

# **Diffusivity and Ionic Conductivity in Lithium Niobate and Related Glasses and Glass Composites**

Von der Naturwissenschaftlichen Fakultät

der Universität Hannover

zur Erlangung des Grades eines

Doktors der Naturwissenschaften

Dr. rer. nat.

genehmigte Dissertation

von

**M. Sc. Muayad Masoud**

geboren am 24. September 1973 in Burqa-Nablus, Palästina

Institut für Physikalische Chemie und Elektrochemie  
Hannover, 2005

Referent: Prof. Dr. Paul Heitjans  
Institut für Physikalische Chemie und Elektrochemie, Universität Hannover  
Korreferent: Prof. Dr. Josef-Christian Buhl  
Institut für Mineralogie, Universität Hannover

Tag der Promotion (Disputation): 19. Dezember 2005

Referenten der Disputation: Prof. Dr. Paul Heitjans (Physikalische Chemie), Prof. Dr. Josef-Christian Buhl (Mineralogie), Prof. Dr. Peter Behrens (Anorganische Chemie)

### **Erklärung an Eides statt**

Hiermit erkläre ich, dass ich die vorliegende Arbeit selbständig verfasst und nur unter Verwendung der angegebenen Quellen und Hilfsmittel angefertigt habe. Die Dissertation ist nicht schon als Diplomarbeit oder ähnliche Prüfungsarbeit verwendet worden.

Hannover, den 27. Oktober 2005

Muayad Masoud



## Abstract

NMR and impedance spectroscopy were employed to investigate the Li-ion diffusivity in four different forms of  $\text{LiNbO}_3$ , namely nanocrystalline, microcrystalline, single crystalline, and amorphous  $\text{LiNbO}_3$ . Likewise a composite of nanocrystalline  $\text{LiNbO}_3$  and sodium silicate glass as well as alkali niobium silicate glasses and glass ceramics were studied.

Amorphous  $\text{LiNbO}_3$  samples were prepared by a double alkoxide (sol-gel) route with both full and partial hydrolysis. Nanocrystalline samples were prepared by high-energy ball milling of coarser grained microcrystalline  $\text{LiNbO}_3$ , and time and temperature controlled calcination of the amorphous precursor.

The ionic conductivity at, e.g., 450 K increases by about seven orders of magnitude when going from the single crystal to the amorphous  $\text{LiNbO}_3$  passing through the microcrystalline and nanocrystalline materials. This is accompanied by a decrease in the activation energy from 1.2 down to 0.6 eV. The activation energies obtained from the diffusion induced  $^7\text{Li}$  NMR spin-lattice relaxation rates show trends similar to those of the conductivity. The  $^7\text{Li}$  NMR lines of the nanocrystalline samples show heterogeneous structures composed of a wide and a narrow contribution due to the Li ions in the grains and the grain-boundary regions, respectively. The nanocrystalline samples having comparable grain sizes (around 25 nm) show different behavior depending on their preparation routes. The ball-milled samples resemble the amorphous one with respect to the conductivity and its activation energy. The relative area of the narrow contribution under the  $^7\text{Li}$  NMR lines here amounts to about 32 %. Thus, in this case the grain-boundary regions have a large volume fraction and are possibly of amorphous nature. The latter finding is supported by EXAFS results of a ball-milled nanocrystalline  $\text{LiNbO}_3$  sample. The spectra can be fitted assuming nearly equal contributions from the microcrystalline and the amorphous forms. Moreover, TEM images show amorphous regions enclosing the grains of this sample.

Contrarily, the conductivity and the NMR relaxation results of the sol-gel prepared nanocrystalline sample are similar to those of the microcrystalline one. Furthermore, the relative area of the narrow contribution under the  $^7\text{Li}$  NMR lines is smaller than about 4 %, implying that the grain-boundary regions have a smaller volume fraction in this nanocrystalline form. The partially hydrolyzed sol-gel prepared amorphous sample showed also some differences from the fully hydrolyzed one. It showed two overlapping semicircles in the complex plane of impedance, and a reduced linewidth in the rigid-lattice range. These differences were attributed to a kind of heterogeneity in the structure.

Furthermore,  $^{18}\text{O}$  diffusion was investigated in single crystalline  $\text{LiNbO}_3$ , and showed the presence of oxygen vacancies. However, oxygen cannot be regarded as the main diffusing species.

Upon heating the  $\text{LiNbO}_3$  nanoparticles embedded in  $\text{Na}_2\text{Si}_3\text{O}_7$  glass powder,  $\text{LiNbO}_3$  was found to be transformed into  $\text{NaNbO}_3$ . The effects of varying the temperature and the composition were investigated. This transformation was found to start at a relatively low temperature (673 K). Beside this exchange, extra phases showed up such as  $(\text{Li},\text{Na})_2\text{Si}_2\text{O}_5$ , crystalline silica (quartz low and cristobalite low) and probably  $\text{Li}_2\text{SiO}_3$ . The composition was varied in  $(x)\text{n-LiNbO}_3 \cdot (1-x)\text{g-NaSi}_{1.5}\text{O}_{3.5}$  with  $0 \leq x \leq 1$  at 1173 K. The  $\text{LiNbO}_3$ -to- $\text{NaNbO}_3$  conversion proceeded toward completion as long as the Li molar fraction was less than that of Na in the glass (i.e. for  $x \leq 0.5$ ). Several mechanisms were proposed and discussed.

Glasses with the composition  $0.33[x \text{Li}_2\text{O} \cdot (1-x)\text{Na}_2\text{O}] \cdot 0.33\text{Nb}_2\text{O}_5 \cdot 0.33\text{SiO}_2$  ( $0 \leq x \leq 1$ ) were prepared by conventional quenching method. According to  $^{29}\text{Si}$  NMR results, in the pure lithium glass the silica network is more polymerized than in the pure sodium or the mixed glass. This implies that  $\text{Li}^+$  ions prefer to be located nearby the  $[\text{NbO}_6]^-$  octahedra. The effect of varying  $\text{Li}_2\text{O}$  and  $\text{Nb}_2\text{O}_5$  contents were investigated in the glass series  $x\text{Li}_2\text{O} \cdot (1-x)/3[\text{Nb}_2\text{O}_5 \cdot 2\text{SiO}_2]$  with  $0.35 \leq x \leq 0.45$ , and  $(1-y)/2[\text{Li}_2\text{O} \cdot \text{SiO}_2] \cdot y\text{Nb}_2\text{O}_5$  with  $0.1 \leq y \leq 0.33$ . The results exclude the possibility that  $\text{Nb}^{5+}$  can act as a glass modifier. The dc-conductivities probed by impedance spectroscopy exhibit a minimum at  $x = 0.37$  whereas the corresponding activation energies ( $0.61 \text{ eV} \leq E_a^{\sigma_{\text{dc}}} \leq 0.91 \text{ eV}$ ) show a maximum at this composition (mixed alkali effect). With multi pulse NMR techniques, the Li and Na diffusion can be studied separately; e.g., solid-echo  $^7\text{Li}$  NMR line narrowing showed an enhancement of Li diffusivity with both increasing temperature and Li content  $x$ . Consistently, lithium jump rates  $\tau_{\text{echo}}^{-1}$ , directly probed by recording two-time correlation functions via spin-alignment echoes, decrease exponentially with the introduction of  $\text{Na}^+$  ions. The corresponding activation energies  $E_a^{\text{echo}}$  reveal an exponential increase with increasing Na content.

Keywords: Li diffusion, solid state NMR, impedance spectroscopy, lithium niobate, glasses, glass composites, mixed alkali effect.



## Kurzfassung

Die Li-Diffusion in mikro- und nanokristallinem sowie einkristallinem und amorphem  $\text{LiNbO}_3$  wurde NMR- und impedanzspektroskopisch untersucht. Desgleichen wurden die Struktur und Dynamik eines Kompositsystems aus nanokristallinem  $\text{LiNbO}_3$  und einem Natriumsilikatglas sowie Alkali-Niobsilikatgläser unterschiedlicher Zusammensetzungen und weitere Glaskeramiken studiert.

Amorphes  $\text{LiNbO}_3$  wurde mit Hilfe eines Sol-Gel-Verfahrens über den Weg der vollständigen Hydrolyse hergestellt. Nanokristalline Proben wurden einerseits durch Hochenergie-Kugelmahlen des grobkörnigen mikrokristallinen  $\text{LiNbO}_3$ , als auch durch zeit- und temperaturkontrollierte Kalzination des amorphen  $\text{LiNbO}_3$ -Precursors erhalten. Die Ionenleitfähigkeit bei, z. B. 450 K, steigt um etwa sieben Größenordnungen wenn die verschiedenen Formen von  $\text{LiNbO}_3$  in der Reihenfolge einkristallines  $\text{LiNbO}_3$ , mikrokristallines, nanokristallines und amorphes  $\text{LiNbO}_3$  miteinander verglichen werden. Gleichzeitig sinkt die Aktivierungsenergie der Li-Diffusion von 1.2 eV auf 0.6 eV ab. Aktivierungsenergien, die aus  $^7\text{Li}$  NMR Spin-Gitter-Relaxationsmessungen erhalten wurden, folgen dem gleichen Trend. Die  $^7\text{Li}$ -NMR-Resonanzlinien von nanokristallinem  $\text{LiNbO}_3$  setzen sich aus einer breiten und einer schmalen Resonanzlinie zusammen und deuten somit auf eine heterogene Struktur des Materials hin. Die beiden Linienanteile können den Li-Ionen in den kristallinen Körnern bzw. den Grenzflächenregionen zugeordnet werden. Die Eigenschaften von nanokristallinem  $\text{LiNbO}_3$  mit vergleichbarer Partikelgröße zeigen eine Abhängigkeit von der gewählten Präparationsroute. Ionenleitfähigkeit und Aktivierungsenergien von durch Kugelmahlen hergestelltem nanokristallinem  $\text{LiNbO}_3$  ähneln denen von amorphem Lithiumniobat. Der relative Flächenanteil der schmalen NMR-Resonanzlinie beträgt etwa 32 %, d. h. die Grenzflächenregionen zeigen einen hohen Volumenanteil und haben möglicherweise amorphe Struktur. Auf eine amorphe Struktur der Grenzflächenregionen weisen auch EXAFS-Untersuchungen an einer nanokristallinen  $\text{LiNbO}_3$ -Probe hin, die durch Kugelmahlen hergestellt wurde. EXAFS-Spektren von dieser Probe können gut angepasst werden, wenn angenommen wird, dass sich das Material zu gleichen Teilen aus einer kristallinen und einer amorphen Struktur zusammensetzt. Die mit dem Sol-Gel-Verfahren präparierte nanokristalline  $\text{LiNbO}_3$ -Probe zeigt hinsichtlich ihres Li-Diffusionsverhaltens deutliche Verwandtschaft mit dem mikrokristallinen Material. Der Flächenanteil der schmalen NMR-Resonanzlinie von nur 4 % zeigt, dass der Volumenanteil an Grenzflächen in diesem Fall deutlich geringer ist.

Zusätzlich zur Li-Diffusion konnte die  $^{18}\text{O}$ -Diffusion mit der Sekundärionen-Massenspektroskopie in  $\text{LiNbO}_3$ -Einkristallen untersucht werden. Die Studien deuten auf Sauerstofflückenstellen im Material hin und zeigen erwartungsgemäß, dass Sauerstoff um Größenordnungen langsamer diffundiert als z. B. Li.

NMR- und XRD-Untersuchungen zeigen, dass in glasigem  $\text{Na}_2\text{Si}_3\text{O}_7$  eingeschlossenes nanokristallines  $\text{LiNbO}_3$  sich bei Temperaturerhöhung kontinuierlich in das Natrium-Analogon  $\text{NaNbO}_3$  umwandelt. Dabei wurde der Einfluss von Temperatur und Zusammensetzung auf diesen Prozess untersucht. Die Transformation beginnt bei einer relativ geringen Temperatur von 673 K und wird begleitet mit der Bildung neuer Phasen wie z. B.  $(\text{Li,Na})_2\text{Si}_2\text{O}_5$ , kristallinem Siliciumdioxid und wahrscheinlich  $\text{Li}_2\text{SiO}_3$ .

Die Zusammensetzung des Kompositsystems  $(x)\text{n-LiNbO}_3 \cdot (1-x)\text{g-NaSi}_{1.5}\text{O}_{3.5}$  wurde im Bereich von  $0 \leq x \leq 1$  variiert. Die Abhängigkeit des Kationenaustauschs von der Zusammensetzung konnte bei 1173 K eingehend studiert werden. Verschiedene Mechanismen der  $\text{LiNbO}_3$  zu  $\text{NaNbO}_3$  Transformation werden in diesem Zusammenhang diskutiert.

Ferner ist die Struktur und Li-Dynamik verschiedener Mischalkaligläser der Zusammensetzung  $0.33[x\text{Li}_2\text{O} \cdot (1-x)\text{Na}_2\text{O}] \cdot 0.33\text{Nb}_2\text{O}_5 \cdot 0.33\text{SiO}_2$  ( $0 \leq x \leq 1$ ) mit einer Reihe spektroskopischer Methoden detailliert studiert worden.  $^{29}\text{Si}$ -NMR-Ergebnisse zeigen z. B., dass im reinen Li-Glass das  $\text{SiO}_2$ -Netzwerk einen höheren Polymerisationsgrad aufweist, als im reinen Na-Glass. Die Li-Ionen befinden sich bevorzugt in der Nähe von  $[\text{NbO}_6]$ -Oktaedern. Der Einfluss des  $\text{Li}_2\text{O}$ - und  $\text{Nb}_2\text{O}_5$ -Gehaltes auf die Materialeigenschaften der Gläser wurde exemplarisch anhand einer Serie von Gläsern mit der Zusammensetzung  $x\text{Li}_2\text{O} \cdot (1-x)/3[\text{Nb}_2\text{O}_5 \cdot 2\text{SiO}_2]$  und  $(1-y)/2[\text{Li}_2\text{O} \cdot \text{SiO}_2] \cdot y\text{Nb}_2\text{O}_5$  mit  $0.35 \leq x \leq 0.45$  und  $0.1 \leq y \leq 0.33$  untersucht. Die Ergebnisse zeigen, dass  $\text{Nb}^{5+}$  offenbar nicht als Netzwerkwandler agiert. Impedanzuntersuchungen zeigen unabhängig von der Temperatur ein Leitfähigkeitsminimum bei  $x = 0.37$ . Bei dieser Zusammensetzung offenbaren die entsprechenden Aktivierungsenergien ( $0.61 \text{ eV} \leq E_a^{\sigma_{dc}} \leq 0.91 \text{ eV}$ ) ein Maximum. Dieser Mischkalieffekt wurde darüber hinaus mit Festkörper-Echo-NMR Experimenten und stimulierten Echo-NMR-Experimenten eingehender untersucht.

Stichworte: Li-Diffusion, Festkörper-NMR, Impedanzspektroskopie, Lithiumniobat, Gläsern, Glas-Komposite, Mischkalieffekt.





## **Dedication**

To those candles who burn themselves to enlighten my road,

to the soul of my father,

to my mother, my teachers,

my brothers, my sisters,

my friends, my students,

and

to those who are looking forward to enrich their knowledge.

Muayad Masoud



## Acknowledgements

This thesis was carried out at the Institute of Physical Chemistry and Electrochemistry, University of Hannover. Here I would like to express my gratitude to all those who gave me the possibility to complete this thesis.

I would like to express my sincere appreciation to my supervisor **Prof. Dr. P. Heitjans** for giving me the chance to do my PhD in his group and introducing me to the fascinating field of diffusion in solid state. His guidance, help and encouragement throughout the course research work are highly appreciated. He has been helpful, earnest as well as supportive in the implementation of novel suggestions that have made this study a full fledged thesis. My sincere gratitude is due to him for his tireless effort discussing this thesis and his support in the various stages of its realization.

My sincere gratefulness is due to **Dr. R. Winter** (University of Wales, Aberystwyth, UK). He had earnestly taken care of my well being while I had a chance to work with him on solid state MAS NMR in Aberystwyth during my stay abroad, also for giving me the great chance to visit the CLRC Daresbury Laboratory (UK). He was exceptionally enthusiastic in providing new ideas in glass science. I also highly appreciate his reading and commenting for my thesis.

I thank all my colleagues in the group for providing support and a cordial atmosphere. I am especially thankful to **Dr. M. Wilkening** for his valuable help in all the scientific and practical aspect of NMR and experimental work. I am mainly thankful to him for our fruitful collaboration in measuring the spin-alignment echoes on the mixed alkali niobiosilicate glasses and for continued assistance. I also highly appreciate his reading and commenting for my thesis. Earlier help of **Dr. S. Indris** and **Dr. R. Kappes** are appreciated.

I am heavily indebted to **PD. Dr. C. Rüscher** (Institut für Mineralogie Universität Hannover) for giving me the chance to do all my impedance, infrared, DSC/TG and UV-Vis measurements in the labs of the mineralogy institute under his direct administration. His sincere support, valuable help and beneficial discussions have been invaluable to many experiments throughout my research. I am thankful to him for his efforts.

Special thanks are extended to **PD. Dr. T. Gesing** (Institut für Mineralogie Universität Hannover) for allowing me to measure all my XRD patterns on the diffractometers of the mineralogy institute. I am also appreciative to his invaluable help in refining my XRD patterns using the Rietveld method.

I am indebted to **Prof. Dr. J.-C. Buhl** for his help and for allowing me to use the XRD as well as other facilities in the mineralogy institute. His tireless effort in the reading and the discussion of my thesis is highly appreciated.

From the University of Wales-Aberystwyth, I am grateful to **Prof. N. Greaves** for his corporation during my stay there and for the constructive discussion concerning the EXAFS data. From the CLRC Daresbury Laboratory (UK) I am extremely thankful to **Dr. J. Charnock** for introducing me to the software for analyzing the EXAFS in solid state materials. From the Materials Science Laboratory MSL (Daresbury-UK), I wish to thank **Mr. R. Jones** for giving the chance to use the rotating anode to measure the *in-situ* XRD.



My grateful appreciations are due to **Dr. P. Fielitz** and **Prof. G. Borchardt** (Institut für Metallurgie, Technische Universität Clausthal) and to **Dr. R. De Souza** and **Prof. M. Martin** (Institut für Physikalische Chemie I, RWTH Aachen) for their kind support in measuring  $^{18}\text{O}$  diffusion in single crystalline  $\text{LiNbO}_3$  and for their data analysis and constructive discussion.

I greatly remember the help of **Prof. Dr. C. Vogt** and her coworkers (Institut für Anorganische Chemie Universität Hannover) in doing the trace chemical analysis for my  $\text{LiNbO}_3$  sample by ICP-AES

Great thanks are due to **Prof. Dr. Y. Yue** (Section of Chemistry-Aalborg University-Denmark) for his trial to prepare amorphous  $\text{LiNbO}_3$  by the method of cascade crank for hyperquenching.

I wish to acknowledge the great technical assistance of each of the following people:

- **PD. Dr. H. Behrens** (Institut für Mineralogie Universität Hannover) for his constructive help in fixing the impedance cell and giving me the chance to use their impedance analyzer for my measurements.
- **Dr. M. Klüppel**, **Dr. J.-G. Meier** and **Dr. B. Huneke** (Deutsches Institut für Kautschuktechnologie) for the conductivity measurement on the  $\text{LiNbO}_3$  single crystal.
- **Dr. S. Freimann** (Institut für Mineralogie Universität Hannover) for measuring the Guinier XRD pattern of the single crystalline  $\text{LiNbO}_3$ .
- **PD. Dr. S. Dultz** (Institut für Bodenkunde Universität Hannover) for an early DTA/TG measurement on the amorphous  $\text{LiNbO}_3$  sample.

I am respectfully indebted to the ministry of Science and Culture, Land Niedersachsen, Germany for providing the "**Georg-Christoph-Lichtenberg- Stipendium**" (Feb. 2002-Jan. 2005). I should mention the wonderful organization of the Graduate Program "New Materials with Tailored Properties" organized by the "Center for Solid State Chemistry and New Materials, Hannover". It was of invaluable benefit for me. Here I would like to thank all the participating professors in developing such a great program mainly: **Prof. Dr. P. Behrens**, **Prof. Dr. P. Heitjans**, **Prof. Dr. J. C. Buhl**, and **PD. Dr. T. Bredow**.

From my institute, the Institut für Physikalische Chemie und Elektrochemie, Universität Hannover:

- I am deeply thankful to **Dr. A. Feldhoff** for measuring the SEM and TEM images of the nanocrystalline  $\text{LiNbO}_3$  samples
- Thanks are extended to **Dr. J. Woenckhaus** and **Prof. Dr. J. Becker** for giving me the opportunity to use their Raman spectrometer.
- The continuous help of the group secretary **Mrs. Y. Gabbey** has been invaluable.
- Great thanks are extended to the technical staff in the mechanical and electrical workshops in the institute. The help of **Mrs. K. Majoni** and **Mrs. K. Janze** in cutting  $\text{LiNbO}_3$  single crystals is highly appreciated.

Last, but in no way least, special thanks fly back to Palestine to my former supervisor **Prof. Dr. H. S. Hilal** who introduced me to the world of research. The patience and encouragement given to me by my family and friends are truly appreciated.

Muayad M. M. Masoud  
Hannover-Germany  
October, 2005



# Table of Contents

<b>1</b>	<b>Introduction.....</b>	<b>1</b>
1.1	MOTIVATION .....	1
1.2	HISTORICAL BACKGROUND .....	2
1.3	THESIS OVERVIEW .....	4
<b>2</b>	<b>Materials .....</b>	<b>7</b>
2.1	CRYSTALLINE AND NON-CRYSTALLINE MATERIALS .....	7
2.1.1	Single Crystal and Microcrystalline Materials .....	7
2.1.2	Nanocrystalline Materials .....	7
2.1.3	Glass and Amorphous Materials .....	9
2.1.3.1	The random network model .....	10
2.1.3.2	Modified random network.....	11
2.1.3.3	Preparation of amorphous materials.....	11
2.1.4	Glass Composites .....	12
2.2	DIELECTRIC AND FERROELECTRIC MATERIALS .....	13
2.3	PHYSICAL AND CHEMICAL PROPERTIES OF MATERIALS .....	14
2.3.1	Lithium Niobate .....	14
2.3.2	Sodium Niobate .....	19
2.3.3	Sodium Silicate Glasses .....	20
2.3.4	Alkali-Niobium Silicate-Glasses and Glass-Ceramics .....	20
<b>3</b>	<b>Fundamentals of diffusion in solids.....</b>	<b>23</b>
3.1	FLUX OF PARTICLES (FICK'S LAWS).....	23
3.1.1	Uniform Concentration Gradients (Fick's 1 <sup>st</sup> law).....	23
3.1.2	Non-Uniform Concentration Gradients .....	24
3.2	MECHANISMS OF DIFFUSION AND DIFFUSION COEFFICIENTS....	25
3.3	IONIC CONDUCTORS .....	27
3.4	STRUCTURE SENSITIVE DIFFUSION .....	27
3.5	TECHNIQUES FOR STUDING DIFFUSION <sup>7</sup> .....	28
3.6	THE MIXED-ALKALI EFFECT .....	29
<b>4</b>	<b>Principles of Probing Techniques.....</b>	<b>33</b>
4.1	DIELECTRIC RELAXATION AND IMPEDANCE SPECTROSCOPY ...	33
4.1.1	Method and Expressions for Presentation of Dielectric Data.....	33
4.1.2	Basics of Impedance Spectroscopy <sup>-</sup> .....	35
4.1.2.1	Series and parallel circuits .....	36
4.1.2.2	Series RC circuits.....	36
4.1.2.3	Resistors and capacitors in parallel.....	38
4.1.2.4	The constant phase element .....	40

4.1.3	Dielectric Behavior of Ceramic Materials .....	42
4.1.4	Measurement Methods (A Summary of Capacitance Bridge Functioning).....	44
4.1.4.1	Manual bridges .....	44
4.1.4.2	Automatic bridges .....	46
4.1.4.3	Inductance .....	47
4.1.5	Main Types of Dielectric Functions .....	48
4.1.5.1	Debye relaxation .....	48
4.1.5.2	General dipolar responses .....	49
4.1.5.3	Universal relaxation .....	50
4.1.5.4	Hopping carrier systems .....	50
4.1.5.5	Ionic conduction.....	51
4.1.5.6	Low-frequency dispersion.....	51
4.1.5.7	Low-loss materials - 'flat' losses.....	52
<b>4.2</b>	<b>NUCLEAR MAGNETIC RESONANCE.....</b>	<b>53</b>
4.2.1	Introduction.....	53
4.2.2	Basics of Experimental Setup .....	54
4.2.3	Fundamental Concepts.....	54
4.2.3.1	Zeeman splitting and spin states.....	54
4.2.3.2	Energy population and magnetization .....	56
4.2.3.3	Getting a signal.....	56
4.2.4	Basic Quantum Mechanical Description (Interactions That Modifies $\nu_0$ ) .....	58
4.2.4.1	Chemical shift interaction .....	58
4.2.4.2	Dipolar interaction.....	58
4.2.4.3	Quadrupolar interaction.....	59
4.2.5	Magic Angle Spinning.....	59
4.2.6	Static and MAS NMR Lineshapes.....	60
4.2.7	NMR Spin Relaxations and Diffusion Effect .....	61
4.2.7.1	Spin-lattice relaxation (longitudinal relaxation) <sup>8</sup> .....	61
4.2.7.2	Spin-lattice relaxation in the rotating frame .....	65
4.2.7.3	Spin-spin relaxation.....	66
4.2.7.4	Motional narrowing of NMR lines .....	66
4.2.7.5	Spin-alignment echo NMR <sup>-</sup> .....	67
4.2.8	NMR Applications in Nanomaterials and Glasses.....	68
<b>4.3</b>	<b>EXTENDED X-RAY ABSORPTION FINE STRUCTURE.....</b>	<b>70</b>
4.3.1	Introduction.....	70
4.3.2	Simple Theoretical Description (EXAFS Equation).....	70
4.3.3	Some Experimental Considerations.....	75
4.3.4	X-ray absorption transmission and fluorescence .....	75
4.3.5	EXAFS-Data Analysis.....	76
<b>4.4</b>	<b>SECONDARY-ION MASS SPECTROSCOPY .....</b>	<b>80</b>
4.4.1	Definition and Types .....	80
4.4.2	Secondary Ion Production.....	81
4.4.3	Quantification .....	82
4.4.3.1	Relative sensitivity factors .....	82
4.4.3.2	Depth profiles.....	83
4.4.3.3	Standards (ion implants).....	83
4.4.3.4	Mass interference .....	84
4.4.4	Analytical Conditions .....	84
4.4.4.1	Sample charging.....	84
4.4.4.2	Ion imaging .....	85
4.4.5	SIMS Instrumentation.....	85
4.4.5.1	Primary ion source .....	85
4.4.5.2	Secondary ion extraction and transfer .....	86
4.4.5.3	Ion energy analyzers.....	86



4.4.5.4	Mass analyzers.....	87
4.4.5.5	Secondary-ion detectors.....	88
4.4.5.6	Faraday cups.....	88
4.4.5.7	Ion image detectors.....	88
4.4.5.8	Related instruments.....	89
4.4.6	Applications.....	89
<b>5</b>	<b>Samples Preparation and Characterization .....</b>	<b>91</b>
<b>5.1</b>	<b>LITHIUM NIOBATE.....</b>	<b>91</b>
5.1.1	Single Crystal and Microcrystalline LiNbO <sub>3</sub> .....	91
5.1.2	Amorphous and Nanocrystalline LiNbO <sub>3</sub> .....	93
5.1.2.1	Sol-gel preparation.....	93
5.1.2.2	High-energy ball milling.....	94
5.1.2.3	XRD and particle size determination.....	94
5.1.3	Differential Scanning Calorimetry and Thermogravimetry.....	97
5.1.4	Raman Spectroscopy.....	100
<b>5.2</b>	<b>NANOCRYSTALLINE LiNbO<sub>3</sub> EMBEDDED IN SODIUM SILICATE GLASS .....</b>	<b>101</b>
5.2.1	Sodium Metasilicate Glass Preparation.....	101
5.2.2	n-LiNbO <sub>3</sub> Embedding (Varying Temperature and Composition).....	102
<b>5.3</b>	<b>(LITHIUM,SODIUM) NIOBIUM SILICATE GLASSES &amp; GLASS CERAMICS.....</b>	<b>102</b>
5.3.1	Glass Preparation.....	102
5.3.2	Glass-Ceramic Formation.....	103
<b>6</b>	<b>Experimental Techniques and Setups.....</b>	<b>105</b>
<b>6.1</b>	<b>IMPEDANCE SPECTROSCOPY.....</b>	<b>105</b>
6.1.1	Impedance Analyzer.....	105
6.1.2	Impedance Cell.....	105
6.1.3	Sample Pressing and Electrode Sputtering.....	106
6.1.4	Temperature and Atmosphere Controlling.....	107
6.1.5	Data Analysis and Fitting Procedures.....	107
<b>6.2</b>	<b>NUCLEAR MAGNETIC RESONANCE.....</b>	<b>108</b>
6.2.1	Apparatuses (Magnets, Spectrometers, Amplifiers).....	108
6.2.2	NMR Samples and Probes (Static and MAS).....	109
6.2.3	NMR Experiment.....	110
6.2.3.1	Structure characterization ( <sup>7</sup> Li, <sup>23</sup> Na, <sup>29</sup> Si, <sup>93</sup> Nb).....	110
6.2.3.2	Spin-lattice relaxation ( <sup>7</sup> Li, <sup>23</sup> Na).....	111
6.2.3.3	Motional narrowing.....	111
6.2.3.4	Spin-alignment echoes.....	111
6.2.4	Data Analysis and Fitting.....	112
<b>6.3</b>	<b>X-RAY ABSORPTION FINE STRUCTURE.....</b>	<b>113</b>
6.3.1	Apparatus Description.....	113
6.3.2	Sample Preparation.....	114
6.3.3	Measurement Conditions.....	114
6.3.4	Fitting Software and Approaches.....	114
<b>6.4</b>	<b>SECONDARY-ION MASS SPECTROSCOPY.....</b>	<b>116</b>

6.4.1	Sample Preparation and $^{18}\text{O}$ Equilibration .....	116
6.4.2	SIMS Apparatus.....	117
6.4.3	Data Analysis and Fitting .....	117
<b>6.5</b>	<b>OTHER TECHNIQUES.....</b>	<b>118</b>
6.5.1	XRD and Structure Refinement.....	118
6.5.2	Transmission and Scanning Electron Microscopy .....	119
6.5.3	Infrared and Raman Spectroscopy.....	120
6.5.4	Thermogravimetric Analysis and Differential Scanning Calorimetry.....	121
<b>7</b>	<b>LiNbO<sub>3</sub> (single crystalline, microcrystalline, nanocrystalline, amorphous).....</b>	<b>123</b>
<b>7.1</b>	<b>STRUCTURAL ASPECTS .....</b>	<b>123</b>
7.1.1	NMR Line-Shapes .....	124
7.1.1.1	$^7\text{Li}$ NMR line-shapes.....	124
7.1.1.2	Discussion of $^7\text{Li}$ NMR lineshapes.....	127
7.1.1.3	$^{93}\text{Nb}$ NMR lineshapes.....	129
7.1.1.4	Discussion of the $^{93}\text{Nb}$ NMR lineshapes .....	131
7.1.2	Extended X-ray Absorption Fine Structure .....	133
7.1.2.1	Temperature dependence of EXAFS of microcrystalline LiNbO <sub>3</sub> .....	133
7.1.2.2	EXAFS of amorphous LiNbO <sub>3</sub> .....	136
7.1.2.3	EXAFS of nanocrystalline LiNbO <sub>3</sub> .....	137
7.1.2.4	(EXAFS) discussions .....	139
7.1.3	X-Ray Diffraction and Transmission Electron Microscopy .....	140
7.1.4	General Discussion of the Structural Aspects.....	141
<b>7.2</b>	<b>DYNAMICS AND DIFFUSION .....</b>	<b>143</b>
7.2.1	Impedance Spectroscopy .....	143
7.2.1.1	Conductivity and master curves .....	143
7.2.1.2	Complex impedance and equivalent circuits .....	145
7.2.1.3	Modulus spectra .....	147
7.2.1.4	Dielectric permittivity .....	149
7.2.1.5	Effect of paramagnetic-impurities .....	151
7.2.1.6	Atmosphere effect .....	152
7.2.1.7	Effect of the preparation route.....	153
7.2.1.8	Discussion .....	156
7.2.2	Nuclear Magnetic Resonance .....	159
7.2.2.1	Grain-size effect on the SLR rate .....	159
7.2.2.2	Effect of impurities on SLR rate .....	160
7.2.2.3	Preparation-route effect studied by SLR .....	161
7.2.2.4	Discussion of SLR rates .....	161
7.2.2.5	Effect of grain size on the motional narrowing (MN) of the $^7\text{Li}$ central line .....	164
7.2.2.6	Effect of the preparation route on the m of the $^7\text{Li}$ central line .....	165
7.2.2.7	Discussion of the motional narrowing.....	167
7.2.3	Secondary-Ion Mass Spectroscopy.....	169
7.2.3.1	Oxygen diffusion studies by SIMS.....	169
7.2.3.2	Discussion of oxygen diffusion in LiNbO <sub>3</sub> .....	171
7.2.4	General Discussion of Diffusion Aspects.....	173
<b>8</b>	<b>Nanocrystalline LiNbO<sub>3</sub> Particles Embedded in Sodium Silicate Glasses Na<sub>2</sub>Si<sub>3</sub>O<sub>7</sub>.....</b>	<b>177</b>
<b>8.1</b>	<b>HEATING EFFECT .....</b>	<b>178</b>

8.1.1	X-ray Diffraction Ex-situ and In-situ .....	178
8.1.2	Raman Spectroscopy .....	181
8.1.3	<sup>29</sup> Si, <sup>93</sup> Nb, <sup>23</sup> Na Nuclear Magnetic Resonance.....	182
8.1.4	Impedance Spectroscopy .....	186
<b>8.2</b>	<b>COMPOSITION EFFECT .....</b>	<b>188</b>
8.2.1	X-Ray Diffraction.....	188
8.2.2	Raman Spectroscopy .....	189
8.2.3	<sup>29</sup> Si, <sup>93</sup> Nb, <sup>23</sup> Na MAS-NMR .....	190
8.2.4	Impedance Spectroscopy .....	192
<b>8.3</b>	<b>DISCUSSION.....</b>	<b>193</b>
<b>9</b>	<b>(Lithium, Sodium) Niobosilicate Glasses and Glass Ceramics</b>	<b>199</b>
<b>9.1</b>	<b>GLASS STRUCTURE.....</b>	<b>199</b>
9.1.1	Effect of Changing the Alkali Ion (Li to Na) .....	199
9.1.1.1	X-ray diffraction .....	199
9.1.1.2	Infrared and Raman spectroscopy .....	200
9.1.1.3	<sup>7</sup> Li, <sup>93</sup> Nb, <sup>23</sup> Na, <sup>29</sup> Si nuclear magnetic resonance .....	202
9.1.1.4	Discussion of the modifier-type effect.....	204
9.1.2	Effect of Changing Li <sub>2</sub> O and Nb <sub>2</sub> O <sub>5</sub> .....	205
9.1.2.1	Raman spectroscopy .....	205
9.1.2.2	<sup>29</sup> Si NMR .....	206
9.1.2.3	Discussion of the Li <sub>2</sub> O and Nb <sub>2</sub> O <sub>5</sub> effect .....	208
9.1.3	Glass-ceramic Formation (XRD and DSC).....	210
9.1.4	General Discussion.....	213
<b>9.2</b>	<b>DYNAMICS AND DIFFUSION: MIXED-ALKALI EFFECT .....</b>	<b>217</b>
9.2.1	Impedance Spectroscopy of (Li,Na) Niobosilicate Glasses .....	217
9.2.2	<sup>7</sup> Li and <sup>23</sup> Na NMR Spin-Lattice Relaxation Rate.....	219
9.2.3	NMR Solid-Echoes (Motional Narrowing of <sup>7</sup> Li and <sup>23</sup> Na Central Transitions) .....	221
9.2.4	The Dependence of the Central Linewidth on the Lithium Content .....	223
9.2.5	<sup>7</sup> Li Spin-Alignment Stimulated Echoes .....	225
9.2.6	Discussion .....	228
	<b>References .....</b>	
	<b>List of Figures .....</b>	
	<b>List of Tables .....</b>	
	<b>Curriculum Vitae.....</b>	
	<b>Appendixes .....</b>	



# 1 Introduction

## 1.1 MOTIVATION

In recent years, the study the diffusivity and ionic conductivity in solid state materials has been of great importance. This type of research becomes of special interest when the material under testing has potential applications, e.g., as a solid electrolyte in primary or secondary batteries. It was found that the ionic diffusivity can in some cases be increased by going over from the single crystalline and microcrystalline forms to the corresponding nanocrystalline<sup>1</sup> or amorphous<sup>2</sup> forms. This enhancement of atomic transport is attributed to the increased volume fraction of the interfacial regions in the case of nanocrystalline materials. On the other hand the increase of the free volume may be the reason behind the enhanced diffusivity in the amorphous form. Fig. 1.1.1 shows a simplified visualization of the structure of the different forms of solid materials. The grains of the nanocrystalline form are described as highly ordered or crystalline, whereas

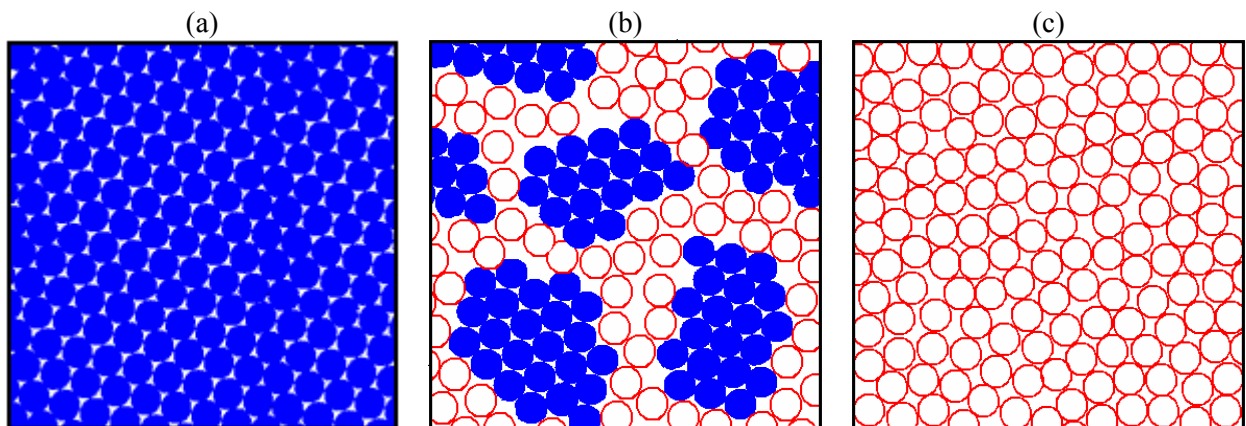


Fig. 1.1.1: Illustration diagram for the reduction of the order degree in solids. (a) Microcrystalline materials show highly ordered single pattern. (b) In the nanocrystalline solid high ordered crystalline grains are enclosed within grain boundaries of low order. (c) Glassy or amorphous materials show an unordered structure.

the grain boundary regions are postulated to have amorphous-like nature. Alternatively, the diffusivity can be enhanced by admixture of an ionic insulator.<sup>3</sup> Following this hypothesis, it was recently possible to show by nuclear magnetic resonance (NMR) that in  $\text{LiNbO}_3$  the mean jump rate of the Li ions increases by several orders of magnitude when going from the microcrystalline to the nanocrystalline and amorphous materials.<sup>4–6</sup> However, the effect of these structural changes on the ionic conductivity has not been fully investigated. In addition, the disordered materials (amorphous or nanocrystalline) can be prepared by several methods. Consequently, many questions remain of interest to the researcher: Is there any correlation between structural disorder and the appearance of fast diffusion of atoms or ions? Can the previous correlation be generalized with respect to disordered materials prepared by different routes? And to which degree is this affected by the structural nature of the grain-boundary regions?

In its most basic form, a composite material is composed of at least two elements working together to produce material properties that are different from the properties of those elements on their own. Glass nanocomposites have one of these components as a glassy phase whereas the second consists of crystalline particles, mostly in the nano-scale. To fully attribute the role and application of composite materials to their structure, an understanding is required of the composing materials themselves and of the conditions under which they can be processed. The effect of temperature and composition on the cation exchange between the crystalline phase and the glassy matrix is important in determining the degree of the disorder and its consequent effect on the novel properties of the composite.

A further type of disorder can be introduced to an already disordered glassy system by having more than one type of ions, in general, and cations, in particular. The resultant deviation from linearity in the total ionic diffusivity or ionic conductivity is well known as the “mixed alkali effect” (MAE). There is wide agreement on that the latter effect is due to the reduced diffusivity of one alkali ion as the second ion is introduced. However, the reason behind that is not known yet. Hence, it is an exciting experience to measure such a deviation by impedance spectroscopy. Moreover, it is of great advantage to use a new method that can probe the jump rate of each ion separately such as NMR spin-alignment echo.

## 1.2 HISTORICAL BACKGROUND

Diffusion in disordered systems has been intensively targeted, mainly in nanocrystalline, amorphous, glassy materials, and glass- or nano-composites. In the last two decades, a huge number of publications dealt with the impedance spectroscopy and the NMR of such disordered systems. Here, a brief insight on the work done in our group and the results achieved are exemplified, for more extensive reviews see Refs [7–8].

Nanocrystalline calcium fluoride ( $\text{CaF}_2$ ), hereafter denoted by ‘n-’, was obtained by the inert gas condensation technique with grain size of 9 nm, see Ref. [9]. In this material, the diffusion-induced peak of

the  $^{19}\text{F}$  spin-lattice relaxation (SLR) rate ( $T_1^{-1}$ ) appeared at considerably lower temperatures than in single crystalline  $\text{CaF}_2$ , hereafter denoted by 's-'. The activation energy estimated from the slope of the peak was found to be reduced to 0.4 eV compared to 1.6 eV in s- $\text{CaF}_2$  where the fluoride ion jumps via thermally activated vacancies in the anion sublattice. These results reveal an increased  $\text{F}^-$ -diffusivity due to the influence of the interfacial regions. Furthermore, at 500 K the ratio obtained from a comparison of the corresponding conductivities of n- $\text{CaF}_2$  and s- $\text{CaF}_2$  amounts to about  $10^4$ , see Ref. [10].  $^{19}\text{F}$  NMR<sup>9</sup> showed single Gaussian broad lines whose linewidth (expressed as full width at half maximum, fwhm) remains unchanged with heating up to 440 K. After that, a motionally narrowed line (Lorentzian) started to superimpose on the broad one. The two components are due to the localized  $\text{F}^-$  ions in the grain interiors and the highly mobile ones in the interfacial regions. At 440 K, the mass fraction of the mobile  $\text{F}^-$  in the interfacial regions was about 10 %.

Ball-milled nanocrystalline  $\text{Li}_{0.7}\text{TiS}_2$  was prepared with grain size of 11.8 nm.<sup>11</sup> Above 250 K, the  $^7\text{Li}$  NMR spectra showed a central transition of the spectra that decomposes into a broad and a narrow component. The relative intensity of the narrow line increases with temperature, finally reaching a saturation value of 50%. The temperature dependent intensity of the narrow component was interpreted in terms of an inhomogeneous interface structure with disk-like particle shape<sup>12</sup>. The results are compared to those obtained for some three-dimensional structures, to which the standard spherical model is applicable in most cases. Furthermore, n- $\text{Li}_{0.7}\text{TiS}_2$  was compared with the corresponding amorphous and microcrystalline forms<sup>11</sup>. The activation energy of the low-temperature flank of the diffusion induced peak was about 0.2 eV, which is not considerably smaller than that in the microcrystalline material and larger than that in the amorphous one (about 0.1 eV). This was attributed to the similar diffusion pathways in the micro- and nanocrystalline forms.

The ball milled n- $\text{LiNbO}_3$ , the microcrystalline source material (m- $\text{LiNbO}_3$ ) and the sol-gel prepared amorphous  $\text{LiNbO}_3$  were previously studied in comparative Li-ion dynamic studies<sup>4-6</sup>. Only the low- $T$  sides of the diffusion-induced SLR rate peaks superimposed on background relaxation rates were observable for m- and n- $\text{LiNbO}_3$  in the accessible temperature ranges up to 1400K and 500 K, respectively. The low- $T$  flank is shifted to lower temperatures in n- $\text{LiNbO}_3$  indicating, in an indirect way, a much faster diffusion. The activation energy of n- $\text{LiNbO}_3$  is reduced to about one third of that m- $\text{LiNbO}_3$  (0.75 eV).

The SLR rate,  $T_{1e}^{-1}$ , in the pulsed rotating reference frame was also measured for m- $\text{LiNbO}_3$ . The maxima of the curves and parts of their high-temperature sides were detected here. Accordingly the value of motional correlation time,  $\tau_c$ , at 890 K was estimated to be  $3 \cdot 10^{-6}$  s for m- $\text{LiNbO}_3$ . This corresponds to a diffusion coefficient  $D$  for the uncorrelated jumps of  $8 \cdot 10^{-15}$   $\text{m}^2 \text{s}^{-1}$  [according to Einstein-Smoluchowski equation (see Eq. 3.2.4)]. The activation energy of 0.88 eV obtained from the high-T side applies to long-range diffusion. It is greater than the value 0.75 eV of the low-T side which agrees with that from the measurements of  $T_1^{-1}$  and reflects short-range motion.

The lineshapes were also investigated.<sup>5,6</sup> The central lines of the  $^7\text{Li}$  spectra are motionally narrowed for all three samples. In n-LiNbO<sub>3</sub> it also reveals a superposition of two contributions at relatively low temperature (450 K). Contrarily, the spectra of m-LiNbO<sub>3</sub> do not show any heterogeneous structure at any temperature indicating homogenous sites in the crystalline bulk. The narrowing in the amorphous LiNbO<sub>3</sub>, hereafter denoted by ‘a-’, starts at temperatures similar to those in n-LiNbO<sub>3</sub>, but the lineshape has only one contribution. This is due to the homogeneous disorder.

It was found that the motional narrowing for Li ions in the interfacial regions of the nanocrystalline material starts at a temperature 400 K below that in the microcrystalline form and very similar to that in the amorphous material. The temperature dependence of the linewidth was analyzed to give activation energies of 0.35 eV for a-LiNbO<sub>3</sub>, 0.39 eV for n-LiNbO<sub>3</sub>, and 1.25 eV for m-LiNbO<sub>3</sub>. These values agree well with those obtained by SLR measurements on the same samples. This implies that the diffusion pathways in the interfacial regions of ball-milled nanocrystalline LiNbO<sub>3</sub> are fast and similar to those in the amorphous material.

### 1.3 THESIS OVERVIEW

In the present section, this thesis is introduced to the reader. In the preceding two sections an overview over the basic hypothesis of this thesis and some literature examples were given.

The following three chapters deal with the fundamentals of this thesis. In chapter 2 the classes of the materials treated here are introduced. The main properties of each class are described as well as their preparation methods and applications. Firstly, the materials are classified according to crystallinity and disorder from single crystalline and microcrystalline materials to nanocrystalline, amorphous, or glassy materials, ending with the glass composites. Secondly, ferroelectric and dielectric materials are introduced. And finally, physical and chemical properties of the material used in this research are described. Chapter 3 deals with some fundamentals of diffusion in solids: Fick’s laws, mechanisms of diffusion in solids, grain boundary diffusion, and the techniques used for probing diffusion, in addition to some ideas about the ionic conductors and the mixed alkali effect.

The 4<sup>th</sup> chapter gives a detailed description (fundamental concepts, types, data analysis, and applications) of the main characterization methods (NMR, impedance spectroscopy, EXAFS, and SIMS).

The preparation and the characterization methods for the three systems (different forms of LiNbO<sub>3</sub>, the composite n-LiNbO<sub>3</sub> embedded in g-Na<sub>2</sub>Si<sub>3</sub>O<sub>7</sub>, and the alkali niobium silicate glasses) are given in chapter 5. Chapter 6 describes the experimental setups and conditions of the main characterization methods used in this research in addition to the auxiliary methods like Raman, infrared spectroscopy, thermal analysis, XRD, and TEM.



The results are presented in the last three chapters (7-9). In chapter 7, the light is focused on lithium niobate. The dynamic behavior as well as the structural aspects of different forms of  $\text{LiNbO}_3$  (amorphous, nanocrystalline, microcrystalline and single crystal) are examined. First the structural aspects are targeted by NMR line-shapes, EXAFS study, and XRD. For additional characterization of the nanocrystalline and amorphous samples as well as the microcrystalline reference material x-ray diffraction, thermal analysis and transmission electron microscopy as well as x-ray absorption spectroscopy (EXAFS) are described. Secondly, a comparative study of the diffusion behavior by means of NMR and impedance spectroscopy is described. The effects of the grain size, preparation route and the atmosphere are investigated in the different forms. Furthermore,  $^{18}\text{O}$  diffusion in single crystalline  $\text{LiNbO}_3$  is investigated by SIMS.

Chapter 8 reveals the effect of both temperature and composition on the n- $\text{LiNbO}_3$  particles embedded in  $\text{Na}_2\text{Si}_3\text{O}_7$  glass.

In the 9<sup>th</sup> chapter, the alkali niobium silicate glasses are targeted. Firstly structural aspects are examined under the effects of varying the modifier type ( $\text{Li}^+$ ,  $\text{Na}^+$ ), the amount of the modifier or the amount of niobium oxide. In the second part the ion dynamics of the mixed (lithium, sodium) niobosilicate glass (the mixed alkali effect) is investigated by impedance spectroscopy. This is followed by a NMR examination of the  $^7\text{Li}$  and  $^{23}\text{Na}$  SLR rate and motional narrowing, beside  $^7\text{Li}$  spin alignment echoes measurements.



# 2 Materials

## 2.1 CRYSTALLINE AND NON-CRYSTALLINE MATERIALS

The order in crystalline systems makes the movement of atoms or ions possible only via defects.<sup>13-14</sup> Thus by introducing such defects starting from a single crystal, disorder will result in highly defective single crystals, microcrystalline, nanocrystalline and amorphous systems. The defect ranges according to the increase of the dimensionality order from vacancies or interstitials to dislocations to grain boundaries defects.

### 2.1.1 Single Crystal and Microcrystalline Materials

A crystal is a solid in which the constituent atoms, molecules or ions are packed in a regularly ordered, repeating pattern extending in all three spatial dimensions. Fluid substances form crystals when they undergo a process of solidification. Under ideal conditions, the result may be single crystal, where all of the atoms in the solid fit into the same lattice or crystal structure but generally many crystals form simultaneously during solidification leading to a polycrystalline solid. For example, most metals encountered in everyday life are polycrystals.

### 2.1.2 Nanocrystalline Materials

Nanostructured solids are materials with at least one of their dimensions being less than 100 nm.<sup>7,15</sup> The nano-materials share the following three fundamental features: (i) their constituents (grains, layers, or phases) are spatially confined to less than 100 nm, thus they include atom clusters and filaments that can essentially be considered as zero-, one-, two- dimensionally modulated layers, coatings or buried layers, and three dimensionally modulated nanophase materials; (ii) increased volume fraction of atoms belong to the interfacial environments and the enhancements in the properties of these materials are attributed to them, and (iii) the presence of interactions between atomic domains. Such materials incorporate a variety

of size related effects. These effects range from electronic quantum size effects caused by spatial confinement of de-localised valence electrons, altered cooperative atom phenomena such as lattice vibrations or melting, to the suppression of the lattice-defect mechanisms such as dislocation generation and migration in confined grain sizes. Add to this the other structural features such as pores, ultrafine grain sizes and the large number of associated interfaces, grain-boundary junctions, and other crystal defects that do not dominate the overall structure.<sup>16</sup>

Major part of these nanostructures are the nanocrystalline materials which are agglomerates of polycrystals with grain size ranging from 5 to 50 nm and with random orientation of their crystallographic axes. In contrast to amorphous materials which display homogeneous structural disorder, nanocrystalline materials have a heterogeneously distributed structural disorder. They generally consist of two phases: (i) the nanometer-sized (grains) which have a perfect crystal structure that are separated by (ii) a large volume fraction of a grain boundaries or interfacial regions which may represent up to 50 % of the atoms.<sup>16</sup> The dispersed crystalline phase is stabilizing the defect structure of the interfacial regions where the excess energy of such a metastable system is stored.

Due to their superior mechanical, magnetic, electrical, optical, catalytic and thermodynamic properties which are remarkably distinct from their coarser grained microcrystalline counterparts, nanocrystalline materials were intensively investigated in the last few decades. Nanophases showed also increased strength and brittleness in metals, and enhanced ductility, diffusivity and ionic conductivity in ceramics<sup>7-17</sup>. The non-equilibrium structure of the interfacial regions (i.e. reduced density and altered coordination number of their atoms) is responsible for their special physical properties.

Nanocrystalline materials can be prepared by a wide variety of methods that can be assembled into two main categories;<sup>7</sup> (i) They can be grown from smaller building units (atoms or molecules) as in the case of inert gas condensation<sup>17</sup>, chemical vapor deposition, pulsed electro-deposition, reverse micro-emulsion technique, hydrothermal synthesis and sol-gel technique. Nanocrystalline  $\text{LiNbO}_3$  was prepared by simple and convenient hydrothermal synthesis route whereby  $\text{LiOH}$  and  $\text{Nb}_2\text{O}_5$  were used to produce flake-like shaped nanocrystals of  $\text{LiNbO}_3$  with average particle size of 40 – 100 nm<sup>18</sup>. It was also prepared with grain sizes below 10 nm using a modified polymer precursor method (4.5 nm) and a double alkoxide sol-gel method (1.6 nm).<sup>19</sup> Furthermore, it was found that the addition of silica restricts the growth of  $\text{LiNbO}_3$  nanocrystals.<sup>20</sup> Recently,  $\text{Li}$  and  $\text{Nb}(\text{OEt})_5$  dissolved in benzyl alcohol were heated at 493 K in an autoclave for 4 days.<sup>21</sup> The obtained nanocrystalline  $\text{LiNbO}_3$  particles display less uniformed particle shape and sizes of 20 – 50 nm. (ii) Contrarily, the nanocrystalline particles can be obtained by reducing the grain size of their coarser counterparts, e.g. by sputtering with radio frequency fields or heavy ions or by high energy ball milling (H.E.B.M.).<sup>22</sup>

For understanding the basic features of the nanocrystalline materials and consequently tailoring their structure-dependent properties, it is necessary to have a deeper insight about the nature of the GBs and the interfacial regions. Several techniques have been employed to explore the structure of the nanocrystalline

materials such as XRD, TEM, positron lifetime spectroscopy<sup>23</sup>, Mössbauer spectroscopy<sup>24</sup>. However, impedance and NMR spectroscopies are still the master tools used to study the unique properties of the disordered ceramic materials as will be discussed in Sec. 4.1.3 and Sec. 4.2.8.

### 2.1.3 Glass and Amorphous Materials

An amorphous material is a solid which has no long-range order of the atomic positions, that is, it has no regularity in the arrangement of its molecular or atomic constituents on a scale larger than few times the size of these groups. Most classes of solid materials can be prepared in an amorphous form by many ways. When the crystalline phases are molten the periodical ordered structural environment is lost. If a liquid is cooled rapidly enough to avoid crystallization, an amorphous solid called a glass is formed below the glass transition temperature. Every definition of glass defines it as an amorphous solid<sup>25</sup>, or more precisely "a uniform amorphous solid material which exhibits a glass transition" or "a solid materials whose shear viscosity exceeds  $10^{14.6}$  poise". Glass is usually produced when a suitably viscous molten material is cooled very rapidly, thereby not giving enough time for regular crystal lattice to form. This process does not release the latent heat of fusion. For this reason many scientists consider glassy materials to be liquids rather than solids. There is widespread opinion that glasses are super-cooled liquids and therefore have a finite viscosity at ordinary ambient temperatures. Stories are told of glass flowing under their own weight<sup>26</sup> of ancient windowpanes that are thicker at the bottom or of glass that has sagged in storage. These observations must find other explanations, because glasses of commercially useful compositions are in fact rigid solids at ordinary temperatures<sup>27</sup>. Amorphous solids produced by other routes, such as ion implantation or sol-gel, are, technically speaking, not glasses.

The relationship between the volume and the temperature is shown in Fig. 2.1.1. Upon cooling, most melts would crystallize following a first order transition between the liquid and the solid state (the route 1 – 2 – 3 in Fig. 2.1.1) accompanied with a discontinuity in volume (as well as in other properties of the material). Nevertheless, glass-forming melts can be supercooled when using high cooling rate that prevents crystallization. Here, the amplitudes of the atomic vibrations decrease and a denser melt is formed through atomic rearrangements, and both effects lead to a gradual decrease in the volume. The transition from the liquid state to the glass state, at a temperature below the equilibrium melting point of the material, is called the glass transition temperature,  $T_g$ , (point 4 in Fig. 2.1.1). The glass transition temperature is the

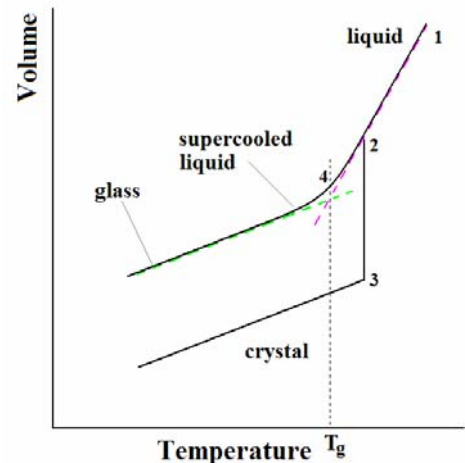


Fig. 2.1.1: The relationship between the volume and the temperature, a comparison between crystalline and glassy materials.

temperature below which the molecules have very little mobility. From practical point of view,  $T_g$  is defined empirically as the temperature at which the viscosity of the liquid exceeds a certain value (commonly  $10^{13}$  Pa · s) where the atomic rearrangements get slower and eventually stop completely. The  $T_g$  depends on the cooling rate, with the glass transition occurring at higher temperatures for faster cooling rate. It is clear that the glass transition is not a first-order thermodynamic transition (such as melting). However, there is a debate as to whether it is a higher-order transition, or merely a kinetic effect.

It is difficult to make a distinction between truly amorphous solids and crystalline solids in which the size of the crystal is very small (less than two nanometers). Even amorphous materials have some short-range order among the atomic positions (over a length scale of about one nanometer).

### 2.1.3.1 The random network model

The Random Network Theory of glass structure developed from the original concept of Zachariasen<sup>28</sup>, has been the most significant model for oxide glasses ( $A_mO_n$  with  $A = B, Si, As, \dots$  etc). It was also supported by the work of Warren on vitreous  $SiO_2$ , see Ref. [29], and by some more recent works.<sup>30–31</sup> Based on the laws of crystal chemistry and the observation that the mechanical properties of glasses are similar to those of crystals of the same composition, Zachariasen concluded that the atoms in a glass are linked together by the same forces as in crystals. He proposed a structure consisting of an extended three-dimensional network made up of well-defined small structural units that are linked together in a random way that no definite chemical compound can exist. The Continuous Random Network may have local order, long range disorder and connectivity. Fig. 2.1.2 shows the atomic arrangements for a hypothetical  $A_2O_3$  oxide in a crystal and a glass are compared. The structural units in both cases are planar  $AO_3$  triangle and randomness of the glass phase is achieved mainly by variation of the bond angles and the distances between the structural units and only to a minor extent by variation of angles and distances within the structural units. According to this concept  $SiO_4$  tetrahedra share corners to form random network, and cations which do not form the the network are pictured as randomly situated in the interstices between the polyhedra. When cations which would not exactly fulfil the requirements of a network former were found to form glasses, the existence of an intermediate group of cations was recognized.  $Nb^{5+}$  appears to belong to this group.

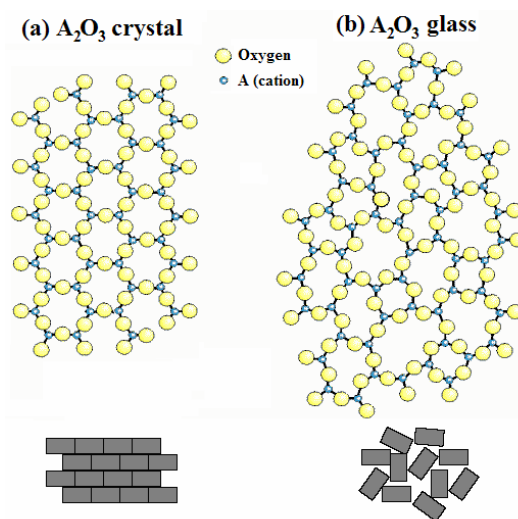


Fig. 2.1.2: Schematic representation of a hypothetical two-dimensional  $A_2O_3$  oxide with  $AO_3$  triangles as structural units: (a) in crystalline phase, and (b) in a glassy phase to demonstrate Zachariasen's random network theory.<sup>59</sup>

### 2.1.3.2 Modified random network

The ‘network-forming’ cations are all cations which form the continuous random network in association with oxygen. This term has been adopted for oxides capable of forming a glass. In a fully-polymerized network such as vitreous  $\text{SiO}_2$  all oxygen atoms act as bridging connecting the corners of adjacent tetrahedra and are called bridging oxygens (BO). Beside the network former, glass can contain many oxides that do not participate in forming the network structure and are called network modifiers. Soda lime silica glass is a prime example, where the alkali and alkaline-earth oxides are incorporated

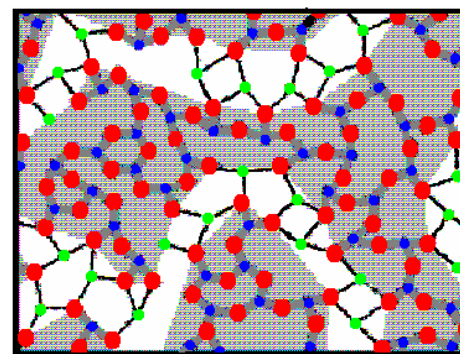


Fig. 2.1.3: Modified Random Network<sup>32</sup>

into the network structure. The introduction of such oxides breaks  $\text{Si—O—Si}$  bonds forming non-bridging oxygens (NBO). These oxygens are therefore bonded to only one Si and bear an increased negative charge. Two NBOs are produced for every formula unit of  $\text{Na}_2\text{O}$  or  $\text{CaO}$  introduced in the structure. The formation of NBOs reduces the connectivity of the glass network and hence, modifies its properties such as ionic diffusion, chemical corrosion and thermal expansion. A model suggested to describe such network modified glasses is the *Modified Random Network* proposed by Greaves<sup>32</sup>, Fig. 2.1.3. The glass structure is proposed to consist of regions of network former interlaced with regions of network modifier. Clustering of alkalis is regarded as a feature of the Modified Random Network model. The structure is therefore partly covalent and partly ionic and this illustrates how network modifier can be incorporated within the context of the continuous random network.

### 2.1.3.3 Preparation of amorphous materials

Glass-forming melts can form a glass when the melt is cooled down with a cooling rate that prevents crystallization. However, in the case of fragile melts, rapid quenching techniques are quite advantageous for preparing the new glasses that cannot be formed by the usual cooling methods. In the 1960s there were many designs for rapid quenching devices<sup>33</sup> including the torsion-catapult<sup>34</sup> and plasma-jet spray-quenching<sup>35</sup> until Chen and Miller<sup>36</sup> described their first twin-roller quenching device. Using such a device, thick and uniform flakes of glasses of many metallic alloys as well as non-metallic materials can be readily prepared. It is relatively easy to fabricate and provides high quenching rates ( $\sim 10^6 \text{ K} \cdot \text{s}^{-1}$ ). It consists of two metallic plated rollers that are held together by a spring system to maintain a uniform thin gap between them during the operation. They rotate with a speed of up to 3000 - 5000 r.p.m. The sample is molten in a heating assembly that consists of a crucible which is surrounded by a wire wound furnace<sup>36</sup>.

On the other hand, amorphisation can be defined as the transformation of a crystalline phase to an amorphous phase without melting and vitrification. It is a progressive process that results from disruption

of the crystalline structure<sup>37</sup>. There are numerous ways of achieving amorphisation, under intensive irradiation<sup>38</sup>, high pressure<sup>39</sup>, or prolonged grinding<sup>40</sup>. As these methods deal with initially solid materials, this order-disorder transition is commonly termed solid-state amorphisation. Amorphisation may also advance by a process of nucleation and growth, nucleating centers being the zones of instability.

While sputtering techniques are useful, it is rather difficult to obtain films with suitable thickness for a number of physicochemical studies. Furthermore, the nonstoichiometry of the sputtered samples creates difficulties in understanding their behavior.  $\text{LiNbO}_3$  can be amorphized by irradiation with 800 keV  $\text{Kr}^+$  ions, the critical amorphisation temperature  $T_c$  above which radiation-induced amorphisation does not occur was 600 K<sup>41</sup>. A thin film of amorphous  $\text{LiNbO}_3$  was also prepared by sputtering with 13.56 MHz r.f. with maximum power of 1.5 kW in an Ar plasma at a constant pressure of  $4 \times 10^{-3}$  torr<sup>42</sup>.

The first pressure-induced amorphisation goes back to 1984 when Mishima *et al.*<sup>43</sup> found that ice-Ih cooled down to 77 K and pressurized to 1 GPa failed to transform into crystalline ice-IX and became amorphous. Since then, a large number of materials were found to undergo similar transitions at different pressures and temperatures. Quartz was found to amorphize at room temperature at pressure between 15 and 25 GPa<sup>44</sup>. Crystalline  $\text{LiNbO}_3$  amorphizes at about 31 GPa and this transition becomes irreversible above 35.8 GPa<sup>45</sup>,  $\text{LiTaO}_3$  becomes irreversibly amorphous at 33.2 GPa.<sup>46</sup>

#### 2.1.4 Glass Composites

Glass-ceramic was defined as a two-phase system comprising crystals that have been controllably grown from a parent glass by careful heat treatment.<sup>47</sup> However, another definition considered any two-phase system where one phase is a crystal and the other is glass as a glass-ceramic.<sup>48</sup> The glass-ceramic processing offers many advantages over both single crystals and conventional powder processing (sintered ceramic) including: (i) Easy formability because pure forms of these materials have little glass forming ability, (ii) low cost of glass due to the convenient processing of glass-ceramics, (iii) increased homogeneity, pore free microstructures, and shape forming versatility, (iv) optical transparency, and (v) the temperature independence of the dielectric constant. Glass can be crystallized not only by annealing but also by photo induced<sup>49</sup> or ion-exchange induced crystallization.

Ferroelectric glass-ceramics are of great interest due to their unique properties and their potential for commercial applications. The ferroelectric nanoparticle can be treated as built-in electrical dipole which produces effects like the electro-optic effect<sup>50</sup> (change of optical index with electrical field), harmonic generation (changing frequency of light), photorefraction<sup>51</sup> (index change in response to light). High optical transparency is very important for the electrooptical phenomenon. Optical transparency can be obtained in a glass-ceramic by limiting crystal growth to a size less than the shorter wavelengths of the visible spectrum, thereby minimizing light scattering, and by matching the refractive indices of the crystalline and the glass phase<sup>52</sup>. The volume fraction of the ferroelectric phase and the grain size has critical param-



ters dictating the properties of any ferroelectric phase, which grows from the glass matrix. Generally, glass-ceramic materials also have high fracture strengths and increased chemical and thermal stability. In addition, the crystallite size and concentration can be varied in order to produce desired material properties and characteristics by separately controlling the degree of nucleation and the rate of crystal growth.

The crystallization of a homogeneous phase, liquid or glass, begins and extends progressively from discrete centers distributed throughout the mass. Two stages can be distinguished, the nucleation and the growth. The (nucleation) process involves conversion of a small volume of reactant into a stable particle of product, and continued reaction (growth) occurs preferentially at the interfacial zone of contact between these two phases. A metastable state evolves towards the stable equilibrium state via localized droplet fluctuations of a critical size. The critical energy for the formation of a droplet is determined by a competition between a volume term (which favors creation of the droplet) and a surface term (which favors its dissolution). The critical radius  $R_c$  results from this competition: droplets of size  $R > R_c$  grow while droplets with  $R < R_c$  shrink. Several nucleation processes have been identified, instantaneous nucleation, single-step nucleation gives either an exponential or a linear law and multi-step nucleation gives a power one.

At present, the process of homogeneous nucleation<sup>53-56</sup> is quite well understood. This is also the case for late time phase separation, known as Ostwald ripening. Experimentally, nucleation, growth and coarsening have been well-studied in systems like crystallization of melt<sup>57</sup>, glasses and amorphous materials<sup>58</sup>.

## 2.2 DIELECTRIC AND FERROELECTRIC MATERIALS

Dielectric materials have poor electrical conductivity as they do not have free charges. However, they increase the charge storing capacity of a capacitor according to their dielectric constant which depends in turn on their polarizability<sup>59</sup>. The polarizability of a material is determined by contributions from various polarization mechanisms, including electronic, ionic, dipole, and space charge polarization. Electronic and ionic polarizations are the important ones in the case of ceramic materials. Electronic polarization results from shifting the electron cloud of an atom in response to the applied field, while ionic polarization evolves from movement of ionic species in the material under the influence of the field. Both mechanisms are dependent on frequency. Electrons can respond to frequencies up to  $10^{16}$  Hz, and ions up to  $10^{12}$  Hz. When an electric field is applied to such materials there is a tendency to produce charge displacement within the atoms or molecules of the material (i. e. polarization) without long range migration of charges. For many of their applications dielectric materials are made to hold a large electrostatic charge when they are subjected to high voltages without any damage (high dielectric strength) while dissipating minimal energy in the form of heat (low dielectric loss). The parameter used to describe the dielectric behavior is the dielectric constant (relative permittivity),  $\epsilon'$ , which is equal to the ratio between the capacitance of par-

allel plates capacitor when the dielectric material is placed between its plates relative to that of an empty one.

Dielectric losses in ceramics result mainly from three processes: ion migration, ion vibration, and deformation electron polarization<sup>59</sup>. The first results from dc conductivity and ion jump or dipole relaxation and is responsible for the majority of dielectric losses in ceramic dielectrics, while the last two are not significant at low frequencies ( $< 10^{10}$  Hz). Conductivity losses are negligible at room temperature where most ceramics are insulators. At higher temperatures, the loss factor can be expressed in terms of conductivity

$$\text{by} \quad \tan \delta = \frac{\sigma}{2\pi f \varepsilon' \varepsilon_0} \quad (2.2.1)$$

where  $\sigma$  is the electrical conductivity,  $f$  is the frequency, and  $\varepsilon_0$  is the permittivity of the free space. Conductivity losses are predominant at frequencies  $< 100$  Hz.

Ion jump relaxation results from an ion jumping between two equivalent sites. The frequency at which the jumps occur is dependent on the energy barrier between the two sites. When the applied field frequency is lower than the jump frequency, losses are low because the ion can follow the field. At frequencies much higher than the jump frequency, the ion is unable to jump at all, which also results in a low dielectric loss. Losses are greater when the frequency of the applied field is of the same amplitude as the jump frequency.

In polyphases or nanocrystalline ceramics, interfacial region or space polarization due to the difference in conductivities of the grain and grain boundary could arise.<sup>59</sup> This polarization results in a high apparent dielectric constant and a peak in the loss factor.

## 2.3 PHYSICAL AND CHEMICAL PROPERTIES OF MATERIALS

### 2.3.1 Lithium Niobate

Lithium niobate is a well-known human-made oxide material that has been an especially interesting candidate for both basic science and technological applications. It was successfully grown in a single crystal form by Ballman<sup>60</sup> with Czocharalski method. Then, it has been extensively studied and the major breakthrough of crystal growth was made by Lerner *et al.*<sup>61</sup> Up to 1483 K,  $\text{LiNbO}_3$  is a member of the noncentrosymmetric space group R3c. This ferroelectric phase is a derivative of corundum structure<sup>[62,63]</sup>. It has a hexagonal-close-packed oxygen lattice with distorted octahedra sharing faces. The cations are stacked in the oxygen octahedra down the hexagonal c-axis according to the sequence Nb, Li, vacancy (V or  $\square$ ), Nb, Li, V, etc<sup>62</sup>, Fig. 2.3.1(a). A more abstract version is given in Fig. 2.3.1(b) indicating the existence of planes containing triangles of  $\text{O}^{2-}$  ions, being parts of a hexagonal close-packed structure. The cations sit between these planes, Nb near the center of an octahedral, Li more off-centered resulting in a polar

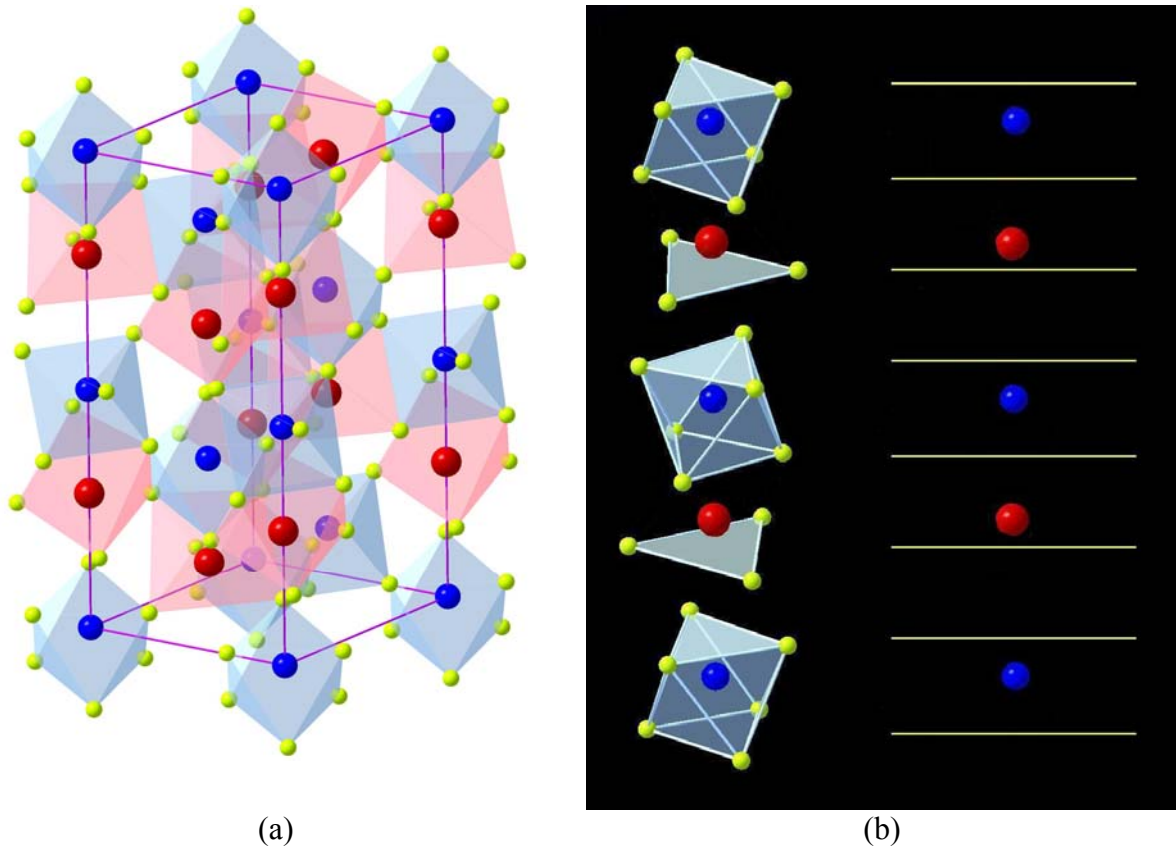


Fig. 2.3.1: (a) The crystal structure of the ferroelectric phase of LiNbO<sub>3</sub>, a hexagonal-close-packed oxygen lattice with distorted octahedra sharing faces.(b) An abstract version indicating the existence of planes containing triangles of O<sup>2-</sup> ions. The cations sit between these planes, Nb near the center of an octahedral, Li more off-centered resulting in a polar symmetry.

asymmetry that gives rise to large ferroelectric, pyroelectric, and piezoelectric coefficients.<sup>64</sup> Two unusual optical properties exhibited in bulk LiNbO<sub>3</sub> that are also related to this asymmetry are known as the photorefractive effect and photovoltaic effect.<sup>51,65</sup> Furthermore, LiNbO<sub>3</sub> possesses useful electro-optic and acousto-optic properties that make it a unique promising non-linear optical material that finds applications in waveguide switches, frequency conversion, and acoustic devices.<sup>64,66-67</sup> Due to this outstanding richness in its physical properties, during the last three decades it was the subject of a large number of papers, reviews and even books.<sup>64,68-69</sup> The columns of octahedral are packed together such that in the basal plane every Li ion has three nearby Nb ions and three nearby structural vacancies; each Nb ion has three nearby Li ions and three nearby structural vacancies; and each vacancy has three of each Li and Nb ions, Fig.2.3.2. In the mid 1960s, the crystal structure of the congruent composition had been determined with XRD method by Abrahams *et al.*<sup>62,70-71</sup>, and theoretically treated by Megaw<sup>63</sup>.

This structure can also be related to that of the ABO<sub>3</sub> perovskite (with tolerance factor,  $t = 0.74$ ,  $t = (r_A + r_O) / [1.4(r_B + r_O)]$ ). However, the structures are different because, unlike the perovskite A and B ions, Li<sup>+</sup> and Nb<sup>5+</sup> here have nearly identical ionic radii and thus they have similar environment; both ions are surrounded by distorted octahedral of six O<sup>2-</sup> ions. Because of this similarities and since the Nb<sup>5+</sup>—O<sup>2-</sup>

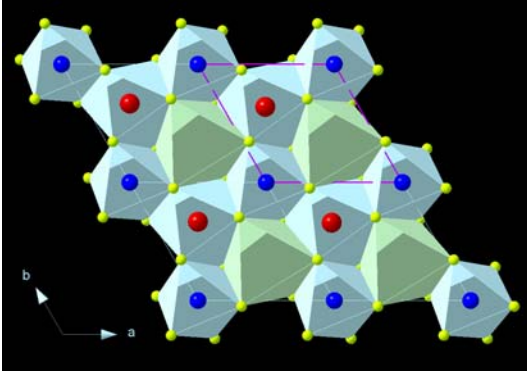


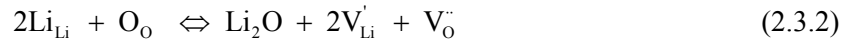
Fig. 2.3.2: The basal plane of the crystal structure of  $\text{LiNbO}_3$ , where every Li ion has three nearby Nb ions and three nearby structural vacancies; each Nb ion has three nearby Li ions and three nearby structural vacancies; and each vacancy has three of each Li and Nb ions.

bond is stronger than the  $\text{Li}^+ - \text{O}^{2-}$  one,  $\text{LiNbO}_3$  has a tendency to be nonstoichiometric with  $[\text{Li}]/[\text{Nb}] = 0.942$ . However,  $\text{LiNbO}_3$  single crystal has a wide solid solution region extending from stoichiometric point (50 %  $\text{Li}_2\text{O}$ ) to the niobium rich side (47 %  $\text{Li}_2\text{O}$ )<sup>61</sup>. It can be readily grown from a melt of  $\text{Li}_2\text{O} - \text{Nb}_2\text{O}_5$  mixture with a content of about 48.5 %  $\text{Li}_2\text{O}$ <sup>72-73</sup>. This composition is known as the congruent composition. It melts at 1526 K. The following equation describes the relationship between the melt composition and the crystal composition.<sup>74</sup>

$$c_{\text{Li}} = 48.5 + 0.3436 \times (c_{\text{Li, melt}} - 48.5) - 0.02897 \times (c_{\text{Li, melt}} - 48.5)^2 \quad (2.3.1)$$

The Li content can be changed by prolonged equilibration in contact with  $[\text{Li}_3\text{NbO}_4$  and  $\text{LiNbO}_3$  ( $\text{Li}_2\text{O}$  source)] or  $[\text{LiNb}_3\text{O}_8$  and  $\text{LiNbO}_3$  ( $\text{Li}_2\text{O}$  sink)] at temperatures approaching but lower than the Curie temperature for 300 hours<sup>75</sup>.

In order to sustain this nonstoichiometry, LN usually processes a high concentration of intrinsic defects<sup>68,76</sup> including cation and anion vacancies, interstitial ions and impurities.<sup>77-79</sup> So far, several defect models have been proposed for  $\text{LiNbO}_3$ . Some authors preferred the model where lithium vacancies are charge compensated by oxygen vacancies *anion or oxygen vacancies model*,  $[\text{Li}_{1-2x}\square_{2x}][\text{Nb}][\text{O}_{3-x}\square_x]$ .<sup>80</sup> This model was based mostly on  $\text{OH}^-$  infrared absorption measurements and density data<sup>81</sup>. The obtained infrared band consists of two components attributed to  $\text{OH}^-$  either substituting  $\text{O}^{2-}$  ions or occupying interstitial sites. This was in agreement with the suggestion that lattice sites are conserved<sup>77</sup>:



The work of Jorgensen and Bartlett on high-temperature transport in  $\text{LiNbO}_3$  also supported the presence of oxygen vacancies.<sup>82</sup> They investigated the electrical conductivity at different oxygen partial pressure as a function of temperature. The electrical conductivity was found ionic at  $p_{\text{O}_2} = 1$  atm, and electronic at  $p_{\text{O}_2} < 10^{-6}$  where it is proportional to  $p_{\text{O}_2}^{-1/4}$  atm. This was attributed to a defect model involving singly ionized oxygen and free electrons ( $\text{O}_{\text{O}} \rightleftharpoons \text{V}_{\text{O}}' + \text{e}^- + 1/2\text{O}_{2(\text{g})}$ ). The differences in electrical conductivity and oxygen diffusion for the  $a$  and  $c$  directions were within the experimental error of the measuring techniques. The enthalpy of formation of singly charged oxygen vacancies was calculated to be 97.7 cal/mol. The oxygen diffusion at a partial pressure of 70 Torr was described by the equation

$D = 3.03 \times 10^{-6} \exp(-29.4 \text{ kcal mole}^{-1}/RT)$  and the rate of oxygen diffusion was not affected by the surface exchange. Afterwards it was proved again that oxygen vacancies are present in the crystal.<sup>76,83–85</sup> Annealing the as grown  $\text{LiNbO}_3$  crystal in argon atmosphere at 1373 K gave firstly an optical absorption maxima at  $\lambda_1 = 360 \text{ nm}$  ( $E_1 = 3.55 \text{ eV}$ ), followed by the appearance of another one within 10 – 15 min of continued annealing at  $\lambda_2 = 530 \text{ nm}$  ( $E_2 = 2.32 \text{ eV}$ )<sup>85</sup>.  $E_1$ ,  $E_2$  bands were attributed to  $F^+$  and F centers which are generated when the oxygen vacancies trap one or two electrons, respectively. The appearance of  $E_1$  first implies that the oxygen vacancies are already present in the single crystal and that the electrons which result from the thermal reduction are distributed among all the available oxygen vacancies. This means that in the as-grown  $\text{LiNbO}_3$  crystal the Fermi level of electrons is lower than  $E_1$ . Firstly it is filled by the electrons leading to the formation of  $F^+$  centers and increasing the absorption at 3.55 eV. With time and under reducing conditions the Fermi level is shifted to a higher value. This results in the second energy level  $E_2$  which generates F centers resulting in the appearance of the second optical absorption band at 2.32 eV. Bredikhin *et al.*<sup>86</sup> found the congruent  $\text{LiNbO}_3$  crystal to be an oxygen and lithium conductor at temperatures between 573 and 1073 K. The conductivities [in  $(\Omega\text{cm})^{-1}$ ] at 973 K of the  $\text{LiNbO}_3$  crystal were found to be:  $2 \cdot 10^{-6}$  (oxide-ion conductivity in the as grown crystal),  $3 \cdot 10^{-6}$  (oxide-ion conductivity in the thermally reduced crystal),  $8 \cdot 10^{-6}$  (lithium-ion conductivity) and  $10^{-4}$  (electronic conductivity). The slight increase in  $\text{O}^{2-}$  conductivity upon reduction emphasizes that the oxygen vacancies did not change so much. The concentration of oxygen vacancies  $N_{\text{ox}}^{\text{V}}$  was found to be more than  $10^{19} \text{ cm}^{-3}$ . Lithium-ion conductivity has the same order of magnitude as that of oxide ion while the electronic conductivity exceeds the ionic conductivities. The electronic conduction has activation energies of 1.4 and 0.54 eV for the as grown and the thermally reduced  $\text{LiNbO}_3$  crystal. Bredikhin *et al.*<sup>86</sup> could detect the formation of regions with changed stoichiometry with respect to O and Li by applying an electrical field to the samples. The same two optical bands mentioned above were also observed in the cases of oxygen vacancies or lithium ions electrically injected by double layer electrodes. These identities of the electrical and optical absorption properties for both the thermally and electrically reduced crystal emphasize the conclusion that they have the same origin. Moreover, ionizing radiation may turn these vacancies into color centers, such as F or  $F^+$  that can be identified by their optical absorption spectra.

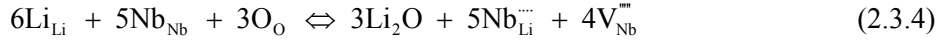
However, an increase in the density of the Nb-rich composition was observed which could not be interpreted by the oxygen vacancy model. This implies that oxygen vacancies are not the major defects in  $\text{LiNbO}_3$  or that the oxygen vacancy model is completely unfeasible to account for the nonstoichiometry in  $\text{LiNbO}_3$ .<sup>61–62,87–88</sup>

The assumption of *cation stacking faults* was adopted to account for the nonstoichiometry of  $\text{LiNbO}_3$  and was presented by a suggested formula like:  $[\text{Li}_{1-5x}\text{Nb}_{5x}][\text{Nb}_{1-4x}\text{O}_3]^{73,293}$ ,  $[\text{Li}_{1-5x}\text{Nb}_x\text{Nb}_{4x}]\text{NbO}_3$ <sup>61</sup>. Lerner *et al.* proposed that unit cells are lost in proper stoichiometric ratios as the  $\text{Li}_2\text{O}$  content decreases, according to

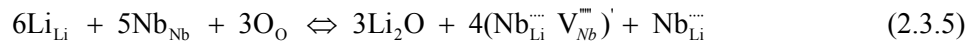


The Nb left over by the loss of unit cell moves into the crystal and substitute for some of the missing Li creating  $Nb_{Li}$  antisite. The latter is preferred over  $V_{Nb}$  on the basis of excess charge. A controversy emerges according to the type of defects that compensates the excess charge introduced by the  $Nb_{Li}$  antisites.

In the *Nb vacancy model*<sup>79</sup>, charge is compensated at the expense of  $V_{Nb}$ . The nonstoichiometry defects are  $Nb_{Li}$  (4.6 %) and  $V_{Nb}$  (3.7 %) according to



However, it is unlikely that such a set of highly charged individual defects would be the lowest energy solution to accommodate the loss of  $Li_2O$ . Smyth assumed that each Nb vacancy is located adjacent to an antisite Nb to give a singly charged defect complex<sup>88-90</sup>



This complex may be simply derived from a Li-vacancy by the movement of an adjacent lattice



The congruent  $LiNbO_3$  contains regions where the normal cation stacking sequence is replaced by ilmenite ordering  $Li\ Nb \square\ Nb\ Li \square\ Li\ Nb \square\ Nb\ Li$ . This configuration is only slightly less stable than the normal  $LiNbO_3$  structure. A complex  $(Nb_{Li}\ V_{Nb})$ , as referred to in the normal cation sequence of  $LiNbO_3$ , then corresponds to a Li vacancy,  $V_{Li}$ , in ilmenite domain in the crystal.

Later, and based on a NMR study<sup>293</sup>, another kind of cation-substitution model was proposed. The presence of Nb vacancies was assumed according to the formula  $[Li_{1-5x}Nb_{5x}][Nb_{1-4x}\square_{4x}]O_3$ . This defect model was also supported by the x-ray structure analysis of congruent and stoichiometric  $LiNbO_3$  crystal done by Abrahams and Marsh<sup>71</sup>. They assigned a value of  $x = 0.118$  for the congruent composition. However, it was pointed out on an energetic basis<sup>91</sup> that the Nb-site vacancy defects are more unfavorable than Li-site vacancy type. The authors considered that the microscopic ilmenite-like stacking could overcome the energy difference of 6 eV per  $Li_2O$  without any quantitative data for this assumption. Iyi *et al.*<sup>87</sup> also obtained a structure refinement for XRD and TOF neutron diffraction data of  $LiNbO_3$  crystals with four different compositions. Their refinement disagreed with that of Abrahams and showed that the amount of Nb occupancy was composition-independent and that  $Li^+$  ions were replaced by the  $Nb^{5+}$  ions, creating vacancies at the Li site.

The most supported defect model<sup>61-62</sup> was given by Lerner *et al.*,  $[Li_{1-5x}Nb_x\square_{4x}]NbO_3$ . In this *Li-vacancy model* the nonstoichiometry defects are now  $Nb_{Li}$  (3.7 %) and  $V_{Li}$  (0.9 %). According to this model, the lithium site is partially occupied by  $Nb^{5+}$ , each Nb atom replacing five Li atoms. This suggests the presence of  $4x$  vacancies in this site. This model has been in agreement with recently experiments<sup>95-93</sup> and several new discussions<sup>94-95</sup>.

The chemical analysis presents an absolute method to determine the real chemical composition of the crystal; but generally it is not sensitive enough for any of the main components of the host material ( $\cong 10^{-1}$

mole %). Add to this the complicated chemical processing procedure<sup>96</sup>. The crushed samples were dissolved with HNO<sub>3</sub>-HF solution in a closed Teflon vessel at 323 K overnight. The resulting solution was passed through an anion exchanger (SA-1) to separate Li and Nb ions. The Li content was measured by atomic absorption analysis of the effluent. Nb ions, eliminated from the resin by HCl-HF solution, were precipitated by Cuperon, and the precipitate was dried and incinerated. Weighting of the yielded Nb<sub>2</sub>O<sub>5</sub> gave the Nb content<sup>87</sup>. The practical physical methods are more sensitive ( $\cong 10^{-2}$  mole %), but they are generally relative and highly affected by various impurities. The Curie temperature varies with the composition according to the following relation<sup>97</sup>

$$T_C = 9368.4 - 369.05 c + 4.228 c^2 \text{ (K)} \quad (2.3.7)$$

Each method has its own inconveniences; Curie temperature measurements can be performed over 1273 K<sup>98</sup>. The phase matching temperature of the second harmonic generation can be measured only by precision laser optical system. The installation of this method therefor is too expensive. The measurement of the extraordinary reflection index with acceptable accuracy demands a very high level of crystal processing.<sup>99</sup> The refractivity is also influenced by impurities.<sup>100</sup> The shift of the UV-absorption edge was applied to determine the LiNbO<sub>3</sub> crystal composition.<sup>101</sup> The accuracy of the method was about 10<sup>-2</sup> mole % using a simple commercial UV-spectrophotometer. The edge position reflects the amount of Nb<sup>5+</sup> ions in Li sites. The ion impurities that prefer the Nb<sup>5+</sup> sites are not expected to disturb the number of Nb<sub>Li</sub>, consequently they have no effect on the absorption edge. Contrarily, ions occupying the lithium sites can move the Nb ion from the Li positions and shift the absorption edge. Thus, care must be taken for defects and impurities and a perfectly oxidized LiNbO<sub>3</sub> crystal in which neither Nb<sup>4+</sup> nor oxygen vacancies exist.

### 2.3.2 Sodium Niobate

The phase transformations in sodium niobate (NaNbO<sub>3</sub>) are complicated<sup>102</sup>. Sodium niobate is orthorhombic at room temperature, changing to tetragonal at  $643 \pm 5 \text{ K}$ <sup>103-106</sup>. Tetragonal to cubic phase transformation was observed at 698 K using x-ray analysis. At 913 K, this transition can only be detected by optical techniques because of the very small changes in structure associated with the transformation.<sup>106-107</sup> Further studies showed that sodium niobate transforms from an orthorhombic to tetragonal structure at 643 K, and from tetragonal to a cubic

Table 2.3.1: the seven phases of sodium niobate and their space groups and temperatures of transformation<sup>102</sup>

<i>T</i> (K)	Phase	Lattice symmetry	Space group	Formula per unit cell
173	N	Rhombohedral	<i>F3c</i>	2
633	P	Orthorhombic	<i>Pbma</i>	8(4)
753	R	Orthorhombic	<i>Pnmm</i>	24(8)
793	S	Orthorhombic	<i>Pnmm</i>	8
848	T(1)	Orthorhombic	<i>Ccmm</i>	4
913	T(2)	Tetragonal	<i>F4/mmb</i>	2
	Aris-totype	Cubic	<i>Pm3m</i>	1

structure at 913 K<sup>104–107</sup>. The lattice parameters of the tetragonal phase of sodium niobate are temperature dependant and the axial ratio ( $c/a$ ) approaches one as the temperature approaches 913 K.

### 2.3.3 Sodium Silicate Glasses

Fig. 2.3.3 shows the phase diagram of the  $\text{Na}_2\text{O} - \text{SiO}_2$  system.<sup>108</sup> It reveals the compounds that can form from the melt at various temperatures. Inspection of the phase diagram reveals that  $\text{Na}_2\text{O} \cdot 2\text{SiO}_2$  and  $\text{Na}_2\text{O} \cdot \text{SiO}_2$  are possible de devitrification products when the  $\text{SiO}_2$  contribution is close to 66.6 mole %. In addition to these phases  $2\text{Na}_2\text{O} \cdot \text{SiO}_2$  is also a possible phase when the  $\text{SiO}_2$  content is close to 50 %. Babushkin *et al.*<sup>109</sup> presented a thermodynamic analysis of the reaction between  $\text{SiO}_2$  and  $\text{Na}_2\text{CO}_3$ . Measuring the stability of the formed silicate the value of the free energy, he concluded that the stability of the product was higher with greater  $\text{SiO}_2$  content (in the reaction product). The temperature for the formation of the silicate phases was such that the phase would form in the order  $\text{Na}_2\text{O} \cdot 3\text{SiO}_2$ ,  $\text{Na}_2\text{O} \cdot 2\text{SiO}_2$ ,  $\text{Na}_2\text{O} \cdot \text{SiO}_2$ , and  $2\text{Na}_2\text{O} \cdot \text{SiO}_2$ , with increasing temperature. It was determined that theoretically  $\text{Na}_2\text{O} \cdot 2\text{SiO}_2$  could form above 400 K and  $\text{Na}_2\text{O} \cdot \text{SiO}_2$  above 500 K. However, thermodynamic findings should only be used as an indicator of the possible phases that could form at various temperatures since thermodynamics is based on the equilibrium state and does not incorporate kinetic consideration.

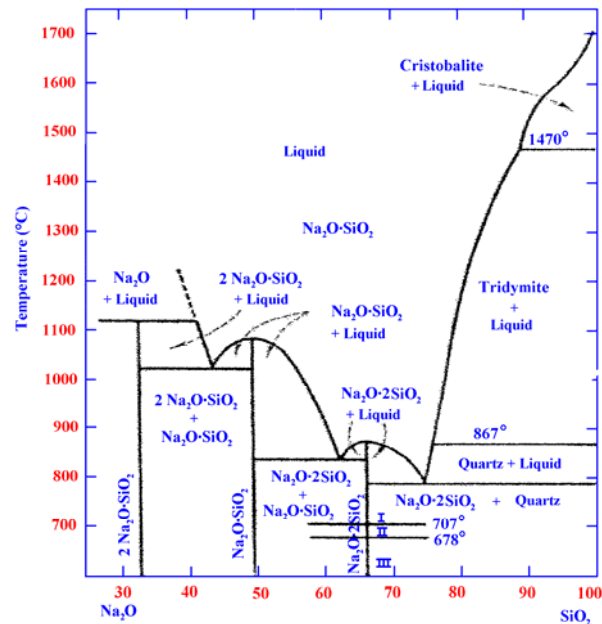


Fig. 2.3.3: Phase diagram of  $\text{Na}_2\text{O} - \text{SiO}_2$  system.<sup>108</sup>

### 2.3.4 Alkali-Niobium Silicate-Glasses and Glass-Ceramics

The incorporation of  $\text{Nb}_2\text{O}_5$  in inorganic glasses exerts a favorable effect on a number of their physical and chemical properties awarding them considerable practical interest. The participation of  $\text{Nb}_2\text{O}_5$  in silicate systems contributes to the development of new materials with higher non-linear optical coefficients<sup>110</sup> with piezoelectric, semiconducting and improved radiation optical properties<sup>111</sup>, and laser glasses of high-stimulated emission parameters.<sup>112</sup>

Several studies have been reported on lithium, sodium, and potassium niobium silicate glasses and the corresponding glass-ceramics systems due to their unique dielectric and electro-optical properties, the



ferroelectric behavior of the crystalline phases, and their potential for commercial applications<sup>107,113–120</sup>. The glass-ceramic processing offers many advantages over conventional powder processing methods including increased homogeneity, pore-free microstructures, and shape forming versatility. Generally, glass-ceramic materials also have high fracture strengths and increased chemical and thermal stability. In addition, the crystallite size and concentration can be varied in order to produce desired material properties and characteristics by separately controlling the degree of nucleation and the rate of crystal growth. Formation of ferroelectric crystalline phases and their solid solutions, in glass-ceramic materials has been demonstrated by many investigators. Commercial titanate and niobate capacitor dielectrics with properties comparable to sintered ceramics have been made through glass-ceramic of glass forming compositions of low network former content.<sup>117</sup> In addition, a number of these transparent ferroelectric glass-ceramics exhibit the electro-optic effect<sup>114,115</sup>.

The crystallization behavior of sodium niobium silicate glasses was studied by Layton and Herczog<sup>121,120</sup>. They focused on glasses containing  $\leq 50$  mol % silicate and equimolar concentrations of alkali and niobium oxides. The samples showed two crystallization steps; the first due to the formation of  $\text{NaNbO}_3$  at 1023 K, and the second at 1023 K due to the formation of  $\beta$ -cristobalite. They obtained transparent glass-ceramics only with samples containing  $\leq 25$  mol % silica. Such glasses have a very high crystallization rate. The rate of nucleation increases with decreasing silica content while the onset temperature of crystallization and crystals size decreases. The rapid nucleation was attributed to the coalescence of niobia-rich phase separated regions that form from the supersaturation of the silica network with niobium. The short range order of the resulting microheterogeneities is similar to that of crystalline  $\text{NaNbO}_3$ <sup>121</sup>.

Crystallization of potassium niobium and tantalum silicate glasses containing 30 – 50 %  $\text{Nb}_2\text{O}_5$  or  $\text{Ta}_2\text{O}_5$  oxide was attributed to the nucleation from phase separated regions caused by the incompatibility between  $\text{SiO}_4$  tetrahedra and  $\text{NbO}_6/\text{TaO}_6$  octahedra.<sup>107,118</sup> Potassium niobium silicate glasses containing equimolar of potassium and niobium and 24 mol % silica showed two crystallization peaks. The activation energy of the first decreased with increasing the silica content, whereas the second peak exhibited a minimum at 28 mol % silica. The phases formed were  $\text{KNbO}_3$ ,  $\text{K}_3\text{NbO}_4$ ,  $\text{K}_8\text{Nb}_{18}\text{O}_{49}$  and a new phase  $\text{K}_6\text{Nb}_6\text{Si}_4\text{O}_{26}$ . The last was labeled as the stable high-temperature phase that results from the chemical reaction of  $\text{KNbO}_3$  with the silica rich grain boundary. The ferroelectric  $\text{KNbO}_3$  was formed successfully in these glasses with a silica content  $\leq 36$  mol %.



# 3 Fundamentals of diffusion in solids

## 3.1 FLUX OF PARTICLES (FICK'S LAWS)

Mass transport in a gas or liquid generally involves the flow of fluid although atoms also diffuse. Solids on the other hand, can support shear stresses and hence do not flow except by diffusion involving the jumping of atoms on a fixed network of sites. Diffusion is a process in which the uniformity of concentration of the species under consideration is attained through its migration from the denser to its less abundant part<sup>122</sup> or under a concentration gradient<sup>123</sup>.

### 3.1.1 Uniform Concentration Gradients (Fick's 1<sup>st</sup> law)

Atomic jumps can be achieved in the solid state with a rate  $\nu$  with each jump over a distance  $\lambda$ . For random jumps, the root mean square distance is

$$\bar{x} = \lambda\sqrt{n} = \lambda\sqrt{\nu t} \quad (3.1.1)$$

where  $n$  is the number of jumps,  $t$  is the time. The concentration of solute is  $C$  (atom/m<sup>3</sup>) and each plane has  $C \cdot \lambda$  (atoms/m<sup>2</sup>), (see Fig. 3.1.1).

$$\delta C = \lambda \left( \frac{\partial C}{\partial x} \right) \quad (3.1.2)$$

Thus, the atomic flux,  $J$  (atoms/(m<sup>2</sup>·s)), between left and right is

$$J_{L \rightarrow R} = \frac{1}{6} \nu C \lambda \quad \text{and} \quad J_{R \rightarrow L} = \frac{1}{6} \nu (C + \delta C) \lambda \quad (3.1.3)$$

Therefore, the net flux along  $x$  is given by

$$J_{\text{net}} = -\frac{1}{6} \nu \delta C \lambda = -\frac{1}{6} \nu \lambda^2 \left( \frac{\partial C}{\partial x} \right) = -D \left( \frac{\partial C}{\partial x} \right) \quad (3.1.4)$$

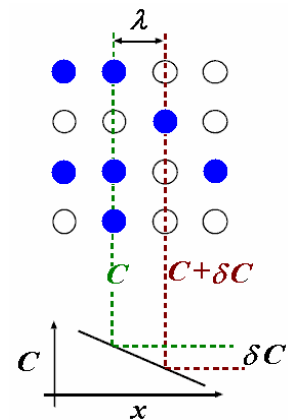


Fig. 3.1.1: Diffusion in a uniform concentration gradient.

This is Fick's first law where the constant of proportionality is called the tracer diffusion coefficient or diffusivity ( $\text{m}^2/\text{s}$ ). Fick's first law applies to steady state flux in a uniform concentration gradient. Thus, Eq. (3.1.1) can now be expressed in terms of the diffusivity as

$$\bar{x} = \lambda\sqrt{vt} \quad \text{with } D = \frac{1}{6}v\lambda^2 \quad \text{giving } \bar{x} = \lambda\sqrt{6Dt} \cong \sqrt{Dt} \quad (3.1.5)$$

### 3.1.2 Non-Uniform Concentration Gradients

If the concentration gradient is not uniform, Fig. 3.1.2, then

$$\text{Flux in} = -D\left(\frac{\partial C}{\partial x}\right)_1 \quad (3.1.6)$$

$$\text{Flux out} = -D\left(\frac{\partial C}{\partial x}\right)_2 = -D\left[\left(\frac{\partial C}{\partial x}\right)_1 + \delta x\left(\frac{\partial^2 C}{\partial x^2}\right)\right] \quad (3.1.7)$$

In the time interval  $\delta t$ , the concentration changes  $\delta C$

$$\delta t \delta C = (\text{Flux in} - \text{Flux out}) \delta t \quad (3.1.8)$$

$$\frac{\partial C}{\partial t} = D \frac{\partial^2 C}{\partial x^2} \quad (3.1.9)$$

This is Fick's second law of diffusion. This partial differential equation simplifies if  $D$  is constant and can be solved for particular initial and boundary conditions.<sup>124</sup> This allows one to determine  $D$  from measurements of concentration profiles  $c(x, t)$ .

This agrees with numerical solutions for the general case, but there are a couple of interesting analytical solutions for particular boundary conditions. For a case where a fixed quantity of solute is plated onto a semi-infinite bar, Fig. 3.1.3, the boundary conditions are

$$\int_0^{\infty} C(x, t) dx = B \quad \text{and} \quad C\{x, t=0\} \quad (3.1.10)$$

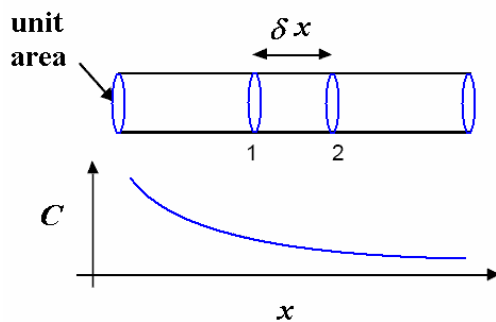


Fig. 3.1.2: Non-uniform concentration gradient

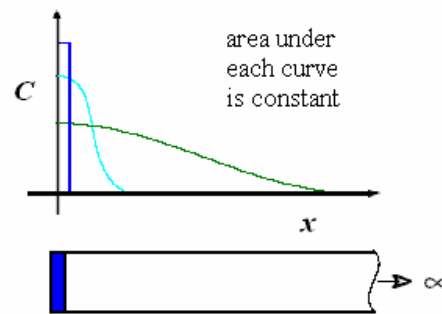


Fig. 3.1.3: Exponential solution. Note how the curvature changes with time.

$$C\{x,t\} = \frac{B}{\sqrt{\pi Dt}} \exp\left\{\frac{-x^2}{4Dt}\right\}. \quad (3.1.11)$$

The diffusion couple, illustrated in Fig. 3.1.4, can be made by stacking an infinite set of thin sources on the end of one of the bars. Diffusion can thus be treated by taking a whole set of the exponential functions obtained above, each slightly displaced along the  $x$  axis, and summing (integrating) up their individual effects. The integral is in fact the error function

$$\operatorname{erf}(x) = \frac{2}{\sqrt{\pi}} \int_0^x \exp(-u^2) du. \quad (3.1.12)$$

So the solution to the diffusion equation with the boundary conditions  $C(x=0, t) = C_s$  and  $C(x, t=0) = C_0$  is

$$C(x, t) = C_s - (C_s - C_0) \operatorname{erf}\left(\frac{x}{2\sqrt{Dt}}\right). \quad (3.1.13)$$

This solution can be used in many cases where the surface concentration is constant and the concentration profiles would be the same as in Fig. 3.1.4.

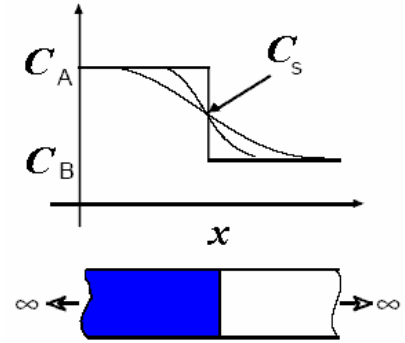


Fig. 3.1.4: The error function solution. Notice that the “surface” concentration remains fixed.

## 3.2 MECHANISMS OF DIFFUSION AND DIFFUSION COEFFICIENTS\*

Atoms in the solid-state migrate by jumping into vacancies (Fig. 3.2.1). There is a barrier to the motion of the atoms because the motion is associated with a transient distortion of the lattice. Assuming that the atom attempts jumps at a frequency  $\nu_0$ , the rate of successful jumps is given empirically by an Arrhenius relation

$$\nu = \nu_0 \exp\left\{-\frac{G^*}{k_B T}\right\} = \underbrace{\nu_0 \exp\left\{-\frac{S^*}{k_B}\right\}}_{\text{independent of } T} \times \exp\left\{-\frac{H^*}{k_B T}\right\} \quad (3.2.1)$$

where  $k_B$  and  $T$  are the Boltzmann constant and the absolute temperature respectively, and  $H^*$  and  $S^*$  the activation enthalpy and activation entropy respectively. As  $D \propto \nu$

$$\Rightarrow D = D_0 \exp\left(-\frac{H^*}{k_B T}\right) \quad (3.2.2)$$

A plot of the logarithm of  $D$  versus  $1/T$  should therefore give a straight line, the slope of which is  $-H^*/k_B$ .  $H^*$  is frequently called the activation energy for diffusion and is often designated by  $Q$ .

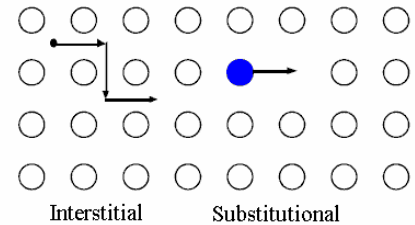


Fig. 3.2.1: Mechanism of interstitial and substitutional “vacancy” diffusion.

\* The last part of this section follows Ref. [7]

The activation enthalpy of diffusion can be separated into two components, the enthalpy of migration (due to distortions) and the enthalpy of formation of a vacancy in an adjacent site. For the atom to jump it is necessary to have a vacant site; the equilibrium concentration of vacancies can be very small in solids. Since there are many more interstitial vacancies, and since most interstitial sites are vacant, interstitial atoms diffuse far more rapidly than the “vacancy” or substitutional solutes. However, the most common mechanism is the vacancy mechanism.

At first sight, diffusion is difficult to appreciate for the solid state. A number of mechanisms have been proposed historically. This includes a variety of ring mechanisms where atoms simply swap positions, but controversy remained because the strain energies associated with such swaps made the theories uncertain. One possibility is that diffusion occurs by atoms jumping into vacancies. But the equilibrium concentration of vacancies is very small particularly at low temperatures. The theory was therefore not generally accepted until an elegant experiment by Smigelskas and Kirkendall.<sup>125</sup> The net effect is described by the usual Fick’s laws, but with an interdiffusion coefficient  $\bar{D}$  which is a weighted average of the two intrinsic diffusion coefficients

$$\bar{D} = x_B D_A + x_A D_B \quad (3.2.3)$$

where  $x$  represents a mole fraction. The interdiffusion coefficient is measured in most experiments. The tracer diffusion coefficient  $D$  can be defined by the Einstein-Smoluchowski relation<sup>126,127</sup>

$$D^T = \lim_{t \rightarrow \infty} \frac{\langle r^2(t) \rangle}{2dt} \quad (3.2.4)$$

Where  $\langle r^2(t) \rangle$  is the mean square displacement of the particles after the time  $t$ , and  $d$  is the dimensionality of the movement. The diffusion coefficient for uncorrelated jumps,  $D^{\text{uc}}$ , can be given by

$$D^{\text{uc}} = \frac{l^2}{2d\tau} \quad (3.2.5)$$

This can be related to the tracer diffusion coefficient by

$$D = f D^{\text{uc}} \quad (3.2.6)$$

$f$  is the correlation factor that equals 1 when the movement is purely random hopping, and  $0 < f < 1$ , when the correlated motion of the atoms has enhanced backward hopping probability.

The dc-conductivity,  $\sigma_{\text{dc}}$ , can be extracted and related to the diffusion coefficient  $D^\sigma$  by applying the Nernst-Einstein equation

$$D^\sigma = \frac{\sigma_{\text{dc}} k_B T}{N q^2} \quad (3.2.7)$$

$N$  here is the density of the charge carriers and  $q$  is their charge. The diffusion coefficient  $D^\sigma$  is related to the tracer diffusion coefficient  $D$  by

$$D = H_R D^\sigma \quad (3.2.8)$$

$H_R$  is the Haven ratio which gives information on whether the conductivity results from one charge carrier or a superposition of several contributions<sup>128,129</sup>.

### 3.3 IONIC CONDUCTORS

In many ionic solids, the transference number for one of the constituting ions approaches unity. A solid material that has a high ionic diffusivity or conductivity may be a good candidate for commercial application as solid electrolyte in state batteries or fuel cells. This technological importance of fast- or super-ionic conductors provided the motivation for studying their structure and dynamics<sup>130</sup>. Such research aims to enhance our understanding of the conduction mechanism and to determine the important factors for the production of better ionic conductors. Structural studies have shown that these materials often exhibit extensive disordering of the mobile ions amongst interstitial sites in the crystal structure, providing further evidence of the ionic nature of the conduction via a thermally activated hopping motion.

Ionic conductors have been intensively studied because of their interesting properties (partly solid like, partly liquid like). It has been noted<sup>131</sup> that in a material in which the cation is the mobile ion, the following conditions should be met: (i) There must be a large number of connected and vacant sites in the crystal structure. (ii) The difference in the energies of the cation-anion interactions on different sites should be small. (iii) The cations should be stable with a coordination number of 4 or less. (iv) The fast ion should be small and singly charged. The extent of the observed disorder and the energy barriers associated with hopping between the interstitial sites can be calculated from the measured conductivity. In the simplest case this leads to ohmic behavior in the bulk at moderate fields and the conductivity shows an exponential dependence on reciprocal temperature.<sup>132</sup> Impurity effects and structural transformations may complicate the picture considerably.<sup>130</sup>

### 3.4 STRUCTURE SENSITIVE DIFFUSION

The physical properties of nanocrystalline solids differ substantially from those of the coarser grained crystals of the same chemical composition. In particular, the nanocrystalline solids synthesized in non-equilibrium conditions exhibit anomalously enhanced diffusion. For instance, the self-diffusion coefficient in nanocrystalline face centered cubic materials (FCC) exceeds by two to four orders of magnitude the grain-boundary diffusion coefficient in microcrystalline FCC materials of the same chemical composition.<sup>133–135</sup> According to<sup>133</sup>, there are three factors that account for the enhanced diffusion in nanocrystalline solids: (i) Relaxation of grain-boundary regions is impeded in nanocrystalline solids due to the fact that the geometric conditions of relaxation of adjacent grain boundaries are usually poorly compatible because of the small nanocrystallite size. Such relaxation occurs through relative grain displacements and reduces the free volume of grain-boundary regions. (ii) In nanocrystalline solids, the volume fraction of triple grain-boundary junctions, where diffusion proceeds faster than in the usual grain boundaries, is extremely large. (iii) The concentration of impurities, which interfere frequently with grain-boundary diffu-

sion, is lower in nanocrystalline solids than in polycrystals.

Crystals may contain nonequilibrium concentrations of defects such as vacancies, dislocations and grain boundaries. These may provide easy diffusion paths through a perfect structure. Thus, the grain-boundary diffusion coefficient  $D_{gb}$  is expected to be much greater than the diffusion coefficient associated with the perfect structure,  $D_p$ . On the cross section of an assumed cylindrical grain, the area presented by a boundary is  $2\pi r\delta$  where  $\delta$  is the thickness of the boundary, (Fig. 3.4.1). However, the boundary is shared between two adjacent grains so the thickness associated with one grain is  $1/2 \delta$ . The ratio of the areas of grain boundary to grain is therefore

$$\text{ratio of areas} = \frac{1}{2} \times \frac{2\pi r\delta}{\pi r^2} = \frac{\delta}{r} = \frac{2\delta}{d} \quad (3.4.1)$$

where  $d$  is the grain diameter. For a unit area, the overall flux is the sum of that through the lattice and that

$$\text{through the boundary} \quad J \cong J_p + J_{gb} \frac{2\delta}{d} \Rightarrow D_{\text{measurd}} = D_p + D_{gb} \frac{2\delta}{d} \quad (3.4.2)$$

Although the diffusion through the boundary is much faster, the fraction of the sample present in the grain-boundary phase is usually small. Consequently, grain boundary or defect diffusion in general is only of importance at temperatures where  $D_p \ll D_{gb}$ , (Fig. 3.4.2).

### 3.5 TECHNIQUES FOR STUDING DIFFUSION<sup>7</sup>

Several experimental techniques are employed to probe diffusion in solid-state materials. Fig. 3.5.1 shows typical ranges of the diffusivity  $D$  and motional correlation time  $\tau_c$  for macroscopic and microscopic methods. Macroscopic methods are sensitive to long-range diffusion while microscopic methods give access to microscopic diffusion parameters like hopping rates of atoms or ions and the barrier heights for the jump processes. Following an alternative way of classification, these measurement techniques can be clas-

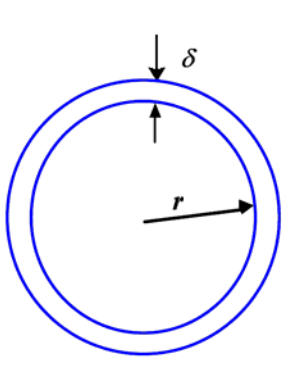


Fig. 3.4.1: A schematic plot of an idealized cylindrical grain.

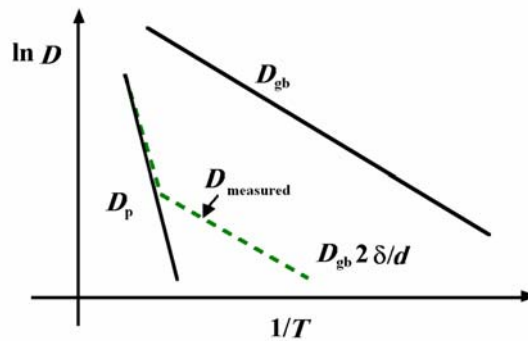


Fig. 3.4.2: Effect of grain-boundary diffusion on the diffusion of a perfect crystalline structure according to Eq 3.4.2.



sified to nuclear or non-nuclear methods. Nuclear methods are those which use radioactive or stable nuclei or elementary particles as probes. A combination of different techniques and experimental set-ups is usually of great advantage as the length scale for the probed diffusion processes may vary with the applied measurement frequency. Furthermore, this may enable the experimentalist to evaluate the correlation factor  $f$  that gives information about the observed diffusion mechanism<sup>136</sup>.

Tracer diffusion methods are macroscopic ones that may be sensitive to a radioactive or a stable isotope which can be tracked by its radioactive emission or mass. The tracer isotope is deposited on the surface of the sample. Then it is annealed at the temperature at which the diffusion coefficient is to be determined. Then the concentration profiles of the tracer are determined. For large penetration depths ( $> 1 \mu\text{m}$ ), classical radiotracer techniques can be used, while SIMS profiling can be applied for penetration depths  $< 1 \mu\text{m}$ , for more details see Sec 4.4.

In this work, diffusion in ceramics and glasses is studied by conductivity measurements, NMR line-shape and spin-lattice relaxation techniques, in addition to secondary-ion mass spectroscopy (SIMS) as an example of tracer diffusion methods. However, additional techniques like<sup>7</sup> QENS,  $\beta$ -NMR, muon spin resonance/relaxation ( $\mu\text{SR}$ ) spectroscopy or deuterium effusion experiments can give a deeper insight into the diffusion mechanisms.

### 3.6 THE MIXED-ALKALI EFFECT

The mixed-alkali effect (M.A.E.) can be defined as the noticeable deviation from linearity in the properties of alkali glasses with the addition of a second alkali. It has been observed in many glass systems as well as in certain porcelains, molten salts and salts and crystals.<sup>137–138</sup> Properties exhibiting the MAE usually show a minimum or a maximum with increasing concentration of the second alkali. The properties associated with alkali-ion diffusivity, such as electrical conductivity, dielectric loss, alkali diffusion, inter-

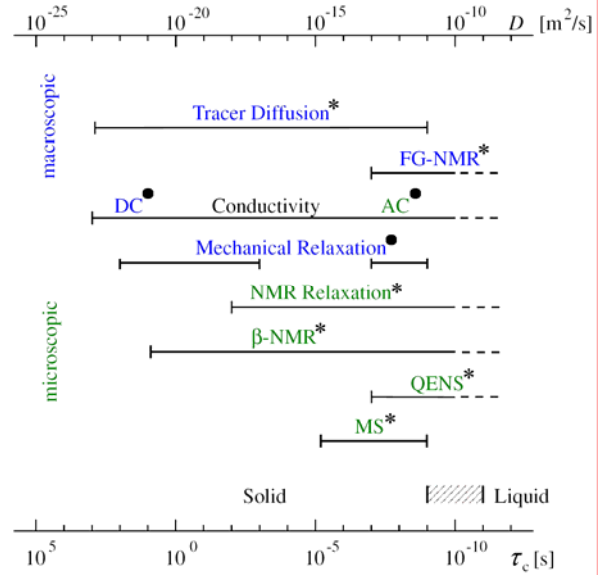


Fig. 3.5.1: Typical ranges of the diffusivity  $D$  and motional correlation time  $\tau_c$  of some macroscopic and microscopic methods used for studying diffusion in solids: field gradient NMR (FG-NMR),  $\beta$ -radiation-detected NMR ( $\beta$ -NMR), quasi-elastic neutron scattering (QENS), Mössbauer spectroscopy (MS). \* indicates nuclear methods while  $\bullet$  for non-nuclear ones. The dashed line indicates the transition from the solid to the liquid where the motional correlation time is reduced by about two orders of magnitude.

nal friction and chemical durability are the most affected by the MAE. Electrical conductivity has been observed to decrease by five orders of magnitude in a mixed-alkali glass<sup>139</sup>.

The MAE in properties that depend on alkali-ion movement is explained by the change in diffusion coefficients of alkali ions in a mixed-alkali glasses<sup>139</sup>. As an example, the diffusion coefficients of A and B ions,  $D_A$  and  $D_B$ , respectively, in a  $(1-x)A_2O \cdot xB_2O \cdot 3SiO_2$  glass will be discussed as a function of A to B ratio. The addition of a second alkali to an alkali glass always reduces the diffusion coefficient of the original ion, whatever the second alkali is. However, the magnitude of change in the diffusivity of the original ion, depends on the second alkali. The value of  $D_A$  of the A ion in  $A_2O \cdot 3SiO_2$  glass decreases with the addition of a second alkali, B. The greater the size difference between A and B the bigger the decrease in  $D_A$  (and  $D_B$  as well).

When the  $x_B \ll x_A$ , then  $D_B < D_A$ .  $D_A$  decreases as  $x_B$  increases, while  $D_B$  increases.  $D_A$  and  $D_B$  eventually cross at some alkali ratio, after which the  $D_B > D_A$ . The ratio of the two alkalis at the crossover point is dependent on the identity of the two alkalis present (i.e. their size ratio), the glass composition (i.e. total alkali concentration, identity of the glass former), and in some cases, temperature<sup>139,137</sup>.

The deviation from linearity of the diffusion coefficient of the individual ion is small; the deviation from linearity for the slowest ion and the fastest moving ion is significant. Properties controlled by alkali ion movement are usually determined by the diffusivity of the slowest or the fastest moving ion, and therefore exhibit a minimum or a maximum. Extremes in alkali ions movement related properties in mixed alkali systems are usually located around the crossover point. The question that remains unanswered is why the diffusivity of the original ion decreases in a glass, regardless of the identity of the second alkali. Several theories have been developed to explain the MAE, but none of them has been universally accepted. Initial models tried to explain the MAE in terms of phase separation and grouping of atoms in regions. Mazurin<sup>140</sup> proposed that the MAE results from the effect of the polarizability of the non-bridging oxygens on the alkali-ion diffusivity. Another model was based on specific diffusion pathways of the alkalis in glass<sup>141</sup>. Stevels<sup>142</sup> attempted to define the MAE in terms of glass structure. He hypothesized that a random network of silicon-oxygen tetrahedra could geometrically incorporate ions of different sizes easier than ions of the same size. The resulting binding energy of the ions to the structure and hence the activation energy for diffusivity, were higher because of a more stable structure. The MAE according to Hendrickson and Bray<sup>143,144</sup> results from an electrodynamic interaction between unlike neighboring ions in a glass. The electrodynamic interaction, which results from the coupling of vibrations of dissimilar neighboring ions, leads to the splitting of vibrational energy levels with most of the ions occupying the lower energy state. The increased stability in the bond leads to an increase in the energy required for the diffusion of the ions. Tomandl and Schaeffer's<sup>145</sup> model combined the Hendrickson and Bray model mathematically with pathway specific models.

LaCourse<sup>146</sup> used a site specific diffusion approach, where alkali ions of one type can only exist in sites occupied by similar ions. Diffusion of these ions occurs by the formation of "mixed-alkali defects" which

result when an ion of one type occupies a site of the second ion and vice versa. The reduction of alkali diffusivity in this case results because of the need for high energies to form the mixed-alkali defect.

Tomozawa<sup>147</sup>, using a thermodynamic approach, attributes the mixed-alkali effect to an increase in activation energy that results from the negative enthalpy associated with mixing of the alkalis. Tomozawa and McGahay<sup>148</sup> claim that the MAE in conductivity is limited to dc measurements since conductivity measurements at high frequencies fail to exhibit the MAE. The MAE arises from the difference in dielectric relaxation strength between single and mixed-alkali glass.

Non-transport properties such as the glass transition temperature, thermal expansion coefficient and density also exhibit the mixed-alkali effect<sup>139</sup>. The deviation from linearity in density and thermal expansion are relatively small ( $\leq 10\%$ ). Deviation from linearity in properties that do not depend on alkali movement have been observed in several systems. Significant deviations from linearity have been noted in the glass transformation temperatures of mixed-alkali galliosilicate<sup>149,150</sup>, borate<sup>151</sup>, and germinate<sup>152</sup> glasses. The thermal expansion coefficient may exhibit a positive deviation from linearity in some systems like in sodium potassium borate glasses, sodium potassium, and sodium rubidium germinates. Other glasses can exhibit a negative deviation as in the case of sodium cesium germinate.



# 4 Principles of Probing Techniques

## 4.1 DIELECTRIC RELAXATION AND IMPEDANCE SPECTROSCOPY

### 4.1.1 Method and Expressions for Presentation of Dielectric Data

The dielectrics science combines the fields of physics, chemistry and electrical engineering. The motivation for chemists is to track the dielectric relaxation and to use it as a probe on molecular dynamics and to utilize both the temperature dependence of the permittivity at constant frequency and its frequency dependence at constant temperature to monitor diffusion processes, the progress of chemical reactions or the nonlinear behavior of some materials such as ferroelectrics.

Relaxation is the recovery of strain upon sudden removal or sudden application of a steady stress. This process implies a time dependence which can be measured in the time-domain (TD) measurement<sup>153</sup>. Alternatively the material can be subjected to a harmonically varying stress of an angular frequency ( $\omega$ ) in the frequency-domain (FD) measurements<sup>154</sup>. In materials responding linearly with respect to the amplitude of the applied signal, TD and FD responses are Fourier transforms of one another

$$\chi'(\omega) = \int_0^{\infty} f(t) \cos(\omega t) dt, \quad \chi''(\omega) = \int_0^{\infty} f(t) \sin(\omega t) dt \quad (4.1.1)$$

$$f(t) = (2/\pi) \int_0^{\infty} \chi'(\omega) \cos(\omega t) d\omega = (2/\pi) \int_0^{\infty} \chi''(\omega) \sin(\omega t) d\omega \quad (4.1.2)$$

The TD response is the variation of the current in time and thus it is a real function  $f(t)$ . FD response defines two components of amplitude variation in phase and in quadrature with respect to the driving harmonic signal and has to be defined as real and imaginary functions  $\chi'(\omega)$  and  $-i \chi''(\omega)$  of the real fre-

quency variable, where  $\omega = 2\pi\nu$  is the angular frequency,  $\nu$  is the circular frequency (Hz) and  $i = \sqrt{-1}$ .

Relaxation phenomena in the FD involve a fortune of information in comparison with the static measurement. It can be presented in various ways and it is important to choose the most suitable method of presentation for particular requirements. The following dielectric functions may be defined:

(a) The complex permittivity  $\varepsilon^*(\omega)$  and susceptibility  $\chi^*(\omega)$ ,

$$\chi^*(\omega) \equiv \frac{\varepsilon^*(\omega) - \varepsilon_\infty}{\varepsilon_0} = \chi'(\omega) - i\chi''(\omega). \quad (4.1.3)$$

$\varepsilon_0 = 8.854 \times 10^{-12}$  F/m is the free space permittivity,  $\varepsilon_\infty$  is the high-frequency permittivity and the physical emphasis is on *parallel* processes contributing to the real and imaginary components of the polarization.

(b) The dielectric modulus, which emphasizes *series* processes.

$$M^*(\omega) = M'(\omega) + iM''(\omega) = \frac{1}{\varepsilon^*(\omega)} = \frac{\varepsilon'(\omega) + i\varepsilon''(\omega)}{[\varepsilon'(\omega)]^2 + [\varepsilon''(\omega)]^2} \quad (4.1.4)$$

(c) The complex capacitance relates to a sample of planar geometry of area  $A$  and thickness  $l$ .

$$C^*(\omega) = \frac{A}{l} \cdot \varepsilon^*(\omega) \quad (4.1.5)$$

The susceptance is the quantity corresponding to susceptibility; both are recommended wherever the geometry of the sample is not well defined. They emphasize *parallel* processes acting in the sample.

$$\chi^*(\omega) = C^*(\omega) - C_\infty, \quad (4.1.6)$$

(d) The impedance of the sample is a complex number that is a generalized proportionality constant between voltage ( $V$ ) and current ( $I$ ), and represents the equivalent *series* resistance  $R$  and reactance  $X$ .

$$Z^*(\omega) = \frac{V}{I} = R(\omega) + iX(\omega) \quad (4.1.7)$$

(e) The admittance, the reciprocal of the impedance, represents the equivalent *parallel* conductance  $G(\omega)$  and capacitance  $C(\omega)$

$$Y^*(\omega) = I/V = i\omega C^*(\omega) \equiv G(\omega) + i\omega C(\omega). \quad (4.1.8)$$

There are several ways of presenting the previous dielectric functions and the most common ones are:

(1) Plots of the real and imaginary components (in logarithmic or in linear coordinates) vs. frequency or even the magnitude of the quantity and its phase angle vs. the frequency which is known as bode plots, Fig. 4.1.2(b) and Fig. 4.1.4(b). The (log-log) form is particularly useful in representing dielectric functions which are often power-law functions of frequency which is referred to as the ‘universal’ law

$$\chi^*(\omega) \propto (i\omega)^{n-1}, \quad (4.1.9)$$

where  $0 < n < 1$  in the frequency region above any loss peaks.

(2) Polar plots of the imaginary component against the real component, on a linear presentation typically, and called complex plane plots, Fig. 4.1.2(a) and Fig. 4.1.4(a).

### 4.1.2 Basics of Impedance Spectroscopy <sup>155-157</sup>

The introduction of Electrochemical impedance spectroscopy (EIS) concept occurred in the 1880s by O. Heaviside. Its development in terms of vector diagrams and complex representation was done by A. E. Kennelly and C. P. Steinmetz. Two of the more detailed works about impedance spectroscopy are Digby D. Macdonald's "Transient Techniques in Electrochemistry" <sup>158</sup> and J. Ross Macdonald's "Impedance spectroscopy" <sup>155</sup>.

EIS is a very powerful technique that is widely used in studying the conductivity of electronic, ionic, as well as mixed conductors. EIS deals with the theory of interpreting equivalent resistance and capacitance values with respect to various fields such as surface engineering, corrosion research, electrochemical power generation, catalysis, diffusion and electrochemical basis research <sup>160-159</sup>. EIS is one of the potential sweep methods in which a large perturbation is applied to the system. The working electrode is driven to a condition far from equilibrium. Then the response is measured. Another approach is the application of an alternating perturbation potential of small amplitude at a fixed direct current (dc) bias potential. Then the system follows the perturbation at steady state <sup>160</sup>. Perturbation of the cell by alternating voltage or alternating current (ac) has several advantages. Once ac flows, one has to distinguish between purely ohmic resistance and the frequency dependent resistances (impedances). Investigation of the frequency dependence of the electrode reactions allows the separation of different contributions <sup>161</sup>. The small magnitude of the signal induces a linear current-voltage dependence, which allows the theoretical treatment of the response by linearized current-potential characteristics <sup>160</sup>. The wide frequency range scanned ( $10^{-4} - 10^{12}$  Hz) allows eliciting responses corresponding to the various processes which occur with different rate constants in the cell. As an example in solid ceramic samples, the resistance of grain boundaries and that of the grain interiors can be separated in many cases. Furthermore, EIS gives a vast amount of data in a short period of time, from a very simple experimental setup. Furthermore the measurement can be implemented using a variety of electrodes suitable for different purposes.

In EIS, the applied ac monochromatic voltage signal differs from the DC one in having a magnitude, frequency and a phase which are commonly combined into one complex number using the Euler formula

$$e^{i\omega t} = \cos \omega t + i \sin \omega t \quad (4.1.10)$$

thus, the voltage will be 
$$V(t) = V_0 \sin(\omega t) = V_0 e^{i\omega t} \quad (4.1.11)$$

This voltage is driving a circuit with various circuit elements connected in series, Then the current response will be

$$I(t) = I_0 \sin(\omega t - \varphi) = I_0 e^{i(\omega t - \varphi)} \quad (4.1.12)$$

where  $\varphi$  is the phase difference between the voltage and the current. This phase angle is zero for purely resistive behavior. Substituting for  $V(t)$  and  $I(t)$  in (4.1.7) gives

$$V_0 e^{i\omega t} = Z \cdot I_0 e^{i(\omega t - \varphi)} = Z \cdot I_0 e^{i\omega t} e^{-i\varphi} \quad (4.1.13)$$

The time dependent exponential can be eliminated from both sides to find that  $V_0 = Z \cdot I_0 e^{-i\varphi}$ .

### 4.1.2.1 Series and parallel circuits

When circuit elements are connected *in series*, the total impedance is the sum of the individual impedances of each element,

$$Z_T = Z_1 + Z_2 + Z_3 + \dots \quad (4.1.14)$$

and

$$I_0 = V_0 / |Z_T| \quad \text{and} \quad \varphi = \delta \quad (4.1.15)$$

On the other hand, the total admittance for circuit elements *in parallel* is the sum of the individual admittances,

$$Y_T = Y_1 + Y_2 + Y_3 + \dots \quad (4.1.16)$$

So the amplitude and phase of the current response are

$$I_0 = V_0 \cdot |Y_T| \quad \text{and} \quad \varphi = -\delta \quad (4.1.17)$$

In EIS, a purely electronic model can be applied to simulate the behavior of the electrochemical cell in the measurement frequency range. The undergoing processes in the sample like slow electrode kinetics, slow preceding reactions, and diffusion can all be considered analogous to specific electronics elements or a combination of them that impede the flow of electrons in an ac circuit. The most encountered elements are ohmic resistance, capacitor, and inductors which are shown in Table 4.1.1 with their frequency response, applications and complex plane impedance plots. In practice, the obtained impedance plot can be correlated with one or more equivalent circuits. Accordingly a suitable mechanistic model can be chosen for the system or at least the incorrect models can be ruled out. When we have an ac circuit with several elements that are in parallel and series, first the equivalent admittance for any parallel elements should be found and followed then by the total impedance for the series elements.

In an ideal ac capacitor circuit, where the resistance of the dielectric is assumed to be infinite, the impedance ( $Z_C$ ) can be denoted, (as shown in Table 4.1.1

$$Z_C = -i/\omega C \quad \text{and} \quad \varphi = -90^\circ \quad (4.1.18)$$

The current leads the voltage by  $90^\circ$ , and the average work done by the circuit ( $I \cdot V$ ) is zero.

### 4.1.2.2 Series RC circuits

A series circuit provides only one route for the current to flow between two points in a circuit, Fig. 4.1.1(a) shows a resistor in series with a capacitor between the points A and B. In ac analysis both the resistor and capacitor are treated as phasor quantities, so  $X_C$  is  $-90^\circ$  out of phase from the perturbing voltage signal and therefore is expressed in complex form as

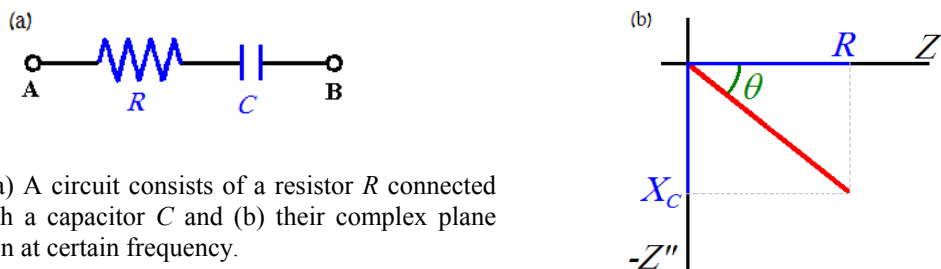


Fig. 4.1.1: (a) A circuit consists of a resistor  $R$  connected in series with a capacitor  $C$  and (b) their complex plane representation at certain frequency.



$$X_C = -iX_C \quad (4.1.19)$$

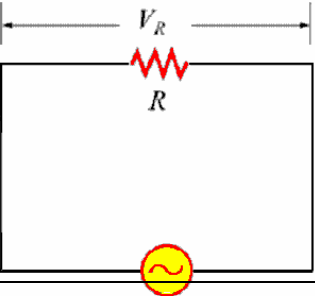
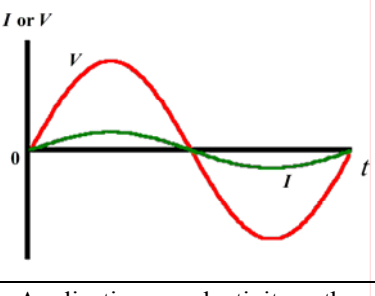
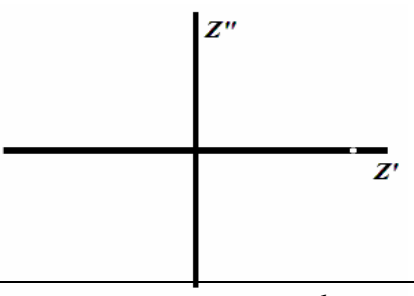
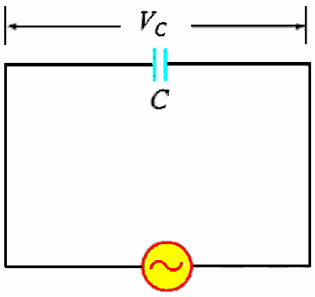
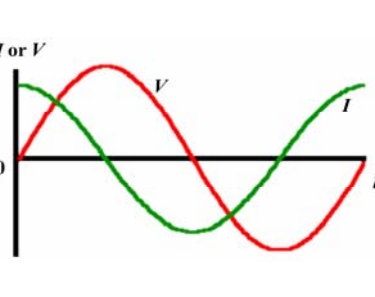
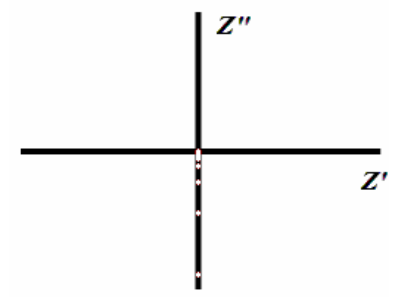
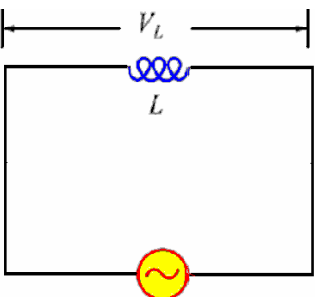
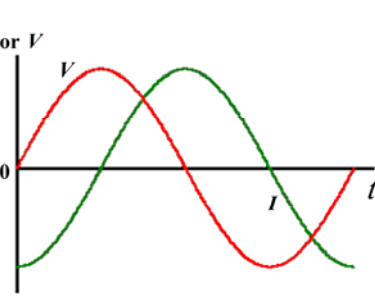

Since  $Z$  is a phasor sum the result is presented on a complex plane diagram, Fig. 4.1.1(b). The total impedance of this circuit is the contribution from both the capacitor and resistor.

$$Z^* = R - iX_C \quad (4.1.20)$$

The magnitude of the impedance, the length of vector, can be calculated using

$$|Z| = \sqrt{R^2 + X_C^2}$$

Table 4.1.1: Different circuit elements, their symbols, frequency response of the of  $V(t)$  and  $I(t)$  in their circuits and the complex plane impedance plots.

	circuit component	frequency response	complex plane impedance
Resistance ( $R$ )			
	$V = Z_R \cdot I, \quad \varphi = 0$	Application: conductivity path (electrolyte resistance, charge transfer resistance)	$Z_R = R \quad Y_R = \frac{I}{R}$
Capacitor ( $C$ )			
	$I = C \cdot \left(\frac{dV}{dt}\right), \quad \varphi = -90^\circ$	Application: double layer (adsorption)	$Z_C = -\frac{i}{C\omega} \quad Y_C = iC\omega$
Inductor ( $L$ )			
	$V = L \cdot \left(\frac{dI}{dt}\right), \quad \varphi = 90^\circ$	Application: voltage built up due to self induction in current carrying conductors	$Z_L = iL\omega \quad Y_L = -\frac{i}{L\omega}$

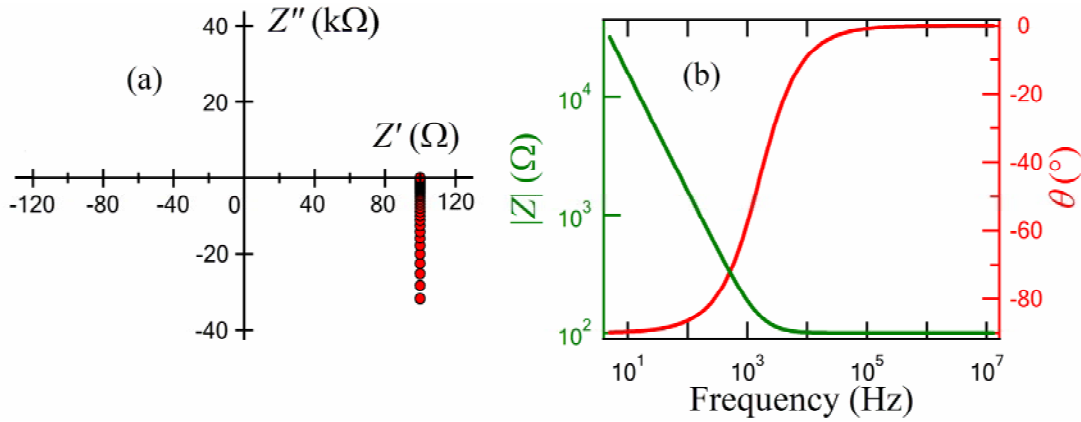


Fig. 4.1.2: The response of series  $RC$  circuit with changing frequency, (a) the complex plane diagram, (b) the Bode plots. (real example for  $R=100\ \Omega$  and  $C=1\ \mu\text{F}$  in the frequency range 1 Hz-10 MHz)

and the phase factor is given by 
$$\varphi = -\tan^{-1}(X_C/R) \quad (4.1.21)$$

However, as the frequency is altered both the magnitude and the phase will change. The obtained response will resemble that in Fig. 4.1.2 shown in both representations complex plane impedance diagram (a), and in bode plots (b). The modulus and phase are given by

$$|Z_T| = \sqrt{R^2 + \left(\frac{1}{\omega C}\right)^2} \quad \text{and} \quad \delta = \tan^{-1}\left(-\frac{1}{\omega CR}\right) \quad (4.1.22)$$

The total impedance is 
$$Z_T = Z_R + Z_C = |Z_T| e^{i\delta} \quad (4.1.23)$$

The voltage and current (as complex numbers) are,

$$V_o e^{i\omega t} = |Z_T| e^{-i\delta} I_o e^{i\omega t} e^{-i\varphi} \quad (4.1.24)$$

We solve for the amplitude and phase of the current response just as in the previous case,

$$I_o e^{-i\varphi} = \frac{V_o}{|Z_T|} e^{-i\delta} \quad (4.1.25)$$

Comparing these complex numbers we see that

$$I_o = \frac{V_o}{|Z_T|} = \frac{V_o}{\left(R^2 + (1/\omega C)^2\right)^{1/2}} \quad \text{and} \quad \varphi = \delta = \tan^{-1}\left(\frac{-1}{\omega CR}\right) \quad (4.1.26)$$

where for the phase factor  $-\pi/2 < \varphi < 0$  holds.

#### 4.1.2.3 Resistors and capacitors in parallel

In a real circuit, the dielectric has a finite resistance. This circuit can be modeled with an ideal capacitor and an ideal resistor in parallel, Fig. 4.1.3. Here, the current has alternative pathways to follow and the route taken depends upon the relative 'resistance' of each branch. The voltage across the capacitor and the resistor equals the voltage between the points A and B and can be given by

$$V_C = V_R = V_0 e^{i\omega t} \quad (4.1.27)$$

The current through the capacitor is

$$I_C = \frac{dQ(t)}{dt} = \frac{d(CV(t))}{dt} = C \left( \frac{dV_0 e^{i\omega t}}{dt} \right) = i\omega C V_0 e^{i\omega t} \quad (4.1.28)$$

and that through the resistor is

$$I_R = \frac{V_0 e^{i\omega t}}{R} = \frac{V(t)}{R}. \quad (4.1.29)$$

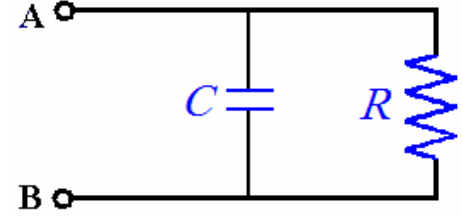


Fig. 4.1.3: A circuit of a resistor ( $R$ ) connected in parallel with a capacitor ( $C$ ).

The net current flow is equal to the sum of  $I_C$  and  $I_R$ , and is no longer out of phase with the voltage by  $90^\circ$ . The current through the resistor is lost to the system as heat. The angle of deviation of the current from  $90^\circ$  is denoted by  $\delta$ , and  $\tan \delta$  is known as the dissipation factor.

The total current is

$$I_{tot} = I_R + I_C = \frac{V(t)}{R} + i\omega C V(t). \quad (4.1.30)$$

To calculate the total impedance (resistance) of this circuit we use the capacitive reactance  $X_C$  as the equivalent resistance of the capacitor. Then we use the rules for summing resistors in parallel remembering that now we are dealing with phasor quantities.  $Z$ , the complex impedance, is defined as the ratio between the voltage and current, which is here

$$Z^* = \frac{V(t)}{\left( \frac{V(t)}{R} \right) + i\omega C V(t)} = \frac{1}{\left( \frac{1}{R} \right) + i\omega C} \quad (4.1.31)$$

The impedance can be separated into its real,  $Z'$ , and imaginary,  $Z''$ , parts to give

$$Z^* = \frac{\frac{1}{R}}{\left( \frac{1}{R} \right)^2 + (\omega C)^2} - i \frac{\omega C}{\left( \frac{1}{R} \right)^2 + (\omega C)^2} \quad (4.1.32)$$

The impedance magnitude and phase angle is given by the following

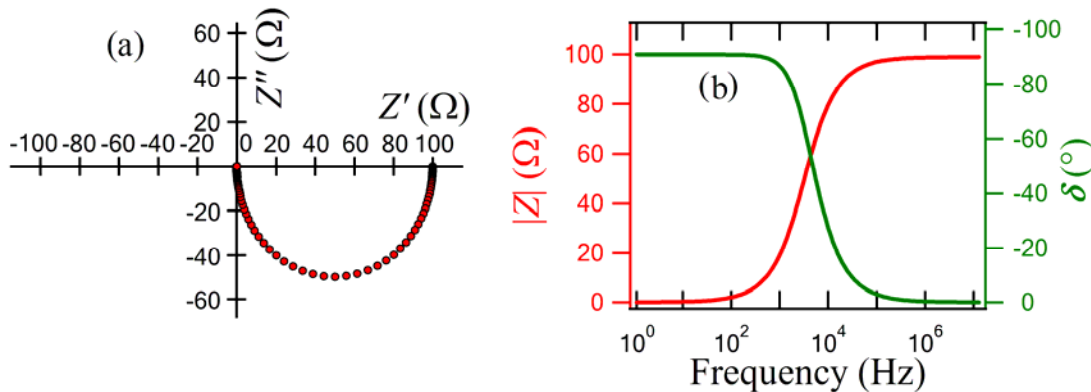


Fig. 4.1.4: The response of  $RC$  parallel circuit with changing frequency: (a) complex plane plot revealing a semi-circle in the fourth quadrant, (b) Bode plots.

$$|Z| = \frac{R \cdot X_c}{\sqrt{R^2 + X_c^2}} \text{ and } \delta = \tan^{-1} \left( \frac{R}{X_c} \right). \quad (4.1.33)$$

The phase angle is seen to change from  $0^\circ$  at low frequencies where the current flows almost completely through the resistor arm to  $-90^\circ$  at high frequencies where the current flow is through the branch containing the capacitor. The frequency response of this type of circuit is shown in Fig. 4.1.4 using the complex plane diagram (a) and the Bode plots (b).

The most familiar is a plot of  $Z'$  vs.  $Z''$  (as parametric functions of  $\omega$ ) will result in a semicircle of radius  $R/2$  in the fourth quadrant. The time constant of this simple circuit is defined as

$$\tau_0 = RC = \frac{1}{\omega_0} \quad (4.1.34)$$

and corresponds to the characteristic relaxation time of the sample. Substituting  $\omega_0$  from Eq. (4.1.34) into Eq. (4.1.32) gives  $Z' = R/2$ ,  $Z'' = R/2$ , so that the characteristic frequency lies at the peak of the semi-circle, Fig 4.1.4(b). The impedances of  $RC$  circuits are summarized in Table 4.1.2.

Table 4.1.2: Comparison between the impedance  $Z^*$  of a resistor ( $R$ ) and a capacitor ( $C$ ) connected in series (s) and in parallel (p)

Series	Parallel
$Z^* = Z' + Z'' = R_s + 1/i\omega C_s$	$Y^* = Y' + Y'' = 1/Z^* = 1/R_p + i\omega C_p$
$R_s = Z'$ , $C_s = 1/(Z'' \cdot i\omega)$	$R_p = 1/Y'$ , $C_p = Y''/(i\omega)$

From the calculated value of capacitance one infers the dielectric constant by capacitance of parallel plate samples

$$C = \epsilon' \epsilon_0 \frac{A}{l}. \quad (4.1.35)$$

This formula is an approximation based on the assumption that all of the electromagnetic flux is directly from one electrode to the other and that there is no stray capacitance through the surrounding air from one electrode to the other (fringing capacitance) which can be a serious problem with low permittivity samples and samples with thick geometries.

There are other circuit elements which are used in special cases like the Warburg impedance which is applied in cases of linear diffusion of reactants and contains information about reaction parameters and the diffusion coefficient and the constant phase element.<sup>255</sup>

#### 4.1.2.4 The constant phase element

The constant phase element (CPE) is a circuit element invented while looking at the response of real-world systems where the complex impedance plane plot was an arc of a circle with its centre some distance below the  $x$ -axis. These depressed semicircles are explained by several phenomena; however, all the explanations indicate a kind of inhomogeneity or some distribution (dispersion) of the value of some

physical property of the system.

Its admittance is given by 
$$Y_{\text{CPE}} = Q^\circ (i\omega)^\alpha \quad (4.1.36)$$

where  $Q^\circ$  is the admittance at  $\omega = 1$  rad/s. Thus, the phase angle of the CPE impedance is independent of the frequency and has a value of  $-(90 \cdot \alpha)^\circ$  and this gives the CPE its name. When  $\alpha = 1$ , this is the same equation as that for the impedance of a capacitor, where  $Q^\circ = C$ .

$$1/Z = Y = i\omega Q^\circ = i\omega C \quad (4.1.37)$$

When  $\alpha$  is close to 1.0, the CPE resembles a capacitor, but the phase angle is not  $-90^\circ$  but less at all frequencies. If the exponent,  $\alpha$ , is not close to 1.0, the value of  $Q^\circ$  should be the capacitance value<sup>162</sup>.

The impedance of an equivalent circuit for parallel connection of CPE and  $R$  can be expressed by<sup>163</sup>

$$Z(\omega) = \frac{R}{1 + (i\omega CR)^\alpha} \quad (4.1.38)$$

The differential capacity,  $C_{\text{diff}}$ , derived from Eq. (4.1.44.38) is

$$C_{\text{diff}} = (C_{\text{dl}})^\alpha (\omega R)^{\alpha-1} \sin(\alpha\pi/2) \quad (4.1.39)$$

$$Z' = \frac{R[1 + (\omega CR)^\alpha \cos(\alpha\pi/2)]}{1 + 2(\omega CR)^\alpha \cos(\alpha\pi/2) + (\omega CR)^{2\alpha}} \quad (4.1.40)$$

and

$$Z'' = \frac{R(\omega CR)^\alpha \sin(\alpha\pi/2)}{1 + 2(\omega CR)^\alpha \cos(\alpha\pi/2) + (\omega CR)^{2\alpha}} \quad (4.1.41)$$

For many real metal or solid electrodes, the measured impedance in the double-layer region (no faradaic current) follows a power law, such as that for the CPE, with a value of  $\alpha$  between 0.9 and 1. The phase angle of this "capacitance" is not  $-90^\circ$ , but is given by  $-(\alpha \cdot 90^\circ)$ . The observed angle is something between  $-80^\circ$  ( $\alpha = 0.89$ ) and  $90^\circ$  ( $\alpha = 1$ ). When this "capacitance" is in parallel with a charge-transfer resistance ( $R$ ), the complex plane plot is an arc of a circle, with the center of the circle below the  $x$ -axis. i.e., it is the "depressed semi-circle" shown in Fig. 4.1.5(a). This behavior is not seen on a mercury electrode

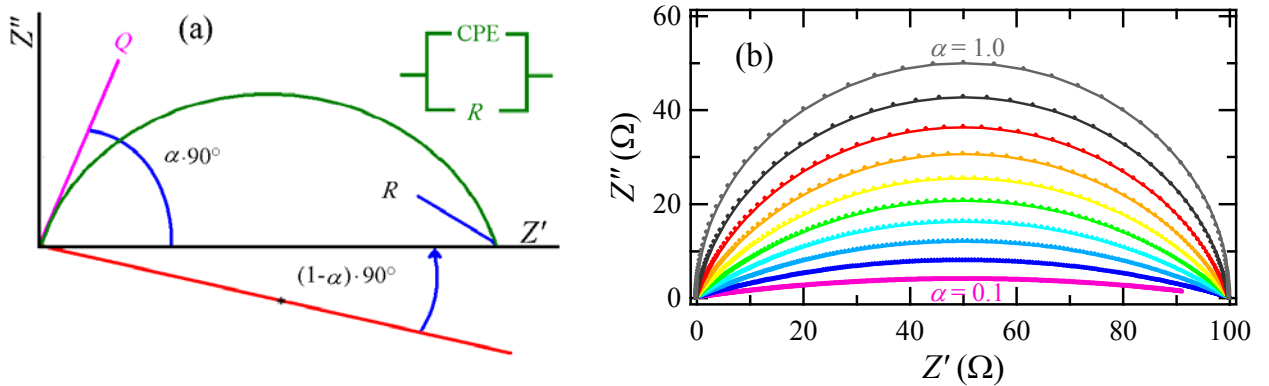


Fig. 4.1.5: The complex impedance plane plot for: (a) a CPE connected in parallel to a resistor ( $R$ ); for a solitary CPE ( $Q$ ) is a straight line which makes an angle of  $(\alpha \cdot 90^\circ)$  with the  $x$ -axis and the ( $RQ$ ) circuit is represented by the green semicircle with its centre being depressed by an angle of  $(1 - \alpha) \cdot 90^\circ$ ; (b) similar circuit with different values of CPE ranging from 0.1 to 1.0 obtained from Eqs (4.1.40-41) with the values of  $C = 1 \times 10^{-4}$  F and  $R = 100 \Omega$ .

because, as a liquid, it is atomically smooth.

One physical explanation for CPE behavior is electrode roughness where the fractal dimension ( $D$ ) of the surface is between 2 and 3; 2 for an absolutely flat surface (fills between 2 dimensions), and it is 3 for a surface branching through space when filling three dimensions and resembling a porous cube. It has been shown that for these electrodes, the interfacial impedance (electron transfer or double layer capacitance) is modified by an exponent,  $\alpha = 1/(D - 1)$ . For a smooth surface  $D$  is 2 and  $\alpha = 1$ . The impedance is unchanged. For a highly contorted surface we have  $D = 3$ , and  $\alpha = 0.5$ <sup>164</sup>.

Another explanation is inhomogeneous reaction rates on a surface, such as might be seen at polycrystalline metal surfaces or carbon electrodes with a distribution of active sites (with varying activation energies) on the surface.

A third possible explanation may be varying thickness or composition of a coating. For example, if the bulk conductivity of a coating changes with distance through the coating, then the resultant impedance spectrum can closely approximate that of a CPE.

MacDonald, *et al.*<sup>155</sup> indicated that in spite of the absence of a particular theory that explains the CPE behavior exactly, mostly CPE behavior fits the experimental data very well. This is increasingly true as the complexity of a circuit model grows. In short, a CPE can provide a useful modeling element, even if the true nature of the system is unknown.

### 4.1.3 Dielectric Behavior of Ceramic Materials

A dielectric material is an insulator that increases the charge storage capacity of a capacitor. The increase in the amount of charge stored is dependent on the dielectric constant of the material, which in turn is dependent on its polarizability<sup>59</sup>. The polarizability of a material is determined by contributions from various polarization mechanisms, including electronic polarization, ionic polarization, dipole polarization, and space charge polarization. Dipole polarization plays a significant role in the ferroelectric materials. Of these mechanisms, electronic and ionic polarizations are important in ceramic materials. Electronic polarization results from the shifting of the electron cloud of an atom in response to the applied field, while ionic polarization results from the movement of ionic species in the material under the influence of a field. Both mechanisms are frequency-dependent. Electrons can respond to frequencies up to  $10^{16}$  Hz, and ions to frequencies up to  $10^{12}$  Hz (Dielectric relaxation will be discussed in detail in Sec. 4.1.5).

There are several models for an electrolyte under an applied voltage. The most common one is a resistor and CPE in parallel, as shown in Fig. 4.1.5(a). In an ideal polycrystalline sample, the complex plane plot exhibits an arc at high frequency, a second arc at intermediate frequencies, and a linear portion at the lowest frequencies which may be a part of a large arc, as shown in Fig. 4.1.6, with the corresponding equivalent circuit model shown at the top of the figure. Three parallel RC circuits are lumped together. The first circuit is assigned to represent the grain interior behavior "gi", the second one the grain-boundary

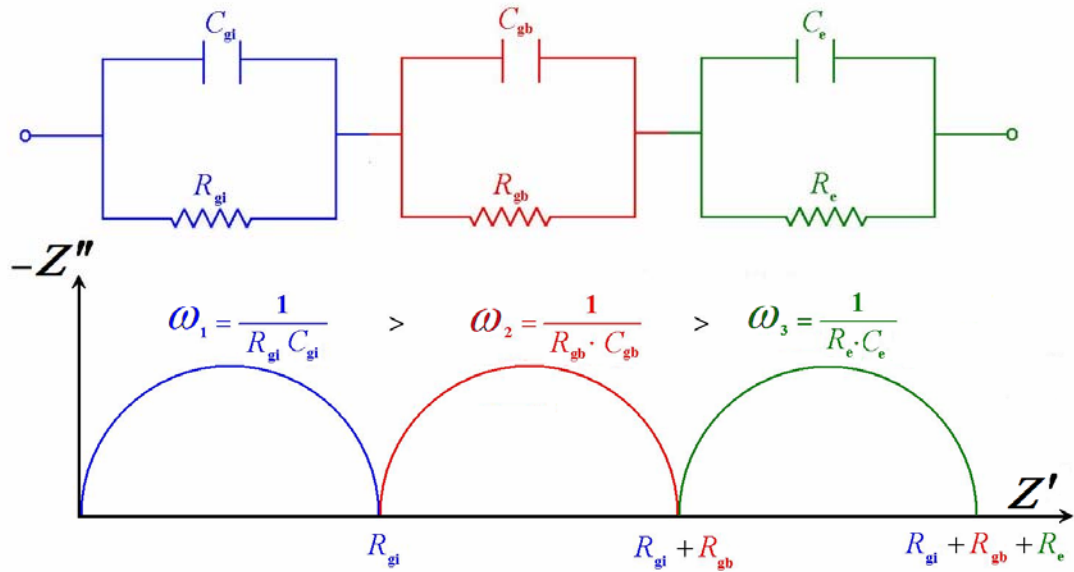


Fig. 4.1.6: Expected equivalent circuit model (top) and complex plane diagram (bottom) of a nanocrystalline material in which the parallel  $RC$  circuits have been lumped together.

behavior "gb", while the third one is the electrode behavior "e".

The measurement of the bulk conductivity is straightforward from the complex plane plot, while the measurement of specific grain-boundary conductivity requires knowledge of the grain size and grain-boundary thickness. In order to determine the grain-boundary conductivity without detailed microstructural and electrical information, one can adopt a "brick layer model" in which the grains are assumed to be cube-shaped, and grain boundaries to exist as flat layers between grains. This is sketched in

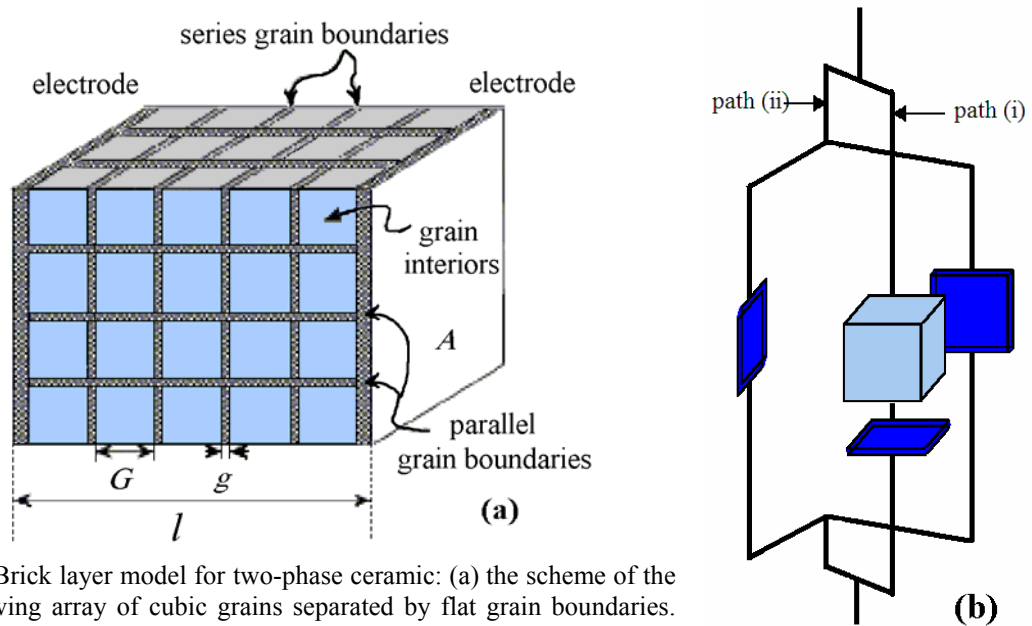


Fig. 4.1.7: Brick layer model for two-phase ceramic: (a) the scheme of the model showing array of cubic grains separated by flat grain boundaries. (b) Exploded view of a single cell showing parallel electrical paths: (i) through the grains and grain boundaries, (ii) along the grain boundaries.

Fig 4.1.7(a), where  $l$  is the sample length,  $A$  is the sample cross-sectional area,  $G$  is the edge length of the grains and  $g$  is the grain-boundary thickness. The implication of the “brick-layer model” and its application is discussed in detail in Ref. [157]. Here we list some of the conclusions.  $\sigma_{\text{gi}}$  and  $\sigma_{\text{gb}}$  are defined as the specific conductivity of the bulk and grain boundary, respectively. Depending on their relative magnitudes, one of the two paths may dominate, Fig 4.1.7(b). For the situation where  $\sigma_{\text{gi}} \gg \sigma_{\text{gb}}$ , the conductivity along the grain boundaries (path ii) is negligible, and the conduction through the grains and across the grain boundaries dominates. The behavior can be described by

$$\rho_{\text{tot}} = \rho_{\text{gi}} + \frac{x_{\text{gb}}}{3} \rho_{\text{gb}} \quad (4.1.42)$$

where  $\rho$  is the resistivity and  $x$  is the mole fraction. On the other hand, when  $\sigma_{\text{gi}} \ll \sigma_{\text{gb}}$ , conduction along the grain boundaries is dominant. The complex conductivity  $\psi$  is given by

$$\psi_{\text{tot}} = \psi_{\text{gi}} + \frac{2}{3} x_{\text{gb}} \psi_{\text{gb}} \quad (4.1.43)$$

#### 4.1.4 Measurement Methods (A Summary of Capacitance Bridge Functioning)

All the capacitance bridges apply a known voltage to the high side of the sample and a known current to the low side of the sample, Fig. 4.1.8. Then the current is adjusted, either manually with the general radio bridges or automatically by the LCR meters until a balance is reached at point A, which means that the voltage there is 0 with respect to the system common. At this point, the voltage across the sample and the current through it are known and the impedance can be calculated. Thus the natural property of the sample measured by the bridges is not capacitance, dielectric constant, or permittivity; nevertheless they measure the complex impedance and model to calculate the capacitance and the dielectric loss. This balanced condition is important in finding the impedance and for shielding by virtual ground, i.e. a point in an electric circuit that being held close to the ground level electric potential.

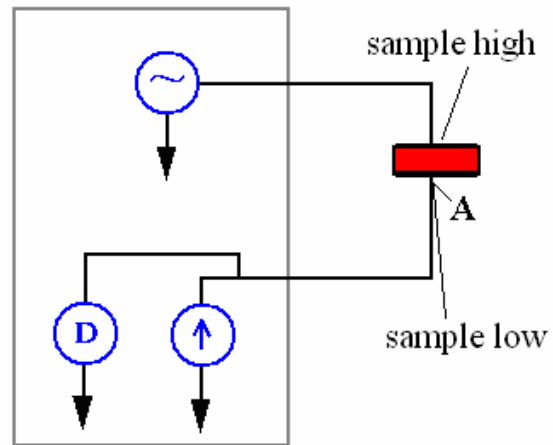
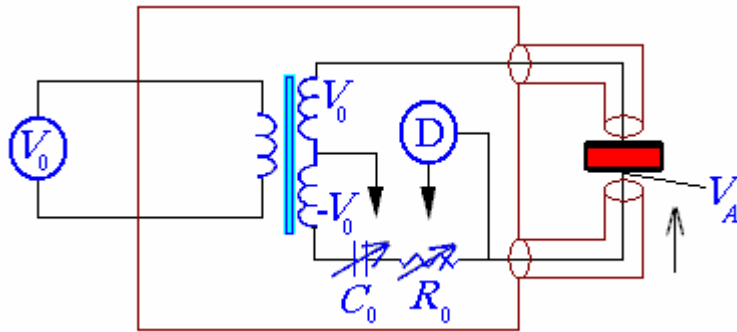


Fig. 4.1.8: The basic principle of capacitance bridges; the sample is connected to a voltage source (top), an adjustable current source. The balance point at A is measured by a detector.

##### 4.1.4.1 Manual bridges

The manual bridges use a center-tapped transformer to create a negative voltage which is applied to standard capacitors and resistors to make the balance current, Fig. 4.1.9. An extremely precise broadband transformer and an external generator are used to supply the measurement signal. The transformer has a





If  $V_A = 0$  then

$$I = \frac{V_o}{R_o + 1/\omega C_o}$$

If the sample is assumed to be modeled by  $C_o$  and  $R_o$  then  $C_o = C_s$ ,  $R_o = R_s$  and since  $D = \omega RC$ ,  $D$  can be calculated.

Fig. 4.1.9: Basic principle of the manual bridge; using tapped transformer and variable standard resistor ( $R_0$ ) capacitor ( $C_0$ ) until the balance point is detected at (A).

total turns ratio of two, and due to the center tap, the output is two voltages, which are equal in magnitude to the generator signal with the signal in the reference arm exactly inverted with respect to the generator. The user looks at the signal present at the detector and adjusts the variable components until there is no signal at the balance point. The measurement circuit has then a voltage source ( $V_0$ ) connected to the sample high and a current source connected to the sample low. The current is determined by the inverted generator voltage ( $-V_0$ ) divided by the impedance of the variable standard capacitor and resistor ( $C_0$  and  $R_0$ ). This "current source" is only correct when the bridge is in balance, because only then the voltage across the sample is equal to the (inverted) voltage across the standard components, Fig. 4.1.9.

The balance condition of the bridge results in several advantages; because the balance point is held at exactly 0 V, the high and low sides of the measurement circuit can be shielded from each other by ordinary metal shielding as long as the shielding is connected to the system common. Also an electrode held at 0 V (grounded) can be used as a guard for high impedance samples. Furthermore, loading of the transformer is not a first-order error and so it does not affect the bridge balance. There is still another second order error resulting from resistance in the transformer winding and in the cable connecting the sample to the bridge which can have some effect on the answer. This can be minimized by keeping the cables as short as possible especially when attempting to measure larger samples at higher frequency.

Another effect that is always present results from the distributed capacitance, resistance, and inductance in a coaxial cable, Fig. 4.1.10. In any coaxial cable the distributed impedances act as a low pass filter. The magnitudes of these impedances are not a large problem at low frequency but for the most accurate measurements some sort of compensation is necessary.

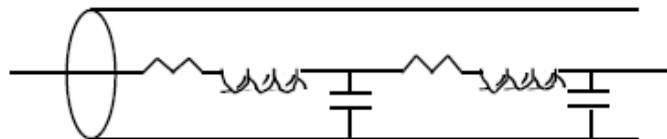


Fig. 4.1.10: The distributed capacitance, resistance, and inductance in a coaxial cable

#### 4.1.4.2 Automatic bridges

The automatic bridges use the same principles as the manual bridges but perform the functions using electronics rather than passive components. The simplified bridge is similar to the hypothetical 3 terminal bridge shown in Fig. 4.1.8. This simplified bridge uses voltage and current generated by electronic sources with a detector. However, since automatic bridges are supposed to work over the widest possible range of samples and since the difference between a capacitor, resistor and inductor (at any one frequency) is just the phase of the

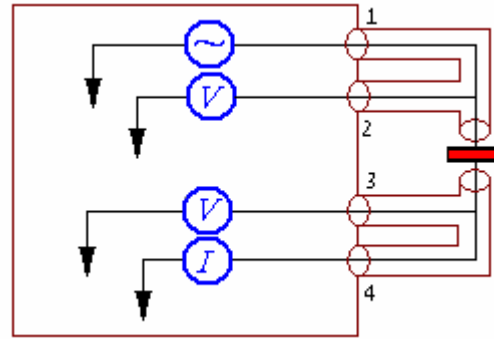


Fig. 4.1.11: The four-terminal configuration.

current passing through it. Thus, by building a current source which is adjustable over the entire  $\pm 90^\circ$  phase range it is possible to build one bridge which will measure any type of component. To allow for the greatest range of impedance magnitude, the problem is the impedance of the lead mainly with samples of relatively low impedance (small value resistors and inductors and large value capacitors). In such case, lead impedance can contribute significantly to the measurement error. The solution is the 4-terminal configuration (the exact ac analog of the 4 terminal DC resistance measurement), Fig. 4.1.11. Here, terminals 1 and 4 function only as generator and current source as before. Voltage drop in them is insignificant as long as terminal 2 is connected next to the sample approximating an ideal ac voltmeter. Current loss from terminal 4 would be significant but basically current in this lead is not interested in going anywhere except to the sample because of the virtual ground. Terminal 3 is just a detector but it has now been brought out to the front panel of the bridge so that it can also be connected next to the sample, once again eliminating the effect of lead resistance. Interestingly since the voltage at this point is 0 at the balance point, this terminal does not have to be an ideal voltmeter or current detector. Since the voltage at both ends of this cable should be 0 there will be no current flowing in this cable regardless of the nature of the detector so lead resistance would not create a voltage drop. Newer automatic bridges can also reduce the effects of lead impedance by compensating for it digitally. The idea is that the impedance of the test fixture and cables in both the open circuit and short circuit states can be measured before the sample measurement is performed and the bridge corrects for these impedances in the final result. However, these corrections can be perturbed by the presence of the sample, movement of the cables, thermal expansion in the cables or test fixture, change of resistance in the cables and test fixture due to temperature changes, and simple imperfection in the measurement of the cable impedance. Furthermore, if the cable impedance becomes significant compared to the sample impedance then the bridge has to subtract two similar numbers to find the answer, which leads to big error.

#### 4.1.4.3 Inductance

An electrical inductor stores energy in the magnetic field formed when current flows through the coil. This energy is released when the current decreases and the magnetic field collapses. The effects of inductances are often seen at the highest frequencies (as impedances below the  $x$ -axis in  $-Z''$  vs.  $Z'$  plot). The impedance of an inductor increases with frequency. High-frequency inductive effects may be due to (i) the actual physical inductance of the wires and, possibly, of the electrode itself. These "stray" inductances are generally only few microHenry ( $\mu\text{Hy}$ ). (ii) Instrumental artifacts, mainly capacitance of the current measuring resistor, however, many manufacturers have already made corrections for this in their EIS software.

Inductive behavior at low frequencies is hardly understandable. It is in the range of 1 Hy, or larger and may be attributed to an adsorption process at the electrode surface or an instrumental artifact in some cases like high impedance, low capacitance systems and samples with coatings or microelectrodes<sup>165</sup>. To overcome the high impedance of the sample, it is often advantageous to place it inside of a conducting box (a Faraday cage) to minimize the effects of stray pickup from the surrounding electronic devices. However, there is some small capacitance between the electrodes or wires and the surrounding 'cage' or conducting box. Since both the cage and the electronic measuring equipment are grounded together, some small stray current will flow through the sample then through this capacitance to ground. In many applications this current is negligible. Fig. 4.1.12 illustrates that, due to current flow through the stray capacitance, the current flowing into the ammeter is smaller than the current which enters the sample. This causes the measured impedance to appear to be too big. One of the most important conditions when making low capacitance measurements is shielding. When any two conductors are held apart a geometrical capacitor is formed between them. The two leads (electrodes) and the sample test fixture have a geometrical capacitance which will appear as error in the measurement and affect the loss measurement in proportion to the ratio of stray capacitance,  $C_{\text{stray}}$ , to sample capacitance. This capacitance itself can never be eliminated but with a proper design and moderate attention to the sample setup  $C_{\text{stray}}$  can be diverted. Inserting a piece of metal between the

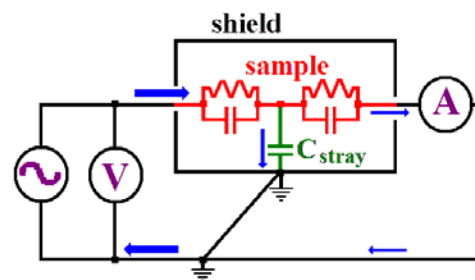


Fig. 4.1.12: The sample is inside a Faraday cage. This produces small capacitance between the electrodes and the cage. Thus some small stray current flow through the sample then through this capacitance to ground. Consequently, the ammeter current is smaller than the sample current and the measured impedance appears too big.

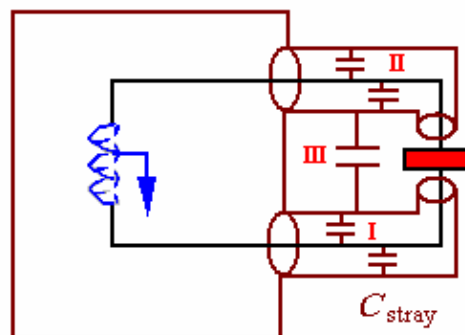


Fig. 4.1.13: Principle of the virtual ground "shielding", where  $I_{\text{stray}} = \omega C_{\text{stray}}(V_a - V_{\text{shield}}) = 0$ .

leads will not reduce  $C_{\text{stray}}$  nor will grounding that piece of metal ensure its shielding properties. The shielding property of conductors is a consequence of the way that precision capacitance bridges are built and this may be not possible in sufficiently crude capacitance meters without building external electronics. The ability to shield  $C_{\text{stray}}$  is a result of the virtual ground used in all sophisticated capacitance bridges. When the bridge is in balance, point A is at 0 V because of the current flowing through the sample is precisely balanced by the current through the reference arm. Such a point, actively held at 0 V, is called a virtual ground. The idea in a capacitance bridge is to know the voltage applied to the sample and the resulting current flowing through the sample. Since point A (and the entire lead to point A) is at 0 V, any capacitance existing between point A and a conductor held at 0 V, like the bridge's shielding which is connected to the system common, will not cause any current to flow from the low terminal, because there is no voltage across the capacitor, Fig. 4.1.13(I). Therefore  $C_{\text{stray}}$  has no tendency to affect the measurement. In principle it is sufficient to shield only one side of the measurement circuit, but practically speaking the other side is also always shielded both to help cover "holes" in the low side shielding and to reduce noise pick-up from environmental fields. Fortunately capacitance on the high side of the bridge can also be shielded without affecting the bridge balance. As shown in Fig. 4.1.13(II), capacitance in the high lead simply loads the system generator. The capacitance between the shields, Fig. 4.1.13(III), has no effect on the measurement because it affects neither the voltage nor the current being measured.

### 4.1.5 Main Types of Dielectric Functions

The two main types of dielectric behavior are "dipolar" and "charge carrier". Dipolar polarization leaves zero residual polarization on discharging, and it has a finite integral of  $f(t)$  over time. On the other hand, charge carriers give a partial recovery on discharge but typically leave a finite polarization in the system, and it has divergent character in the TD, Fig. 4.1.14. In FD the reversible systems have loss peaks, while irreversible systems do not show any loss peaks and give a continuing rise of  $\chi'(\omega)$  and  $\chi''(\omega)$  towards low frequencies.

#### 4.1.5.1 Debye relaxation

The dipolar "Debye" polarization was introduced in 1912<sup>166</sup> and the derivation of the archetypal dipolar response followed later<sup>167</sup> and is given by

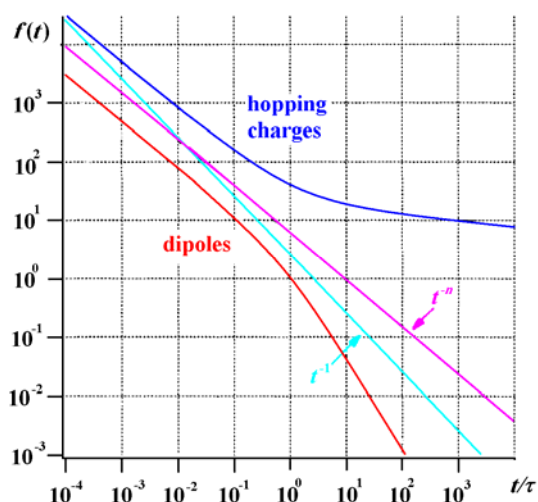


Fig. 4.1.14: Schematic TD response  $f(t)$  of two types of dielectric materials one dominated by dipoles and the other by hopping charge carriers. The line  $t^{-1}$ , corresponding physically to 'flat' loss, is drawn as a guide to show the logarithmic slopes of the two curves. The line  $t^{-n}$  shows the short-time dependence of both the carrier and dipolar systems.<sup>180</sup>

$$\chi^*(\omega) = \frac{B}{1+i\omega/\omega_p} = B \left[ \frac{1-i\omega/\omega_p}{1+\omega^2/\omega_p^2} \right] \quad (4.1.44)$$

where  $B$  is a constant and  $\omega_p$  is the loss peak frequency with the fwhm of the loss peak  $\lambda_D = 1.144$  decades, Fig. 4.1.15. This is the response of a group of ideal dipoles which do not interact together and have the same waiting time before making a transition, or for an assembly of identical dipoles which have a loss of energy proportional to frequency. The Debye response is also obtained with a series combination of a frequency-independent capacitance ( $C$ ) and resistance ( $R$ ) which give the peak frequency  $\omega_p = (RC)^{-1}$ .

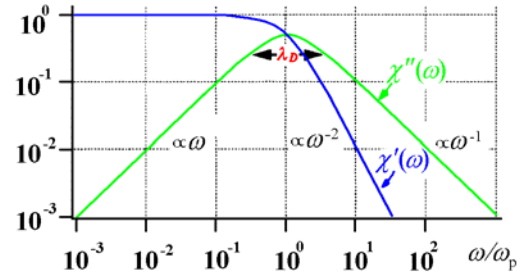


Figure 4.1.15: The real and imaginary components of the complex dielectric susceptibility for the Debye process. Note the symmetric shape of the loss peak and its width at half-height of  $\lambda_D = 1.144$  decades.<sup>180</sup>

#### 4.1.5.2 General dipolar responses

Pure Debye behavior is hardly found in reality and natural systems deviates from it slightly, as in Fig. 4.1.16(a), or more markedly, Fig. 4.1.16(b), or more drastically moved towards nearly ‘flat’ frequency dependence. The prevailing forms of frequency dependence are fractional power laws

$$\chi''(\omega) \propto \omega^m \text{ for the rising part with } \omega \ll \omega_p \quad (4.1.45)$$

$$\chi''(\omega) = \cot(n\pi/2) \chi'(\omega) \propto \omega^{1-n} \text{ for the falling part with } \omega \gg \omega_p \quad (4.1.46)$$

where the exponents  $m$  and  $n$  fall in the range between 0 and 1.

The dielectric decrement  $\chi(0) - \chi'(\omega)$  below the loss peak follows the complementary power-law relation

$$\chi(0) - \chi'(\omega) = \tan(m\pi/2) \chi''(\omega) \quad (4.1.47)$$

as shown by the dashed-dotted curve in Fig. 4.1.15(a) and (b).

The generalized loss peaks can be represented by the empirical analytical expression

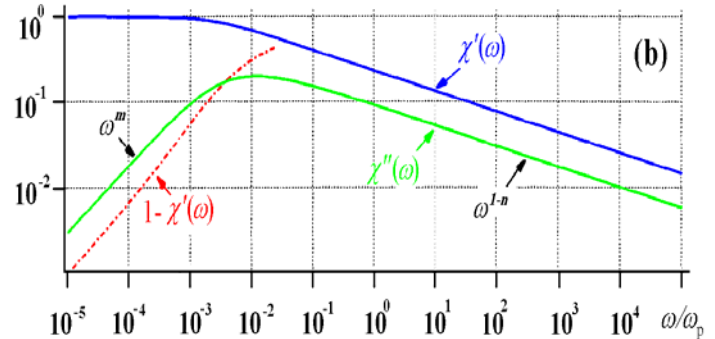
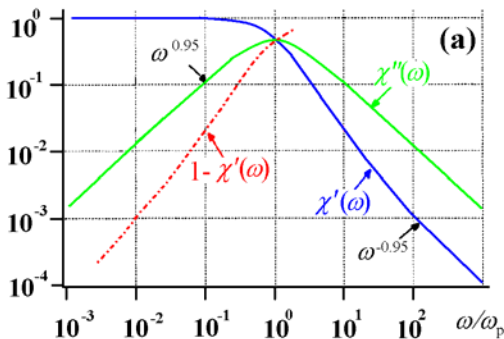


Fig. 4.1.16: (a) A near-Debye response showing the characteristic deviation from the Debye shape of  $\chi'(\omega)$  towards parallelism with  $\chi''(\omega)$ . (b) The generalized form of a non-Debye loss peak with the rising and falling branches following power laws with exponents  $m$  and  $1-n$ , respectively. The dashed-dotted curve below the loss peak shows the dielectric decrement  $\chi(0) - \chi'(\omega)$ .<sup>154</sup>

$$\tilde{\chi}(\omega) \propto \left[1 + (i\omega/\omega_p)^m\right]^{(n-1)/m} \quad (4.1.48)$$

This has the correct behavior of Eqs (4.1.45) and (4.1.46) and may be used to approximate the experimental data<sup>168</sup>.

In materials that undergo glass-to-crystalline transition there are differences between the responses below and above the glass transition temperature  $T_g$ . Below  $T_g$  the loss peaks are broader and their temperature dependence follows typically the Vogel-Fulcher law,

$$\omega_p \propto \frac{1}{(T - T_0)} \quad (4.1.49)$$

where  $T_0$  is some characteristic temperature. Above  $T_g$  the peaks are narrower and the loss peak frequency follows a temperature dependence with activation energy  $W$ , described by the Arrhenius relation

$$\omega_p \propto \exp(-W/kT) \quad (4.1.50)$$

### 4.1.5.3 Universal relaxation

When the polarization is dominated by slowly hopping charge carriers the material will show ‘shallow’ fractional power laws, Eq. (4.1.9), with exponents  $0.1 < 1 - n < 0.3$  at “high” frequencies instead of the loss peaks. This ‘universal’ dielectric response is common to dipoles and to charge carriers at high frequencies<sup>169</sup>. Its unique feature is the independence of frequency of the ratio

$$\chi''(\omega)/\chi'(\omega) = \cot(n\pi/2) \quad (4.1.51)$$

which distinguishes the universal law from all other spectral forms. This behavior is shown in Fig. 4.1.17 as steadily falling lines of  $(-1 + n_H)$  slope. The high-frequency limit of the applicability of this relation is difficult to ascertain experimentally, but is most likely in the short microwave or infrared region.

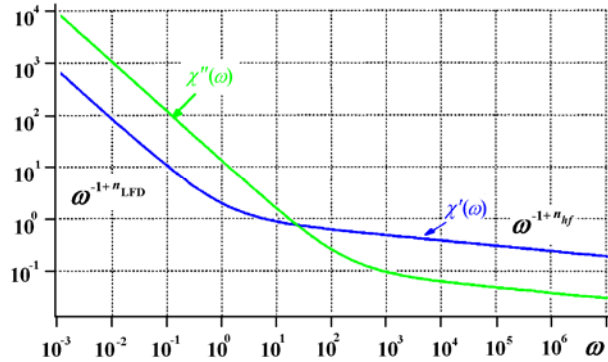


Fig. 4.1.17. The dielectric behavior of a material in which slowly mobile charge carriers such as ions or hopping electrons dominate the dielectric response. There is no loss peak, since no dipolar processes are involved; instead the low-frequency part follows another fractional power law of the type of Eq. (4.1.46) with a much smaller exponent  $n_{LFD}$ , for LFD.<sup>154</sup>

### 4.1.5.4 Hopping carrier systems

The conducting and dielectric response can be dominated by movements of charge carriers, typically ion or hopping electrons. Those charge carriers are relatively free to move in extended trajectories between the electrodes, they will produce ‘giant’ polarizabilities.

In a simplistic argument a system of hopping carriers should be a dc conductor. It is true that a random walk on a spatially homogenous medium gives dc only<sup>170</sup>, but there are further complicating features such as carrier-carrier interactions and various probabilities of the hopping transitions. The general impression

is that experimental data follow broadly the same descending fractional power law, Eq. (4.1.9), as was found for dipolar materials above  $\omega_p$  but there are also other findings.

While the complications of the various models are very considerable, the overriding impression is that the dielectric spectra remain relatively flat in frequency even if they do not follow the fractional power law, but follow some such logarithmic relations as<sup>171</sup>

$$\chi'(\omega) \propto [\ln(2\omega_0 / \omega)]^5 \text{ and } \chi''(\omega) \propto [\ln(2\omega_0 / \omega)]^4 \quad (4.1.52)$$

where  $\omega_0$  is a suitably chosen ‘vibration frequency’. The frequency dependence of these relations is shown in Fig. 4.1.18(a,b) and it is evident that, while these differ from the universal fractional power law and do not obey the same mathematical expression, they nevertheless represent very broad featureless spectra.

As pointed out by Dyre<sup>170</sup>, while electrons are fermions and ions are bosons, *de facto* hopping ions have a similar coulombic restriction of double occupancy as do electrons and thus their FD behavior in disordered solids is very similar. Some of the theories for behavior under alternating fields are therefore equally applicable to ions and to electrons.

#### 4.1.5.5 Ionic conduction

At enough temperatures high all materials may show increasing movements of ions either intrinsic or extrinsic. This will result in dc conduction or low-frequency dispersion. The conduction may be dominated by motion of ions which relies on the formation of lattice defects under the action of thermal excitation. Thus creating vacancies through which ionic motion may proceed under the action of external electric fields. This leads to Arrhenius temperature dependence with an activation energy given by the energy of migration plus formation of a defect. In an extreme case, fast ionic conductors have lattices which contain significant densities of vacant lattice sites and the ionic motion may proceed between pre-existing vacancies with much lower energy being the migration energy alone.

The frequency dependence of the conductivity of the ionic conducting material (with  $\sigma > 10^{-5} \Omega^{-1} \text{cm}^{-1}$ ) has been theoretically studied, see e.g. Refs [172–176]. The treatment was extended to the optical region of the spectrum and the results for low and intermediate frequencies agree with other theories. Many studies of the frequency dependence of conductivity were done on glassy materials<sup>177–178</sup> and as they vary in composition, many models were developed to represent their properties, although most of the analysis appears to be concerned with steady-state properties. Some authors obtain various logarithmic/power laws of the type of Eq. (4.1.52) and similar, while others find good fractional power laws of the ‘universal’ type, with little common ground between them. It is possible that the former relate to more conducting samples, while the latter are less conducting.

#### 4.1.5.6 Low-frequency dispersion

At low frequencies, a second power-law regime with  $1-n$  much closer to unity may be obtained,

Fig. 4.1.16. This remarkable behavior known as low-frequency dispersion (LFD)<sup>179</sup> appeared in the form of a weakly-frequency-dependent conductivity,

$$\sigma(\omega) = \varepsilon_0 \omega \chi''(\omega) \propto \omega^{n_{\text{LFD}}} \quad (4.1.53)$$

found in the case of silicon monoxide films, which were relatively conducting and in which the low-frequency branch corresponded to small values of the exponent  $n_{\text{LFD}}$  giving a ‘not-quite-dc’ response. This type of dielectric behavior was described in a wide range of materials, usually in the presence of humidity either on the surface or in the volume<sup>180</sup>. The strong rise of  $\chi'(\omega)$  at low frequencies implies a finite and reversible storage of charge in the material or at the interface, something which distinguishes it from DC conduction in which there can be no charge storage, and consequently  $\chi'(\omega)$  is independent of frequency as shown by the horizontal line in Fig. 4.1.18. The ratio  $\chi'(\omega) / \chi''(\omega)$  represents the fraction of stored charge (typically 0.01 – 0.1). The LFD behavior represents an extension of the universal law, with a different power-law index.

Widely accepted interpretation of the rise of  $C'(\omega)$  is in terms of the formation of interfacial capacitance, the so-called Maxwell-Wagner effect<sup>181</sup>. The latter is equivalent to a capacitance in series with the resistive volume of the sample, ignoring that the resulting frequency dependence should be that of an  $R$ - $C$  combination, which corresponds to pure Debye behavior. The explanation of LFD in terms of interfacial phenomena does not meet the evident requirements of the experimental situation.

#### 4.1.5.7 Low-loss materials - ‘flat’ losses

Low-loss materials have very ‘flat’ spectral responses, as their  $\chi'(\omega)$  and  $\chi''(\omega)$  are independent of frequency, since if  $\chi''(\omega)$  were not flat then it would not be very low everywhere, while with low  $\chi''(\omega)$  Kramers-Kronig relations demand that  $\chi'(\omega)$  be virtually constant. This is a consequence of the universal law in the limit of  $n \rightarrow 1$ , as in the high-frequency limit of Fig. 4.1.16. There are examples of almost ‘flat’ losses which are neither particularly low nor do they follow the universal law according to which there is an identifiable value of  $\varepsilon_\infty$  to be subtracted from  $\varepsilon'(\omega)$ <sup>182</sup>. The precise physical significance of this behavior is at present not understood.

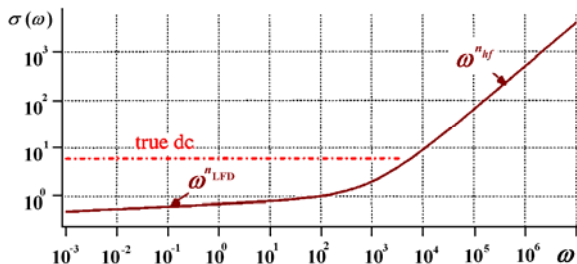


Fig. 4.1.18: The frequency dependence of electrical conductivity  $\sigma(\omega) = \varepsilon_0 \omega \chi''(\omega)$  for the same conditions as those shown for the susceptibility in Fig. 4.1.17. The critical point is the slight but unmistakable slope of the low-frequency part of the response corresponding to LFD. The horizontal line marked ‘true dc’ represents the expected dc response.<sup>182</sup>



## 4.2 NUCLEAR MAGNETIC RESONANCE

### 4.2.1 Introduction<sup>183</sup>

Using simple laboratory equipments, NMR was discovered in the late 1940's using a bottle of water and the earth's magnetic field to record and publish the first signal from protons in water independently by Bloch and Purcell. However, the enormous technological developments in magnets, computers and radio frequency (r.f.) electronics have initiated a tremendous evolution in NMR.

Each element in the periodic table has at least one magnetically active isotope, enabling NMR to inspect a wide range of elements that is mostly undetectable by other techniques in a non-destructive testing way. By probing the magnetic properties of the nuclei one can accomplish a lot of information about both the sample structure and dynamics. NMR has developed starting from the simple continuous wave experiments, to one dimensional pulse sequences, to the more complicated multiple resonance techniques which can be employed to selectively couple, or decouple, nuclei in a sample giving insight onto the atomic environment. By manipulation of the energy functions or time-reversal, it is also possible to investigate classically forbidden multiple quantum coherences, couple spin groups together or determine the chemical and electronic environment of any chosen NMR nucleus. All these techniques including averaging techniques such as magic angle spinning (MAS) have introduced NMR as one of the front running structural elucidation techniques especially when conjugated with crystallographic techniques such as x-ray diffraction. NMR can be used for relaxation time measurements, to investigate variations in chemical shift, diffusivity and even to derive internuclear distances.

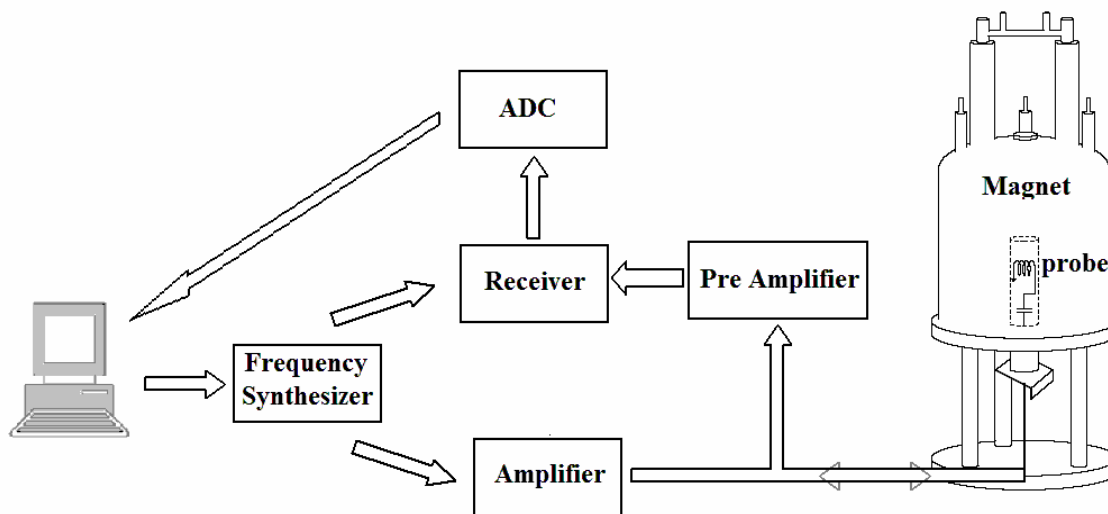


Fig. 4.2.1: A general schematic layout of the main components in the NMR experiment.

## 4.2.2 Basics of Experimental Setup

NMR has a sophisticated set of equipments comprising advanced electronic spectrometer, modern computers and a superconducting magnet, Fig. 4.2.1. Huge developments resulted in the pulsed Fourier Transform (FT) NMR. The superconducting magnet has a strong and homogeneous magnetic field. The cores of such magnets consist of coils of many kilometers of Nb-Ti wire which becomes superconducting at 10 K. Due to absence of resistive losses such a coil is able to maintain a steady, homogeneous field without any power input. Small shimming coils inside the main coil are able to alter the shape of the static field by varying their current to remove any gradients or magnetic field inhomogeneity.

The spectrometer combines the electronics with the superconducting magnet all being controlled by a modern computer system. A frequency synthesizer produces the radio frequencies (r.f.) and can accurately set the phases of pulses within the precision of the digitizer. In the amplifier, the r.f. input is amplified and then it passes through probe which is a tuned LRC circuit. The inductive component is the coil which is used to apply the perpendicular field ( $B_1$ ) to the sample.

The resultant signal passes through the pre-amplifier for a small amplification before passing to the receiver. The receiver is phase sensitive to determine whether the signal frequency is higher or lower than the synthesizer frequency which is subtracted from the signal. The analogue signal is converted to digital format and passed to the computer. The spectrometer computer is used to set the duration, frequency and phase of pulses used in the NMR experiment via pulse programs input by the user. A desktop computer is used to send pulse timings to the spectrometer computer and to save and to process the acquired data.

## 4.2.3 Fundamental Concepts

### 4.2.3.1 Zeeman splitting and spin states

Spin relates to the angular momentum of the nucleus. The spin quantum number of the nucleus depends on the combination of its nucleus constituents. As neutrons and protons are spin- $\frac{1}{2}$  particles, nuclei with odd numbers of protons and neutrons will have integer spin while odd-even combinations give half integer spin. The spin is quantized by certain selection rules and may align (or anti-align) with an applied magnetic field in certain defined directions. For most nuclei, the spins that orientate themselves opposing the external magnetic field are known as being in the higher energy states, and those aligned along the external magnetic field as being in the lower energy state.

Nuclear magnetic resonance is possible for nuclei possessing a spin  $I$  of  $1/2$  or greater. When the sample is in its natural state, i.e. in the absence of a strong external magnetic field, the magnetic moments exist in all possible orientations and all the spin- $I$  nucleus have the same energy (degeneracy). These nuclei exhibit a nuclear magnetic dipole moment,  $\vec{\mu}$ , directly proportional to the nuclear spin vector,  $\vec{I}$

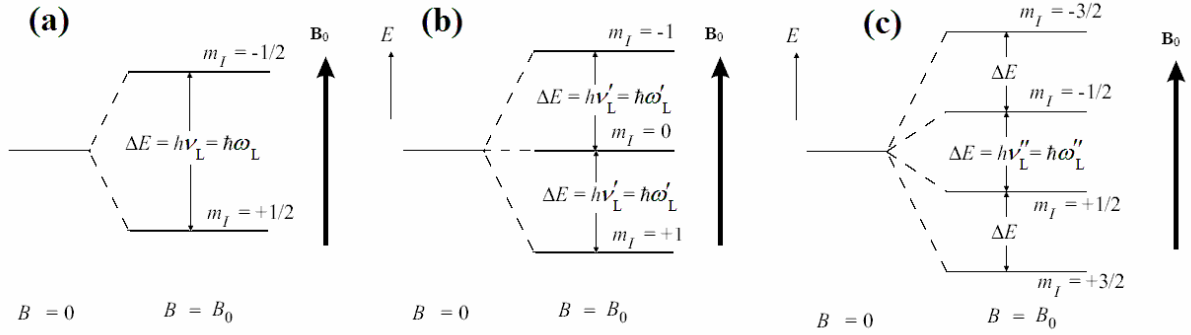


Fig. 4.2.2: Zeeman splitting of the nuclear energy level due to interaction of the nuclear spins with a static external field  $B_0$ , shown here for (a)  $I = 1/2$ , (b) spin  $I = 1$ , and (c) spin  $I = 3/2$   $\gamma > 0$ .

$$\vec{\mu} = \gamma \vec{I} \quad \text{or} \quad \mu = \gamma \hbar I \quad (4.2.1)$$

where  $\hbar = h/2\pi$ ,  $h$  is Planck's constant,  $\gamma$ , the proportionality constant, is the gyromagnetic ratio which can be expressed in terms of the Bohr nuclear magnetron  $\mu_N$  as

$$\gamma = g/\hbar(e \hbar/2m_p) = g\mu_N/\hbar \quad (4.2.2)$$

where  $g$  is the nuclear  $g$ -factor,  $e$  is the proton coulombic charge,  $m_p$  is the proton mass. When a strong magnetic field is applied, the degeneracy is removed and the interaction of the nuclear magnetic moment with the magnetic field yields the quantum mechanical interaction energy

$$E_z = -\vec{\mu} \cdot B_0 = -\gamma \hbar I \cdot B_0 = -\gamma m \hbar B_0 \quad (4.2.3)$$

Here  $B_0$  is the strength of the external magnetic field (the  $z$ -direction is the assumed direction for the static field),  $m$  (the magnetic quantum number) is an integer taking  $2I+1$  values ranging from  $-I$  to  $+I$  as shown in Fig. 4.2.2. The energy of the nucleus is shifted by an amount proportional to the magnetic field strength, the gyromagnetic ratio, and one component of the angular momentum. Furthermore, the nuclei are found to equally populate any available energy levels. However, this is not an energetically favorable situation and the spins arrange themselves. Since the NMR selection rule is  $\Delta m = \pm 1$ , the allowed transitions are between adjacent energy levels with the energy difference

$$\Delta E_z = -\gamma \hbar m B_0 - [-\gamma \hbar (m+1) B_0] = \gamma \hbar B_0 = h\nu_0. \quad (4.2.4)$$

Thus, in the presence of a magnetic field, the non-degenerate  $2I+1$  energy levels established for a spin- $I$  nucleus are equally spaced by  $\gamma \hbar B_0$ . Transitions between these levels are induced by subjecting the nucleus to an electromagnetic wave. The frequency,  $\nu_0$ , is called the Larmor resonance frequency, denoted with a subscript 'L', i.e. the transmitter frequency  $\nu_L = \omega_L/2\pi$ . It is also the frequency with which the spins precess about the static field. Since the resonance frequency region for NMR active nuclei falls in the radio frequency range, the electromagnetic radiation used to induce transitions in spin state is referred to as the radio frequency (r.f.). The r.f. magnetic field oscillates at  $\nu_0$  and is transverse to the external field  $B_0$ .

### 4.2.3.2 Energy population and magnetization

As the sample is placed into the magnetic field, nuclei are found to equally populate any available energy levels. However, this is not an energetically favorable situation. So spins start to re-arrange themselves to an equilibrium ratio governed by Boltzmann distribution according to:

$$\frac{N \downarrow}{N \uparrow} = e^{\frac{-\Delta E}{k_B T}} \quad (4.2.5)$$

where  $\Delta E$  equals  $\hbar\gamma B_0$ ,  $k_B$  is the Boltzmann constant. In the equilibrium state there are fewer spins aligned opposite to the field ( $N \downarrow$ ) than aligned with it ( $N \uparrow$ ). Thus the energy necessary to re-orientate the spins is determined by the thermal energy  $k_B T$ , so there will be only a small probability of the spins to become ordered in the lower energy state ( $N \uparrow$ ). As the value of  $\Delta E/k_B T$  is very small Eq. (4.2.5) can be simplified using  $e^{-x} \approx 1 - x$ , to obtain the normalized population difference equation

$$N \downarrow \approx N \uparrow \left( 1 - \frac{\Delta E}{k_B T} \right) \Rightarrow \frac{N \downarrow - N \uparrow}{N \downarrow + N \uparrow} \approx \frac{-\Delta E}{k_B T} \quad (4.2.6)$$

There is no direct classical analogue of spin, which is fundamentally a quantum mechanical phenomenon. However, it is acceptable to deal with a nucleus as a spinning charged particle. Biot-Savart law states that a spinning charge has a magnetic dipole moment associated with it. Thus, each nucleus can be represented as a small magnet; this means that there will be an overall magnetization in the direction of  $B_0$ . This is the magnetization  $M_z$  which has the value  $M_0$  when the sample is allowed to fully relax to equilibrium.

In any form of spectroscopy, an electromagnetic field excites molecules or atoms from the lower energy state into the upper energy state with the same probability as it induces the reverse transition, from the upper to the lower energy state. The net absorption energy is therefore dependent on the difference in the population between the two levels. The size of this magnetization is clearly dependent on the population difference and the equations above, Eq. (4.2.5) and Eq. (4.2.6), show that the greater  $\Delta E$  and the lower  $T$ , the greater the population difference will be. The population difference is minute ( $\sim 1$  spin in  $10^5$ ) resulting in the need for an accurate experimental setting to optimize the signal strength. The excess number of spins aligned with the field leads to the magnetization in the  $z$ -direction, Fig. 4.2.2.

### 4.2.3.3 Getting a signal

By applying a pulse to the tuned coil, a linearly oscillating magnetic field,  $B_1$ , is generated that varies exactly at the resonance frequency and acts at  $90^\circ$  to the main field. This field is rotating in the  $x$ - $y$  plane with the same frequency as the spins, so in the rotating frame it is a static field, perpendicular to  $B_0$ . If the  $B_1$  field is sufficiently strong and applied at the resonance frequency, the magnetization begins to precess about the  $B_1$  field at a frequency  $\nu_1 = (\gamma/2\pi)B_1$ . So for a  $B_1$  pulse applied along the  $y$ -axis the magnetization is rotated in the  $x$ - $z$  plane, the extent of rotation depends on the pulse duration. If the magnetization reaches the  $x$ -axis the corresponding pulse duration is known as the  $\pi/2$  pulse length, Fig. 4.2.3. The longi-

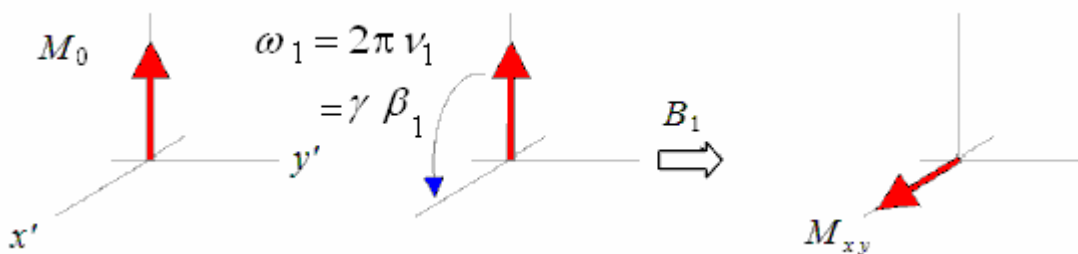


Fig. 4.2.3: The effect of the perpendicular  $B_1$  field on the magnetization vector, note that the diagram is "in the rotating frame" for simplicity

tudinal magnetization,  $M_z$ , is converted into transverse magnetization  $M_{x-y}$  precessing at a frequency  $\omega_0$  within a coil. The variation of the magnetization with time in a coil induces an electrical signal "the NMR signal" which oscillates at or near the frequency  $\nu_0$ . Before being passed to the computer for processing a reference frequency (the input frequency from the transmitter) is subtracted from the signal. If the reference frequency is exactly the same as the precession frequency of the nuclei approximately exponential signal decay is observed as in Fig. 4.2.4(a), and we are said to be "on resonance". If the input pulse is "off resonance" the signal will look more like that in Fig. 4.2.4(b) since the spins are rotating at a frequency different to that of the rotating frame. If the net magnetization is placed in the  $xy$ -plane, with respect to the applied magnetic field, it will rotate about the  $z$ -axis. The frequency of rotation will be equal to that of a photon which would cause the transition between the lower and the upper transition levels. If energy is absorbed by the nucleus, the angle of precession of the macroscopic magnetization will change. This absorption of radiation causes the magnetic moments to "flip" such that it opposes the applied field. The magnetic moment will then relax emitting a photon.

When nuclei are placed in the magnetic field, the spins can only exist in one of  $(2I+1)$  possible orientations according to the rules of quantum mechanics, Fig. 4.2.2. In case (a),  $I = 1/2$ , there will be two possible energy states which depend on the orientation of the spin (i.e. whether the spin is in state  $\langle +1/2 \rangle$  or  $\langle -1/2 \rangle$ ). These two states have different energy. It is energetically more favorable for a nucleus to be lined up with the  $B_0$  field than to be against it, therefore the  $\langle +1/2 \rangle$  state has the lower energy. In case (b),  $I = 2/3$ , there will be four possible energy states. This energy level splitting is known as Zeeman splitting and depends on the field strength.

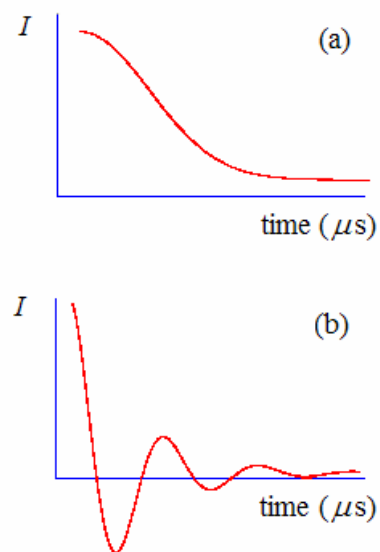


Fig. 4.2.4: the obtained FID's for when the reference frequency and the precession frequency of the nuclei are: (a) "on resonance", (b) "off resonance".

## 4.2.4 Basic Quantum Mechanical Description (Interactions That Modifies $\nu_0$ )

In NMR spectroscopy, photons or quanta are used to induce transitions between nuclear energy levels. The energy levels are set up by a variety of interactions. A Hamiltonian that yields the relevant energies can represent each of these interactions. The nuclear spin Hamiltonian can be written as a sum of internal and external parts

$$H = H_{\text{int}} + H_{\text{ext}}. \quad (4.2.7)$$

With this separation,  $H_{\text{int}}$  combines the intrinsic effects to the spin system while  $H_{\text{ext}}$  contains terms due to the actions performed on the spin system by experimental setup. The  $H_{\text{int}}$  can be subdivided into the basic interactions resulting from the environment of the nucleus:

$$H_{\text{int}} = H_J + H_{\text{CS}} + H_{\text{D}} + H_{\text{Q}} \quad (4.2.8)$$

where  $H_J$  is the indirect spin-spin coupling or ( $J$  coupling),  $H_{\text{CS}}$  is the chemical shift shielding (or chemical shift),  $H_{\text{D}}$  is the direct dipole-dipole coupling, and  $H_{\text{Q}}$  is the quadrupolar coupling. Each of these interactions is intrinsic to the spin system and primarily depends on the chemical environment of the nucleus.

The experimenter is able to interact with the spin through  $H_{\text{ext}}$ , and this has been the focus of much of the NMR field<sup>184</sup>. The  $H_{\text{ext}}$  can usually be expressed as:

$$H_{\text{ext}} = H_Z + H_{\text{RF}} \quad (4.2.9)$$

Both the Zeeman component,  $H_Z$ , and radio frequency component,  $H_{\text{RF}}$ , were discussed in the previous sections. With extensive awareness of the information that is intrinsically available from  $H_{\text{int}}$  of Eq. (4.2.8), we can tailor  $H_{\text{ext}}$  to extract the desired information.

### 4.2.4.1 Chemical shift interaction

The field experienced by the nucleus generally is not exactly the applied  $B_z$ ; instead, it is shielded by the surrounding bonding electrons, and the field it experiences varies accordingly. This chemical shielding Hamiltonian can be written as

$$H_{\text{CS}} = \gamma I \cdot \sigma \cdot B_0 \quad (4.2.10)$$

where  $\sigma$  represents the chemical shift tensor describing the chemical shielding. The total chemical shielding Hamiltonian is described by

$$H_{\text{CS}} = -\omega_0 \sigma_{\text{iso}} I_z - 1/2 \omega_0 \Delta \sigma [(3 \cos^2 \beta - 1) + \eta \sin^2 \beta \cos 2\alpha] I_z. \quad (4.2.11)$$

Here  $\alpha$  and  $\beta$  relate the principle axis system of the chemical shielding tensor to the laboratory frame where the field is oriented along the z-axis.

### 4.2.4.2 Dipolar interaction

In solid samples containing many nuclei each moment interacts with its neighboring moments. All nuclei possessing magnetic moments act like small magnets and can influence the magnetic environments of the surrounding nuclei. This interaction is the dipole-dipole interaction, also called dipolar coupling; it is small in magnitude compared to the Zeeman energy and is roughly proportional to  $r_{jk}^{-3}$ , ( $r_{jk}$  is the dipole-dipole distance, i.e. the vector joining the  $j^{\text{th}}$  and the  $k^{\text{th}}$  nuclei)

$$H_D = \frac{1}{4} \gamma^2 \hbar \sum_{j,k} \frac{(1-3\cos^2 \theta_{jk})}{r_{jk}^3} (3I_{zj}I_{zk} - I_j \cdot I_k). \quad (4.2.12)$$

Here  $\theta_{jk}$  is the angle between the external field  $B_0$  and the vector  $r_{jk}$  and  $I_z$  is the  $z$ -component of the spin vector. The effect of dipolar coupling gives rise to a symmetric distribution about the resonance frequency  $\nu_0$ . Often for glasses, Gaussian and/or Lorentzian distribution functions can be used to represent the spread in resonance frequency about  $\nu_0$ .

#### 4.2.4.3 Quadrupolar interaction

The quadrupolar interaction, referred to as quadrupole coupling, exists only for nuclei with  $I > 1/2$ . The

interaction can be expressed by 
$$H_Q = \frac{eQ}{2I(2I-1)} I \cdot V \cdot I \quad (4.2.13)$$

where  $I$  is the spin of the nucleus,  $e$  is the charge of electron,  $Q$  is the quadrupole moment of the nucleus, and  $V_{\alpha\alpha}$  are the components of the electric field gradient tensor in the PAS. If we define  $\eta = (V_{xx} - V_{yy})/V_{zz}$  as the asymmetry,  $q$  as the field gradient, and the quadrupolar frequency as

$$\omega_Q = \frac{3e^2qQ}{4I(2I-1)\hbar}, \quad eq = V_{zz} \quad (4.2.14)$$

we have 
$$H_Q = \omega_Q \left[ \left( I_z^2 - \frac{1}{3} I^2 \right) + \frac{\eta}{3} (I_x^2 - I_y^2) \right] \quad (4.2.15)$$

with the main values of the electric field gradient tensor  $|V_{xx}| \leq |V_{yy}| \leq |V_{zz}|$  and the asymmetry  $0 \leq \eta \leq 1$ .

#### 4.2.5 Magic Angle Spinning

In liquids the molecules are tumbling much faster than the frequency of the above mentioned interactions so that any directional dependence is averaged out. Contrarily, in solids the molecules are more localized relative to the NMR timescale, resulting in significant broadening of the spectrum. The main idea in MAS, is to overcome these anisotropies by rapid rotation of the sample about the "magic angle" ( $54.74^\circ$ ). The first order CS anisotropy, the dipolar coupling and the quadrupole coupling all vary with  $(3\cos^2\theta - 1)$ . The coil is housed in a stator through which the necessary bearing and drive airflow is channeled efficiently to the sample holder, or rotor. If the sample is spun at a frequency greater than that of the dominant interaction about the magic angle, this orientation dependence is averaged out and an isotropic peak with a dis-

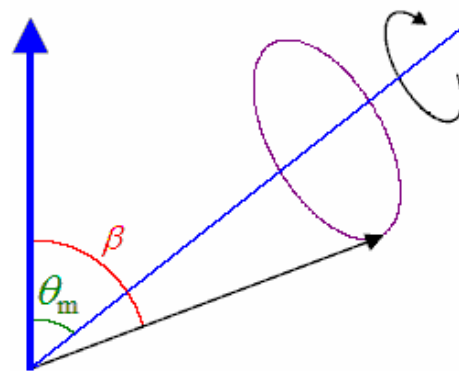


Fig. 4.2.5: the internuclear vector at an angle  $\beta$  to the static field is rotated about the magic angle  $\theta_m$  by spinning of the rotor to give an average orientation similar as the magic angle.

crete frequency rather than a range of frequencies is obtained. Fig. 4.2.5 shows how an internuclear vector at an angle  $\beta$  to the static field is rotated about the magic angle by spinning of the rotor. Thus, its average orientation is the same as the magic angle  $\theta_m$ . Recent maximum MAS rates exceed 30 kHz; this may not be fast enough to average strong interactions and certainly cannot average strong quadrupole coupling which has an additional orientational dependence to second order of  $\cos 4\theta$ . This, too, can be averaged by spinning about a second angle, and the technique of double rotation (DOR) involves spinning the sample about both angles simultaneously. If the spinning rate is not sufficient to average the interactions out, signal decay occurs during the first half of a rotor period (that is, the time it takes for the rotor to get half way through a revolution). Since all spins are inverted after half a rotor period, the following half of the rotor period sees the refocusing of the spins meaning the signal recovers just as in the echo sequence "rotor echo".

#### 4.2.6 Static and MAS NMR Lineshapes

The simulated spectra in Fig. 4.2.6 illustrate the effect of variable chemical shift asymmetry parameters,  $\eta_{CS}$ , on the lineshape. The simulations are for typical static  $^{29}\text{Si}$  NMR spectra of different  $Q^n$  species.  $Q^0$  and  $Q^4$  are symmetric; therefore the CSA is very small resulting in a very small spread in the values of  $\sigma_{11}$ ,  $\sigma_{22}$ , and  $\sigma_{33}$ . This leads to a symmetric lineshape, Fig. 4.2.6(a.1). Fig. 4.2.6(a.2) is characteristic of an axially symmetrically distributed electron density, as is the case in  $Q^3$  or  $Q^1$ . The intense peak at  $\sigma_{11} = \sigma_{22}$  is due to the most common orientation, with shielding symmetry axis orthogonal to  $B_0$ . The value of the chemical

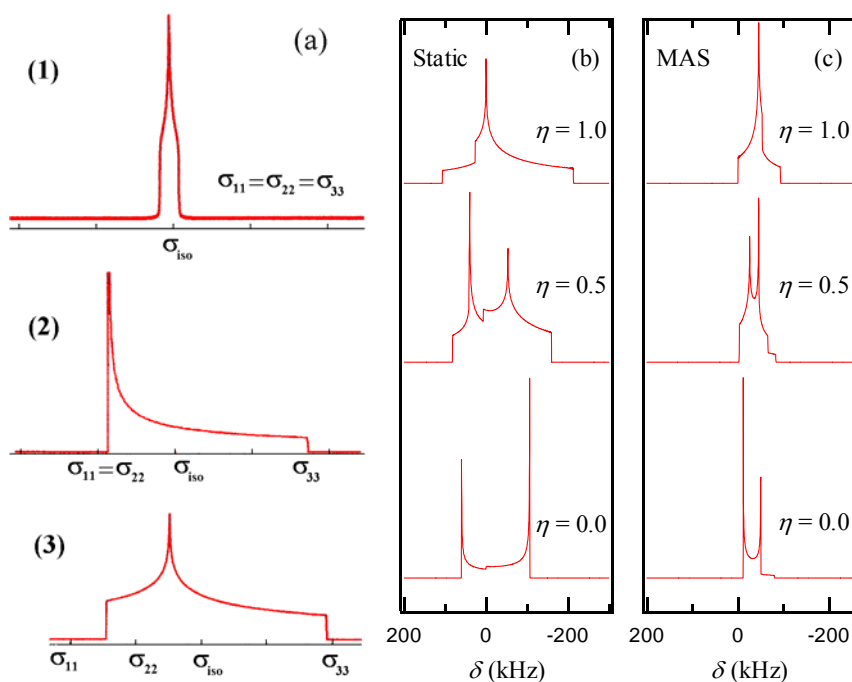


Fig. 4.2.6: (a) The dependence of the static NMR lineshape on the symmetry and orientation of the molecular segment relative to the applied field: (1) spherical symmetry: the shielding is similar in all directions and the values if  $\sigma_{11}$ ,  $\sigma_{22}$ , and  $\sigma_{33}$  are very close as in the case of  $Q^4$  and  $Q^0$ , (2) Axial symmetry: Maximum shielding when symmetry axis is parallel to  $B_0$  as in the case of  $Q^3$  and  $Q^1$ , (3) Asymmetric: the shielding is different in the three directions as in the case of  $Q^2$ ; (b) and (c) are the stimulated Static and MAS lineshapes, respectively for a nucleus that has a coupling constant  $C_Q = 2$  MHz and the indicated asymmetry parameters  $\eta_Q$ .



shift  $\sigma_{33}$  is due to sites with symmetry axis parallel to  $B_0$ . The orthogonal orientation gives maximum shielding whereas the parallel orientation gives maximum deshielding. Fig. 4.2.6(a.3) is characteristic for complete anisotropy of electron distribution that gives rise to three different values of  $\sigma_{11}$ ,  $\sigma_{22}$ , and  $\sigma_{33}$ . This is the case with  $Q^2$  where the lack of symmetry is evident. Figs. 4.2.6(b) and (c) demonstrate simulated static and MAS quadrupole lineshapes (typical for  $^{23}\text{Na}$  or  $^{93}\text{Nb}$ ) for the central transition ( $m = 1/2 \leftrightarrow m = -1/2$ ) with various  $\eta_Q$ . The effect of MAS can be seen by the narrowing of lines. This happens by reducing the second order quadrupole interactions. The lineshapes are very sensitive to the changes in  $C_Q$  as well as  $\eta_Q$ . Broadened lines would be observed for real spectra of glassy samples as a result of the dipolar broadening. The presence of a distribution of environments and the overlapping resonances from several sites may result in a complicated spectra that is not easy to be deconvoluted.

## 4.2.7 NMR Spin Relaxations and Diffusion Effect

NMR relaxation methods are different from other forms of spectroscopy. The mechanisms of nuclear spin relaxation are generally magnetic interactions, mainly dipolar coupling. As the molecules translate, rotate and vibrate,  $r$  and  $\theta$  vary in a complicated way causing the instantaneous dipolar interactions to fluctuate rapidly. This will cause the nuclear spins to experience a time-dependent local magnetic field which can induce transitions to return to equilibrium. The topic of spin relaxation is well discussed in Ref. [8] and the coming sections follow it in particular.

### 4.2.7.1 Spin-lattice relaxation (longitudinal relaxation)<sup>8</sup>

The spins usually rearrange themselves to the low-energy equilibrium population difference governed by the Boltzmann distribution, Eqs (4.2.5) and (4.2.6). The spin system can flip among its available states. The *energy exchange* between the spin system and the surroundings is called "spin-lattice relaxation". The emission of a photon ( $\Delta E = h\nu_0$ ) is stimulated by fluctuations of the local fields at the position of the nucleus under inspection. The significance of the fluctuations in causing energy level transitions increases when they have a component oscillating at or near the NMR Larmor frequency. These fluctuations result from motions such as diffusion, translation, rotation, thermal vibration and ion hopping. The intensity of fluctuations varies as a function of temperature and  $T_1$  varies accordingly. Thus  $T_1$  relaxation couples the spins (very weakly) to the motion of the molecules and its rate  $T_1^{-1}$  can tell us about motions on that time-scale (the motion is within the time scale of the reciprocal of the Larmor frequency).

In other words, spin-lattice relaxation brings spins into thermal contact with the lattice, enabling equilibration with the surroundings. The energy absorbed or released during the process of spin-lattice relaxation is transferred from or to the motions of the molecules, causing a slight temperature fluctuation of the lattice. Since the spin energies are minute in comparison to the rotational, vibrational and translational energies of the molecules, nuclear spins are relaxed with an infinitesimally small temperature

change of the sample. Thus spin-lattice relaxation (SLR) can be probed by NMR. This can be simplified by imagining a picture of a probe spin precessing in an external magnetic field  $B_0$  with a Larmor precession frequency  $\omega_L = \gamma B_0$ . The transition probability of the nuclear spin will peak up when  $\omega_L$  is in resonance with the frequency of a transverse alternating field  $B_1$ . The latter can be an external radio-frequency field or internal fluctuating fields due to dipolar magnetic fields from neighboring nuclei and quadrupolar electric fields from local electric field gradients. This fluctuating field can be described by the correlation function  $G(t)$  which contains the temporal information on the atomic diffusion process. The correlation time characterizing  $G(t)$ ,  $\tau_c$ , is related to the mean residence time between successive atomic jumps,  $\tau$ . The spectral density function of the fluctuating local field,  $J(\omega)$ , which is the Fourier transform of the correlation function  $G(t)$  and extends up to frequencies of the order of  $\tau_c^{-1}$ , is related to the SLR. The latter becomes effective, when  $J(\omega)$  has components at the transition frequencies inducing transitions between the energy levels of the spin system. The transition probability is measured by the SLR rate  $T_1^{-1}$  which can be

$$\frac{1}{T_1} = \frac{2}{3} \gamma^4 \hbar^2 I(I+1) [J^{(1)}(\omega_L) + J^{(2)}(2\omega_L)] \quad (4.2.16)$$

for the relaxation due to dipolar interaction between like spins, while for unlike spins one has

$$\frac{1}{T_1} = \gamma_I^2 \gamma_S^2 \hbar^2 S(S+1) \left[ \frac{1}{12} J^{(0)}(\omega_I - \omega_S) + \frac{3}{2} J^{(1)}(\omega_I) + \frac{3}{4} J^{(2)}(\omega_I + \omega_S) \right]. \quad (4.2.17)$$

The essential features of  $T_1^{-1}$  in a 3D system with random jump diffusion are derived from the exponential correlation function

$$G(t) = G(0) \cdot \exp(-|t|/\tau_c) \quad (4.2.18)$$

assumed by Bloembergen, Purcell and Pound (BPP)<sup>185</sup>. The corresponding Lorentzian shaped spectral density function is given by

$$J(\omega) = G(0) \cdot \frac{2\tau_c}{1 + (\omega\tau_c)^2} \quad (4.2.19)$$

The correlation time  $\tau_c$ , like the mean residence time  $\tau$ , will generally depend on temperature  $T$  according to the Arrhenius relation

$$\tau_c = \tau_{c0} \cdot \exp(E_A/k_B T), \quad (4.2.20)$$

where  $E_A$  is the activation energy of the diffusion process. Fig. 4.2.7 shows  $J(\omega)$  for three different temperatures. The SLR rate passes through a maximum at intermediate temperature for each  $\omega_L$  which is determined by the condition  $\omega_L \tau_c = 0.62 (\approx 1)$ .

The standard behavior of  $\log T_1^{-1}$  vs.  $1/T$  in a 3D system is

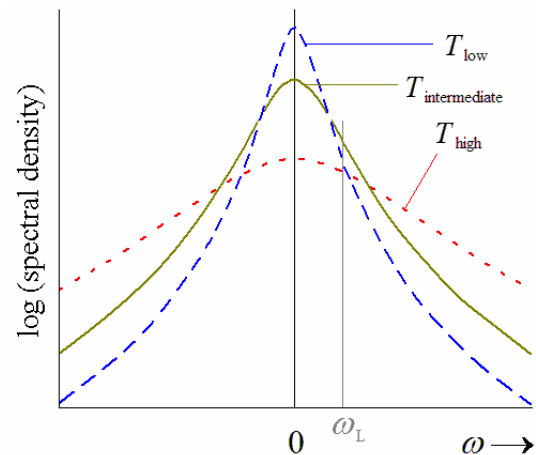


Fig. 4.2.7: Lorentzian spectral density functions for three different temperatures. For a chosen value of the Larmor frequency  $\omega_L$  the spectral density will be maximum for the intermediate  $T$  value where  $\omega_L \tau_c \approx 1$ .

shown in Fig. 4.2.8 for three different Larmor frequencies (magnetic fields). The peaks are symmetric and the slopes at temperatures above and below the maximum which correspond to the limiting cases  $\omega_L \tau_c \ll 1$  and  $\omega_L \tau_c \gg 1$ , respectively, yield the activation energy  $E_A$ . In the high- $T$  limit, the SLR rate shows no  $\omega_L$  dependence while it follows the power law  $T_1^{-1} \propto \omega_L^{-2}$  in the low- $T$  limit. The information about the jump diffusion mechanism can be extracted from the slopes of the high- $T$  and low- $T$  flanks of the log

$T_1^{-1}$  vs.  $1/T$  plot. In contrast to the standard BPP model<sup>185</sup>, predominantly asymmetric peaks are found. In most solids the activation energy extracted from the low-temperature side turn out to be smaller than the activation energy determined from the high-temperature side. This may be ascribed to non-uniform diffusion energy barriers in a non-ideal, defective solid and how they are seen by NMR relaxation with its inherent time window of the order  $\omega^{-1}$ . The activation energy  $E_A^{\text{IT}}$  of the low- $T$  side ( $\omega^{-1} \ll \tau_c$ ) can be attributed to the short-time limit of the diffusion process, i.e. the elementary jump, whereas  $E_A^{\text{HT}}$  should refer to long-range diffusion because at high temperatures many jumps occur before one precession is completed ( $\omega^{-1} \gg \tau_c$ )<sup>8</sup>. Since long-range diffusion implies an increases probability to surmount barriers of higher energy,  $E_A^{\text{HT}}$  should exceed  $E_A^{\text{IT}}$ .

In the disordered and low-dimensional systems, deviation from the BPP model is expected. In Table 4.2.1 the corresponding predictions from simple models for low-dimensional diffusion<sup>186–187</sup> are compared with the standard 3D behavior. It is noted that dimensionality effects show up only in the high- $T$  region where several jumps occur before one precession of the probe spin is completed ( $\tau_c \ll \omega_L$ ). The functional dependences are valid not only in the case of discrete jump vectors pertaining to ordered solids but also in the case of continuous diffusion. In the low- $T$  region, however, the  $\tau_c^{-1} \omega_L^{-2}$  dependence, Fig. 4.2.8, which applies to the 1D through 3D cases is true only for jump diffusion. In the case of continuum diffusion a  $\tau_c^{-1/2} \omega_L^{-3/2}$  dependence is predicted, which is thus weaker than for jump diffusion in both variables.

SLR in disordered systems is not explicitly included in Table 4.2.1. However, continuum diffusion is discussed as bearing resemblance to diffusion in disordered solids due to varying dis-

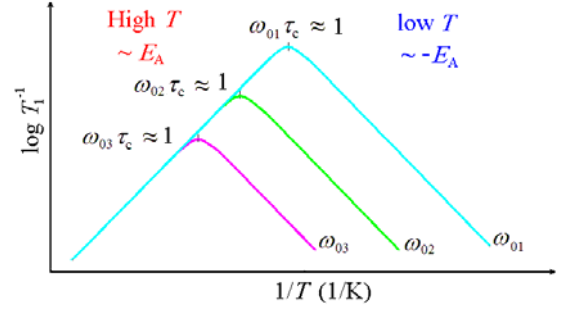


Fig. 4.2.8: schematic plot demonstrating the characteristic temperature and frequency dependence of the diffusion induced SLR rate ( $1/T_1$ ) for 3D systems at three different Larmor frequencies,  $\omega_0$ .

Table 4.2.1: Asymptotic behaviour of  $T_1^{-1}(\tau_c, \omega_L)$  for diffusion with different dimensionalities.

	$\omega_L \tau_c \ll 1$ (high $T$ )	$\omega_L \tau_c \gg 1$ (low $T$ )	
		Jump diffusion	Continuum diffusion
3D	$\propto \tau_c$	} $\propto \tau_c^{-1} \omega_L^2$	} $\propto \tau_c^{-1/2} \omega_L^{-1/2}$
2D	$\propto \tau_c \ln(1/\omega_L \tau_c)$		
1D	$\propto \tau_c (\omega_L \tau_c)^{-1/2}$		

tances of atomic sites. Indeed, the SLR rate in amorphous and defective crystalline materials has often been found to show an asymmetric  $\log T_1^{-1}$  vs.  $1/T$  peak with a smaller (absolute) slope on the low-T side and an  $\omega_L$  dependence characterized by

$$T_1^{-1} \propto \omega_L^{-\alpha} \text{ with } \alpha \leq 2. \quad (4.2.21)$$

There are models for SLR in disordered ion conductors<sup>188-191</sup>. These models claim a relation between the activation energies  $E_a^{\text{IT}}$  and  $E_a^{\text{hT}}$  obtained from the low- and high-temperature side, respectively, and the parameter  $\alpha$  characterizing the frequency dependence of the SLR<sup>192</sup>.

$$T_1^{-1} \propto \omega_L^{-\alpha} \cdot \exp\left(-\frac{E_a^{\text{IT}}}{k_B T}\right) \quad (4.2.22)$$

with  $1 < \alpha < 2$  on the low-T side. The deviation from this value indicates the influence of correlated motion and Coulomb interaction if  $1 \leq \beta \leq 2$  is found. The corresponding activation energy  $E_{\text{NMR}}^{\text{IT}}$  should be related to  $E_a^{\text{hT}}$  characterizing the slope on the high-T side, by

$$\frac{E_a^{\text{IT}}}{E_a^{\text{hT}}} = \alpha - 1 \quad (4.2.23)$$

Figs. 4.2.9 and 4.2.10 summarize the expected behavior of the diffusion-induced SLR rate as a function of correlation time and frequency, respectively, for diffusion in 2D ordered system and 3D disordered system in comparison with the BPP case.

Practically, after saturation of the spin system by introducing the sample into the static field, the magnetization recovers in the  $z$ -direction exponentially as a function of the delay time  $\tau$ , Fig. 4.2.11 according

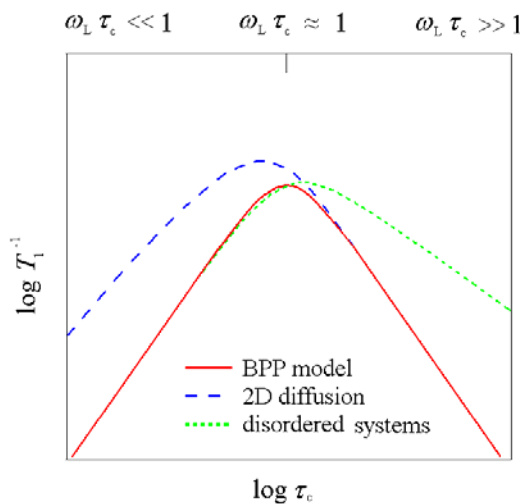


Fig. 4.2.9. Schematic representation of  $\log$  (SLR rate) vs.  $\log$  (correlation time) (corresponding to reciprocal temperature) for diffusion in the BPP case and the expected deviations for 2D systems and disordered systems.<sup>8</sup>

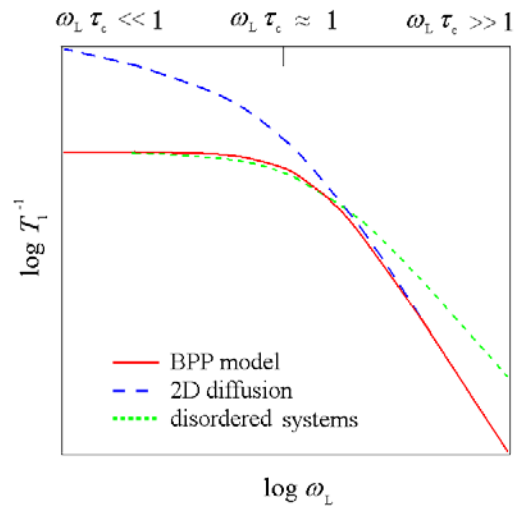


Fig. 4.2.10. Schematic representation of  $\log$  (SLR rate) vs.  $\log$  (Larmor frequency) (or magnetic field) for the BPP case and the expected deviations for 2D systems and disordered systems.<sup>8</sup>

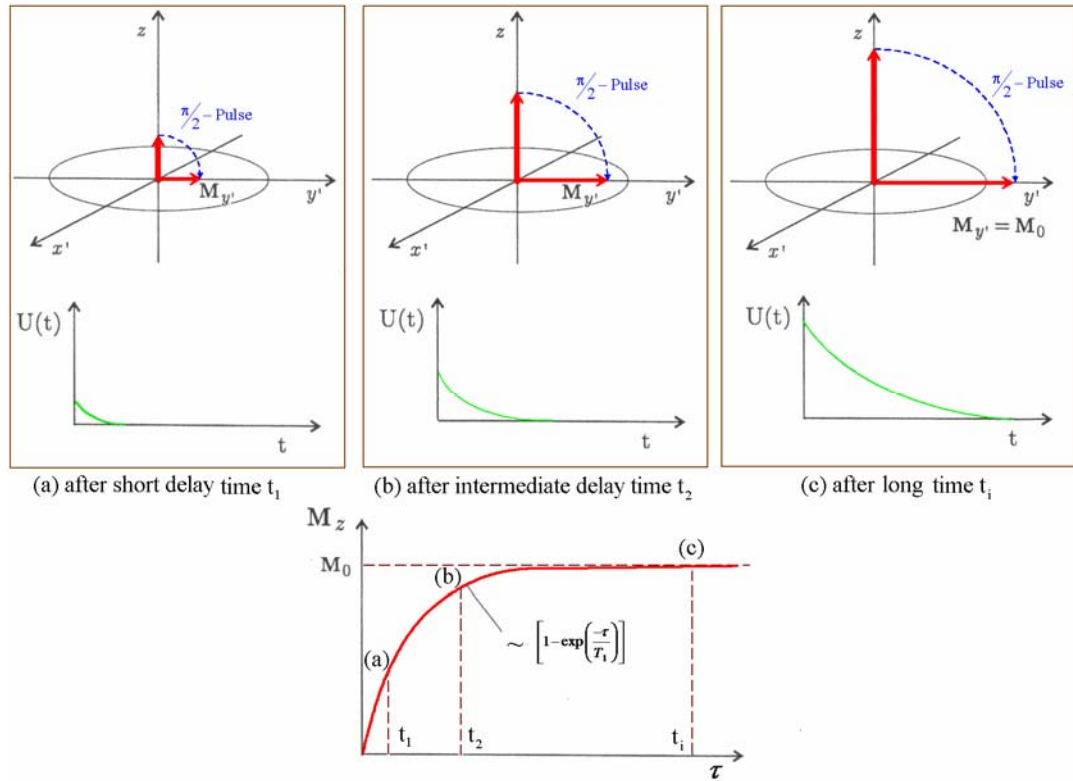


Fig. 4.2.11: Illustration for the recovery of the magnetization as a function of the delay time ( $\tau$ ). It shows the exponential recovery to the maximum magnetization  $M_0$  at three different stages: (a) after short delay time  $t_1$ , (b) after intermediate delay time  $t_2$ , and (c) after long delay time  $t_i$ .

to the equation

$$M_z(\tau) = M_0 \left[ 1 - \exp\left(\frac{-\tau}{T_1}\right) \right]. \quad (4.2.24)$$

The time constant describing how the longitudinal magnetization,  $M_z$ , returns to the equilibrium position is known as the spin-lattice relaxation time,  $T_1$ . It can range from less than a second to days depending on the nature of the sample.  $M_z$  takes the time  $T_1$  to recover to 0.632 of the maximum magnetization  $M_0$ . As the magnetization is tipped into the  $x$ - $y$  plane, a reasonably strong signal cannot be obtained unless the magnetization is allowed to recover completely between acquisitions by waiting a time more than  $T_1$  ( $5T_1$  is recommended).

#### 4.2.7.2 Spin-lattice relaxation in the rotating frame

Instead of using the static external field  $B_0$  as a reference, if spin-lattice relaxation is probed with reference to a resonant alternating field  $B_1$ , then the SLR rate in the rotating frame,  $T_{1\rho}^{-1}$ , is measured. It follows nearly the relation

$$T_{1\rho}^{-1} \propto J(2\omega_1) \quad (4.2.25)$$

where  $\omega_1 = \gamma B_1$ . As  $B_1 \ll B_0$ , the condition  $\omega_1 \tau_c \approx 0.5$  for the maximum of  $T_{1\rho}^{-1}(T)$  implies that  $T_{1\rho}^{-1}$  can 'look into' correlation times that are longer than those probed by  $T_1^{-1}$  measurements. Thus, it is usually ap-

plied to the systems in which the maximum and the high-temperature side are not accessible with SLR in the laboratory reference frame.

#### 4.2.7.3 Spin-spin relaxation

In the relaxed state the spins in the precession cone exist according to the random phase approximation, that is, there is no phase relationship between the spins. In the relaxed state of the spin system the “excess” spins in the z-direction which cause the net magnetization  $M_0$  obey the random phase approximation and populate all orientations of the “spin cone”. After a sufficiently strong  $B_1$  field, rotating at the resonance frequency, is applied along the  $x'$ -axis, the system will be quantized along the  $x'$ -axis by the new field, thus the spins “drop” onto the positive or negative half of the new spin cone aligned with the  $B_1$  field. The spins now precess around this field. After the  $B_1$  pulse has been applied for a time equal to the  $90^\circ$  pulse length, the *excess* spins have precessed together about the field. When the field is removed, a *phase coherence* has been imposed on the spins and the net magnetic moment now points along the  $y'$  axis, in this way the magnetization has been converted from the z-direction into the  $x$ - $y$  plane. It is worth noting at this stage that the population of spin states are equal, exactly the same situation as when the system is *saturated*. In addition to the rotational, vibrational and translational motions, the net magnetization starts to dephase because each of the individual spin packets encounters a slightly different magnetic field. Consequently, each group will rotate at different Larmor frequencies. The time constant describing the return to equilibrium of the transverse magnetization,  $M_{xy}$ , is known as the spin-spin relaxation time,  $T_2$ , which can be thought of as an entropy relaxation.

$$M_{xy} = M_{xy0} \left[ \exp\left(\frac{-t}{T_2}\right) \right] \quad (4.2.26)$$

$T_2$  is affected by a number of key interactions which cause the variations in precession frequency. The net magnetization in the  $xy$  plane will then tend to zero and the longitudinal magnetization will grow until  $M_0$  is along the z-axis. The transverse component rotates about the direction of the applied magnetization and dephases.

#### 4.2.7.4 Motional narrowing of NMR lines

Ion dynamics is related to the structural details of the sample. It should be possible to distinguish between the ions dynamics in the two structural zones, grain-boundary region and grain interior. The temperature dependence of the linewidth of the central transition is an important concern of Li NMR. The observation of motional narrowing (MN) of the linewidth starts when  $\tau_c \leq (2\pi\delta\nu_{RL})^{-1}$ , where  $\delta\nu_{RL}$  is the linewidth of the rigid lattice, which is due to the spatial variation of the static dipolar field. When the dynamics of the probed Li atoms in the grain-boundary regions and the grain interiors vary significantly, it should be possible then to determine the fraction of atoms ascribed to each of them.

In addition, the study of the MN allows to calculate the activation energy for the Li diffusion which corresponds to  $E_a^{\text{IT}}$  because the evaluation of the linewidth is normally restricted to the range  $\omega^{-1} \ll \tau_c \ll (2\pi\delta\nu_{\text{RL}})^{-1}$ . The  $\text{MN}(T)$  curves can be fitted with the following function<sup>193</sup>

$$\Delta\nu(T) = \Delta\nu_{\text{R}} \left[ 1 + \left( \frac{\Delta\nu_{\text{R}}}{B} - 1 \right) \exp\left(-\frac{E_a^{\text{MN}}}{k_{\text{B}}T}\right) \right] + D. \quad (4.2.27)$$

$\Delta\nu(T)$  is the linewidth of the central transition at a temperature  $T$ ,  $\Delta\nu_{\text{R}}$  and  $B$  are parameters related to the linewidths of the rigid lattice and the thermally activated ions, respectively.  $D$  is a temperature-independent linewidth caused, e.g. by the inhomogeneity of the external static magnetic field. Moreover, the activation energy  $E_a^{\text{MN}}$  can be obtained by fitting the motional narrowing data according to the *ad hoc* formula<sup>194</sup>

$$\Delta\nu(T) = \sqrt{\Delta\nu_{\text{RL}}^2 \frac{2}{\pi} \arctan\left[\alpha\Delta\nu(T)\tau_{\infty} \exp\left(\frac{E_a^{\text{MN}}}{k_{\text{B}}T}\right)\right] + \Delta\nu_{\infty}^2}. \quad (4.2.28)$$

where  $\Delta\nu$  is the width of the central line at the temperature  $T$ ,  $\Delta\nu_{\text{RL}}$  its respective width in the rigid lattice, and  $\Delta\nu_{\infty}$  the residual linewidth caused by non-dipolar interactions when the MN is completed.  $\alpha$  represents a fit parameter here chosen to be one.  $\tau_{\infty}$  is the pre-exponential factor in the Arrhenius relation assumed for the temperature dependence of the correlation time  $\tau_c$ .

An alternative method to determine the activation energy from the MN data especially when only the onset of the MN can be determined, without the full range of MN being covered, is the Waugh-Fedin method<sup>195</sup>

$$E_a^{\text{MN}} (\text{eV}) = 1.617 \times 10^{-3} \cdot T_{\text{onset}} (\text{K}) \quad (4.2.29)$$

$T_{\text{onset}}$  is the absolute temperature at which the motional narrowing starts.

#### 4.2.7.5 Spin-alignment echo NMR<sup>196–197</sup>

Ultraslow ionic motions with jump rates in the range between kHz to sub-Hz are difficult to be monitored by lineshape or spin-spin measurements. This is because such a slow motions has only a marginally effect on the lineshape. However, the measurement of the multiple time correlation function is possible by spin-alignment echo (SAE) method. The SAE NMR spectroscopy takes advantage of the interaction between the nuclear quadrupole moment and the electric field gradient (EFG) tensor at the nucleus site. The Zeeman frequency  $\omega_0/2\pi$  is altered by this interaction according to  $\omega_0 \pm \omega_Q$ . The quadrupole frequency is

$$\text{given by} \quad \omega_Q / 2\pi = \frac{1}{4} C_Q \left( 3 \cos^2 \Theta - 1 - \eta \sin^2 \Theta \cos(2\Phi) \right) \quad (4.2.30)$$

$C_Q = e2qQ/h$  is the quadrupole coupling constant with the proton charge  $e$ , Planck's constant  $h$  and the electric quadrupole moment  $Q$  of the nucleus.  $\eta$  denotes the asymmetry parameter of the quadrupole interaction. The polar angles  $\Theta$  and  $\Phi$  determine the orientation of the external field  $B_0$  in the principle axis system of the EFG tensor at the nucleus site. Provided electrically inequivalent sites are visited within a

given diffusion pathway by the jumping ion, the information about the dynamic process is coded in terms of a change in the quadrupole frequency  $\omega_Q$ . The spin-alignment technique allows one to measure directly a single particle correlation function yielding information about dynamic as well as geometric parameters of the hopping process.

The pulse sequence used to sample spin-alignment echoes is based on the Jeener-Broekaert experiment  $90^\circ_x - t_p - 45^\circ_y - t_m - 45^\circ_x - t^{198}$ .  $t_p$  is the evolution and  $t_m$  is the mixing time. In the ideal case, the first two pulses generate pure quadrupole spin-order. The third or reading pulse of the JB-sequence transforms spin-alignment back into an observable transverse coherent magnetization leading to an echo at  $t = t_p$ . The amplitude of the spin-alignment echo is given by<sup>199</sup>

$$S_2(t_p, t_m) = \frac{9}{20} \left\langle \sin[\omega_Q(t_m = 0)t_p] \sin[\omega_Q(t_m)t_p] \right\rangle \quad (4.2.31)$$

$\langle \dots \rangle$  denote powder average. The decay of the alignment echo amplitude  $S_2(t_p; t_m)$  for fixed  $t_p$  and as a function of  $t_m$  is in general due to two processes, i. e., (i) individual jumps of the ions and (ii) longitudinal relaxation. The first one, characterized by the decay constant  $\tau_{SAE}$  being directly related to the motional correlation time, will affect the echo formation when the ions are jumping between magnetically and electrically inequivalent sites, respectively. Simultaneously, the second process gives rise to a decay of the longitudinal order and thus to a decrease of the alignment echo amplitude, too. Therefore the experimental time window to investigate ionic motions is limited by longitudinal relaxation, i. e.,  $\tau_{SAE} < T_1$ .

Experimentally, even at very small evolution times  $t_p$ , in the case of  ${}^7\text{Li}$  being subject to relatively strong dipole-dipole interactions as compared to, e. g.,  ${}^9\text{Be}$ , the complete suppression of dipolar ( $D$ ) order simultaneously with generation of quadrupolar ( $Q$ ) order is difficult to realize<sup>200-201</sup>. Nevertheless the two corresponding time constants  $\tau_{SAE,D}$  and  $\tau_{SAE,Q}$  determining the echo decay will be of the same order of magnitude and will differ by about a factor of two, if at all (cf., e. g., an analogous relaxation study in Ref. [202]). Whereas SAE-NMR leads directly to a single-particle correlation function, the decay of dipolar order is described by a two-particle correlation function.

#### 4.2.8 NMR Applications in Nanomaterials and Glasses

NMR is able to investigate the heterogeneous structure of nanocrystalline ceramic materials. Via temperature dependent measurements NMR is able to distinguish between the two different structural regions and to differentiate between the ion diffusion in these distinct areas. Some previous results from NMR spectra, mainly  ${}^7\text{Li}$  lineshape studies, emphasized the structural properties for several nanocrystalline systems as well as the discussion of the diffusion-induced motional narrowing of the central line in the  ${}^7\text{Li}$ .

NMR is a powerful tool for the investigation of short-range order of glasses due to its high sensitivity to structural and chemical changes in the 1<sup>st</sup> and 2<sup>nd</sup> coordination spheres of the probe nuclei. In silicate glasses, a silicon atom is surrounded by  $n$  bridging oxygens (BO) and other  $(4 - n)$  non-bridging oxygens



(NBO). According to this it is designated as  $Q^n$  species, where Q represents silicon bonded tetrahedrally to four oxygen atoms and  $n$  ( $=0 - 4$ ) is the number of bridging oxygen atoms connected to silicon. The Si nucleus becomes more deshielded as the number of NBOs increase. Following this trend in the chemical shift, it is usually possible to distinguish between the different Q-species.  $^{29}\text{Si}$ -NMR spectra are deconvoluted quantitatively into several Gaussian distributions<sup>203</sup>.

Each Q-species is characterized by Gaussian linewidth, intensity, and position. The linewidth reveals the range of Si—O—Si bond-angle and bond length distributions. The position, i.e. the chemical shift of the  $Q^n$  species is generally between  $-70$  and  $-115$  ppm while that of six-coordinated Si is between  $-190$  and  $220$  ppm.<sup>204</sup> Fig. 4.2.12 shows the chemical shifts in ppm with respect to TMS for various possible  $^{29}\text{Si}$  species in silicate structural configurations  $Q^n$ .

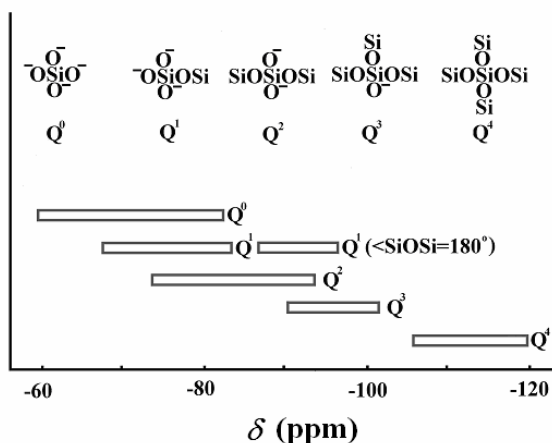


Fig. 4.2.12:  $^{29}\text{Si}$  chemical shift (ppm) with respect to TMS for various possible silicate structural configurations  $Q^n$ .<sup>204</sup>

## 4.3 EXTENDED X-RAY ABSORPTION FINE STRUCTURE

### 4.3.1 Introduction

Over the last three decades X-ray Absorption Fine Structure (XAFS) spectroscopy remains a mature incisive probe applied for investigating the local atomic environment surrounding selected variable atomic species in dilute, amorphous, nanophase or molecular gases. XAFS remains the best choice for investigating the GBs regions as it does not require extreme thinning of the sample as it is the case for TEM. This avoids any change in the structure by contaminating the surface or altering its stress. Both the phenomenon and its basic explanation have been known since the 1930's, however, it did not become a practical experimental tool until: (i) the fundamental physics of process was distilled into the standard XAFS equation and the consequent simple method of data analysis; and (ii) the availability of tunable, high flux, high energy-resolution synchrotron radiation beam lines. XAFS as short-range order technique is most powerful when combined with complementary long range techniques such as x-ray diffraction. XAFS experiments have many applications in physics, chemistry, materials science, biology, and environmental science.

### 4.3.2 Simple Theoretical Description (EXAFS Equation)

When monochromatic x-rays are allowed to pass through the sample, the incident and transmitted x-ray fluxes are monitored. For a homogeneous sample of uniform thickness  $x$ , the absorption coefficient  $\mu(E)$  is related to the transmitted ( $I$ ) and incident ( $I_0$ ) fluxes by

$$I = I_0 e^{-x\mu(E)}. \quad (4.3.1)$$

$\mu(E)$  is related to the cross section  $\sigma$  ( $\text{cm}^2/\text{g}$ ) and the density  $\rho$  ( $\text{g}/\text{cm}^3$ ) by

$$\mu = \rho\sigma \approx \sum_i \rho_i \sigma_i = \rho \sum_i (m_i / M) \sigma_i. \quad (4.3.2)$$

The sum is over  $i$  in the sample of mass fraction  $m_i/M$ . This expression is approximate as the total absorption is not the sum of the atomic absorption coefficients, the proximity of neighboring atoms strongly modulates the absorption coefficient as a function of energy, and this is the basis of XAFS. Thus XAFS is the oscillatory modulation in the x-ray absorption coefficient on the high-energy side of the edge<sup>205</sup>.

Fig. 4.3.1 shows that by increasing the energy  $E$ , the  $\mu(E)$  decrease approximately as  $1/E^3$ . However, each element shows a characteristic sudden increase called (absorption edges). The edge occurs when an incident x-ray photon has just sufficient energy to cause transition of an electron from the 1s state (K-edge) to an unfilled state of predominantly p-character. In the "Extended X-ray Absorption Fine Struc-

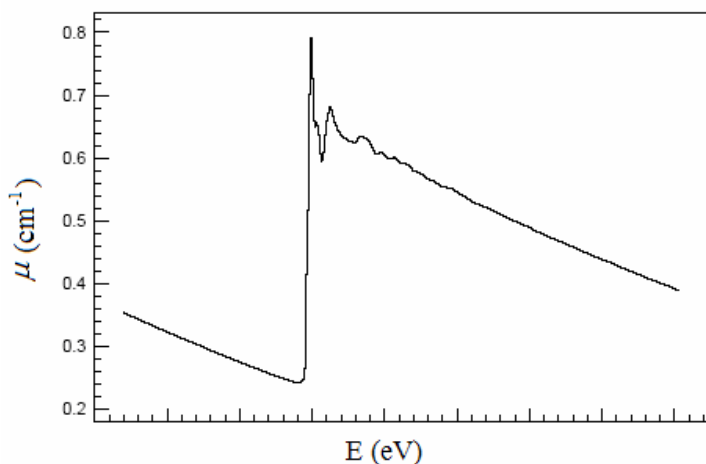


Fig. 4.3.1: the K X-ray absorption edge.

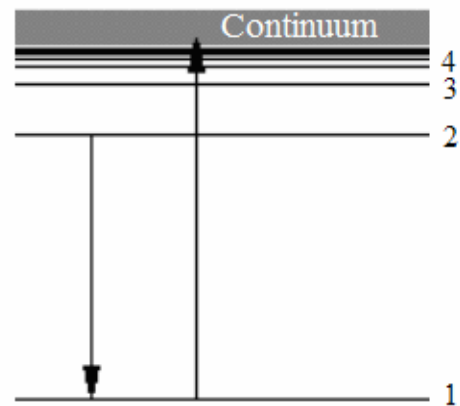


Fig. 4.3.2: Excitation of photoelectron from

ture" (EXAFS) region, ( $\geq 30$  eV) above the absorption edge, transitions to continuum states occur. Whereas in the "X-ray Absorption Near Edge Structure" (XANES), transitions may occur to unfilled bound states, nearly-bound states (resonances), or continuum states of the appropriate symmetry, Fig. 4.3.2.

The L-edges are also suitable for measuring EXAFS, mainly for heavy elements and transition metals as their K-edges are difficult to reach and due to the interesting information about d-symmetry states (in the case of  $L_{II}$  and  $L_{III}$  edges). It should be noted that the structure in the pre-edge region and on the rising part of the edge is sensitive to details of the local site symmetry, bond length, charge state, and orbital occupancy. This XANES information can often be exploited to provide information on the chemical state of the sample, even in case where EXAFS spectra cannot be obtained with adequate signal to noise ratio.

The EXAFS is defined as

$$\chi = \frac{\mu - \mu_0}{\mu_0} \quad (4.3.3)$$

where  $\mu_0$  is the hypothetical smooth background absorption coefficient due to the transition of interest; and  $\mu$  is the observed absorbance. When a core electron with binding energy ( $E_0$ ), absorbs an x-ray photon of energy ( $E$ ), which is higher than  $E_0$  then a photoelectron of the energy ( $E - E_0$ ) will be generated. The EXAFS arises from the interaction of the absorbing atom with photoelectron waves backscattered by neighboring atoms. According to the de Broglie relation this photoelectron has the wavelength

$$\lambda_e = \frac{h}{p_e} \quad (4.3.4)$$

where  $h$  is Planck's constant and  $p_e$  is the momentum of the photoelectron. The energy of the photoelectron is related to the momentum by the kinetic energy equation

$$E_e = \frac{p_e^2}{2m_e} \quad (4.3.5)$$

where  $m_e$  is the mass of the electron. Combining Eqs (4.3.4) and (4.3.5), the wavelength of the photoelectron is

$$\lambda_e = \frac{h}{\sqrt{2m_e E_e}} = \frac{h}{\sqrt{2m_e (E - E_0)}} \quad (4.3.6)$$

In EXAFS, the quantity  $2\pi/\lambda_e$  is called the photoelectron wave vector,  $k$

$$k = 2\pi / \lambda_e = \hbar^{-1} \sqrt{2m_e (E - E_0)} \quad (4.3.7)$$

The absorption probability  $\mu(E)$  is given in time dependent perturbation theory as the square of the transition matrix element

$$\left| \langle \psi_f | \hat{\epsilon} \cdot \vec{r} e^{i\vec{k} \cdot \vec{r}} | \psi_i \rangle \right|^2 \quad (4.3.8)$$

where  $|\psi_i\rangle$  is the initial state wave function that has significant magnitude only near the absorbing atom,  $|\psi_f\rangle$  is the final state wave functions, and  $\hat{\epsilon}$  and  $\vec{k}$  are the x-ray electric polarization and wave vector.

The absorbance varies with the magnitude of  $\psi_f$  in the vicinity of the absorber. In the dipole approximation the exponential is neglected and the dipole-coupled absorption cross-section is

$$\sigma = \left| \hat{\epsilon} \int \psi_i^* \cdot \hat{r} \cdot \psi_f d\tau \right|^2 \quad (4.3.9)$$

Here the absorption probability is independent of the direction of propagation of the x-ray, and depends only on the relative orientation of the sample axes with respect to  $\hat{\epsilon}$ .

In an isolated atom the continuum final state wave function  $\psi_f$  consists of a spherical wave emerging from the central absorbing atom, and the spectrum shows little fine structure. However, if the atom is placed into condensed matter, the final state wave function consists of the outgoing wave and the part scattered from neighboring atoms which may interfere either constructively or destructively, depending on the electron wavelength and the distance to the backscattering atom. Fig. 4.3.3 shows an absorbing atom emitting a photoelectron wave of wavelength  $\lambda_e$ . This wave is scattered from another atom at a distance  $R_{as}$  and returns to the absorber. To complete the round trip, the photoelectron wave travels a distance  $2R_{as}$ . This corresponds to  $2R_{as}/\lambda_e$  wavelengths or a change in phase of

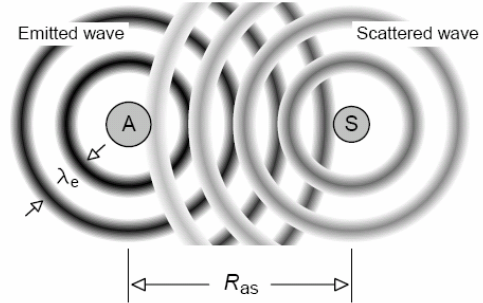


Fig. 4.3.3: A photoelectron wave emitted from the absorbing atom (A) is back-scattered by a scattering atom (S).

$$\Delta_{phase} = 2\pi(2R_{as} / \lambda_e). \quad (4.3.10)$$

The phase difference between the emitted and scattered waves is  $2kR_{as}$  at the absorbing atom. As the phase of the wave is also changed in traversing the potentials of the absorbing and scattering atoms, a correction  $\alpha_{as}(k)$  must be added

$$\Delta_{phase} = 2kR_{as} + \alpha_{as}(k) \quad (4.3.11)$$

As the incident x-ray energy  $E$  is scanned above the absorption threshold  $E_0$ , the kinetic energy of the

photoelectron  $E - E_0$  is varied, and consequently its momentum  $\hbar k$  and wavelength  $2\pi/k$ , which by conservation of energy are related by  $\hbar^2 k^2 / 2m = E - E_0$ . This interference modulates the matrix element and the absorption probability, which gives rise to oscillations in the absorption coefficient which are periodic in the wave number  $k$ . In this way the absorption coefficient literally records an interferogram of the spatial distribution of neighboring atoms. The transition matrix element can be expressed in terms of the Green's function

$$\mu(E) \propto \langle \psi_i | H_{\text{int}} G H_{\text{int}} | \psi_i \rangle \quad (4.3.12)$$

where  $G = \sum_n |n\rangle (E - \hbar\omega + i\varepsilon)^{-1} \langle n|$  and  $H_{\text{int}}$  is the interaction Hamiltonian. The Green's function can be expanded as a series of terms corresponding to zero, single, double and higher order scatterings from neighboring atoms:  $G = G_0 + G_0 T G_0 + G_0 T G_0 T G_0 \dots$ , where  $G_0$  is the Green's function of the central atom alone and  $T$  is the total scattering matrix of the surrounding atoms. Because the absorption coefficient depends linearly on the Green's function,  $\chi(k)$  can similarly be expressed as a sum of contributions corresponding to increasing numbers of scattering events. Experiment and theory have shown that in most cases relatively low orders of multiple scattering are needed to obtain agreement with experiment.

It is convenient to express the total absorption coefficient  $\mu(E)$  as the isolated atom absorption  $\mu_0(E)$  times a correction factor

$$\mu = \mu_0(1 + \chi). \quad (4.3.13)$$

$\chi$  is the fractional change in absorption coefficient that is induced by neighboring atoms. Within the context of the single scattering approximation, Stern, Sayers and Lytle<sup>206</sup> derived a very simple and useful expression for  $\chi$ , which has come to be called the standard EXAFS equation. For K-edge excitation, a group of individual atoms (each index  $i$ ) at relative distance  $r_i$  make a total contribution to the EXAFS of

$$\chi(k) = - \sum_i \frac{3 \cos^2 \theta_i}{k r_i^2} |f_i(k)| S_0^2 \varepsilon^{-2r_i/\lambda_e} \sin \{2k r_i + 2\delta_1(k) + \arg(f_i(k))\} \quad (4.3.14)$$

where  $\theta$  is the angle between the x-ray polarization vector  $\hat{\varepsilon}$  and the vector  $\vec{r}_i$  connecting the central atom with the atom in question.  $|f_i(k)|$  and  $\arg(f_i(k))$  are the modulus and phase of the complex electron scattering amplitude for each atom;  $\delta_1(k)$  is the  $l = 1$  partial wave phase shift of the central absorbing atom; and  $S_0^2$  and the photoelectron mean free path  $\lambda_e$  account for losses of coherence due to multi-electron excitations. The  $1/r^2$  factor accounts for the  $1/r$  decrease in intensity of the photoelectron wave propagating out to the scatterer and then back to the central atom.

Several approximations support the simple theory: the potential energy of the photoelectron propagating through the solid is approximated as that of spherically symmetric atoms with a constant region between them (muffin tin approximation); only a single electron is directly excited, which interacts with the electron gas in the solid; only backscattering from each neighboring atoms is included, i.e. multiple scattering is neglected; and in the scattering process the photoelectron is approximated as a plane wave.

The plane wave and single scattering approximations are known to be inadequate, and modern theory

properly takes account of them. When spherical wave effects are included, the basic structure of the EXAFS equation can be preserved if the plane wave scattering amplitude  $f(k)$  is replaced by an effective scattering amplitude  $f_{\text{eff}}(k, r)$  the scattering amplitude acquires a weak  $r$  dependence. Also, in the case of oriented samples, additional terms proportional to  $\sin^2 \theta$  appear at low  $k$  which may be not negligible.

Neglecting the multiple scattering implies that the total  $\chi(k)$  is a simple linear sum of contributions from backscattering atoms. This is a useful first approximation, but it is known that multiple scattering can be important, particularly when the absorbing atom and scatterers are collinear. The overall structure of the simple equation is that of a sum of damped sine waves: a  $k$ -dependent amplitude pre-factor times the sine of a phase which is approximately linear in  $k$ . In other words each atom contributes a sinusoidal signal which, when plotted vs.  $k$ , oscillates more rapidly when the distance is larger. When the scattering amplitude is stronger the signal becomes larger. In an oriented sample, the signal from a given atom is largest when its radius vector lies along the direction of the x-ray polarization vector.

The contributions from multiple scattering also oscillate more rapidly when their path length is long. For this reason single scattering contributions from higher shells may oscillate at about the same frequency as multiple scattering contributions of similar path length. This complicates interpretation of higher shell data. This problem may be essentially solved by recent theoretical advances.

In a real experiment one averages over many sites in the sample. The instantaneous positions of atoms may differ because of thermal and quantum zero point motion, and structural heterogeneity. XAFS essentially takes a snapshot of the instantaneous configurations of atoms. This is because the lifetime of the excited state is limited by the lifetime of the core hole (i.e. the vacancy in the initial  $1s$  state), and core hole level widths  $\Delta E$  are 1 eV or greater. This corresponds to a time scales of  $\tau = \hbar / \Delta E < 10^{-15}$  sec, approximately  $10^3$  times shorter than periods of interatomic vibration.

For randomly oriented polycrystalline or solution samples an isotropic average over angles must be performed. In this case the contributions from atoms of the same atomic number and at similar distances from the absorbing atom may not be resolvable from each other, and the atoms must be conceptually grouped together into "coordination shells". For small variations in distance within a shell, the equation

becomes

$$\chi(k) = - \sum_i \frac{N_i}{k r_i^2} |f_i(k)| e^{-2r_i/\lambda_e} e^{-2k^2 \sigma_i^2} \sin \{2k r_i + 2\delta_1(k) + \arg(f_i(k))\} \quad (4.3.15)$$

where  $N_i$  is the number of atoms in the coordination shell, and  $\sigma_i^2$  is the mean square variation of distances about the average  $r_j$  to atoms in the  $i^{\text{th}}$  shell. This is the classic EXAFS equation.

There are numerous exact expressions for the full multiple scattering  $\chi(k)$ , and most of them involve computationally inefficient nested sums over angular momenta up to high order. Rehr and Albers<sup>207</sup> have recently shown that the simplicity of the path by path approach is retained if the scattering amplitudes at each vertex of a scattering path are replaced by matrices  $F$ ; six by six matrices seem to provide essentially exact results. Their expression for a path, (either single or multiple scattering) is

$$\chi_{\Gamma}(p) = \text{Im} S_0^2 \frac{e^{i(\rho_1 + \rho_2 + \dots + \rho_N + 2\delta_1)}}{\rho_1 \rho_2 \dots \rho_N} e^{-\sigma_{\Gamma}^2 p^2 / 2} \times \text{Tr} M F^N \dots F^2 F^1, \quad (4.3.16)$$

where  $M$  is a termination matrix,  $\bar{\rho}_i = p(\bar{R}_i - \bar{R}_{i-1})$ ,  $p^2/2m = E - V_{\text{MT}}$  and  $V_{\text{MT}}$  is the zero energy of the muffin tin potential. The effects of disorder are approximated by the Debye Waller-like factor, where  $\sigma_{\Gamma}$  is the mean square variation in total length of path.

### 4.3.3 Some Experimental Considerations

Most of XAS measurements depend on the continuous spectrum of x-rays produced by synchrotrons<sup>208</sup>. This radiation is emitted when electrons or positrons, circulating in a ring at near the speed of light, are accelerated by a magnetic field. The x-rays are emitted in the direction of the electron or positron beam and are polarized in the plane of the ring. Polychromatic x-rays are produced by a synchrotron radiation source and a desired energy bandwidth of approximately 1 eV is then selected by diffraction from a monochromator, typically constructed of two crystals arranged as shown in Fig. 4.3.4. Only those x-ray photons that are of the correct wavelength  $\lambda$  to satisfy the Bragg condition ( $n\lambda = 2d \sin \theta$ ) at the selected angle  $\theta$  will be reflected from the first crystal; the others are absorbed. The parallel second crystal is used as a mirror to restore the beam to its original direction.

The undesired higher harmonics ( $n > 1$ ) can be removed in a number of ways. The first method uses a mirror reflecting x-rays only below a certain energy<sup>205</sup>. The second method rejects the harmonics by rotating the second monochromator crystal slightly out of parallel to the first. This takes advantage of the fact that the rocking curves for the higher harmonics are much narrower and are displaced with respect to the fundamental<sup>209</sup>.

### 4.3.4 X-ray absorption transmission and fluorescence

The simplest XAFS experiments are done in transmission mode. The intensity of the x-ray beam is meas-

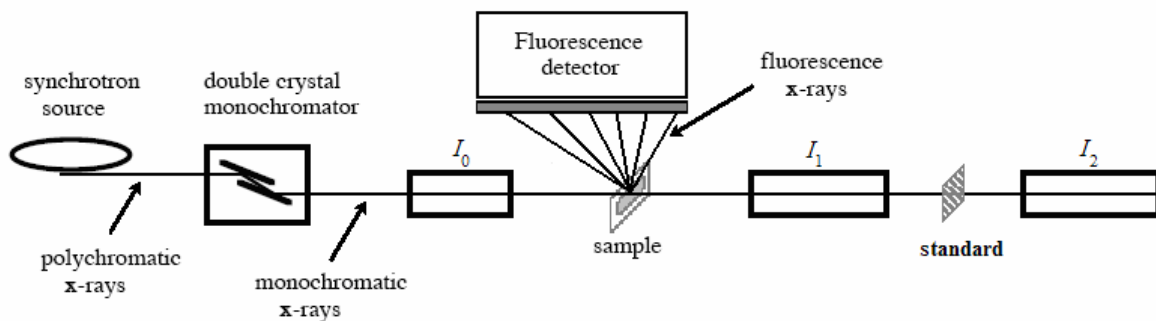


Fig. 4.3.4: Schematic illustration of the apparatus for a transmission and fluorescence EXAFS experiment.  $I_0$ ,  $I_1$  and  $I_2$  are ionization detectors for incident, transmitted and accurate energy flux calibration. The fluorescence detector is usually an ionization detector or a solid-state detector.

ured before and after a sample and the absorbance ( $\mu t$ ) calculated using the expression

$$\mu_t x = -\ln(I_1/I_0) \quad (4.3.17)$$

where  $x$  is the thickness of the sample. The intensity of the x-ray beam is typically measured using ionization detectors which measure the (photo-ion) current passing between the plates which in turn is proportional to the x-ray intensity. A third detector is often added to allow the concurrent measurement of the XAS from a standard. This standard spectrum is used to calibrate the energy scale using the position of features (transitions and inflection points) with known energy.

Fluorescence experiments are more sensitive than transmission. This is why they are used for dilute samples<sup>205</sup>. Here, the absorbance of the sample is measured by monitoring the intensity of the x-ray fluorescence produced when higher-shell electrons relax into the hole left by the photoelectron. The absorption coefficient is

$$\mu_x = C(F/I_0) \quad (4.3.18)$$

where  $F$  is the intensity of the fluorescence x-rays,  $C$  is approximately constant. The sample is commonly oriented at  $45^\circ$  to the beam and the fluorescence detector placed at  $90^\circ$ , see Fig. 4.3.4. Because the x-rays do not have to pass through the fluorescence detector, a solid state detector or an ionization detector filled with a gas of high x-ray cross-section to maximize detection is normally used.

### 4.3.5 EXAFS-Data Analysis

The aim of data analysis is to determine the structural parameters contained in the EXAFS equation like: distances ( $r$ ), coordination numbers ( $N$ ), disorder parameters ( $\sigma^2$ ) and types of atoms ( $T$ ) in the various coordination shells for the "unknown" sample. In addition to the atomic functions in the sample ( $f(k), \delta_1(k), \lambda(k)$ ). These scattering amplitudes and phases can be obtained to a good approximation by comparing the "unknown" sample with standard compounds of known structure. This is the preferred method of analyzing EXAFS data. The extent to which this is possible depends on the nature of the system, the quality of standards and the data.

The traditional method of data analysis involves a sequence of steps: correction for instrumental effects such as detector dead time losses and energy resolution; spectrum averaging and removal of monochromator "glitches"; normalization of the spectrum to unit edge step to compensate for variations in sample thickness or concentration; selection of the energy threshold  $E_0$  and interpolation to  $k$ -space; subtraction of smooth background (typically using cubic spline functions) to generate  $\chi(k)$ ; Fourier transformation and filtering to produce single shell amplitude and phase; determination of model parameters using the "ratio method" or nonlinear least squares fitting of data using empirical or theoretical standards.

(i) Data reduction: data reduction means the extraction of the EXAFS curve from the raw absorption data. To extract the EXAFS, one should remove the underlying background absorbance and the featureless background edge absorbance from the total absorbance. The background or "pre-edge" absorbance is estimated by fitting a polynomial function with low order (linear or quadratic) to the absorbance curve prior



to the edge using a least-squares procedure and extrapolating to the end of the data, Fig. 4.3.5(a). The observed EXAFS signals appear to be multiplied by energy dependent absorption factors due to the uncertainties in the concentration and sample thickness, in addition to a variety of materials such as mylar windows, and the sample matrix itself that enter into the beam path between the  $I_0$  monitor and the detector  $I_1$ . Thus the absorbance is scaled to an edge step of 1.0 so that the final EXAFS is relative to the edge ( $\mu_0$ ). Before background subtraction, the value of the threshold energy,  $E_0$ , must be specified somewhere near the bottom of the edge, close to the Fermi level. Then, the data are converted to  $k$ -space so that the background fit does not preferentially follow the data at high energy (which oscillate slowly in energy space). The sampling frequency must be high enough that the shortest wavelength in the data is sampled twice in a period; otherwise a rapid oscillation in the data will be confused with an oscillation at half the frequency. The differences between the data and the fit are weighted by an increasing function of  $k$  (such as  $k^3$ ) so that the data at high  $k$  (which are of small amplitude) are adequately fit. After that, the hypothetical smooth background absorbance above the edge is estimated by fitting a polynomial spline function to the normalized absorbance. The  $k$ -space data range is divided into several regions, and separate cubic polynomials are fit to the data over each region. The cubic polynomials are constrained so that their values, first and second derivatives are smooth at the junctions, Fig. 4.3.5(b). A least squares procedure is used to

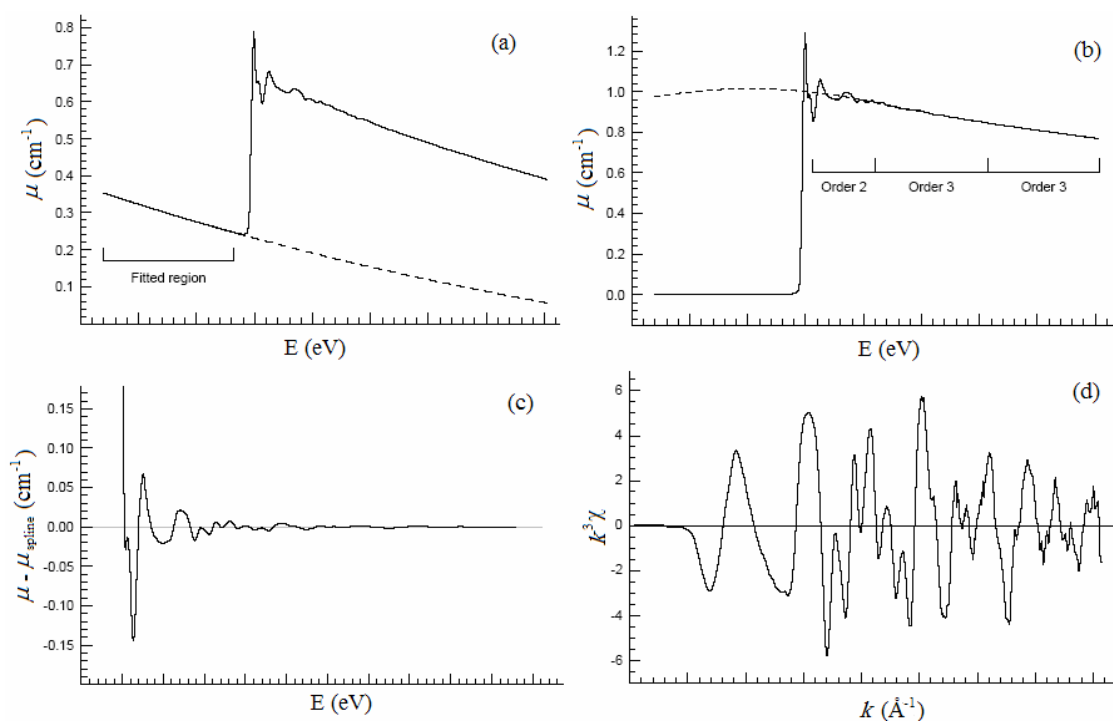


Fig. 4.3.5: EXAFS data reduction for K-edge example: (a) the background absorbance estimated by fitting a quadratic curve to the absorbance. (b) Normalised  $K$  x-ray absorption with the featureless background edge absorbance estimated using a polynomial spline curve. The spline curve consisted of a segment of order 2 and other two segments of order 3. (c) Difference between the normalized  $K$ -edge absorption and the featureless background edge absorbance estimated using a polynomial spline curve. (d)  $K$ -edge EXAFS has been graphed as a function of  $k$  and multiplied by  $k^3$  to compensate for the rapid attenuation with increasing energy.

fit the spline curve to the normalized absorbance (by minimizing  $\sum [k^3 (\mu_{normalized}(E) - \mu_{spline}(E))]^2$ ).

The weight given to the data points is increased with increasing energy as the fit has to be better at high energy due to the decreasing magnitude of the EXAFS oscillations. Then the spline curve is subtracted to obtain the curve shown in Fig. 4.3.5(c). Finally the difference between the normalized absorbance and the spline curve is divided by the normalized background absorbance due to the edge ( $\mu_{0,normalised}$ ).  $\mu_{0,normalised}$  is estimated using the expression

$$\mu_{0,normalised} = \lambda^3(C_a - C_b) - \lambda^4(D_a - D_b) \quad (4.3.19)$$

where  $\lambda$  is the X-ray wavelength and  $C_b$  and  $D_b$  and  $C_a$  and  $D_a$  are the Victoreen coefficients before and after the edge as tabulated in the International Tables for x-ray Crystallography<sup>210</sup>. The final EXAFS, plotted as a function of  $k$  and multiplied by  $k^3$  to compensate for the rapid attenuation with increasing energy, is shown in Fig. 4.3.5(d)

The obtained data consist of sums of damped sine waves corresponding to the different shells of atoms. The EXAFS equation is used as the basis for interpretation. To reduce the number of fitting parameters, it is useful to separate the signals from different shells using Fourier filtering methods to get the amplitude and phase functions<sup>211</sup>.

The modulus of  $\chi(r)$  exhibits peaks that correspond to the various coordination shells. The position of the peak corresponds to the average frequency of the corresponding shell's EXAFS, which is related to the average distance in the shell. The peak height is related to the average amplitude of the (weighted) EXAFS over the data range, and is therefore related to the number of atoms in the shell, the disorder parameter  $\sigma^2$ , the atomic number of the atoms in the shell, and the  $k$ -space window chosen. Thus the modulus of the fourier transform is analogous to a radial distribution function, but it absolutely should not be called or naively interpreted as "the radial distribution function". The transform depends on many factors including the  $k$ -range, and in responsible analysis several transforms with different  $k$  weightings and  $k$ -ranges are examined until an understanding of the data is achieved. The transform peak position is only a crude measure of the average distance in most cases (it really just measures the average phase slope) and cannot generally be used for accurate distance determination. Moderate to large disorder ( $k_{max} \sigma \approx 1$ ) in distances can cause significant peak shifts that do not correspond to the average distance. This effect can be dealt with appropriately in  $k$ -space using cumulant methods or nonlinear least squares fitting. Similarly the peak heights cannot be used to determine coordination numbers except in a very approximate manner, because atomic number, disorder, and other effects are important.

The transformed data actually consist of a complex function, which has real and imaginary parts, or alternatively a modulus and phase. The modulus is the most frequently used quantity, but the real and imaginary parts exhibit significantly more structure. They do not suffer from nonlinear interference. The Fourier transform is a linear operation while calculating the modulus is a nonlinear operation (the modulus of the sum is not the sum of the moduli); this is why adjacent peaks can interfere with or superimpose on

each other in (transform modulus) plots. Inter-shell interference causes considerable confusion as peaks which are not resolved from each other interfere strongly enough that there is a sharp dip in the modulus between the peaks, which may approach zero.

The *ratio method* is appropriate when the shell in the unknown consists of only one type of atoms. According to the EXAFS equation the logarithm of the ratio of the amplitude of the unknown to that of the standard is a linear function of  $k^2$ . In the simplest form of the ratio method, this quantity is plotted and fitted with a line. The intercept gives the ratio of coordination numbers, and the slope gives the difference in mean square disorder. Similarly, the phase difference, when plotted versus  $k$ , has zero intercept, and slope equal to twice the difference in average distance for the shell. This method is valid for small disorder  $k\sigma \ll 1$ . Otherwise, some curvature may be observed that is greater than can be explained by noise in the data. This curvature can be analyzed to determine the first few cumulants of the distribution of atoms in the shell <sup>Ref2</sup>.

On the other hand, *nonlinear least square fitting* is performed using amplitude and phase functions obtained from empirical standards or theoretical work. Then, using the EXAFS equation, it is a simple matter to synthesize the EXAFS corresponding to any particular hypothetical structure. This spectrum can be compared to the spectrum of the unknown, using a least-squares or other criterion. Comparison can be made to the amplitude  $A$  and phase  $\varphi$  separately, a weighted combination, or to  $A\sin\varphi$ . Fitting to a weighted combination of  $A$  and  $\varphi$  is flexible; fitting to  $A\sin\varphi$  tends to give more weight to the phase. The sum of squares function, which measures the goodness of fit, is a function of the hypothetical structural parameters. By minimizing the mean square error (according to any of a number of standard numerical algorithms) the parameter values for the best fit to the data are obtained.

## 4.4 SECONDARY-ION MASS SPECTROSCOPY<sup>212</sup>

### 4.4.1 Definition and Types

Most of the recent developed materials attained their superior properties from being multi-layered or having a heterogeneous distribution of one or more element. For such cases, conventional bulk analysis is not sufficient and it is necessary to have a surface analytical technique. It is crucial to have a simple way for the elemental-composition determination of the outermost atomic layer, including the chemical binding states, precise sites of atoms in the crystal structure, surface homogeneity and the state of adsorbates. SIMS uses ions as a probe to detect species at atomic densities below 1 part per million atomic (ppma) for all elements, and 10 ppma for some elements, with a resolution of few nanometers.

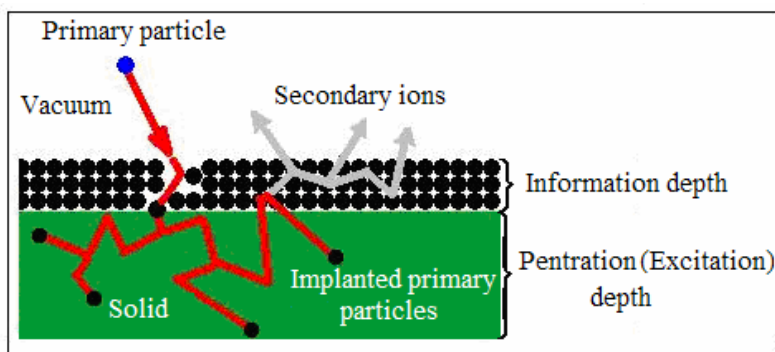
SIMS involves bombardment of sample surface under vacuum with a several keV focused primary ion beam. The final result of the ion-solid interaction is the emission of particles (1 % of the emitted particles are ions in the ground state as well as in the excited state). They are subsequently monitored by a mass spectrometer and then detected. In TOF-SIMS, the material is irradiated with a pulsed (very short pulses of < 1 ns) and focused beam of energetic ions (usually Ar or Ga). The resulting secondary ions will be accelerated to a constant kinetic energy by applying a potential between the sample surface and the mass analyzer and then allowed to pass a certain distance in a field free environment before they are collected on an intensity sensitive detector. Secondary ions travel through the TOF analyzer with different velocities, depending on their mass to charge ratio ( $E_k=1/2mv^2$ ). For each primary ion pulse, a full mass spectrum is obtained by measuring the arrival times of the secondary ions at the detector which will be related to individual masses and then performing a simple time to mass conversion.

The analysis area in TOF-SIMS is very small (~100 nm), which allows it to be used for making, combined chemical images of sample surface. It is possible to make different types of analyses such as: (i) Static SIMS, non-destructive surface analysis, in which only the outermost (1 – 2) atomic layers of the sample surface are sputtered away very slowly. To ensure that the analyzed secondary ions come from the outer surface of the sample, a primary ion dose of less than  $10^{12}$  ions/cm<sup>2</sup> is employed. Below this "static limit," roughly less than 0.001 of surface atoms or molecules are struck by a primary ion. The actual desorption of material from the surface is caused by a "collision cascade" which is initiated by the primary ion impacting the surface. This slow sputtering mode minimizes the damage of sample surface offering useful information for identifying molecular species. (ii) Dynamic SIMS or depth profiling is used to get quantitative information a function of depth. An ion gun is operated in the DC mode for sputtering, and the same ion gun or a second ion gun is operated in the pulsed mode for data acquisition. Depth profiling by TOF-SIMS allows monitoring of all species of interest simultaneously, and with high mass resolution.

(iii) Ion imaging is achieved by slow sputtering conditions similar to the static SIMS besides controlling the position where the primary ion beam strikes the sample surface. An image is generated by rastering a finely focused beam across the sample surface. Due to the parallel detection nature of TOF-SIMS, the entire mass spectrum is acquired from every pixel in the image. The mass spectrum and the secondary ion images are then used to determine the surface lateral distribution of elements and compound on a microscopic scale. (iv) Temperature dependent measurements, i.e. surface analysis as a function of temperature.

#### 4.4.2 Secondary Ion Production

The bombarding primary ion beam produces emission of electrons, photons and surface particles (mono-atomic and polyatomic), in charged, uncharged and also excited states, along with re-sputtered primary ions. All these emission products are emitted with a certain angular distribution.



$\text{Cs}^+$ ,  $\text{O}_2^+$ ,  $\text{O}$ ,  $\text{Ar}^+$ , and  $\text{Ga}^+$  at energies of 1 – 30 keV are the most

useful species for primary beam in SIMS. Primary ions are implanted and mixed with sample atoms to depths of 1 to 10 nm. Sputter rates in typical SIMS experiments vary between 0.5 and 5 nm/s. Sputtering rates depend on primary beam intensity, sample material, and crystal orientation.

The sputter yield is the ratio of the number of atoms sputtered (in any state) to the number of imposing primary ions (typically 5 – 15). According to collision cascade model, Fig. 4.4.1, a fast primary ion passes energy and momentum to target atoms and to a limited area around the point of particle impact by a series of binary collisions. This will result in: (i) A change in the lattice structure, as atoms from the sample's outer monolayer can be driven in 10 – 15 nm for a keV-range energy, penetration (excitation) depth, thus producing surface mixing. (ii) The energetic target atoms (called recoil atoms) will move and become a source of collision cascade with more target atoms inside the sample, some of which will recoil back through the sample surface causing loss of surface material by sputtering. The bombardment can be regarded as a sequence of single event with no overlapping of the collision cascades and the sputtering phenomenon can be studied by means of transport theory with the use linear Boltzmann equation<sup>213</sup>. Sputtering results in surface roughness in the sputter craters assisted by lattice imperfections. Polycrystalline materials form rough crater bottoms because of differential sputter rates depend on crystal orientation. A comprehensive analysis of sputtering process has been given by Sigmund<sup>214</sup> as

$$S(\cos \theta, E) = \frac{3F_D(\cos \theta, E)}{4\pi^2 N U_0 C_0} \quad (4.4.1)$$

where  $S$  is the sputtering yield,  $E$  is the energy of the incident ion,  $\theta$  is the incidence angle,  $N$  is the atom density of the sample,  $U_0$  is the surface binding energy,  $C_0$  is a constant appearing in the power approximation of the scattering cross section, and  $F_D$  is the average energy density deposited on the sample surface by the incident particle and can be defined as

$$F_D = \alpha N S_n(E) \quad (4.4.2)$$

where  $S_n(E)$  is the nuclear stopping power. This is a dimensional factor which takes into account various process parameters such as electronic screening, the energy, the angle of incidence of the primary beam, and the ratio between the mass of the primary ions and that of the lattice atoms. For normal incidence (linear collision cascade) the amount of the sputtered material can be written as

$$S(E) = 0.042 \alpha \frac{S_n(E)}{U_0 10^{-16}}. \quad (4.4.3)$$

The SIMS ionization efficiency is called "ion yield", defined as the fraction of sputtered atoms that become ionized. It depends on the element and its chemical environment as well as the primary beam. Ion yields vary over many orders of magnitude for the various elements. (i) The ion yield decreases with increasing ionization potential for positive ions and (ii) increases with increasing electron affinity for negative ions. By going from a pure metal to an oxide, the ionization probability of the same species (the metal atom) may be changed by several orders of magnitude. Oxygen bombardment increases the yield of positive ions while cesium bombardment increases the yield of negative ions. The variability in ionization efficiencies leads to different analysis conditions for different elements.

### 4.4.3 Quantification

#### 4.4.3.1 Relative sensitivity factors

Quantitative analysis by SIMS uses relative sensitivity factors defined according to

$$\frac{I_M}{C_M} = \text{RSF}_E \cdot \frac{I_E}{C_E} \quad (4.4.4)$$

where  $\text{RSF}_E$  is the relative sensitivity factor for the element,  $I_E$ ,  $I_M$  are secondary ion intensities for the element and for the matrix,  $C_E$ ,  $C_M$  are concentration of the element and the matrix. In trace element analysis, the matrix elemental concentration is assumed to remain constant. The matrix concentration can be combined with  $\text{RSF}_E$  to give a more convenient constant,  $\text{RSF}$ , where  $\text{RSF} = C_M \cdot \text{RSF}_E$ . This  $\text{RSF}$  is a function of the element of interest and the sample matrix. This leads to the most common form of the  $\text{RSF}$

equation

$$C_E = \text{RSF} \cdot \frac{I_E}{I_M}. \quad (4.4.5)$$

RSF Range (atom/cc)																			
H																	He		
Li	Be													B	C	N	O	F	Ne
Na	Mg													Al	Si	P	S	Cl	Ar
K	Ca	Sc	Ti	V	Cr	Mn	Fe	Co	Ni	Cu	Zn	Ga	Ge	As	Se	Br	Kr		
Rb	Sr	Y	Zr	Nb	Mo	Tc	Ru	Rh	Pd	Ag	Cd	In	Sn	Sb	Te	I	Xe		
Cs	Ba	La	Hf	Ta	W	Re	Os	Ir	Pt	Au	Hg	Tl	Pb	Bi	Po	At	Rn		
Fr	Ra	Ac																	
			Ce	Pr	Nd	Pm	Sm	Eu	Gd	Tb	Dy	Ho	Er	Tm	Yb	Lu			
			Th	Pa	U	Np	Pu	A	Cm	Bk	Cf	Es	Fm	Md	No	Lr			

	< 1.0·10 <sup>21</sup>		1.0·10 <sup>22</sup> - 1.0·10 <sup>23</sup>		1.0·10 <sup>24</sup> - 1.0·10 <sup>25</sup>
	1.0·10 <sup>21</sup> - 1.0·10 <sup>22</sup>		1.0·10 <sup>23</sup> - 1.0·10 <sup>24</sup>		> 1.0·10 <sup>25</sup>

X O<sub>2</sub><sup>+</sup> Primary (Positive Secondary)
X Cs<sup>+</sup> Primary (Negative Secondary)

Fig. 4.4.2: The periodic table of elements showing the elements which give positive secondary ions (outlined letters) and those which give negative secondary ions (underlined letters). The colors of the background indicate the RSFs measured for oxygen primary ion bombardment, positive secondary ions, and silicon matrix.

The tables of RSF values, Fig. 4.4.2, show how sensitivity depends on the element of interest. Low RSF values mean high sensitivity. The ordinary concentrations of high sensitivity elements can saturate electron multiplier ion detectors. The SIMS detection limits for most trace elements are between 10<sup>12</sup> and 10<sup>16</sup> atoms/cc. Two cases can limit this sensitivity: (i) If the secondary ion signal produced by sputtering is less than the detector dark current. (ii) Analyte atoms sputtered from mass spectrometer parts back onto the sample by secondary ions constitute another source of background. (iii) Mass interferences also cause background limited sensitivity.

#### 4.4.3.2 Depth profiles

The depth profile is the secondary ion count rate of selected elements as a function of time. To convert the time axis into depth, the SIMS analyst uses a profilometer, a separate instrument that determines depth by dragging a stylus across the crater and noting vertical deflections. Total crater depth divided by total sputter time provides the average sputter rate. Relative sensitivity factors convert the ion counts or intensity into concentration. Depth resolution depends on flat bottom craters. Modern instruments provide uniform sputter currents by sweeping a finely focused primary beam in a raster pattern over a square area. In some instruments, apertures select secondary ions from the crater bottoms, not the edges.

#### 4.4.3.3 Standards (ion implants)

Quantitative SIMS analysis requires standard materials to measure RSF values from. RSFs must be measured for each analyte element, sputtering species, and sample matrix. It is possible to implant virtually any element into any matrix to form ion implants which are good standards. Ions can be passed through a mass

analyzer before implantation to insure implant purity. The implant ion current can be integrated to determine the total ion dose. Dividing the total signal by the measurement time gives  $I_i$ , the average secondary ion signal during the measurement. The implant dose and the crater depth are required to calculate the average implant concentration

$$C_1 = \text{Dose} / \text{Crater Depth} \quad (4.4.6)$$

Inclusion of the matrix current,  $I_M$ , provides for *RSF* calculation according to the rearranged *RSF* equation

$$RSF = C_1 \cdot \frac{I_M}{I_i} \quad (4.4.7)$$

For samples with homogeneously dispersed analyte, *bulk analysis* provides more than an order of magnitude better detection limit than depth profiling. Mass spectra sample the secondary ions by continuously monitoring the ion signal while scanning a range of mass-to-charge ( $m/z$ ) ratios in small steps. The mass spectrum detects both atomic and molecular ions.

#### 4.4.3.4 Mass interference

Mass interferences occur whenever another ion has the same nominal mass as the analyte ion. However, their exact masses differ by a fraction of a mass unit. The exact mass minus the nominal masses is called the mass defect which arises from differences in the nuclear binding energies that hold the protons and neutrons together in the nucleus. The curve of mass defects gives atomic ions higher masses than molecular interferences at relatively low masses and the opposite at higher masses. Mass spectrometers with sufficient mass resolution can separate atomic ions from molecular ion interferences. Mass resolution is usually specified in terms of  $m/\Delta m$  where  $m$  is the nominal mass of the two ions and  $\Delta m$  is their difference. Minor isotopes can often resolve interference problems. However, minor isotope secondary ion intensities are lower and their detection limits are correspondingly worse, and the *RSF* values must be adjusted. Natural abundance isotope ratios cannot always be used for these adjustments because some processes, such as ion implantation of a specific isotope, alter the ratios.

#### 4.4.4 Analytical Conditions

##### 4.4.4.1 Sample charging

Insulator samples undergo charge build up due to the net electric current produced by the SIMS primary ion beam, secondary ions, and secondary electrons at the sample surface. This can diffuse or divert the primary beam from the analytical area, and subsequently eliminates the secondary ion signal or change the energy distribution of the secondary ions, which affects their transmission and detection by the mass spectrometer. For a thin dielectric sample on a conducting substrate, a strong electric field develops. Mobile ions (such as  $\text{Li}^+$ ) migrate in the electric field and depth profiles are no longer representative for the layers true composition. Several techniques are available to compensate for sample charging: (i) Electrons bom-



bardment compensates for positive charge buildup in the case of positive primary ions and/or negative secondary ions and electrons. Low energy electron beams work better because high energies electron beams produce more than one secondary electron for an incoming electron. (ii) Placing conducting grids over the sample reduces the effects of charging on ion optics and brings a source of electrons near to the positively charged areas of the sample. When struck by a primary ion, the conductors emit secondary electrons that migrate to the charged area. Samples are often coated with conducting materials such as gold. Before starting the analysis, the coating must be sputtered away only in the analytical area. (iii) The use of negative primary ion beams like  $O^-$  which is most common and available from the same duoplasmatron sources which is widely used for insulating geological samples. (iv) For samples that are only slightly charging, a continuously variable voltage offset can be applied to the accelerating voltage automatically. After every cycle in a depth profile analysis, the instrument software adjusts the voltage offset as needed to keep the peak of the distribution constant according to the last measurement.

#### 4.4.4.2 Ion imaging

The secondary ion intensities are shown as a function of location on sample surfaces. Ion images can be acquired in two ways: (i) Stigmatic imaging which requires a combination of ion microscope and mass spectrometer able to transmit a mass of selected ion beam from the sample to the detector without loss of lateral position information. Ion microscope images are usually rounded like the ion detectors. (ii) Raster scanning: a finely focused primary ion beam sweeps the sample in a raster pattern and software saves secondary ion intensities as a function of beam position. Microbeam imaging uses standard electron multipliers and image shape follows raster pattern shape, usually square.

#### 4.4.5 SIMS Instrumentation

##### 4.4.5.1 Primary ion source

In typical SIMS instruments, primary ion source is either a duoplasmatron and/or a surface ionization source. The duoplasmatron operates with any gas, but oxygen is the most commonly used and its plasma contains both  $O^-$  and  $O^{2+}$ , and either can be extracted. The cesium surface ionization source produces  $Cs^+$  ions as Cs atoms vaporize through a porous tungsten plug. Primary ions are extracted from the sources and passed to the sample through the primary ion column, Fig. 4.4.3, which usually contains a primary beam mass filter that transmits

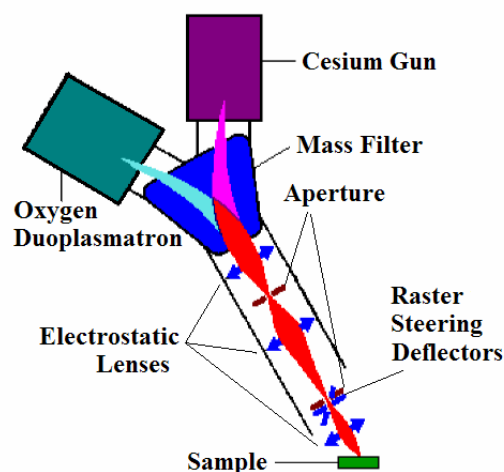


Fig. 4.4.3: Primary ion column contains primary ion source, primary beam mass filter and number of electrostatic lenses and apertures.

only ions with a specified mass-to-charge ( $m/z$ ) ratio. This filter eliminates impurity in the beam. Without a primary beam mass filter, contaminants deposit onto the sample surface, raising their detection limits.

The intensity and width of the primary ion beam are controlled by number of electrostatic lenses and apertures with several diameters. A finely focused and rastered primary ion beam delivers uniform primary beam intensity to an area on the sample leading to flat bottom sputter craters. Other deflectors are located near the apertures to tune the primary beam through the middle of the electrostatic lenses.

#### 4.4.5.2 Secondary ion extraction and transfer

Secondary ions are extracted from the sample as they are produced. Large mass spectrometer components are held at ground potential, while the sample must be held at high accelerating potential. The secondary ions accelerate toward the ground plate of the first electrostatic "the immersion" lens. The second "transfer lens" focuses the ion beam onto the mass spectrometer entrance slits or aperture. This two-lens system constitutes an ion microscope. The secondary ions could be projected onto an image detector for viewing the sample surface. Different transfer lenses produce different magnifications.

The field aperture "the contrast diaphragm" is located approximately at the point where the ion beam image comes into focus. Smaller aperture diameters intercept ions with off-axis energy components reducing image aberrations and lower mass resolution; however, it reduces ion intensity. These off axis ions arise because the primary beam raster pattern sputters an area not the single point where the axis intercepts the sample. The dynamic emittance deflectors adjust the secondary ion beam back on-axis. The deflectors operate in synchrony with the primary beam raster generator to provide continuous adjustment.

#### 4.4.5.3 Ion energy analyzers

The sputtering process produces ions with wide energy range. The high energy ions are intercepted by energy slit. The energy analyzer deflects lower energy ions by a larger angle. A physical barrier intercepts the low energy ions, Fig. 4.4.4. Ions with higher translational energies pass through to the mass analyzer. The voltage offset technique uses the energy analyzer of a mass spectrometer to select secondary ions from the high range of translational energies. The offset is a reduction in acceleration voltage. It reduces both monatomic and multi-atomic ion intensities; however, multi-atomic ions are reduced more. The inner and outer sector electrodes have voltages of opposite

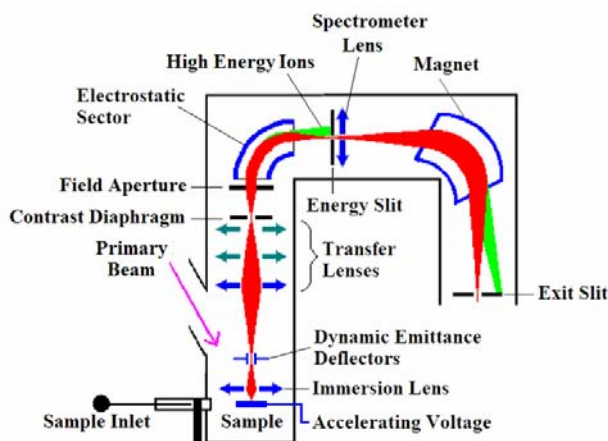


Fig. 4.4.4: schematic drawing of a SIMS instrument showing all part except the primary ion column (shown in Fig. 4.4.3).

polarity with a magnitude about 10 % of the ion accelerating voltage. The ion image comes into focus, producing a virtual image inside the electrostatic sector behind the field aperture. The active surfaces of the electrostatic sector are spherical to transfer the image to the mass analyzer with minimal distortion. The spectrometer lens adjusts the ion beam focus (cross over) to meet the input requirements of the mass analyzer.

#### 4.4.5.4 Mass analyzers

The most common kind of mass analyzers are *magnetic sectors* in which the ion beam passes through the magnetic field, the particles are acted on by a force at right angles, both to the direction of motion and to the direction of the magnetic field. The following equation shows the relationship between the magnetic field ( $B$ ), the ion accelerating voltage ( $V$ ), the mass-to-charge ratio ( $m/q$ ), and the radius of ion curvature

$$\left(\frac{m}{q}\right) \text{ in the magnetic field} = \frac{B^2}{2V} r^2 \quad (4.4.8)$$

Fewer ions strike metal surfaces and the ion beam focuses better at the exit slit with nonnormal pole faces. The entrance and exit slits can be arranged at ion beam crossovers for the cleanest separation (highest mass resolution) between ions with similar  $m/z$  values. The combination of a magnetic and an electrostatic sector produces a double focusing instrument. A magnetic analyzer introduces chromatic aberrations into an ion beam. In a series arrangement of one electrostatic and one magnetic sector, the energy dispersion of the electrostatic sector can compensate the energy dispersion of the magnet. The system will have the mass dispersive properties of the magnet, except that it will produce higher mass resolution. The spectrometer lens adjusts the cross-over from the electrostatic sector to the location required for the magnetic sector.

SIMS, like many kinds of analysis, employs quadrupoles. Ideally, the rods have hyperbolic shapes, but this geometry can be approximated with closely spaced circular rods, Fig.4.4.5. In a typical quadrupole spectrometer, the rods are 1 cm in diameter and 20 cm long and capable to separate ions with energy range of about 25 eV. Since SIMS ions can have a wider energy range than 25 eV, electrostatic sectors usually lead the quadrupole. Alternating and direct voltages on the rods cause the ions to oscillate after entering the quadrupole. For a given set of voltages, Ions with a single  $m/z$  undergo stable oscillation and traverse through the rods. All other ions have unstable oscillations and strike the rods. The alternating frequency and the ratio between the alternating and direct voltages remain constant. Scanning the voltages scans the mass spectrum.

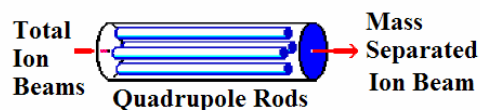


Fig.4.4.5: the quadrupole used as mass analyzer.

#### 4.4.5.5 Secondary-ion detectors

Most of the used SIMS instruments have four detectors; ion counting electron multiplier, a Faraday cup, and two ion image detectors, Fig.4.4.6. The first is the most sensitive and should be protected from intense ion beams. The Faraday cup detector moves on a solenoid to cover the electron multiplier when the incoming ion signal is too high. An electrostatic sector precedes the electron multiplier to eliminate the high energy neutral species formed when an ion beam strikes a surface from the ion signal by charge exchange. The projector lenses bring an image of the sample into focus on the image detectors.

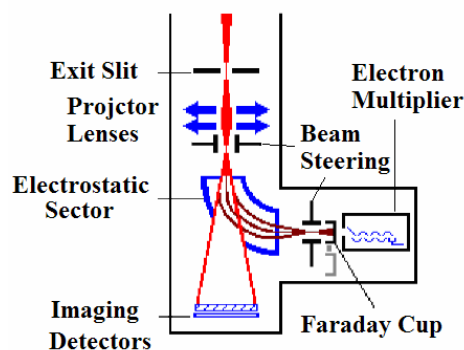


Fig. 4.4.6: the arrangement of detectors in the SIMS instrument.

An electron multiplier consists of a series of electrodes called dynodes, each connected along a resistor string. The signal output end of the resistor string attaches to positive high voltage. The other end of the string goes to the electron multiplier case and ground. The dynode potentials differ in equal steps along the chain. When a particle (electron, ion, high energy neutral, or high energy photon) strikes the first dynode it produces secondary electrons. The secondary electrons are accelerated into the next dynode where each electron produces more secondary electrons. A cascade of secondary electrons ensues. The dynode acceleration potential controls the electron gain.

#### 4.4.5.6 Faraday cups

A Faraday cup is an electrode from which electrical current is measured while a charge particle beam (electrons or ions) impinge on it, Fig. 4.4.7. The shape helps minimize loss of secondary electrons that would alter the current measurement. A deep cup with an electron repeller plate minimizes secondary electron loss.

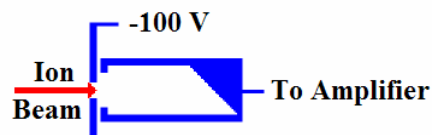


Fig. 4.4.7: Faraday cup

#### 4.4.5.7 Ion image detectors

Ion image detectors depend on micro-channel plate electron multiplier arrays, Fig. 4.4.8. These plates consist of large arrays of small channel electron multipliers. The channels are 7 degrees from perpendicular to the array surface. The voltage across single channel plate can produce gains as high as  $1 \times 10^5$ . For SIMS use, two micro-channel plates

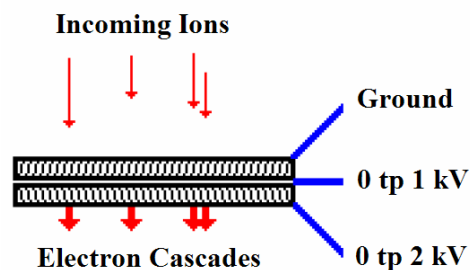


Fig. 4.4.8: Lateral section of an ion image detector.

combine to easily produce gains of  $1 \times 10^6$ . Two kinds of anode provide either direct visualization, or computer compatible ion position data. Two micro-channel plates followed by a phosphor screen for visualizing the electron cascade provide an easy way to monitor the secondary ion beam. SIMS analysts call this combination a dual micro-channel plate (DMCP). As the electrons are accelerated into the phosphor anode, they generate more than one photon per electron. Thus, the anode provides additional gain.

#### **4.4.5.8 Related instruments**

Time-of-flight SIMS instruments are common. However, the sputtering duty cycle is low. A time-of-flight instrument is appropriate for static SIMS in contrast to dynamic SIMS. Only dynamic SIMS will be treated in this surface analysis tutorial because only dynamic SIMS yields quantitative information.

#### **4.4.6 Applications**

Due to its high sensitivity, good depth resolution achievable high mass resolution, the SIMS technique was widely used in electronic materials industries (semiconductors, opto-electric devices, etc.)<sup>215</sup>. The geologists also utilize SIMS for laterally resolved isotopic and elemental analysis<sup>216</sup>. It has been successfully applied to the study of various doping method in optical materials where a good knowledge of diffusion constant, activation energy and solid solubility is crucial to predict the dopant profile in the active component and to ensure adequate control over the optical and the physical properties of the crystal. In particular, results obtained on diffusion of metals, like Mg, Ti, and Cr, rare earths like Er and protons in  $\text{LiNbO}_3$  crystals, with different techniques such as thermal diffusion from thin films, ion-exchange and ion implantation<sup>69</sup>.



# 5 Samples Preparation and Characterization

## 5.1 LITHIUM NIOBATE

### 5.1.1 Single Crystal and Microcrystalline LiNbO<sub>3</sub>

The LiNbO<sub>3</sub> single crystal was delivered by MaTecK (Jülich, Germany) and characterized by the x-ray Guinier method. Rietveld refinement gave the following cell parameters:  $a = 5.15289 \text{ \AA}$ ,  $c = 13.87161 \text{ \AA}$ . A diffraction measurements in the range 47 – 49.8 mol % Li<sub>2</sub>O have shown an overall decrease of  $0.004 \text{ \AA}$  ( $\cong 0.077 \%$ ) and  $0.014 \text{ \AA}$  ( $\cong 0.1 \%$ ) for the lattice constants  $a$  and  $c$ , respectively<sup>87</sup>. However, the unit-cell volume is the property which shows more linear dependence on the Li content than the lattice constants. The unit-cell volume,  $V$  (in  $\text{\AA}^3$ ), obtained from the refinement is  $318.977 \text{ \AA}^3$ , and upon substituting in the equation<sup>74,87</sup>

$$V = 334.7 - 0.3338 c_{\text{Li}} \quad (5.1.1)$$

a Li<sub>2</sub>O mol %,  $c_{\text{Li}}$ , of about 47.1 % was obtained.

Another method that can be applied to measure the stoichiometry of the single crystal was measuring the intrinsic UV/Vis absorption of a plate of the single crystal (1.44 mm thick). The measurement was conducted using a diode array Carl-Zeiss Specord S10. The obtained data were corrected for the reflected light using the equation<sup>217</sup>

$$I_t = I_0(1 - R)^2 \exp(-\alpha d) \Leftrightarrow \alpha = \frac{-\ln(T/(1 - R)^2)}{d} \quad (5.1.2)$$

where  $I_t$  and  $I_0$  are the intensities of the transmitted and the incident light respectively,  $\alpha$  is the absorption coefficient,  $d$  is the sample thickness,  $T (= I_t/I_0)$  is the transmittance, and  $R$  is the reflection coefficient which can be calculated from the refractive index according to the equation<sup>217</sup>

$$R = \frac{(n - 1)^2 + k^2}{(n + 1)^2 + k^2} \approx \frac{(n - 1)^2}{(n + 1)^2} \quad (5.1.3)$$

Here  $n$  is the real refractive index (sometimes called index of refraction), and  $k$  is the attenuation index

Table 5.1.1: The results of the chemical analyses done by ICP-AES and/or delivered by the manufacturing companies for the different LiNbO<sub>3</sub> samples (in ppm).

element	single crystal	Alpha Aesar		Sigma-Aldrich			amorphous (sol-gel)
		microcrystalline		microcrystalline		nano. 16 h	
		(1)	(2)	(1)	(2)	HEBM	
Mg	1.16	1.0 *	36.22	20 •	39.69	472.7	133.8
Si	-	1.0 *	-	-	-	-	-
Al	115.1	0.0 *	207.0	-	226.8	161.7	8650.1
Ca	291.73	0.0 *	148.8	405 •	2257.1	2337.0	5173.5
Cr	7.19	3.0 **	5.68	-	43.37	4.0	96.5
Mn	61.22	-	2.51	8.4 •	9.18	4.4	29.9
Fe	71.06	2.0 **	34.17	150 •	338.78	94.0	803.9
K	228.84	-	174.4	20 ••	371.94	427.9	181.0
Na	268.60	-	234.7	400 ••	637.76	2499.1	3808.5
Rb	-	-	-	6.0 ••	-	-	-

- For samples that have two analyses: the first one is delivered by the manufacturing company and the second one is done here.
- Unlabeled numbers were measured by ICP-AES otherwise: \* by trace emission spectroscopy, \*\* by mass spectroscopy, • by trace analysis ICP, •• by atomic absorption.

(also called the extinction coefficient). The values of  $n$  for LiNbO<sub>3</sub> were taken from the literature<sup>218-219</sup>, and  $k$  was set to zero. The corrected absorption coefficient data were compared with the calibration curve given in Ref. [220], where the absorption edge position (taken at absorption coefficient = 20 cm<sup>-1</sup>) corresponded to 46.4 Li<sub>2</sub>O mol %. The chemical analysis by ICP-AES<sup>†</sup> showed that the single crystal contains some metal impurities, Table 5.1.1.

Highly pure coarse-grained microcrystalline LiNbO<sub>3</sub> was obtained from Alpha Aesar (Product no. 10741-100 g). According to the manufacturing company's chemical analysis, it consists of 99.9995 % lithium niobate, with Li<sub>2</sub>O mol % of 48.55 ± 0.04 as determined by DTA. The sample is remarkably pure; however, it contains several metal impurities, Table 5.1.1.

Early investigations were done on a microcrystalline 99.9 %<sup>‡</sup> LiNbO<sub>3</sub> sample obtained from Sigma Aldrich (Product no. 254290-100 g). The chemical analysis delivered by the producing company and also the one done here showed that the sample contains a relatively high level of metal impurities, mainly Fe among other paramagnetic impurities, Table 5.1.1. This sample was excluded from the results except some examples to show the effect of paramagnetic impurities on both the conductivity and the SLR rate and their activation energies.

<sup>†</sup> ICP-AES was done by the group of Prof. C. Vogt (Inorganic Chemistry Institute, Hannover University)

<sup>‡</sup> The producing company admitted that the purity of this product (with the same product number) has changed from 99.995 % to 99.99 % in 1986 then to 99.98 % in 1993 and finally to 99.9% in 2000.



## 5.1.2 Amorphous and Nanocrystalline LiNbO<sub>3</sub>

Many attempts were made to prepare amorphous LiNbO<sub>3</sub> by melt-quenching methods like single roller quenching<sup>221</sup>, twin-roller quenching<sup>222–227</sup> or cascade crank for hyper-quenching<sup>228</sup>, but unfortunately none of them succeeded. This was mainly due to the lack of the extremely high cooling rate, 10<sup>6</sup> K/s, see Refs [229–230], needed to quench such a fragile melt (for more details about those trials see appendix A.1). Hence, amorphous LiNbO<sub>3</sub> was prepared by double alkoxide sol-gel route. Nanocrystalline LiNbO<sub>3</sub> was prepared by two methods: (i) grain-size reduction starting from the coarser grained microcrystalline LiNbO<sub>3</sub> using the high-energy ball milling technique, (ii) particle growth from the sol-gel prepared amorphous LiNbO<sub>3</sub> applying time-temperature controlled heating under dry oxygen.

### 5.1.2.1 Sol-gel preparation

Two amorphous LiNbO<sub>3</sub> samples, prepared by a sol-gel double alkoxide route, were investigated. The first one was prepared as follows<sup>231–233</sup>: equimolar ratios of lithium ethoxide, LiOEt, obtained as 1 M solution in absolute ethanol (Aldrich, Product no. 400246-100 ml) and niobium ethoxide, Nb(OEt)<sub>5</sub>, neat liquid 99.999 % (Alpha Aesar, product no. 014689-50 g) were dissolved in absolute ethanol (0.2 M each). Then, the solution was refluxed at 352 K for 24 h with continuous magnetic stirring to prepare lithium niobium double alkoxide solution (LiNb(OEt)<sub>6</sub>). Due to the high reactivity of the ethoxides the preparation was conducted under flow of dry argon and the whole system was enclosed under argon inside an Atmos bag [Aldrich (Product no. Z11, 282-8/1ea)]. Then, the double alkoxide was completely hydrolyzed with 7.5 equivalent moles of deionized water dissolved in absolute ethanol (2 M). Slow addition of water/ethanol solution with further stirring and refluxing yielded the white lithium niobium hydroxide hydrated gel. After the gel was filtered and dried up, it was calcined up to 470 K for 2 h under O<sub>2</sub> flow to get the amorphous LiNbO<sub>3</sub>. The product of this preparation route contains some organic residual impurities (as will be shown in Sec. 5.1.3). The ICP-AES analysis showed that the resultant amorphous LiNbO<sub>3</sub> contains some metal impurities, Table 5.1.1.

The second amorphous LiNbO<sub>3</sub> sample<sup>§</sup> was prepared by similar alkoxide sol-gel route with minor alterations<sup>234</sup>; the Nb(EtO)<sub>5</sub> solution was mixed with LiEtO solution and refluxed for 1 h (instead of 24 h). The resultant double alkoxide solution was partially (1/3) hydrolyzed (instead of complete hydrolysis). Then the sample was dried for several hours at 470 K in O<sub>2</sub> atmosphere, followed by heating for 5 min at 620 K to get rid of the unhydrolyzed alkyl residues, however, it continued to have some organic residues.

The morphology of the samples was tested by scanning electron microscopy (SEM) and found to consist of irregular particles with diameters of 1 – 20 μm<sup>234</sup>. Hereafter they will be denoted as "the fully hydrolyzed" and "the partially hydrolyzed", respectively. The fully hydrolyzed sample was used as a precursor to prepare nanocrystalline LiNbO<sub>3</sub> (see also appendix A, pages n, o for SEM images).

<sup>[§]</sup> Delivered by Dr. M. Dinges and Prof. H. Fueß (Technische Universität Darmstadt)

### 5.1.2.2 High-energy ball milling

Nanocrystalline ceramics were prepared from the microcrystalline powder by the high-energy ball milling technique<sup>4-5,235</sup>, using a SPEX 8000 device equipped with an alumina vial set and a 4-g ball made of the same material, (Fig. 5.1.1). Alumina was chosen because of its high hardness to minimize the contamination of the milled sample by abrasion. Despite the chemical stability of  $\text{LiNbO}_3$  in air, the vial was loaded under argon atmosphere and enclosed in a gas tight steel container to decrease the contamination during milling. This was done as a precaution to suppress the reaction with water vapor and  $\text{CO}_2$ , mainly during milling due to the high reactivity and hygroscopicity of the nanocrystalline interfaces at the elevated temperature. The average grain size was varied by milling for different durations of time ranging from one up to 64 hours. The ball-to-powder weight ratio was kept at unity to maintain the reproducibility of the results (for more details see Ref. [236]). The ICP-AES chemical analysis showed that the impurity level increases by the milling process. See Table 5.1.1 for trace metal analysis for e.g. the nanocrystalline  $\text{LiNbO}_3$  sample milled for 16 h. It was previously estimated that milling for 128 h introduces about 13 wt % (by weighing the ball before and after the milling)<sup>5</sup>, however, no XRD reflections due to  $\alpha\text{-Al}_2\text{O}_3$  were detected. In this work the diffractograms were accurate and Rietveld structure refinement showed that the sample milled for 16 h contains about 5 % of crystalline  $\text{Al}_2\text{O}_3$ . The peaks of the  $\alpha\text{-Al}_2\text{O}_3$  phase<sup>237</sup> are marked on the diffractogram of the sample milled for 64 h, (Fig. 5.1.2).



Fig. 5.1.1.: Loading of the SPEX 8000 mill.

### 5.1.2.3 XRD and particle size determination

All the  $\text{LiNbO}_3$  samples produced by HEBM and by sol-gel were subjected to x-ray powder diffraction. The effect of varying the milling time XRD patterns is shown in Fig. 5.1.2(a). The peaks are getting weaker and broader by increasing the milling time, i.e. from the highest intensity and minimum broadening from the microcrystalline starting material (0 h of HEBM) to the lowest intensity and maximum broadening after 64 h of milling.

On the other hand, Fig. 5.1.2(b) shows the evolution of the crystalline phase with varying the temperature and the period of the calcinations. The XRD patterns for the as-dried sol-gel  $\text{LiNbO}_3$  and the gel powder calcined for 2 h at 473 K show no diffraction peaks, confirming their amorphous nature. The sample heated for 1 h at 573 K shows broadened peaks with low intensities; however, they have the XRD pattern characteristic for  $\text{LiNbO}_3$  in addition to the diffuse background (broad humps) of the amorphous form. This background disappeared only after heating at 773K.

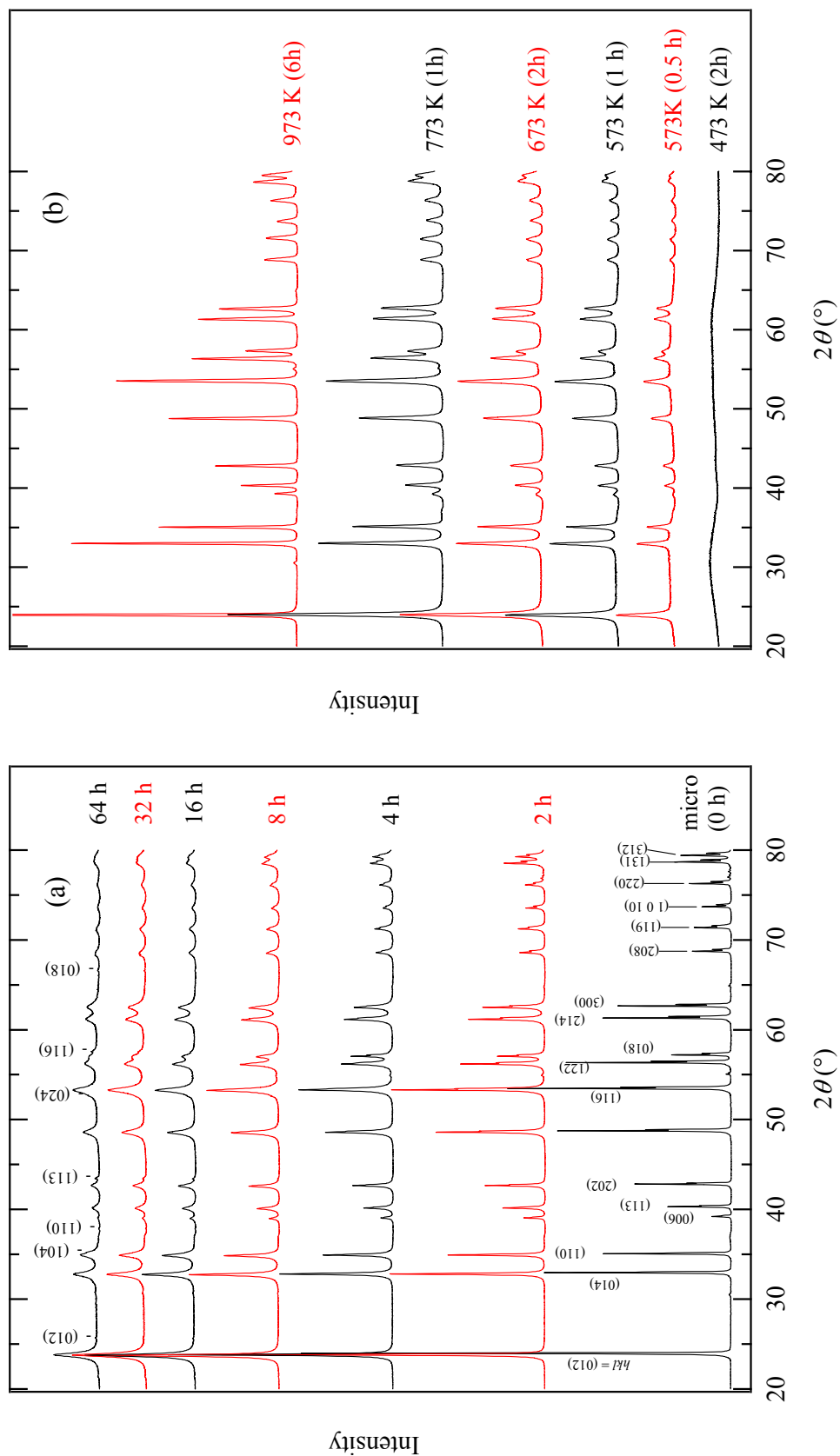


Fig. 5.1.2: The XRD patterns for  $\text{LiNbO}_3$ : (a) high-energy ball-milled for the indicated periods, (b) prepared by double alkoxide sol-gel route followed by calcining under oxygen at the indicated temperatures and periods (in a progressive way). The values of  $(hkl)$  for  $\text{LiNbO}_3$  are shown on the diffractograms of the microcrystalline starting material, while those shown at the diffractogram for the sample milled for 64 h (top of part (a)) belong to the  $\alpha\text{-Al}_2\text{O}_3$  introduced as impurities from the abrasion of the milling vial and ball.

The peak seen in the diffractograms of the microcrystalline material at  $2\theta = 30.5^\circ$  is attributed to the presence of minute amount of  $\text{LiNb}_3\text{O}_8$ , (Fig. 5.1.2(a)). This is expected due to the high degree of  $\text{Li}_2\text{O}$  deficiency in the sample; the peak was broadened with increasing milling time. In Fig. 5.1.2(b) this peak was absent for most of the samples indicating that only the stoichiometric  $\text{LiNbO}_3$  phase is present except in the sample calcined at 975 K for 6 h in which a similar peak appears probably due to the  $\text{Li}_2\text{O}$  loss during prolonged heated at such relatively high temperature.

The average grain size of the nanocrystalline  $\text{LiNbO}_3$  was determined from the line broadening of the XRD pattern. The microcrystalline  $\text{LiNbO}_3$  peaks were used as references to separate the instrumental broadening. Prior to measuring the broadening, the XRD peaks were stripped off the  $K_{\alpha 2}$  contribution using Rachinger correction<sup>238-240</sup>, then the obtained broadening was substituted in the Scherrer equation<sup>240-241</sup>

$$L_0 = \frac{k \cdot \lambda}{\beta \cdot \cos \theta} \quad (5.1.4)$$

where  $L_0$  is the average grain size (i.e. the diameter of the crystal particle);  $\lambda$  is the wavelength of the x-ray source, (in the present work Cu  $K_{\alpha 1}$  radiation was used with  $\lambda = 1.54056 \text{ \AA}$ );  $\theta$  is the Bragg angle of the used peak,  $k$  is a constant that depends on the shape of the crystallites (0.89 for spherical particles);  $\beta$  is the total broadening of diffraction line measured at half its maximum intensity (in radians). The assumption of the spherical particles shape is reasonable as the SEM images for the sol-gel prepared samples show that they consist of spherical particles, whereas the milled particles have an irregular shape that can be well approximated with spheres (for more details c.f. Sec. 5.1.2.1 and Appendix A.2). When Gaussian fitting is used the broadening is given by

$$\beta^2 = B_m^2 - B_s^2 \quad (5.1.5)$$

while in the case of Lorentzian curve fitting

$$\beta = B_m - B_s \quad (5.1.6)$$

where  $B_s$  is the measured full width at half maximum (fwhm) of the standard line and  $B_m$  is the measured fwhm of the unknown line. The resultant grain sizes are listed in Table 5.1.2.

Table 5.1.2: The grain sizes  $L_0$  (nm) and the strain  $\varepsilon$  for the nanocrystalline  $\text{LiNbO}_3$  prepared by HEBM. The calculations were done using both the Gaussian and the Lorentzian fitting to extract the broadening followed by applying the Scherrer equation without considering the strain and equation introduced by Williamson and Hall which accounts for the strain using two couples of harmonic reflections [(012), (024) and (104), (108)].

milling time (h)	Lorentzian fit					Gaussian fit				
	$L_0$	(012) and (024)		(104) and (208)		$L_0$	(012) and (024)		(104) and (208)	
		$L_0$	$\varepsilon \cdot 10^{-3}$	$L_0$	$\varepsilon \cdot 10^{-3}$		$L_0$	$\varepsilon \cdot 10^{-3}$	$L_0$	$\varepsilon \cdot 10^{-3}$
1	695.3	513.5	–	513.5	–	133.3	308.1	0.4	154.1	–
4	119.4	308.1	0.6	271.2	0.3	54.5	126.3	0.9	110	0.3
8	64.4	220.1	1.2	220.1	1.0	37.2	90.6	1.7	77	1.2
16	31.7	128.4	1.8	73.4	1.5	23.2	64.2	2.3	45.3	1.6
32	20.6	51.4	2.8	33.5	2.2	17.3	35	2.8	24.1	1.7
64	16.8	29.6	3.0	32.1	2.3	15.2	28	3.3	19.8	1.9

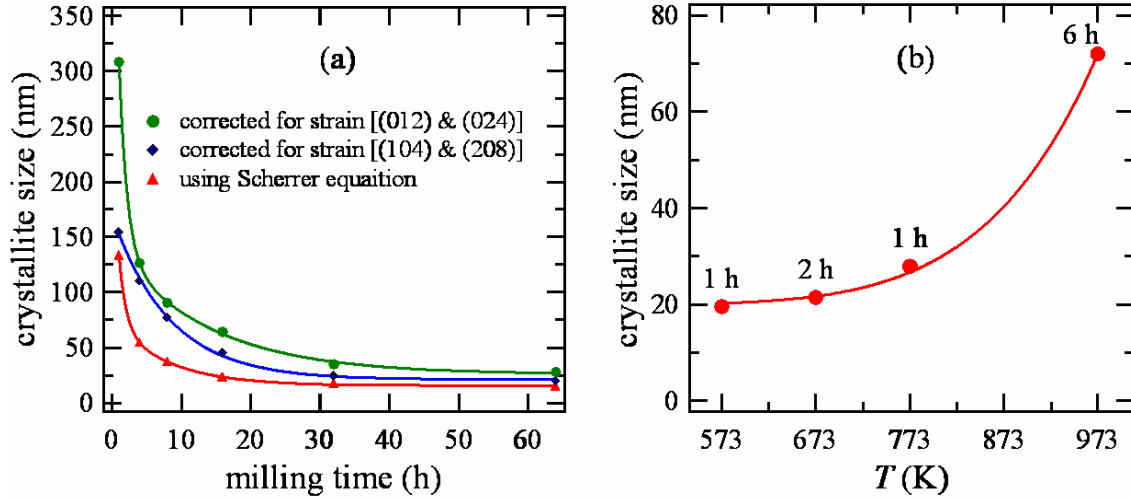


Fig. 5.1.3: (a) The decrease of crystallite size for the HEBM nanocrystalline  $\text{LiNbO}_3$  with increasing the milling times. The crystallite sizes were calculated using Scherrer equation, furthermore, strain effects on the broadening were separated from the effect of the reduced grain size by applying Eq. (5.1.7) to two couples of harmonic reflections, (b) the increase of the crystallite size with increasing the temperatures of calcinations of the amorphous  $\text{LiNbO}_3$  prepared by sol-gel for the indicated periods (Only the results of the Gaussian fit are shown). The solid lines are guides for the eye.

For the ball-milled samples, the Scherrer equation is not appropriate as it neglects the influence of strain on the peak broadening, mainly in the case of long milling times. In such situations both grain size ( $L_0$ ) and strain ( $\varepsilon$ ) of the crystallites are determined from an analysis of the shape of the peak (where  $\varepsilon = \Delta d/d$ ,  $d$  is the lattice spacing). Assuming that the broadening of the peak is the sum of the contributions due to the grain size ( $\beta'$ ) and the strain ( $\beta''$ ), the equation of Williamson and Hall<sup>242-243</sup> can be applied to obtain the relationship between broadening, strain, and size as follows

$$\beta = \beta' + \beta'' = \frac{\lambda}{L_0 \cos \theta} + 4\varepsilon \tan \theta \Rightarrow \beta \cos \theta = 4\varepsilon \sin \theta + \frac{\lambda}{L_0} \quad (5.1.7)$$

Thus the strain and the grain size can be determined by plotting ( $\beta \cos \theta$ ) vs. ( $4 \sin \theta$ ) for each couple of harmonic peaks, [(012), (024) and [(104), (208) were used here]. With increasing milling time, the crystallite size decreases while the strain increases as shown in Table 5.1.2 and Fig 5.1.3(a). For the nanocrystalline samples prepared by heating the sol-gel precursor, the grain size increases with increasing the temperature and the heating period. In this case, strain was not expected so the particle size was determined using Eq. (5.1.4) and the results are listed in Fig 5.1.3(b).

### 5.1.3 Differential Scanning Calorimetry and Thermogravimetry

Fig. 5.1.4(a) shows a DSC curve for the (as prepared) gel, with a characteristic broad endothermic peak that extends from 325 K to 475 K associated with the TG first weight loss step which can be attributed to the removal of water, alcohol and the loosely bonded organic groups. At 600 K there is a strong exother-

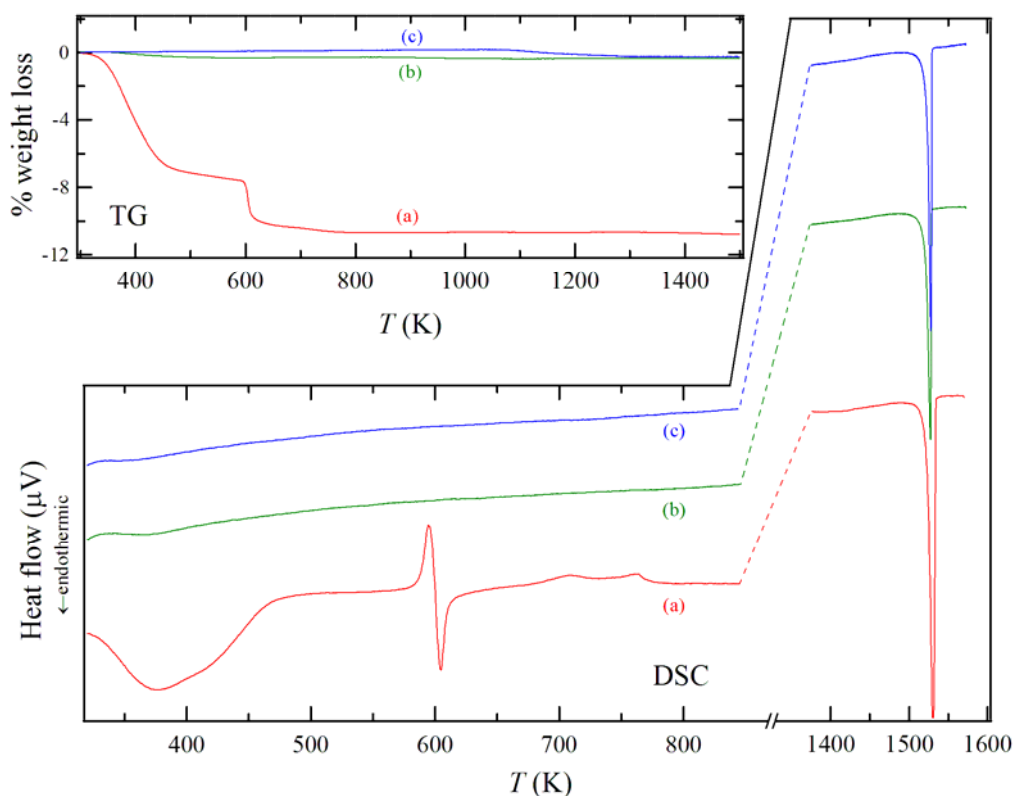


Fig. 5.1.4: TG graphs (top) for the sol-gel prepared  $\text{LiNbO}_3$ : (a) the parent or as prepared gel (dried at 353 K), and after calcination under oxygen: (b) at 773 K for 1 h, and (c) at 973 K for 6 h. The DSC curves (bottom) are for the same samples with rescaled region to show the melting peaks. All measurements were done using a heating rate of 10 K/min and He as carrier gas.

mic peak followed directly by an endothermic one. The former one is due to the completion of the pyrolysis of organic residuals as confirmed by the weight loss step, followed by a subsequent crystallization of the  $\text{LiNbO}_3$ . After this no significant weight loss can be seen. The DSC curve further shows two exothermic peaks at 707 K and 762 K. These may be attributed to the pyrolysis of relatively more complex organic residues which may have been formed during the first pyrolysis process (at 600 K). Similar peaks were encountered during the synthesis of  $\text{LiNbO}_3$  using a metal alkoxide-metal nitrite precursor where they were attributed to the chemical decomposition of  $\text{NO}_3^-$  and  $\text{CO}_3^{2-}$  groups in that system.<sup>244</sup> The presence of these residues is important in preventing the complete crystallization and maintaining smaller crystallite size even after calcination at relatively high temperatures. However, another grain growth and secondary recrystallization occur sequentially at higher temperatures.<sup>244</sup> Thus the amorphous  $\text{LiNbO}_3$  was prepared by calcination of dried gel under oxygen at 473 K for 2 h to avoid crystallization. However, the resultant amorphous form will continue to have alkyl residue less than 3.7 wt. %. The same amorphous form was used to prepare nanocrystalline  $\text{LiNbO}_3$  by calcination at 773 K for 1 h and at 973 K for 6 h. The DSC/TG curves, Fig. 5.1.4(b,c), did not show any significant DSC or weight loss peaks in the whole temperature range up to the melting point. Hence, these samples were regarded as thermally stable up to the

calcination temperatures used to prepare them. The melting points are about 1530 K which indicates that the prepared gel maintains well the chemical composition of  $\text{LiNbO}_3$ .

The DSC/TG curves for the single crystal and the microcrystalline  $\text{LiNbO}_3$  are shown in Fig. 5.1.5(a,b). As expected, they show no significant thermal changes or weight loss up to the melting point. Nanocrystalline sample (16 h HEBM) showed a broad endothermic peak at temperatures extending from 350 to 500 K associated with a TG weight-loss peak of about 3 wt % followed by a second characteristic broad exothermic peak between 540 and 700 K, Fig. 5.1.5(c), which is absent in the case of the microcrystalline form (see the small framed area in the figure for comparison). The first peak may be attributed to the loss of the water strongly adsorbed on the highly reactive interfacial regions. Hence, special attention was paid to avoid the water absorption and its consequences on the NMR relaxation times and the conductivity measurements. All the preparation steps of the nanocrystalline samples were conducted under dry and inert conditions in an argon glove box where they were also stored during the whole research period. The NMR samples were filled inside the glove box followed by evacuation and sealing. However, in the case of impedance samples, it was not possible to press and sputter the electrodes inside the glove box; however, this was overcome by a special drying procedure inside the impedance cell prior to the measurement (see Sec. 6.1.4). The second peak can be attributed to grain-boundary relaxation and grain growth. Such a peak was absent in the case of the nanocrystalline  $\text{LiNbO}_3$  prepared by sol-gel which implies that the interfacial regions differ according to the preparation route. Since DSC is a dynamical

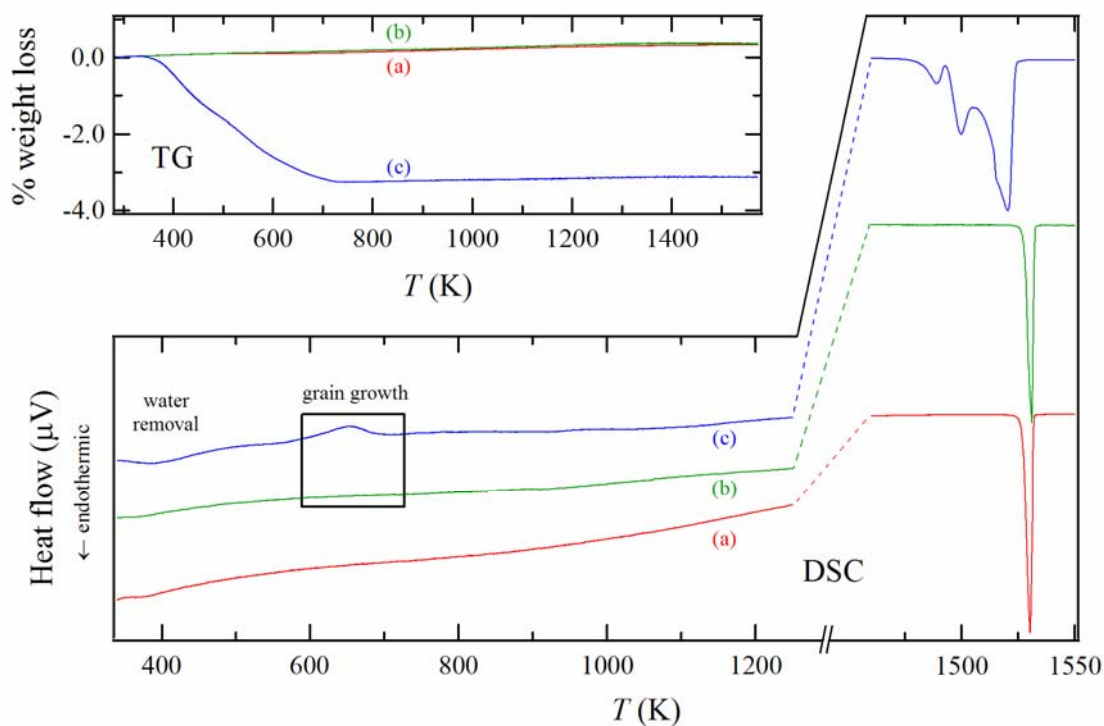


Fig. 5.1.5: TG graphs (top) for  $\text{LiNbO}_3$ : (a) single crystal, (b) microcrystalline, and (c) nanocrystalline HEBM for 16 h. The DSC curves (bottom) are for the same samples with rescaled region to show the melting peaks. All measurements were done using a heating rate of 10 K/min and He as carrier gas.

technique and grain-boundary relaxation and grain growth cannot be ascribed to definite transition temperatures, the temperature 540 K was proposed to be the upper limit for the safe temperature range for all the experiments. However, the reproducibility tests for both NMR and impedance measurements showed that the temperature should not exceed 450 K for the milled nanocrystalline  $\text{LiNbO}_3$ .

### 5.1.4 Raman Spectroscopy

The Raman spectra for microcrystalline and HEBM nanocrystalline  $\text{LiNbO}_3$  are shown in Fig. 5.1.6. They agree very well with the literature values<sup>245–248</sup> (see Table 5.1.3). In spite of being widely studied, the full mode assignment has not been conclusive until now. In the ferroelectric phase, there are two chemical formulas per rhombohedral unit, i.e. ten atoms in a unit cell of  $\text{LiNbO}_3$ . This implies a total of 30 degrees of freedom. According to group theory, the vibrational symmetry of the optical modes at zero wave vector is  $4A_1 + 9E + 5A_2$ . The  $A_1$  and  $E$  modes are polar phonons and both Raman and infrared active, whereas  $A_2$  modes are nonpolar phonons and inactive. Therefore, there are 13 directional dispersion branches of phonons.  $\text{LiNbO}_3$  possesses the major Raman band at  $620\text{ cm}^{-1}$  and a shoulder at  $579\text{ cm}^{-1}$ . These bands correspond to slightly different Nb–O bond lengths and are assigned to the symmetric stretching mode of the  $\text{NbO}_6$  octahedra. The peak at  $874\text{ cm}^{-1}$  is assigned to the antisymmetric stretching mode of the Nb–O–Nb linkage, and the associated bending modes of the Nb–O–Nb linkage appear at  $431$  and  $366\text{ cm}^{-1}$ , see

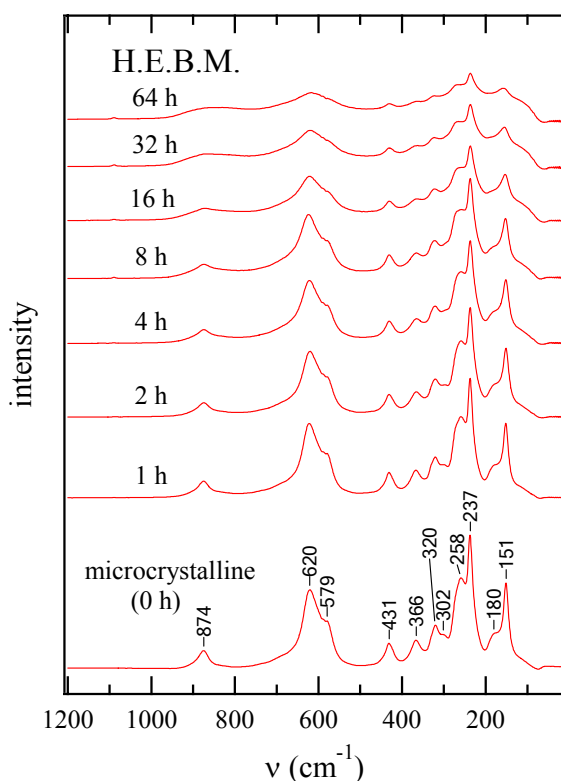


Fig. 5.1.6: The effect of grain-size reduction with increasing the milling time on the Raman spectra for the nanocrystalline  $\text{LiNbO}_3$ .

Table 5.1.3: Band locations ( $\text{cm}^{-1}$ ) for the observed Raman bands for  $\text{LiNbO}_3$  in comparison with those found in the literature:

this work	previous works (Refs.)			symmetry
	[246]	[247]	[248]	
151	152 vs*	152	152	$E_T$
180	180 m			
237	238 vs	238	238	$E_T$
258	256 vs	255	253	$A_{1(T)}$
			265	$E_T$
	276 s	277	276	$A_{1(T)}$
302	308 w		299	$E_L$
320	322 m	321	321	$E_T$
	334 m		333	$A_{1(T)}$
366	370 w	369	368	$E_T$
431	432 w	430	432	$E_T$
579	582 w	580	580	$E_T$
620	628	632	632	$A_{1(T)}$
874	876 w		873	$A_{1(L)}$
		883	881	$E_L$

\* vs, s, m, w, and vw correspond to: very strong, strong, medium, weak, and very weak, respectively, whereas L and T stand for longitudinal and transversal modes.



Ref. [245]. A Raman peak at  $738\text{ cm}^{-1}$  is missing in our case indicating the absence of a defect structure that has ilmenite-like stacking which was previously found in nonstoichiometric  $\text{LiNbO}_3$ , see Ref. [249]. The effect of grain size reduction on the Raman spectra can clearly be seen; the intensity of all Raman bands decreases with increasing milling time and after large milling time most of the weak peaks or shoulders disappeared. Fig. 5.1.7 shows the evolution of the Raman band characteristics for  $\text{LiNbO}_3$  upon heating the hydrated double alkoxide precursor. At the beginning, the "as-dried" gel shows very broad diffuse peaks indicating wide distributions of bond angles. It was difficult to monitor the evolution of the Raman peaks at the beginning of the calcinations due to the fluorescence of the combustion residues formed at low temperatures of calcination. The first clearly-distinguished Raman bands were obtained after heating at  $773\text{ K}$  where most of the organic residues were burnt out and the sample turned to the off-white color characteristic for  $\text{LiNbO}_3$ .

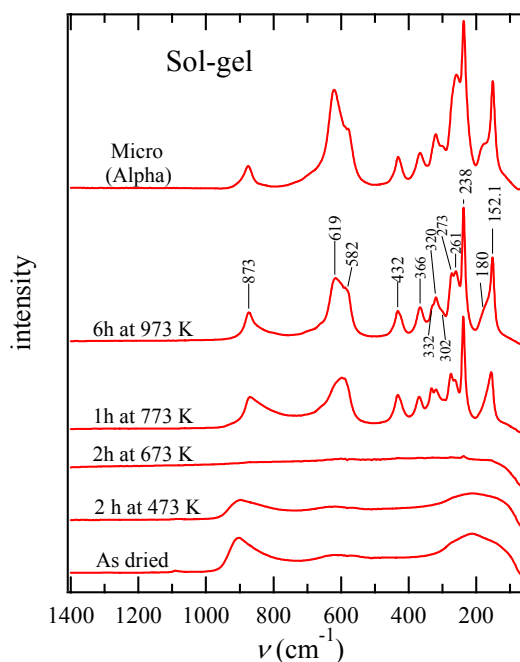


Fig. 5.1.7: Raman spectra for the sol-gel precursor showing the evolution of the nanocrystalline  $\text{LiNbO}_3$  upon heating with the spectrum of the commercial  $\text{LiNbO}_3$  for comparison.

The first clearly-distinguished Raman bands were obtained after heating at  $773\text{ K}$  where most of the organic residues were burnt out and the sample turned to the off-white color characteristic for  $\text{LiNbO}_3$ .

## 5.2 NANOCRYSTALLINE $\text{LiNbO}_3$ EMBEDDED IN SODIUM SILICATE GLASS

### 5.2.1 Sodium Metasilicate Glass Preparation

To prepare  $\text{Na}_2\text{Si}_3\text{O}_7$  glass, high purity quartz ( $\text{SiO}_2$ ) and sodium carbonate ( $\text{Na}_2\text{CO}_3$ ) were dried in an electrical oven at  $393\text{ K}$  overnight. Then  $22.324\text{ g SiO}_2$  and  $13.126\text{ g Na}_2\text{CO}_3$  were weighed and well mixed using pestle and mortar for 10 minutes. The mixture was placed in a sintered alumina crucible and heated in a bottom loaded electrical oven (Carbolite™, Fig. 5.1.8), at  $1573\text{ K}$  (1 h), then at  $1673\text{ K}$  (1.5 h), and finally at  $1723\text{ K}$  (0.5 h). This heating procedure provided good efficiency in mixing reactants and getting rid of the gas bubbles. At the end of the heating period, the melt was poured onto a steel plate at room temperature. About 30 g-batch of transparent bulk glass was obtained which was manually crushed into a powder of about  $100\text{ }\mu\text{m}$  grain size by pestle and mortar.  $\text{Fe}_2\text{O}_3$  (0.2 wt %) was in-



Fig. 5.1.8: Bottom loading (elevator hearth) furnaces.

tentionally added as a source of paramagnetic impurities to the samples used for  $^{29}\text{Si}$  NMR to enhance the SLR rate and to make the measurements possible within reasonable experimental time.

## 5.2.2 n-LiNbO<sub>3</sub> Embedding (Varying Temperature and Composition)

To study the heating effect, 5g-batches of 1:1 lithium-to-sodium molar ratio were prepared by mixing 2.75 g HEBM nanocrystalline LiNbO<sub>3</sub> with 2.25 g-Na<sub>2</sub>Si<sub>3</sub>O<sub>7</sub> glass powder (to indicate the equimolar ratio of alkalis, hereafter, this mixture will be denoted as n-LiNbO<sub>3</sub>·g-NaSi<sub>1.5</sub>O<sub>3.5</sub>). Each batch was packed together manually in a sintered Al<sub>2</sub>O<sub>3</sub> crucible, and then heated at a certain temperature (873, 973, 1073, 1173, and 1273 K) for 2 h, and finally taken out of the furnace and allowed to cool in air. To study the composition effect, a new series of different batches having the composition (x)n-LiNbO<sub>3</sub>·(1-x)g-NaSi<sub>1.5</sub>O<sub>3.5</sub> with  $0 < x < 1$  were prepared by mixing n-LiNbO<sub>3</sub> with the glass powder according to Table 5.2.1. All the batches were heated at 1173 K for 2 h. This temperature was chosen according to the results obtained from the temperature-effect study.

Table 5.2.1: Weights of n-LiNbO<sub>3</sub> and g-Na<sub>2</sub>Si<sub>3</sub>O<sub>7</sub> used to prepare 5-g batches the composite (x)n-LiNbO<sub>3</sub>·(1-x)g-NaSi<sub>1.5</sub>O<sub>3.5</sub> with different x values

x	wt. Na <sub>2</sub> Si <sub>3</sub> O <sub>7</sub> (g)	wt. LiNbO <sub>3</sub> (g)
0.9	0.42	4.58
0.8	0.85	4.15
0.7	1.30	3.70
0.6	1.77	3.23
0.5	2.25	2.75
0.4	2.76	2.24
0.3	3.28	1.72
0.2	3.83	1.17
0.1	4.40	0.60

## 5.3 (LITHIUM,SODIUM) NIOBIUM SILICATE GLASSES & GLASS CERAMICS

### 5.3.1 Glass Preparation

Samples of the glass  $0.33[x\text{Li}_2\text{O} \cdot (1-x)\text{Na}_2\text{O}] \cdot 0.33\text{Nb}_2\text{O}_5 \cdot 0.33\text{SiO}_2$  with  $x = 1, 0.85, 0.7, 0.6, 0.5, 0.4, 0.3, 0.15, 0$ , were prepared from reagent grade silica (SiO<sub>2</sub>), lithium carbonate (Li<sub>2</sub>CO<sub>3</sub>), sodium carbonate (Na<sub>2</sub>CO<sub>3</sub>), and niobium oxide (Nb<sub>2</sub>O<sub>5</sub>) according to Table 5.3.1. The preparation followed the same procedure used to prepare pure lithium niobium silicate glass<sup>250-251</sup> and the pure sodium niobium silicate glass<sup>252-253</sup>. The reagents were dried overnight at 393 K in an electrical oven before taking the amounts required to prepare 5-g batches, and then they were well-mixed using pestle and mortar for 5 minutes. The melts were so fragile that they were completely absorbed by the sintered alumina crucible, thus the mixtures were molten in platinum crucibles applying the same temperature program used in the preparation of Na<sub>2</sub>Si<sub>3</sub>O<sub>7</sub> glass (Sec. 5.2.1). At the end of the heating period, the melts were quenched by dipping the bottom of the crucible into water kept at room temperature to aid in removing the glass from the crucible. Then they were annealed at 773 K for 2 h. The result was a fade yellowish transparent glass for all compo-

Table 5.3.1: Weights of  $\text{Li}_2\text{CO}_3$ ,  $\text{Na}_2\text{CO}_3$ ,  $\text{Nb}_2\text{O}_5$ , and  $\text{SiO}_2$  used to prepare 5-g batches of  $0.33[x\text{Li}_2\text{O} \cdot (1-x)\text{Na}_2\text{O}] \cdot 0.33\text{Nb}_2\text{O}_5 \cdot 0.33\text{SiO}_2$  glass with different compositions,  $x$ .

$x$	$\text{Li}_2\text{CO}_3$ wt. (g)	$\text{Na}_2\text{CO}_3$ wt. (g)	$\text{Nb}_2\text{O}_5$ wt. (g)	$\text{SiO}_2$ wt. (g)
0.00	0.00	1.23	3.08	0.70
0.15	0.13	1.05	3.11	0.70
0.30	0.26	0.88	3.15	0.71
0.40	0.35	0.76	3.17	0.72
0.50	0.44	0.64	3.20	0.72
0.60	0.54	0.51	3.22	0.73
0.70	0.63	0.39	3.25	0.73
0.85	0.78	0.20	3.28	0.74
1.00	0.92	0.00	3.32	0.75

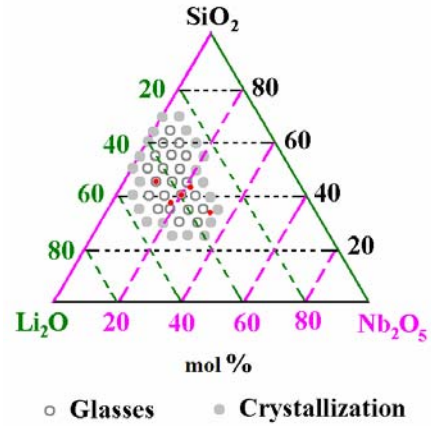


Fig. 5.3.1: The ternary phase diagram of  $\text{Li}_2\text{O}$ - $\text{SiO}_2$ - $\text{Nb}_2\text{O}_5$ , Ref. 254. The red points represent the prepared compositions.

sitions. Except for the pure sodium one,  $x = 0$ , the product was a miscible glass with milky color.

To investigate the role of  $\text{Nb}^{5+}$  in the silicate glasses, another two series of glasses were prepared. The first with the general formula  $(1-y)/2[\text{Li}_2\text{O} \cdot \text{SiO}_2] \cdot y\text{Nb}_2\text{O}_5$  has  $y = 0.1, 0.2, 0.33$  and the second has the composition  $x\text{Li}_2\text{O} \cdot (1-x)/3[\text{Nb}_2\text{O}_5 \cdot 2\text{SiO}_2]$  with  $x = 0.35, 0.4, 0.45$ , Table 5.3.2. These compositions were chosen in the glass forming region according to the ternary phase diagram of the  $\text{Li}_2\text{O} \cdot \text{SiO}_2 \cdot \text{Nb}_2\text{O}_5$  system, (Fig. 5.3.1)<sup>254</sup>. They were prepared according to the same heating procedure mentioned above.

Table 5.3.2: Weights of  $\text{Li}_2\text{CO}_3$ ,  $\text{Na}_2\text{CO}_3$ ,  $\text{Nb}_2\text{O}_5$ , and  $\text{SiO}_2$  used to prepare 5-g batches the glasses  $(1-y)/2[\text{Li}_2\text{O} \cdot \text{SiO}_2] \cdot y\text{Nb}_2\text{O}_5$  and  $x\text{Li}_2\text{O} \cdot (1-x)/3[\text{Nb}_2\text{O}_5 \cdot 2\text{SiO}_2]$  with different  $y$  and  $x$  values:

$(1-y)/2[\text{Li}_2\text{O} \cdot \text{SiO}_2] \cdot y\text{Nb}_2\text{O}_5$				$x\text{Li}_2\text{O} \cdot (1-x)/3[\text{Nb}_2\text{O}_5 \cdot 2\text{SiO}_2]$			
$y$	wt. of $\text{Li}_2\text{CO}_3$ (g)	wt. of $\text{Nb}_2\text{O}_5$ (g)	wt. of $\text{SiO}_2$ (g)	$x$	wt. of $\text{Li}_2\text{CO}_3$ (g)	wt. of $\text{Nb}_2\text{O}_5$ (g)	wt. of $\text{SiO}_2$ (g)
0.10	1.91	1.53	1.56	0.45	1.60	2.34	1.06
0.20	1.38	2.49	1.13	0.40	1.38	2.49	1.13
0.33	0.92	3.32	0.75	0.35	1.18	2.63	1.19

### 5.3.2 Glass-Ceramic Formation

It was not planned to study the kinetics of crystallization or particle growth inside the glass matrixes. However, while heating the glass samples at elevated temperatures during characterizing the samples by *in-situ* XRD (Sec. 6.5.1) and by DSC (Sec. 6.5.4), some useful information about the glass-ceramics was collected.



# 6 Experimental Techniques and Setups

## 6.1 IMPEDANCE SPECTROSCOPY

### 6.1.1 Impedance Analyzer

Most of the impedance measurements were done over the frequency range 5 Hz – 13 MHz using an LF impedance analyzer (HP 4192A). It works as an auto balancing bridge with an impedance detection range from 0.1 m $\Omega$  to 1 M $\Omega$ . It applies a test signal level in the range from 5 mV to 1.1 V and has an accuracy of 0.1 %. The device is manufactured by Hewlett-Packard.

In the case of single crystalline LiNbO<sub>3</sub> and due to its low conductivity, an Alpha™ high-resolution dielectric analyzer was used. It works in the frequency range from 3  $\mu$ Hz to 10 MHz and in the impedance range from 10<sup>-2</sup> to 10<sup>14</sup>  $\Omega$  (16 orders of magnitude). It has a high accuracy in measuring the loss factor ( $\tan \delta$ ) which is less than  $3 \cdot 10^{-5}$  (resolution < 10<sup>-5</sup>); furthermore, it is specified to measure capacities as low as 1 fF within the frequency range from 10 Hz to 500 kHz. The device is manufactured by Novocontrol-GmbH.

### 6.1.2 Impedance Cell

The conductivity measurements were performed using a home-built Duran glass apparatus placed in a horizontal tube furnace. Fig. 6.1.1 shows the sample holder which has a four-terminal configuration (discussed previously in Sec. 4.1.4.2). On the other hand the Alpha analyzer uses a BDS1200 connection head as the standard sample cell for the low-frequency range from DC to 10 MHz including a PT100 temperature sensor. The cell is connected by four or two wire BNC cables to the impedance analyzer.

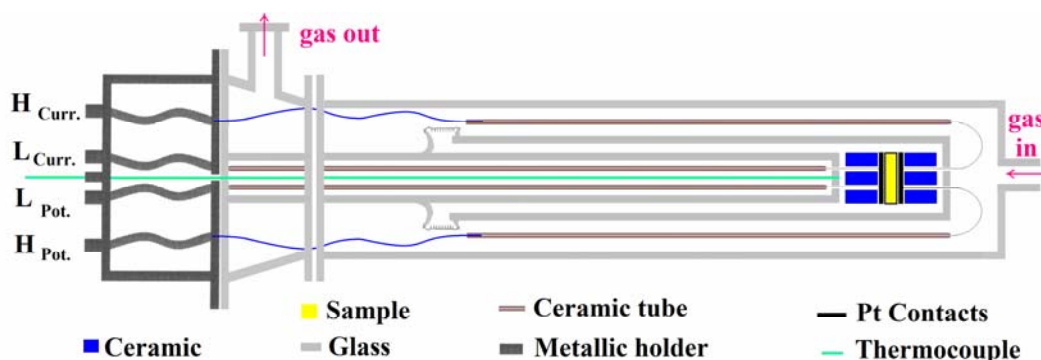


Fig 6.1.1: Impedance cell (the four terminal pair (4TP) configuration) the Pt wires pass through ceramic tubes painted with Pt paste for shielding. The cell is gas tight and has an inlet and an outlet to pass the gas.

### 6.1.3 Sample Pressing and Electrode Sputtering

Powder samples were prepared for impedance measurements by pressing into pellets under uniaxial pressure of about 0.75 GPa using a SPEX pressing die of 13 mm diameter (maximum pressure = 10 ton). The thickness of the pellets was in the range 0.2 – 0.4 mm. Then it was cut into the shape of a smaller disk with diameter smaller than 9 mm to fit inside the cell. Afterthat, each pellet was sputtered with gold using metal rings with inner diameters of 6.5 mm as masks to print two opposite circular gold spots (electrodes) on the parallel sides of the pellets as illustrated in Fig. 6.1.2.

The  $\text{LiNbO}_3$  single crystal was cut into plates with a thickness of 0.6 mm and an area of  $15 \times 12 \text{ mm}^2$ . The two largest surfaces were polished down to the fineness of  $1 \mu\text{m}$  using diamond paste to achieve parallel surfaces. The final sample thickness was 0.45 mm. The large surfaces were then sputtered with gold. High attention was paid to avoid sputtering on the sides of the pellets in order not to short circuit the electrodes. The gold sputtering was conducted using bench-top sputter coater (Scancoat Six™) originally designed by BOC Edwards Company to prepare specimens for conventional scanning electron microscopy.

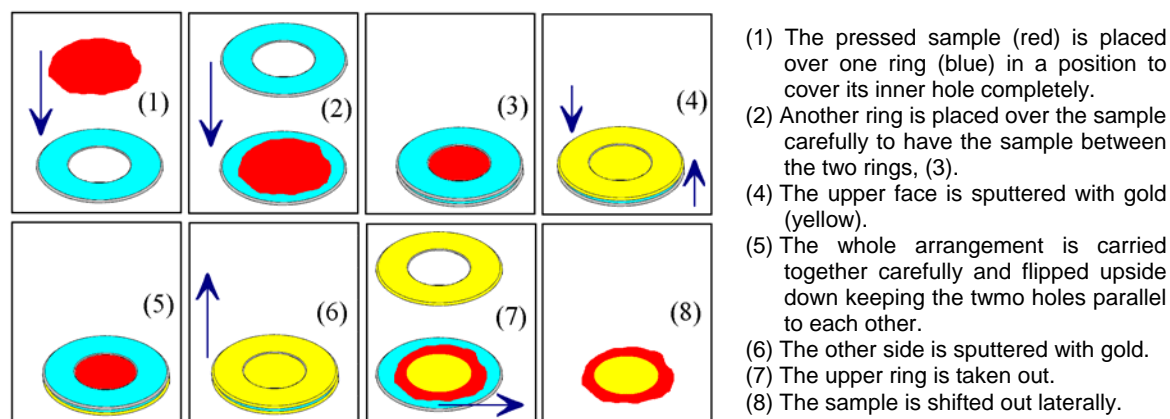


Fig. 6.1.2: Illustration of sample sputtering with gold to make the electrodes for the impedance-spectroscopy measurements.

No degradation (peeling off or cracking) of the electrodes was observed even after heating for prolonged periods. The areas of the electrodes were calculated and all the measured conductivities were normalized to the cell factor  $l/A$  where  $l$  is the sample thickness and  $A$  is the electrode area.

#### **6.1.4 Temperature and Atmosphere Controlling**

The home-built impedance cell is placed in a horizontal-tube furnace controlled by a Eurotherm 818 programmable temperature controller. Temperature is measured with a chromel/alumel thermocouple (type K) that is best suited for measurements in the range from ambient temperature up to 750 K range. It was situated just 3 mm away from the sample. Axial temperature gradients are less than 0.1 K/mm at 423 K. The accuracy of temperature is estimated to be better than 0.5 K. While the Alpha dielectric analyzer is equipped with a Novocool system that controls the temperature in the range from 173 K to 523 K with an accuracy of 0.3 K. The temperature is measured at the lower electrode of the sample cell. The temperature is adjusted by means of evaporated liquid nitrogen in conjugation with an electrical heater both controlled by the Novocontrol software WinDETA.

In spite of keeping the nanocrystalline samples under dry argon and using a gas-tight milling vial for milling, it was not possible to prevent moisture from being adsorbed at least on the surface of the sample. As a result a hysteresis in conductivity was obtained, i.e. the conductivity was high at the beginning and started to decrease with drying as the temperature was raised and then it started to increase again with heating. To get rid of this behavior, the cell was flushed with dry oxygen for several minutes after inserting the sample to remove the air and the water vapor, then the system was heated up to 383 K overnight to eliminate any adsorbed water or water vapor. After that, the temperature was raised to the upper limit of the temperature range, followed by a waiting period to reach the thermal equilibrium at the new temperature. Then the cell was flushed with oxygen followed by a waiting period of 5 minutes to retain the thermal equilibrium, after that the measurement was conducted. During the experiments, the temperature was changed in 10 degrees steps for  $\text{LiNbO}_3$  samples and 15 – 20 degrees for other glasses and composites. Over the whole temperature range of the experiment, the measured conductivity was reproducible on repeated runs.

#### **6.1.5 Data Analysis and Fitting Procedures**

The Novocontrol software, WinDETA, was used to control the temperature and to record the measurements automatically. However, in all cases, complex plane impedance plots were analyzed according to the method of electrical “Equivalent Circuit” software. This program works in an environment developed for equivalent electric circuits being based on the fitting and simulation of emittance spectra using non-linear least square (NLLS) methods.<sup>255</sup>

## 6.2 NUCLEAR MAGNETIC RESONANCE

### 6.2.1 Apparatuses (Magnets, Spectrometers, Amplifiers)

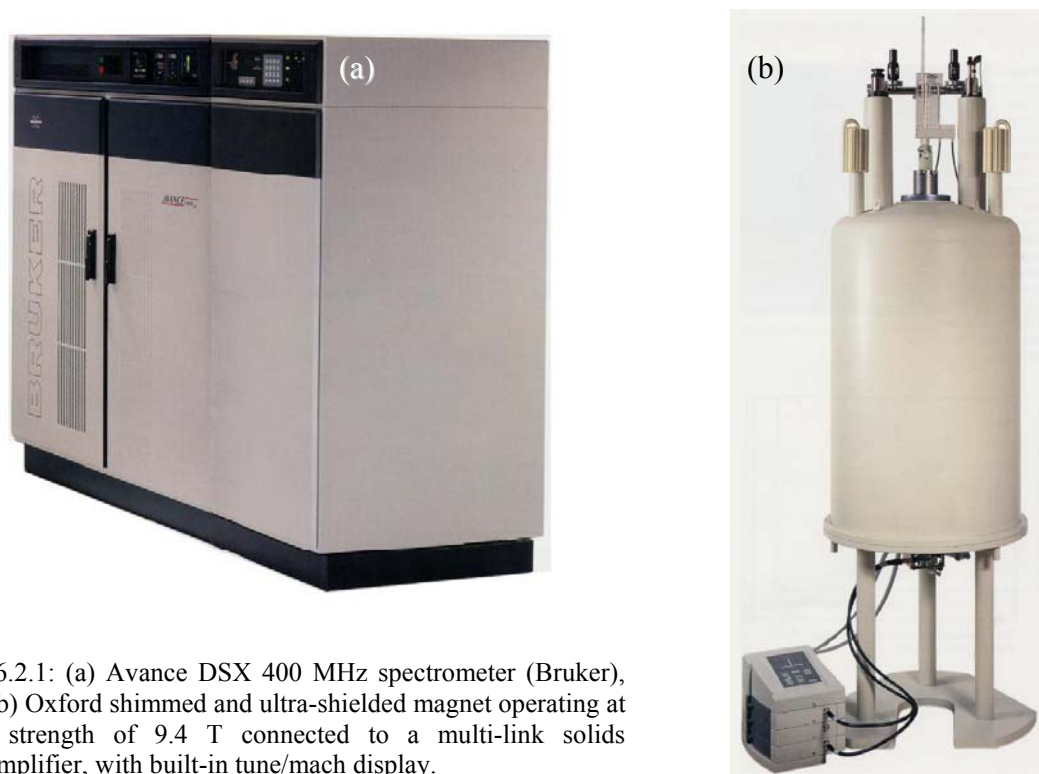


Fig. 6.2.1: (a) Avance DSX 400 MHz spectrometer (Bruker), and (b) Oxford shimmed and ultra-shielded magnet operating at field strength of 9.4 T connected to a multi-link solids pre-amplifier, with built-in tune/mach display.

For structure characterization,  ${}^7\text{Li}$ ,  ${}^{23}\text{Na}$ ,  ${}^{29}\text{Si}$ ,  ${}^{93}\text{Nb}$  spectra were collected on a Bruker Avance DSX 400 MHz spectrometer. This spectrometer is well designed for solid-state NMR, especially high-resolution NMR of solids containing quadrupolar nuclei. It has a 4 MHz receiver bandwidth, with a digital phase switching in  $0.05^\circ$  step, an ultra fast (50 ns) and ultra clean four-phase modulator, and dual 1 kW rf amplifiers that provide very long, high power output bursts free of instabilities and limitations usually caused by component heating in most semiconductor-based amplifiers. The used magnet was an 89 mm wide-bore shimmed and ultra-shielded Oxford magnet operating at field strength of 9.4 T. The resonance frequencies ( $\nu_L = \omega_L/2\pi$ ) were 155.5, 105.84, 79.49, and 97.78 MHz, respectively. Two-channel:  ${}^1\text{H}/{}^{19}\text{F}$ , and one broad-banded 40-amp gradient amplifiers are used.

The SLR rates ( $T_1^{-1}$ ) were measured using a tunable (0 – 8 Tesla) non-shimmed (Teslatron H<sup>TM</sup>, Oxford) cryomagnet with an 89 mm wide bore. They were performed in the laboratory reference frame for  ${}^7\text{Li}$  and  ${}^{23}\text{Na}$  at a fixed field of 5 T corresponding to a resonance frequency,  $\nu_L$ , of 77.72 and 52.90 MHz, respectively. A modified Bruker MSL 100 console with a Kalmus LP 400 W high-frequency amplifier was connected to the magnet.



## 6.2.2 NMR Samples and Probes (Static and MAS)

The powder samples were filled in a Duran (or quartz-glass) tube under dry conditions in an argon-glove box to minimize the amount of water adsorbed on the surface of the sample, mainly in the case of the nanocrystalline sample. Then the tube was evacuated and closed by melting the neck of the glass tube to give a sealed ampoule, (Fig. 6.2.2(a)). The samples to be probed by MAS NMR were finely ground and packed very well into the sample container in order to avoid tumbling which may damage the MAS probe. The sample container (the rotor) consists of a cylindrical zirconia tube (4 mm in diameter), (Fig. 6.2.2(b)). A full rotor has a sample volume  $\approx 80 \mu\text{l}$ . The maximum spinning rate for such a rotor is about 15 kHz, but is limited to lower speeds of about 12.5 kHz in all experiments. The rotor caps are made of a type of plastic called Kel-F® (a homopolymer of chlorotrifluoroethylene), which can be used in a temperature range from 283 K to 323 K. The cap does not only close the rotor, but it also provides the driving of the rotor. For this purpose, it has a turbine-shaped design such that when air is streamed over the cap it will spin around its axis of symmetry. The DSX spectrometer is equipped with a microprocessor-based MAS pneumatic unit capable of insertion and ejection of MAS rotors, besides an intelligent MAS controller that brings the rotor up to speed and regulates the speed within 0.1 %. It regulates two gas stream, one for drive and one for bearing gas and stabilizes the MAS rotors typically to less than  $\pm 5$  Hz over the entire operating speed.

For the static measurements at temperatures from 150 to 450 K, a commercial Bruker probe was used. The temperature was measured using a thermocouple inserted in the probe to reach the nearest point to the sample. The temperature is read by an intelligent temperature controller unit, ITC 4-Oxford. This controlling unit stabilizes the temperature within 0.5 K using a flow of freshly evaporated liquid nitrogen for temperatures below room temperature or a stream of electrically heated air for high temperatures. The high-temperature measurements ( $T > 450$  K) were conducted

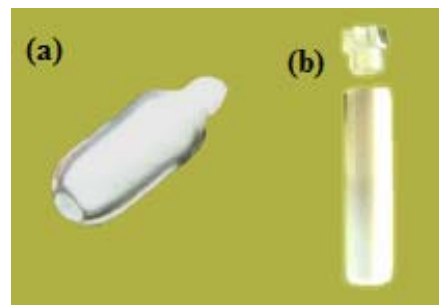


Fig. 6.2.2: NMR samples; (a) sealed quartz ampoule, (b) 4-mm diameter cylindrical zirconia tube with its plastic turbine-shaped rotor cap.

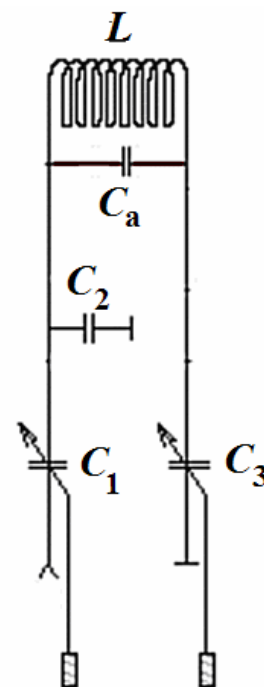


Fig. 6.2.3: A schematic electronic diagram for the LRC circuit used in the home-built NMR probe. The capacitance values  $C_1 = 6$  pF,  $C_3 = 6$  pF,  $C_2 = 10$  pF,  $C_a = 12$  pF. For the coil number of turns  $N = 10$ , has been assumed, length  $l = 29$  mm, and diameter  $D = 9$  mm yields an inductance of approximately  $L = 250$  nH

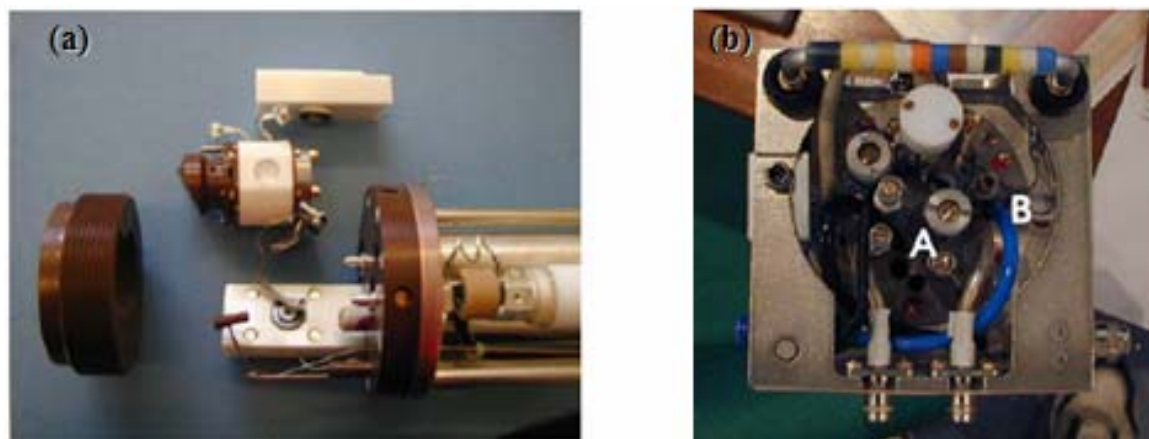


Fig. 6.2.4: (a) Top of MAS probe after being disassembled, (b) Bottom of the MAS probe showing knob A used to match the resonance circuit to the  $50\ \Omega$  cable coming from the spectrometer and knob B for tuning the correct frequency for the sample nucleus capacitors<sup>257</sup>.

using an electrically heated home-built probe with the electronic LRC-circuit shown in Fig. 6.2.3. This probe was designed to be two-channel probe as described in detail elsewhere<sup>256</sup>.

In an MAS mode, the sample is inserted into the probe via a tube at the top of the magnet which leads directly to the probe. Then it is inserted into the correct position within the coil by using a timed burst of compressed air. After that, the sample is brought to rotate at the desired speed (e.g.  $\nu_r = 12.5\ \text{kHz}$ ), using the control panel on the NMR control unit. Figure 6.2.4 (a) shows the MAS probe after being disassembled. When the desired spinning speed is achieved the control unit will lock the drive and bearing pressures in order to maintain this spinning speed. The NMR spectrometer is matched and tuned to the nucleus to be probed by applying some alterations to the RLC circuit used to provide the resonance conditions. On the bottom of the MAS probe there are two knobs conveniently situated for the purpose of matching and tuning the spectrometer for the experiments, (Fig. 6.2.4(b))<sup>257</sup>.

## 6.2.3 NMR Experiment

### 6.2.3.1 Structure characterization ( $^7\text{Li}$ , $^{23}\text{Na}$ , $^{29}\text{Si}$ , $^{93}\text{Nb}$ )

$^7\text{Li}$  spectra were acquired by a  $\pi/6$  pulse with 2 s delay and 1000 scans and spectral width of 100 kHz.  $^{23}\text{Na}$  spectra were acquired with a  $\pi/12$  pulse, recycle delay of 3 s and 2000 signal averages and spectral width of 150 kHz, while for Nb, a  $\pi/6$ -pulse with 100 ms delay and 16,000 scans were used and spectral width of 1 MHz. Si spectra were acquired by  $\pi/6$  flip angle, and spectral width of 150 kHz, and recycle delay of 20 s for the glassy samples and using 5000 scans to collect spectra with good signal to noise ratio (S/N). In the samples with crystalline silicate a delay of 400 s with 2000 scans was necessary due to the slow relaxation. Relatively short pulses were used here to assure a quantitative, uniform and selective excitation of the central transition

of all the sites in the atomic sample. 1 M LiCl solution, 1 M NaCl solution, saturated solution of NbCl<sub>5</sub> in "wet" acetonitrile, and TMS were used as references for Li, Na, Nb, and Si, respectively.

### 6.2.3.2 Spin-lattice relaxation (<sup>7</sup>Li, <sup>23</sup>Na)

The SLR rates for <sup>7</sup>Li and <sup>23</sup>Na were measured in the laboratory reference frame at resonance frequencies  $\nu_L = 77.72$  and 52.9 MHz, respectively. All the experiments were done in the temperature range from 153 K to 453 K using a commercial single-channel broad band probe, OBSERVE – Z 31 v HP, designed by Bruker to measure <sup>1</sup>H NMR at 100 MHz. The saturation recovery pulse sequence<sup>258</sup> ( $n \cdot \pi/2 - \tau - \pi/2$ ) was used with  $n = 10$  pulses. The pulses are separated by a delay of about 50  $\mu$ s. After that, a  $\pi/2$ -pulse follows with lengths of about 5.5 or 3.2  $\mu$ s for <sup>7</sup>Li and <sup>23</sup>Na, respectively. The spectral width was kept at 2 MHz in the case of <sup>23</sup>Na whereas it was ranging between 0.5 and 2 MHz in the case of <sup>7</sup>Li depending on the temperature and the diffusivity of the Li<sup>+</sup> ion. The magnetization

$$M(\tau) = M_0 \left\{ 1 - \exp\left(-\frac{\tau}{T_1}\right) \right\} \quad (6.2.1)$$

was recorded at each temperature for 30 different fractions of the delay time,  $\tau$ , which is usually taken to be  $5T_1$  or more when stretched exponential behavior is expected. The delay time ranged between 0.8 and 300 s for <sup>7</sup>Li and between 0.1 and 6 s for <sup>23</sup>Na. Each data point of the magnetization curve was obtained by integrating the area under the free induction decay (FID). The number of transients accumulated for each FID was increased at high temperatures and for sample with low content of the probed nucleus from 4 to 32 scans for <sup>7</sup>Li and from 8 to 64 scans for <sup>23</sup>Na.

### 6.2.3.3 Motional narrowing

The solid-echo pulse sequence was used to register the <sup>7</sup>Li and <sup>23</sup>Na NMR spectra to overcome receiver-deadtime problems and to obtain all the accessible information from the spectra. As both nuclei have  $I = 3/2$ , the amplitude will be at maximum using a refocusing pulse of 64°. The echoes were recorded in the temperature range 150 – 670 K. The solid echo sequence is: 64° –  $t_e$  – 90° –  $t_e$  – echo. The inter-pulse delay,  $t_e$ , had values between 10 and 100 ms. Under the condition  $t_e \ll T_2$  the trailing half of the echo is equal to the FID. FT was performed beginning from the echo top.

### 6.2.3.4 Spin-alignment echoes<sup>259</sup>

<sup>7</sup>Li spin-alignment echoes were measured at 77.72 MHz in the temperature range between 150 and 450 K. Spin-alignment echoes under static conditions were measured using the three-pulse Jeener-Broekaert sequence<sup>198</sup>. Two-time correlation functions were recorded for constant evolution time  $t_p = 12 \mu$ s as a func-

tion of the mixing time  $t_m$  ranging from 1  $\mu\text{s}$  up to 100 s. The recycle delay was about  $5T_1$ . Appropriate phase cycling<sup>260</sup> was employed in order to pick out the correct coherence pathway and to eliminate unwanted coherences and to decrease the effects of pulse imperfections.

## 6.2.4 Data Analysis and Fitting

The  $^7\text{Li}$ ,  $^{23}\text{Na}$ ,  $^{29}\text{Si}$ , and  $^{93}\text{Nb}$  NMR spectra were quantitatively analyzed with DmFit software<sup>261</sup>. Li and Na lines are fitted by Gaussian or Lorentzian lines for slow and fast moving ions, respectively, and the full width at half maximum (fwhm) is extracted from the fit to describe the temperature dependence of the linewidth (the motional narrowing).

Gaussian distributions are used as a standard method for fitting  $^{29}\text{Si}$  NMR spectra<sup>203</sup>. The linewidth, peak position and amplitude of each Gaussian component are varied until the best fit is obtained. The percentage of non-bonding oxygens to the total number of oxygen atoms in the silicon-oxygen tetrahedra,  $NBO \% = NBO / (BO + NBO) \times 100 \%$ , can be obtained from the percentage of each  $Q^n$  species in the glass<sup>262</sup>.  $Q^3$  shares three BOs and has one NBO, which accounts for 2.5 oxygen/tetrahedron, therefore  $NBO / (BO + NBO) = 2/5$ . For  $Q^2$  there are 2 unshared NBOs leading to  $NBO / (BO + NBO) = 2/3$ , while  $Q^4$  has no NBO. The average  $NBO \%$  is given by

$$\sum f(Q^n) \times \left[ \frac{NBO}{BO + NBO} \right]_n \quad (6.2.2)$$

where  $f(Q^n)$  is the relative percentage of the  $Q^n$  species which equals the relative area of the Gaussian line to the total area under the Si NMR line.

For  $T_1$  determination, the evolution of the magnetization  $M(\tau)$  was fitted with single exponentials in the microcrystalline and the amorphous forms of  $\text{LiNbO}_3$ , however, for the nanocrystalline form and the glasses a Kohlrausch stretched exponential was used.

In heterogeneously disordered systems such as nanocrystalline materials, there are different structural zones. In the ideal case, they should each show a single-exponential relaxation, especially when they have relaxation times which are very different from each others<sup>263</sup>. However, in some cases they may show a single-exponential relaxation due to the spin diffusion, i.e. as a result of polarization transfer between the grains and the interfacial regions. The obtained spin-lattice relaxation rate is plotted against the reciprocal of the temperature. The low-temperature side of the diffusion-induced peak is clearly detected but the SLR rate maximum and the high-temperature flank were not accessible in the measurable temperature range. To extract the pure diffusion induced relaxation rate,  $T_{1\text{diff}}^{-1}$ , the background (bgr) rate,  $T_{1\text{bgr}}^{-1}$ , is fitted with a power law  $T_{1\text{bgr}}^{-1} \propto T^\gamma$  where the exponent  $\gamma$  describes the temperature dependence of the background rate, and extrapolated to higher temperatures and subtracted from the measured data.

$$T_{1\text{diff}}^{-1} = T_1^{-1} - T_{1\text{bgr}}^{-1} \quad (6.2.3)$$

The low-temperature flank follows an Arrhenius relation

$$T_{1\text{diff}}^{-1} \propto \exp\left(-\frac{E^{\text{IT}}}{k_B T}\right) \quad (6.2.4)$$

where  $k_B$  is the Boltzmann constant, and  $E^{\text{IT}}$  is the activation energy of the low-temperature side of the diffusion-induced peak.

## 6.3 X-RAY ABSORPTION FINE STRUCTURE\*\*

### 6.3.1 Apparatus Description

EXAFS experiments were done in the Daresbury Synchrotron Radiation Source (SRS) which delivers radiation with wavelengths from the infrared to hard x-ray. The SRS is a 2 GeV electron storage ring which routinely operates at high circulating currents with lifetimes of more than 24 h. It has three electron accelerators, two feeding successively into the main storage ring which serves many experimental stations.

Station 9.2 is on the Wiggler I beam line suitable for EXAFS measurements in the range 10 keV to 33 keV. It has a water-cooled harmonic rejecting double crystal monochromator which is constructed of two silicon single crystal plates with crystallographic orientation (220). The station is equipped with a Canberra 13-element solid state detector. The station is used to make measurements at higher energy edges. The benchmark is defined as an EXAFS scan of a 30-micron Rh foil in the middle of the wavelength range of the station.

Our measurements were conducted at the Nb K-edge, with a beam minimum current of 125 mA at 2 GeV and beam dimensions were 10 mm by 0.6 mm. The detectors were standard ion chambers filled with Ar/ Kr; 20 % absorbing  $I_o$  and 80 % absorbing  $I_t$ , backfilled to 1000 mbar with He. The ion chambers consist of two metallic plates with a 500 V potential difference between them, supplied by an Ortec 456 HT. In transmission EXAFS the ion chambers measure the x-ray beam intensity both before and after the sample. The current between the plates is amplified by a Keithley 428 current amplifier (with a gain of  $10^7$ , rise time of 100 ms) and shown on the Digital Volt Meters (DVMs). This amplified signal is also fed to a voltage-to-frequency converter and the digital output is then fed into a scalar counter, which feeds into the station computer.

---

[\*\*] These measurements were done in the UK by: experimental team: Dr. D. Bork (now in KNH, Patent Postfach 26 02 32 D-80059 München-Germany), Dr. D.-M. Fischer (now in Baker Hughes INTQ, Christensenstraße 1, D-29221 Celle, Germany), and Dr. R. Winter (Institute of Mathematical and Physical Sciences, University of Wales Aberystwyth, Ceredigion SY23 3BZ, Wales UK); Station scientist: Dr. F. Mossemans. Data analysis: Dr. A. Dent, Dr. J. Charnock (both from CRLS labs Daresbury), Prof. N. Greaves (Institute of Mathematical and Physical Sciences, University of Wales Aberystwyth, Ceredigion SY23 3BZ, Wales UK), Prof. P. Heitjans and M.Sc. M. Masoud.

### 6.3.2 Sample Preparation

Powder samples were pressed into pellets with 8 mm diameter and 0.5 mm thickness for the cryostat and 13 mm diameter and 0.25 mm thickness for the oven. The samples were perpendicular or inclined (with variable angles) to the beam in the cryostat and the oven, respectively.

### 6.3.3 Measurement Conditions

The temperature was varied in the range from 80 to 300 K for all LiNbO<sub>3</sub> samples using a liquid nitrogen bath cryostat (Oxford instruments) connected to an adjustable temperature control unit. The microcrystalline sample is thermally stable up to higher temperatures; therefore it was possible to perform runs at 450, 550 and up to 975 K using an electrical DL/RI furnace.

The measurements scan the  $k$  space from 2 to 18 Å<sup>-1</sup> using a step of 0.04 Å<sup>-1</sup> and a time of 2 s/point (about ~ 13 minutes to scan the entire range), with  $k = 0$  weighting. The resulting data usually have  $S/N$  better than 60 at  $k = 12$  Å<sup>-1</sup> and better than 20 at  $k = 16$  Å<sup>-1</sup>. Several independent scans were taken for each sample to examine the reproducibility of the experiments and to enhance the signal to noise ratio.

### 6.3.4 Fitting Software and Approaches

The data were stored on the SRS computer system (XRSSERV1) and analyzed using the Daresbury suite for EXAFS programs (EXCALIB, EXSPLINE, LINCOM and EXCURV98<sup>264</sup>). First, EXCALIB was used to read, calibrate the energy scale and to average the spectra measured for the same sample to get a better signal to noise ratio. Then, EXSPLINE was used to fit and subtract the baseline (smooth background). The pre-edge was fitted with a curve of order 1, and the post-edge was fitted with spline curve which consists of 3 – 4 adjacent polynomial segments, then it was subtracted and the resultant EXAFS was normalized to the smooth background. The obtained EXAFS spectra were modelled using EXCURV98 applying the curved wave theory<sup>265</sup>. EXAFS spectra were collected for the microcrystalline LiNbO<sub>3</sub> to verify the calculated Nb–O, Nb–Li, and Nb–Nb phase shift and to refine the Debye-Waller factors,  $\sigma^2$ . A simplified structural model for LiNbO<sub>3</sub> was constructed as a radial distribution derived from the crystallographic data for LiNbO<sub>3</sub> with a congruent composition [atomic positions ( $x, y, z$ ) for: Nb (0,0,0), Li (0,0,0.27909), O (0.0479,0.34299,0.06385), and cell parameters  $a = 5.15052$  Å,  $c = 13.864961$  Å]<sup>79</sup> (the model will be shown later in Table 7.1.1(a)).

The EXAFS (or its FT) for the nanocrystalline material was compared with the corresponding counterparts for the microcrystalline and amorphous forms by two methods. *Method (i)* (linear combination of EXAFS): the experimental EXAFS spectra measured at the same temperature for lithium niobate in the microcrystalline (M) and amorphous (A) forms are used as standards. Using a small program called LINCOM<sup>264</sup> that runs a least square routine to minimize the difference between the experimental EXAFS

spectrum of the nanocrystalline LiNbO<sub>3</sub> (N) and a linear combination of the standards. Thus, it minimizes

$$\sum_i^n (N_i - mM_i - aA_i) \quad (6.3.1)$$

with the constrains:  $m, a < 1, m + a = 1$ . It returns the values of the mixing coefficients  $m, a$ , and  $R$  for the fit. *Method (ii)* (multiple clusters): the excited Nb central atoms in the nanocrystalline form are visualized to be distributed between two different phases: grains and GBs. They are supposed to interact with two different environments. For each of them, a radial cluster must be generated; one for the crystalline grains and another for the "likely" amorphous GBs. The relative contribution of each cluster to the total model can be adjusted by altering the shell occupation number of the excited central atoms for each cluster. To find the suitable model for the nanocrystalline materials the occupation number for the microcrystalline cluster was changed from 0 to 1 in steps of 0.1 and for the amorphous cluster from 1 to 0. A meaningful indication of the consistency of the fit can be obtained by comparing the EXAFS  $R$ -factor,  $R_{\text{EXAFS}}$ , being

defined as<sup>265</sup>

$$R_{\text{EXAFS}} = \sum_i^n \frac{1}{\bar{\sigma}_i} (|\chi_i^{\text{exp}}(k)| - |\chi_i^{\text{th}}(k)|) \cdot 100 \% \quad (6.3.2)$$

where  $\bar{\sigma}_i$  is the standard deviation,  $\chi_i^{\text{exp}}$  and  $\chi_i^{\text{th}}$  are the values of the experimental EXAFS signal and the corresponding theoretical fit, respectively.

The Debye-Waller factor is obtained for each shell as the sum of two contributions

$$\sigma^2 = \sigma_{\text{stat}}^2 + \sigma_{\text{vib}}^2. \quad (6.3.3)$$

The former is temperature independent and corresponds to the dispersion of bond lengths without vibration while the latter is due to thermal vibration and is thus related to the vibrational spectrum. There are two approximations for describing the vibrational contributions. For the first shell in an oxide, the cation-oxygen vibration can be approximately regarded as the optical mode of the phonon spectrum. In this case, an Einstein model is appropriate because the vibrational frequency of the diatomic optical mode is typically high and relatively wavelength independent. For the following shells, the involved cation-cation vibrations are clearly not optical modes. Since longer wavelength acoustic modes of the cation network are probably more important in this case, the Debye model can be adopted with a distribution of vibrational frequencies to analyze the second shell data.

The vibrational contribution, based on Einstein model, can be written as

$$\sigma_{\text{vib}}^2 = \frac{h}{8\pi^2 \bar{\mu} \nu} \coth\left(\frac{h\nu}{2kT}\right), \quad (6.3.4)$$

and for Debye model it is

$$\sigma_{\text{vib}}^2 = \frac{3k_B^2 T^2}{8\pi^2 M h \nu^2} \int_0^{h\nu/kT} \left(\frac{1}{e^x - 1} + \frac{1}{2}\right) x dx \quad (6.3.5)$$

where,  $\bar{\mu}$  is the reduced mass of the cation-oxygen (Nb—O) pair,  $M$  is the cation (Nb) mass,  $T$  is the absolute temperature, and  $h$  is Planck's constant. The frequency  $\nu$  is the Einstein frequency for the optical mode in Eq. (6.3.4) or the Debye frequency, which is the maximum vibrational frequency of the acoustic

mode in Eq. (6.3.5). Combining Eq. (6.3.3) and (6.3.4), the Nb—O data can be fitted to determine the Einstein vibrational frequency and the static distortion. Likewise, from Eqs (6.3.3) and (6.3.5) the Debye frequency and the static distortion can be obtained for the Nb—Nb shell.

## 6.4 SECONDARY-ION MASS SPECTROSCOPY

### 6.4.1 Sample Preparation and $^{18}\text{O}$ Equilibration <sup>††</sup>

The  $\text{LiNbO}_3$  single crystal was cut into plates with dimensions of  $5 \times 5 \times 1 \text{ mm}^3$  in such a way that their largest surfaces are perpendicular to the optical  $c$ -axis in some samples and parallel to it in some others. The samples were polished with diamond paste down to the fineness of  $1 \mu\text{m}$  and cleaned with ethanol in an ultrasonic bath. A pre-annealing in  $^{16}\text{O}$ -gas (200 mbar) at 1333 K was performed to remove the stress induced while polishing, but the crystals turned out to have a milky colour instead of their usual transparent appearance. This was probably due to Li out-diffusion and the separation of the  $\text{Li}_2\text{O}$ -deficient phase ( $\text{LiNb}_3\text{O}_8$ ), see Ref. [266]. Thus, the pre-annealing temperature was reduced and new samples were pre-annealed at 1273 K for about 15 hours. Using these conditions, no change in the appearance of the crystals was observed.

The samples were attached to an alumina holder and introduced into a furnace, which was evacuated to a pressure of about  $10^{-3}$  mbar. After evacuation,  $^{16}\text{O}$ - or  $^{18}\text{O}$ -gas, respectively, was introduced into the furnace at a pressure of 200 mbar. A mechanical transport system allowed the rapid transfer of the sample from the hot to the cold zone of the furnace. Prior to the  $^{18}\text{O}$ -diffusion experiments all samples were annealed in  $^{16}\text{O}$ -gas (200 mbar) to achieve thermal equilibrium at the given temperature. To achieve an identical diffusion treatment, couples of samples of both orientations (with the largest surface parallel or per-

Table 6.4.1: Annealing conditions of the  $\text{LiNbO}_3$  single crystal samples with the diffusion parallel to ( $\parallel$ ) or perpendicular to ( $\perp$ ) the optical  $c$ -axis.

Orientation	Pre-annealing in $^{16}\text{O}_2$ (200 mbar)				Annealing in $^{18}\text{O}_2$ (200 mbar)	
	Stress removal		Equilibration		$T$ (K)	Time (s)
	$T$ (K)	Time (h)	$T$ (K)	Time (h)		
$\parallel$	1223	15	1188	6	1188	4200
$\parallel$	1223	15	1073	92	1073	23700
$\parallel$	1223	14	983	276	983	184200
$\perp$	1223	15	1188	6	1188	4200
$\perp$	1223	15	1073	92	1073	23700
$\perp$	1223	14	983	276	983	184200

<sup>†††</sup> The  $^{18}\text{O}$ -exchange experiments and the early SIMS measurements were conducted by Dr. P. Fielitz and Prof. G. Borchardt, Institut für Metallurgie, Technische Universität Clausthal.



pendicular to the  $c$ -axis) were placed in the furnace together and annealed at the same temperature for the same duration (see Table 6.4.1). The  $^{18}\text{O}$  gas concentration in the furnace,  $c_g$ , was measured by a Residual Gas Analyzer (RGA 200, Stanford Research Systems).

### 6.4.2 SIMS Apparatus

The diffusion profiles of the  $^{18}\text{O}$  tracer were first determined using the Cameca IMS 3f SIMS instrument<sup>††</sup> under the following conditions: 14.5 keV  $\text{O}^-$  primary beam with a current of about 100 nA. The rastered area was  $250 \times 250 \mu\text{m}^2$ , and the diameter of the analyzed zone was 60  $\mu\text{m}$ . Positive secondary ions were used in the analysis of the samples. Charging effects were prevented by coating the samples with a 45 nm thick gold film and using negative primary oxygen ions. However, the disadvantage of the use of oxygen as primary ions is that the measured  $^{18}\text{O}$  concentration is somewhat distorted. Nevertheless, those measurements helped to find optimised annealing conditions for the samples. To get quantitatively accurate depth profiles of the  $^{18}\text{O}$  tracer the samples were measured using a TOF-SIMS IV (ION-TOF GmbH, Münster-Germany)<sup>‡‡</sup>. Measurement conditions were: 25 keV  $\text{Ga}^+$  ions (burst mode) rastered over 60  $\mu\text{m}^2$  with the cycle time set at 50  $\mu\text{s}$  ( $I = 35 \text{ pA}$ ), sputtering was accomplished with 2 keV  $\text{Cs}^+$  ions rastered over 250  $\mu\text{m}^2$  ( $I = 130 \text{ nA}$ ). A beam of 20 eV electrons were used for charge compensations, see Ref. [267] for more details about the analysis method.

### 6.4.3 Data Analysis and Fitting

A detailed explanation how to evaluate measured  $^{18}\text{O}$  depth profiles of isotope exchange experiments is given in Ref. [124]. In thermal equilibrium the  $^{18}\text{O}$  isotope flux out of the sample equals the  $^{18}\text{O}$  isotope flux into the sample (neglecting the very low concentration of  $^{17}\text{O}$ ). This means that the total oxygen concentration is constant.

$$c_{^{16}\text{O}}(x, t) + c_{^{18}\text{O}}(x, t) = c_{\text{O}}^{\text{tot}} = \text{constant} \quad (6.4.1)$$

There is only a small instrumental mass fractionation that occurs during the measurement of oxygen isotope ratios by SIMS and it can be ignored in TOF-SIMS. Furthermore, for isotopes of the same elements, differences in sputter and ionization yield can be neglected. Therefore, it is justified because of Eq. (6.4.1) (to convert the intensity signals,  $I$ , of the measured oxygen isotopes into the  $^{18}\text{O}$  atomic frac-

tion,  $c$ , as follows

$$c = \frac{I(^{18}\text{O})}{I(^{18}\text{O}) + I(^{16}\text{O})} \quad (6.4.2)$$

For the sake of simplicity, the term “concentration” is used instead of “atomic fraction” throughout the following text. The assumption is made that the oxygen incorporation can be phenomenologically described as a first order reaction

<sup>††</sup> The final SIMS measurements were done by Dr. R. De Souza and Prof. M. Martin, Institut für Physikalische Chemie I, RWTH Aachen.

$$j_{18}^{\text{in}} = (c_g - c_s)K \quad (6.4.3)$$

where  $K$  is the surface exchange coefficient of oxygen,  $c_g$  is the  $^{18}\text{O}$  concentration in the gas phase and  $c_s$  is the  $^{18}\text{O}$  concentration in the solid near the specimen surface. This flux must be equal to the diffusional flux of  $^{18}\text{O}$  into the bulk of the sample, i.e. at  $x = 0$

$$-D \left( \frac{\partial c}{\partial x} \right)_{x=0} = (c_g - c_s)K \quad (6.4.4)$$

where  $D$  is the self-diffusivity of oxygen. To calculate the expected  $^{18}\text{O}$  depth profile one has to solve the diffusion equation with respect to this boundary condition (Eq. 6.4.4).

$$\frac{\partial c(x, t)}{\partial t} = D \frac{\partial^2 c(x, t)}{\partial x^2} \quad (6.4.5)$$

The solution is given by Crank<sup>124</sup>

$$c(x, t) - c_\infty = (c_g - c_\infty) \left[ \operatorname{erfc} \left( \frac{x}{\sigma} \right) - \exp \left( 2 \frac{x}{\sigma} \sqrt{\frac{t}{\tau}} + \frac{t}{\tau} \right) \operatorname{erfc} \left( \frac{x}{\sigma} + \sqrt{\frac{t}{\tau}} \right) \right] \quad (6.4.6)$$

where  $c_g$  is the constant  $^{18}\text{O}$  gas concentration in the gas phase,  $c_\infty$  the natural abundance of  $^{18}\text{O}$  in the sample (for  $x = \infty$ ),  $\sigma = 2\sqrt{Dt}$  is the diffusion length and  $\tau = D/K^2$  is a characteristic time constant. The physical meaning of  $\tau$  is obvious if one considers the time dependence of the  $^{18}\text{O}$  concentration near the surface of the solid ( $c_s(t) = c(x = 0, t)$ )

$$c_s(t) - c_\infty = (c_g - c_\infty) \left[ 1 - \exp \left( \frac{t}{\tau} \right) \operatorname{erfc} \left( \sqrt{\frac{t}{\tau}} \right) \right] \quad (6.4.7)$$

The characteristic time constant,  $\tau$ , determines the duration that is necessary to reach equilibrium between the  $^{18}\text{O}$  concentration in the gas phase and the  $^{18}\text{O}$  concentration near the surface of the solid. Eq. (6.4.6) enables the simultaneous determination of  $D$  and  $K$  from the measured SIMS depth profiles.

## 6.5 OTHER TECHNIQUES

### 6.5.1 XRD and Structure Refinement

Most of the samples were subjected to powder x-ray diffraction (XRD) analysis either to examine their glassy nature, or to determine their composition or grain size. PHILLIPS PW 1800 diffractometer, with Bragg-Brentano geometry equipped with graphite monochromize  $\text{Cu } K_\alpha$ -radiation, Ni-filter, and a proportional counter was used. Most measurements were done in the  $2\theta$  range  $5^\circ - 80^\circ$  with a step size of  $0.02^\circ$  and a step time of 17 s. The total time used for measuring one sample was about 18 h.

The resultant diffractograms were refined using the Rietveld method<sup>88</sup>. The refinements were performed using the TOPAS 2.1 software suite (Bruker AXS)<sup>268</sup> a graphics based profile and structure analysis program built on a general non-linear least squares fitting system. The reference data were obtained from the Inorganic Crystal Structure Database (ICSD) in (\*.cif) electronic format. Lattice parameters, displacement parameters and the scale factor were refined to get the best fit for the measured XRD profile.

*In-situ* XRD measurements were carried out at the Materials Science Laboratory MSL in CLRC Daresbury Laboratory (UK) using a FR571 Enraf Nonius Cu rotating anode x-ray generator with an independently mounted INEL detector. This diffractometer works in transmission geometry and records a scattering angular range from 5° to 80° ( $2\theta$ ) simultaneously using a linear detector. The glass samples were ground and pressed into pellets which were mounted on a support finger hung from the top of the furnace. The temperature was varied from room temperature up to 1273 K and held at specific temperatures to acquire data as long as some changes were taking place. Data were recorded in 5 min slices.

### 6.5.2 Transmission and Scanning Electron Microscopy \*\*\*

Field-Emission TEM was conducted using a JEOL JEM-2100F-UHR, Fig. 6.5.1, capable of the following: (i) taking bright field (BF), dark field (DF), and high resolution TEM (HRTEM) using a Schottky field-emitter ZrO/W(100) and an acceleration voltage of 200 kV (160 kV) with a point-resolution of  $\leq 0.19$  nm ( $C_s = 0.5$  mm). (ii) Scanning Transmission Electron Microscopy (STEM) with BF, High Angle Annular Dark Field (HAADF) with a lattice resolution  $\leq 0.2$  nm. (iii) Electron Diffraction: selected area electron diffraction (SAED), convergent beam electron diffraction (CBED), also Energy-Filtered Transmission Electron Microscopy (EFTEM). (iv) Energy-Dispersive X-ray Spectroscopy (EDXS), Oxford Instruments INCA 200, detection from Be on.



Fig. 6.5.1: JEOL JEM-2100F-UHR TEM microscope



Fig. 6.5.2: Field-Emission SEM JEOL JSM-6700F.

Field-Emission Scanning Electron Microscopy images were recorded using a JEOL JSM-6700F microscope, (Fig. 6.5.2). This microscope is equipped with a secondary electron detector, a semi-in-lens detector for a small working distances and a backscattered electron detector (BSE). The energy-dispersive x-ray spectrometry (EDXS) can be measured with an Oxford INCA 300 Instrument (detection from Be on). It has a resolving power of 1 nm at 15 kV and 2.2 nm at 1 kV and an acceleration voltage of 0.5 - 30 kV.

### 6.5.3 Infrared and Raman Spectroscopy

Infrared spectra were recorded on a Bruker optics IFS 66v/S vacuum FT-IR spectrometer (Fig. 6.5.3 (top)), with a spectral range coverage from the very far infrared ( $< 5 - 370 \text{ cm}^{-1}$ ) up to  $400 \text{ cm}^{-1}$ . Spectra were recorded with a resolving power of less than  $1 \text{ cm}^{-1}$  spectral resolution. The KBr method was used in which 1 – 2 mg of the material is mixed with 200 mg dried KBr. The pellets are made at a pressure of about 10 kbar. Far infrared (FIR) measurements use polyethylene pellets for which 100 mg of polyethylene with 2 mg of the sample are mixed and then pressed under a 5-kbar pressure. An extended range FIR beam splitter allows measurements from approximately  $700$  to  $20 \text{ cm}^{-1}$  without using multiple mylar films. It is possible to record spectra free from gas interferences ( $\text{H}_2\text{O}$  or  $\text{CO}_2$ ) by evacuating the housing that surrounds the spectrometer optics to give higher sensitivity and stability especially for FIR.

Raman spectra were recorded using a Bruker RFS100/S spectrometer equipped with a broad-range quartz beam splitter, (Fig. 6.5.3 (bottom)). This instrument is equipped with a patented frictionless interferometer with its ROCKSOLID™ alignment with Gold-coated optics for highest throughput. The diode-pumped, air-cooled Nd:YAG laser source is providing the 1064 nm excitation wavelength controlled through the software. Furthermore, the system is equipped with a proprietary high-sensitivity liquid  $\text{N}_2$  cooled Ge diode detector working at  $90^\circ$  scattering geometry. The standard configuration provides a spectral range from  $3600$  to  $70 \text{ cm}^{-1}$  (Stokes shift) and from  $-100$  to  $-2000 \text{ cm}^{-1}$  (anti-Stokes shift). Optimized sample position is achieved by motorized sample stage.



Fig. 6.5.3: IFS 66v/S Vacuum FT-IR spectrometer (top) and Bruker RFS100/S Raman spectrometer (bottom).

#### **6.5.4 Thermogravimetric Analysis and Differential Scanning Calorimetry**

The thermal properties were measured using a SETSYS Evolution analyzer (SETARAM). Simultaneous TGA/DSC measurements were obtained at temperatures ranging from 293 up to 1573 K. The weights of the powdered samples were about 37.5 mg (equal the reference sapphire crystal). Then they were placed in a couple of Pt crucibles capped with hats and loaded on the balance. After that, the balance and the furnace were evacuated and flushed out with He gas under which the measurements were conducted. The data were analyzed using the thermal analysis software SETSOFT 2000.



## 7 LiNbO<sub>3</sub> (single crystalline, microcrystalline, nanocrystalline, amorphous)

### 7.1 STRUCTURAL ASPECTS

Recently nanocrystalline materials were intensively considered due to their superior properties which are remarkably distinct from those of their coarser grained microcrystalline counterparts. Nanocrystalline materials can be prepared by a wide variety of methods that can be classified into two main categories<sup>7</sup>: (i) growing the nanocrystalline particles from smaller building units as it is the case in the sol-gel preparation method, or contrarily (ii) by reducing the grain size of their coarser-grained counterparts; e.g., by high-energy ball milling (HEBM). It is believed that the enhancements in the properties of the nanocrystalline materials result from the increased volume fraction of the interfacial region between the nanocrystalline grains, i.e., the grain-boundary (GB) regions. For understanding the basic features of nanocrystalline materials and consequently tailoring their properties, it is necessary to have a deeper insight about the nature of the GB regions and their dependence on the preparation route.

Several techniques have been employed to explore the structure of nanocrystalline materials such as XRD, TEM, Mössbauer spectroscopy<sup>24</sup>. However, NMR is the method which gives direct information about the real structure. LiNbO<sub>3</sub> contains four different quadrupolar nuclei; <sup>17</sup>O (natural abundance 0.037 %, spin quantum number  $I = 5/2$ ), <sup>6</sup>Li (7.42 %, 1), <sup>7</sup>Li (92.58 %, 3/2), and <sup>93</sup>Nb (100 %, 9/2)<sup>269</sup>. The <sup>17</sup>O NMR signal can only be detected in enriched samples because of its low natural abundance. Here, we have employed <sup>7</sup>Li and <sup>93</sup>Nb NMR to explore the structure of different forms of LiNbO<sub>3</sub>.

EXAFS also is one of the most powerful tools which can be applied to investigate the local atomic environment surrounding particular types of element in dilute, amorphous or nanophase. The choice of

EXAFS for investigating the GB regions is advantageous for the following reasons: (i) The result can be directly interpreted; this makes it advantageous over the XRD measurements which can have more than one way of interpretation. (ii) It does not require an extreme thinning of the sample as it is the case for TEM, thus avoiding any change in the structure by contaminating the surface or altering its stress.

In spite of its wide applications and the consequent demanding interest it has been receiving,  $\text{LiNbO}_3$  is still regarded as a nonstoichiometric material with an unresolved defect structure<sup>95,249</sup>, in addition to the intrinsic metastability of the non-stoichiometric (congruent) composition at room temperature<sup>266</sup>. These facts impose several obstacles in the way of any structure analysis for  $\text{LiNbO}_3$  as many of the properties of  $\text{LiNbO}_3$  will show a composition dependence and can in principle be used to determine the stoichiometry of  $\text{LiNbO}_3$ . However, the reliable standard needed for such utilization is missing as no precise quantitative chemical analysis can be obtained for  $\text{LiNbO}_3$ , see Ref. [68]. Hence, it is also difficult to compare the obtained results to the literature due to the uncertainty in composition. Furthermore the properties of  $\text{LiNbO}_3$  are known to be highly affected by impurities<sup>64</sup>.

In the first part of this chapter the nanocrystalline  $\text{LiNbO}_3$  prepared by HEBM and by sol-gel are treated; trying to participate in solving the puzzling structure of the GB regions and its dependence on preparation route, meanwhile keeping our eyes on the two opposite ends of the structural order/disorder scale as standards. In other words, most of the structural features of the nanocrystalline form will be extracted by comparing the measured characteristics with those obtained from the microcrystalline and the amorphous  $\text{LiNbO}_3$ . For this purpose we utilize NMR and EXAFS as main characterization techniques in addition to XRD- and TEM-measurements as auxiliary tools.

## 7.1.1 NMR Line-Shapes

### 7.1.1.1 $^7\text{Li}$ NMR line-shapes

With the aim of obtaining structural information about  $\text{LiNbO}_3$  in different modifications,  $^7\text{Li}$  NMR lines were recorded for amorphous, nanocrystalline, and microcrystalline  $\text{LiNbO}_3$ . The central transition of the  $^7\text{Li}$  NMR line for amorphous and microcrystalline  $\text{LiNbO}_3$  can be described with a homogeneous line, which can be fitted with a Gaussian line in the rigid lattice regime at low temperatures or a Lorentzian line at higher temperatures, as shown in Fig. 7.1.1(a,d). Contrarily, the central line of the 16 h HEBM nanocrystalline  $\text{LiNbO}_3$  sample begins to split into two contributions: a narrow component that is attributed to the highly mobile ions in the disordered interfacial regions and a broad contribution caused by the slow Li ions inside the crystalline grains. The onset of this separation can be seen at 333 K, Fig. 7.1.1(b). The ratio of the area under the narrow contribution to the area under the whole line is proportional to the fraction of atoms that are highly mobile. At lower temperatures, only a single contribution can be seen, or more likely, two contributions with comparable widths at that temperature regime which are practically



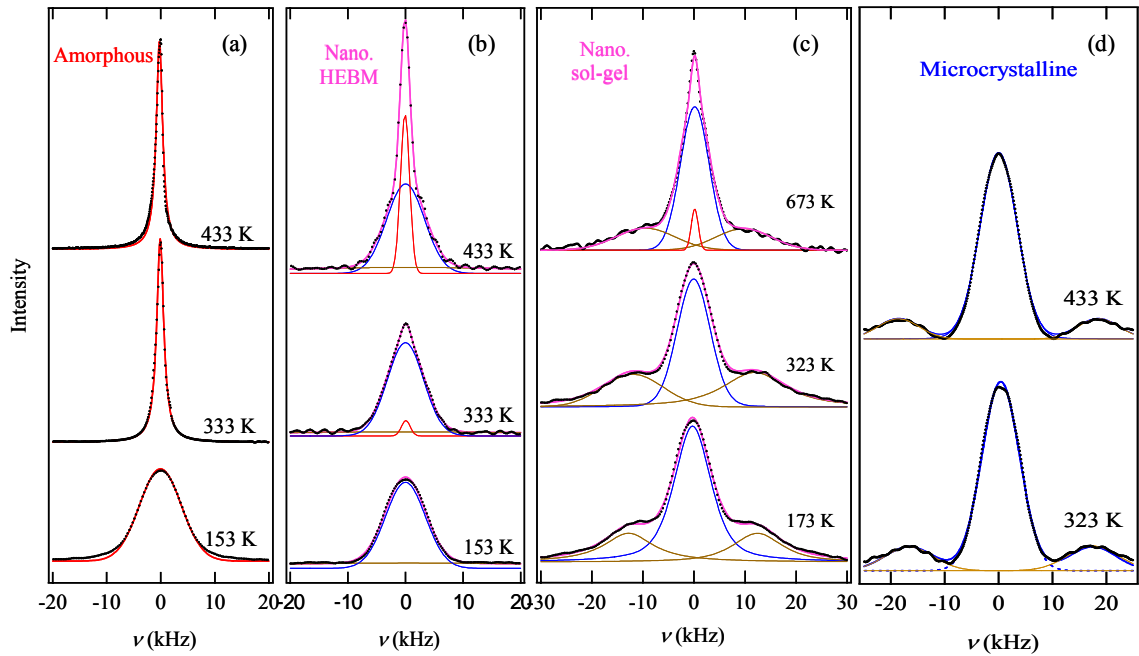


Fig. 7.1.1:  ${}^7\text{Li}$  NMR spectra for: (a) amorphous, (b) 16 h HEBM nanocrystalline (23 nm), (c) sol-gel prepared nanocrystalline (27 nm), and (d) microcrystalline  $\text{LiNbO}_3$  measured at 77.7 MHz at the indicated temperatures. The measured data are shown as black dots and the total fit as solid lines. The contribution due to fast ions, slow ions, and quadrupolar satellites are shown in red, blue and brown, respectively.

difficult to separate. To investigate the effect of the preparation route, another nanocrystalline  $\text{LiNbO}_3$  sample was prepared from the amorphous  $\text{LiNbO}_3$  (sol-gel route: full hydrolysis of the double alkoxide) by heating at 773 K for 1 h. The obtained sample had a grain size (27 nm) that is comparable to the 16 h HEBM sample (23 nm). The  ${}^7\text{Li}$  NMR spectra for this sample are shown in Fig. 7.1.1(c), they are consistent with those of the HEBM sample in owning a heterogeneous structure composed of a narrow and a wide contribution. However, they reveal some considerable differences. As can be conceived from Fig. 7.1.2, the narrow contribution of the chemically prepared sample begins to separate only at 473 K and continues to show a nearly constant relative contribution of about 3.8 %. For the HEBM sample, however, the narrow contribution emerged at 330 K with a relative contribution which increases continuously up to 32 % with raising the temperature to 450 K. In the last case the relative con-

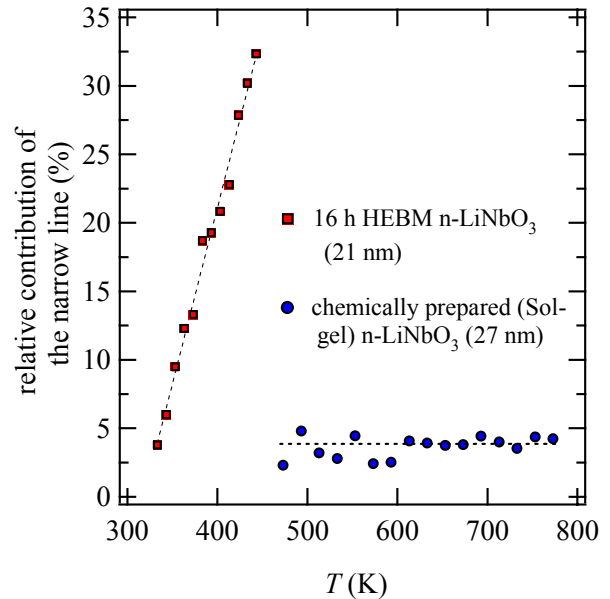


Fig. 7.1.2:  ${}^7\text{Li}$  NMR narrow line relative contribution to the total area under the whole line. For nanocrystalline samples of comparable grain sizes, one prepared by sol-gel (27 nm) and the other by HEBM (23 nm).

tribution of the narrow line does not reach a saturation value and may probably continue to rise with heating implying that the percentage of the atoms in the interfacial region larger than 32 %. However, the upper temperature limit was 450 K to avoid grain-boundary relaxation and grain growth.

Furthermore, several amorphous samples were also investigated; they show high degrees of similarity in lineshapes. However, there are some small differences in the fwhm and their temperature-dependent motional narrowing (MN) which will be discussed in detail in Sec. 7.2.2.6.

The second remarkable observation in the  ${}^7\text{Li}$  NMR spectra is the appearance of quadrupole satellites. In the spectra measured at 77.7 MHz, a couple of well-defined quadrupole satellites appears in the case of microcrystalline  $\text{LiNbO}_3$  and in the case of nanocrystalline  $\text{LiNbO}_3$  prepared by sol-gel, Fig. 7.1.1(d,c), respectively. Such satellites can be seen as slight diffuse background in the nanocrystalline  $\text{LiNbO}_3$  prepared by HEBM for 16 h. However, they are completely absent in the spectra of the amorphous form (Fig. 7.1.1(b) and (a), respectively). The relative intensities of the microcrystalline sample begin with 0.9 : 4 : 0.9 at 300 K and decrease to 0.5 : 4 : 0.5 when the temperature is raised to 433 K. In the case of the sol-gel prepared nanocrystalline sample the intensities are 1.8 : 4 : 1.8 at 300 K and decreased to 0.7 : 4 : 0.7 by raising the temperature to 473 K. It is noticeable that the intensity of the quadrupolar satellites is less than the expected theoretical value for  ${}^7\text{Li}$  (3 : 4 : 3 for atoms with  $I = 3/2$ , see Ref. [194]) mainly in the microcrystalline sample and that the satellites intensity decreases with increasing temperature.

Another parameter that can be extracted is the quadrupolar coupling constant which equals twice the

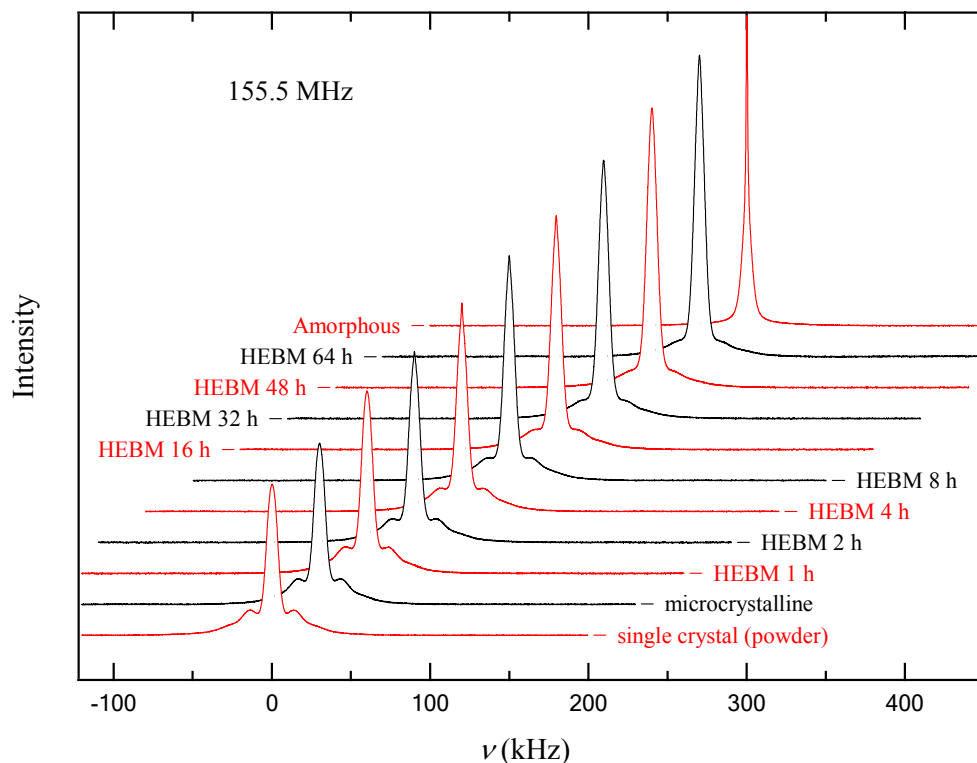


Fig. 7.1.3: Illustration of the effect of the introduction of crystal imperfections on the intensities of the quadrupolar satellites in static  ${}^7\text{Li}$  NMR lines measured at 155.5 MHz going from the single crystal and microcrystalline through the nanocrystalline HEBM for different periods ending with the amorphous  $\text{LiNbO}_3$ .

distance between the quadrupolar satellites, i.e.  $2 \cdot \Delta\nu$ <sup>194,269–270</sup>. The microcrystalline LiNbO<sub>3</sub> sample has a quadrupole coupling constant of 68.8 kHz at room temperature which increases gradually with increasing the temperature to reach 74.3 kHz at 433 K. On the other hand the chemically prepared nanocrystalline sample shows a slight decrease in the quadrupole coupling constant from 47.7 to 44.4 and 38.1 kHz with increasing the temperature from room temperature to 473 and 673 K, respectively.

To examine the effect of introducing crystal imperfections, spectra were recorded for different samples at room temperature using a higher magnetic field (155.5 MHz). It was found that the intensity of the quadrupolar satellites decreases while going from the single crystal and microcrystalline through the nanocrystalline to the amorphous LiNbO<sub>3</sub>, Fig 7.1.3. For nanocrystalline samples, HEBM for more than 32 h, the quadrupolar satellites were "smeared out" because of a wide distribution of coupling constants to give a broad background which can hardly be seen in the amorphous case.

### 7.1.1.2 Discussion of <sup>7</sup>Li NMR lineshapes

Due to the ionic nature of the lithium oxygen bonds and the small value of the shielding factor that is close to unity [(1 -  $\gamma_{\infty}$ ) = 0.744], <sup>7</sup>Li has a small quadrupole coupling constant,  $e^2qQ/h$ , and a <sup>7</sup>Li spectra can usually be described by first order perturbation theory<sup>271</sup>. In LiNbO<sub>3</sub>, being a trigonal crystal (*C3v*), the non-cubic crystal system imposes an electric field gradient with a cylindrical symmetry on the Li sites. Consequently, the NMR spectrum is composed of three lines: a central transition line ( $\pm 1/2 \leftrightarrow \mp 1/2$ ) at the Larmor NMR frequency and its two satellites corresponding to  $\pm 3/2 \leftrightarrow \pm 1/2$ .

The linewidth of the central line (measured as full width at half maximum, fwhm) at room temperature was found to be 8.3, 8.8, 7.8 kHz for the microcrystalline, chemically- and mechanically prepared nanocrystalline, respectively. These values agree with the values found in literature, 10 kHz<sup>272–273</sup> and 7.8 kHz<sup>274</sup>. But they are all significantly broader than the calculated, Van Vleck, dipolar linewidth of about 5.9 kHz<sup>272</sup>. The additional broadening may be due to second-order quadrupolar effects caused by crystal imperfections. The amorphous sample showed fwhm of 5.4 kHz at room temperature which indicated that motional narrowing had already started whereas the rigid lattice value of fwhm for this sample was 8.8 kHz.

For spin 3/2 nuclei, the distance between the quadrupolar satellites,  $\Delta\nu$ , is given by<sup>194,269,270</sup>

$$\Delta\nu = \pm(e^2qQ/h) \left[ (3\cos^2\theta - 1)/2 \right] \quad (7.1.1)$$

here  $\theta$  is the angle between the major electric field gradient direction and the magnetic field and  $e^2qQ/h$  is the quadrupole coupling constant. The shape function for the NMR lines for powders was calculated by Pound<sup>275</sup>, however, the field-gradient directions are randomly orientated with respect to the applied magnetic field resulting in broad lines in addition to the dipolar broadening. This leads to a significant uncertainty in the estimation of the quadrupolar coupling constant. Several values for the quadrupolar coupling constant were found for LiNbO<sub>3</sub> in the literature, Table 7.1.1, see Refs [272–283]. The quadrupolar split-

ting of the  ${}^7\text{Li}$  NMR spectrum was found to be sensitive to stoichiometry only at elevated temperatures not at room temperature as can be seen from the agreement of the values shown in Table 7.1.1 for samples from different sources. This implies that changing the crystal composition from congruent to stoichiometric does not affect the gradient of the internal crystal electric fields.<sup>278</sup> The value measured here for the sol-gel prepared nanocrystalline samples (47.7 kHz) is comparable to the value obtained by Burns<sup>276</sup>, and not far from the average of the single crystals shown in Table 7.1.1.

It is interesting to note that at high temperatures the quadrupolar satellites became more separated from the central line, i.e.,  $\Delta\nu$  depends linearly on temperature. This behavior suggests that with increasing temperature the Li ion moves towards the lower oxygen planes<sup>281</sup>. The linear increase in the coupling constant with increasing temperature was attributed to a change in the time average of the gradients "seen" or sampled by the nucleus which is in thermal motion. Because gradients vary in the region of space around a lattice point, the magnitude of the time average depends on the shape, and extent, of the region of space in which the nucleus moves. Thus, because the thermal motion of an atom is usually a function of temperature, the time average of the gradient, and hence also the quadrupolar coupling constant, is temperature dependent.

Yatsenko *et al.*<sup>284</sup> observed additional  ${}^7\text{Li}$  NMR lines for  $\text{LiNbO}_3$  with  $\Delta\nu$  equal to 1.49 times the basic value of  $\Delta\nu$ . This was attributed to the presence of four minima on the potential surface in the distorted  $\text{LiO}_6$ . Three of them constitute the basic lines. They are equivalent and shifted from the  $c$ -axis and related by a three-fold symmetry axis. In addition, there is another minimum sited on the  $c$ -axis to which the weak additional lines were attributed<sup>285</sup>. It was also shown that  ${}^6\text{Li}$  occupy only the sites on the  $c$ -axis<sup>286</sup>. This may help in explaining the high quadrupole coupling constant obtained for the microcrystalline sample (68.8 kHz) which also agrees with the literature value of 63 kHz<sup>277</sup>. It is known that the intensity of the quadrupole satellites depends on the degree of crystallinity of  $\text{LiNbO}_3$ . The presence of various defects in the crystal such as impurities, vacancies and dislocations leads to a decrease in the intensity of the satellites<sup>274</sup>.

The shapes of  ${}^7\text{Li}$  spectra are not sensitive to the type of intrinsic defects and the observed additional quadrupole satellites are related to the peculiarities of the potential surface and to the diffusivity of  $\text{Li}^+$  ions in the distorted  $\text{LiO}_6$  octahedra<sup>287</sup>.

Table 7.1.1 : Literature values of the quadrupolar coupling constant for  $\text{LiNbO}_3$  in single crystal and powder forms at room temperature ( $R = [\text{Li}_2\text{O}]/[\text{Nb}_2\text{O}_5]$  in the melt):

Sample nature	Quadrupolar coupling constant (kHz)	Comments
powder	46	[276]
	63	[277]
	72	(At 975 K) [5]
	77.6	[273]
	55.2	$R = 0.95$ [277]
Single crystals	54	$R = 0.95$ [278,279]
	55	$R = 1.2$ [278,279]
	53.8	$R = 0.95$ [272]
	55.2	[273]
	53	$R = 0.95$ [274]
	55	$R = 0.95$ [281]
	55	[282]
	53.34	[283]

In the whole temperature range both the microcrystalline and the amorphous samples show a single-structured central lines that can be fitted with a Gaussian line at low temperatures, while a Lorentzian line fits the central line better at higher temperatures. This behavior can be realized taking into account that the amorphous form is a homogeneously disordered material and that the microcrystalline form is a homogeneously ordered material. In contrast to that, nanocrystalline  $\text{LiNbO}_3$  can be visualized as a heterogeneous mixture of crystalline grain interiors and a highly disordered *amorphous* phase of interfacial regions. As a result, it should be possible to deconvolute the central line of the nanocrystalline  $\text{LiNbO}_3$  into a broad and a narrow contribution that can be ascribed to the Li ions being located in the two distinct environments of such a heterogeneous structure. The broad contribution agrees with that obtained for the microcrystalline form and can be ascribed to the slow Li ions in the grain interiors, whereas the narrow contribution matches that of the amorphous form and thus can be ascribed to the highly mobile ions in the interfacial regions.

Considering the assumption<sup>16</sup> that the average thickness of the interfacial regions in nanocrystalline materials ranges from 0.5 to 1 nm, it is possible to estimate the fraction of atoms residing in the interfacial regions. For the 16 h HEBM sample (23 nm) for example, it is expected that 8 – 15 % of the atoms are located in the interfacial regions. For the chemically prepared sample (27 nm) the expected percentage decreases to 5 – 12 %, see Ref. [16]. However, the percentages of the mobile ions obtained from  $^7\text{Li}$  NMR measurements deviate considerably from these values. For the ball milled nanocrystalline samples, the ratio of mobile ions in the interfacial regions were found to exceed 32 % which is much higher than the predicted value from their grain sizes. This finding may suggest that they have thicker interfacial regions, or more reasonably, nanocrystallites are embedded in a thick matrix of amorphous  $\text{LiNbO}_3$ . In the chemically prepared nanocrystalline sample the highly mobile ions do not exceed 4 % of the total number of ions. In this case the grain-boundary region can be visualized to be much thinner than expected from their grain size and may be described as crystalline grains surrounded by very thin and probably not even disordered interfacial surfaces. This can clearly indicate that the nature of disorder in nanocrystalline materials, in general, depends on the preparation route. Ball-milled  $\text{LiNbO}_3$  is much more disordered than that prepared chemically via sol-gel technique. Previous results found in our group on nanocrystalline  $\text{CaF}_2$  prepared by noble gas condensation revealed a similar characteristics of the structure of the  $^{19}\text{F}$  NMR line; a superposition of a narrow contribution caused by mobile ions in the interfacial regions and a broad contribution due to the immobile ions in the gains.<sup>9</sup>

### 7.1.1.3 $^{93}\text{Nb}$ NMR lineshapes

Quadrupolar nuclides, such as  $^{93}\text{Nb}$ , interact with both the external magnetic field and the surrounding electric field gradient of their environment, leading typically to broad NMR resonances. Fig. 7.1.4 shows the  $^{93}\text{Nb}$  MAS-NMR lines for different forms of  $\text{LiNbO}_3$  measured at a Larmor frequency of 97.78 MHz

and a spinning rate of 12.5 kHz. The central transition ( $-1/2 \leftrightarrow 1/2$ ) for the powder of the single crystal and for microcrystalline  $\text{LiNbO}_3$  splits into two overlapping contributions. This splitting was previously observed by others<sup>288–289</sup>. The measured spectra were simulated using the program DmFit 2003, see Ref. [261]. The fits are acceptable for the single crystal and the microcrystalline forms except for some deviations in the relative intensities of the two peaks. However, for nanocrystalline phases the deviation is so big that the disorder (represented by a Gaussian line) masks the details of the lines. It seems unreasonable to fit the line with a single contribution as it will describe the Nb atoms inside the crystallites and ignore those in the disordered grain-boundary regions. The quadrupole coupling constant for the powder obtained from part of the single crystal was 22.18 MHz and the asymmetry parameter of the quadrupolar tensor was 0. The line has as huge isotropic chemical shift as  $-1003.9$  ppm from the reference (saturated solution of  $\text{NbCl}_5$  in "wet" acetonitrile)<sup>288</sup>. These results agree with the results previously reported by Prasad *et al.*<sup>290</sup> who found by MQMAS  $^{93}\text{Nb}$  NMR that the single crystal  $\text{LiNbO}_3$  has  $\delta_{\text{iso}} = -1004$  ppm and quadrupolar coupling constant of 22.1 MHz. The obtained results here are also consistent with values reported from measurements on single crystal and powder samples ( $\delta_{\text{iso}} = -1009$  ppm, quadrupolar coupling constant = 22.1 MHz, and asymmetry parameter of the quadrupolar tensor  $\eta_Q = 0$ , see Ref. [291]). Davis *et al.* also measured  $^{93}\text{Nb}$  NMR for  $\text{LiNbO}_3$  and found a quadrupole coupling constant for the single crystal  $\text{LiNbO}_3$  of 22 MHz and  $\eta_Q = 0.2$  and  $\delta_{\text{iso}} = +237$  ppm relative to the reference made by dissolving Nb in HF<sup>288</sup>. It was previously stated that the asymmetry parameter  $\eta_Q$  of the electric-field-gradient tensor is zero for Li and niobium atoms as they occupy sites with threefold symmetry<sup>273</sup>. No significant change in  $\delta_{\text{iso}}$  was found for the different forms of  $\text{LiNbO}_3$  while the quadrupolar coupling constant decreased to about 21 MHz after milling for 64 h. The amorphous form showed a very broad line with a fwhm of about 69.8 kHz.

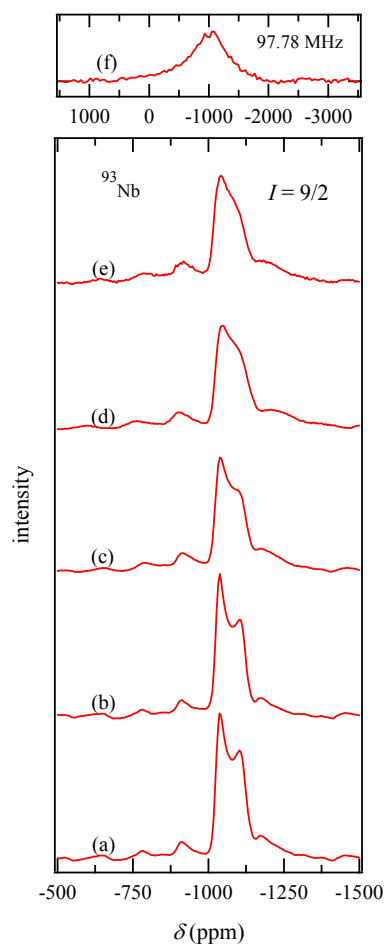


Fig. 7.1.4:  $^{93}\text{Nb}$  MAS-MNR spectra measured at Larmor frequency 97.98 MHz with spinning rate 12.5 kHz for: (a) single-crystal powder, (b) microcrystalline, nanocrystalline HEBM for (c) 4 h, (d) 16 h, and (e) 64 h and (f) amorphous  $\text{LiNbO}_3$  (Note the different scale due to the huge broadening).

### 7.1.1.4 Discussion of the $^{93}\text{Nb}$ NMR lineshapes

$^{93}\text{Nb}$  has  $I = 9/2$ , and a large quadrupole moment  $Q = 0.4 \text{ b}$  ( $-2 \cdot 10^{-29} \text{ m}^2$ ), which is ten times higher than that of  $^7\text{Li}$ . The quadrupole coupling constant  $e^2qQ/h$  of the  $^{93}\text{Nb}$  nucleus must be 200 times that of  $^7\text{Li}$  in  $\text{LiNbO}_3$  (assuming that the electrical field gradient at the niobium is the same as at lithium, in fact it is larger). Thus  $e^2qQ/h$  for  $^{93}\text{Nb}$  is expected to be about 10 MHz. The first  $^{93}\text{Nb}$  NMR study determined the quadrupolar coupling constant for single crystal  $\text{LiNbO}_3$  (22.02 MHz)<sup>273</sup>. Due to the large quadrupole coupling constant, second order powder pattern perturbation should be used to describe the resonance of the central transition ( $-1/2 \leftrightarrow 1/2$ ), (Fig. 7.1.5). There are two peaks, one at  $A$  and the other at  $-16/9A$ , where  $A$  is expressed as<sup>292</sup>

$$A = \frac{(e^2qQ/h)^2}{384\nu_0} \quad (7.1.2)$$

Here  $\nu_0$  is the NMR resonance frequency. To account for the huge chemical shift, the coordination shell

distortion,  $D$ , was proposed as

$$D = \frac{100}{d_a^2} \sum_{i=1}^n (d_i - d_a)^2 \% \quad (7.1.3)$$

where  $d_a$ , ( $= \frac{1}{n} \sum_{i=1}^n d_i$ ), is the average Nb—O bond length, and the  $d_i$  are the lengths of the individual Nb—O bonds. The Nb octahedra in  $\text{LiNbO}_3$  have three Nb—O bonds of 1.879 Å lengths and another three with 2.126 Å, thus  $d_a$  will be 2.0025 Å and  $D$  will equal 2.28 %. The shielding of the  $^{93}\text{Nb}$  nucleus is much less efficient in  $\text{LiNbO}_3$  (with octahedra sharing edges) and this is the reason for the large chemical shift. The quadrupolar tensor is close to axial symmetry, i.e.  $\eta_Q = 0$ . It should be recalled that  $\text{LiNbO}_3$  has an unusual ferroelectric behavior. The macroscopic dipole is parallel to the  $c$ -axis, which may be related to the near axial symmetry in the perovskite structure<sup>288</sup>.

Several earlier works have dealt with the  $^{93}\text{Nb}$  NMR signal as a couple of contributions. It was employed to differentiate between the two defect models proposed for Li deficiency by observing the asymmetry of the central transition. Due to the large chemical shift range of Nb, different signals are expected for  $^{93}\text{Nb}$  in different environments. In the Li-vacancy model, besides the prominent  $^{93}\text{Nb}$  NMR signal of the regular lattice, an additional signal of about 1 % intensity should result from  $\text{Nb}_{\text{Li}}^{4+}$  antisite. On the other hand, in the Nb-vacancy model, the relative intensity of the additional signal is expected to be about 5 % from Nb occupying larger Li octahedra. This model was favored by Peterson and Carnevale<sup>293</sup>. Also Hu *et al.*<sup>294</sup> supported this idea and attributed the splitting in the NMR spectra of the  $^{93}\text{Nb}$  central transi-

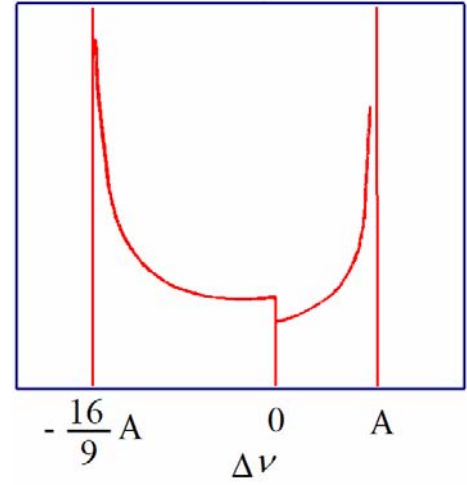


Fig. 7.1.5: Second-order powder pattern neglecting the effects of dipolar broadening<sup>292</sup>.

tion to the presence of  $\text{Nb}^{5+}$  in two different environments; the main peak due to  $\text{Nb}_{\text{Nb}}$ , and the extra side peak due to  $\text{Nb}_{\text{Li}}^{4+}$ . They noticed that the side peak vanished at 5 mole % MgO dopant which is equal to the  $\text{Nb}_{\text{Li}}$  concentration determined by Abrahams. However, a careful measurement combined with elaborate simulation studies showed that the interpretation of the  $^{93}\text{Nb}$  is less straightforward than thought before.<sup>295</sup>

The half-width of the low field derivative of the  $^{93}\text{Nb}$  NMR line showed appreciable sensitivity to stoichiometry in the composition range 48 – 50 %  $\text{Li}_2\text{O}$ , see Ref. [73].

Yatsenko *et al.*<sup>287</sup> modeled the intrinsic defects in congruent single crystals of  $\text{LiNbO}_3$  with complex  $(\text{Nb}_{\text{Li}} + 3\text{V}_{\text{Li}})$  and isolated  $\text{V}_{\text{Li}}$  defects. They assumed that the potential surface of the Li ion in the distorted  $\text{LiO}_6$  octahedron has four minima.<sup>296</sup> An additional  $^{93}\text{Nb}$  NMR line was observed in Ref. [297] only in some  $\text{LiNbO}_3$  crystals but it was attributed to defects in the growth of those crystals.

A second point of view in explaining the  $^{93}\text{Nb}$  NMR lines for  $\text{LiNbO}_3$  relayed on the fact that the second order quadrupolar interactions are too great to be removed by MAS alone. Even at 12.5 kHz rotation frequency the isotropic lines cannot be resolved, (Fig. 7.1.4). In another study<sup>95</sup>, crystals were rotated about the crystallographic  $c$ -axis; none of them gave a second signal or even a shoulder, and the linewidth varied between 5 and 22 kHz. Thus, it was deduced that the second resonance found earlier was an artifact due to low magnetic field strengths. A recent XRD result supports the Li-vacancy model which requires a second resonance signal of 1 % intensity<sup>87,298</sup>. The latter may not be detected due to strong quadrupolar nuclei or it may have a behavior similar to the main signal and thus is hidden under it and NMR cannot distinguish them. Two-dimensional nutational NMR also showed no second signal for  $\text{LiNbO}_3$  single crystal when its  $c$ -axis was aligned with the external magnetic field.<sup>95</sup>

For most metal niobates such as  $\text{LiNbO}_3$ , the second-order quadrupolar interaction is dominating the lineshape and cannot be removed by MAS NMR (alone), even at high magnetic fields and high spinning rates. The magnitude of the second-order quadrupolar interaction is inversely proportional to the magnetic field. The fwhm of  $^{93}\text{Nb}$  MAS NMR spectra of  $\text{LiNbO}_3$  powder was found to show marginal improvement from 11 to 9 kHz by changing the magnetic field from 9.4 to 14.1 T. The field dependence and the broadening are consistent with chemical shift dispersion which is due to disorder in the material.<sup>290</sup> The observed fwhm of the centerband in the isotropic dimension of the  $^{93}\text{Nb}$  DAS NMR spectrum of  $\text{LiNbO}_3$  was 5.8 kHz which is likely dominated by homonuclear dipolar interactions which are expected to be significant for  $^{93}\text{Nb}$  due to the natural abundance of 100 %. Finally, the 3QMAS NMR spectrum of  $\text{LiNbO}_3$  showed one order of magnitude higher resolution than the DAS. The obtained fwhm was about 0.7 kHz which is comparable to the homogeneous linewidth  $(1/\pi T_2)$  where  $T_2$  measured for a static sample is 375  $\mu\text{s}$ , see Ref. [290].



## 7.1.2 Extended X-ray Absorption Fine Structure

### 7.1.2.1 Temperature dependence of EXAFS of microcrystalline $\text{LiNbO}_3$

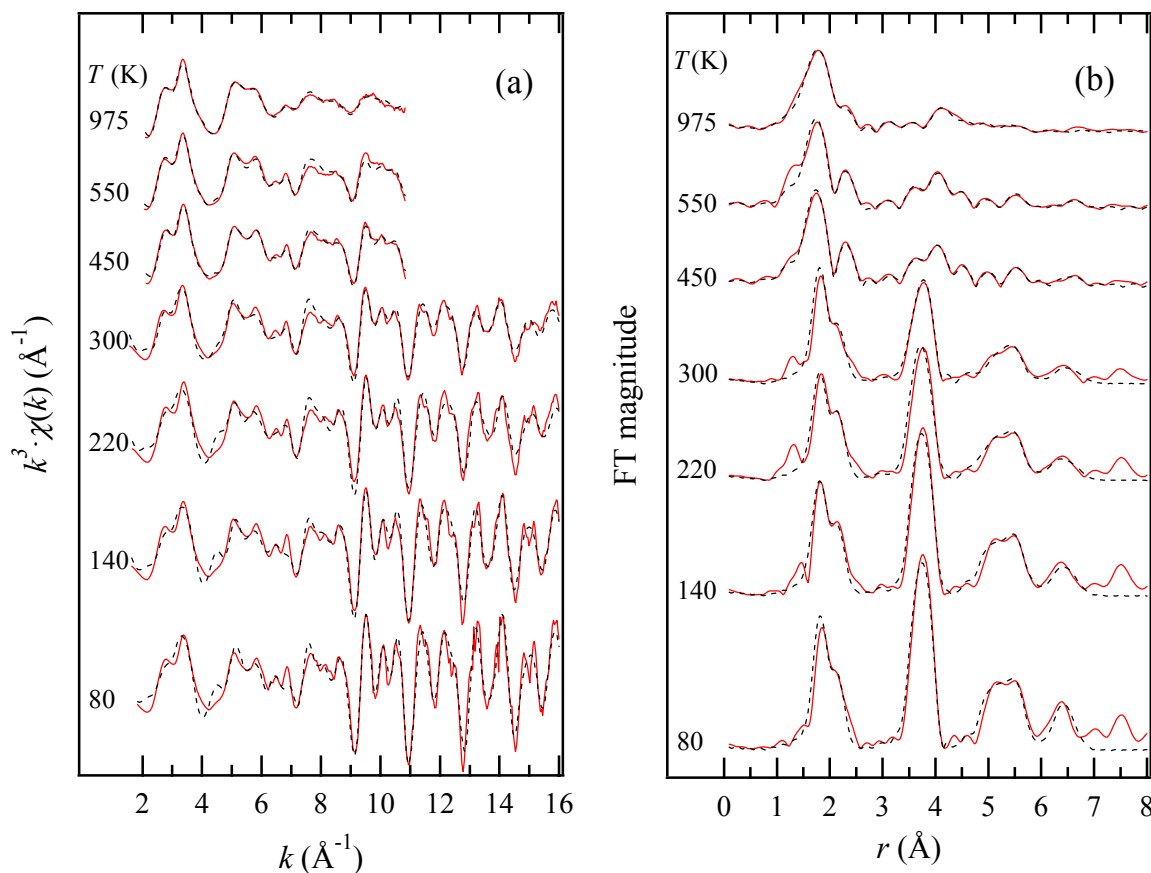


Fig. 7.1.6: (a) Nb K-edge EXAFS for microcrystalline  $\text{LiNbO}_3$  obtained in transmission mode at the indicated temperatures (in K). (b) The FTs of the EXAFS. Experiments are shown by solid curve with theory indicated by dashed curves. The fitting parameters are listed in Table 7.1.1(b).

EXAFS spectra were measured for microcrystalline  $\text{LiNbO}_3$  as a model compound at temperatures extending from 80 to 975 K. The spectra are shown with their Fourier transformations (FTs) in Fig. 7.1.6(a) and (b). The best theoretical models are shown by dashed lines, and the structural parameters obtained from these calculations are listed in Table 7.1.2(b), for 80 K as example. These parameters agree with those of the crystallographic model, Table 7.1.2(a), in e.g. the type and the number of atoms in each shell and the average distance from the excited atom (bond lengths) as well.

The peaks at about 2 Å in the Fourier transformed (FT) spectra correspond to the nearest couple of Nb—O shells. Each consists of three atoms, at 1.866 and 2.120 Å. These two shells constitute the distorted octahedral surrounding the excited Nb atom. The next two Li shells contain a sum of seven Li atoms and appear as very weak contributions between the first and the second main peaks. The second peak is com-

posed of four shells: two shells of oxygen (three O atoms each) at 3.665 Å and 3.684 Å, one shell of Nb (six atoms) at 3.751 Å and a combined shell (three O atoms, one Li atom, and three O atoms) at 4.034 Å. The third peak originates from the contribution of one oxygen shell (nine atoms) at 5.014 Å, and two niobium shells (six atoms each) at 5.127 and 5.477 Å. The fourth peak is mainly attributed to a Nb shell (six atoms) at 6.402 Å. The peaks at about 2 Å in the Fourier transformed (FT) spectra correspond to the nearest couple of Nb—O shells. Each consists of three atoms, at 1.866 and 2.120 Å. These two shells constitute the distorted octahedral surrounding the excited Nb atom. The next two Li shells contain a sum of seven Li atoms and appear as very weak contributions between the first and the second main peaks. The second peak is composed of four shells: two shells of oxygen (three O atoms each) at 3.665 Å and 3.684 Å, one

(a) Crystallographic model			(b) Microcrystalline LiNbO <sub>3</sub> 80 K					(c) Amorphous LiNbO <sub>3</sub> 80 K			
<i>N</i>	Atom	<i>R</i> (Å)	<i>j</i>	<i>N</i>	Atom	<i>R</i> (Å)	$\sigma^2$ (Å <sup>2</sup> )	<i>N</i>	Atom	<i>R</i> (Å)	$\sigma^2$ (Å <sup>2</sup> )
1	Nb	0.000	0	1	Nb	0	0.01	1	Nb	0	0.01
3	O	1.879	1	3	O	1.86573	0.00506	2	O	1.79822	0.02032
3	O	2.126	2	3	O	2.12001	0.0085	4	O	1.99227	0.02462
1	Li	3.063	3	4	Li	3.00189	0.01525	5	Li	2.81961	0.02699
3	Li	3.067	4	3	Li	3.39539	0.01435	4	O	3.41925	0.02479
3	Li	3.357	5	3	O	3.66522	0.00206	3	O	3.82739	0.00262
3	O	3.624	6	3	O	3.68386	0.00277	3	Nb	3.8942	0.02489
3	O	3.738	7	6	Nb	3.75107	0.00635	8	O	4.73589	0.04683
6	Nb	3.766	8	7	O	4.03372	0.0049				
3	O	3.859	9	9	O	4.56689	0.01954				
1	Li	3.870	10	9	O	5.01374	0.00672				
3	O	4.210	11	6	Nb	5.12676	0.01022				
3	O	4.437	12	6	Nb	5.47692	0.00986				
6	O	4.531	13	6	O	5.51569	0.04834				
3	O	4.848	14	9	O	5.7986	0.04964				
3	O	4.843	15	9	Li	5.97809	0.05003				
3	O	4.927	16	3	Li	6.14815	0.05015				
3	O	4.949	17	9	O	6.2962	0.0528				
6	Nb	5.151	18	6	Nb	6.40228	0.00753				
3	O	5.489									
6	Nb	5.496									
3	O	5.559									
3	O	5.729									
3	O	5.821									
3	O	5.886									
6	Li	5.992									
3	Li	5.995									
3	Li	6.142									
3	O	6.270									
3	O	6.358									
3	O	6.376									
6	Nb	6.380									

Table 7.1.2: Comparison between the radial distributions for LiNbO<sub>3</sub> obtained from: (a) the crystallographic-structure model for single crystal data (from the literature<sup>79</sup>), (b) the EXAFS fitting results for microcrystalline and (c) amorphous LiNbO<sub>3</sub>. *N* is the coordination number of the *j*<sup>th</sup> shell, *R* is the bond length and  $\sigma_j$  is the Debye-Waller factor.

shell of Nb (six atoms) at 3.751 Å and a combined shell (three O atoms, one Li atom, and three O atoms) at 4.034 Å. The third peak originates from the contribution of one oxygen shell (nine atoms) at 5.014 Å, and two niobium shells (six atoms each) at 5.127 and 5.477 Å. The fourth peak is mainly attributed to a Nb shell (six atoms) at 6.402 Å.

The FTs of the EXAFS for the microcrystalline form obtained at different temperatures are shown in Fig. 7.1.6(b). The characteristic features of the spectra, in terms of the peak positions and shapes remain unchanged through out the whole temperature range, indicating the absence of phase transformation and that the main effect of the temperature was related to the amplitude. In the temperature range from 80 to 300 K the amplitude decreases slightly while the decrease becomes more drastic above 300 K, especially for the outer shells. Starting from 450 K, the outer peaks diminished so much that they are no longer detectable. Fig. 7.1.7 shows the values of the Debye-Waller factor *vs.* temperature. These data are fitted by the Einstein model (Eq. (6.3.4)) and the Debye model (Eq. (6.3.5)) for Nb–O and Nb–Nb shells, respectively. Both equations give nonzero  $\sigma_{\text{vib}}^2$  values at 0 K, corresponding to a zero point motion. The results of the fittings are summarized in Table 7.1.2.

With respect to the Nb–O shells, the  $\sigma_{\text{stat}}^2$  has increased from 0.00225 Å<sup>2</sup> for the first oxygen shell (Nb–O<sub>I</sub>) to 0.00541 Å<sup>2</sup> for the second one (Nb–O<sub>II</sub>). This value increases when moving away from the excited Nb atom. On the contrary, in the case of Nb–Nb shells, the curves are very near to each other and the variation in the value of  $\sigma_{\text{stat}}^2$  is much smaller. The value obtained for the mean vibrational frequency ( $\bar{\nu}$ ) for the first two Nb–O shells are not far from each other and compare well to the literature value, where the major Raman bands for LiNbO<sub>3</sub> are found at 620 cm<sup>-1</sup> and a shoulder at 579 cm<sup>-1</sup> (symmetric stretching mode of the NbO<sub>6</sub> octahedra with slightly different Nb–O bond lengths), and a peak at

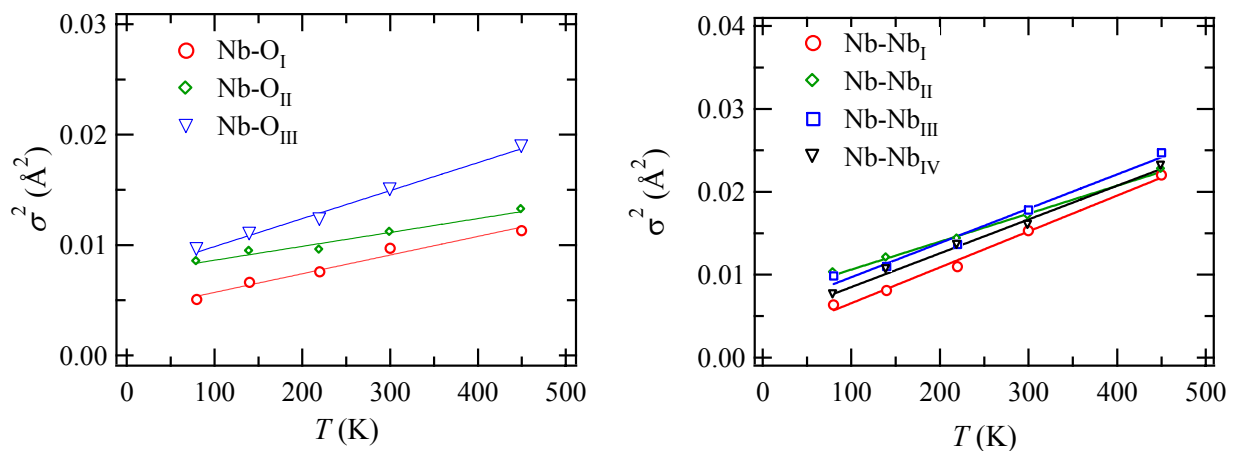


Fig. 7.1.7: The temperature dependence of the Debye-Waller factors for microcrystalline LiNbO<sub>3</sub>. Comparison between experimental data (points) and calculated results (lines) for the niobium-oxygen and niobium-niobium shells. Fitting parameters are listed in Table 7.1.3.

Table 7.1.3: Static and vibration frequency of Nb-O and Nb-Nb shells obtained from fitting the curves in Fig. 7.1.7.

Bond	$R$ (Å)	$N$	$\sigma_{\text{stat}}^2$ (Å <sup>2</sup> )*	$\bar{\nu}$ (cm <sup>-1</sup> )*	$\bar{\nu}_{\text{ref}}$ (cm <sup>-1</sup> )
Nb-O <sub>I</sub>	1.86573	3	0.00225	844.09	500–750, and
Nb-O <sub>II</sub>	2.12001	3	0.00541	783.38	750–1000 <sup>[245]</sup>
Nb-Nb <sub>I</sub>	3.75107	6	0.00223	-	-

\* Einstein model used for Nb-O shells and Debye model used for Nb-Nb shells

874 cm<sup>-1</sup> (antisymmetric stretching mode of the Nb—O—Nb linkage)<sup>245</sup>.

### 7.1.2.2 EXAFS of amorphous LiNbO<sub>3</sub>

The EXAFS spectrum for amorphous LiNbO<sub>3</sub> at 80 K is shown at the top of Fig. 7.1.8(a), and its FT at the top of Fig. 7.1.8(b). The structural parameters, the average bond lengths and the coordination numbers of the fitting model are listed in Table 7.1.2(c) for 80 K. These spectra were measured to be used as models for fitting the nanocrystalline form. However, a lot of useful information about the local structure of amorphous LiNbO<sub>3</sub> can be extracted from them. The first peaks at about 2 Å in the FT spectra correspond to the nearest couple of Nb—O shells at 1.798 and 1.992 Å with 2 and 4 O atoms, respectively. These two shells constitute the octahedron around the central atom which is less distorted and smaller than in the case of the microcrystalline form. It is surrounded by a fewer number of Li and Nb atoms in the nearest neighboring spheres (5 Li instead of 7 and 3 Nb instead of 6 in the microcrystalline form). The first Nb—Nb distance in the amorphous form (3.894 Å) is larger than that in the microcrystalline LiNbO<sub>3</sub>

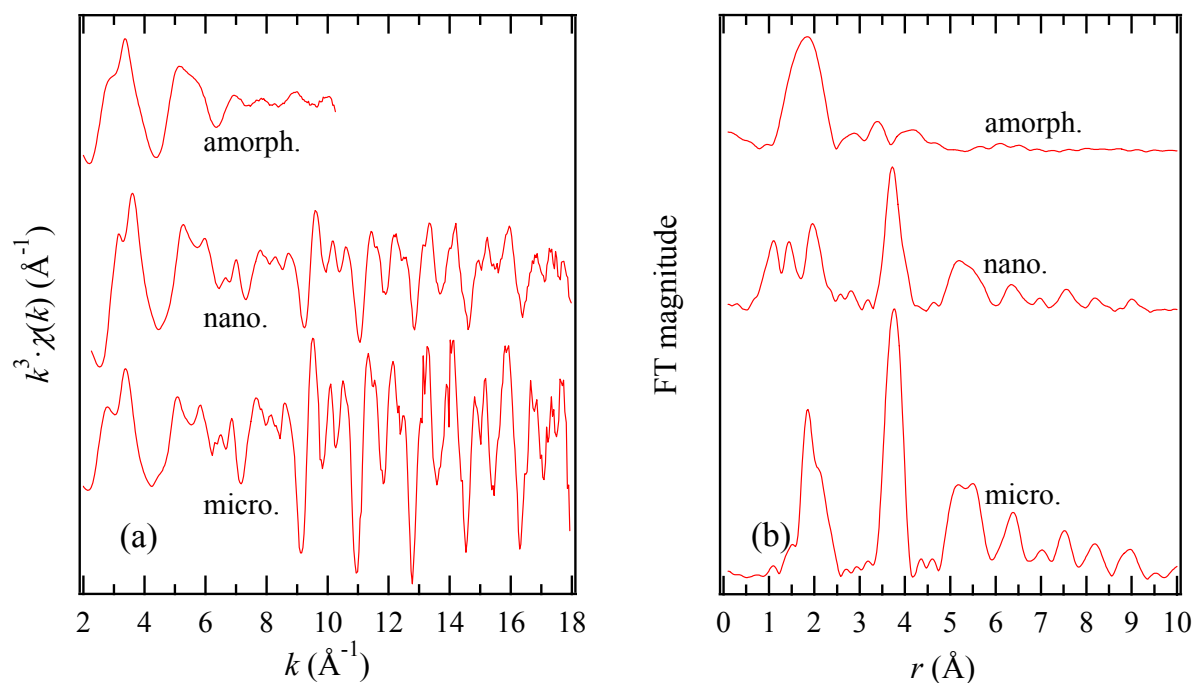
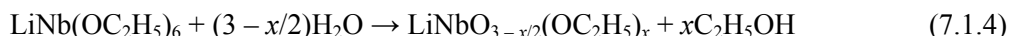


Fig. 7.1.8: Niobium K-edge measured at 80 K for: the microcrystalline, ball milled nanocrystalline, and sol-gel prepared amorphous LiNbO<sub>3</sub>: EXAFS spectra (a), and their FT's (b).

(3.751 Å). From these findings we can conceive that the amorphous  $\text{LiNbO}_3$  is composed of the same building units as the microcrystalline form which are  $\text{NbO}_6$  octahedra, however, they are loosely connected to each other by fewer Li moieties (tetrahedra or octahedra).

It is known that  $\text{Nb}(\text{OR})_5$  has a bi-octahedral structure (edge shared) with two bridging  $\text{Nb—O—Nb}$  bonds and eight terminal  $\text{Nb—O}$  bonds with bridging alkyl groups<sup>299</sup>. Prominent atomic pairs in the lithium niobium double alkoxide,  $\text{LiNb}(\text{OC}_2\text{O}_5)_6$ , can be related to the crystal structure of  $\text{LiNbO}_3$ . Considering the XRD studies of  $\text{LiNb}(\text{OC}_2\text{O}_5)_6$  and FTIR investigations of amorphous  $\text{LiNbO}_3$  gels<sup>300</sup>, it was found that the structure of the  $\text{LiNb}(\text{OC}_2\text{O}_5)_6$  is composed of infinite helical polymers comprised of alternating  $\text{Nb}(\text{OC}_2\text{O}_5)_6$  octahedral units linked by severely distorted tetrahedrally coordinated Li atoms with bridging alkoxide ligands. NMR investigations have shown that the Li environment changes during hydrolysis<sup>301</sup>, while Nb octahedra are stable even with changing water concentration in the gel<sup>302</sup>. In the hydrolysis reaction the double alkoxide is converted to amorphous  $\text{LiNbO}_3$  which acts as the building block of the crystalline  $\text{LiNbO}_3$  in the sol according to the following equation



The products depend on the degree of hydrolysis  $(3 - x/2)$ , where  $0 < x < 6$ . However,  $\text{LiNbO}_2(\text{OC}_2\text{H}_5)_2$  and amorphous  $\text{LiNbO}_3$  are known to be thermodynamically stable compounds. Short-range order in the amorphous phase is usually very similar to that of the crystal which will grow from the amorphous phase.

### 7.1.2.3 EXAFS of nanocrystalline $\text{LiNbO}_3$

Fig. 7.1.8(a) shows the EXAFS spectra for nanocrystalline  $\text{LiNbO}_3$  in comparison with the corresponding microcrystalline and amorphous forms measured at 80 K. A high degree of resemblance between the microcrystalline and the nanocrystalline forms can be seen, except that the latter shows reduced peak intensities. The EXAFS spectra of amorphous  $\text{LiNbO}_3$  show less details and the intensity of the peaks is much more reduced. The most remarkable change in the FT of the nanocrystalline form, shown in Fig. 7.1.8(b), is the splitting of the first main peak into three medium-intensity peaks in the nanocrystalline form. The first one can be regarded as an artifact as it appears at 1 Å while the last two of the peaks are due to the nearest couple of  $\text{Nb—O}$  shells which form the distorted octahedron around the excited Nb atom. Otherwise the FTs of the nanocrystal-

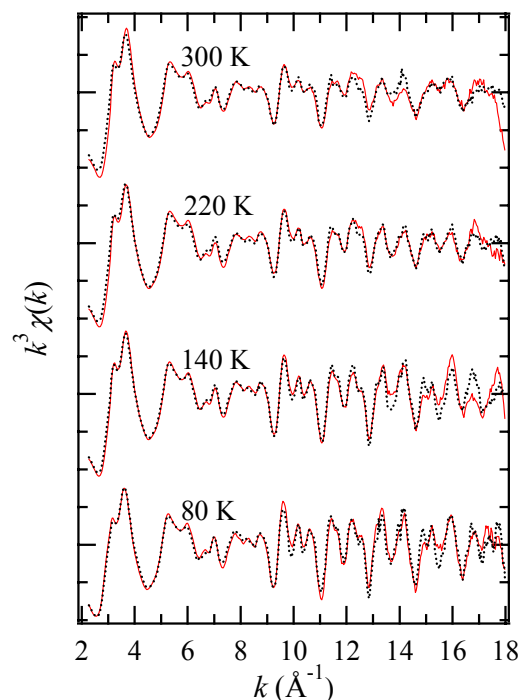


Fig. 7.1.9.: Nb K-edge XAFS of nanocrystalline  $\text{LiNbO}_3$  (solid curves), with the dotted curves representing the fitting obtained by a linear combination of the EXAFS curves for the microcrystalline and the amorphous measured at the same temperatures and the mixing coefficients ( $m$ ,  $a$ ) shown as percentages in table 7.1.3.

line form show similar peak positions to those of the microcrystalline form but with reduced intensities.

Using the LINCOM program, the experimental EXAFS spectrum of the nanocrystalline  $\text{LiNbO}_3$  was modeled with a linear combination of the standards which are the EXAFS spectra of the microcrystalline and amorphous  $\text{LiNbO}_3$  measured at the same temperature, Fig. 7.1.9 (for more details about the fitting procedure see section 6.3.4). This procedure was applied for the different temperatures. The values of the obtained coefficients of Eq. 6.3.1 ( $m$  and  $a$ ) are listed in Table 7.1.4. The mixing coefficients range between 50 % and 55 % for the microcrystalline form and 45 % and 50 % for the amorphous form.

Using another fitting procedure two radial clusters were generated according to the multiple cluster approach (section 6.3.4). The first cluster is for the grain environment which is the same cluster used to model the EXAFS of the microcrystalline sample (the first excited Nb atom and the subsequent 17 shells), Table 7.1.2(b). The second cluster represents the GB environment which is modeled by the cluster used to fit the EXAFS of the amorphous sample (the second excited Nb atom and the subsequent last seven shells), Table 7.1.2(c). The relative contribution of each cluster to the total model was adjusted by changing the shell occupation number of the excited central atoms for each cluster, i.e.,  $N_0$  for the first (micro-

Table 7.1.4: The values of the mixing coefficients for the microcrystalline (M) and the amorphous (A) standards that gave the best fit for the nanocrystalline EXAFS using LINCOM software.

$T$ (K)	$m$ (%)	$a$ (%)
80	49.9	50.1
140	55.4	44.6
220	53.4	46.6
300	55.4	44.6

Using another fitting procedure two radial clusters were generated according to the multiple cluster approach (section 6.3.4). The first cluster is for the grain environment which is the same cluster used to model the EXAFS of the microcrystalline sample (the first excited Nb atom and the subsequent 17 shells), Table 7.1.2(b). The second cluster represents the GB environment which is modeled by the cluster used to fit the EXAFS of the amorphous sample (the second excited Nb atom and the subsequent last seven shells), Table 7.1.2(c). The relative contribution of each cluster to the total model was adjusted by changing the shell occupation number of the excited central atoms for each cluster, i.e.,  $N_0$  for the first (micro-

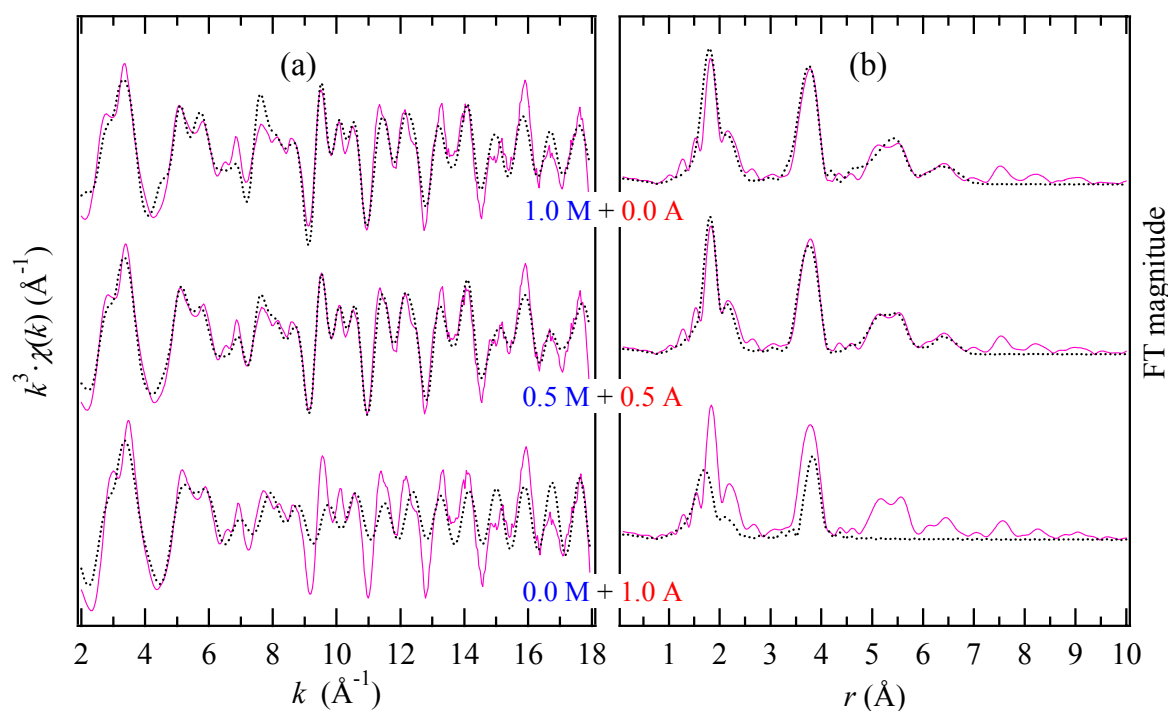


Fig. 7.1.10: Niobium K-edge (a) EXAFS for nanocrystalline  $\text{LiNbO}_3$  at 140 K, and (b) their FTs. Experimental data are shown by solid curves whereas the dashed curves represent the result obtained using the multiple cluster model with the indicated different mixing coefficients

crystalline) cluster and  $N_{I9}$  for the second (amorphous) cluster. Fig. 7.1.10 shows three examples of fitting for the nanocrystalline sample at 140 K for three different ratios of the clusters' contributions [(0 M + 1 A), (0.5 M + 0.5 A), (1 M + 0 A)]. It is clear that the best fit is obtained in the case of (0.5 M + 0.5 A) mixing ratio. Furthermore, it is obvious that the microcrystalline cluster (1 M + 0 A) fits better than the amorphous cluster (0 M + 1 A). The occupation number for each cluster was changed from 0 to 1 in steps of 0.1 for the temperatures 80, 140, 220, 300 K. Fig. 7.1.11 summarizes  $R_{\text{EXAFS}}$  values for the different temperatures and variable mixing ratios of the two clusters. The best fit is obtained at a mixing ratio of 40 – 50 % microcrystalline with 60 – 50 % amorphous.

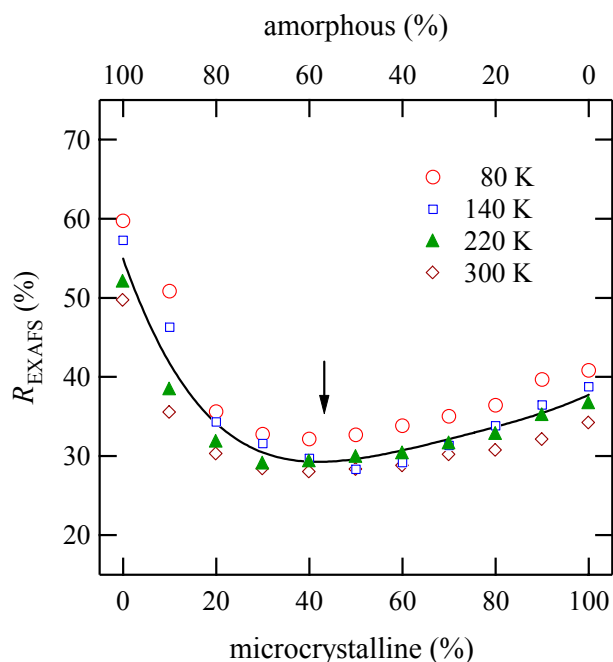


Fig. 7.1.11: The change in  $R_{\text{EXAFS}}$  (%) for the multiple clusters fitting with changing ratio of amorphous and microcrystalline clusters.

#### 7.1.2.4 (EXAFS) discussions

EXAFS was employed to investigate the structure of microcrystalline  $\text{LiNbO}_3$  over a wide temperature range. The structural parameters extracted from the measured EXAFS spectra agree with those obtained from the XRD crystallographic model. Furthermore, the temperature dependence of the Debye-Waller factor for microcrystalline  $\text{LiNbO}_3$  was modeled to extract the vibration frequency of the Nb—O bond.

EXAFS also gave useful details about the local structure of the amorphous  $\text{LiNbO}_3$ . It consists of smaller and less distorted  $\text{NbO}_6$  octahedra which are connected to fewer and farther situated  $\text{NbO}_6$  octahedra by a smaller number of Li-oxygen polyhedra (octahedra or tetrahedra). This idea emphasizes that the short range order in the amorphous form is similar to that of the microcrystalline form (at least with respect to niobium). However, they differ with respect to long range order as the building units in the amorphous form are more separated and enclose a lot of free volume in the structure.

From the analysis of the EXAFS of the microcrystalline form as a model material, it was clear that EXAFS measurements on  $\text{LiNbO}_3$  cannot be easily interpreted. Firstly, because the crystal structure is not that simple as each peak in the FT spectra belongs to several adjacent shells. The second reason is the low atomic number of Li and consequently its scattering factor, implying that the amplitude (the occupancies) and the atomic positions cannot be reliably obtained by using EXAFS or by any other conventional diffraction method. This also may affect the fitting parameters for the neighboring shells as well.

EXAFS was also employed to explore the nature of the grain boundaries in the nanocrystalline  $\text{LiNbO}_3$  prepared by HEBM. The analysis of the nanocrystalline form was not possible using the conventional descriptions used for similar cases. Hence, the measured EXAFS of the coarse grained microcrystalline and the sol-gel prepared amorphous  $\text{LiNbO}_3$  were utilized as standards to model the experimental EXAFS results of the nanocrystalline form by applying the "multiple cluster" and "linear combination" approaches. Both methods showed that 16 h HEBM nanocrystalline  $\text{LiNbO}_3$  consists of approximately equal contributions of the microcrystalline grains and the amorphous grain-boundary regions.

Simultaneously with the present one an EXAFS study of nanocrystalline  $\text{LiNbO}_3$  was conducted on samples prepared by ball milling (14 nm), double alkoxide sol-gel (1.6 nm), and a polymer precursor method (4.5 nm).<sup>19</sup> However, the analysis focused on the reduction in the amplitude of the second peak. This reduction was attributed to the reduced dimensionality of the grains as there is a significant number of 'surface' Nb sites which lack an Nb–Nb interaction reducing the coordination number especially when the grain diameter is less than the dimensions of the unit cell. Otherwise this reduction in amplitude was attributed to the presence of an amorphous phase with a reduced average coordination number.<sup>19</sup>

Unfortunately, the chemically prepared nanocrystalline sample was not measured by EXAFS so no clues about the nature of its grain boundaries could be obtained. However, it was found that the nanocrystalline samples of a number of simple binary oxides prepared by sol-gel<sup>303–304</sup>, and recently also of  $\text{LiNbO}_3$ , see Ref. [20], are highly ordered with the interfaces between the crystallites being very similar to those in bulk materials.

### 7.1.3 X-Ray Diffraction and Transmission Electron Microscopy

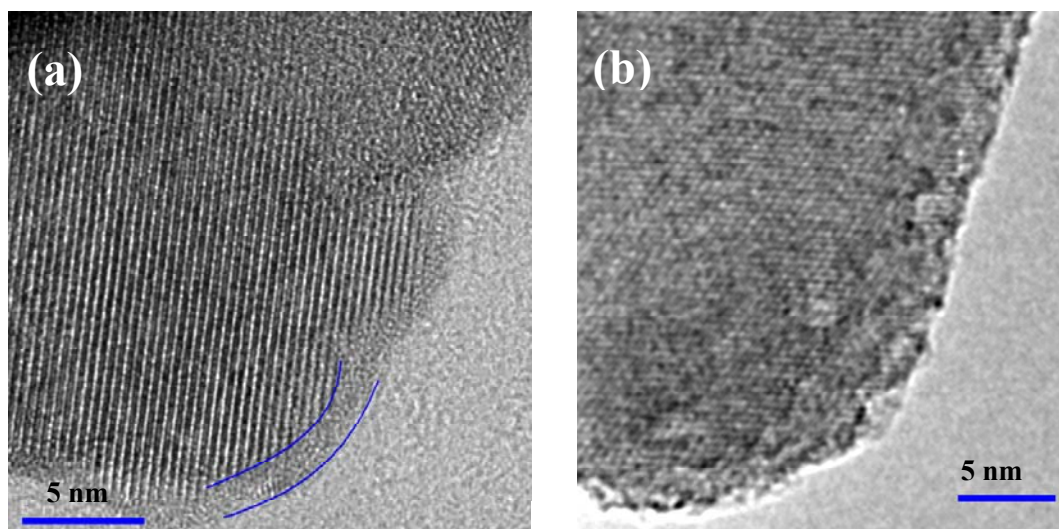


Fig. 7.1.12: The TEM image of nanocrystalline  $\text{LiNbO}_3$  prepared by: (a) HEBM for 32 h (average crystallite size 23 nm) where the amorphous layer is covering the surface at the right top and surrounding the rest of the grain with a thick amorphous grain boundary region, (b) heating the double alkoxide sol-gel amorphous sample for 1 h at 773 K (average grain size 27 nm).



The diffractograms of the nanocrystalline  $\text{LiNbO}_3$  were shown in Fig. 5.1.2. They showed that the broadened peaks due to the reduced crystallite size of the grains are superimposed over the broad humps which are the characteristic background for the amorphous grain-boundary regions. In the case of HEBM the amorphous background started to be noticeable after 8 h of milling and continued to increase for higher milling times. On the other hand, this background disappeared completely after heating the amorphous  $\text{LiNbO}_3$  at 773 K.

In the TEM images of the nanocrystalline  $\text{LiNbO}_3$  HEBM for 32 h, it is possible to observe a large amount of the amorphous form, Fig. 7.1.12(a). The right top part of the crystallites is covered by this amorphous material which also surrounds the rest of the nanocrystals with a thick layer of interfacial regions. On the other hand, the sol-gel prepared sample shows a lower degree of crystallinity, and the grain-boundary regions are disordered and defective however, they are thin and the crystallite can be seen through them, Fig. 7.1.12(b). There are some terraces and surface steps; however, no thick grain-boundary regions could be detected as in the case of HEBM sample. For more TEM and SEM images, see appendix A.2.

#### 7.1.4 General Discussion of the Structural Aspects

The majority of the lithium ions have one crystallographic position in the  $\text{LiNbO}_3$  crystalline forms (microcrystalline, single crystals as well as in the crystalline grains of the nanocrystalline samples). However, a certain degree of disorder can be introduced in the Li lattice when preparing both the amorphous and the nanocrystalline forms. This can be accomplished by sol-gel preparation of the amorphous and the nanocrystalline forms as well as by HEBM of the parent microcrystalline material to convert it into nanocrystals. The amorphous form is believed to be highly defective and disordered, with the disorder being homogeneously distributed in the long range sense, leading to “free volume” enclosed in its disordered network. In spite of the intensive research directed to the nanocrystalline materials, it is not clear up to now whether the GB regions in nanocrystalline materials prepared by different routes have similar local structure. One point of view was that the GB regions in nanocrystalline metals are completely disordered like a gas without even the short-range order of liquids or amorphous solids<sup>15,305</sup>. This hypothesis is based on an XRD analysis of 6 nm Fe<sup>306</sup> and an EXAFS study of 10 – 24 nm grained Cu<sup>307</sup>. On the other hand, TEM<sup>308</sup> and XRD<sup>309</sup> studies on Pd, beside other EXAFS studies on Cu<sup>310</sup> and Pd<sup>311</sup> showed that the GBs are not anomalous. Recently, many EXAFS studies have targeted nanocrystalline oxides. Some nanocrystalline oxides showed well-ordered crystallites with GBs similar to those in bulk materials such as sol-gel prepared, tin oxide<sup>312</sup>, zinc oxide<sup>313</sup>, or yttrium stabilized cubic  $\text{ZrO}_2$  prepared by the polymer spin coating<sup>243</sup> and  $\text{CeO}_2$ <sup>314</sup>. On the other hand, ball milled nanocrystalline oxides have a large level of disorder in the interfacial regions<sup>303</sup>.

The findings obtained here by means of  $^7\text{Li}$  NMR line-shape analysis were able to distinguish between the Li ions residing in the ordered crystalline grains and those which are residing in the highly disordered interfacial regions of the nanocrystalline  $\text{LiNbO}_3$ . The ratio of the highly mobile Li ions in the interfacial regions was more than 32 % in the HEBM nanocrystalline  $\text{LiNbO}_3$ , while this ratio did not exceed 4 % in the chemically prepared nanocrystalline  $\text{LiNbO}_3$ .

The local environment around niobium in ball milled nanocrystalline  $\text{LiNbO}_3$  was probed by EXAFS. The analysis of the resultant spectra were modeled with a combination of microcrystalline and amorphous  $\text{LiNbO}_3$  EXAFS spectra with about 1:1 ratio. This would be helpful in understanding the structure of the nanocrystalline  $\text{LiNbO}_3$  prepared by HEBM as being composed of crystalline grains and amorphous GB regions. This has also been found by others for HEBM  $\text{LiNbO}_3$ , see Ref. [19]. The XRD investigations and TEM images support the presence of amorphous grain-boundary regions in the HEBM nanocrystalline sample while they were absent (or extremely thin) in the chemically prepared one.

In general, it seems to be true that the degree of disorder in the nanocrystalline  $\text{LiNbO}_3$ , i.e. the nature of the GB regions, is strongly dependent on the preparation route. The nanocrystalline  $\text{LiNbO}_3$  sample prepared by HEBM has a high volume fraction of the amorphous grain-boundary regions, or it can be pictured as nanocrystallites embedded in an amorphous  $\text{LiNbO}_3$  matrix.

## 7.2 DYNAMICS AND DIFFUSION

### 7.2.1 Impedance Spectroscopy

#### 7.2.1.1 Conductivity and master curves

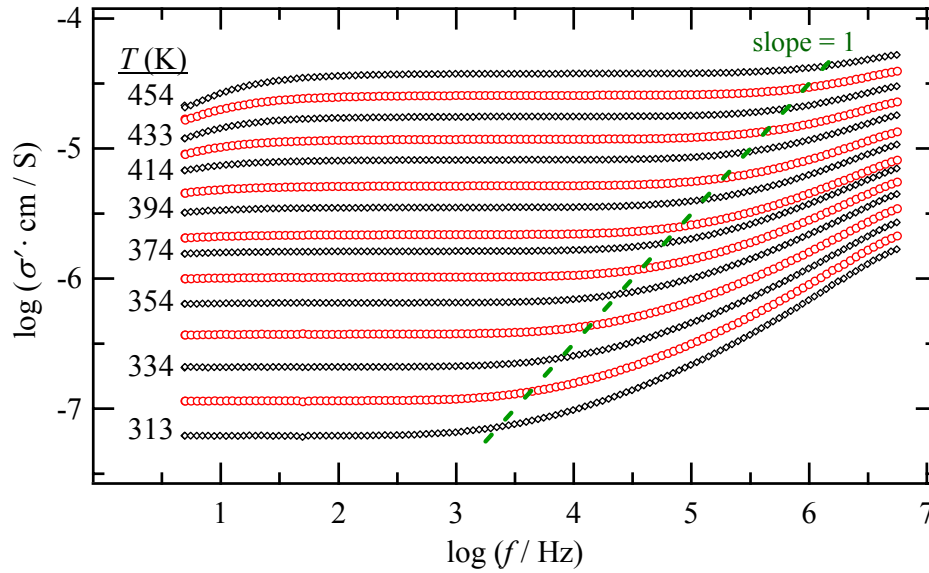


Fig. 7.2.1: Conductivity log-log spectra for amorphous  $\text{LiNbO}_3$  for temperatures from 313 to 454 K measured under oxygen atmosphere in the frequency range from 5 Hz to 13 MHz. The dashed line has a slope of 1 and connects the onsets of the dispersion regions for the different temperatures.

Fig. 7.2.1 shows typical (log-log) conductivity spectra for amorphous  $\text{LiNbO}_3$  at temperatures in the range 313 – 454 K. Here  $\sigma'$  is obtained by normalizing  $G$  for the sample geometric parameters [i.e.  $\sigma' = G \cdot l/A$ , where  $G$  is the conductance, the real part of the complex admittance ( $Y^*$ ),  $l$  and  $A$  are the sample thickness and the contacts area, respectively]. The obtained response shows typical characteristics of an ionic conductor. At low frequencies the conductivity spectra consist of true  $\sigma_{\text{dc}}$ -plateaus which are completely frequency independent and become more pronounced at elevated temperatures. They originate from thermally activated-long range diffusion of mobile ions. On the other hand, in the high-frequency range the conductivity becomes strongly frequency dependent, that is the dispersive regime. This is due to the fact that the time window,  $\Delta t = 1/\omega$ , is getting shorter with increasing the frequency so that the experiment is capable to register more hops before they are cancelled by the correlated backward hops. Contrarily, in the low-frequency regime where  $\Delta t$  is long enough to allow the backward hops to cancel number of the hops. Thus the experiment is capable to register only a smaller number of successful “i.e. uncorrelated” hops

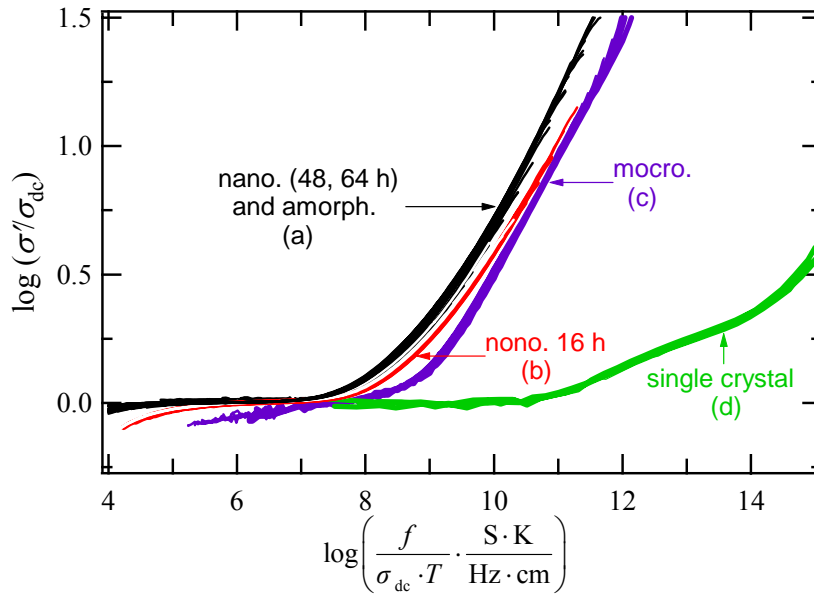


Fig. 7.2.2: Conductivity master curves obtained by normalizing the  $y$ -axis over  $\sigma_{dc}$  and the  $x$ -axis over the product  $(\sigma_{dc} \cdot T)$  for different  $\text{LiNbO}_3$  samples: (a) amorphous, nanocrystalline HEBM for 64 h and 48 h, (b) nanocrystalline HEBM for 16 h, (c) microcrystalline, and (d) single crystalline  $\text{LiNbO}_3$ .

which correspond to long range motion<sup>315</sup>. The frequency dependent conductivity data can be approximated by a power law

$$\sigma' = \sigma_{dc} + A\omega^s \quad (7.2.1)$$

with  $0.55 \leq s \leq 0.77$ ,  $s$  is a temperature-dependent parameter that is related to the conduction process (polarization conductivity or dielectric loss)<sup>316</sup>. The decrease of  $\sigma'$  for  $f < 10$  Hz, visible in the high-temperature conductivity curves, is due to a blocking-electrode effect. This polarization effect occurs when the electrode is unable to dissipate or replenish ions arriving or departing from the electrode in any half cycle. The importance of this effect appears at high temperatures and low frequencies ( $< 1000$  kHz). With increasing the temperature the onset frequency of the dispersive regime shifts towards higher frequencies following a straight line with slope of about 1, shown by the dashed line in Fig. 7.2.1. Sliding the conductivity isotherms for amorphous  $\text{LiNbO}_3$  along this line makes them collapse into a common curve, Fig. 7.2.2(a) for amorphous  $\text{LiNbO}_3$ . This implies that the underlying transport processes become faster with increasing temperature without any alteration in the conduction mechanism<sup>317</sup>. According to the time-temperature superposition principle, this can be achieved by scaling the  $y$ -axis with  $\sigma_{dc}$  and the  $x$ -axis with  $(\sigma_{dc} \cdot T)$ .

Fig. 7.2.2 displays the master curves for different forms of  $\text{LiNbO}_3$ . The curve (a) for amorphous  $\text{LiNbO}_3$  coincides with those of the nanocrystalline samples prepared by HEBM for 64 h and 48 h, while the 16 h HEBM curve (b) deviates towards the curve (c) which belongs to the microcrystalline form that is shifted towards higher  $(f / \sigma_{dc} \cdot T)$ . The single crystal curve (d) exhibits an extra shift. At a given 'normalized frequency' value  $(f / \sigma_{dc} \cdot T)$ , the normalized conductivity  $(\sigma' / \sigma_{dc})$  increases by going from the single crystal  $\text{LiNbO}_3$  to the microcrystalline material passing through the nanocrystalline and ending with the

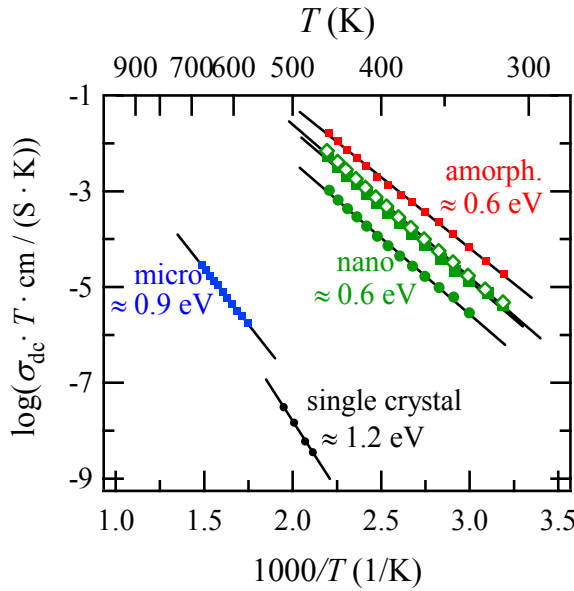


Table 7.2.1: Comparison between the activation energy of the dc conductivity,  $E_{a,\sigma}$ , and the activation energy of the semicircle relaxation frequency,  $E_{a,r}$

LiNbO <sub>3</sub>	$E_{a,\sigma}$ [eV]	$E_{a,r}$ [eV]
single crystal	1.16	–
microcrystalline	0.93	0.88
nanocrystalline	16 h	0.63
	48 h	0.63
	64 h	0.63
amorphous	0.59	0.60

Fig. 7.2.3: Temperature dependence of  $\sigma_{dc}$  for the single crystalline (●), microcrystalline (■), nanocrystalline HEHM for [16 h (●), 48 h (■), 64 h (◇)] and amorphous (■) LiNbO<sub>3</sub>.

amorphous material. There may be two reasons for this behavior: (i) One reason may be the increased number of highly mobile ions due to the interfacial regions and the free volume in the nanocrystalline and amorphous forms, respectively. (ii) Alternatively, one may conceive that in the amorphous material and in the interfacial regions of the nanocrystalline material the disorder leads to a lack of Brillouin zones and selection rules causing the vibrations to dominate the ionic movement which is described by the following characteristic frequency dependence [ $\sigma(\omega) \propto \omega^2$ ]<sup>315</sup>.

Fig.7.2.3 shows the temperature dependence of the dc-conductivity for the different forms of LiNbO<sub>3</sub>. At a certain temperature, e.g. 450 K, the conductivity increases by seven orders of magnitude by going from the single crystal to the amorphous LiNbO<sub>3</sub>. Each sample shows single Arrhenius behavior over the measured temperature range indicating no change in the conduction mechanism.

$$T \cdot \sigma_{dc} = A' \exp(-E_{a,\sigma} / k_B T), \quad (7.2.2)$$

The activation energy decreases from that of the single crystal and microcrystalline via nanocrystalline to that of amorphous LiNbO<sub>3</sub>. Note that the activation energies of the amorphous and nanocrystalline forms are practically the same, (Table 7.2.1).

### 7.2.1.2 Complex impedance and equivalent circuits

The complex impedance analysis was used to separate  $\sigma_{dc}$  of the sample from electrode effects. Here the complex resistivity,

$$\rho^* = Z^* \cdot A / l, \quad (7.2.3)$$

is used instead of the impedance  $Z^*$  to eliminate any differences due to the geometries of the different samples. The complex plane plots of the resistivity for different forms of LiNbO<sub>3</sub> at 370 K are shown in

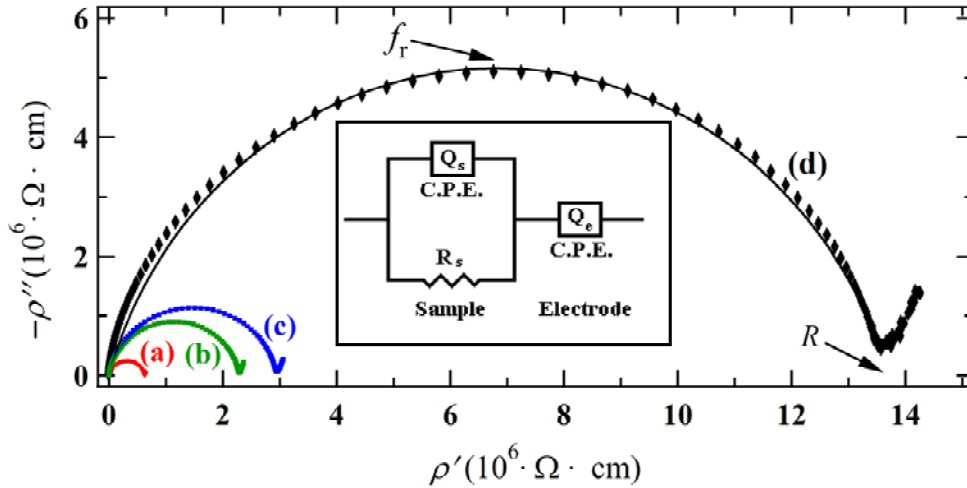


Fig. 7.2.4: Complex plane representation of resistivity data (markers) at 370 K for: (a) amorphous  $\text{LiNbO}_3$ , (b) nanocrystalline  $\text{LiNbO}_3$  HEBM for 64 h, (c) 48 h, (d) 16 h. The solid lines indicate the theoretical fits obtained using the Equivalent Circuit program, with the equivalent circuit,  $(R_s Q_s) Q_e$ , shown in the inset.

Fig. 7.2.4. The semicircle in each case represents the sample's response, in addition to a well-behaved low-frequency inclined spike which is attributed to polarization of electrodes. These plots were analyzed using software called the Equivalent Circuit<sup>©255</sup>. The equivalent circuit, shown in Fig. 7.2.4 (inset), represents the electric and dielectric properties of the  $\text{LiNbO}_3$  samples. A resistor,  $R_s$ , and a constant phase element,  $Q_s$ , connected in parallel are used to represent the response of the sample (denoted by the subscript "s"). This sub-circuit is connected in series with another constant phase element,  $Q_e$ , which represents the electrode response. The parameters  $Q_s$  and  $Q_e$  are non-ideal capacitances which allow for a distribution of relaxation times. They are physically determined by the parameters  $Q^\circ$  and  $\alpha$  ( $\alpha \leq 1$ ), where  $Q^\circ$  is the admittance of the constant phase element at angular frequency  $\omega = 1$  rad/s and  $n$  is the power of the constant phase element. For more details see Sec. 4.1.2. To calculate the values for the equivalent ideal capacitor,  $C$ , the values of  $R$ ,  $Q^\circ$ ,  $\alpha$ , obtained from the complex plane fit can be inserted into the relation

$$C = R \left( \frac{1-\alpha}{\alpha} \right) Q^\circ \left( \frac{1}{\alpha} \right). \quad (7.2.4)$$

The relaxation frequency of the sample,  $f_r$ , for different temperatures is obtained by substituting the values of  $R$  and  $C$  into the equation  $f_r = 1 / (2\pi RC)$ . The relaxation frequencies are thermally activated according to the equation  $f_r = \exp(-E_{a,r} / k_B T)$ , and the resultant activation energies,  $E_{a,r}$ , are comparable to those for  $\sigma_{dc}$  (cf. Table 7.2.1). The advantage of using the relaxation frequency is its complete independence of the sample dimensions.

The HEBM nanocrystalline  $\text{LiNbO}_3$  shows only one depressed semicircle for both the grain interior and boundary. This might be explained by (i) the fact that the grain-boundary semicircle is absent (highly conductive grain boundary), (ii) the time constants for both processes are identical, or alternatively, (iii)

the grain interior contribution is too small to be detectable<sup>318</sup>. In the actual case, the second explanation is more probable suggesting that the depressed semicircle is composed of two inseparable semicircles with very similar relaxation frequencies. The impedance semicircles overlap significantly if their relaxation times differ by less than three orders of magnitude<sup>319</sup>.

### 7.2.1.3 Modulus spectra

An alternative approach to inspect ionically-conducting materials is to use the complex electric modulus, given in Eq. 4.1.4 or by

$$M^*(\omega) = M' + iM'' = i\omega C_0 Z^*(\omega). \quad (7.2.5)$$

This formalism was proposed by Macedo *et al.* and it is suitable to minimize the electrode interface capacitance contribution and to detect the conductivity-relaxation times ( $\tau_\sigma$ ) and many other phenomena.<sup>320–321</sup> The peak shape of the modulus curves appears to call for a non-exponential approach to the electrical functions, which can describe the dielectric relaxation through the Kohlrausch-William-Watts (KWW) function which has the form<sup>322</sup>

$$\varphi(t) = \exp\left[-\left(\frac{t}{\tau}\right)^\beta\right], \quad 0 < \beta < 1 \quad (7.2.6)$$

where  $\tau$  is the conductivity-relaxation time and  $\beta$  is the stretching factor which represents the deviation from single exponential behavior ( $\beta = 1$ ), and gives a measure of the distribution of relaxation times. It has been proposed that the parameter  $\beta$  reflects the effects of many-body interactions between the jumping ion and other species present in the structure. The complex electric modulus  $M^*$  is given as an expression related to the Fourier transform of the time derivative of the decay function  $\varphi(t)$

$$M^* = M_s \left[ 1 - \int \exp(-i\omega t) \left( \frac{d\varphi(t)}{dt} \right) dt \right] \quad (7.2.7)$$

The curves of the real part of the electric modulus  $M'$ , vs. log frequency, increase from zero at low frequency towards  $M_s$ , the high-frequency limit. The dispersion shifts toward high frequency with increasing temperature, Fig. 7.2.5(a). Meanwhile, the imaginary parts  $M''$ , having uniform peak shape, are broader than single relaxation time curves on both sides of the maximum in  $M''(\omega)$  but asymmetric and skewed towards the high-frequency

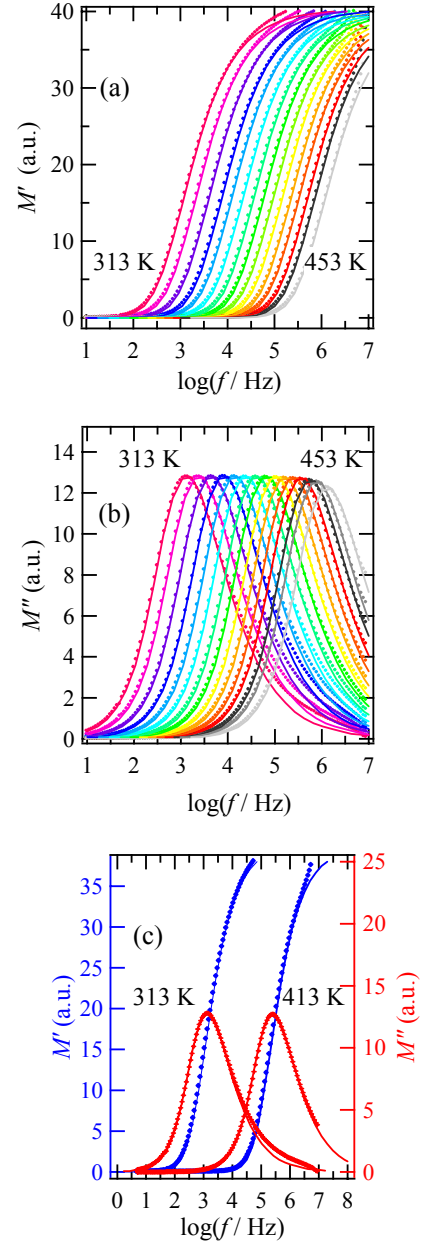


Fig.7.2.5: (a) Real and (b) imaginary parts of the electric modulus for nanocrystalline LiNbO<sub>3</sub> HEBM for 64 h at temperatures from 313 to 453 K, (c) shows the positioning of the  $M''$  peak at around the center of the dispersion region of  $M'$  (markers are the measured points while the solid lines are the fits with the KWW stretched function).

side of the maximum, Fig. 7.2.5(b). The low-frequency side of the peak represents the range of frequencies in which the ion can do 'successful', long distance hops. The high-frequency side of the peak represents the range of frequencies in which the ion is spatially confined and can do only localized motions, i.e. 'correlated hops' in their potential wells. This peak is positioned at around the centre of the dispersion region of  $M'$ , Fig. 7.2.5(c). The peak frequency,  $f_p$ , is shifted to a higher value with increasing temperature. Peak-relaxation times,  $\tau_p$ , were obtained by fitting both the real and the imaginary parts of the modulus,  $M'$  and  $M''$  vs. frequency using Moynihan's tables<sup>323</sup> [for more details see appendix A.3]. The obtained  $\tau_p$  values follow an Arrhenius behavior which can be described by the following relation

$$\tau_p = \tau_0 \exp(W/k_B T) \quad (7.2.8)$$

where  $W$  is the activation energy and  $\tau_0$  is the pre-exponential factor. Fig. 7.2.6 shows the Arrhenius plots for the relaxation times of the electric modulus for the HEBM nanocrystalline (16 h, 48 h, and 64 h) and the amorphous  $\text{LiNbO}_3$ . The stretching exponents used for the fitting procedures for both the real and the imaginary parts of the electric modulus ranged between 0.55 and 0.60 going from low to high temperatures for all samples. The fitting parameters are listed in Table 7.2.2. Hwang *et al.* found that the imaginary part of the dielectric constant  $\varepsilon''(\omega)$  has a relaxation stretching exponent  $\beta_{dc} \approx 0.6$  for amorphous  $\text{LiNbO}_3$  and  $\text{KNbO}_3$  prepared by twin-roller quenching<sup>324</sup>. In general, the relaxation time,  $\tau_p$ , decreases with increasing temperature for all samples. For any given temperature, the lowest relaxation time is obtained for both the amorphous and the nanocrystalline sample HEBM for 64 h, then it increases gradually via the sample milled for 48 h and continuing to that milled for 16 h. After that, a sudden and larger increase happens in the case of the microcrystalline sample. This behavior is consistent with the results obtained for  $\sigma_{dc}$  (Fig. 7.2.3), for  $f_i$  of the complex plane plot, and for their activation energies, Table 7.2.1.

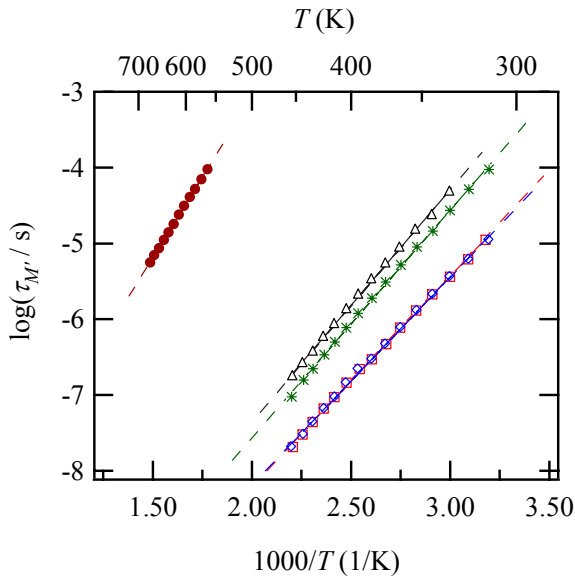


Table 7.2.2: The fitting parameters (activation energies,  $W$ , and the logarithm of the pre-exponential factors,  $\log(\tau_0)$ ) obtained from the Arrhenius plots for  $M'$ , Fig. 7.2.6 and for  $M''$  (not shown here).

LiNbO <sub>3</sub>	$M'$		$M''$	
	$\log(\tau_0)$	$W$ [eV]	$\log(\tau_0)$	$W$ [eV]
Micro	-11.57	0.85	-11.96	0.90
16 h Nano	-13.46	0.61	-13.42	0.61
48 h Nano	-13.58	0.60	-13.58	0.60
64 h Nano	-13.68	0.55	-13.68	0.55
Amorphous	-13.74	0.55	-13.71	0.55

Fig. 7.2.6: Temperature dependence of relaxation time of the electric modulus,  $\tau_p$ , for microcrystalline ( $\bullet$ ), nanocrystalline [16 h ( $\Delta$ ), 48 h ( $*$ ), 64 h ( $\diamond$ )] and amorphous ( $\square$ )  $\text{LiNbO}_3$ .



In general, there are remarkable similarities between the amorphous and the ball milled nanocrystalline  $\text{LiNbO}_3$  in several aspects, mainly in the case of the samples milled for long periods (48 h and 64 h]: (i) the comparable values of  $E_{a,\sigma}$  and  $E_{a,r}$ , Table 7.2.1, and  $W$ , in Table 7.2.2, (ii) the coincidence of their master curves, Fig. 7.2.2. This leads us to say that the disorder in the amorphous material and the interfacial regions of the nanocrystalline one can be visualized to have the same structure. The minor differences between them, mainly in the values of conductivity or relaxation time, can be due to the difference in their chemical origin, and in the volume fraction of the disordered region which increases in the nanocrystalline materials with increasing milling time, whereas the amorphous form can be regarded as homogeneously disordered.

#### 7.2.1.4 Dielectric permittivity

The dielectric constant,  $\varepsilon^*$ , can be calculated from the impedance using

$$\varepsilon^* = \varepsilon' - i\varepsilon'' = \frac{1}{i\omega C_0} \frac{1}{Z^*} = \frac{Z''}{\omega C_0 (Z''^2 + Z'^2)} - i \frac{Z'}{\omega C_0 (Z''^2 + Z'^2)} \quad (7.2.9)$$

By examining Fig. 7.2.7, one can see that the real part of the dielectric constant,  $\varepsilon'$ , drops down to nearly zero at relatively low frequencies, indicating a relatively low electrode polarization. A weak dispersion behavior can be seen only for the amorphous sample, which becomes more pronounced with increasing temperature. Rescaling the  $\varepsilon'$ -axis, the inset of Fig. 7.2.7, a step-like dispersion appears which is shifted towards higher frequency with increasing temperature. This relaxation peak is only noticeable for the amorphous sample and believed to be due to the motion of conducting Li ions. These curves can be normalized over the frequency of the peak maxima to show that the shapes of the high-frequency side are the same, but those of the low-frequency side are strongly dependent on temperature. Ion hopping results in

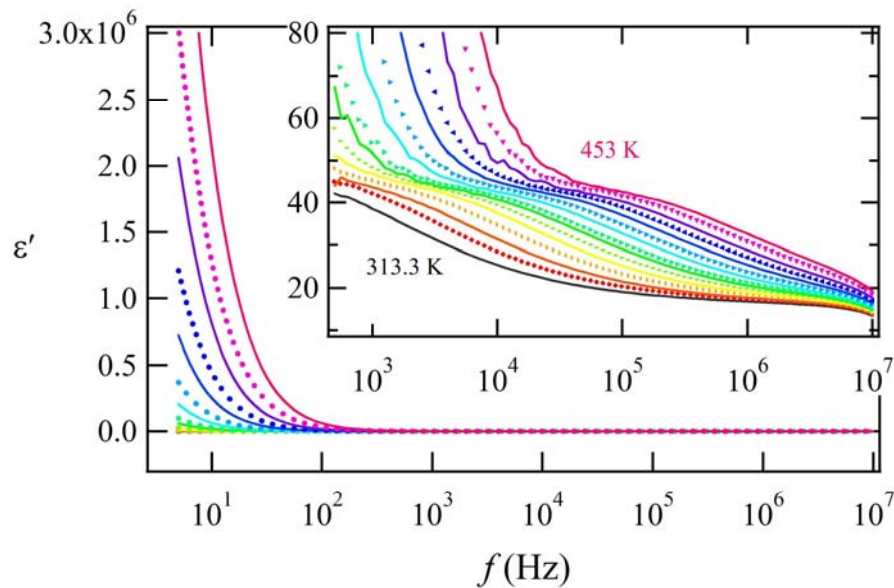


Fig. 7.2.7: The frequency dependence of  $\varepsilon'$  for amorphous  $\text{LiNbO}_3$  for different temperatures between 313 K and 453 K from 5 to  $10^7$  Hz, the inset shows the re-scaled area from  $10^2$  to  $10^7$  Hz.

an electric current (dielectric loss) and due to the presence of a random distribution of potential well depths in amorphous materials, the compensation of those with the high energy is possible only at high temperatures not at lower ones. The hopping ions create space charge at the surface of the electrodes as they cannot penetrate through the electrode resulting in additional capacitance<sup>325</sup>. Similar dispersion behavior was previously found in amorphous  $\text{LiNbO}_3$  prepared by twin roller quenching and the behavior was fitted by ion-hopping conduction and Davidson-Cole relaxation mechanisms.<sup>325–326</sup>

Fig.7.2.8 shows the dielectric constant plots obtained by two distinct methods:

(a) taking the values of  $\epsilon'$  at any arbitrary chosen frequency from Fig. 7.2.7 and re-plotting them versus the temperatures at which the measurements were done.

(b) calculating  $\epsilon'$  at the relaxation frequencies of the complex impedance semicircle for each temperature (illustrated in Sec. 7.2.1), by substituting the value of  $C$ , extracted using Eq. 7.2.4, in the following equation

$$C = \epsilon' \epsilon_0 \frac{A}{l} \quad (7.2.10)$$

It should be noted that the values of the dielectric constant calculated at the relaxation frequencies (method (b)) have the following features: (i) when compared with the real part of the dielectric constant obtained at arbitrary frequencies they match the curve that has a frequency similar to  $f_r$  at the temperature of the measurement. Each temperature has its characteristic relaxation frequency, indicated at the bottom of Fig. 7.2.8. (ii) they show only minor variation in the measured temperature range<sup>327</sup>. This emphasizes

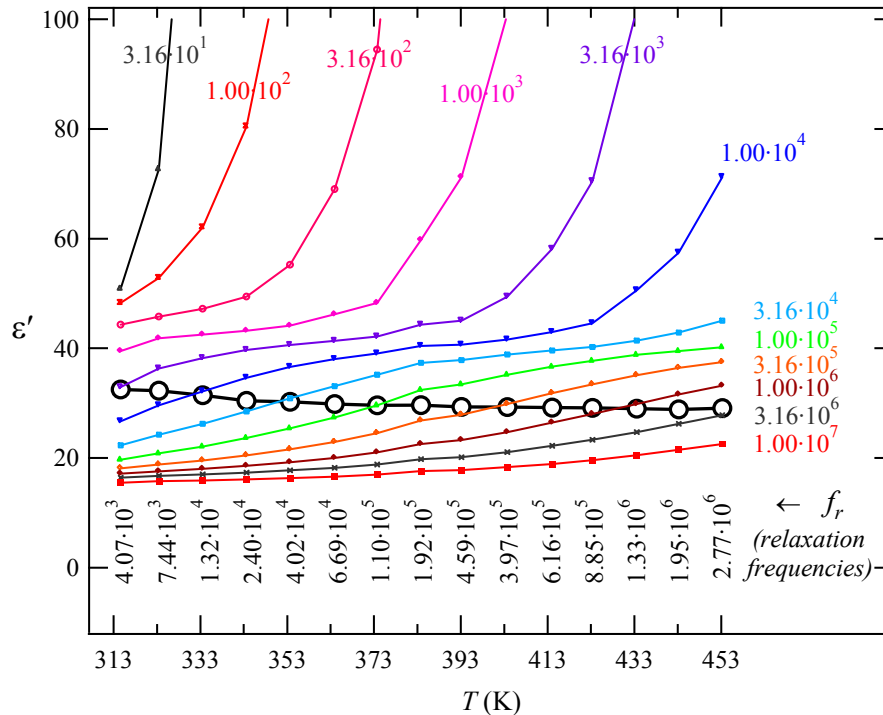


Fig. 7.2.8: Temperature dependence of the real part of the dielectric constant measured at different arbitrary frequencies (with the frequency of each curve indicated by the same color) and the dielectric constant calculated at the relaxation frequency (the black open circles with the relaxation frequency of each point written in black adjacent to the temperature at which it was measured at the bottom of the figure).

that the  $\varepsilon'$  values calculated at the relaxation frequency of the sample are more reliable and represent the real behavior of the sample, unlike those obtained at frequencies far from the relaxation frequencies which may deviate by many orders of magnitude. Following this procedure, it was possible to construct similar curves for all  $\text{LiNbO}_3$  forms. In Fig. 7.2.9 one can see that the values of the dielectric constant increases with decreasing grain size. In the interfacial regions of the nanocrystalline ceramics, space charge polarization may occur due to the difference in conductivities of the grains and the grain boundaries<sup>59</sup>. This additional polarization results in a high apparent dielectric constants. Space charge polarization effects become important at high temperatures when the difference in conductivities between the two phases becomes significant. The intermediate value of the amorphous sample may be due to the fact that the material is homogeneously disordered or it may depend on the organic residuals in the sample resulting from the chemical preparation route.

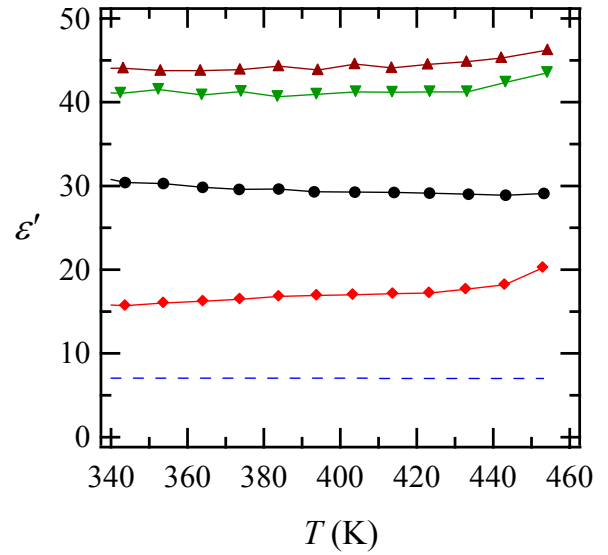


Fig. 7.2.9: Dielectric constants, calculated at the relaxation frequencies for microcrystalline (---), nanocrystalline [16 h (♦), 48 h (▼), 64 h (▲)] and amorphous (●)  $\text{LiNbO}_3$ .

### 7.2.1.5 Effect of paramagnetic-impurities

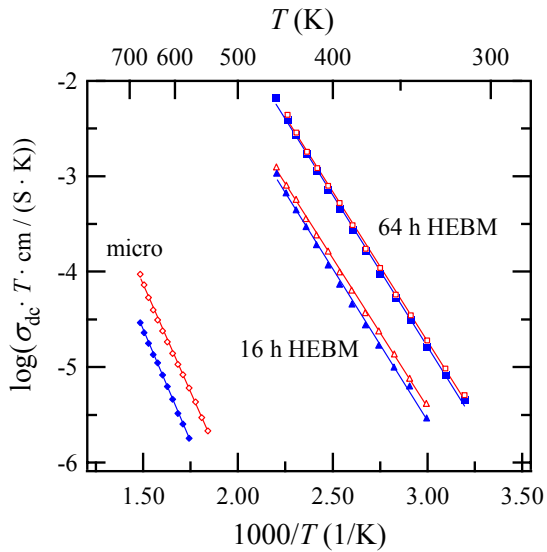


Fig. 7.2.10: Temperature dependence of  $\sigma_{dc}$  for microcrystalline (◇), nanocrystalline [16 h (Δ), 64 h (□)]  $\text{LiNbO}_3$ . A comparison between the pure samples (the closed blue symbols) with the impure sample (the open red symbols)

Table 7.2.3: Comparison between the activation energy of the dc conductivity,  $E_{a,\sigma}$ , of the pure  $\text{LiNbO}_3$  samples (Alfa) with the impure sample (Aldrich).

$\text{LiNbO}_3$	$E_{a,\sigma}$ [eV]	
	Aldrich	Alfa
microcrystalline	0.93	0.89
nanocrystalline 16 h	0.63	0.62
HEBM 64 h	0.63	0.62

Two sets of samples were investigated to study the effect of impurities. The first sample was obtained from Alfa Aesar (pure) and the second one from Aldrich (with high level of impurities), see Table 5.1.1 for trace analysis of the most encountered impurities. Fig. 7.2.10 shows their  $\sigma_{dc}$  Arrhenius plots. The corresponding activation energies are listed in Table 7.2.3. The effect of the impurities is recognizable mostly on the microcrystalline sample. The conductivity of the impure microcrystalline sample is higher by about half an order of magnitude compared with that of the pure counterpart. However, this difference decreases for the samples milled for 16 h and vanishes after 64 h of milling. This can be attributed to the significant amounts of impurities introduced by the milling process that mask the effect of impurities originally present in the parent material. The changes in activation energies are so tiny that they can be neglected.

### 7.2.1.6 Atmosphere effect

The important effect of the atmosphere on the conductivity measurement emerges from the fact that one kind or more of the charge carriers can be created or blocked as a result of the interaction between the atmospheric gas and the system under investigation. Fig. 7.2.11 shows the change in conductivity as a result of changing the atmosphere from oxygen (open symbols) to helium (closed symbols) for different forms of  $\text{LiNbO}_3$  with their activation energies listed in Table 7.2.4. The oxygen atmosphere results in a decrease in the conductivity of the HEBM nanocrystalline samples with the extent of decrease being higher in the case of shorter milling times. This can be attributed to the reduction of  $\text{LiNbO}_3$  which introduces additional oxygen vacancies among other kinds of vacancies and defects during the milling process. The importance of the oxygen vacancies decreases with increasing milling time due to the creation of additional numbers of other kinds of vacancies with longer milling periods. In other words, these oxygen vacancies will have less important effect on the overall conductivity. The formation of oxygen vacancies during milling is probable because the milling vial was loaded under argon and enclosed in a gas tight container. Moreover, the friction that accompanies the milling process causes a rise in the temperature. The attained

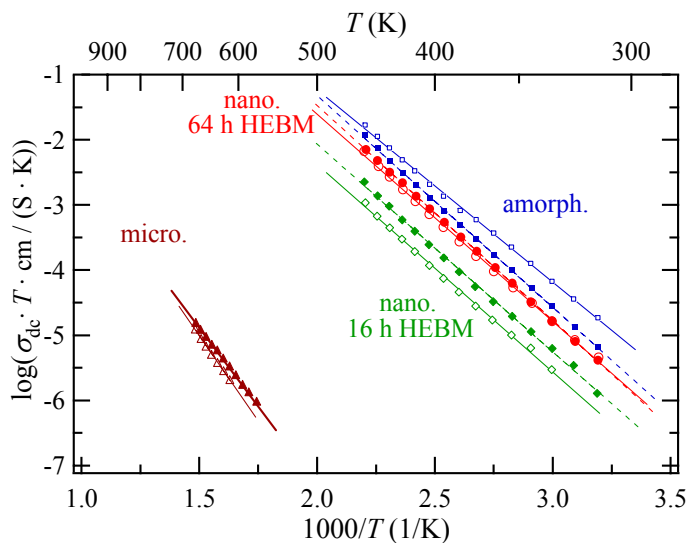


Fig. 7.2.11: Temperature dependence of  $\sigma_{dc}$  for, microcrystalline ( $\Delta$ ), nanocrystalline [16 h ( $\diamond$ ), 64 h ( $\circ$ )], and amorphous ( $\square$ )  $\text{LiNbO}_3$ ; a comparison between the conductivities measured under oxygen atmosphere (the opened symbols) with those measured under helium (the closed symbols)

temperature is not that high, nevertheless it can be sufficient to cause a reduction for the disordered and highly reactive grain-boundary regions. Anyway, the reduced conductivity of nanocrystalline samples measured under oxygen atmosphere is still five orders of magnitude higher than the conductivity of the bulk microcrystalline  $\text{LiNbO}_3$ , confirming that the oxygen vacancies are not the main charge carriers. Contrarily, in the case of amorphous  $\text{LiNbO}_3$  in He atmosphere the conductivity decreases in comparison

with the results obtained in  $\text{O}_2$  atmosphere. In the last preparation stage of the amorphous  $\text{LiNbO}_3$  it was calcined under oxygen for two hours; this leads one to say that measuring under He may lead to reduction of the rest of the alkyl residue. The complex resultant products obstruct the diffusing Li ions and thus decrease the conductivity and increase its activation energy, as can be seen from Table 7.2.4. The maximum measurement temperature, 673 K, is not high enough to cause any oxidation or reduction for the bulk microcrystalline form; and this explains its lack of dependence on the atmospheric condition.

Table 7.2.4: Comparison between the activation energy of the dc conductivity,  $E_{a,\sigma}$ , for different forms of  $\text{LiNbO}_3$  under oxygen and under helium.

$\text{LiNbO}_3$	$E_{a,\sigma}$ [eV]	
	$\text{O}_2$	He
microcrystalline	0.93	0.92
nanocrystalline	16 h	0.63
	64 h	0.64
amorphous	0.59	0.65

### 7.2.1.7 Effect of the preparation route

Unlike the fully hydrolyzed amorphous  $\text{LiNbO}_3$ , the complex impedance plane plots for the partially hy-

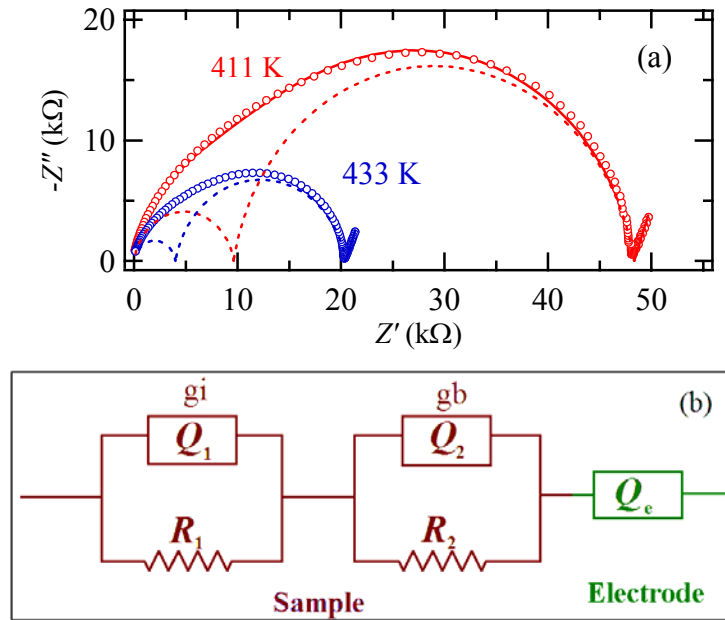


Fig. 7.2.12: (a) The complex plane plot of impedance data (circles) for partially (1/3) hydrolyzed  $\text{LiNbO}_3$  at 413 and 433 K. The solid lines indicate the theoretical fits obtained using the Equivalent Circuit program, (b) The equivalent circuit,  $(R_1Q_1)(R_2Q_2)Q_e$ . The dashed lines in (a) represent the individual contribution of the sub-circuits  $(R_1Q_1)$  and  $(R_2Q_2)$  independently.

drolyzed amorphous sample revealed an electrical behavior that is composed of two overlapping semicircles corresponding to two different diffusion processes besides the electrode-polarization spike, Fig. 7.2.12(a). A resistor,  $R_1$ , and a constant phase element,  $Q_1$ , connected in parallel ( $R_1Q_1$ ), are used to model the response of the grains (the high-frequency semicircle). This sub-circuit is connected in series with another similar sub-circuit ( $R_2Q_2$ ) to represent the grain-boundary regions (the low-frequency semicircle), in addition to a constant phase element,  $Q_e$ , which represents the electrode response. Thus, the total electric response of the partially hydrolyzed amorphous  $\text{LiNbO}_3$  sample is modeled with the equivalent circuit  $(R_1Q_1)(R_2Q_2)Q_e$ , Fig. 7.2.12(b). The value of  $\sigma_{dc}$  obtained from  $R_1$  was four times that calculated from  $R_2$  at the same temperature ( $\sigma_{dc} = R \cdot l/A$ ).

Fig. 7.2.13 shows a comparison between the Arrhenius plots of the fully and the partially hydrolyzed amorphous samples. The latter showed two contributions with similar activation energies (0.64 and 0.67 eV). The completely hydrolyzed sample has a lower activation energy (0.59 eV) and a slightly higher conductivity. The larger the amount of water used in the hydrolysis helps in getting rid of a larger amount of residual organic groups. Thus reduces the energy barrier for the diffusing ions. The high-frequency contribution is comparable to that of the fully hydrolyzed sample which indicates a very similar composition and Li content.

The presence of the two contributions in the partially hydrolyzed samples may be attributed to any of the following reasons: (i) the partially hydrolyzed sample maintain a high amount of alkyl residuals, according to Eq. (7.1.4). Thus the resultant octahedra may have different numbers of alkoxide groups surrounding them; (ii) during the second calcination step (5 min at 620 K), which was done only for the partially hydrolyzed sample, there is a possibility to form very small crystals (2 – 3 nm). These crystallites will enclose some of the Li-ions, restricting their motion, to give rise to the high-frequency conductivity.

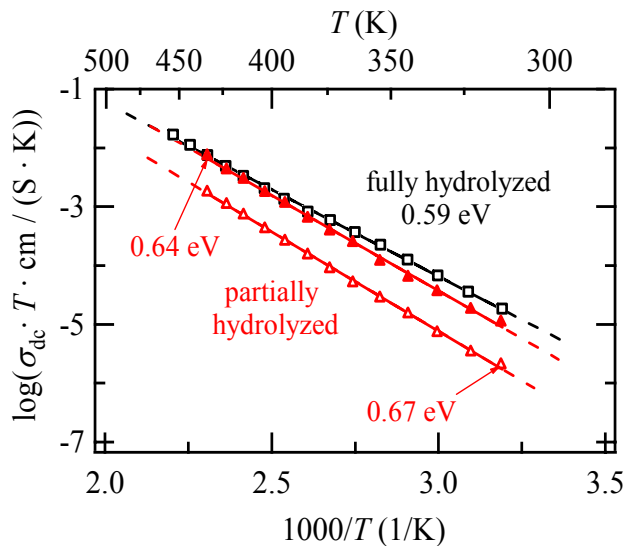


Table 7.2.5: Comparison between the activation energy of the dc conductivity,  $E_{a,\sigma}$ , and the activation energy of the semicircle relaxation frequency,  $E_{a,r}$

$\text{LiNbO}_3$	$E_{a,r}$ [eV]	$E_{a,\sigma}$ [eV]
Completely hydrolyzed amorphous	0.60	0.59
Partially (1/3) hydrolyzed amorphous	0.63	0.64
Nano (1 h at 773 K)	0.76	0.79
Nano (6 h at 973 K)	0.85	0.84

Fig. 7.2.13: Comparison between the temperature dependence of  $\sigma_{dc}$  for the sol-gel prepared amorphous  $\text{LiNbO}_3$ : fully hydrolyzed ( $\square$ ) and partially hydrolyzed the low-frequency contribution ( $\blacktriangle$ ) and the high-frequency one ( $\blacktriangle$ ).

ity-semicircle; (iii) while preparing lithium niobium double alkoxide, the refluxing time which was limited to 1 h for the partially-hydrolyzed sample may not be enough to prepare a homogeneous double alkoxide. As a result, this sample may contain zones in which the Li-ion concentration is high and other zones with low Li-ion concentration and consequently the conductivity will be increased or reduced, respectively. The ambiguity between the previous three possibilities arises from the lack of an effective structural characterization tools for the amorphous phases. The two samples were characterized by XRD which can only confirm their amorphous nature but it cannot distinguish between two amorphous structures having similar compositions as in case (i). By using XRD it is also not possible to detect the crystallites when their size is only a few nanometers as in case (ii). XRD can tell the exact structure only after complete crystallization of the sample. However, the obtained structural information will not reflect the differences between the disordered states. This is because many diffusion processes take place during calcination which homogenize the structure. This makes XRD rather useless in case (iii), as well. The first assumption is the least reasonable as the fully-hydrolyzed sample also contains a certain amount of alkyl residues. The second assumption is probable but unlikely to be the reason behind the two contributions as it was not possible to detect two separate contributions in the HEBM samples with bigger crystallite sizes. The third assumption is the most plausible one as it is supported by the structural study of Hirano *et al.*<sup>233</sup> They found by NMR and XRD that the minimum refluxing time to obtain a homogenous  $\text{LiNbO}_3$  is 22 h; otherwise the product will be a mixture of  $\text{LiNbO}_3$  and other Li-rich and Li-poor phases, i.e.,  $\text{Li}_3\text{NbO}_4$  and  $\text{LiNb}_3\text{O}_8$ , respectively.

The chemically and the mechanically prepared nanocrystalline  $\text{LiNbO}_3$  samples appear to be similar in their conductivity behavior as far as the general trend of decreasing electrical conductivities with increasing grain size is concerned, (Fig. 7.2.14(a)). The increase in the grain size is here is due to the increase in

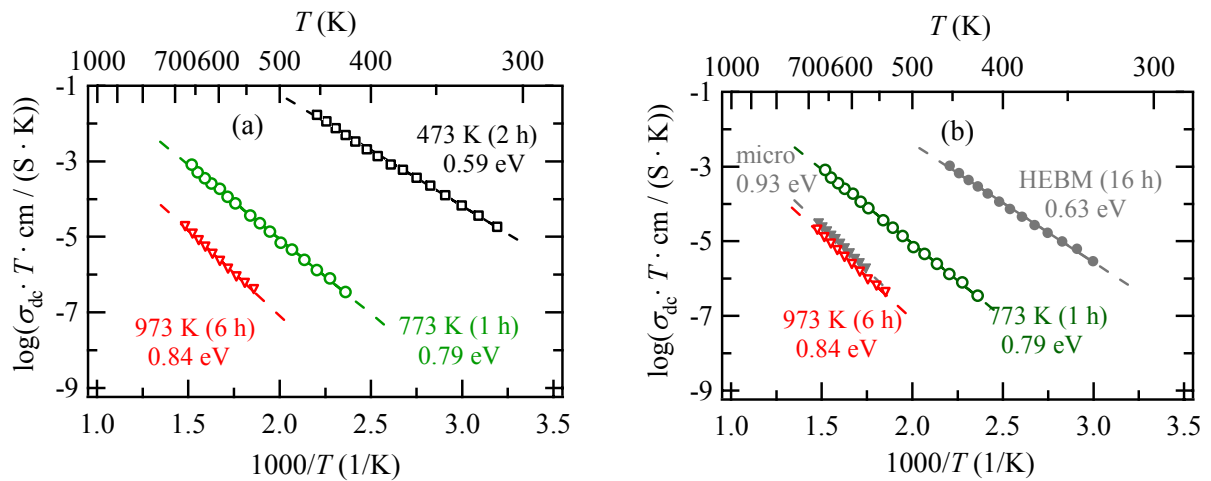


Fig. 7.2.14: Temperature dependence of  $\sigma_{dc}$  for: (a) the chemically prepared (sol-gel)  $\text{LiNbO}_3$  heat treated at different temperatures and times: ( $\square$ ) 473 K 2 h (amorphous), ( $\circ$ ) 773 K 1 h (27 nm), and ( $\nabla$ ) 973 K 6 h (72 nm). (b) Comparison with the ( $\nabla$ ) commercial microcrystalline (Alfa) and ( $\bullet$ ) nanocrystalline HEBM for 16 h.

the treatment temperature going from the amorphous (2 h at 473) to the nanocrystalline with grain size of 27 nm sample (1 h at 773 K) to that of 72 nm grains (6 h at 973 K). The activation energy first increases from 0.59 eV for the amorphous sample to 0.79 eV for the “27 nm-sample” and then to 0.84 eV for the “72 nm-sample”. This can be attributed to the formation and the growth of the crystalline grains which enclose large numbers of the Li ions in an environment where they have more restricted diffusion paths with higher energy barriers leading to increasing activation energies.

Fig. 7.2.14(b) reveals that, in general, the chemically prepared nanocrystalline  $\text{LiNbO}_3$  samples have a much lower conductivity than those prepared by ball milling. Let us recall that the nanocrystalline sample prepared by heating the amorphous precursor 1 h at 773 K is comparable in grain size to that HEBM for 16 h (27 and 23 nm, respectively); nevertheless, its conductivity is lower by about three orders of magnitude, i.e. shifted towards the microcrystalline sample. Moreover, the sample heated for 6 h at 973 K has a conductivity which is even lower than that of the commercial microcrystalline form. These findings imply that the nature of the chemically prepared nanocrystalline  $\text{LiNbO}_3$  is indisputably different from the mechanically prepared one. The latter is believed to consist of crystalline grains embedded in highly defective grain-boundary regions (or massive amorphous matrix) which is not likely the case with the chemically prepared one. The results obtained here imply that the chemically prepared nanocrystalline  $\text{LiNbO}_3$  consists of crystalline grains with thin grain-boundary regions, as can be concluded from its low conductivity which is comparable to that of the microcrystalline form. Table 7.2.5 summarizes the values of the activation energies for the amorphous and nanocrystalline samples prepared chemically. In general we can conclude that disordered materials prepared by different methods may differ in their properties due to differences in their microstructures.

### 7.2.1.8 Discussion

In the previous sections the effect of grain size and order/disorder on the Li-ion diffusivity and ionic conductivity were investigated. Impedance spectroscopy has shown that the electrical conductivity increases in the following sequence: single crystal < microcrystalline < nanocrystalline chemically prepared (sol-gel) << nanocrystalline mechanically prepared (HEBM) < amorphous. This sequence of increasing conductivity is attributed to the increased disorder in the grain-boundary regions and the free volume in the nanocrystalline and amorphous materials, respectively. In such areas the mobile ions have a reduced coordination number and at a certain temperature they are relatively less restricted to move than in the corresponding ordered phase.

The electrical conductivity was intensively investigated for pure and doped single crystalline  $\text{LiNbO}_3$ . According to the dominant conduction mechanism, the conductivity has been categorized into three main regions<sup>68–69</sup>: (i) at temperatures below 400 K the conductivity is assumed to result from random hopping of electrons<sup>328</sup>. The activation energies for  $\sigma_{\text{dc}}$  in this region are usually measured by indirect methods. (ii)



In the range 400 to 1000 K there is a kind of agreement that the conduction is extrinsic and due to mobile protons diffusing in the form of  $\text{OH}^-$ . The activation energies range from 1 to 1.5 eV<sup>329-332</sup>. The conductivity-activation energy value obtained here for the single crystal (1.2 eV) agrees with the literature values within this range. (iii) The intrinsic conduction starts at temperatures higher than 1000 K, where the conductivity depends on the oxygen partial pressure,  $\sigma \propto p_{\text{O}_2}^{1/4}$ , with electrons being the main charge carriers for  $p_{\text{O}_2} < 1$  atm, whereas for  $p_{\text{O}_2} > 1$  atm the ionic conductivity dominates the electrical response. This was explained by singly-ionized oxygen vacancies. At constant  $p_{\text{O}_2}$  the activation energy of the conductivity was found to vary between 2 and 2.5 eV.<sup>82,331,333</sup>

The presence of paramagnetic impurities in  $\text{LiNbO}_3$  causes only a small increase in the conductivities. However, it seems to have no effect on the activation energy. This may be due to the small concentrations of such impurities that cannot change the overall conductivity or its mechanism.

In the measurement conducted here the atmosphere has only a small effect on the conductivity of the microcrystalline form. The measurements were conducted at relatively low temperatures that no oxidation or reduction of the bulk material can take place. The most pronounced effect was in the case of the ball-milled (16 h) nanocrystalline  $\text{LiNbO}_3$  sample which showed a decreased conductivity when measured under oxygen. This sample was milled under an oxygen-deficient environment which was able to cause a reduction for the grain-boundary regions, at least. Thus, if the measurement is conducted under He, the oxygen vacancies will be kept and will take part in the conduction. On the other hand, if the measurement is done under oxygen atmosphere, this will block most of the oxygen vacancies and inhibit the conduction, consequently.

The microcrystalline form shows a behavior similar to that of the single crystal, that means low conductivities and high activation energies (0.93 eV). Lanfredi *et al.*<sup>327</sup> prepared microcrystalline  $\text{LiNbO}_3$  by a chemical evaporation method followed by calcination at 820 K. Their sample showed an activation energy of about 1.15 eV in the temperature range from 720 to 1070 K.

Amorphous  $\text{LiNbO}_3$  was previously prepared by several methods. Early attempts were done by twin-roller quenching and gave activation energies of 0.4 eV<sup>334</sup> and 0.502 eV<sup>335</sup>, independently. Ono *et al.* prepared amorphous  $\text{LiNbO}_3$  by a sol-gel method using the same chemical route applied here. They found a conductivity activation energy of 0.47 eV<sup>231</sup>. The Li-ion diffusion in amorphous material is clearly enhanced (up to seven orders of magnitude) when compared with bulk  $\text{LiNbO}_3$ .

The dielectric anomaly of the roller quenched glassy  $\text{LiNbO}_3$  film was considered as a ferroelectric-like anomaly<sup>336</sup>. Lines<sup>337</sup> has attempted to explain it by assuming the existence of small dielectrically soft, ordered regions in which the dielectric behavior is considered to be similar to that in macroscopically crystalline parent materials. A radio-frequency sputtered thin film of  $\text{LiNbO}_3$  showed a similar dielectric

anomaly. This behavior was explained by the presence of crystalline clusters in the amorphous film as confirmed by HRTEM. The tissue material is the cause of the anomaly rather than the clusters.

The conductivity of nanocrystalline  $\text{LiNbO}_3$  is relatively large so that it is comparable with that of the amorphous form. The high degree of similarity emerges mainly in the case of the ball milled nanocrystalline samples especially after long milling periods. The samples HEBM for 48 h and more showed high degrees of similarities with the amorphous sample in most aspects of the electrical behavior, e.g., the value of the conductivity and its activation energy, the activation energy of the semicircle relaxation frequency, the activation energy of the relaxation time of the electrical modulus, in addition to the coincidence of the conductivity master curves. It seems reasonable to assume that the enhancement is due to diffusion in the amorphous grain-boundary regions of these nanocrystalline samples. Nanocrystalline-ionic conductor thin films have shown enhanced conductivity which was assigned to space-charge effects recently<sup>338</sup>. A similar explanation may be valid for the present situation.

On the other hand, the nanocrystalline  $\text{LiNbO}_3$  samples prepared by sol-gel showed also some enhancements of  $\text{Li}^+$  diffusion “i.e. Li conductivity”, but they are still far away from the amorphous form and tend towards the microcrystalline form. In other words, the behavior of the nanocrystalline materials proved to be highly dependent on the preparation route. As the sol-gel prepared nanocrystalline materials seem to be composed of grains with thin (or even ordered) grain-boundary regions, there is no way to enhance their ionic diffusivity in the same way as in the ball milled samples. Similar results have recently been reported by other workers.<sup>20</sup>

The presence of impurities in the measured sample causes a little increase of the conductivity of the pure forms, however, this effect vanishes with increasing milling time due to the large amount of impurities introduced while milling. Furthermore these impurities showed no effect on the activation energy of conductivity.

## 7.2.2 Nuclear Magnetic Resonance

### 7.2.2.1 Grain-size effect on the SLR rate

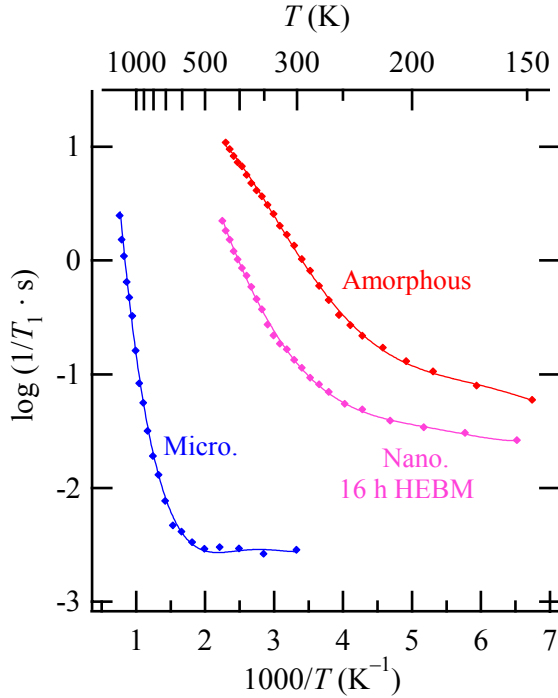


Table 7.2.6.: Values of the activation energies of the low-temperature flank of  ${}^7\text{Li}$  SLR rates ( $1/T_1$ ) obtained from the plots of Fig. 7.2.15 (with and without background correction).

LiNbO <sub>3</sub>	$E_{T_1}^{\text{IT}}$ [eV]	
	w/o corr.	w. corr.
Amorphous	0.17(6)	0.22(3)
Nanocrystalline 16 h HEBM	0.25(5)	0.27(3)
Microcrystalline	0.79(8)	0.80(9)

Fig.7.2.15: Temperature dependence of the  ${}^7\text{Li}$  spin-lattice relaxation rates ( $1/T_1$ ) for amorphous, nanocrystalline and microcrystalline LiNbO<sub>3</sub> measured at  $\omega_0/2\pi = 77.7$  MHz. The activation energies are calculated from the low-temperature flank for the uncorrected data and for the pure diffusion induced relaxation rate after the subtraction of the non-diffusive background relaxation. <sup>[†††]</sup>

Fig. 7.2.15 displays the spin-lattice relaxation (SLR) rates ( $T_1^{-1}$ ) (as a function of  $T^{-1}$ ) measured at a resonance frequency  $\nu_L = \omega_L/2\pi = 77.7$  MHz for the microcrystalline, the 16 h HEBM nanocrystalline (23 nm), and the fully-hydrolyzed sol-gel prepared amorphous LiNbO<sub>3</sub>. In all cases, the plot of  $T_1^{-1}$  vs. the reciprocal of the absolute temperature consists of a superposition of a diffusion-induced SLR rate peak that sharply rises with increasing temperature to give the expected maximum (not apparent here within the measured range), and a non-diffusional "background" SLR rate which shows up at low temperatures and has no or only a weak diffusive temperature dependence and is mostly attributed to the presence of paramagnetic impurities. The SLR rate background has only little influence on the data at the highest temperatures, whose slope yields the low-temperature flank activation energy,  $E_{T_1}^{\text{IT}}$ , as can be seen by comparing the values with and without background correction, shown in Table 7.2.6. <sup>[†††]</sup>

<sup>[†††]</sup> The curve of the microcrystalline sample is taken from Ref. [235]

The diffusion-induced relaxation peaks for nanocrystalline and amorphous  $\text{LiNbO}_3$  are shifted to lower temperatures.  $T_{\text{diff}}^{-1}$  is proportional to the motional correlation rate  $\tau_c^{-1}$  that is directly related to the mean jump rate. Thus, for a given temperature the SLR rate  $T_1^{-1}(T)$ , and in turn  $\tau_c^{-1}$ , increases with increasing Li-ion diffusivity starting from the microcrystalline form through the nanocrystalline form, ending at the amorphous form. It is worth noting that there is a high degree of similarity between the diffusivity in the nanocrystalline and the amorphous forms. One similarity is the temperature at which the steep increase in  $T_1^{-1}$  begins: 230 and 285 K for the amorphous and the HEBM nanocrystalline forms, respectively, while the microcrystalline material shows only the temperature independent background in this temperature range and its drastic increase starts at about 700 K. Another aspect of similarity is that the amorphous sample and the nanocrystalline one have very similar  $E_{T_1}^{\text{IT}}$  values (0.22 and 0.27 eV) while that of the microcrystalline form is about three times higher values (0.81 eV).

### 7.2.2.2 Effect of impurities on SLR rate

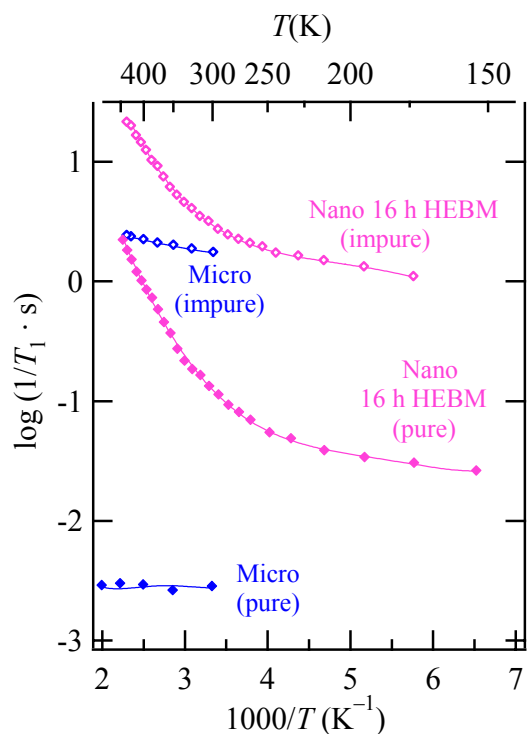


Fig. 7.2.15: The temperature dependence of the  $^7\text{Li}$  NMR SLR rates ( $1/T_1$ ) measured at  $\omega_0/2\pi = 77.7$  MHz for the microcrystalline and the HEBM nanocrystalline  $\text{LiNbO}_3$  showing the impurity effect. The rate is increased by three orders of magnitude in the background of the microcrystalline form by increasing the impurity level. Also in the HEBM nanocrystalline there is a high increase (1.75 orders of magnitude) but the activation energy remains the same.

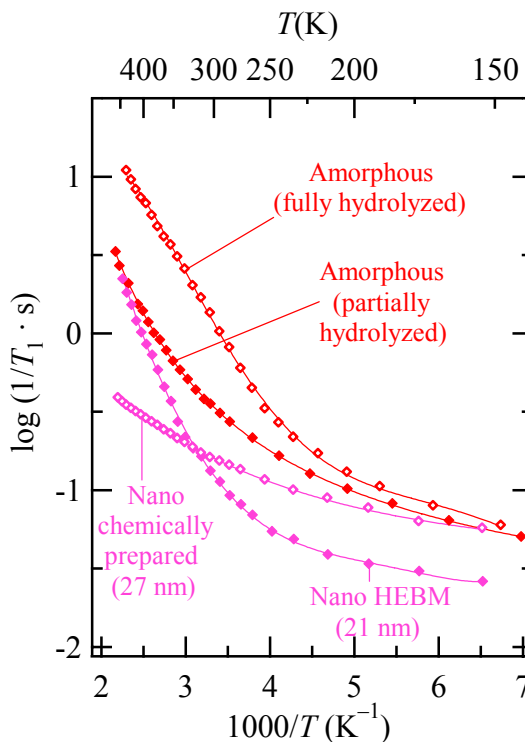


Fig. 7.2.16: The temperature dependence of the  $^7\text{Li}$  NMR SLR rates ( $1/T_1$ ) measured at  $\omega_0/2\pi = 77.7$  MHz for the microcrystalline and the HEBM nanocrystalline  $\text{LiNbO}_3$  showing the preparation route effect on the amorphous  $\text{LiNbO}_3$  prepared by double alkoxide sol-gel with partial and full hydrolysis and on the nanocrystalline form prepared by HEBM and chemically by sol-gel.

Paramagnetic impurities, in particular, can increase the SLR rate of the diffusing ions. This can be clearly seen in Fig. 7.2.16 where the SLR rate of microcrystalline  $\text{LiNbO}_3$  was increased by three orders of magnitude just by changing the purity of 99.99 % to 99.9 % for  $\text{LiNbO}_3$  obtained from the same producer, (for more details about the samples refer to section 5.1.1). In the case of 16 h HEBM nanocrystalline  $\text{LiNbO}_3$  the difference in the SLR rate is 1.75 orders of magnitude for the non-diffusive background while it decreases to about one order of magnitude with the evolution of the low-temperature flank of the diffusion induced maximum. Nevertheless, the activation energies of the two samples are similar ( $E_{T_1}^{\text{IT}} = 0.27$  eV for the pure sample and 0.29 eV for the impure one). In the case of the microcrystalline sample the effect of impurities is much more pronounced (2.75 orders of magnitude) for the non-diffusional backgrounds as shown in Fig. 7.2.16.

### 7.2.2.3 Preparation-route effect studied by SLR

Fig. 7.2.17 shows the SLR rate for the amorphous  $\text{LiNbO}_3$  prepared by double alkoxide sol-gel method for two samples; the fully hydrolyzed sample has a SLR rate higher by about half an order of magnitude, however, the activation energies are not affected, Table 7.2.7. In the case of the nanocrystalline  $\text{LiNbO}_3$  two samples with comparable grain sizes were examined: the 16 h HEBM sample (23 nm) and a chemically prepared sol-gel one (27 nm). At low temperatures, the SLR rate of the chemically prepared sample is lower by about one order of magnitude. In this case, it seems that the low-temperature flank is inaccessible within the measured temperature range, thus no low-temperature flank activation energy can be obtained. It is clear that the behavior of this sample is different from that of the mechanically prepared (HEBM) one as it deviates from the amorphous sample and resembles the microcrystalline one.

Table 7.2.7: The activation energies for the low-temperature flank of the  $^7\text{Li}$  SLR rates ( $1/T_1$ ) obtained from the plots of Fig. 7.2.17 (with and without background correction).

$\text{LiNbO}_3$		$E_{T_1}^{\text{IT}}$ [eV]	
		w/o corr.	w. corr.
Amorphous	Fully hydrolyzed	0.17(6)	0.22(3)
	Partially hydrolyzed	0.16(7)	0.22(3)
Nanocrystalline	mechanically 16 h HEBM	0.25(5)	0.27(3)
	chemically sol-gel	low temperature flank was not detected	

### 7.2.2.4 Discussion of SLR rates

The diffusion-induced SLR rate curves,  $T_1^{-1}(T)$  vs.  $1/T$ , were shifted towards lower temperatures and their background got higher by going from the microcrystalline to the nanocrystalline (16 h HEBM) ending with the amorphous form. The shift means that Li diffusion is starting at lower temperatures due to the increased Li-ion diffusivity when going from the highly ordered microcrystalline to the heterogeneously

disordered nanocrystalline form and then to the homogeneously disordered amorphous form. The first increase is believed to arise from the increased volume fraction of the disordered grain-boundary regions, whereas the increased free volume in the amorphous form is responsible for the second increase. The necessity to restrict NMR experiments to temperatures below 450 K prohibits the detection of the  $T_1^{-1}$  maxima with increasing the temperature for both the milled and the amorphous samples. Thus little quantitative information can be extracted from the data obtained about the diffusion parameters.

The SLR rate proved to be dependent on the preparation route. Firstly, the  $1/T_1$ -rate of the amorphous samples which were prepared by the double alkoxide sol-gel showed a dependence on the amount of water used for the hydrolysis. The partially hydrolyzed sample showed lower SLR rate than the fully hydrolyzed sample. This can be attributed to the amount of residual organic material being large in the case of partial hydrolysis (in accordance with Eq. 7.1.4). Moreover, the nanocrystalline sample prepared by the sol-gel route showed a much lower SLR rate than that of the ball-milled nanocrystalline that possesses a similar grain size. The behavior of the chemically prepared nanocrystalline sample tends to resemble that of the microcrystalline one. Although it does not reveal a diffusion-induced low-temperature flank, it was clear that the cause of the enhancement of the diffusion in the ball-milled sample, i.e. the increased volume fraction of the disordered grain-boundary region, is absent in the chemically prepared one. Thus the grain-boundary regions in the chemically prepared nanocrystalline sample can be postulated to have ordered structure similar to that of the bulk material. Alternatively, it might be disordered and so thin that they do not dominate the overall relaxation behavior of the sample.

Recently,  $^7\text{Li}$  dynamics in microcrystalline, nanocrystalline<sup>4-5,235</sup>, and amorphous  $\text{LiNbO}_3$  prepared by sol-gel method<sup>6</sup> were probed intensively. The previous results showed that the SLR rates for the ball-milled nanocrystalline samples increase and the activation energies decrease with increasing the milling times. The curves of the samples milled longer than 48 h showing a kind of saturation limit. The  $E_A^{\text{IT}}$  values were frequency independent, whereas the SLR rate for the same region was frequency dependent ( $T_{1\text{diff}}^{-1} \propto \nu^\alpha$ ). The exponent  $\alpha$  was found to be 1.7, 1.1, and 1.2 for amorphous, nano-, and microcrystalline  $\text{LiNbO}_3$ , respectively. The ideal Bloembergen-Purcell-Pound (BPP) behavior, incorporating random isotropic diffusion, would imply  $\alpha = 2$ . This deviation indicates the influence of structural disorder and Coulomb interactions between the diffusing Li ions according to the jump-relaxation model<sup>191</sup>.

The background rate for amorphous  $\text{LiNbO}_3$  was found to follow an empirical power law  $T_{1\text{bgr}}^{-1} \propto T^\gamma$  with  $\gamma$  ranging from 1.6 to 2 in amorphous  $\text{LiNbO}_3$  in the frequency range 23 – 78 MHz. The frequency dependence of the background rate can be described by a power law  $T_{1\text{bgr}}^{-1} \propto \nu^\beta$  with  $\beta = 1.4 \pm 0.1$ . This behavior of the background rate may be ascribed to the presence of paramagnetic impurities. Furthermore, the activation energy extracted from the slope of the high-temperature side visible in  $T_{1c}^{-1}(T^{-1})$  was 0.88 eV and was attributed to the long-range motion of the Li ion. At the maximum of

$T_{1e}^{-1}(T^{-1})$  peak, the condition  $\omega\tau_c \approx 1$  is valid. Thus, applying the Einstein-Smoluchowski equation resulted in a self-diffusion coefficient  $D$  of  $7.3 \times 10^{-15} \text{ m}^2/\text{s}$  (at  $T = 890 \text{ K}$ ).

The impurities have a large effect on the SLR rate, mainly on  $T_{1\text{bkg}}^{-1}$  and to a lesser degree on  $T_{1\text{diff}}^{-1}$ ; however, they show only a minor effect on the activation energy. This was previously concluded from the saturation behavior seen in the growing  ${}^7\text{Li}$  SLR rates and the decreasing activation energies with increasing milling time which proved that the influence of (non-paramagnetic) impurities introduced by ball-milling on NMR results is limited. This is also in agreement with introducing Fe impurities into the nanocrystalline  $\text{LiNbO}_3$  by using a stainless steel milling vial which showed that there was no significant change in the activation energy from the low-temperature flank and only the background was increased in the steel milled sample which is probably caused by the paramagnetic impurities.

### 7.2.2.5 Effect of grain size on the motional narrowing (MN) of the $^7\text{Li}$ central line

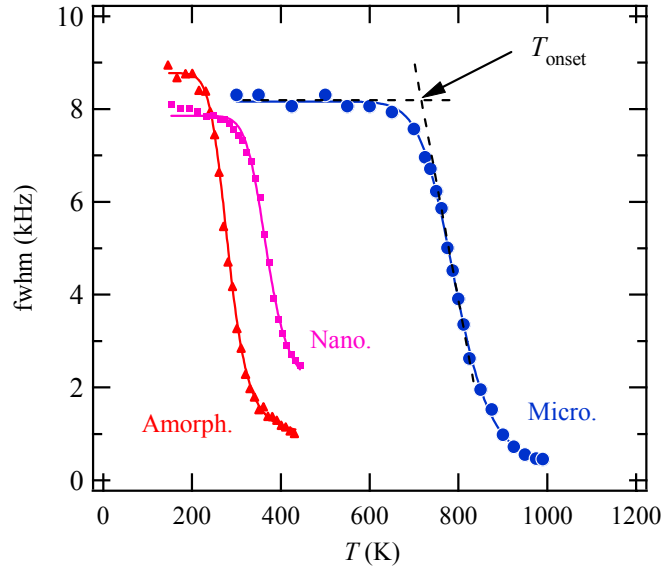


Fig. 7.2.18: The temperature dependence of the full width at half maximum (fwhm) of the  $^7\text{Li}$  central transition NMR-line for the amorphous, the nanocrystalline (16 h HEBM), and the microcrystalline  $\text{LiNbO}_3$  sample. (the data for the microcrystalline sample are taken from Ref. [5])

Further insight into the dynamics is achieved by investigating the temperature dependence of the central transition linewidth (fwhm) of the  $^7\text{Li}$  NMR lines. Fig. 7.2.18 shows the temperature dependence of the fwhm of the lines measured at 77.7 MHz for microcrystalline, 16 h HEBM nanocrystalline, and amorphous  $\text{LiNbO}_3$ . The difference between these forms can be obtained by monitoring  $T_{\text{onset}}$ , the temperature

Table 7.2.8: Fitting parameters of the temperature-dependent MN obtained by different equations (ad hoc, and Waugh Fedin), the activation energies of the low-temperature flank of the SLR rate are also given for comparison

Parameter	Amorphous		Nanocrystalline 16 h HEBM	Microcrystalline	Method of calculation
	Fully hydrolyzed	Partially hydrolyzed			
$\Delta v_R$ [kHz]	7.04	5.45	6.13	6.53	
$\Delta v_\infty$ [kHz]	0.86	0.78	1.84	0.0071	
$\tau_\infty$	$5.75 \cdot 10^{-5}$	$9.16 \cdot 10^{-5}$	$1.34 \cdot 10^{-5}$	$5.55 \cdot 10^{-7}$	ad. hoc.
$E_a^{\text{MN}}$ [eV]	0.18	0.21	0.29	0.83	
$\Delta v_R$ [kHz]	7.77	5.87	5.90	7.89	
$B$ [kHz]	$2.565 \cdot 10^{-5}$	$2.215 \cdot 10^{-5}$	$1.753 \cdot 10^{-6}$	$3.126 \cdot 10^{-8}$	
$D$ [kHz]	1.00	0.93	1.96	0.27	Hedrickson and Bray
$E_a^{\text{MN}}$ [eV]	0.31	0.36	0.48	1.32	
$T_{\text{onset}}$ [K]	237.91	279.5	324.75	714.05	
$E_a^{\text{MN}}$ [eV]	0.38	0.45	0.53	1.15	Waugh Fedin
$E_a^{\text{IT}}$ [eV]	0.22	0.22	0.27	0.81	SLR



at which the MN starts which is shifted by about 475 K from the microcrystalline  $\text{LiNbO}_3$  to the amorphous form (714 to 238 K). The ball-milled nanocrystalline sample shows a  $T_{\text{onset}}$  of about 325 K which is about 85 K higher than the  $T_{\text{onset}}$  amorphous form. However, it is still closer to it than to the microcrystalline form. The values of  $T_{\text{onset}}$  for the different samples were substituted in the Waugh Fedin equation (Eq. 4.2.31) and the obtained activation energies are listed in Table 7.2.8. The amorphous and the 16 h HEBM nanocrystalline samples have low values of  $E_a^{\text{MN}}$  that are relatively near to each other (0.38 and 0.53 eV, respectively), while the microcrystalline form has a higher value of 1.15 eV. The motional narrowing is nearly complete at 400 K for both the nanocrystalline and the amorphous forms. The magnetic field inhomogeneity may account for the large residual linewidth at high temperatures for the amorphous form. However, in the nanocrystalline case the residual linewidth ( $\cong 2$  kHz) is unlikely to be attributed to magnetic field inhomogeneity as it is considerably high. Furthermore, the nanocrystalline and the amorphous samples were measured using the same magnet with limited period of time.

These data can be fitted with ad hoc (Eq. 4.2.30), Hedrickson and Bray (Eq. 4.2.29), and Waugh Fedin formulas [for more details refer to section 4.2.7], from which the activation energies,  $E_a^{\text{MN}}$ , were calculated and shown in Table 7.2.8. In general, the obtained activation energies were reduced to one third of their value when going from the microcrystalline to the nanocrystalline and amorphous forms, in agreement with the trend of activation energies of the low-temperature  $T_1^{-1}$  flank, listed also for comparison.

### 7.2.2.6 Effect of the preparation route on the m of the $^7\text{Li}$ central line

Fig. 7.2.19 shows the effect of the preparation route on the MN in the case of amorphous  $\text{LiNbO}_3$  prepared by the double alkoxide sol-gel route but using different amounts of water for the hydrolysis. The MN for the fully hydrolyzed sample starts at a lower temperature than that of the partially hydrolyzed one, 238 K and 280 K respectively. This indicates that the Li ions in the fully hydrolyzed sample are more mobile than those in the partially hydrolyzed one, resulting in lower values of the activation energies, which is in agreement with the results obtained from impedance spectroscopy and SLR NMR, Table 7.2.8. Another remarkable observation is the great difference in the measured

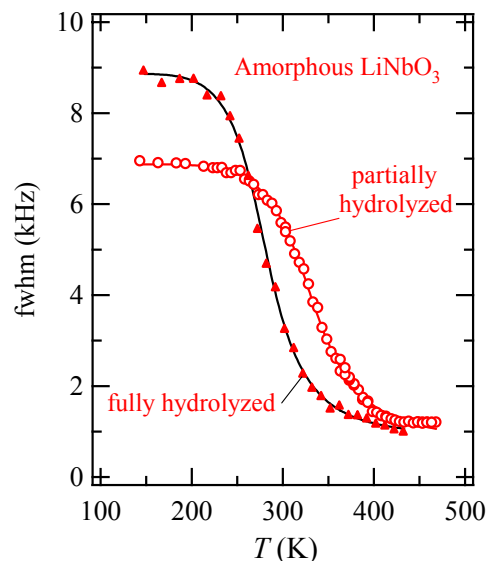


Fig. 7.2.19: The temperature dependence of the full width at half maximum (fwhm) of the central transition  $^7\text{Li}$ -NMR line for the amorphous  $\text{LiNbO}_3$  prepared by the double alkoxide sol-gel method with one of them fully hydrolyzed and the other partially (1/3) hydrolyzed.

fwhm in the rigid lattice range. The linewidth is linked with the Li-ion pair distance ( $r$ ) in accordance with the Van-Vleck formula over the second moment

$$\text{fwhm} \propto \sum_k \frac{1}{r_{jk}}. \quad (7.2.11)$$

As the two samples were prepared to give stoichiometric  $\text{LiNbO}_3$  (i.e. to have a Li:Nb ratio of 1), this difference can be understood as a homogeneous, random distribution of  $^7\text{Li}$  cations in the fully hydrolyzed sample while in the case of the partially hydrolyzed sample the distance between two adjacent Li cations is larger.

The MN was also investigated in a couple of nanocrystalline  $\text{LiNbO}_3$  samples prepared by different routes, namely HEBM and sol-gel. At the beginning, the lines of HEBM nanocrystalline  $\text{LiNbO}_3$  were fitted with single lines and their fwhm were used to obtain the MN curve shown in Fig. 7.2.20(a). However, it was discussed in Sec. 7.1.1 that these lines show two distinct contributions, one of which is narrow due to the grain-boundary regions and the other is wide due to the grain interiors. When the two contributions are separable, i.e. after the emergence of the narrow contribution, it is more appropriate to fit them with two lines. Fig. 7.2.20(a) shows that the emergence of the narrow contribution and the narrowing of the entire line occurred simultaneously at 330 K. At this temperature the amorphous sample is completely narrowed (see the shadowed dotted red curve in Fig. 7.2.20(a)). Hence, one can infer that the grain-boundary regions of the HEBM sample are amorphous and that the appearance of their narrow contribution is the cause of the narrowing in the entire line because the relative contribution of the narrow line

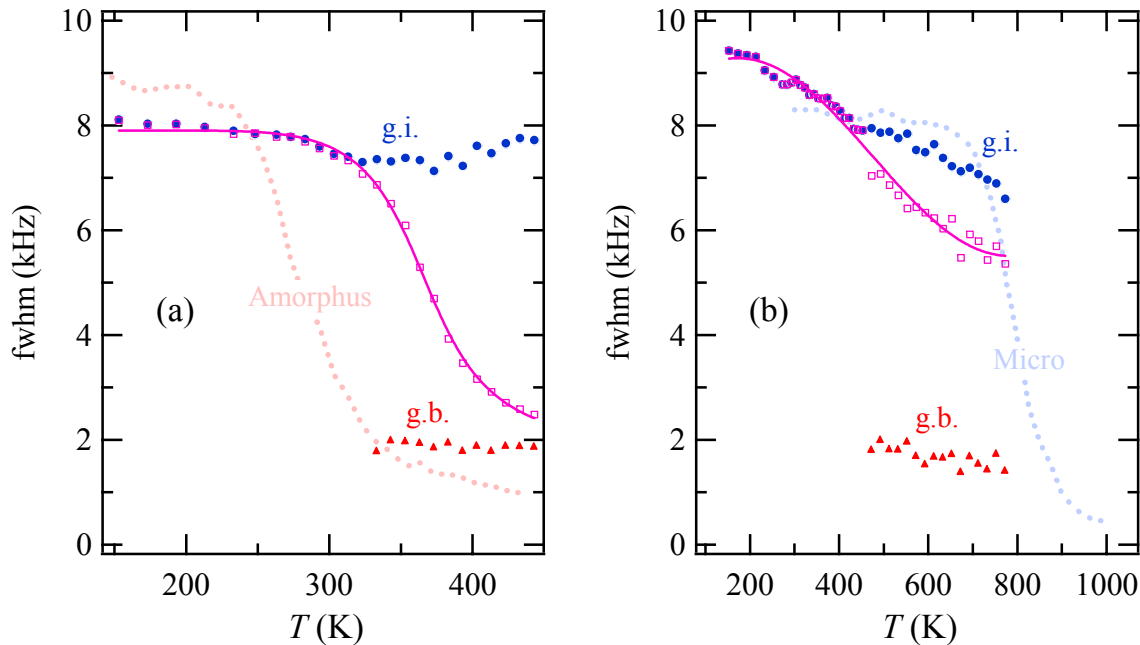


Fig. 7.2.20: The temperature dependence of the full width at half maximum (fwhm) of the  $^7\text{Li}$  central transition for nanocrystalline  $\text{LiNbO}_3$  prepared by (a) HEBM for 16 h, and (b) double alkoxide sol-gel fully hydrolyzed and heated for 1 h at 773 K (with the amorphous and the microcrystalline MN curves shown as shadowed dotted curves in red and blue, respectively).

starts to be significant under these conditions (up to 32 %, see Fig. 7.1.3).

On the other hand, Fig. 7.2.20(b) shows the MN for the sol-gel prepared nanocrystalline sample heated for 1 h at 773 K (grain size  $\approx 27$  nm). Over the whole temperature range measured, the fwhm of the entire line was not completely narrowed. By trying to fit the entire line with two contributions, the broad contribution obtained has a fwhm comparable to that of the microcrystalline form (the shadowed dotted blue curve in Fig. 7.2.20(b)), and thus it was attributed to the grain interiors. The sharp contribution started to be separable only at 470 K; it has a fwhm comparable to that of the amorphous form (the shadowed dotted red curve in Fig. 7.2.20(a)) and showed only a minor effect on the narrowing of the entire line despite having the same fwhm as the amorphous form. However, this may be attributed to its small relative contribution which does not exceed 4 % (see Fig. 7.1.3).

### 7.2.2.7 Discussion of the motional narrowing

Narrowing of the NMR linewidth occurs when the interactions, containing both nuclear spin and space coordinates, are partially averaged out by the thermal motion of atoms in a solid which increases with increasing temperature (the motional narrowing effect)<sup>194</sup>. The temperature dependence of the fwhm of the  $^7\text{Li}$  NMR central transitions showed an increase in the diffusivity of lithium ion with decreasing the grain size and increasing the structural disorder. This was concluded from the fact that the microcrystalline form has the highest  $T_{\text{onset}}$  (the lowest Li-ion diffusivity) followed by the HEBM nanocrystalline form, which is not far from the amorphous material (highest Li-ion diffusivity). The fact that MN was nearly complete for both the nanocrystalline and the amorphous forms at a lower temperature than where it started in the microcrystalline form, indicates a large difference in diffusivity (a few orders of magnitude) between them. The estimated  $E_a$  was found to increase slightly from the amorphous form to the ball-milled nanocrystalline one. On the contrary, the microcrystalline  $\text{LiNbO}_3$  showed an  $E_a^{\text{MN}}$  which is bigger by a factor of two to three times than the previous amorphous and nanocrystalline forms. The reason behind this is that crystalline materials usually possess equal and high energy barriers, whereas, the disordered amorphous and nanocrystalline materials have a wide distribution of energy barriers with different height from which ions prefer the ones with lower energy barriers.

The preparation route of disordered materials reveals a significant effect on the diffusivity in both the amorphous and the nanocrystalline  $\text{LiNbO}_3$ . The fully-hydrolyzed amorphous sample shows Li-ion diffusivity higher than that of the partially-hydrolyzed one, as can be seen from the shift of the MN curve toward lower temperatures. Furthermore, there is a noticeable difference in the fwhm measured in the rigid-lattice range. According to Van Vleck formula, the smaller fwhm in the case of the partially hydrolyzed sample can be attributed to the bigger distance ( $r$ ) between the Li-ions. This agrees with the findings of the complex plane impedance measurements (Sec. 7.2.1.7). Where structural differences were assumed to be present and attributed to: (i) the presence of small crystallites due to the second heating process, or

(ii) the presence of a second Li-rich phase due to the limited mixing time in the preparation of the double alkoxide.

For the nanocrystalline sample, the heterogeneous disorder and the separation of the central transition into two components contradict with using a single line fit. Accordingly, two lines were used (narrow and wide). The wide line is used to fit the contribution due to the restricted ions inside the grain. The width of this contribution matches the width of the microcrystalline line in the rigid lattice region. This is expected as the grains are known to have a crystalline structure similar to that of the microcrystalline parent material. On the other hand, the narrow line is used to fit the contribution due to the fast-moving ions in the grain-boundary regions. The width of this contribution matches the width of the amorphous line after narrowing. Furthermore the narrow contribution starts to be separable only at the temperatures at which the amorphous line is considerably narrowed. This can be regarded as additional supporting evidence that the grain-boundary regions of the nanocrystalline form have amorphous nature in accordance with our previous conclusions from the impedance and SLR measurements.

The nanocrystalline  $\text{LiNbO}_3$  is regarded as a heterogeneous ionic conductor that combines crystalline and amorphous phases. In such systems, the Li-ion diffusivity is dominated by the ions in the highly defective and disordered regions. Hence the diffusivity of Li ions in these materials should be comparable to that of the purely amorphous form. This fact was specifically true in the case of the HEBM nanocrystalline  $\text{LiNbO}_3$ .

MN in a  $\text{LiNbO}_3$  single crystal was first investigated by Halstead<sup>272</sup>. He reported a diffusion coefficient for Li of about  $1.8 \times 10^{-5}$  and  $2.0 \times 10^{-5}$   $\text{m}^2/\text{s}$  and activation energies of 1.62 and 1.46 eV for the pure  $\text{LiNbO}_3$  single crystal and a vacuum-annealed crystal, respectively, at temperatures above 820 K. The line narrows slowly between 423 and 823 K due to a motion that may only partially remove the dipolar interaction having a low activation energy, possibly a to-and-fro motion. Then it narrows rapidly between 823 and 923 K due to a motion that completely removes the dipolar interaction, having high activation energy, probably diffusion.

## 7.2.3 Secondary-Ion Mass Spectroscopy

### 7.2.3.1 Oxygen diffusion studies by SIMS

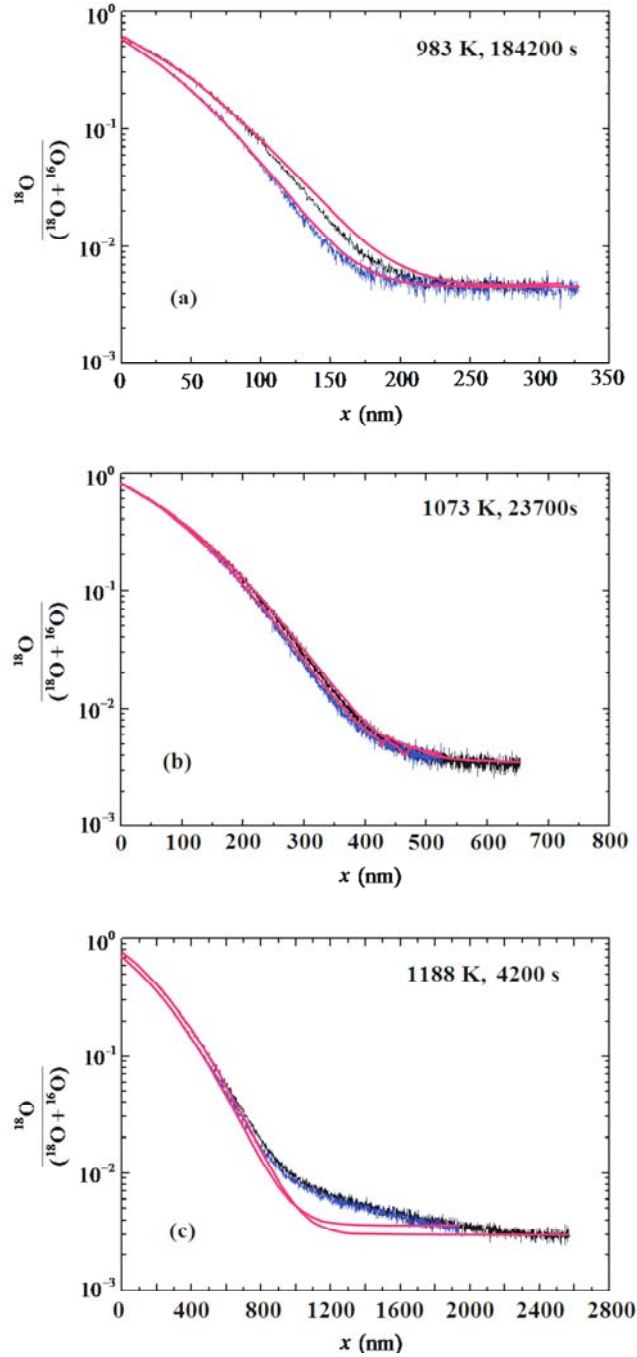


Fig. 7.2.21: SIMS depth profiles of the relative  $^{18}\text{O}$  concentration measured in  $\text{LiNbO}_3$  single crystal after diffusion annealing in  $^{18}\text{O}_2$  gas atmosphere (200 mbar) at: (a) 973, (b) 1073, and (c) 1188 K for 184200, 23700, and 4200 s, respectively, with diffusion direction parallel to the  $c$ -axis (black curves) and perpendicular to it (blue curves). The solid red lines represent mean squares fits using Eq. (6.4.6).

Fig. 7.2.21 shows typical SIMS depth profiles of the relative  $^{18}\text{O}$  concentration measured in the  $\text{LiNbO}_3$  single crystal after diffusion annealing in an  $^{18}\text{O}_2$  gas atmosphere (200 mbar). The red solid lines in this figure are the result of a least squares fit according to Eq. (6.4.6). The results of the least squares fit and all the experiment parameters are listed in Table 7.2.9. The penetration depth along the optical  $c$ -axis is slightly larger than perpendicular to it (the black and the blue curves, respectively). The difference between them decreases with increasing annealing temperature. This difference is not significant taking into account that the error in the SIMS crater depth measurement is about 10 %.

The measured background value of the relative  $^{18}\text{O}$  concentration is about 0.004 whereas its natural abundance is 0.002. However, it was recently found<sup>339</sup> that the  $^{18}\text{O}$  fraction in pre-annealing gases may be significantly higher than the literature value of 0.204 %<sup>340</sup>. It was shown by means of simulations that these effects are important when analyzing grain-boundary diffusion, but they can be neglected when investigating bulk diffusion and surface exchange, as in our case here.

The actual fit parameters determined from the measured SIMS depth profiles are the diffusion length,  $\sigma$ , and the reduced annealing time,  $t/\tau$ , (see Eq. 6.4.6). From these fitting parameters one can calculate the physical parameters  $D$  and  $K$ , because the annealing time,  $t$ , is measured independently. For  $t/\tau > 10$  the calculated surface exchange coefficient,  $K$ , can become very erroneous because of error accumulation<sup>341</sup>. To evaluate the surface exchange coefficient,  $K$ , it is necessary to measure quantitatively the  $^{18}\text{O}$  concentration in the gas phase,  $c_g$ , and in the solid very near the surface,  $c_s$ . These concentrations were measured by RGA and SIMS, respectively, thus they contribute independently to the error accumulation. Simple error estimation can show that the scatter of the measured  $K$  values in Fig.7.2.22 can be explained by error accumulation which is mainly caused by errors in the concentration measurements (for more details see appendix A.4). The straight lines in Fig. 7.2.22(a) represent the following Arrhenius relations for  $D$

$$D = D_0 \exp\left(\frac{-E_{a,D}}{RT}\right) \quad (7.2.12)$$

while the straight lines in Fig. 7.2.22(b) represent the following Arrhenius relations for  $K$

Table 7.2.9: The experimental parameters obtained from fitting the curves in Fig. 7.2.20 for  $983 \text{ K} \leq T \leq 1188 \text{ K}$ .

Orientation	$T$ (K)	$t$ (s)	$c_g$	$c_\infty$	$t/\tau$	$\sigma$ (nm)	$c_s$	$\tau$ (s)	$D$ ( $\text{m}^2/\text{s}$ )	$K$ ( $\text{m}/\text{s}$ )
	983	184200	0.95	0.0047	1.73	103.4	0.61	106474	$1.45 \cdot 10^{-20}$	$3.69 \cdot 10^{-13}$
	1073	23700	0.95	0.0035	13.7	210.2	0.81	1730	$4.66 \cdot 10^{-19}$	$1.64 \cdot 10^{-11}$
	1188	4200	0.95	0.003	8.4	493.6	0.76	500	$1.45 \cdot 10^{-17}$	$1.70 \cdot 10^{-10}$
⊥	983	184200	0.95	0.0046	1.3	90.5	0.58	141692	$1.11 \cdot 10^{-20}$	$2.80 \cdot 10^{-13}$
⊥	1073	23700	0.95	0.0039	14.2	200.4	0.81	1669	$4.24 \cdot 10^{-19}$	$1.59 \cdot 10^{-11}$
⊥	1188	4200	0.95	0.0036	4.0	486.5	0.71	1050	$1.41 \cdot 10^{-17}$	$1.16 \cdot 10^{-10}$

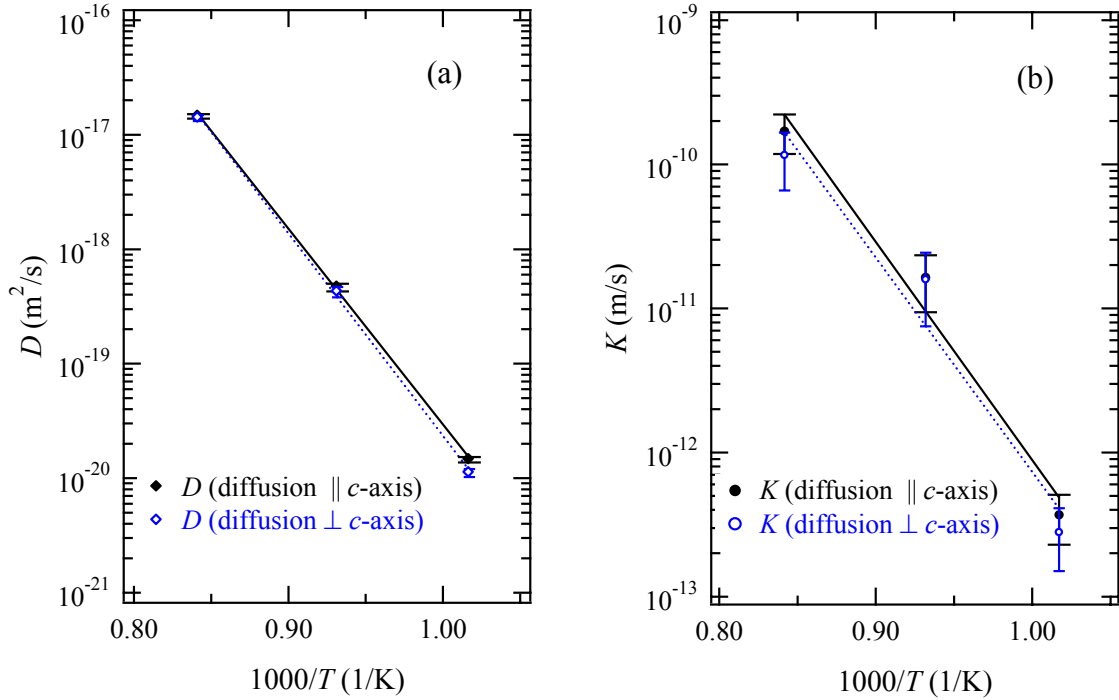


Fig. 7.2.22: (a) Oxygen diffusion coefficients ( $D$ ) and (b) oxygen exchange coefficients ( $K$ ) measured in single crystal  $\text{LiNbO}_3$ , with the filled markers representing the diffusion  $\parallel$  the optical  $c$ -axis (fitted with the solid line) while the open markers are used for the diffusion  $\perp$  the optical  $c$ -axis (fitted with the dotted line).

Table 7.2.10: Summary for the fitting parameters of the Arrhenius plots of the oxygen diffusion coefficients and oxygen exchange coefficients obtained by fitting the plots in Fig. 7.2.22:

oxygen diffusion coefficients			oxygen exchange coefficients				
parameter	diff. $\parallel$ $c$ -axis	diff. $\perp$ $c$ -axis	parameter	diff. $\parallel$ $c$ -axis	diff. $\perp$ $c$ -axis		
$D_0$ (m <sup>2</sup> /s)	$3.63 \cdot 10^{-03}$	$1.08 \cdot 10^{-02}$	$K_0$ (m/s)	$1.22 \cdot 10^{03}$	$5.37 \cdot 10^{02}$		
$E_{a,D}$ {	(kJ/mol)	327.15	338.1	$E_{a,K}$ {	(kJ/mol)	289.82	284.53
	(eV)	3.4	3.51		(eV)	3.01	2.95

$$K = K_0 \exp\left(\frac{-E_{a,K}}{RT}\right) \quad (7.2.13)$$

The fitting parameters are summarized in Table 7.2.10.

### 7.2.3.2 Discussion of oxygen diffusion in $\text{LiNbO}_3$

The diffusion coefficient is a second rank tensor which is supposed to be isotropic in the basal plane of a hexagonal system and different in directions perpendicular to it. However, only slight differences were found for the oxygen diffusivity and the oxygen exchange at the surface when diffusion is perpendicular or parallel to the optical  $c$ -axis. This agrees with electrical conductivity<sup>82,342</sup> and early oxygen diffusion<sup>82</sup> measurements which showed only minor differences along different crystallographic orientations. A

similar result was observed for the oxygen diffusivity in a 2/1-mullite single crystal<sup>343</sup>. This may be due to the contraction of the  $c$ -axis and the expansion of the  $a$ -axis as the temperature is increased within the measured temperature range (973 – 1073 K)<sup>344</sup>. Consequently, the number of oxygen planes to be passed by an ion diffusing within a certain distance along the  $c$ -axis is increasing. This leads to hindering the diffusion, whereas the ion diffusing perpendicular to the  $c$ -axis will be faced by a smaller number of oxygen planes and thus can diffuse faster. As a result, the diffusion will slow down along  $c$ -axis and become faster perpendicular to it, and the difference between the two directions will get smaller or even vanish. D. Birnie III<sup>345</sup> reviewed diffusion data in  $\text{LiNbO}_3$  for several elements and found that diffusion is very close to isotropic also for H, Li, O, Ti, Mg, and Er.

The only available oxygen tracer diffusion measurement in  $\text{LiNbO}_3$  was conducted in 1969.<sup>82</sup> The oxygen diffusion rates were obtained by monitoring the ratio of  $^{18}\text{O}$  to  $^{16}\text{O}$  as a function of time in a limited volume containing a well-mixed oxygen mixture and a partial pressure of 70 Torr. Only the residual  $^{18}\text{O}$  concentration in the gaseous phase was measured without any indication about the real concentration in the solid crystal. Plane sheet geometry with one-dimensional non-steady state diffusion was applied and the diffusion process was described by

$$D = 3.125 \times 10^{-10} \frac{\text{m}^2}{\text{s}} \exp\left(-\frac{123.5 \text{ kJ/mole}}{R T}\right) \text{ for } 973 \text{ K} \leq T \leq 1273 \text{ K} \quad (7.2.8)$$

This result is significantly different to the findings obtained in this work, see Fig. 7.2.23 for comparison.

The diffusion coefficients obtained are higher by 2.5 – 4 orders of magnitude than ours over the measured temperature range. The activation energy,  $E_{a,D} \approx 1.3 \text{ eV}$ , is much lower than our value of 3.5 eV. However, the measurement of Jorgensen and Bartlett may be unreliable as they measured the concentration of the residual  $^{18}\text{O}$  in the gaseous phase which could have a large error mainly because  $^{18}\text{O}$  was diluted with normal oxygen to yield a  $^{18}\text{O}/^{16}\text{O}$  ratio of 5 – 10 %. They used several  $\text{LiNbO}_3$  sheets of constant thickness in each run and waited until the total  $^{18}\text{O}$  uptake reached 50 %. After that, they applied plane sheet geometry without measuring the  $^{18}\text{O}$  concentration in the solid. Moreover, they argued the possibility of leakage in the gas container and the absorption of  $^{18}\text{O}$  on the surface of the experimental setup. Another possible explanation is the fact that the mixture of oxygen iso-

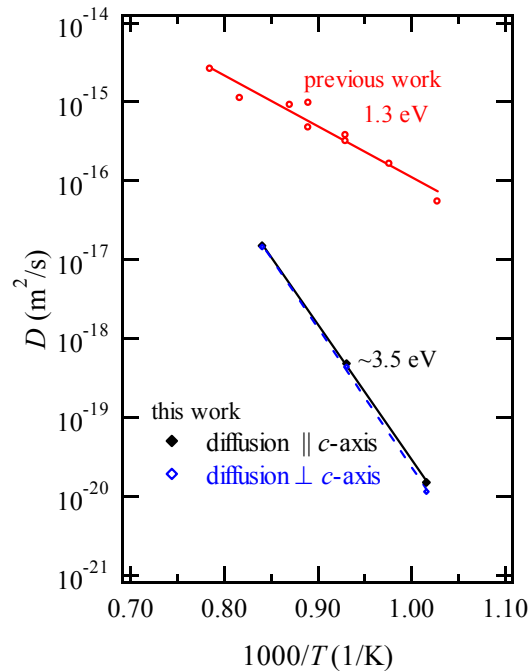


Fig. 7.2.23: Oxygen diffusion coefficients,  $D$ , measured here by SIMS in single crystalline  $\text{LiNbO}_3$ , a comparison between this work and the results presented in Ref. [82].



topes in which our single crystals were annealed is regarded as an oxidizing atmosphere which will decrease the number of oxygen vacancies, whereas in Ref. [82] the annealing was done at oxygen partial pressure of 70 Torr which may create such vacancies.

The electrical transport measurement showed that the electrical conductivity of  $\text{LiNbO}_3$  at 1 atm of oxygen is completely ionic.<sup>82</sup> By substituting the diffusion coefficient obtained for oxygen into the Nernst-Einstein equation, the resulting transport number of oxygen is significantly less than 1. It is unreasonable to assume oxygen to be the major diffusing ion. It is even less probable that  $\text{Nb}^{5+}$  is the main diffusing ion because of its relatively large size and higher charge. This implies that the Li ions are the main diffusing species. However, the presence of oxygen vacancies in the  $\text{LiNbO}_3$  crystal was confirmed again recently<sup>76,83-84</sup>. Annealing the as-grown crystals in Ar at 1373 K gave two successive optical absorption maxima at  $\lambda_1 = 360$  and  $\lambda_2 = 530$  nm.<sup>85</sup> They were attributed to  $\text{F}^+$  and F (colored centers generated by oxygen vacancies trapping one or two electrons, respectively). The successive appearance of these maxima implies that oxygen vacancies were already present in the single crystal and that the electrons, which result from the thermal reduction, are distributed among all the available oxygen vacancies. The congruent  $\text{LiNbO}_3$  crystal was found to act as oxygen and lithium conductor at temperatures between 573 and 1073 K using reversible electrodes<sup>85-86</sup>. The oxide-ion conductivities at 973 K were  $2 \cdot 10^{-6}$  and  $3 \cdot 10^{-6} (\Omega \cdot \text{cm})^{-1}$  for the as-grown and the thermally reduced  $\text{LiNbO}_3$  crystals, respectively. The slight increase in  $\text{O}^{2-}$ -conductivity emphasizes that the oxygen vacancy concentration did not change so much upon reduction. The concentration of oxygen vacancies was greater than  $10^{19} \text{ cm}^{-3}$ . The same two optical bands mentioned above were observed in the cases of oxygen vacancies or lithium ions electrically injected by double layer electrodes. These identities of the electrical and optical absorption properties for both the thermally and electrically reduced crystal emphasize the conclusion that they have the same origin<sup>85-86</sup>. Ionizing radiation may turn these oxygen vacancies into color centers, such as F or  $\text{F}^+$  that can be identified by their optical absorption spectra.<sup>84</sup>

## 7.2.4 General Discussion of Diffusion Aspects

The discovery of high-ionic conductivity in several ceramic materials over the past decades has stimulated considerable interest in these materials. Great attention was paid to: (i) the conduction mechanism operative in these systems, (ii) their potential utilization in technological applications, and (iii) methods for tailoring their properties such as increasing their conductivity. Whatever the structure of an ionic material is, its physical properties are strongly related to the degree of disorder [Ref.]. Crystalline materials usually have equal potential energy barriers while in disordered materials (amorphous and nanocrystalline forms) there is a wide distribution of energy barriers with different heights. In such a situation, ions prefer the diffusion paths with lower energies, particularly at low temperatures. It was found that diffusivity and

ionic conductivity in solid-ionic conductors can be increased in most cases by going from the microcrystalline form to the corresponding nanocrystalline<sup>1,4-5,7</sup> or amorphous<sup>2,6</sup> forms.

It is relatively straightforward to obtain information about the short-range order using classical spectroscopic techniques like wide angle x-ray diffraction, EXAFS, etc. and about the long-range order by XRD. In spite of this, such opportunities are limited in the case of heterogeneously disordered materials where it is much more difficult to investigate the disorder from a qualitative as well as quantitative point of view. The only available tool is to monitor some of their physical properties such as the dielectric behavior in comparison with the behavior expected or observed in ordered systems.<sup>346</sup>

Following the previous concepts, the temperature dependence of the ionic conductivity and the NMR SLR rate and MN were investigated in different forms of LiNbO<sub>3</sub>. The results obtained from these measurements revealed that microcrystalline LiNbO<sub>3</sub> possesses slower Li ions (the smallest values of  $\sigma_{dc}$ ,  $f_r$ ,  $T_{1\text{diff}}^{-1}$  and the longest  $\tau_{M'}$  with the highest activation energies). It is followed by the nanocrystalline and then the amorphous sample in which the Li ions have the highest diffusivity (the largest values of  $\sigma_{dc}$ ,  $f_r$ ,  $T_{1\text{diff}}^{-1}$  and the shortest  $\tau_{M'}$  with the lowest activation energies). As an example of the enhanced diffusivity, the ionic conductivity was found to increase by seven orders of magnitude at 450 K when going from the single crystalline to amorphous LiNbO<sub>3</sub>. This enhancement is attributed to the increased "free volume" in the amorphous sample. The high resemblance of electrical behavior (including the values of  $\sigma_{dc}$ ,  $f_r$ , and  $\tau_{M'}$  and their activation energies) implies that the disorder in the interfacial regions of HEBM nanocrystalline LiNbO<sub>3</sub> is similar to that of the amorphous form. The increase of the volume fraction of these interfaces with increasing milling time is the cause of the faster atomic transport in the milled samples. Despite having a crystallite size similar to that of the HEBM sample, the chemically prepared nanocrystalline material showed a behavior which is nearer to that of the microcrystalline form in both the conductivity and SLR. It was misleading to estimate the fwhm of the <sup>7</sup>Li central NMR line of the nanocrystalline forms by a single line; instead it should be dealt with as a superposition of two contributions: a narrow one whose fwhm matches that of the amorphous sample and a broad one whose fwhm matches that of the microcrystalline sample. This explains the incomplete MN of both samples when fitted with single lines, where the HEBM nanocrystalline sample showed more narrowing than the chemically prepared one due to a larger relative contribution of the narrow line in the former case. All these findings emphasize the visualized picture about the microstructure of the nanocrystalline samples: ball-milled material possesses a large volume fraction of grain-boundary regions. Or, in other words, the nanocrystallites are embedded in an amorphous matrix. In such systems, the Li-ion diffusivity is dominated by the ions in the structural disordered regions. Hence the Li diffusivity in these materials should be comparable to that of the purely amorphous form. This fact was obvious particularly in the case of the HEBM nanocrystalline LiNbO<sub>3</sub>. The MN and the NMR SLR as well as the  $\sigma_{dc}$  results confirmed this trend; the Li jump rate is higher in the amorphous

phase than in the microcrystalline phase. Moreover, the activation energy of amorphous and HEBM nanocrystalline  $\text{LiNbO}_3$  are identical.

It is now clear that the nature of disorder depends on the preparation route. Despite having grain size comparable to that of the HEBM sample, the chemically prepared nanocrystalline sample did not show the expected enhancement in Li diffusivity. This was clear from its MN and SLR as well as the conductivity, which was much lower than that of the amorphous samples and tends to resemble the behavior of the microcrystalline form. Accordingly, the conclusion was drawn that the chemically prepared nanocrystalline form has a small volume fraction of interfacial regions or that the grain-boundary regions are so thin that the ions inside them are not able to affect the overall diffusivity of the system.

The calculated dielectric constant shows no significant variation in the temperature range studied and yields consistent and precise results when compared to the real part of the dielectric constant obtained at arbitrary frequency. This dielectric constant showed a general increase with decreasing grain size for the same material. The paramagnetic impurities showed only a small effect on the conductivity and no effect on its activation energy. The small electronic part of the conductivity, which may appear in the reduced samples due to the oxygen vacancies, was blocked by conducting the measurements in an oxygen atmosphere.

$^{18}\text{O}$  SIMS showed that oxygen has a very low diffusion coefficient in single crystal  $\text{LiNbO}_3$  (even lower than previously reported in Ref. [82]). Nevertheless, the tracer diffusivities reported at 1273 K are  $^{345} D_{\text{Li}}^* = 6.8 \times 10^{-8} \text{ cm}^2/\text{s}$ ,  $D_{\text{Nb}}^* = 1.2 \times 10^{-11} \text{ cm}^2/\text{s}$ , and  $D_{\text{O}}^* = 2.8 \times 10^{-11} \text{ cm}^2/\text{s}$ . One may thus conclude that Nb and O are immobile compared to Li. The slow rate for oxygen motion is important in the light of rather rapid oxidation and reduction kinetics; samples are observed to darken or become black rapidly when reduced at high temperatures  $^{347,348}$ . The low diffusion coefficient obtained for oxygen implies that oxygen vacancies cannot be regarded as the main species responsible for the electrical conductivity in  $\text{LiNbO}_3$  single crystals.



## **8 Nanocrystalline $\text{LiNbO}_3$ Particles Embedded in Sodium Silicate Glasses $\text{Na}_2\text{Si}_3\text{O}_7$**

A glass-ceramic was defined as a two-phase system that comprises crystals grown from the parent glass by careful heat treatment<sup>47</sup>. Moreover, it was recently defined as any two-phase system where one phase is crystalline and the other one is glassy<sup>349</sup>. Glass-ceramics are highly regarded for their unusual mixture of physical properties which combines those of the crystalline phase as well as the glass properties, which are otherwise difficult to achieve. Recently a number of glass-ceramics comprising some well-known ferroelectric crystalline phases such as  $\text{LiNbO}_3$  and  $\text{NaNbO}_3$  in a glassy matrix have been investigated<sup>229,349–350</sup>. Preparing a ferroelectric glass-ceramics has a number of advantages over single crystals; the easy formability, optical transparency, low cost of glass, the temperature independence of the dielectric constant, and having a built-in electrical dipole (the ferroelectric nanoparticles) which produce phenomena such as electro-optic, harmonic generation, and photo-refraction effects.

Ferroelectric glass-ceramics can be prepared by controlled crystallization of a ferroelectric phase from the parent glass; however, this method has many challenges because the pure forms of such materials have little glass-forming ability. It is difficult to control the nucleation rate of glass under normal quenching conditions due to the nature of the material and the lack of fundamental understanding of the crystallization process upon glass quenching. The other way to prepare a glass-ceramic is to embed the particles in the glass matrix.

Ion-exchange inter-diffusion of cations in a glass forms the basis for the technological synthesis of gradient-index optical and acoustic elements and also of ion-exchange strengthening of glass. This determines investigators' interest in studying ion exchange and diffusion in glass.

Here, we try to prepare a glass-ceramic by embedding  $\text{LiNbO}_3$  nanoparticles in a sodium metasilicate glassy matrix. The preliminary purpose to initiate such a system was to focus on the mixed-ionic dynamics of the Li and Na ions in the resultant glass-ceramic. However, the results did not show any mixed cation effect but they were more interesting from the structural point of view. There was evidence for complete conversion of  $\text{LiNbO}_3$  into  $\text{NaNbO}_3$  under different heating and variable composition conditions.

## 8.1 HEATING EFFECT

### 8.1.1 X-ray Diffraction Ex-situ and In-situ

Fig. 8.1.1 shows the diffractograms obtained in the  $2\theta$  range from  $20^\circ$  to  $70^\circ$  for the  $n\text{-LiNbO}_3 \cdot g\text{-NaSi}_{1.5}\text{O}_{3.5}$  batches. They reveal the effect of heating for 2 h at the temperatures 873, 973, 1073, 1173, and 1273 K where the diffraction peaks of  $\text{LiNbO}_3$  are gradually substituted by those of  $\text{NaNbO}_3$ . The Rietveld structure refinement of these diffractograms (appendix A.5.1) demonstrates the

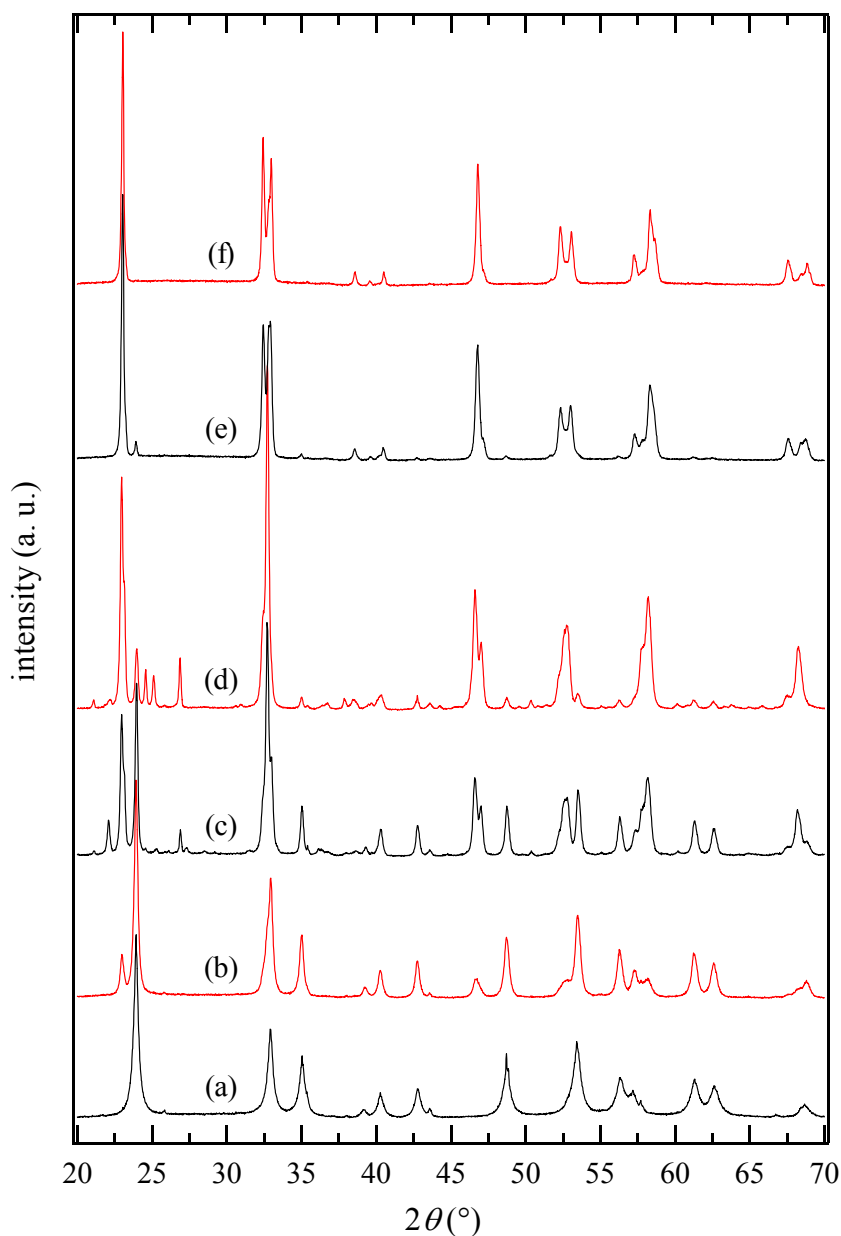


Fig. 8.1.1: Ex-situ XRD patterns for the composite  $n\text{-LiNbO}_3 \cdot g\text{-NaSi}_{1.5}\text{O}_{3.5}$  after 2 h of heating at: (b) 873, (c) 973, (d) 1073, (e) 1173, (f) 1273 K, (a) is  $n\text{-LiNbO}_3$  for comparison.

presence of 33.7 % of NaNbO<sub>3</sub> after 2 h of heating at 873 K which indicates that the lithium-sodium inter-change between the crystalline LiNbO<sub>3</sub> and the Na<sub>2</sub>Si<sub>3</sub>O<sub>7</sub> glass starts at relatively low temperatures. Few peaks that belong to new phases appeared at 973 and 1073 K but they did not appear after heating at 1173 K or higher temperatures. Rietveld structure refinement showed that the new crystalline phases are lithium disilicate doped with sodium, (Li,Na)<sub>2</sub>Si<sub>2</sub>O<sub>5</sub>, derived from the lithium phyllo-disilicate<sup>351,352</sup>, Li<sub>2</sub>Si<sub>2</sub>O<sub>5</sub>, [space group *C 1 c 1* (no. 9) ICSD-15414<sup>\*\*\*</sup>, quartz low<sup>353</sup> [*P 3 2 1* (no. 154) ICSD-174], and cristobalite low<sup>354</sup> [*P 4<sub>1</sub> 2<sub>1</sub> 2* (no. 92) ICSD-34927]. The result of the structure refinements are summarized in Table 8.1.1 and plotted in Fig. 8.1.2. The conversion of LiNbO<sub>3</sub><sup>355</sup> [*R c 3* (161) ICSD-74469] to NaNbO<sub>3</sub> reached more than 99 % after 2 h of heating at 1173 K with only minor intensity of the LiNbO<sub>3</sub>

Table 8.1.1: The molar percentages of LiNbO<sub>3</sub>, NaNbO<sub>3</sub> (summation of Lueshite high, Lueshite low, and orthorhombic NaNbO<sub>3</sub>) and the other new phases relative to the total crystalline phases obtain by Rietveld-structure refinement of the XRD diffractograms for the composite n-LiNbO<sub>3</sub>.g-NaSi<sub>1.5</sub>O<sub>3.5</sub> after heating for 2 h at the indicated temperatures.

<i>T</i> (K)	% LiNbO <sub>3</sub>	% NaNbO <sub>3</sub>	% other phases		
			quartz low	(Li,Na) <sub>2</sub> Si <sub>2</sub> O <sub>5</sub>	cristobalite low
873	66.35	33.65	–	–	–
973	11.25	51.21	2.70	28.39	6.44
1073	2.63	70.60	6.05	18.29	2.43
1173	2.94	97.06	–	–	–
1273	0.10	99.90	–	–	–

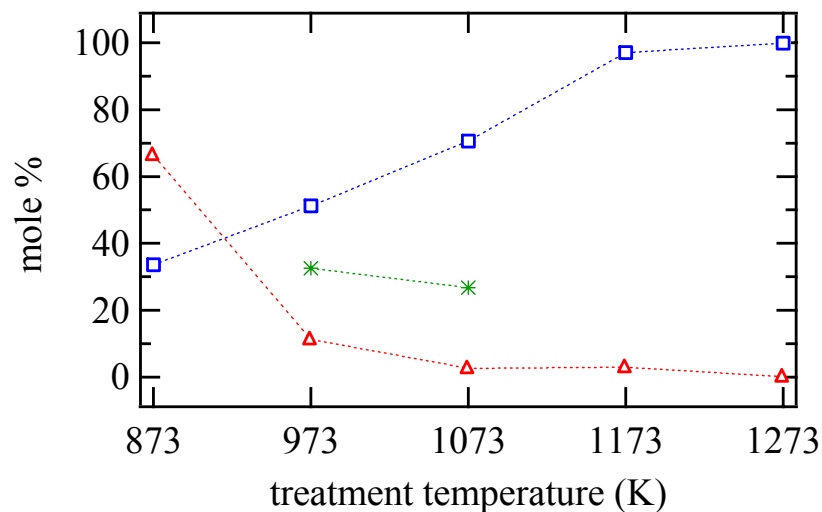


Fig. 8.1.2: The molar % of crystalline phases in the composite n-LiNbO<sub>3</sub>.NaSi<sub>1.5</sub>O<sub>3.5</sub> showing the effect of heating for 2 h at temperatures ranging from 873 to 1273 K for: (Δ) LiNbO<sub>3</sub>, (□) NaNbO<sub>3</sub> [summation of Lueshite high, Lueshite low, and orthorhombic NaNbO<sub>3</sub>], (\*) SiO<sub>2</sub> [quartz low and cristobalite low] and (Li,Na)<sub>2</sub>Si<sub>2</sub>O<sub>5</sub>.

\*\*\* ICSD stands for international crystallographic structure data base

main peak (at  $2\theta = 23.9^\circ$ ). Structure refinement showed that the obtained  $\text{NaNbO}_3$  consists of three different crystalline phases; Lueshite high<sup>356</sup> [space group  $Pm\bar{3}m$  (no. 221) ICSD-28589, orthorhombic  $\text{NaNbO}_3$ <sup>357</sup> [ $Pbma$  (no. 57) ICSD-89317, and Lueshite low<sup>356</sup> [ $P12/m1$  (no. 10) ICSD-28577]. At all temperatures, the Lueshite phases (high and low) were more dominant over the orthorhombic phase; however, the relative percentage of the orthorhombic phase increased at higher temperature. When the sample was heated to 1273 K it showed only minor changes. The crystallite-sizes were obtained from the structure refinement. They were found to increase generally from 25 – 55 nm at 873 K to 73 – 130 nm at 1273 K for all phases (except Lueshite low, and  $(\text{Li,Na})_2\text{Si}_2\text{O}_5$ ). For more details about the crystallographic details for  $\text{LiNbO}_3$  and some of  $\text{NaNbO}_3$  phases see Table 8.1.2.

The *in-situ* x-ray diffractograms show gradual conversion from  $\text{LiNbO}_3$  to  $\text{NaNbO}_3$ , Fig. 8.1.3. The conversion started at the relatively low temperature of 673 K. This can be noticed from the asymmetry of the  $\text{LiNbO}_3$  main diffraction peak ( $2\theta = 23.4^\circ$ ), followed by the formation of a shoulder at 723 K which developed at higher temperature to form the main peak of  $\text{NaNbO}_3$  ( $2\theta = 22.2^\circ$ ). This was accompanied by the emergence of the peaks at  $2\theta = 46.17, 51.9,$  and  $57.36^\circ$  that belong to the  $\text{NaNbO}_3$  phase and the disappearance of the  $\text{LiNbO}_3$  peaks at  $35.04, 42.65, 48.6,$  and  $56.2^\circ$ . All these changes reveal the ongoing conversion of n- $\text{LiNbO}_3$  into  $\text{NaNbO}_3$  up to 973 K where no remarkable changes can be seen. An enduring shift in the peaks' position towards lower  $2\theta$  values, due to the thermal expansion, is seen starting from the beginning up to 823 K. The new crystalline phases found in the *ex-situ* diffractograms could not be resolved here due to the low resolution of the diffractometer.

Table 8.1.2: The crystallographic (literature) details for  $\text{LiNbO}_3$  and some of  $\text{NaNbO}_3$  phases, phases (I, III, V) were detected and refined in the x-ray diffractograms while phases II and IV are known phases which may be metastable phases. (more details in Sec 8.3).

Phase name	Lueshite high (I) <sup>[356]</sup>	Lueshite intermediate (II) <sup>[356]</sup>	sodium niobate (III) <sup>[357]</sup>	Lueshite low (IV) <sup>[368]</sup>	Lueshite low (V) <sup>[356]</sup>	$\text{LiNbO}_3$ (* ) <sup>[355]</sup>
Crystal system	cubic	tetragonal	Orthorhombic	orthorhombic	monoclinic	trigonal
Point group	$U_h$	$D_{4h}$	$D_{2h}$	$C_{2v}$	$C_s$	$C_{3v}$
Space group no.	$Pm\bar{3}m$ (221)	$P4/mmm$ (123)	$Pbma$ (57)	$P21ma$ (26)	$P12/m1$ (10)	$R3c$ (161)
Unit cell dimensions (Å)	$a = 3.9404$	$a = 3.9368$ $c = 3.9418$	$a = 5.5679(3)$ $b = 15.5156(8)$ $c = 5.5029(3)$	$a = 5.569(2)$ $b = 7.790(2)$ $c = 5.518(2)$	$a = 3.9234$ $b = 3.9234$ $c = 3.9234$ ( $\beta = 90.10^\circ$ )	$a = 5.1502(1)$ $c = 13.8653(4)$
Cell volume (Å <sup>3</sup> )	61.18	61.09	475.39(4)	239.38(14)	60.39	318.50(1)
Z	1	1	8	4	1	6
ICSD	28589	28587	89317	39624	28577	74469



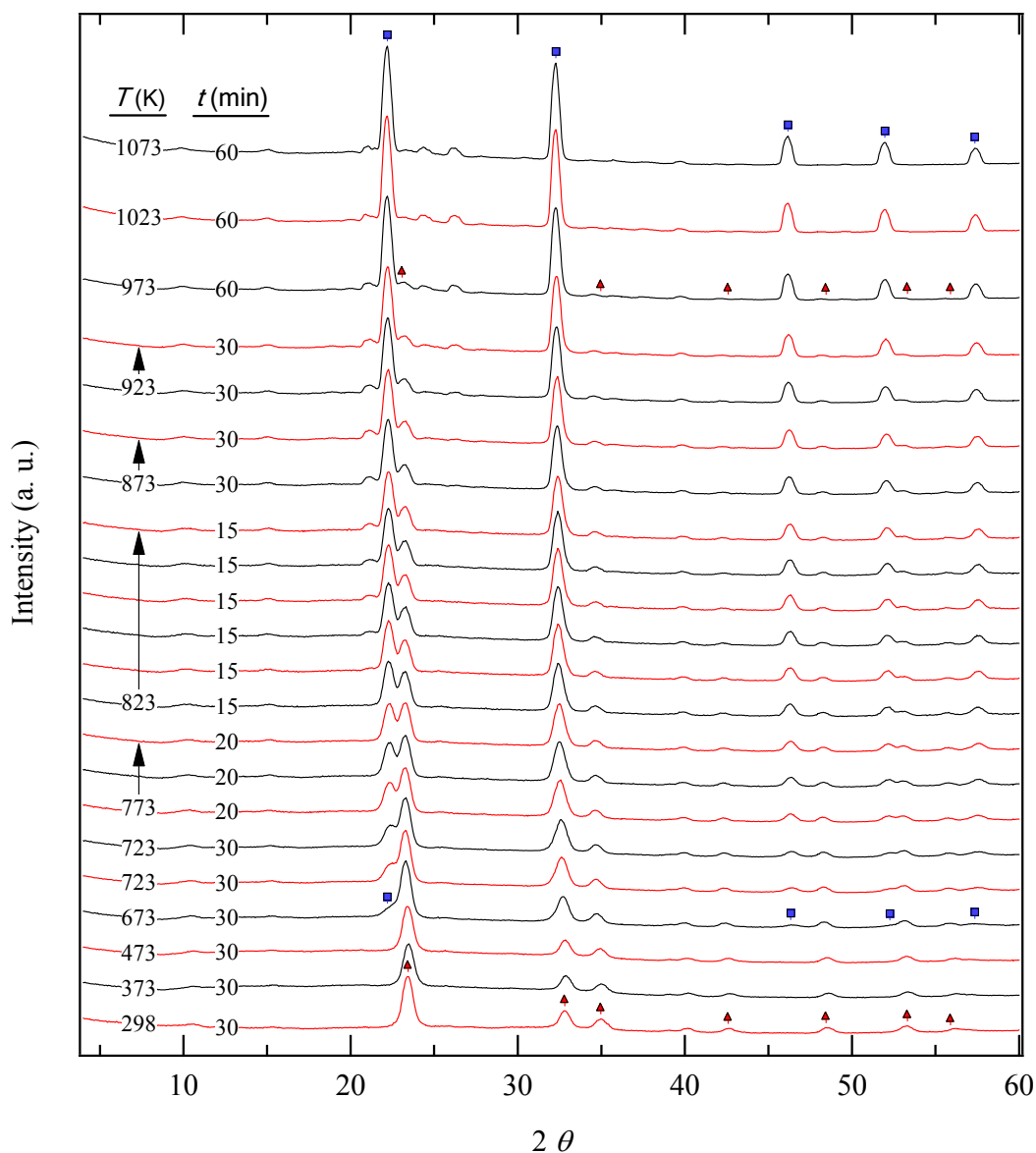


Fig. 8.1.3: In-situ x-ray for the composite  $n\text{-LiNbO}_3\text{-}g\text{-NaSi}_{1.5}\text{O}_{3.5}$  showing the transformation of  $\text{LiNbO}_3$  (▲) to  $\text{NaNbO}_3$  (■) with heating up for the indicated temperatures and periods. The markers indicate the appearance and disappearance of the phase.

### 8.1.2 Raman Spectroscopy

Fig. 8.1.4 shows the Raman spectra for the composite batches heated at different temperatures. The peaks obtained are sharp, thus the main features are attributed to the crystalline phases, not to the glassy matrix. The major Raman band appears in the  $610 - 625 \text{ cm}^{-1}$  region accompanied by a shoulder in the  $575 - 580 \text{ cm}^{-1}$  region. This band and its shoulder correspond to slightly different Nb—O bond lengths and are assigned to the symmetric stretching mode of the  $\text{NbO}_6$  octahedra in both  $\text{LiNbO}_3$  and  $\text{NaNbO}_3$ <sup>245</sup>.  $\text{LiNbO}_3$  contains a hexagonal close-packed structure in which the regular  $\text{NbO}_6$  octahedra are connected

by shared corners with a  $30^\circ$  tilting angle between two adjacent  $\text{NbO}_6$  octahedra and a  $0.26 \text{ \AA}$  off-center displacement of the Nb atom. It possesses similar Raman features as the perovskite  $\text{NaNbO}_3$  compound in the  $500 - 700 \text{ cm}^{-1}$  region. Additional Raman bands appear at  $\sim 874$ ,  $\sim 430$ ,  $\sim 365$ , and  $\sim 320 \text{ cm}^{-1}$  in the spectra of  $\text{LiNbO}_3$  and the composite treated at 873 and 973 K, Fig. 8.1.4 (a), (b), and (c), respectively. The intensity of these Raman bands is significantly decreased for  $\text{NaNbO}_3$  and the composite treated at 1173, 1273 K, Fig. 8.1.4 (g), (e), and (f), respectively. For  $\text{LiNbO}_3$ , the additional band at  $\sim 874 \text{ cm}^{-1}$  is assigned to the antisymmetric stretching mode of the Nb—O—Nb linkage, and the associated bending modes of the Nb—O—Nb linkage appear at  $\sim 430$  and  $\sim 365 \text{ cm}^{-1}$ , see Ref. [245]. For the perovskite modification of  $\text{NaNbO}_3$  the intensity of the Raman bands at  $\sim 874$ ,  $\sim 430$ , and  $\sim 375 \text{ cm}^{-1}$  significantly decreased. This is probably due to the lower tilt angle,  $18^\circ$ , between the adjacent octahedra (and they would disappear in the case of  $\text{KNbO}_3$  as there is no tilting). In our case, not only the  $\text{NaNbO}_3$  formed has perovskite structure but some is low Lueshite which deviates from the perovskite ideal structure and tends toward that of  $\text{LiNbO}_3$ . Furthermore multiple and strong Raman bands in the low wave-number region, between  $100$  and  $300 \text{ cm}^{-1}$ , are also observed mainly for  $\text{NaNbO}_3$  and highly similar to those obtained in the case of the composite treated at 1273 K.

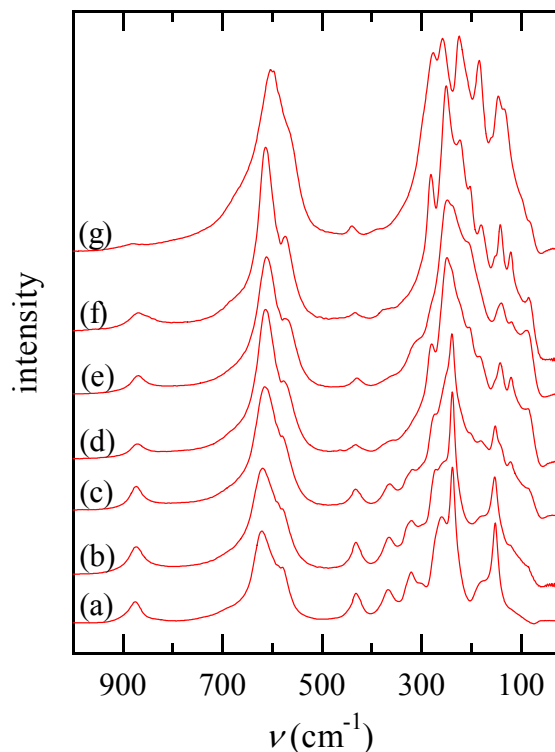


Fig. 8.1.4: Raman spectra showing the heating effect (2 h) on the composite  $n\text{-LiNbO}_3 \cdot \text{NaSi}_{1.5}\text{O}_{3.5}$  at: (b) 873, (c) 973, (d) 1073, (e) 1173, (f) 1273 K, [(a)  $\text{LiNbO}_3$ , and (g)  $\text{NaNbO}_3$  for comparison].

### 8.1.3 $^{29}\text{Si}$ , $^{93}\text{Nb}$ , $^{23}\text{Na}$ Nuclear Magnetic Resonance

Fig. 8.1.5(a) shows the  $^{29}\text{Si}$  MAS-NMR spectra of the composite  $n\text{-LiNbO}_3 \cdot g\text{-NaSi}_{1.5}\text{O}_{3.5}$  heated for 2 h at different temperatures. The figure also demonstrates the statistics obtained from the deconvolution of the  $^{29}\text{Si}$ -NMR lines into Gaussian lines. At 973 and 1073 K some dramatic changes took place; at 973 K, sharp (crystalline) peaks in the  $Q^2$ ,  $Q^3$ ,  $Q^4$  regimes appeared, while at 1073 K the sharp  $Q^2$  was absent and the sharp  $Q^3$  intensified whereas the two sharp peaks in the  $Q^4$  range appeared with opposite relative intensities. According to  $^{29}\text{Si}$  NMR, the pure sodium silicate glass,  $\text{Na}_2\text{Si}_3\text{O}_7$ , consists of two broad Q species; namely  $Q^3$  and  $Q^4$ . Their relative abundance is  $64.3 : 35.7$ , respectively. This is in consistency with the ratio of  $2 : 1$ , as expected from the chemical formula. Heating the composite  $n\text{-LiNbO}_3 \cdot g\text{-NaSi}_{1.5}\text{O}_{3.5}$

up to 973 K increases the percentage of the Q<sup>3</sup> slightly. After that, the Q<sup>4</sup> vanishes, to be replaced by Q<sup>2</sup> at higher temperature, while the Q<sup>3</sup> continues to keep nearly constant percentage. The whole spectra became broader and shifted slightly towards higher  $\delta$  values. These changes in the broad Q species indicate a considerable change in the structure of the glass toward a less polymerized composition at the temperatures between 973 K and 1073 K. Fig. 8.1.5(b) shows that Q<sup>3</sup> is the dominant species in the glass as well as in

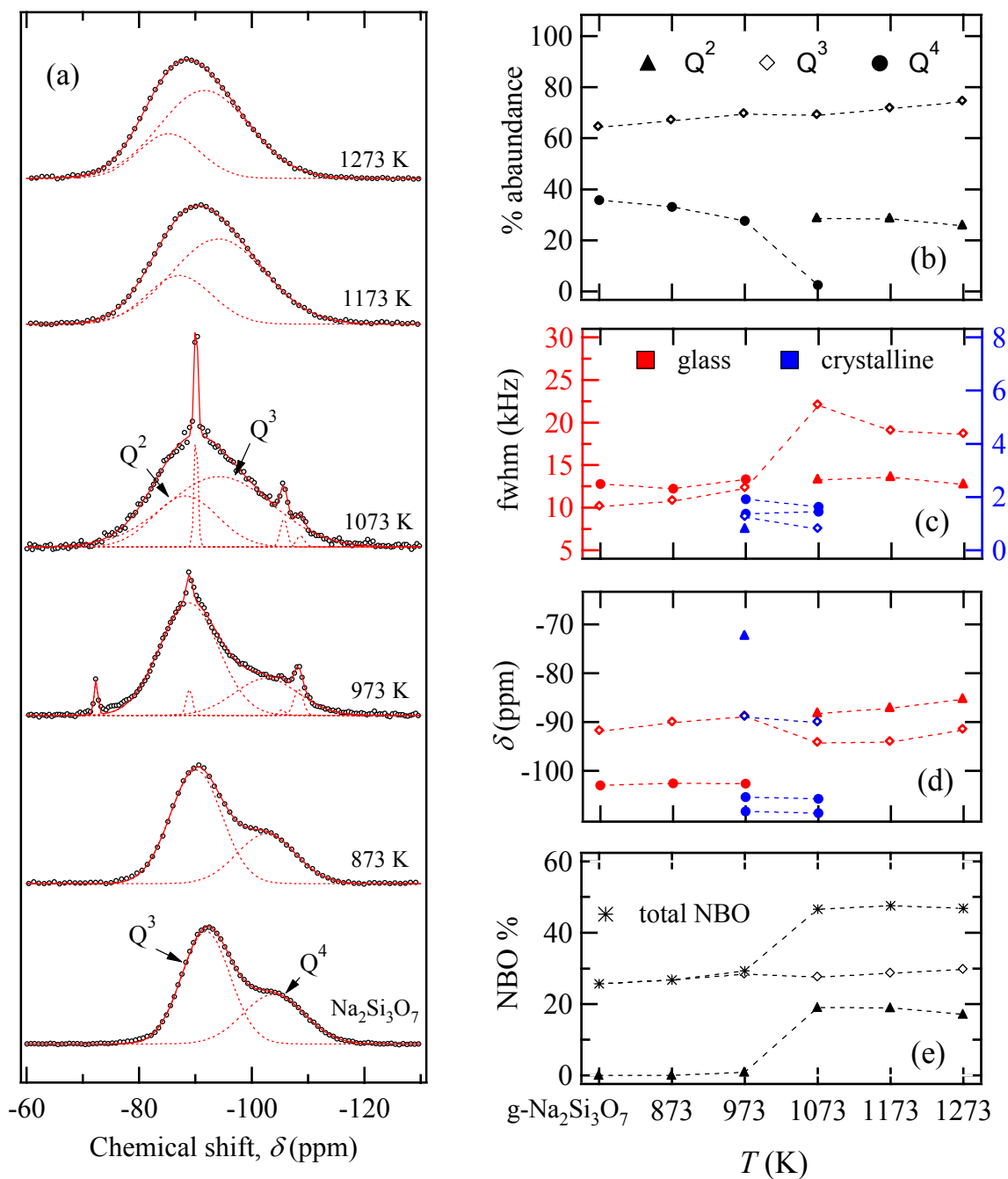


Fig. 8.1.5: (a) <sup>29</sup>Si NMR lines for the composite n-LiNbO<sub>3</sub>-g-NaSi<sub>1.5</sub>O<sub>3.5</sub> heated for 2 h at the indicated temperatures. (b) Abundance, (c) FWHM, (d) chemical shift values of Q<sup>n</sup>s. (e) The percentage of the non-bonding oxygens to the total number of oxygen around <sup>29</sup>Si calculated from the deconvolution of the NMR lines for both the glassy and the crystalline phases. Na<sub>2</sub>Si<sub>3</sub>O<sub>7</sub> glass is given for comparison.

the composite with a relative abundance of 65 to 70 %. Furthermore, it shows the decrease in the percentage of the  $Q^4$  species which reaches its end at 1073 K. Here, the  $Q^4$  species is replaced by a  $Q^2$  with a relative abundance of 28 % to continue at higher temperatures with constant percentage. Fig. 8.1.5(c) shows the full width at half maxima (fwhm) of the Q species. It shows a significant increase in the  $Q^3$  width at 1073 K. With increasing treatment temperature, the positions of the Q species are slightly shifted toward higher values, Fig. 8.1.5(d). The percentage of the non-bridging oxygens (NBO) relative to the total number of oxygens reveals a constant percentage of about 27 % up to 973 K, and then it increases sharply to 47 % at 1073 K and continued at the same level up to 1273 K, Fig. 8.1.5(e).

Heat treatment converts  $\text{LiNbO}_3$  in the composite gradually to several crystallographic modifications of  $\text{NaNbO}_3$ . Thus using any NMR-fitting software to model the obtained  $^{93}\text{Nb}$ -NMR spectra will not be a trouble-free task. Hence,  $^{93}\text{Nb}$  NMR spectra of the microcrystalline  $\text{NaNbO}_3$ ,  $\text{LiNbO}_3$ , and  $\text{Nb}_2\text{O}_5$  were measured for comparison. The spectrum  $\text{Nb}_2\text{O}_5$  was quite different and as a consequence it was excluded. This was also supported by the absence of any  $\text{Nb}_2\text{O}_5$  phase from the XRD diffractograms and their re-

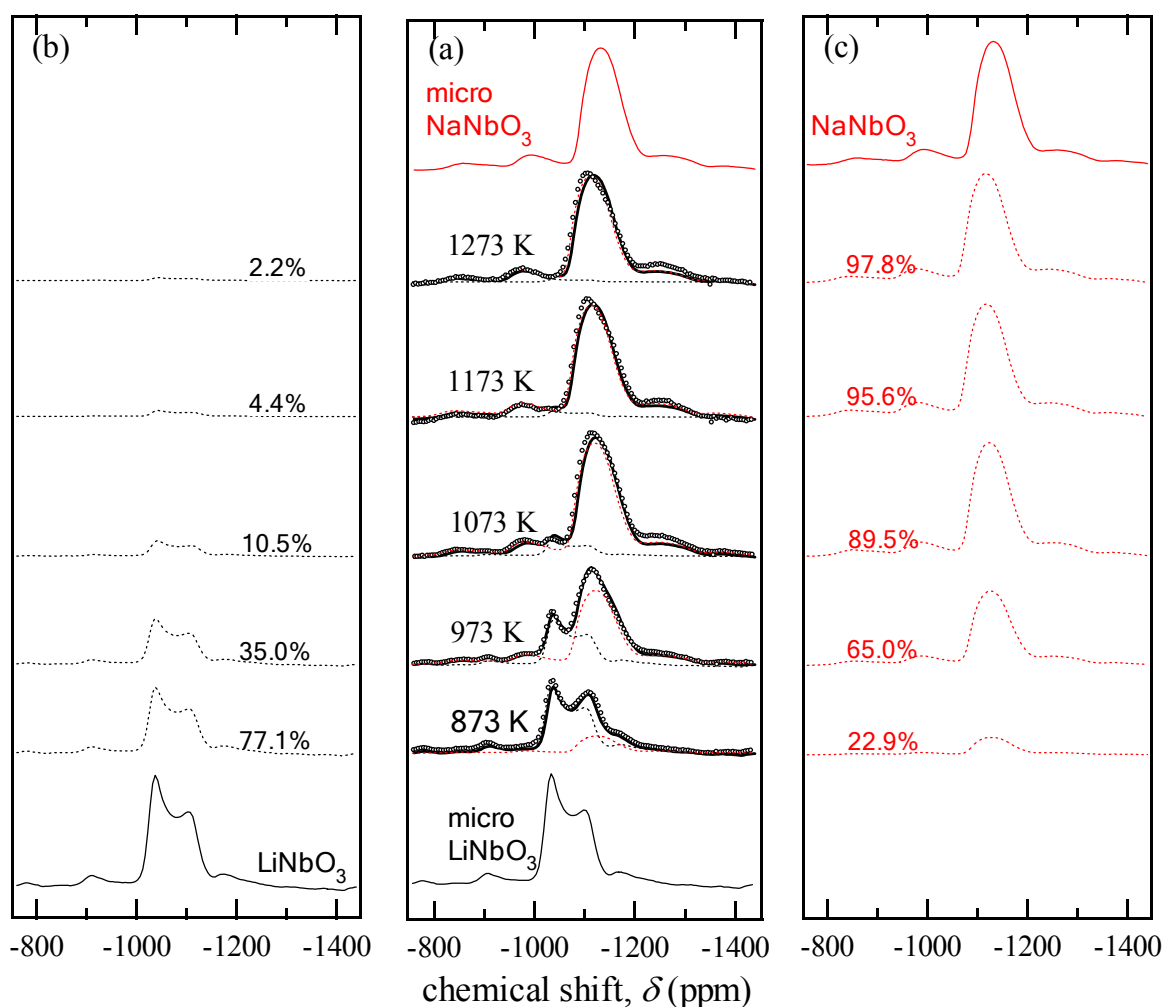


Fig 8.1.6: (a)  $^{93}\text{Nb}$  NMR lines for the n- $\text{LiNbO}_3$ ·g- $\text{NaSi}_{1.5}\text{O}_{3.5}$  composite after heating for 2 h at the indicated temperatures measured at 97.8 MHz and fitted using the  $^{93}\text{Nb}$  NMR lines of commercial  $\text{LiNbO}_3$  (---) and  $\text{NaNbO}_3$  (- - -) as standards. (b) and (c) show the relative contribution of  $\text{LiNbO}_3$  and  $\text{NaNbO}_3$ , respectively.

finement. LiNbO<sub>3</sub> and NaNbO<sub>3</sub> spectra were used as standards for fitting the obtained spectra for the n-LiNbO<sub>3</sub> · g-NaSi<sub>1.5</sub>O<sub>7</sub> composite. The <sup>93</sup>Nb NMR line of LiNbO<sub>3</sub> agrees with the literature as was shown in Sec. 7.1.1.3 and discussed in details in Sec. 7.1.1.4. For NaNbO<sub>3</sub>, the shift of the NMR resonance is about 1095.78 ppm, and a coupling constant  $C_Q = 17.44$  MHz ( $\eta = 0$ ). However, these values have a weak agreement with literature values as Prasad *et al.*<sup>290</sup> found a resonance shift of about 1073 ppm, and  $C_Q = 22.7$  MHz, whereas Wolf *et al.*<sup>358</sup> reported  $C_Q = 19.7$  MHz and  $\eta = 0.82$ . The standard spectra were added with varying mixing ratios until a good fit was achieved, Fig. 8.1.6(a). In Fig. 8.1.6(a) the circles represent the measured data points and the solid lines are the total fit, while the dashed lines stand for the contribution of LiNbO<sub>3</sub> and NaNbO<sub>3</sub> which are shown separately in Fig. 8.1.6(b) and (c), respectively. The relative amount for each compound was obtained by integrating the area under the <sup>93</sup>Nb-NMR spectrum of each phase relative to the whole lines, Fig. 8.1.7 (the solid line). The figure shows a comparison with the percentages obtained from XRD structure refinement. It is clear that the XRD underestimates the LiNbO<sub>3</sub> content and consequently NaNbO<sub>3</sub> is overestimated due to the low atomic scattering factor of the light Li atom. Nevertheless, both techniques, i.e. <sup>93</sup>Nb-NMR and XRD showed a similar trend: At 873 K, 973 K, and 1073 K, the conversion of LiNbO<sub>3</sub> to NaNbO<sub>3</sub> proceeds with a high rate where only ~ 10 % of LiNbO<sub>3</sub> are left at 1073 K. Afterwards the conversion continued with a slower rate towards completion.

<sup>23</sup>Na MAS NMR spectra are shown in Fig. 8.1.8. The Na<sub>2</sub>Si<sub>3</sub>O<sub>7</sub> glass shows a very broad featureless spectrum, while in the case of the n-LiNbO<sub>3</sub> · g-NaSi<sub>1.5</sub>O<sub>3.5</sub> composite heated for 2 h at 873 K the spectrum has a sharp contribution superimposed on the broad one. This sharp part of the

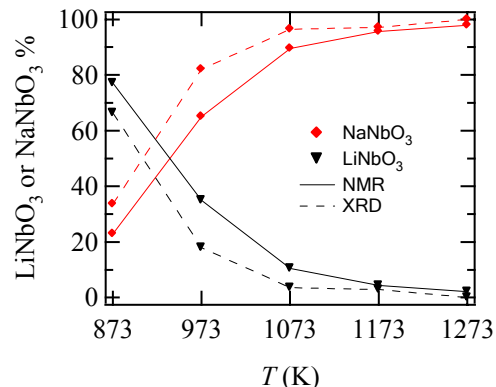


Fig. 8.1.7: The relative percentage of LiNbO<sub>3</sub> and NaNbO<sub>3</sub> obtained from Nb NMR fitting (solid lines) in comparison with those obtained from Rietveld refinement of the XRD data (dashed line).

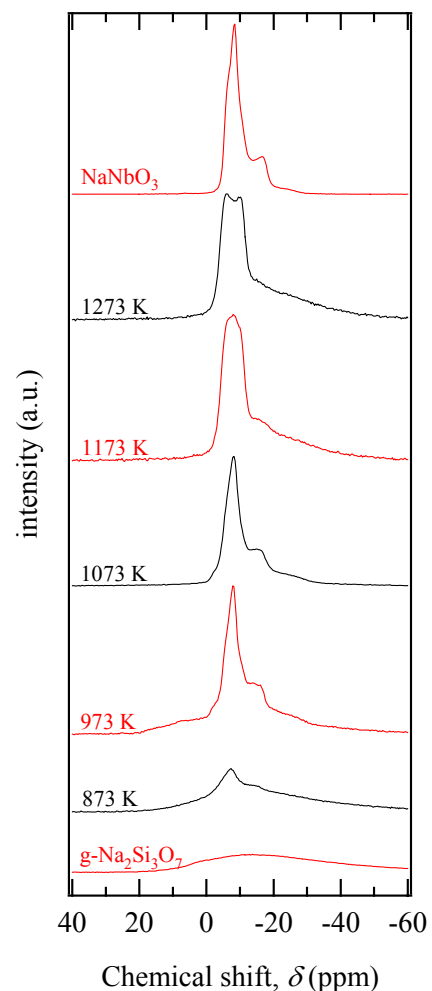


Fig. 8.1.8: <sup>23</sup>Na MAS-NMR lines for the n-LiNbO<sub>3</sub> · g-NaSi<sub>1.5</sub>O<sub>3.5</sub> measured at room temperature and 105.8 MHz after being heated for 2 h at the indicated temperatures at a spinning rate of 12.5 kHz. The spectra for NaNbO<sub>3</sub> and g-Na<sub>2</sub>Si<sub>3</sub>O<sub>7</sub> are shown for comparison.

line became larger at 973 K; however, the broad 'glassy' background is still recognizable. After heating at 1073 K the obtained spectrum resembles that of the commercial microcrystalline  $\text{NaNbO}_3$ . At this stage, the glassy background is nearly absent (or at least in its minimum state) indicating that most of the sodium is in the crystalline niobate phase to compensate for the lost Li with minor amount of sodium, if any, left in the glass phase. After that (at 1173, 1273 K) the line started to broaden and the glassy background re-appeared which may be due to the dissolution of  $\text{NaNbO}_3$  in the glass at these higher temperatures besides the formation of more than one crystalline phase of  $\text{NaNbO}_3$  [Lueshite high and low and the orthorhombic form]. This was confirmed by the broadening of the  $^{23}\text{Na}$  NMR line and its splitting at 1273 K and also by XRD refinement. Another possibility is that a considerable fraction of the sodium may be enclosed in the  $(\text{Li},\text{Na})_2\text{Si}_2\text{O}_5$  crystalline phase at 1073 K which results in a relatively sharp  $^{23}\text{Na}$  NMR line. At higher temperature, this crystalline phase dissolve to bring the Na back to the glass.

### 8.1.4 Impedance Spectroscopy

The temperature dependence of the dc-conductivity reveals Arrhenius behavior in the measured temperature range for the composites  $n\text{-LiNbO}_3 \cdot g\text{-NaSi}_{1.5}\text{O}_{3.5}$  heated for 2 h at different temperatures, Fig. 8.1.9(a). The conductivity values increase slightly for the composite heated at 873 K due to the softening of the glass grain boundaries and the reduction of the porosity which enhances the connectivity between the glass particles in the composite. Then a sharp decrease is observed when the samples are heated up to 973 and 1073 K. This decrease agrees with the appearance of the new crystalline phases and the

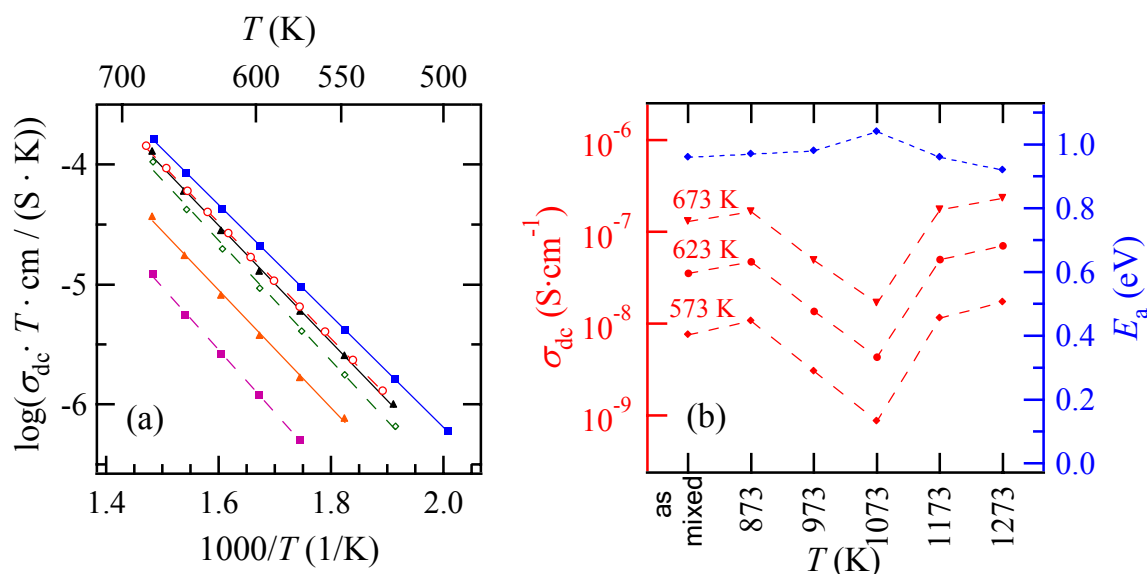


Fig. 8.1.9: (a) Arrhenius plots for the  $n\text{-LiNbO}_3 \cdot g\text{-Na}_2\text{Si}_3\text{O}_7$  composites heated for 2 h at: ( $\blacktriangle$ ) 873, ( $\blacktriangle$ ) 973, ( $\blacksquare$ ) 1073, ( $\circ$ ) 1173, ( $\blacksquare$ ) 1273 K, and ( $\diamond$ ) for the as-mixed composite. The lines represent the best Arrhenius fit. (b) Variation in the dc-conductivity and its activation energy with changing treatment temperature. The dc-conductivity values are shown for three measurement temperatures only (573, 623, and 673 K). The data points of the top curve represent the activation energy (left-hand scale).

dramatic changes in the <sup>29</sup>Si-NMR results and may be attributed to the inclusion of the mobile ions in the new crystalline phase ((Li,Na)<sub>2</sub>Si<sub>2</sub>O<sub>5</sub>) in addition to the formation of the crystalline quartz and cristobalite that may exhibit insulating effects. Afterwards a sharp rise in the conductivity can be seen at 1173 K which continues slightly up to 1273 K. This increase can be ascribed to the disappearance of the insulating silica phases (quartz and cristobalite) and the dissolution of the (Li,Na)<sub>2</sub>Si<sub>2</sub>O<sub>5</sub> crystalline phases which releases the mobile ions again into the glassy phase. The exchanged glass is likely to be more conductive than the parent glass as the majority of its modifier is Li, the faster ion. Furthermore, the dissolution of some of the crystalline niobates with their modifier in the glass at such high temperatures may be behind this increase in conductivity. This can be clearly seen in Fig. 8.1.9(b) which shows the variation in the activation energies as well as in conductivity. The activation energies vary between 0.96 and 0.92 eV, this can be regarded as an insignificant change except a slight maximum (1.04 eV) when the composite is heated at 1073 K and matches the minimum in conductivity. That is where the material is mostly heterogeneous. Consequently, it is difficult for the diffusing ions to find easy (i.e. continuous) pathways.

## 8.2 COMPOSITION EFFECT

### 8.2.1 X-Ray Diffraction

To investigate the composition effect, several batches of  $(x)n\text{-LiNbO}_3 \cdot (1-x)\text{g-NaSi}_{1.5}\text{O}_{3.5}$  were heated for 2 h at 1173 K. This temperature was chosen upon the results of studying the temperature effect as this is the temperature at which the Li-Na exchange reached completion and the intermediate crystalline phases [quartz low, cristobalite low and  $(\text{Li,Na})_2\text{Si}_2\text{O}_5$ ] were absent. The XRD diffractograms in Fig. 8.2.1 show that the  $\text{LiNbO}_3$ -to- $\text{NaNbO}_3$  conversion proceeds toward completion as long as the molar fraction of Li is less than that of Na in the glass (i.e. for  $x \leq 0.5$ ). Otherwise the Na coming from glass will be depleted leaving an excess of unconverted  $\text{LiNbO}_3$  (for  $x > 0.5$ ). The results of the Rietveld-structure refinement of the XRD patterns are summarized in Table 8.2.1, and Fig. 8.2.2.

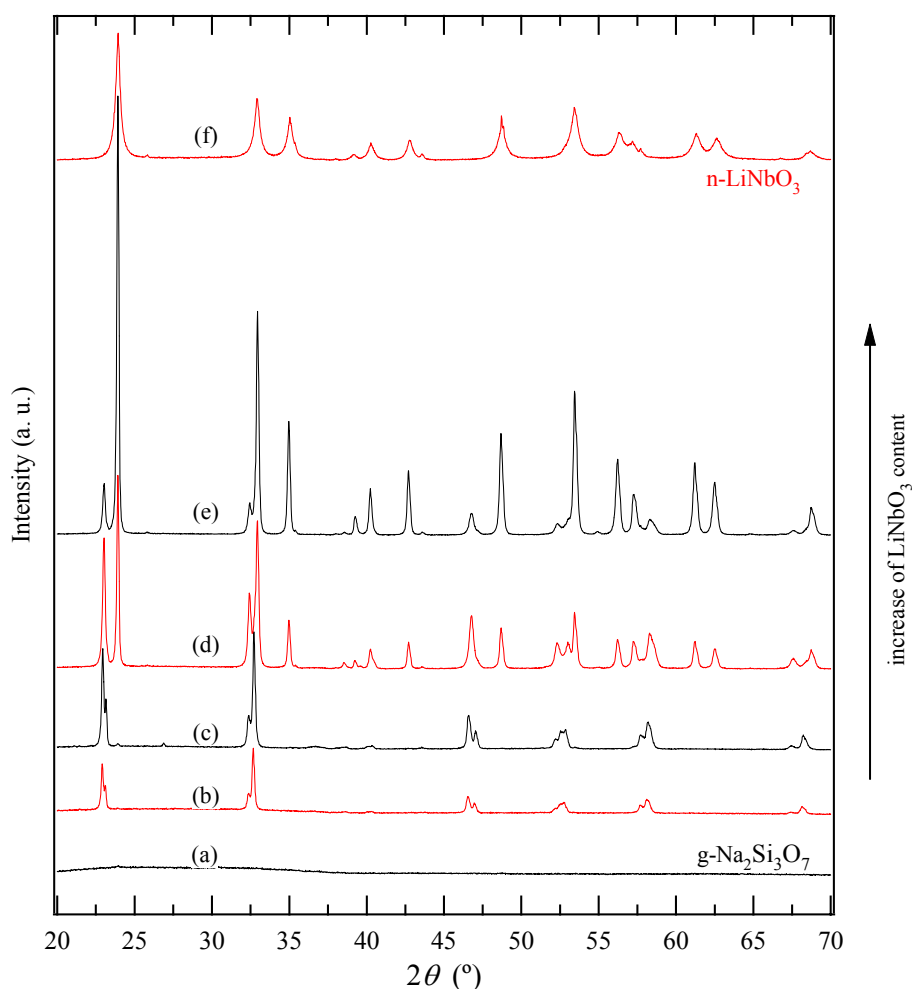


Fig. 8.2.1: Ex-situ XRD pattern for the composite  $(x)n\text{-LiNbO}_3 \cdot (1-x)\text{g-NaSi}_{1.5}\text{O}_{3.5}$  after heating for 2 h at 1173 K with  $x$ : (a) 0.0 ( $\text{g-NaSi}_{1.5}\text{O}_{3.5}$ ), (b) 0.20, (c) 0.40, (d) 0.60, (e) 0.80, (f) 1.00 ( $n\text{-LiNbO}_3$ ).



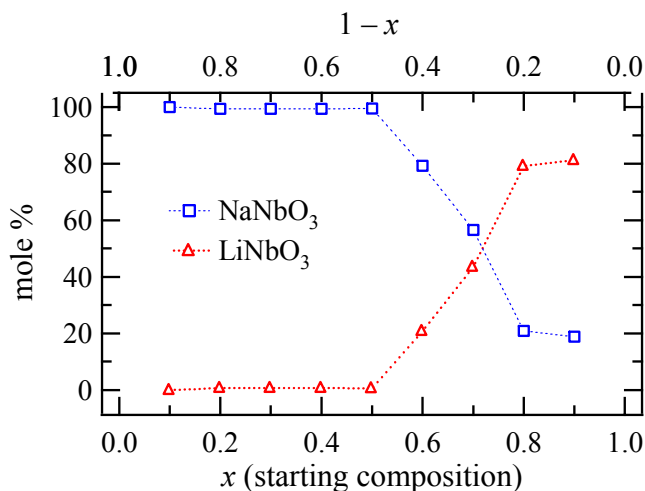


Figure 8.2.2: Mole % of LiNbO<sub>3</sub>, NaNbO<sub>3</sub> in the crystalline phase obtained after heat treatment for 2 h at 1173 K in the composite  $(x)\text{n-LiNbO}_3 \cdot (1-x)\text{g-NaSi}_{1.5}\text{O}_{3.5}$ , showing the effect of varying the starting compositions,  $x$ .

Table 8.2.1: Mole % of LiNbO<sub>3</sub>, NaNbO<sub>3</sub> in the crystalline phase obtained after heat treatment for 2 h at 1173 K for the composite:  $(x)\text{n-LiNbO}_3 \cdot (1-x)\text{g-NaSi}_{1.5}\text{O}_{3.5}$  with different starting compositions,  $x$ .

starting composition	final crystalline phase	
	LiNbO <sub>3</sub>	NaNbO <sub>3</sub>
$x$		
10	0.00	100
20	0.63	99.36
30	0.66	99.34
40	0.63	99.38
50	0.59	99.41
60	20.82	79.18
70	43.46	56.54
80	79.10	20.90
90	81.14	18.86

## 8.2.2 Raman Spectroscopy

Fig. 8.2.3 shows the Raman spectra for the composite  $(x)\text{n-LiNbO}_3 \cdot (1-x)\text{g-NaSi}_{1.5}\text{O}_{3.5}$ . The resulting peaks are sharp and attributed to the crystalline phases. Fig. 8.2.3(b) shows the spectrum obtained for the composite with  $x=0.8$  which looks similar to that of LiNbO<sub>3</sub>, Fig. 8.2.3(a), indicating that the predominant phase is the unconverted LiNbO<sub>3</sub> because of the limited amount of sodium offered by the glass. At  $x=0.5$ , Fig. 8.2.3(c), the spectrum differs from that of LiNbO<sub>3</sub>; the bands at  $\sim 370$  disappeared and those at  $\sim 430$  and  $\sim 320$   $\text{cm}^{-1}$  are weakened implying that all the LiNbO<sub>3</sub> is converted into NaNbO<sub>3</sub>. Taking into account that both sodium and lithium niobate share the main features (i.e. the main band in the  $610 - 625$   $\text{cm}^{-1}$  region, and a shoulder in the  $575 - 580$   $\text{cm}^{-1}$  region), one can see that at  $x=0.2$ , Fig. 8.2.3(d), the spectrum resembles that of sodium niobate, (c.f. mainly the bands at  $280, 250, 220, 177, 140, 120$   $\text{cm}^{-1}$ ). The intensity of the Raman bands at  $\sim 870, \sim 430$ , and  $\sim 370$   $\text{cm}^{-1}$  are significantly decreased due to the conversion to less tilted octahedra as in the perovskite modification of NaNbO<sub>3</sub>.

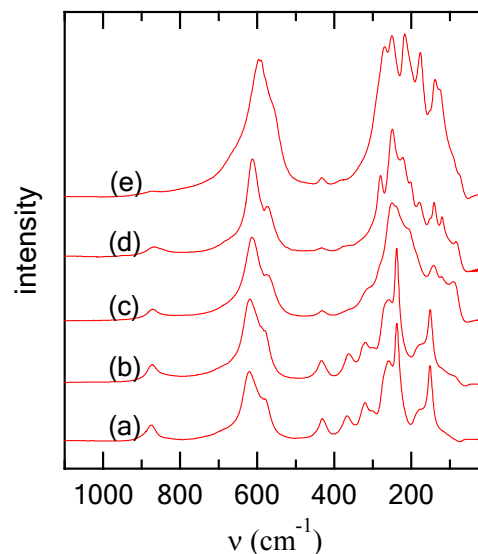


Fig. 8.2.3: Raman spectra for the composite  $(x)\text{n-LiNbO}_3 \cdot (1-x)\text{g-NaSi}_{1.5}\text{O}_{3.5}$  showing the composition effect on samples heated at 1173 K for 2 h with  $x =$  (a) 1.0 (LiNbO<sub>3</sub>), (b) 0.8, (c) 0.5, (d) 0.2, and (e) for NaNbO<sub>3</sub>.

### 8.2.3 $^{29}\text{Si}$ , $^{93}\text{Nb}$ , $^{23}\text{Na}$ MAS-NMR

In Fig. 8.2.4(a), the  $^{29}\text{Si}$  MAS-NMR spectra demonstrate the effect of varying the composition in  $(x)\text{n-LiNbO}_3 \cdot (1-x)\text{g-NaSi}_{1.5}\text{O}_{3.5}$  after heating for 2 h at 1173 K. When increasing  $x$ , the lines get broader and are slightly shifted toward higher  $\delta$ -values. Fig. 8.2.4(b) shows that  $\text{Q}^3$  is the dominant species ( $\sim 65\%$ ) for the glass. This abundance increased to  $\sim 70\%$  when  $x$  was 0.2, then it increased again to 72% and to 92% when  $x$  was raised to 0.5 and 0.8, respectively. In addition, the abundance of the  $\text{Q}^4$  from 36% in the pure glass to 29% in the composite with  $x = 0.2$ . After that it disappears to be replaced by  $\text{Q}^2$ . The fwhm of the  $\text{Q}^3$  increases with increasing  $\text{LiNbO}_3$  content(c).

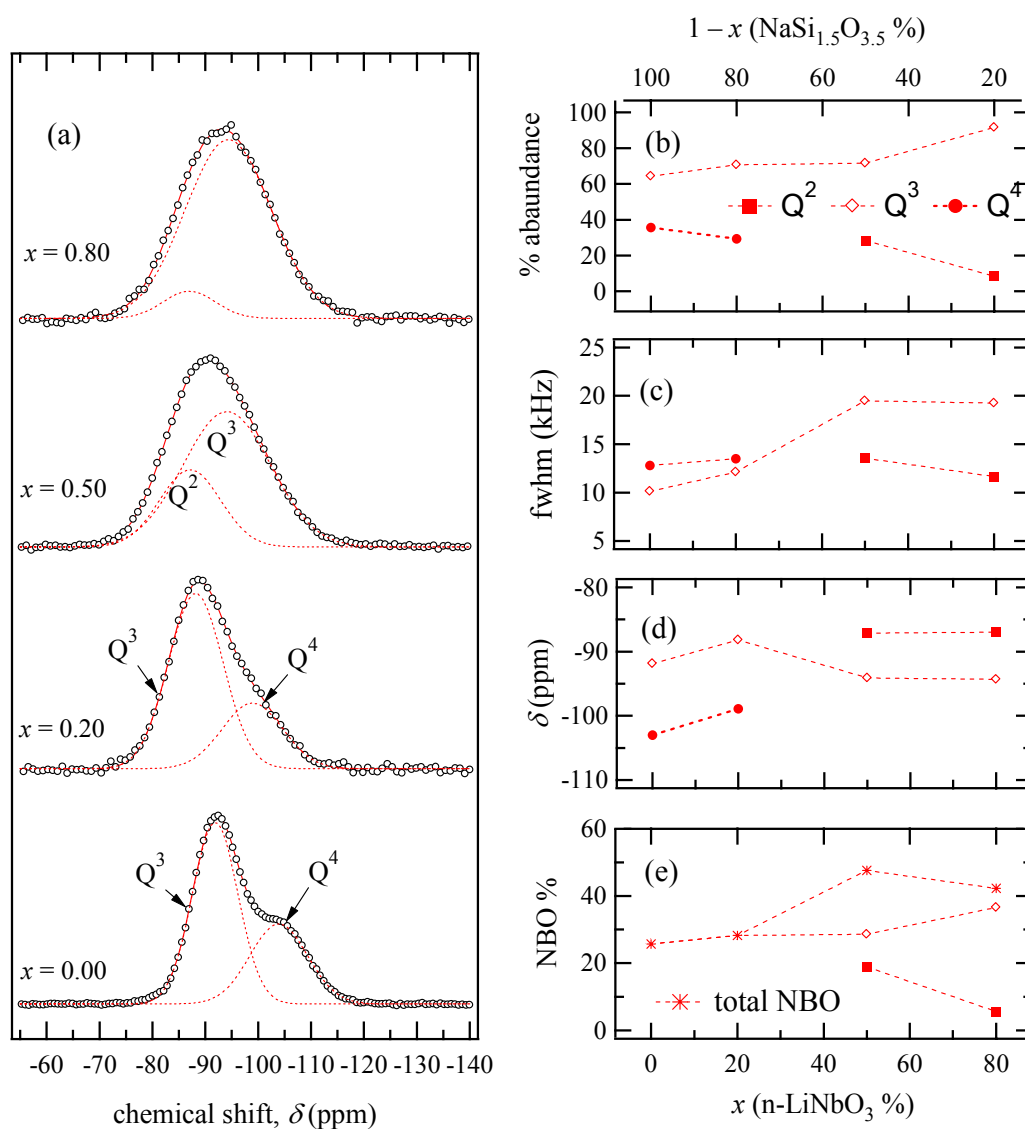


Fig. 8.2.4: (a) Simulated  $^{29}\text{Si}$  MAS NMR spectra of the composite  $(x)\text{n-LiNbO}_3 \cdot (1-x)\text{NaSi}_{1.5}\text{O}_{3.5}$  with  $x = 0$  (glass), 0.20, 0.50, 0.80 after heating for 2 h at 1173 K. (b)  $\text{Q}^n$  abundance, (c) fwhm, (d) chemical shift values  $\delta$ , and (e) the percentage of the NBO to the total number of oxygen atoms around the  $^{29}\text{Si}$  atom.

Upon the introduction of n-LiNbO<sub>3</sub> the position of both Q<sup>3</sup> and Q<sup>4</sup> species is shifted towards higher values. At  $x = 0.2$ , the two Q species seem to keep their relative intensity with being shifted toward higher chemical shift. This may be due to the Li-Na ion exchange without affecting the network structure. Afterwards, when  $x$  reaches 0.5, the network falls apart and the Q<sup>4</sup> is replaced by Q<sup>2</sup> and the entire peak becomes broader. The positions of the peaks remain nearly unchanged at  $x = 0.5$  and 0.8, Fig. 8.2.4(d). The percentage of the NBOs relative to the total number of oxygen atoms increasing from 26 % in the pure sodium silicate glass to 28 % at  $x = 0.2$  to then the network falls apart and this value raises to more than 45 %, Fig. 8.2.4(e).

Fig. 8.2.5 (a) shows the <sup>93</sup>Nb-NMR spectra for the composite  $(x)n\text{-LiNbO}_3 \cdot (1-x)g\text{-NaSi}_{1.5}\text{O}_{3.5}$  heated at 1173 K for 2 h. The composites with  $x = 0.2$  and 0.5 show Nb-NMR lines which resemble that of NaNbO<sub>3</sub> only and not LiNbO<sub>3</sub> which emphasizes that the crystalline LiNbO<sub>3</sub> has completely exchanged its lithium content by sodium. However, at  $x = 0.5$  the intensity is higher due to the higher amount of NaNbO<sub>3</sub> formed. In the case of  $x = 0.8$  the resultant <sup>93</sup>Nb line is a mixture of the lines of LiNbO<sub>3</sub> and NaNbO<sub>3</sub>, as shown in the figure, and the ratio of the areas under the two contributions is 75.6 : 24.4. This

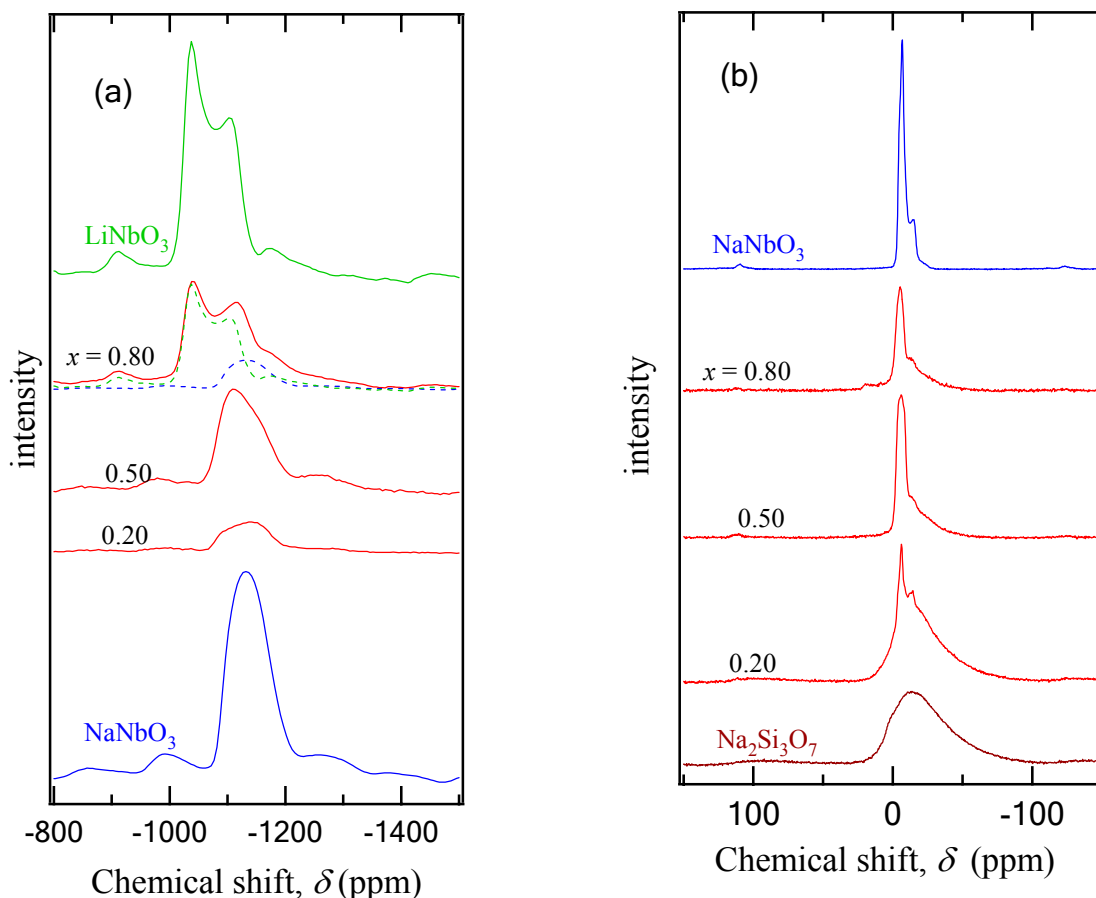


Fig 8.2.5: (a) <sup>93</sup>Nb (b) <sup>23</sup>Na MAS-NMR lines measured for the composite  $(x)n\text{-LiNbO}_3 \cdot (1-x)g\text{-NaSi}_{1.5}\text{O}_{3.5}$  with  $x = 0.2, 0.5, 0.8$  after heating for 2 h at 1173 K, with a spinning frequency of 12.5 kHz. LiNbO<sub>3</sub>, NaNbO<sub>3</sub> and Na<sub>2</sub>Si<sub>3</sub>O<sub>7</sub> spectra are given for comparison.

is equivalent to 3 : 1, the exact ratio expected from complete exchange; as  $\text{Na}^+$  supply from the glass is the limiting factor for the exchange.

The  $^{23}\text{Na}$ -NMR spectra for the same samples are shown in Fig. 8.2.5(b). At  $x = 0.2$ , the spectrum shows a sharp contribution similar to that of  $\text{NaNbO}_3$  mounted on top of a broad line which is attributed to sodium in the  $\text{Na}_2\text{Si}_3\text{O}_7$  glass. This suggests that a fraction of Na ions is now involved in the crystalline niobate phase maintaining a large amount of sodium in the glassy phase. Starting from  $x = 0.5$  the broad line disappeared, implying that the sodium no longer exists in the glass which emphasizes the result obtained from the Nb-NMR and XRD, i.e. that the sodium supply from the glass is the limiting factor for the exchange process; glass is exhausted as a sodium source for  $x \geq 0.5$ .  $^7\text{Li}$  NMR spectra were also measured; however, they are not shown as the high Li diffusivity averages out any information about the structural details or specific environments in the glass composite.

## 8.2.4 Impedance Spectroscopy

Fig. 8.2.6(a) shows the temperature dependence of the conductivity with changing composition of the composite  $(x)\text{n-LiNbO}_3 \cdot (1-x)\text{g-NaSi}_{1.5}\text{O}_{3.5}$ . The plots show a linear temperature dependence (Arrhenius behavior) with rather similar slopes. The values of the dc-conductivity decrease gradually with increasing  $\text{LiNbO}_3$  content,  $x$ . When  $x$  is increased from 0 up to 0.1 there is no significant change in conductivity. In the range  $0.1 \leq x \leq 0.3$ , however, the decrease in the conductivity is sharp. Afterwards it continues to decrease moderately up to  $x = 1$ . These changes can be clearly seen in Fig. 8.2.6(b). The activation energy increases from about 0.8 to 1 eV when changing  $x$  from 0 to 0.3 and then continues to vary moderately and roughly around the value  $\sim 1$  eV over the rest of the composition range. This can be attributed to the

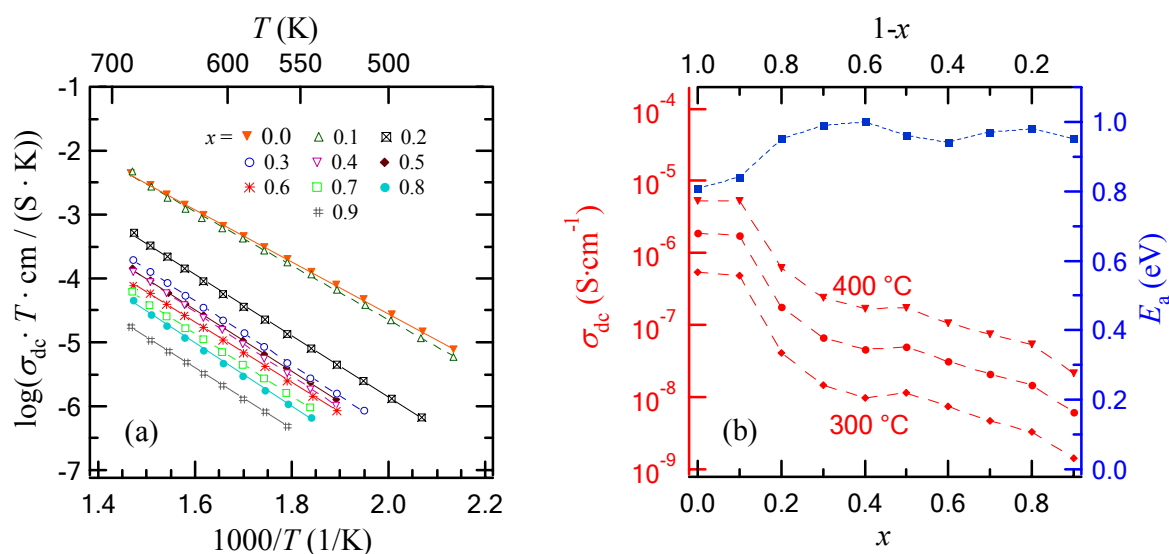


Fig. 8.2.6: (a) Arrhenius plot for the  $(x)\text{n-LiNbO}_3 \cdot (1-x)\text{g-Na}_2\text{Si}_3\text{O}_7$  composite heated for 2 h at 1173 K for  $x$  ranging from 0.0 to 0.9. The lines represent the best linear fit. (b) The variation in the activation energy (top curve) and the dc-conductivity with changing the composite composition at three chosen temperatures 573, 623, 673 K.

fact that the glass is more conductive than the crystalline LiNbO<sub>3</sub>. When the latter is introduced with a small amount ( $x \approx 0.1$ ), the amount of [NbO<sub>6</sub>]<sup>-</sup> that enters the glass is very limited and can be accommodated without the need for charge balance. After that, i.e. at  $x \geq 0.2$ , each [NbO<sub>6</sub>]<sup>-</sup> octahedron will necessitate one alkali ion for charge neutrality to dissolve in the glass which will reduce the number of alkali ions available for conduction.

### 8.3 DISCUSSION

Upon heating the LiNbO<sub>3</sub> nanoparticles embedded in Na<sub>2</sub>Si<sub>3</sub>O<sub>7</sub> glass powder, LiNbO<sub>3</sub> was transformed into NaNbO<sub>3</sub>. This transformation started at the relatively low temperature of about 673 K as can be seen from the *in-situ* XRD measurements. This was also evident from the presence of a considerable amount of NaNbO<sub>3</sub> after heating for 2 h at 873 K, as shown by the <sup>23</sup>Na and <sup>93</sup>Nb NMR results as well as the *ex-situ* XRD results. It is expected that heating up to such high temperatures will induce grain-boundary relaxation and grain growth, and the LiNbO<sub>3</sub> particles will no longer be nanocrystals. Nevertheless starting with nanoparticles may account for the early onset of the cation exchange process by increasing the contact surfaces between the glassy and the crystalline phases. The exchange reached completion (about 99 %) at 973 K in the *in-situ* XRD and after 2 h of heating at 1073 K in the *ex-situ* case, as was also confirmed by <sup>23</sup>Na and <sup>93</sup>Nb MAS-NMR. At the temperatures 973 K and 1073 K dramatic changes occurred: Extra phases started to show up: (i) Lithium disilicate doped with sodium, (Li,Na)<sub>2</sub>Si<sub>2</sub>O<sub>5</sub>, which accounts for ~ 28 % of the crystalline phase at 973 K and ~ 18 % at 1073 K. A sharp <sup>29</sup>Si-NMR peak located at -91.1 ppm (in the Q<sup>3</sup> range) can be attributed to this phase (synthetic Li<sub>2</sub>Si<sub>2</sub>O<sub>5</sub> shows Q<sup>3</sup> at -92.5 ppm and synthetic α-Na<sub>2</sub>Si<sub>2</sub>O<sub>5</sub> at -94.5 ppm<sup>359</sup>). At 973 K, this peak accounts for ~ 3 % of the silicates whereas at 1073 K it rises up to ~ 14 %. (ii) Crystalline silica in the forms of quartz low and cristobalite low constitutes about 9 % of the crystalline phases according to XRD structure refinement. According to <sup>29</sup>Si NMR, it constitutes about 8 % of the silicon present in the sample. The sharp Q<sup>4</sup> peak at -107.36 can be ascribed to the quartz low which has a literature  $\delta$  value of -107.4 ppm<sup>360-361</sup>. The percentage of this Q<sup>4</sup> increased from 0.39 % to 1.73 % with increasing the temperature from 973 to 1073 K. This is in agreement with the increase in the percentage of quartz low from 2.7 % to 6.05 % as obtained from the XRD structure refinement. The second sharp Q<sup>4</sup> peak at -110.82 ppm is attributed to cristobalite low (literature  $\delta$  value is -108.5 ppm<sup>360,361</sup>). The percentage of this Q<sup>4</sup> decreased from 2.55 to 0.79 % by increasing the temperature from 973 to 1073 K. This agrees with the decrease of the percent of cristobalite low from 6.44 % to 2.43 % as estimated by the XRD structure refinement. At 973 K a sharp line at -74.63 ppm (Q<sup>2</sup>) was found to represent 2.3 % of the silicon in the sample which may be attributed to Li<sub>2</sub>SiO<sub>3</sub> (the literature value is -74.5 ppm<sup>362</sup>). This may be undetectable by XRD because of its small amount especially as it contains lithium which has a low atomic scattering factor. Another less likely pos-

sibility is the formation of  $\text{Na}_2\text{SiO}_3$  which shows a specific resonance line in the  $Q^2$  range at  $-76.8 \text{ ppm}^{362,204}$ . With respect to the broad  $Q$  peaks which belong to silicon in glassy environment, the following changes could be seen at the temperatures 973 and 1073 K: a considerable shift in  $Q^3$  position was observed. In addition, there is a sharp decrease in the  $Q^2$  relative abundance accompanied with an increase in  $Q^3$ . Meanwhile, the width of the latter peak reveals a large increase to predominate at temperatures higher than 973 K. All these changes resulted in decreasing the NBO % from 57 to 47 %. To justify this, one may think about the inclusion of alkali modifiers in the crystalline silicate phase  $(\text{Li,Na})_2\text{Si}_2\text{O}_5$ . This can account for the reduction of the conductivity. But it cannot be the main responsible for the decrease in the NBO % because the crystalline  $Q$  species were included in the calculations. Besides that, after heating to 1173 and 1273 K this crystalline phase was not formed without re-increasing the NBO %. At  $T \geq 1073$ , it is possible that  $[\text{NbO}_6]^-$  starts to enter the silicate glass network without any alkali ion for charge neutrality. This may continue up to a certain level of about  $x \approx 0.2$  for  $x\text{Nb}_2\text{O}_5 \cdot (1-x)/3(\text{M}_2\text{O} \cdot 2\text{SiO}_2)$  for M: Na and K, as was proved by EXAFS and Raman spectroscopy and the trend in density and refractive index<sup>363</sup>. After that each  $[\text{NbO}_6]^-$  octahedron will necessitate one alkali ion ( $\text{Li}^+$  or  $\text{Na}^+$ ) to achieve the charge neutrality. As a result, the silica network will be left more deficient in modifier which may account for the decrease in the NBO % at such elevated temperature.

In studying the composition effect in  $(x)n\text{-LiNbO}_3 \cdot (1-x)g\text{-NaSi}_{1.5}\text{O}_{3.5}$ , heated for 2 h at 1173 K, the  $\text{LiNbO}_3$ -to- $\text{NaNbO}_3$  conversion proceeded toward completion as long as the Li molar fraction was less than that of Na in the glass (i.e. for  $x \leq 0.5$ ). Otherwise, all the Na coming from glass will be depleted in converting  $\text{LiNbO}_3$  into  $\text{NaNbO}_3$  leaving an excess of the  $\text{LiNbO}_3$  unconverted (for  $x > 0.5$ ).

Taking into account the aspects of thermodynamics, a glass-forming system at temperatures between its solidus temperature and the glass transition temperature is an under-cooled liquid that stays in a metastable equilibrium state<sup>364</sup>. Annealing within that temperature range can lead the glass forming system to full or partial crystallization, which is a result of the system moving towards its ground state (thermal equilibrium)<sup>365</sup>. Hence, glass crystallization under the high-temperature ion exchange is an expected phenomenon as the ion exchange can lead to some new composition that lies outside the region where glasses can be formed. A compound of this new compositions will leave the glass and crystallize, forming new crystalline phases such as  $(\text{Li,Na})_2\text{Si}_2\text{O}_5$ , obtained in the present case.

One proposed mechanism is that the heating can induce initial de-crystallization of the glass composite. Here, the  $\text{LiNbO}_3$  nanocrystals disappear due to the dissolution of  $\text{Li}_2\text{O}$  into the glass, leading to complete dissolution of the crystallite or leaving  $\text{Nb}_2\text{O}_5$  undissolved. This may then re-crystallize as  $\text{NaNbO}_3$  at an advanced stage (higher temperature and/or different concentration conditions). This may take place when the composition of the obtained glass tends toward phase separation according to the solubility product of the glass forming system. This mechanism is ruled out by many experimental findings like the simultaneous conversion of  $\text{LiNbO}_3$  to  $\text{NaNbO}_3$ , seen by *in-situ* x-ray diffractometry, and the absence of any indication of  $\text{Nb}_2\text{O}_5$  as a separate phase.

The second potential mechanism is similar. However, it combines two steps (de-crystallization and re-crystallization) that take place simultaneously in a spatially limited region. This means that the LiNbO<sub>3</sub> in the interfacial regions at the beginning and in the outermost layers of the crystallites separates at the crys-

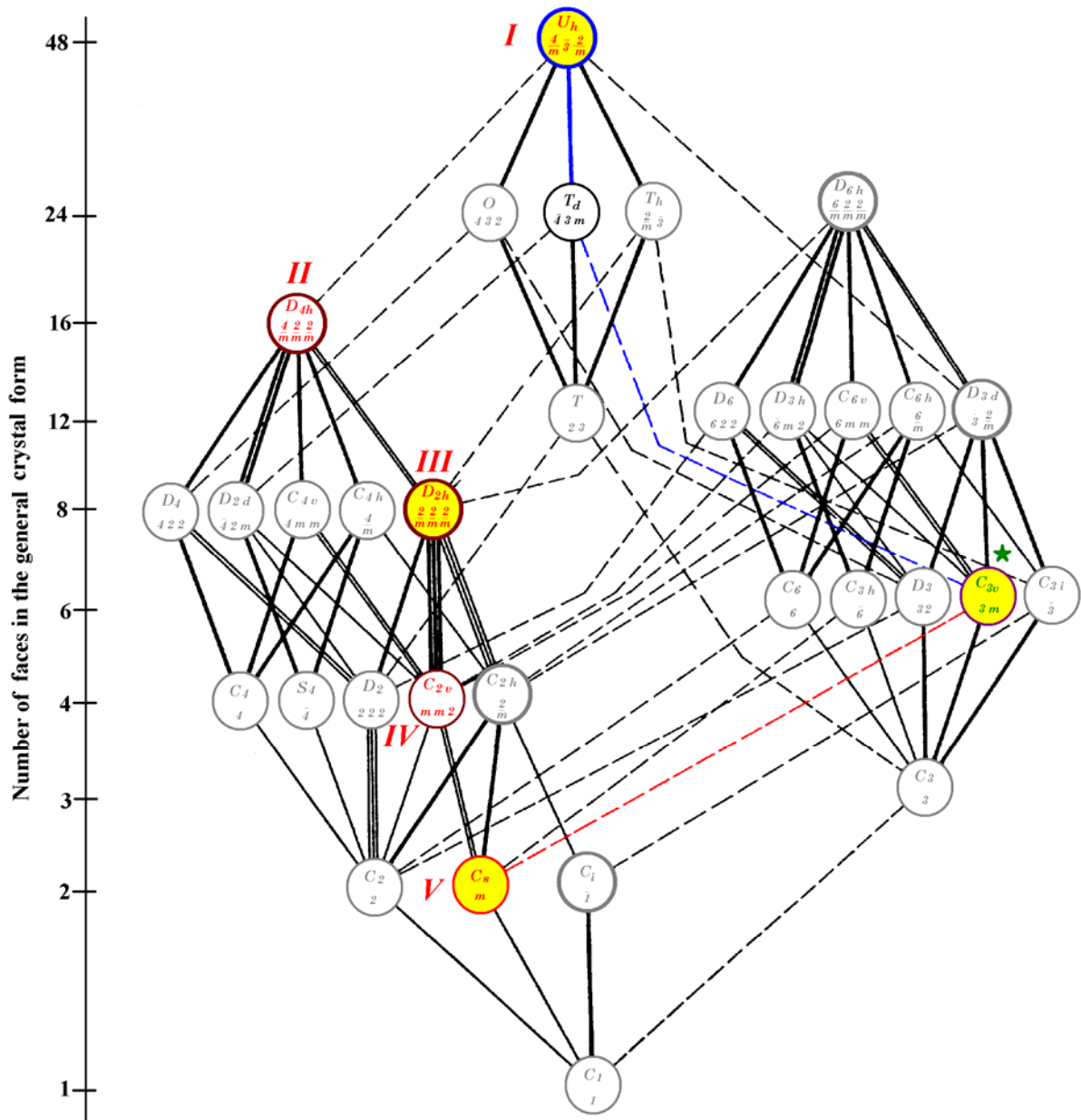
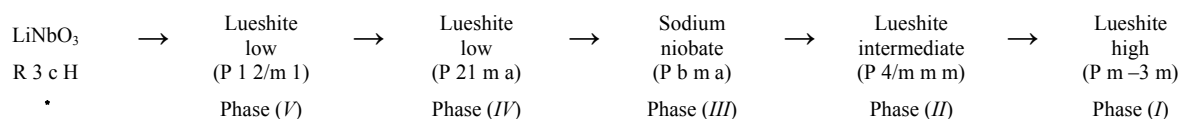


Fig. 8.3.1: The crystallographic point groups and their subgroups, after Hermann<sup>366</sup>. The circles corresponding to the highest symmetry group of each crystal system are outlined in bold. Double or triple lines indicate that the supergroup is related to the subgroup in two or three inequivalent settings. Connecting lines between point groups of same crystal system are bold; all others are plain or dashed. The presence of a line of any sort indicates that the lower group is a subgroup of the higher one. On the ordinate is given the order of the point group, i.e. the number of faces in the general crystal form<sup>367</sup>. The point groups for NaNbO<sub>3</sub> phases are written in red and marked with roman letters and that of the ferroelectric phase of LiNbO<sub>3</sub> is written in green and marked with an asterisk, the circle representing phases detected by XRD are filled with yellow. There are two symmetry pathways from LiNbO<sub>3</sub> to NaNbO<sub>3</sub>. The direct one is represented by a red dashed line and the second one is indicated by the blue dashed line. For more details refer to the text below.

tallite/glass interface into  $\text{Li}_2\text{O}$  and  $\text{Nb}_2\text{O}_5$ ; the former dissolves in the glass and the latter consequently combines with the  $\text{Na}_2\text{O}$  from the glass to form  $\text{NaNbO}_3$ . This can explain the gradual conversion of  $\text{LiNbO}_3$  into  $\text{NaNbO}_3$ , found in the *in-situ* XRD, and the absence of  $\text{Nb}_2\text{O}_5$  as a separate phase. This mechanism cannot be ruled out; however, it cannot account for the decrease in the NBO % as one of its consequences would be the simultaneous conversion of lithium to sodium niobate which is supposed to maintain the NBO %.

A third proposed mechanism is the out-diffusion of Li ion from the  $\text{LiNbO}_3$  to the glass which is simultaneously replaced by Na from the glass to give  $\text{NaNbO}_3$ . The latter has many different phases; most of them are variants of lower symmetry (hettotypes) and one is the perovskite ideal structure (aristotype). Some of these phases are listed in Table 8.1.2 with some of their crystallographic information. Fig. 8.3.1 shows the crystallographic point groups and the symmetry pathways connecting them<sup>367</sup>. The point group of  $\text{LiNbO}_3$ ,  $C_{3v}$ , is shown in green color and marked with a star while those for  $\text{NaNbO}_3$  phases are shown in red and marked with roman numbers (*I-V*). The yellow circles represent the phases found by the structure refinement of the XRD data. There is only one direct symmetry route (the red dashed line) connecting the point group of  $\text{LiNbO}_3$  to that of the monoclinic Lueshite low ( $C_s$ ), phase *V*.

Another symmetry route connects  $\text{LiNbO}_3$  to the cubic Lueshite high, phase *I*. It starts with the blue dashed line to pass through a  $T_d$  point group followed by the bold blue line which ends with phase *I*. The  $T_d$  phase was neither detected by the XRD measurement nor previously reported as one of the phases of  $\text{NaNbO}_3$ . However, as this phase may exist as a high-temperature metastable phase, this route cannot be ruled out. Nevertheless, the cubic Lueshite high (phase *I*) was found by XRD refinement. It may form through several successive transitions according to the following sequence:



Although indirect, this route is more probable than the previous one as most of its products were detected by XRD (phases *I*, *III*, *V*), and the rest (phase *II*, *IV*) are reported phases for  $\text{NaNbO}_3$ .

The fourth proposed mechanism is that  $\text{LiNbO}_3$  dissolves in the glass with the possibility of changing the coordination number and the configuration around the niobium ion.  $^{29}\text{Si}$  NMR results showed that there is a decrease in the average number of bonding oxygens ( $n$ ) in the silicate at temperatures greater than 1000 K. This implies that the number of  $\text{Na}^+/\text{Li}^+$  in the silicate increases and that  $\text{LiNbO}_3$  is supposed to lose  $\text{Li}^+$  to the silicate network. It is implausible to remove  $\text{Li}^+$  from  $[\text{NbO}_6]^-$  octahedral as it is already fully polymerized and needs  $\text{Li}^+$  for charge neutrality. The polarizability of  $\text{Nb}^{5+}$  can accommodate some octahedral without need for alkalis but the amount is very limited. The most  $\text{Li}^+$  transfer that can be obtained is one  $\text{Li}^+$  per formula unit of  $\text{LiNbO}_3$  only when it dissolve tetrahedrally (as  $\text{Q}^3$  with one doubly bonded oxygen and three bonding oxygen) or pyramidally (with five bonding oxygens). It can be calculated that the average number of bonding oxygens decreased from  $3\frac{1}{3}$  in the  $\text{Na}_2\text{Si}_3\text{O}_7$  glass to about 2.7



in the stoichiometric composite heated to a temperature higher than 1073 K. Thus if LiNbO<sub>3</sub> is to go into solution tetrahedrally in our case, then each Si atom will necessitate about 0.63 formula unit of LiNbO<sub>3</sub> per each silicon atom. The previous amount is relatively high but it is still possible. However there was no evidence for four coordinated Nb in the present study.

None of the mentioned mechanisms can explain all the experimental findings. So, a mechanism which combines the second and the third mechanisms should be postulated. The conversion may take place according to the following sequence: at relatively low temperatures (673 – 873 K), the lithium ion is highly mobile and diffuses to the neighboring silicate glassy network. This may be favorable due to the increased entropy of the system. As a result, the sodium ion will be pulled from the Na<sub>2</sub>Si<sub>3</sub>O<sub>7</sub> glass matrix toward the niobate crystalline matrix to re-achieve its charge neutrality. By this, LiNbO<sub>3</sub> is converted to NaNbO<sub>3</sub> (3<sup>rd</sup> mechanism). At a certain stage (873 – 973 K) small amounts of the Nb<sub>2</sub>O<sub>5</sub> will start to dissolve in the glassy matrix to form the alkali niobosilicate glass, in which the niobium oxide plays a role opposite to that of a glass modifier, i.e. former. The Nb<sup>5+</sup> ion in an octahedral [NbO<sub>6</sub>]<sup>-</sup> unit is surrounded by 6 oxygen atoms and thus will acquire a formal charge of -1. The glassy silicate matrix can accommodate some [NbO<sub>6</sub>]<sup>-</sup>-units without the need of alkali ions for charge neutrality because of the polarizability and distortion in the NbO<sub>6</sub> octahedra due to the large size of Nb<sup>5+</sup> cations. The previous situation can continue as long as the amount of Nb<sub>2</sub>O<sub>5</sub> entering the glass is limited. At relatively high temperatures (1073 – 1273 K) the amount of Nb<sub>2</sub>O<sub>5</sub> that dissolves in the glass increases and becomes tolerable only with one mole of alkali for neutralizing each mole of [NbO<sub>6</sub>]<sup>-</sup>. When it exceeds a certain level, the silica network will be left deficient in the modifier in some regions. This may account for the changes observed via <sup>29</sup>Si NMR, in particular the decrease in percentage of the NBO at 1073 and 1173 K. The crystallization (or phase separation) can take place in the neighboring layers which will withdraw some of the modifier from the adjacent regions. Consequently, the resulting modifier-poor (or even free) regions may crystallize as pure quartz low or cristobalite low. At this stage the Nb<sub>2</sub>O<sub>5</sub> enters the glassy phase together with the Li<sub>2</sub>O, with the latter enriching the glassy phase with modifier. When the Li<sub>2</sub>O concentration exceeds the solubility limit in local areas it can initiate sodium-silicate glass crystallization in the form (Li,Na)<sub>2</sub>Si<sub>2</sub>O<sub>5</sub> which is more rich in modifier than the parent glass. At this stage the conductivity of the composite will decrease as a result of enclosing the mobile ions in a crystalline phase.



# 9 (Lithium, Sodium) Niobosilicate Glasses and Glass Ceramics

## 9.1 GLASS STRUCTURE

### 9.1.1 Effect of Changing the Alkali Ion (Li to Na)

#### 9.1.1.1 X-ray diffraction

Samples with the compositions  $0.33[x\text{Li}_2\text{O} \cdot (1-x)\text{Na}_2\text{O}] \cdot 0.33\text{Nb}_2\text{O}_5 \cdot 0.33\text{SiO}_2$ ,  $0 \leq x \leq 1$ , were examined by x-ray diffraction in the  $2\theta$  range from 5 to  $45^\circ$ , Fig. 9.1.1(a). The diffractograms showed only broad humps confirming the glassy nature of the samples. The position of the first sharp diffraction peaks (FSDP) and their full widths at half maxima were obtained by fitting these patterns with several Gaussian lines, Fig. 9.1.1(b,c). Generally, in glasses the length scale is often identified as the size of voids formed due to the awkward arrangement of the polyhedra as a consequence of bond angle disorder. The bigger the voids the lower the density of the glass. The position of the peak corresponds to a characteristic length scale in the microstructure, and the width is related to the structural disorder. From  $x = 1$  to  $x = 0$ , the maxima of the FSDP are displaced toward higher diffraction angles accompanied by a decrease in their width (in reciprocal space). This implies that the structure becomes denser and more ordered (in the real space) when going from the Li-rich to the Na-rich glass sample.

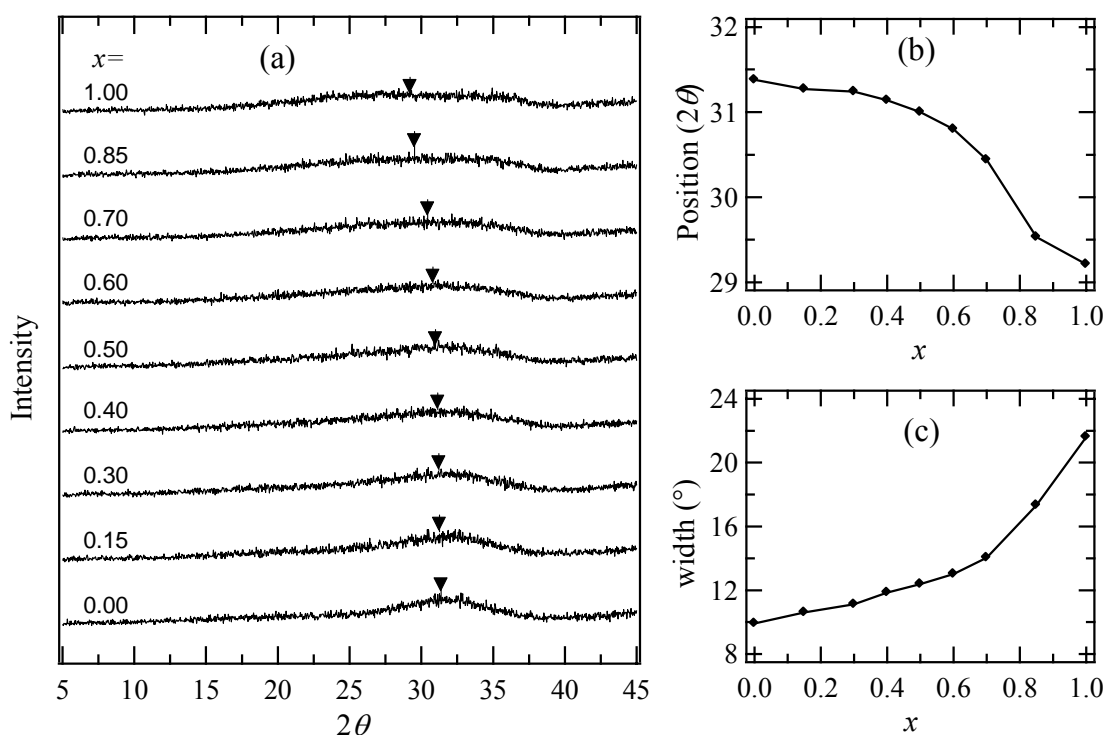


Fig. 9.1.1: (a) XRD pattern for glasses  $0.33[x\text{Li}_2\text{O} \cdot (1-x)\text{Na}_2\text{O}] \cdot 0.33\text{Nb}_2\text{O}_5 \cdot 0.33\text{SiO}_2$ , with  $0 \leq x \leq 1$ , showing only the FSDPs and the change in their: (b) positions indicated by the arrows in (a) and (c) widths vs.  $x$  value.

### 9.1.1.2 Infrared and Raman spectroscopy

Broadening of the bands and decrease in their number and intensity, which is typical for the spectra of vitreous materials, is observed in the infrared spectra of the glass samples, Fig. 9.1.2. According to Kokubo's hypothesis, the alkali-niobium silicate glass is built of a random network of  $\text{SiO}_4$ -tetrahedra and  $\text{NbO}_6$ -octahedra with the alkalis being situated in some holes of the network<sup>369–371</sup>. Using the typical absorption band of pure silica, the band at  $1040 \text{ cm}^{-1}$  is assigned to the anti-symmetric stretching vibrations (S) of the non-bridging silicon-oxygen bond  $\text{Si}-\text{O}^- \text{X}^+$  (alkali) in the depolymerized silica network<sup>112,372–375</sup>. The vibrational modes of deformation of the  $\text{O}-\text{Si}-\text{O}$  and  $\text{Si}-\text{O}-\text{Si}$  bonds (D) appear as a very weak band at  $455 \text{ cm}^{-1}$ , see Refs [373–374,376]. One characteristic peak that usually appears at  $\sim 800 \text{ cm}^{-1}$  for the vibration of a ring

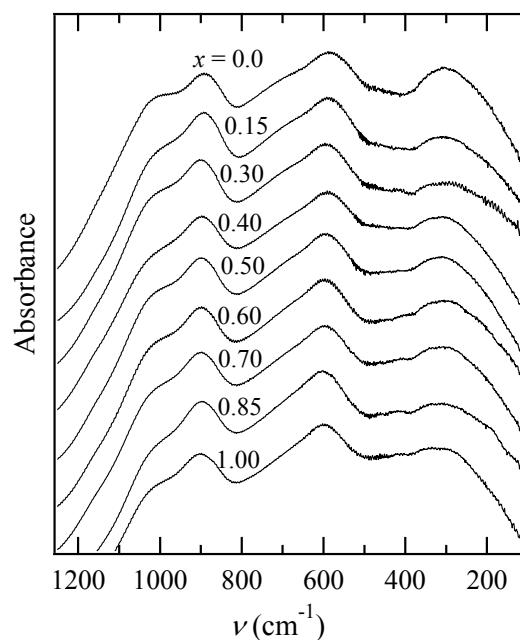


Fig. 9.1.2: Infrared spectra for the glasses  $0.33[x\text{Li}_2\text{O} \cdot (1-x)\text{Na}_2\text{O}] \cdot 0.33\text{Nb}_2\text{O}_5 \cdot 0.33\text{SiO}_2$ , with  $0.0 \leq x \leq 1.0$ .

structure of the tetrahedral  $\text{SiO}_4$  (R)<sup>373</sup> (or the stretching mode of the  $\text{Si-O-Si}$ <sup>374</sup>) is absent due to the dispersion of the Nb octahedra among the Si tetrahedral. This peak does appear in glasses that do not contain niobium. The absorption band at  $900\text{ cm}^{-1}$  is due to the Nb-O bond vibration<sup>377</sup>. The strong band around  $610\text{ cm}^{-1}$  is attributed to the stretching frequency of the Nb-O bond in six-fold coordination ( $\text{NbO}_6$ -octahedra)<sup>378</sup>. At  $700\text{ cm}^{-1}$ , a small but wide hump appears only on the Na-rich side ( $x \leq 0.5$ ) due to the less distorted  $\text{NbO}_6$  octahedra without NBOs<sup>112</sup>. This band appears here indicating that the  $[\text{NbO}_6]^-$  octahedra are left with less amount of modifier in the case of Na-rich side.

Fig. 9.1.3(a) shows Raman spectra for the glasses  $0.33[x\text{Li}_2\text{O} \cdot (1-x)\text{Na}_2\text{O}] \cdot 0.33\text{Nb}_2\text{O}_5 \cdot 0.33\text{SiO}_2$  with  $0 \leq x \leq 1$ . These spectra are analyzed by comparing the bands with the vibrations due to  $\text{SiO}_4$  tetrahedra in silicate glasses and those of niobate crystals. In silicate glasses, the bands at  $850$ ,  $900$ ,  $950$ - $1000\text{ cm}^{-1}$  and  $1050$ - $1100\text{ cm}^{-1}$  have been assigned to the symmetric Si-O stretching motion of silicate containing  $\text{SiO}_4$  tetrahedral units with four, three, two, and one NBOs, respectively.<sup>379</sup> For the glasses studied here, a very weak peak can be seen at  $1050\text{ cm}^{-1}$ . The Si-O symmetric stretching of the BOs vibration in the  $\text{SiO}_4$  unit usually appears in the  $400$  to  $700\text{ cm}^{-1}$  region. In the niobosilicate glasses the latter band appears usually at  $560\text{ cm}^{-1}$  only for samples with high  $\text{SiO}_2$  content and a very limited  $\text{Nb}_2\text{O}_5$  content, e.g. for  $x \leq 0.1$  in glass with the composition  $x\text{Nb}_2\text{O}_5(1-x)/3(\text{M}_2\text{O} \cdot 2\text{SiO}_2)$  with  $\text{M} = \text{Na}$  or  $\text{K}$ .<sup>363</sup> Thus, the high concentration of  $\text{Nb}_2\text{O}_5$  (33.3 %) in the present glass is behind the absence of such a peak as it weakens the Si-O bond.

In silicate glasses containing  $\text{Nb}_2\text{O}_5$ , the  $280\text{ cm}^{-1}$  band is assigned to the bending vibration of O-Nb-O.<sup>380-381</sup> The very strong peak at  $670\text{ cm}^{-1}$  is due to the stretching vibration of the Nb-O bond in the less distorted  $\text{NbO}_6$  octahedra with no NBOs.<sup>382-383</sup> Furthermore, the peak in the range from  $800$  to  $900\text{ cm}^{-1}$  is assigned to the stretching vibration of the Nb-O bond in  $\text{NbO}_6$  octahedra with NBOs and/or with much distortion. Similar peaks were found in crystals with severely distorted  $\text{NbO}_6$  octahedra. The

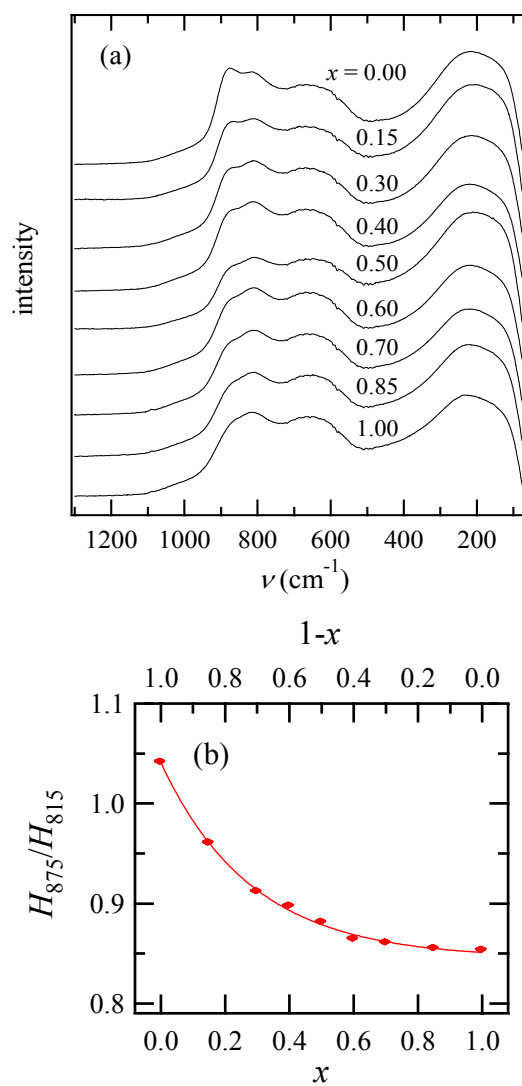


Fig. 9.1.3: (a) Raman spectra for the glasses  $0.33[x\text{Li}_2\text{O} \cdot (1-x)\text{Na}_2\text{O}] \cdot 0.33\text{Nb}_2\text{O}_5 \cdot 0.33\text{SiO}_2$ , with  $0 \leq x \leq 1.00$ ; (b) the ratio between the heights of the Raman at  $875$  and  $815\text{ cm}^{-1}$  vs.  $x$ .

location of such peaks were related to a structural change of  $\text{NbO}_6$  octahedra<sup>380,384–385</sup> (For more details see Appendix A.6). The system shows two adjacent bands in this region. In the pure lithium glass ( $x = 1$ ) the stronger band appears at  $815 \text{ cm}^{-1}$  besides another weaker band at  $875 \text{ cm}^{-1}$  which emerges as a shoulder and starts to grow with increasing the sodium content to become the main peak for the pure sodium glass ( $x = 0$ ). Fig. 9.1.3(b) illustrates this variation expressed as the ratio between the heights of the peak at  $875 \text{ cm}^{-1}$  to that at  $815 \text{ cm}^{-1}$ ,  $H_{875}/H_{815}$ . Thus by replacing lithium by sodium in our glass system, the  $[\text{NbO}_6]^-$  octahedra are getting more deficient with the modifier ions that are needed to neutralize them, and this can be accommodated by one of the following changes: (i) a decrease in the number of NBOs in an  $\text{NbO}_6$  octahedron which already possesses NBOs, or (ii) an increase of distortion and/or increase in the number of oxygens shared by three or four polyhedra. According to Fukumi *et al.*<sup>380</sup>, any one of the previous changes can account for the shift in band (obtained in the  $800 - 900 \text{ cm}^{-1}$  range) to higher wavenumbers.

### 9.1.1.3 $^7\text{Li}$ , $^{93}\text{Nb}$ , $^{23}\text{Na}$ , $^{29}\text{Si}$ nuclear magnetic resonance

Fig. 9.1.4 shows the  $^7\text{Li}$ ,  $^{93}\text{Nb}$ , and  $^{23}\text{Na}$  MAS-NMR lines for the glass samples measured at r.t. The  $^7\text{Li}$  and  $^{23}\text{Na}$  lines do not show any changes with changing the type of the modifier except the change in their intensity, Fig. 9.1.4(a,c). The  $^{93}\text{Nb}$  lines are very broad confirming the presence of the Nb in glassy environment, in addition to small and relatively sharp contributions that resemble the peaks of  $\text{LiNbO}_3$  and  $\text{NaNbO}_3$  in the cases of single alkali modifier, Fig. 9.1.4 (b). These sharp peaks may arise from the similarities between the building units of the glass and those of the crystalline  $\text{LiNbO}_3$  or  $\text{NaNbO}_3$  or may be due to the existence of crystal nuclei which are undetectable by XRD.

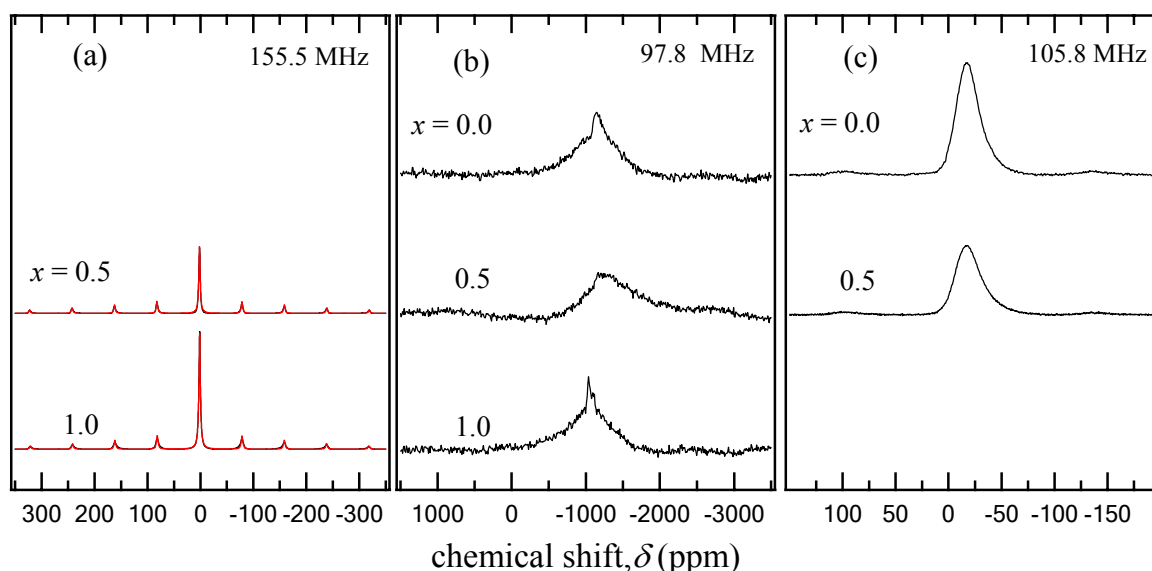


Fig. 9.1.4: (a)  $^7\text{Li}$ , (b)  $^{93}\text{Nb}$ , and (c)  $^{23}\text{Na}$  MAS-NMR for  $0.33[x\text{Li}_2\text{O} \cdot (1-x)\text{Na}_2\text{O}] \cdot 0.33\text{Nb}_2\text{O}_5 \cdot 0.33\text{SiO}_2$  glasses with  $x = 1.00$ ,  $x = 0.50$ , and  $x = 0.0$  measured at room temperature with a spinning frequency of  $12.5 \text{ kHz}$ , at the indicated resonance frequencies.

The  $^{29}\text{Si}$  MAS-NMR spectra are shown in Fig. 9.1.5(a). For  $x = 1$  the line is broader and shifted towards lower  $\delta$  values. These spectra were fitted by Gaussian lines and the results of the fit show the following: (i) the relative abundance of the Q species calculated from the areas under the Gaussian lines relative to the area under the whole line, Fig. 9.1.5(b), (ii) the widths taken as the full width at half the maximum (fwhm) of the lines, Fig. 9.1.5(c), (iii) the chemical shifts of the Qs, Fig. 9.1.5(d), (iv) and the percentage of the non-bridging oxygens (NBO %) with respect to the total number of oxygens surrounding the silicon atom calculated from the relative abundance of the Q species, Fig. 9.1.5(e).

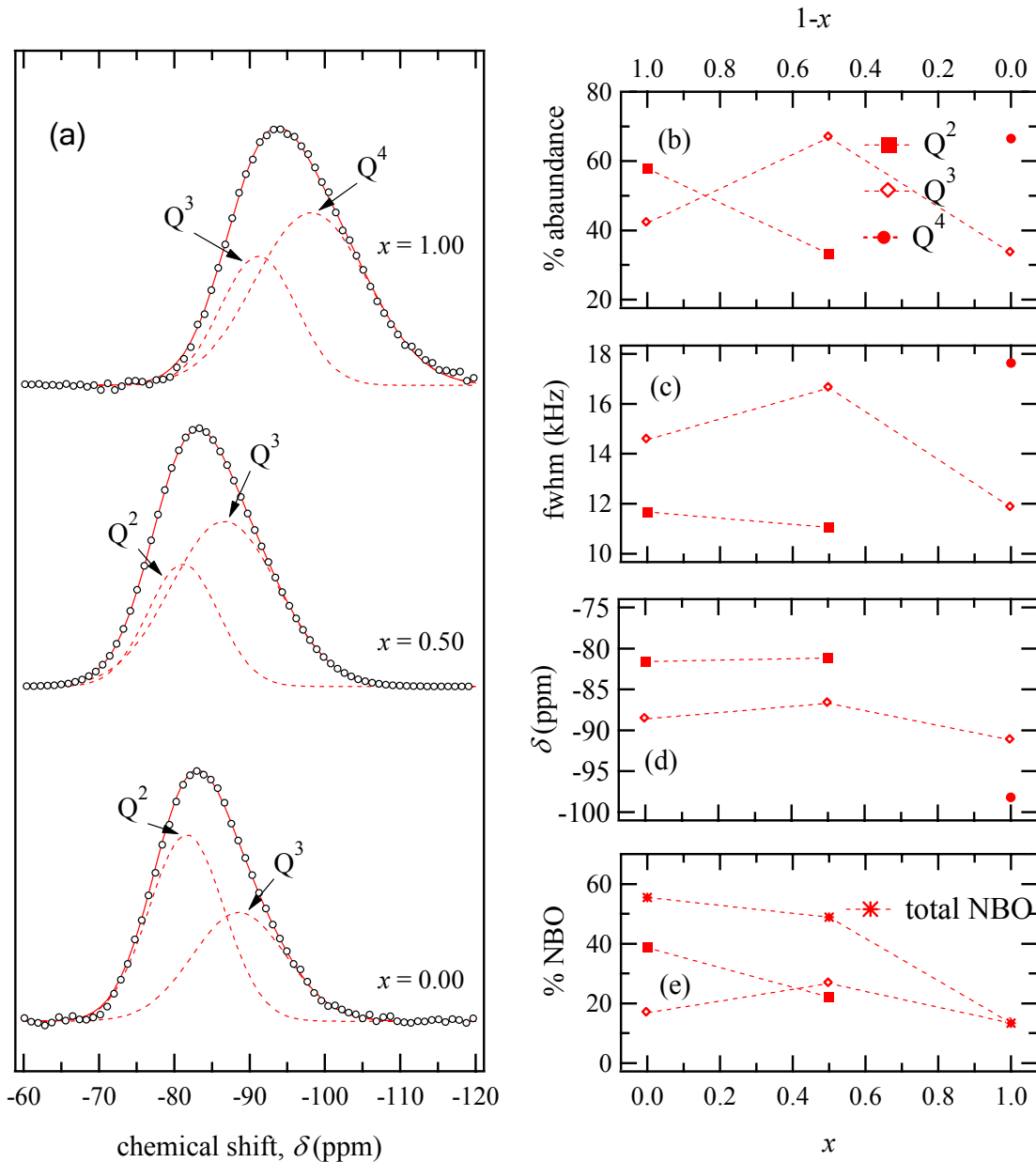


Fig. 9.1.5: (a)  $^{29}\text{Si}$  MAS-NMR for  $0.33[x\text{Li}_2\text{O} \cdot (1-x)\text{Na}_2\text{O}] \cdot 0.33\text{Nb}_2\text{O}_5 \cdot 0.33\text{SiO}_2$  glasses with  $x = 0, 0.5, 1$ , the circles represent the measured spectra, the dashed curves are the Gaussian lines used in the fit and the solid line is the total model. The effect of changing  $x$  is shown on: the relative abundances of the Q species (b), their widths (c), their positions (d), and the percentage of the NBOs to the total number of oxygen surrounding the silicon atoms.

In the pure sodium glass ( $x = 0$ ) the silicate network is de-polymerized and consists of two types of Si species,  $Q^2$  and  $Q^3$ , with the former being more abundant, at  $x \geq 0.5$  the relative abundance of  $Q^2$  decreases to be less than half the value of  $Q^3$ , Fig. 9.1.5(b). When increasing  $x$  from 0 to 0.5 the positions of both Q species remain nearly unchanged. However, with a further increase of the  $x$  to 1 they are shifted to lower chemical shift in spite of the fact that the total amount of the modifier is constant, Fig. 9.1.5(d). The percentage of the NBOs to the total number of oxygens surrounding the silicon atoms decreases from 55 % at  $x = 0$  to  $\sim 49$  % at  $x = 0.5$  and ultimately to  $\sim 13$  % at  $x = 1.0$

#### 9.1.1.4 Discussion of the modifier-type effect

In the glasses  $0.33[xLi_2O \cdot (1-x)Na_2O] \cdot 0.33Nb_2O_5 \cdot 0.33SiO_2$  with  $0 \leq x \leq 1$  the changes in the XRD diffractograms indicate an increase in density and order with replacing lithium by sodium. Each  $Nb^{5+}$  ion in the glass needs 5 BOs to neutralize its positive charge. However, in most cases Nb is accompanied by one extra oxygen ion to form  $[NbO_6]^-$  octahedron that is usually accompanied by an alkali ion, or in few cases it is found as  $NbO_4$  tetrahedral<sup>245</sup>. On the other hand, the coordination number of  $Si^{4+}$  is usually constant at four in silicate glasses and it does not require an alkali ion for charge neutralization in the  $[SiO_4]$  tetrahedra. However, the introduction of alkali ions breaks Si-O-Si bonds forming two non-bridging oxygens (NBO). Each is bonded to only one Si and bears an increased negative charge which is neutralized by an alkali ion. In the glasses  $0.33[xLi_2O \cdot (1-x)Na_2O] \cdot 0.33Nb_2O_5 \cdot 0.33SiO_2$  the Nb:Si ratio is 2:1 and the amount of the alkalis is equivalent to that of Nb. This situation will result in a competition between the  $[NbO_6]^-$  and the  $[SiO_4]$  moieties for the available modifier. The obtained results show two significant facts: (i) In the pure lithium glass the silica network is more polymerized than in the pure sodium or the mixed glass according to  $^{29}Si$  NMR. This implies that the amount of modifier available for the silicate is less in the case of pure lithium glass. At the first glance, one may think about atomic-species vaporization from the oxides at high temperature. However, the vapor pressure of atomic species in ionic crystals decreases with increasing single bond strength<sup>382</sup>. Since the single-bond strength of Na—O is less than Li—O, Na may be more easily vaporizable than Li. A previous study had revealed by chemical analysis that the weight loss due to vaporization after heating at 1823 K was less than 2 wt % in the case of  $Cs_2O$ . If such a loss occurred in case of the Li-glass it would not be able to account for such a great shift of the  $^{29}Si$  NMR line. However, as the maximum temperature used for the preparation was 1723 K and because  $Li_2O$  and  $Na_2O$  are supposed to be the least vaporizable among all the other alkali oxides, one can completely neglect the effect of alkali loss through vaporization. (ii) Both the IR and the Raman spectra showed that, when the amount of sodium exceeds that of lithium in the glass, the  $[NbO_6]^-$  octahedra start to possess a lower number of NBO, i.e. sodium ions are less available for neutralizing of the Nb octahedra than lithium. One can visualize that, in the niobosilicate glasses the  $Na^+$  ions are less preferred by the  $[NbO_6]^-$  octahedra for neutralizing their charges. Accordingly, in the case of the pure Li glass ( $x = 1$ ), a larger



amount of Li will settle somewhere in the neighborhood of the  $[\text{NbO}_6]^-$  octahedra leaving the silica network more deficient of modifier. Contrarily,  $\text{Na}^+$  ions will be more directed to de-polymerize the silica network when  $x = 0$ . This agrees with the FT-IR result which confirmed that Na ions are situated closer to  $\text{SiO}_4$ -tetrahedra than to  $\text{NbO}_6$ -octahedra in the  $\text{Na}_2\text{O} \cdot \text{Nb}_2\text{O}_5 \cdot \text{SiO}_2 \cdot \text{Al}_2\text{O}_3$  glass network<sup>386</sup>.

In the  $[\text{NbO}_6]^-$  octahedra that are accompanied by an alkali ion, the electron clouds in the bonding region between the bridging oxygen core and Nb cores are more attracted towards the alkalis as the field strength of the alkali ion increases<sup>387</sup>. As a result, the ions with high-ionic field strength facilitate a viscous flow in the glasses near to the  $\text{NbO}_6$  units, and favors crystallization of the glasses. The ionic-field strengths, given by  $Z_i/(r_i + r_o)^2$ , are 0.23 and 0.18 for  $\text{Li}^+$  and  $\text{Na}^+$ , where  $Z_i$ ,  $r_i$ , and  $r_o$  are the charge and the radius of the modifier and the oxygen ions, respectively<sup>388</sup>. Thus the  $\text{Na}_2\text{O}$ - $\text{Nb}_2\text{O}_5$ - $\text{SiO}_2$  system has a higher glass forming ability than  $\text{Li}_2\text{O}$ - $\text{Nb}_2\text{O}_5$ - $\text{SiO}_2$  due to the low field strength of  $\text{Na}^+$  relative to  $\text{Li}^+$ . This also accounts for the fact that Li ions prefer the Nb zones over those of silica. In the mixed-alkali glass half of the alkali content is Li which is directed towards the  $\text{NbO}_6$  units leaving the Na part in the silicate network. This explains the high degree of resemblance in the  $^{29}\text{Si}$  NMR spectra between the pure Na glass and the mixed one.

## 9.1.2 Effect of Changing $\text{Li}_2\text{O}$ and $\text{Nb}_2\text{O}_5$

### 9.1.2.1 Raman spectroscopy

Fig. 9.1.6(a) shows the Raman spectra for  $x\text{Li}_2\text{O} \cdot (1-x)/3[\text{Nb}_2\text{O}_5 \cdot 2\text{SiO}_2]$  glasses, where the Nb:Si ratio is kept constant at 1 and the  $\text{Li}_2\text{O}$  content,  $x$ , was varied between 0.35, 0.4, and 0.45. Two distinct broad bands are observed at about  $\sim 230$  and  $\sim 845 \text{ cm}^{-1}$ . The first is a broad band which is not affected by

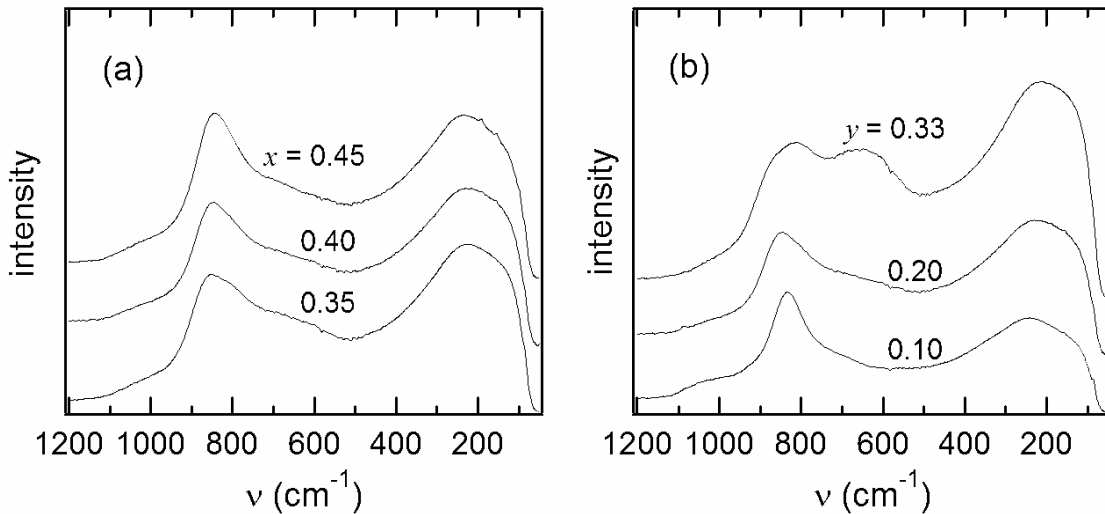


Fig. 9.1.6: Raman spectra of: (a)  $x\text{Li}_2\text{O} \cdot (1-x)/3[\text{Nb}_2\text{O}_5 \cdot 2\text{SiO}_2]$  glasses for various  $\text{Li}_2\text{O}$  concentration,  $x$  ( $x = 0.35, 0.40, 0.45$ ) and (b)  $(1-y)/2[\text{Li}_2\text{O} \cdot \text{SiO}_2] \cdot y\text{Nb}_2\text{O}_5$  glasses for various  $\text{Nb}_2\text{O}_5$  concentration,  $y$ , ( $y = 0.10, 0.20, 0.33$ ).

changing the Li content and is assigned to the bending vibration of O—Nb—O<sup>380–381</sup>. The second band gets slightly stronger with increasing the value of  $x$  and is assigned to the vibration of  $[\text{NbO}_6]^-$  octahedra with NBOs and/or with much distortion. As a result of increasing the  $\text{Li}_2\text{O}$  content from  $x \approx 0.35$  to  $x \approx 0.4$  to  $x \approx 0.45$  the Li:Nb increased from 1.61 to 2 and then to 2.45, which is expected to increase the number of NBOs in the  $[\text{NbO}_6]^-$ . The broad band observed at  $640 \text{ cm}^{-1}$  is assigned to the stretching vibration of the Nb—O bond in the less distorted  $\text{NbO}_6$  octahedra with no NBOs. With increasing  $x$  the intensity of this band decreases slightly indicating that the number of the less distorted  $\text{NbO}_6$  octahedra is affected not by the concentration of the modifier but the Nb:Si ratio that is held at 1 here. The band at  $1030 \text{ cm}^{-1}$  has been assigned to the symmetric Si—O stretching motion of silicate containing  $\text{SiO}_4$  tetrahedral units with one or two NBOs ( $\text{Q}^3$  or  $\text{Q}^2$ , respectively), this band has a very low intensity due to the weakening of the Si—O bond.

Fig. 9.1.6(b) shows the effect of changing the  $\text{Nb}_2\text{O}_5$  content ( $y$ ) on the Raman spectra of the glasses  $(1-y)/2[\text{Li}_2\text{O} \cdot \text{SiO}_2] \cdot y\text{Nb}_2\text{O}_5$ . The  $230 \text{ cm}^{-1}$  peak due to the bending vibration of O—Nb—O is intensified with increasing  $y$ . When  $y$  was increased from 0.1 to 0.2, the Nb:Si ratio was consequently increased from 0.44 to 1. This seems to be just the limit to which the  $\text{NbO}_6$  octahedra can be singly dispersed in the silica network with an alkali ion located in its neighborhood. At  $\text{Nb:Si} \geq 1$ , the bonding between adjacent  $\text{NbO}_6$  octahedra with less number of NBO begins. The previous bonding may start at least by sharing corners. Anyhow it is supposed to increase the number and strength of the Nb—O bonds in the less distorted  $\text{NbO}_6$  octahedra with no NBOs. This is confirmed by: (i) the emergence of the peak at  $650 \text{ cm}^{-1}$  when the Nb:Si ratio reaches 2 ( $y = 0.33$ ). This peak continued to intensify, broaden, and to be shifted towards higher wavenumbers. (ii) the peak in the range from  $800$  to  $900 \text{ cm}^{-1}$  appears at  $835 \text{ cm}^{-1}$  when  $y = 0.1$ . Then it is shifted to  $850 \text{ cm}^{-1}$  when  $y = 0.2$ . At  $y = 0.33$  it broadens and one can see two overlapping bands. One band at  $850 \text{ cm}^{-1}$  and the other one at  $815 \text{ cm}^{-1}$  can be understood as follows: At low  $y$  values, the majority of the  $\text{NbO}_6$  octahedra possess NBOs and their number decreases by increasing  $y$  from 0.1 to 0.2. However, when  $y$  reaches 0.33 there is not enough modifier to neutralize all of the  $\text{NbO}_6$  by alkalis and a part of them will enter the glass network without any NBOs. While the remaining will have fewer NBOs as indicated by the appearance of another peak within this region at  $815 \text{ cm}^{-1}$ . The broad peak at  $1030 \text{ cm}^{-1}$  disappeared with increasing  $\text{Nb}_2\text{O}_5$  content.

### 9.1.2.2 <sup>29</sup>Si NMR

Fig. 9.1.7(a) shows the <sup>29</sup>Si MAS-NMR spectra for the glasses  $x\text{Li}_2\text{O} \cdot (1-x)/3[\text{Nb}_2\text{O}_5 \cdot 2\text{SiO}_2]$ . The line is getting narrower and shifted toward more positive chemical shifts, i.e. more de-polymerized, by increasing the value of  $x$ . All the NMR resonance lines were de-convoluted into sets of Gaussian curves. They show that the glasses are composed of two types of silicon species,  $\text{Q}^2$  and  $\text{Q}^3$ , with  $\text{Q}^2$  being less abundant at  $x = 0.35, 0.4$ . However, it increases with increasing  $x$  to become the most abundant at  $x = 0.45$ ,

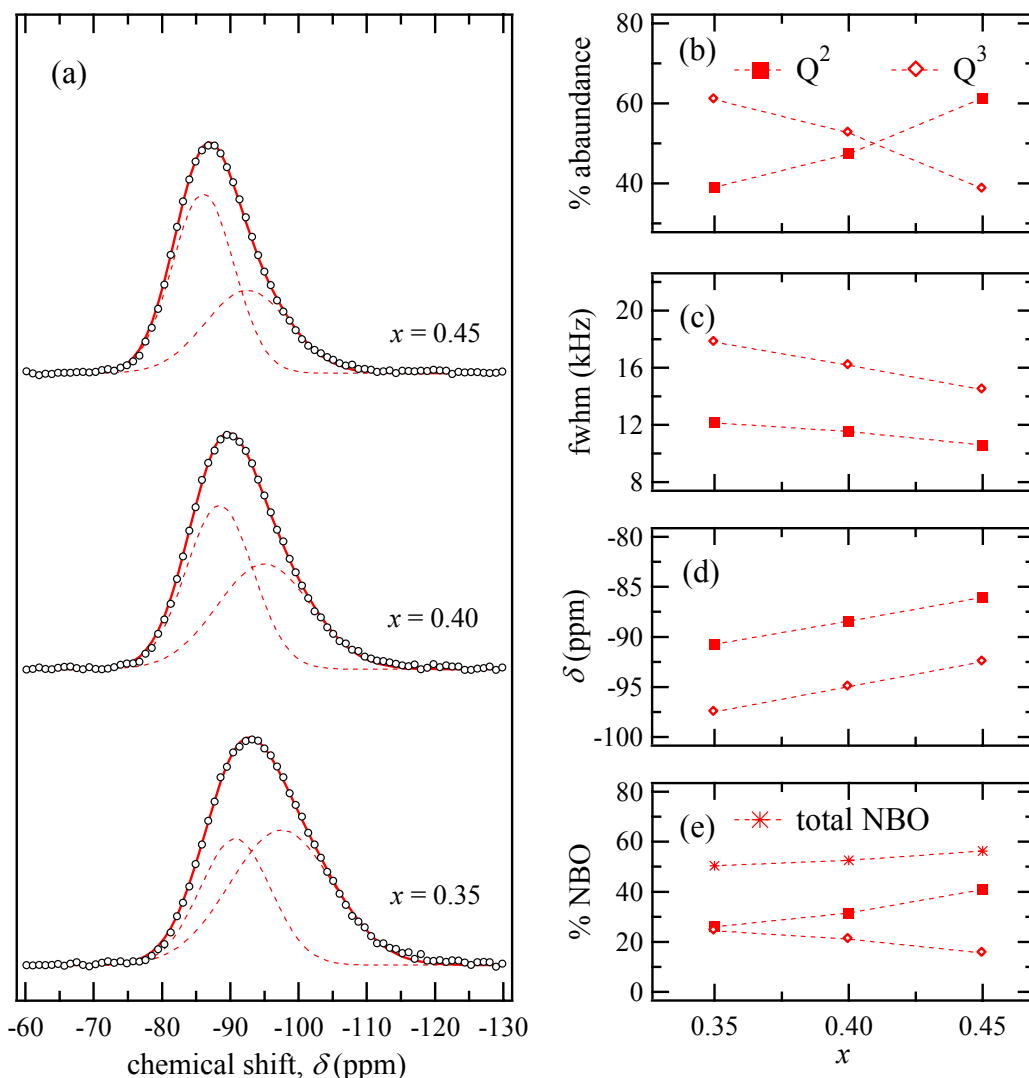


Fig. 9.1.7: (a)  $^{29}\text{Si}$  MAS-NMR spectra for  $x\text{Li}_2\text{O} \cdot (1-x)/3[\text{Nb}_2\text{O}_5 \cdot 2\text{SiO}_2]$  glasses with  $x = 0.35, 0.40, 0.45$ . The circles represent the measured spectra. Dashed curves are Gaussian lines used for fitting procedure. The solid line is the sum of the Gaussian lines. The effect of changing the  $\text{Li}_2\text{O}$  concentration,  $x$ , is shown on: the relative abundances of the Q species (b), their widths (c), their positions (d), and the percentage of the NBOs to the total number of oxygen surrounding the Si atoms.

Fig. 9.1.7(b). The width of both  $Q^2$  and  $Q^3$  decrease with increasing  $x$  value, Fig. 9.1.7(c). Meanwhile, the positions of both Q species are shifted to higher, more de-polymerized values, Fig. 9.1.7(d). The percentage of the NBOs to the total number of oxygens surrounding the silicon atoms increased from  $\sim 50\%$  to  $\sim 56\%$  by the increase of  $x$  from 0.35 to 0.45, Fig. 9.1.7(e)

The  $^{29}\text{Si}$  MAS-NMR spectra for the glasses  $(1-y)/2[\text{Li}_2\text{O} \cdot \text{SiO}_2] \cdot y\text{Nb}_2\text{O}_5$  with  $y = 0.1, 0.2, 0.33$  are shown in Fig. 9.1.8(a). By increasing the  $\text{Nb}_2\text{O}_5$  content,  $y$ , the line gets broader and shifts towards more negative chemical shifts, i.e. becomes more polymerized. The lines were fitted with Gaussian curves which reveal that the glasses consist of  $Q^2$ - and  $Q^3$ -species. At  $y = 0.1$  the most abundant  $^{29}\text{Si}$  species is  $Q^2$ . However, upon the increase of  $y$  it starts to decrease and to be replaced by  $Q^3$  which becomes the most

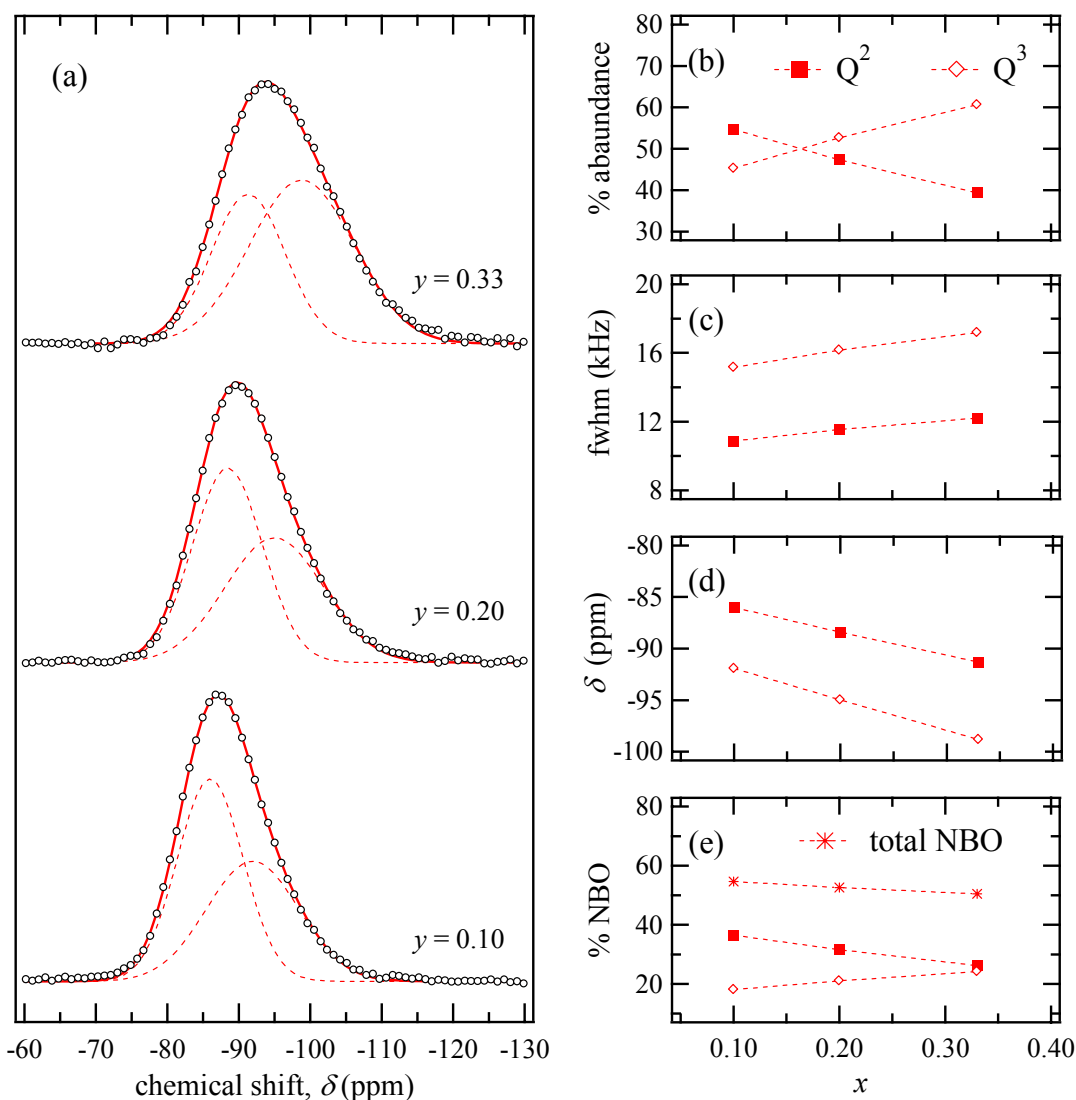


Fig. 9.1.8: (a) <sup>29</sup>Si MAS-NMR for  $(1-y)/2[\text{Li}_2\text{O}\cdot\text{SiO}_2]\cdot y\text{Nb}_2\text{O}_5$  glasses with  $y = 0.10, 0.20, 0.33$ . The circles represent the measured spectra. Dashed curves are Gaussian lines used for the fitting procedure. The solid line is the sum of the Gaussian lines. The effect of changing the Nb<sub>2</sub>O<sub>5</sub> concentration,  $y$ , is shown on: the relative abundances of the Q species (b), their widths (c), their positions (d), and the percentage of the NBOs to the total number of oxygen surrounding the Si atoms.

abundant species at  $y \geq 0.2$ , Fig. 9.1.8(b). The width of both Q<sup>2</sup>- and Q<sup>3</sup>-species increases with increasing  $y$ , Fig 9.1.8(c), while the positions are shifted to lower, more polymerized values, Fig 9.1.8(d). The percentage of the NBOs to the total number of oxygens surrounding the silicon atoms decreases gradually from 54.5 % to ~ 50.5 % by the increase of  $y$  from 0.10 to 0.33, Fig. 9.1.8(e).

### 9.1.2.3 Discussion of the Li<sub>2</sub>O and Nb<sub>2</sub>O<sub>5</sub> effect

In studying the Li<sub>2</sub>O effect, in the glass series  $x\text{Li}_2\text{O}\cdot(1-x)/3[\text{Nb}_2\text{O}_5\cdot 2\text{SiO}_2]$  with  $x = 0.35, 0.4, 0.45$ , the Nb:Si ratio was kept constant at 1. The [NbO<sub>6</sub>]<sup>-</sup> octahedra are dispersed individually in the silica network to accommodate their negative charge. In such a case, the environment around these octahedra is hardly

affected by changing the  $\text{Li}_2\text{O}$  concentration,  $x$ . This can be clearly seen from the unchanged Raman band at  $\sim 230\text{ cm}^{-1}$  while there is only a slight decrease in the band at the  $600 - 700\text{ cm}^{-1}$ . Furthermore, the intensity of the band at  $845\text{ cm}^{-1}$  increases moderately when  $x$  value reached 0.45, Fig. 9.1.6(a). Hence, one can say that at Nb:Si ratio of the order of one, a certain amount of alkali ions is distributed between the silica and niobia. However, the main part of the added alkalis is directed to the silica neighborhood as confirmed by  $^{29}\text{Si}$  NMR measurements. The  $^{29}\text{Si}$  NMR resonance lines shift towards higher values and the percentage of the NBOs increases. In this case, it can be stated that the effect of changing the Nb:Si ratio on the environment of the  $\text{NbO}_6$  octahedra in the niobosilicate glasses is more predominant than the effect of the modifier amount.

On the other hand, the effect of changing the  $\text{Nb}_2\text{O}_5$  content was studied in the glass series  $(1 - y)/2[\text{Li}_2\text{O} \cdot \text{SiO}_2] \cdot y\text{Nb}_2\text{O}_5$  glasses with  $y = 0.1, 0.2, 0.33$ . The  $\text{Li}_2\text{O}/\text{SiO}_2$  ratio was kept at 1, but nevertheless, the changes in the  $^{29}\text{Si}$ -NMR show that with the addition of  $\text{Nb}_2\text{O}_5$  the glass becomes more polymerized and the number of the NBOs decreases. These findings exclude the possibility that  $\text{Nb}^{5+}$  can act as a glass modifier. However, they are in agreement with a previous Raman studies<sup>380</sup> on alkali silicate and alkali germanate glasses which showed that  $\text{Nb}^{5+}$  forms distorted  $\text{NbO}_6$  octahedral units with short Nb—O bonds with and without NBOs. The Nb:Si ratio was changed from 0.44 to 1 and 2. In the case of  $y = 0.1$ , the Nb:Si equals 0.44, the possibility for the  $\text{NbO}_6$  octahedra to be singly dispersed in the silica network is at maximum. However, the Raman spectra showed that the vibration of the  $[\text{NbO}_6]^-$  octahedra with NBOs and/or with much distortion are available while those due to the less distorted  $\text{NbO}_6$  octahedra without NBOs were absent.

## 9.1.3 Glass-ceramic Formation (XRD and DSC)

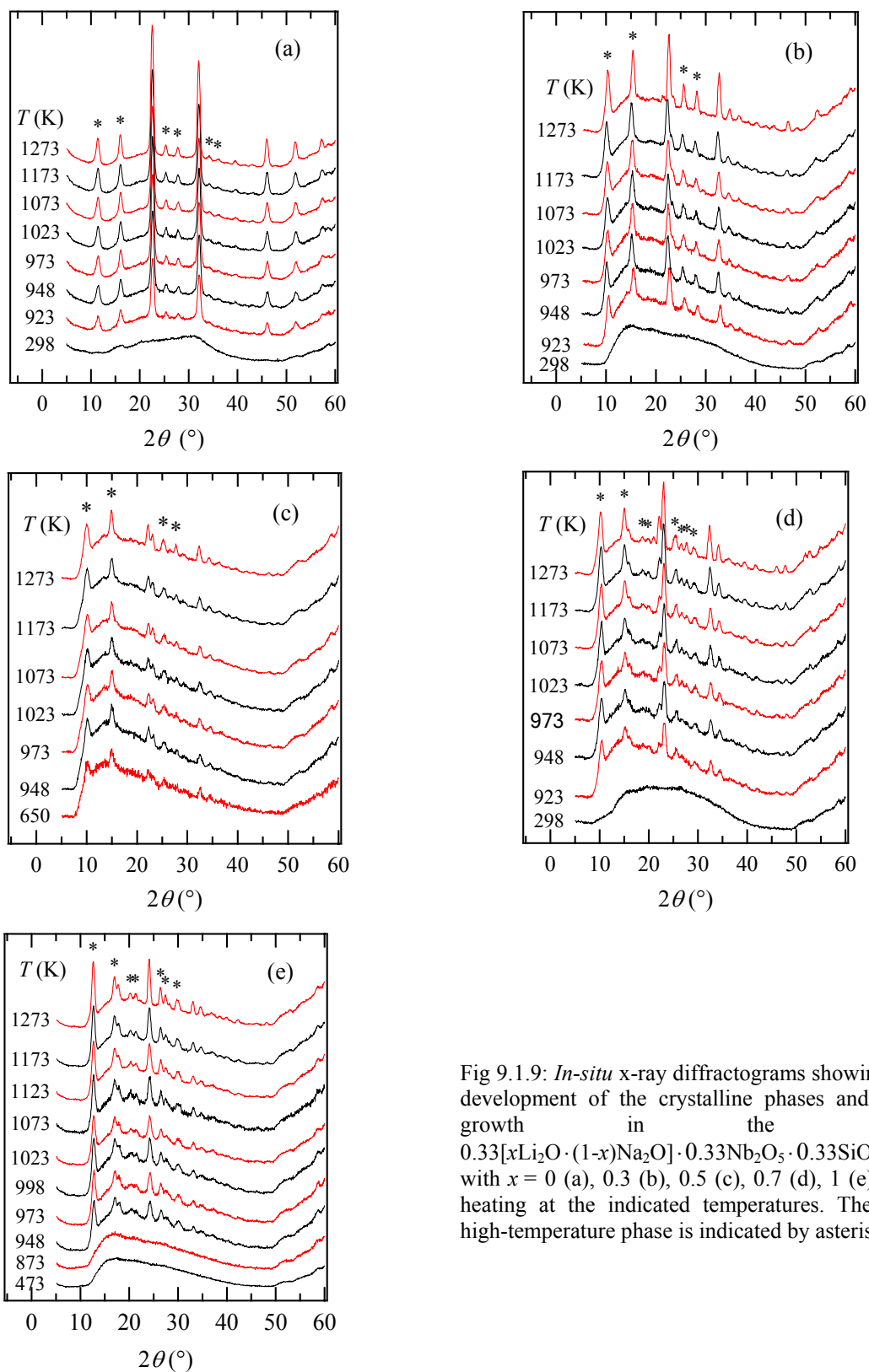


Fig 9.1.9: *In-situ* x-ray diffractograms showing the development of the crystalline phases and their growth in the glass  $0.33[x\text{Li}_2\text{O} \cdot (1-x)\text{Na}_2\text{O}] \cdot 0.33\text{Nb}_2\text{O}_5 \cdot 0.33\text{SiO}_2$  with  $x = 0$  (a), 0.3 (b), 0.5 (c), 0.7 (d), 1 (e) with heating at the indicated temperatures. The new high-temperature phase is indicated by asterisks.

The investigation of the crystallization process and its kinetics for  $\text{LiNbO}_3$ <sup>389–392</sup> or  $\text{NaNbO}_3$ <sup>120,253,393–394</sup> glasses is beyond the scope of this work. Fig. 9.1.9 shows the *in-situ* diffractograms for all glasses  $0.33[x\text{Li}_2\text{O} \cdot (1-x)\text{Na}_2\text{O}] \cdot 0.33\text{Nb}_2\text{O}_5 \cdot 0.33\text{SiO}_2$ , with  $x = 0, 0.3, 0.5, 0.7$ , and  $x = 1$ . They were subjected to the same temperature treatment to monitor the particle growth inside the glassy matrix. No diffraction peaks were detected up to 898 K whereas strong diffraction bands appeared at 923 K in all cases. No further increase in the peak intensities was noticed when the temperature was increased in steps up to 1273 K. The crystalline phases were refined as  $\text{LiNbO}_3$ ,  $\text{NaNbO}_3$  and cristobalite in all cases except in the case of pure sodium glass, where no cristobalite was detected. Beside these main phases there was an additional high-temperature new phase indicated by asterisks in Fig. 9.1.9. Applying the method of Rietveld refinement to the available low resolution data, it was only possible to say that the new phase has a tetragonal crystallographic structure with  $a = 7.91046 \text{ \AA}$  and  $c = 7.65169 \text{ \AA}$ .

After cooling the samples which were used in the *in-situ* experiment higher resolution XRD diffractograms were recorded for them at room temperature, Fig. 9.1.10(a). The high-temperature phase disappeared and the Rietveld refinement, appendix A.5.3, showed the presence of  $\text{LiNbO}_3$  (trigonal,  $R 3 c H$ ),

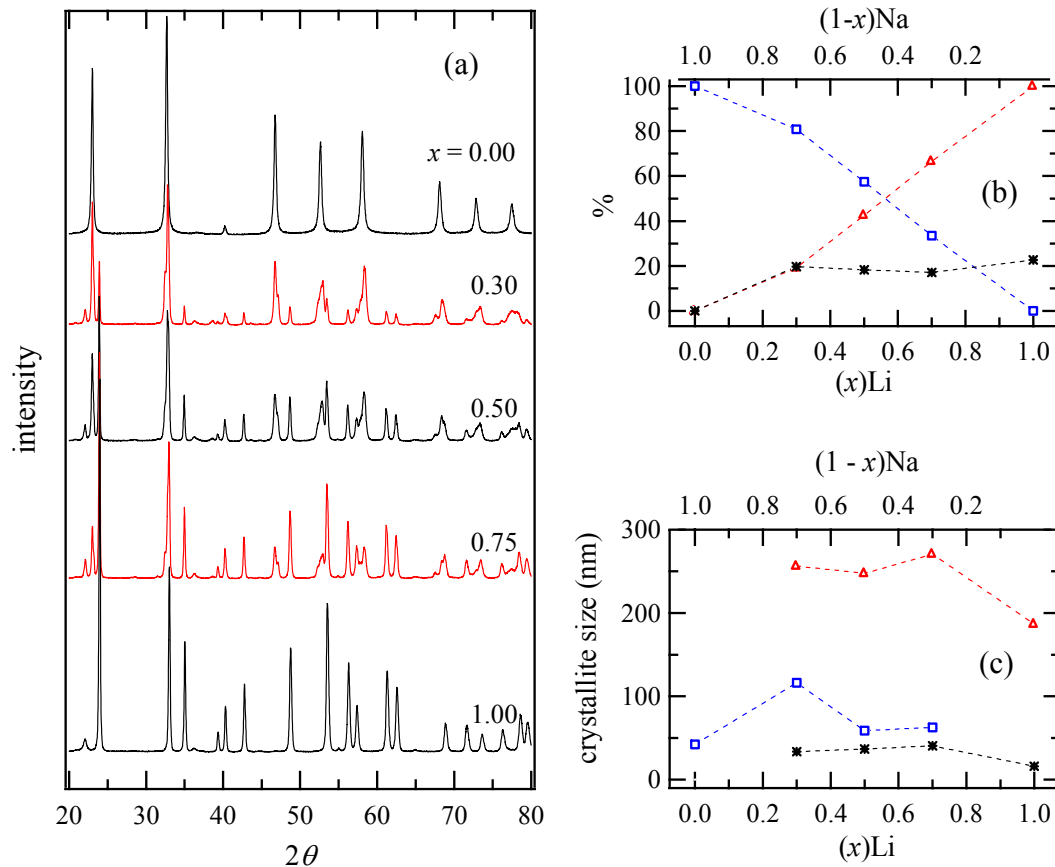


Fig. 9.1.10: Samples  $0.33[x\text{Li}_2\text{O} \cdot (1-x)\text{Na}_2\text{O}] \cdot 0.33\text{Nb}_2\text{O}_5 \cdot 0.33\text{SiO}_2$ , with different  $x$  values after being heated in the *in-situ* experiment: (a) the XRD patterns, (b) the percentage of  $\text{LiNbO}_3$  ( $\Delta$ ) and  $\text{NaNbO}_3$  ( $\square$ ), in the crystalline niobate phase, and the percentage of Cristobalite ( $*$ ) in the total crystalline phase, (c) their particle sizes (in nm).

$\text{NaNbO}_3$  Lueshite high (cubic,  $Pm\bar{3}m$ ),  $\text{NaNbO}_3$  Lueshite low (monoclinic,  $P12/m1$ ), and cristobalite low (tetragonal,  $P41212$ )  $\text{NaNbO}_3$ , the details are listed in Table 9.1.1.

The cristobalite low was formed with nearly constant percentage for the mixed glasses ( $\sim 18\%$ ). However, it was formed much more in the case of the pure Li glass. No cristobalite was found in the pure sodium glass. This fact is in agreement with our previous findings that the  $\text{Li}^+$  ions prefer the Nb network over the silica. Furthermore, this fact may encourage the neutral silica to separate as cristobalite in the glasses which contain Li as a modifier whereas the pure sodium glass, in which the  $\text{Na}^+$  ion prefer the silica side, showed no separation of cristobalite.

It can be clearly seen that the percentage of the crystalline  $\text{LiNbO}_3$  is always less than the percentage of Li in the starting glass contrarily to the  $\text{NaNbO}_3$  percent which was higher than the Na ion percent in the starting glass, Fig. 9.1.10(b). However, this should not be taken as a reliable estimation as the XRD measurement may underestimate the  $\text{LiNbO}_3$  content and consequently  $\text{NaNbO}_3$  is overestimated due to the low atomic scattering factor of the light Li atom, as was discussed in Sec. 8.1.3 (by comparing the percentage obtained from XRD refinement with those obtained from  $^{93}\text{Nb}$ -NMR). Furthermore, it can clearly be seen that  $\text{LiNbO}_3$  has crystallite sizes three times bigger than those of  $\text{NaNbO}_3$  in the mixed glasses. This may be attributed to the fact that  $\text{NaNbO}_3$  nucleates producing higher number of sites for particles growth, hence the precipitated material will be distributed among larger number of particles and thus they remain small. The crystallite sizes show no regular trend with varying the composition,  $x$ ; however, it can clearly be seen that in the case of the single-alkali glasses (i.e. glasses with  $x = 0$  and 1) the crystallite sizes of both  $\text{LiNbO}_3$  and  $\text{NaNbO}_3$  were smaller than their size in the mixed-alkali glasses. This may be

Table 9.1.1: Result of the Rietveld refinement for the crystalline phases in the glass-ceramics with the starting glass compositions  $.33[x\text{Li}_2\text{O}\cdot(1-x)\text{Na}_2\text{O}]\cdot 0.33\text{Nb}_2\text{O}_5\cdot 0.33\text{SiO}_2$  for the indicated  $x$  values after the growth of the crystalline particles by heat treatment.

$x$	Phase	%	Crystallite size (nm)	$a$ (Å)	$b$ (Å)	$c$ (Å)	$\beta$ (°)
1.00	$\text{LiNbO}_3$	77.3	186.5	5.1608	–	13.8291	
	cristobalite low	22.7	16.2	4.9938	–	7.0434	
0.70	$\text{LiNbO}_3$	55.19	270.7	5.1684	–	13.8363	
	$\text{NaNbO}_3$ Lueshite high	0.03	47.4	4.0547	–	–	
	$\text{NaNbO}_3$ Lueshite low	27.69	62.7	3.9171	3.8782	3.9061	90.6987
	cristobalite low	17.10	40.5	4.9984	–	7.0118	
0.50	$\text{LiNbO}_3$	34.8	247.5	5.1677	–	13.8351	
	$\text{NaNbO}_3$ Lueshite low	46.9	58.9	3.9144	3.8797	3.9022	90.6590
	cristobalite low	18.3	36.7	4.9993	–	7.0047	
0.30	$\text{LiNbO}_3$	15.4	256.2	5.1668	–	13.8385	
	cristobalite low	19.7	33.6	4.9944	–	7.01213	
	$\text{NaNbO}_3$ Lueshite low	64.9	116.3	3.9084	3.8771	3.9072	90.7512
0.00	$\text{NaNbO}_3$ Lueshite low	100	42.2	3.9106	3.9015	3.9055	90.2098



attributed to the fact that the formation of the one kind of alkali niobate ( $\text{LiNbO}_3$  or  $\text{NaNbO}_3$ ) may enhance the formation of the other kind, in other words when the first alkali niobate is formed it serves as crystallization nuclei for the second kind.

Raman spectra for these samples are shown in Fig. 9.1.11. The spectra of microcrystalline  $\text{LiNbO}_3$  and  $\text{NaNbO}_3$  are given on the top and the bottom of the figure for comparison, Fig. 9.1.11(a,g). Those were discussed in detail in Sec. 5.1.4 for  $\text{LiNbO}_3$  and in Sec.8.2.2 for  $\text{NaNbO}_3$ . It is clear that the samples with  $x = 1$  and 0.7 have the spectra of  $\text{LiNbO}_3$ , Fig. 9.1.11(b,c). The spectrum of the sample with  $x = 0.5$  shows the main peaks of  $\text{LiNbO}_3$  with very low intensities, Fig. 9.1.11(d). Meanwhile, no peaks can be seen in the case of  $x = 0.3$  or 0, Fig. 9.1.11(e,f). This may be due to the small crystallites size of  $\text{NaNbO}_3$ , the predominant phase, which is not able to give sufficient scattering to detect the Raman spectra of the crystalline phase.

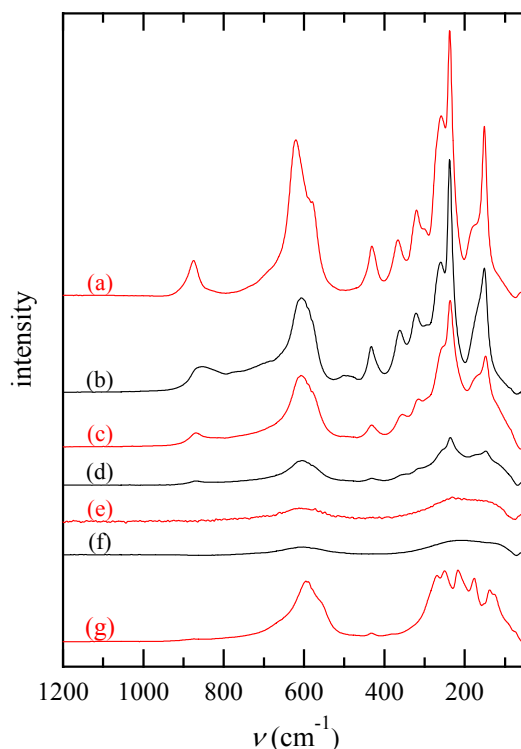


Fig. 9.1.11: Raman spectra for samples  $0.33[x\text{Li}_2\text{O} \cdot (1-x)\text{Na}_2\text{O}] \cdot 0.33\text{Nb}_2\text{O}_5 \cdot 0.33\text{SiO}_2$ , after being heated in the in situ XRD experiment with different  $x$  values: (b) 1.0, (c) 0.7, (d) 0.5, (e) 0.3, and (f) 0.0, while (a) and (g) are the spectra for commercial microcrystalline  $\text{LiNbO}_3$  and  $\text{NaNbO}_3$  for comparison.

#### 9.1.4 General Discussion

The structural role of  $\text{Nb}_2\text{O}_5$  in glasses was intensively targeted by many investigators utilizing several experimental techniques in silicate, phosphate, borate aluminate and galate systems containing  $\text{Nb}_2\text{O}_5$ <sup>363,380,395–400</sup>. However, the main roll played by  $\text{Nb}_2\text{O}_5$  (glass former or modifier), the coordination state of  $\text{Nb}^{5+}$  (4- or 6-coordinated), the deformation for its polyhedra and the mechanism for interaction with other elements have not been sufficiently explored. Earlier results suggest that niobium may function as both a network modifier and former in glasses<sup>397</sup>. Fukumi *et al*<sup>401</sup> proposed that  $\text{Nb}_2\text{O}_5$ , like  $\text{Cs}_2\text{O}$ , creates NBOs and showed the presence of  $\text{AlO}_4$  and  $\text{NbO}_6$  groups containing NBOs and three coordinate oxygens in cesium aluminate glasses. Furthermore, the random network theory considered the  $\text{Nb}^{5+}$  to have a tetrahedral coordination, because the coordination number 4 is the most suitable for a stable three-dimensional random network. The close value of Nb—O bond lengths in  $[\text{NbO}_4]$  tetrahedra (1.9 Å) and  $[\text{NbO}_6]$  octahedra (2.0 Å)<sup>402</sup> resulted in difficulties in determining the coordination state of  $\text{Nb}^{5+}$  from the Raman spectra of niobium containing glasses. One of the high-frequency bands of niobium germinate<sup>403</sup>, niobium phosphate<sup>404</sup>, and niobium borate<sup>405</sup> glasses was assigned to vibration of  $[\text{NbO}_4]$  tetrahedra. Si-

dorov<sup>406</sup> observed the NbO<sub>5</sub> group in the glasses of the Na<sub>2</sub>O·Nb<sub>2</sub>O<sub>5</sub>·SiO<sub>2</sub> system. In  $x\text{Nb}_2\text{O}_5 \cdot (1-x)/3(\text{Na}_2\text{O} \cdot 2\text{SiO}_2)$  glasses, Huanxin *et al.*<sup>363</sup> found by EXAFS and Raman spectroscopy that as  $x$  increases from 0.05 to 0.15, the coordination number of niobium increases from five to six (coordination number 5 was explained as a result of the coexistence of some NbO<sub>4</sub> units with NbO<sub>6</sub> octahedra). Some Raman and EXAFS studies indicate that the coordination number of niobium increases from four to six as the concentration of niobium oxide increases in alkali borate and alkali-silicate glasses<sup>399, 400, 407</sup>. However, the Nb<sup>5+</sup> ion has a too large radius (0.69 Å). Taking into account the radius ratios of the cation to its neighboring oxygen ions there is indication that Nb<sup>5+</sup> should have a higher coordination number than silicon ions (6 fold and 4 fold coordination, respectively). Thus tetrahedrally coordinated Nb<sup>5+</sup> would create anion vacancies which form asymmetry centers of binding forces that in turn would introduce weakness and instability<sup>408</sup>. Moreover, only a few rare-earth ANbO<sub>4</sub> (A = Y, Yb, Sm, and La) compounds have been found to possess tetrahedral coordination, while six-coordinated Nb<sup>5+</sup> examples are numerous<sup>245</sup>.

One possible postulate is that, as the Nb<sub>2</sub>O<sub>5</sub> content of these glasses increases, the number of Si—O—Si linkages should decrease while the number of Si—O—Nb linkages increases. The connectivity of the structure should increase because the niobium ions have a greater coordination number than silicon. Although the niobium-oxygen bonds are weaker than those of silicon-oxygen, as predicted by field strength calculations, and melting temperature of SiO<sub>2</sub> (1996 K) is higher than that of Nb<sub>2</sub>O<sub>5</sub> (1759 K), the number of cation-oxygen bonds is increasing. The increase in the connectivity of the network with the addition of niobium oxide explains the property trends in the constant Li<sub>2</sub>O/SiO<sub>2</sub> glasses with increasing Nb<sub>2</sub>O<sub>5</sub>.

In studying the K<sub>2</sub>O·SiO<sub>2</sub>·Nb<sub>2</sub>O<sub>5</sub> system, Rao<sup>397</sup> observed an increase in the density, refractive index, molar refraction and dielectric constant with increasing Nb<sub>2</sub>O<sub>5</sub> concentration. In addition, he observed an abrupt jump in the trends of chemical durability, coefficient of expansion and softening temperature at particular concentrations which were attributed to niobium functioning as both a network modifier and former. The results obtained for the same system by Vemacotola *et al.*<sup>409</sup> agreed well with the results of Rao<sup>395</sup> and with results of Hirayama and Berg for sodium niobium silicate system<sup>120, 410</sup>. However, the abrupt trend changes observed by Rao were not observed by Vemacotola and Shelby<sup>395, 398</sup>. Their results on the potassium niobium silicate system suggest that niobium acts only as a network former, strengthening the glass network, contrary to the conclusions of Rao, and others<sup>397, 399, 400</sup>. Similar results in the potassium tantalum system suggest that tantalum plays a similar role<sup>25, 395</sup>.

The most accepted structural model for similar glassy systems was suggested by Ito *et al.*<sup>411</sup> for the lithium tantalum silicate and the similar one proposed by Vemacotola and Shelby for the potassium niobium silicate.<sup>395, 398</sup> Their model stated that Nb<sup>5+</sup> (or Ta<sup>5+</sup>) requires an alkali ion in order to balance the six-fold coordinated [NbO<sub>6</sub>] unit charge. Hence, the replacement of a mole of SiO<sub>2</sub> by a mole of Nb<sub>2</sub>O<sub>5</sub> eliminates 2 NBOs from the structure and may introduce a maximum of 4 BOs into it. The replacement of a single mole of alkali with a mole of niobium oxide results in a net gain of 3 BOs and the elimination of 2 NBOs in NbO<sub>6</sub> octahedral. This contributes to a better symmetry of network force<sup>112</sup>. Accordingly, the

connectivity of the glass network is expected to reach its maximum when alkali/niobium ratio of 1 in order to insure the complete neutralization of  $\text{NbO}_6$  units, and thus having a stable glass network. The ability of glasses to be formed at alkali/niobium molar ratios  $< 1$  may be attributed to the distorted state of the octahedral  $[\text{NbO}_6]$  units caused by the high polarizability of the niobium ion<sup>380</sup>. In a similar structural model for mixed alkali and alkaline-earth niobium silicate glasses, Samuneva *et al*<sup>112</sup> assumed that  $\text{Nb}^{5+}$  is a network former. The  $\text{NbO}_6$  groups are assumed to occupy an equivalent position with  $\text{SiO}_4$  tetrahedra, by an ion compensator binding the separate Si—O fragment into a common network. Where  $\text{K}^+$  and  $\text{Ba}^{2+}$  cations are located close to the  $\text{NbO}_6$  octahedra neutralizing the excess negative charges. Another recent work used the following structure model: The parent glass is a random network similar to glassy silica in which the corner sharing  $\text{SiO}_4$ -tetrahedra are partially substituted by  $\text{NbO}_6$ -octahedra. They are linked alternatively to form a three dimensional infinite network which lack of symmetry and long range order. In view of its role of network modifier and of its high diffusivity within the glass structure, the alkali cations (e.g.  $\text{Na}^+$ ) are located in the vicinity of non-bridging oxygen of  $\text{SiO}_4$ -tetrahedra or  $\text{NbO}_6$ -octahedra. The exact position of the alkali cation in the parent glass is rather important for the mechanism of nucleation of the crystal phase<sup>412</sup>.

In  $x\text{Nb}_2\text{O}_5 \cdot (1-x)/3(\text{Na}_2\text{O} \cdot 2\text{SiO}_2)$  glasse<sup>363</sup>, at  $x = 0.05$  the niobium has a coordination number of five as a result of the coexistence of some  $\text{NbO}_4$  units with  $\text{NbO}_6$  octahedra. However, when  $x$  increases to 0.15, the coordination number increases to six. The  $\text{NbO}_6$  octahedra are initially dispersed and connected separately to the Si—O network. At  $x \geq 0.2$ , it was necessary to balance the electrovalence between the  $\text{NbO}_6$  groups and  $\text{R}^+$  by the formation of some holes among the distorted  $\text{NbO}_6$  octahedra and a more loosely glass network resulting in stable density and refractive index. Then, with increasing  $x$ , the  $\text{NbO}_6$  groups will join each other by sharing corners. This is accompanied by an increase in the density and oxygen coordination number. Only at  $x = 0.25$  it was possible to observe the Nb—Nb EXAFS peak at 3.8 Å. In the constant silica and constant alkali-oxide glasses at niobium oxide concentrations  $> 10$ -20 mol %, a competition for the low concentration of alkali ions between the NBO sites and the charged  $[\text{NbO}_6]^-$  sites may occur.

Incompatibility between charged  $[\text{NbO}_6]^-$  and the neutral silica tetrahedral structural units may lead to phase separation. The occurrence of phase separation may also cause the deviation of properties from the trend in the glasses with a high concentration of silica and niobium.

Replacement of silica by an equimolar mixture of niobium and alkali oxides permits glass formation at compositions with as little as 20 mol % silica. Glass transformation temperatures of equimolar alkali oxide/niobium oxide glasses decrease with decreasing silica content, while thermal expansion coefficients and densities increase in the potassium niobium silicate glasses. As the silica content decreases below 50 mol % in the potassium niobium silicate glasses, the densities, thermal expansion coefficients, and glass transformation temperatures level out, as if approaching minima or maxima. These results suggest that the structural role of niobium is changing in the network. The number of Si—O—Nb linkages decreases and

the number of Nb—O—Nb linkages increases as the silica content decreases. Similar behavior has been demonstrated by Shaw and Shelby<sup>413</sup> in the barium gallosilicate system and by Shelby<sup>414</sup> in calcium aluminosilicate glasses. The weaker Nb—O bonds relative to Si—O bonds in a network dominated by Nb—O—Nb linkages and the high atomic weight of niobium explain the decrease in the glass transformation temperatures and the increases in density and thermal expansion coefficients with decreasing silica content.

The property trends in the equimolar potassium oxide/niobium oxide glasses with decreasing silica content indicate that the weaker the niobium-oxygen bond relative to the silicon-oxygen bond has a greater influence on the bulk properties of these glasses than does the higher coordination of a niobium-based network versus a silica-based network.

It should also be noted that small additions of niobium oxide of about 5 mol % largely enhance the durability of the normally hygroscopic potassium silicate glasses. Furthermore it supports the network strengthening effect of niobium oxide on these glasses.

## 9.2 DYNAMICS AND DIFFUSION: MIXED-ALKALI EFFECT

### 9.2.1 Impedance Spectroscopy of (Li,Na) Niobosilicate Glasses

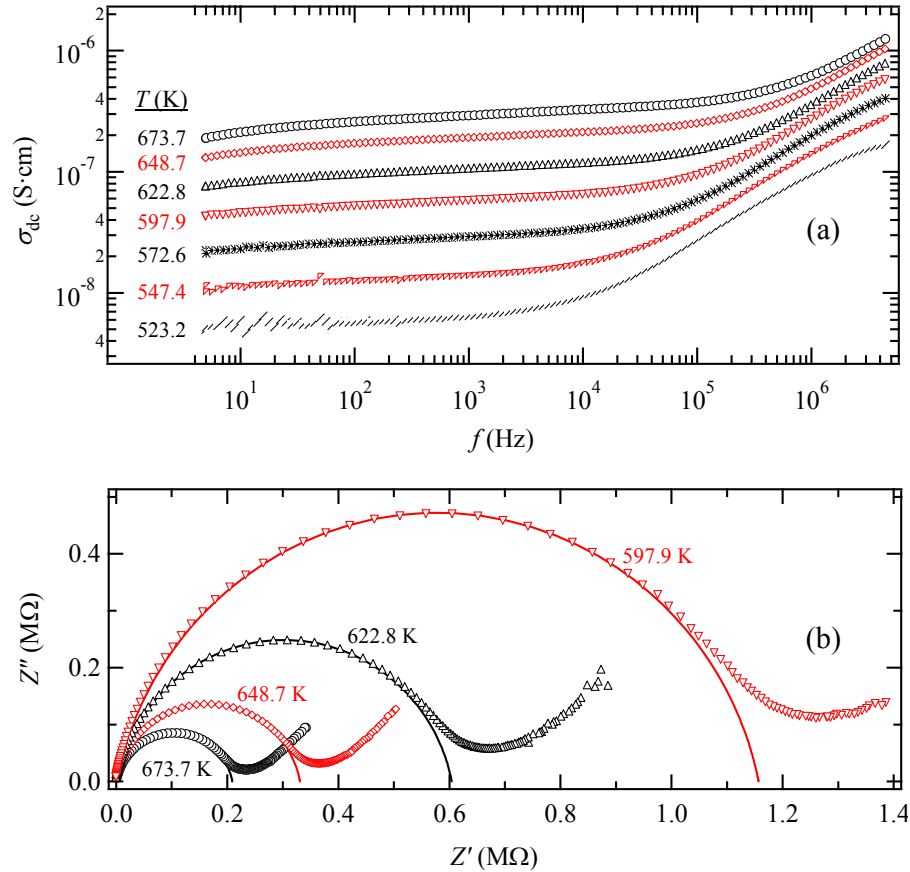


Fig. 9.2.1: (a) the log-log plot for the frequency dependence of the conductivity,  $\sigma$ , for the glass  $0.33[x\text{Li}_2\text{O} \cdot (1-x)\text{Na}_2\text{O}] \cdot 0.33\text{Nb}_2\text{O}_5 \cdot 0.33\text{SiO}_2$  ( $x = 0.5$ ), (b) the complex plane representation for the same sample for temperatures 598–674 K, the solid lines represent the equivalent circuit ( $RQ$ ) obtained for the samples.

The  $0.33[x\text{Li}_2\text{O} \cdot (1-x)\text{Na}_2\text{O}] \cdot 0.33\text{Nb}_2\text{O}_5 \cdot 0.33\text{SiO}_2$  glass samples show typical log-log frequency-dependent conductivity plots, i.e. a frequency independent plateau which corresponds to direct current conductivity ( $\sigma_{dc}$ ) at the low frequencies in addition to a frequency-dependent dispersion region at higher frequencies, Fig. 9.2.1(a). The exact values of  $\sigma_{dc}$  were obtained by fitting the data in the complex plane diagrams, Fig. 9.2.1(b). Depressed semicircles are obtained indicating the presence of a distribution of relaxation processes. This is expected for glassy samples as they have different diffusion pathways with several energy barriers. The semicircle is best fitted with an equivalent circuit which consisting of a resistor and a constant phase element connected in parallel ( $RQ$ ). The  $R$  values can be used to calculate  $\sigma_{dc}$  for the sample at various temperatures.

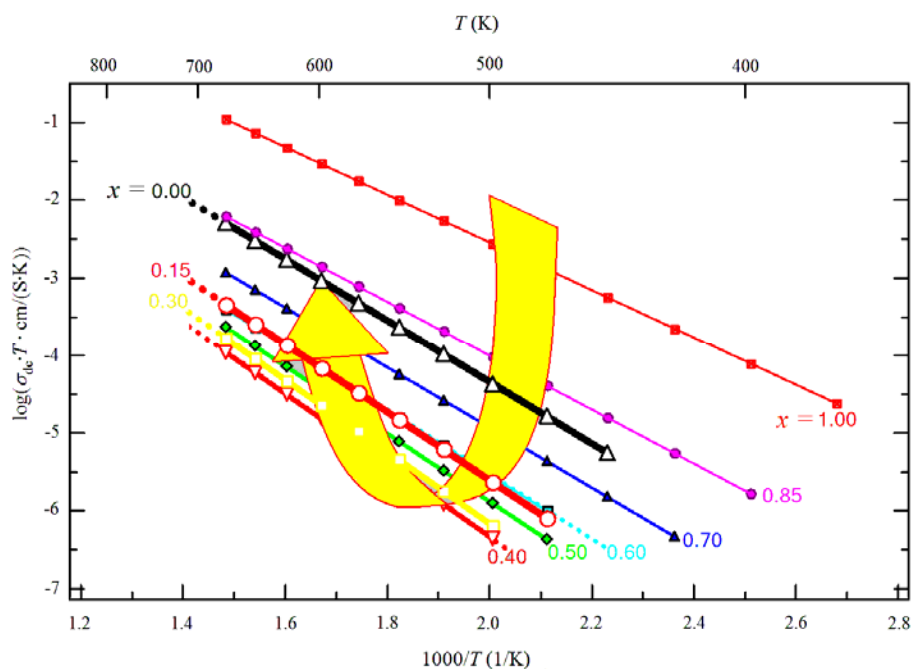


Fig. 9.2.2: Arrhenius plot for the glasses  $0.33[x\text{Li}_2\text{O} \cdot (1-x)\text{Na}_2\text{O}] \cdot 0.33\text{Nb}_2\text{O}_5 \cdot 0.33\text{SiO}_2$ , with  $0 \leq x \leq 1$ . The lines represent the best linear fit. The thin lines represent the part with decreasing conductivity whereas the thick lines represent the side with increasing conductivity.

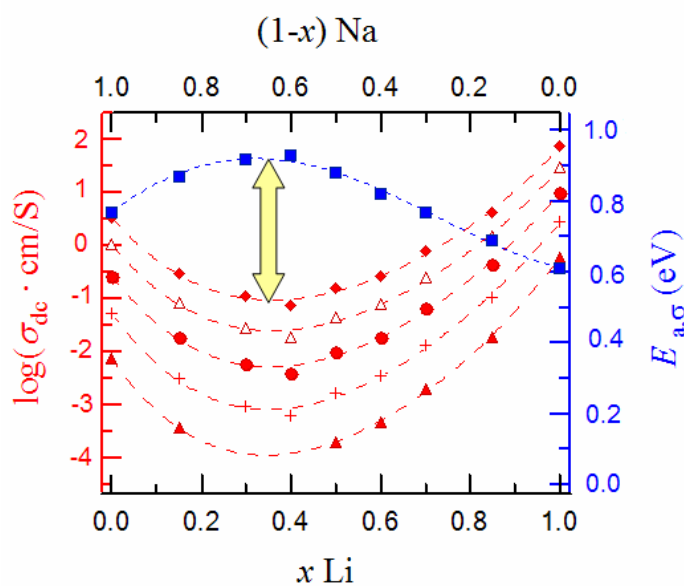


Table 9.2.1: Arrhenius parameters (activation energy,  $E_a^{\sigma_{dc}}$ , and the logarithm of the pre-exponential factor) of the plots shown above in Fig. 7.3.10.

$x$	$\text{Log}(A \cdot \text{K} \cdot \text{S} \cdot \text{cm}^{-1})$	$E_a^{\sigma_{dc}}$ (eV)
0.00	3.5962	0.79
0.15	3.1499	0.87
0.30	3.1088	0.92
0.40	2.8539	0.91
0.50	2.8441	0.87
0.60	2.745	0.82
0.70	2.8233	0.77
0.85	2.9591	0.69
1.00	3.5901	0.61

Fig. 9.2.3: Variation in  $\sigma_{dc}$  with changing  $x$  value.  $\sigma_{dc}$  values are shown for the temperatures ( $\blacktriangle$  473,  $+$  523,  $\bullet$  573,  $\triangle$  623 and  $\blacklozenge$  673 K) in comparison with  $E_a^{\sigma_{dc}}$  ( $\blacksquare$ ). While  $\sigma_{dc}$  shows its MAE minima at  $x = 0.37$ , the  $E_a^{\sigma_{dc}}$  shows an absolute maximum at the same  $x$  value. The resulting Arrhenius parameters are given in table 9.2.1.

ple at various temperatures.

Fig. 9.2.2 shows the temperature dependence of  $\sigma_{dc}$  (plotted as  $\sigma_{dc} \cdot T$  vs.  $1000/T$ ), for the glasses

$0.33[x\text{Li}_2\text{O} \cdot (1-x)\text{Na}_2\text{O}] \cdot 0.33\text{Nb}_2\text{O}_5 \cdot 0.33\text{SiO}_2$  with  $0 \leq x \leq 1$  in the temperature range from 423 K to 673 K in steps of 25 K. However, some compositions showed very low conductivities to be measured in the lower temperature regimes. For all compositions,  $\sigma_{\text{dc}}$  follows an Arrhenius behavior represented by the straight lines shown in the figure. The pure lithium glass sample ( $x = 1$ ) shows a  $\sigma_{\text{dc}}$  which is 1.5 to 2 orders of magnitude higher than that of the pure sodium sample ( $x = 0$ ) indicating that the  $\text{Na}^+$  cation is less mobile than the smaller  $\text{Li}^+$  cation. However, when replacing  $\text{Li}^+$  by  $\text{Na}^+$  and while keeping the total amount of the alkali modifiers constant, a clear trend in the  $\sigma_{\text{dc}}$  values can be perceived by tracking the big arrow in Fig. 9.2.2. When going from  $x = 1$  to  $x = 0.4$ , i.e. with increasing Na content, the Arrhenius plots take lower positions and get steeper, implying that the value of  $\sigma_{\text{dc}}$  is decreasing whereas its activation energy ( $E_{\text{a}}^{\sigma_{\text{dc}}}$ ) is increased. At  $x = 0.4$ , an inflection in the behavior occurs and  $\sigma_{\text{dc}}$  starts to increase while  $E_{\text{a}}^{\sigma_{\text{dc}}}$  decreases with decreasing  $x$  till the pure sodium glass is reached at  $x = 0$ . The values of  $E_{\text{a}}^{\sigma_{\text{dc}}}$  and the pre-exponential factors for all glass samples are listed in Table 9.2.1. This deviation from linear behavior, represented by minima in  $\sigma_{\text{dc}}$  as one of the alkali ions is replaced with another one, is known as the "mixed-alkali effect" (MAE). To illustrate this behavior, in Fig. 9.2.3  $\sigma_{\text{dc}}$  is plotted as a function of  $x$  for temperatures between 473 K and 673 K.  $\sigma_{\text{dc}}$  decreases by three orders of magnitude by going from the pure lithium glass to the absolute minimum at  $x = 0.37$ ; afterwards it increases again by about 1.5 to 2 orders of magnitude until the pure sodium glass is reached. Careful inspection of the figure reveals that the minimum of the MAE gets shallower with increasing temperature. The values of  $E_{\text{a}}^{\sigma_{\text{dc}}}$  also vary with  $x$  but in the opposite way to  $\sigma_{\text{dc}}$ . At  $x = 1$ ,  $E_{\text{a}}^{\sigma_{\text{dc}}}$  is equal to 0.61 eV which is lower than its value of  $E_{\text{a}}^{\sigma_{\text{dc}}} = 0.79$  eV at  $x = 0$ . In-between  $E_{\text{a}}^{\sigma_{\text{dc}}}$  shows an absolute maximum that coincides with the minimum of  $\sigma_{\text{dc}}$  at  $x \approx 0.37$ , indicated by the double arrow in Fig. 9.2.3.

## 9.2.2 $^7\text{Li}$ and $^{23}\text{Na}$ NMR Spin-Lattice Relaxation Rate

Impedance spectroscopy is known to detect the dynamics of the overall charge-carrier including the different ions as well as the electrons. However, with  $^7\text{Li}$  and  $^{23}\text{Na}$  NMR methods it is possible to monitor the dynamics of individual types of mobile species in a relatively more selective way. Nevertheless, even with NMR SLR, the relaxation rate of each type of nucleus is affected by the other type. In the present case, this means that  $^7\text{Li}$  relaxation is due to  $^7\text{Li}$ - $^7\text{Li}$  and  $^7\text{Li}$ - $^{23}\text{Na}$  interactions, whereas,  $^{23}\text{Na}$  relaxation is due to  $^{23}\text{Na}$ - $^{23}\text{Na}$  and  $^7\text{Li}$ - $^{23}\text{Na}$  interactions. However, under the condition that  $\text{Na}^+$  diffuses much slower than the lighter  $\text{Li}^+$ , the predominant movement of the more mobile species can be easily sampled. The measured  $^7\text{Li}$  spin-lattice relaxation rates ( $T_1^{-1}$ ) vs. reciprocal temperature ( $1000/T$ ) are shown for the glass  $0.33[x\text{Li}_2\text{O} \cdot (1-x)\text{Na}_2\text{O}] \cdot 0.33\text{Nb}_2\text{O}_5 \cdot 0.33\text{SiO}_2$  with  $0.15 \leq x \leq 1$  in Fig. 9.2.4(a). The measurements were limited to temperatures below 450 K. Within this temperature range only the background contribu-

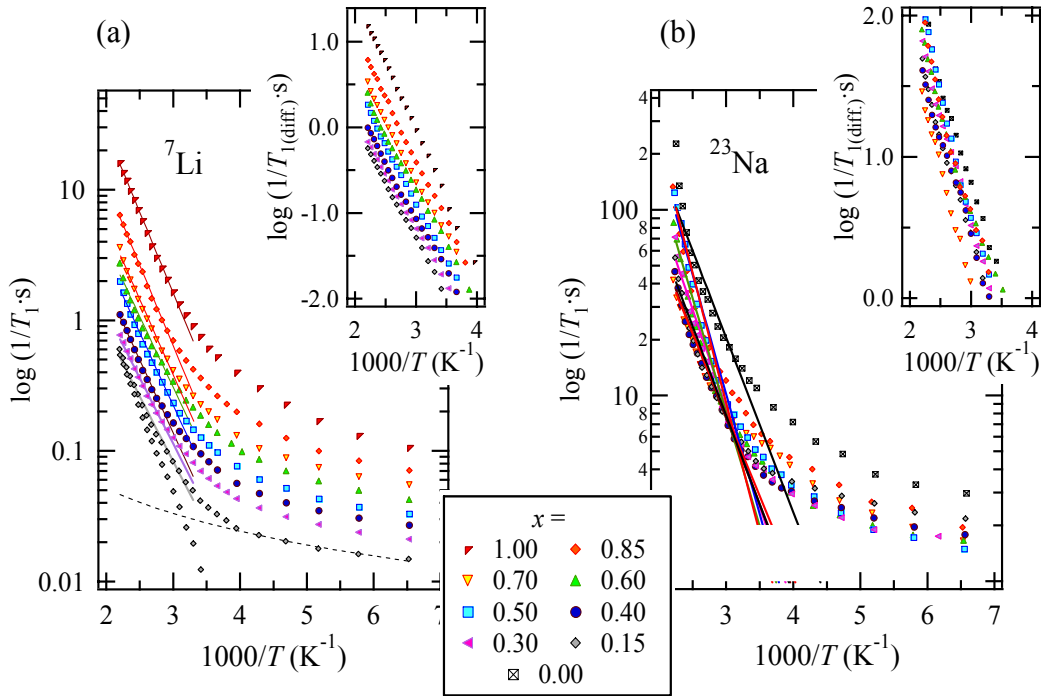


Fig. 9.2.4: The temperature dependence of the spin-lattice relaxation rates ( $1/T_1$ ) for the glasses  $0.33[x\text{Li}_2\text{O} \cdot (1-x)\text{Na}_2\text{O}] \cdot 0.33\text{Nb}_2\text{O}_5 \cdot 0.33\text{SiO}_2$ , with  $0 \leq x \leq 1$ ; (a)  $^7\text{Li}$  SLR rates measured at  $\omega_0/2\pi = 77.7$  MHz, (b)  $^{23}\text{Na}$  SLR rates measured at  $\omega_0/2\pi = 52.9$  MHz. The activation energies, in Table 9.2.2, are calculated from the low temperature flank for the raw data (without correction) and for the pure diffusion-induced rate after the subtraction of the non-diffusive background contribution as shown for the sample with  $x = 0.15$  in the bottom of (a).

tion to  $T_1^{-1}$  and a part of the low-temperature flanks of the diffusion-induced  $1/T_1$  maxima could be observed. This is why it was not possible to extract much information about the  $^7\text{Li}$  dynamics. The background correction of the raw  $1/T_1$  data was done by subtracting the background rates.  $1/T_{1\text{bgr}}$  was fitted with a power law  $1/T_{1\text{bgr}} \propto T^\kappa$  with  $\kappa$  ranging between -1.45 and -0.7. At any temperature,  $T_1^{-1}$  of  $^7\text{Li}$  shows a continuous decrease with increasing Na content ( $1-x$ ). The activation energies of  $T_{1\text{diff}}^{-1}$  for  $\text{Li}^+$ ,  $E_A^{\text{SLR}}$ , for these glasses lie between 0.24(1) and 0.29(7) eV. There is no clear trend as a function of  $x$  for the values of the activation energy with and without background correction, see Table 9.2.2.

For the  $^{23}\text{Na}$  SLR rates the situation is more complicated as shown in Fig. 9.2.4 (b). The samples with  $0 \leq x \leq 0.85$  were measured in the same temperature range. The pure Na glass ( $x = 0$ ) shows noticeably higher  $^{23}\text{Na}$  SLR rates, whereas the rest of the samples are very near to each others and show irregular variation as a function of  $x$ . Here also, as in the case of  $^7\text{Li}$ , the background contributions to  $T_1^{-1}$  beside only small parts of the low-temperature flanks are observed. For  $0 \leq x \leq 0.85$ , the background power  $\kappa$  was in the range of -1.93 to -0.93 and the  $\text{Na}^+$  SLR rates activation-energies  $E_a^{\text{SLR}}$  lie between 0.27(5) to 0.33(9) eV, without any clear dependence on  $x$ .



Table 9.2.2: The activation energies for the  ${}^7\text{Li}$  and  ${}^{23}\text{Na}$  SLR rates ( $1/T_1$ ) obtained from the plots of Fig. 9.2.4 (with and without background correction).

$x$	${}^7\text{Li } E_A^{SLR} \text{ (eV)}$		${}^{23}\text{Na } E_A^{SLR} \text{ (eV)}$	
	w/o correction	w correction	w/o correction	w correction
0.00	–	–	0.18(0)	0.28(6)
0.15	0.19(1)	0.25(5)	0.18(4)	0.28(5)
0.30	0.19(3)	0.24(1)	0.20(4)	0.29(4)
0.40	0.21(4)	0.24(9)	0.17(8)	0.27(5)
0.50	0.21(3)	0.26(6)	0.24(8)	0.32(9)
0.60	0.20(8)	0.24(7)	0.23(6)	0.31(5)
0.70	0.22(2)	0.26(4)	0.16(8)	0.32(1)
0.85	0.26(3)	0.27(9)	0.26(9)	0.33(9)
1.00	0.23(7)	0.29(7)	–	–

### 9.2.3 NMR Solid-Echoes (Motional Narrowing of ${}^7\text{Li}$ and ${}^{23}\text{Na}$ Central Transitions)

${}^7\text{Li}$  solid-echo spectra with delay periods of 40  $\mu\text{s}$  were registered at a resonance frequency of 77.7 MHz. Independent of the lithium content,  $x$ , the spectra, measured within the range of the rigid lattice, consist of two contributions: a Gaussian-shaped distribution for quadrupole background and a central line transition

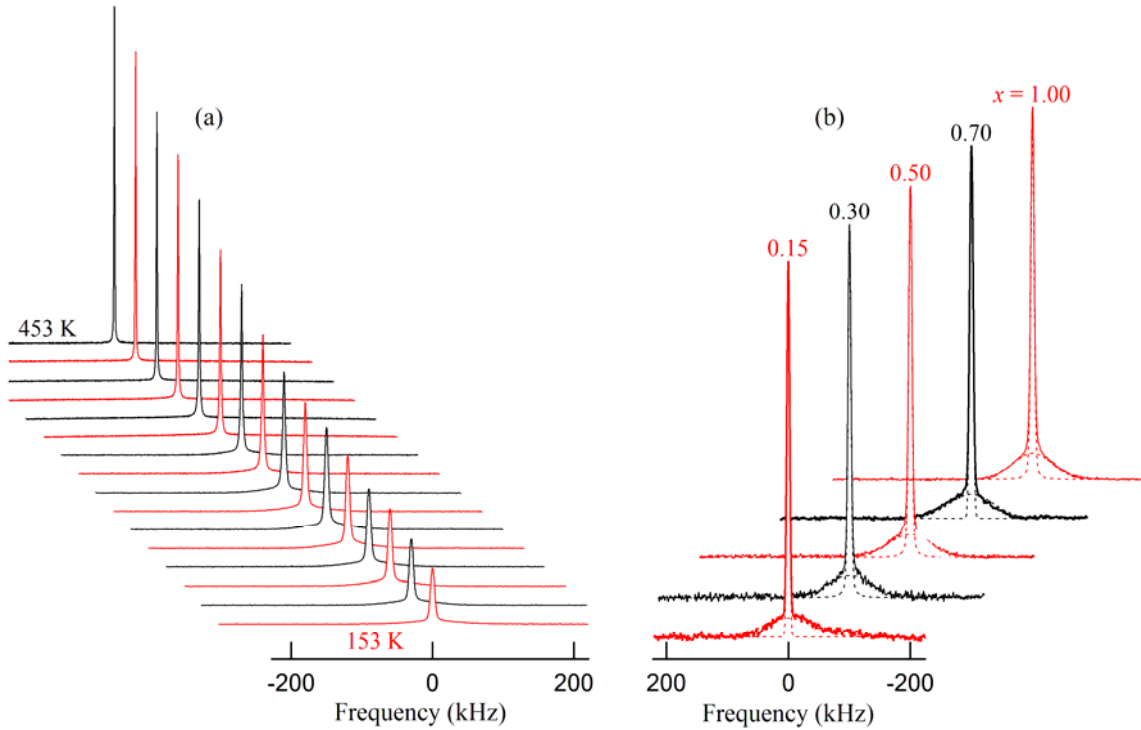


Fig. 9.2.5:  ${}^7\text{Li}$  solid echo spectra measured at 77.7 MHz of  $0.33[x\text{Li}_2\text{O} \cdot (1-x)\text{Na}_2\text{O}] \cdot 0.33\text{Nb}_2\text{O}_5 \cdot 0.33\text{SiO}_2$  glasses: (a) for the pure Li sample ( $x = 1.0$ ) upon heating from 153 to 453 K, showing the disappearance of the contribution of quadrupolar satellites at high temperatures, (b) for different compositions,  $x$ , measured within the rigid lattice range (193 K). Satellite and central line portion are fitted in each case with a Gaussian distribution.

which can be well fitted by a Gaussian line at low temperatures. At higher temperatures the quadrupole contribution usually averages out and Lorentzian lines fit the central transition more properly. Fig. 9.2.5(a) shows these echoes for the sample with  $x = 1$  at temperatures ranging from 153 to 453 K. One can observe the sharpening of the central line and the gradual disappearance of the quadrupole background at high temperatures. As the Li jump rates are larger than the reciprocal of the quadrupole coupling constant, the satellite or the background contributions of the spectra average out. Fig. 9.2.5(b) shows the solid echoes for different contents  $x$ , taken at 193 K. The choice of this temperature was not arbitrary; it was chosen to be low enough for all samples so that all the spectra lie in the rigid-lattice range, i.e. before the lithium-diffusion influence starts to be noticeable. The ratios of the area under the quadrupolar distribution relative to that under the central line contribution are 4:2.9. The quadrupole background shows a fwhm of  $\sim 65$  kHz implying a quadrupole coupling constant of 130 kHz, which is within the usual range for  ${}^7\text{Li}$  spectra. The quadrupole background slightly depends on  $x$ , as it loses intensity with increasing  $x$ .

The  ${}^7\text{Li}$  NMR solid-echoes were measured for all compositions in the temperature range from 153 K to 673 K. The dipolar broadening resulting from the spatial variation of static dipolar fields, seen by the Li spins, is averaged with rising temperature. This is due to Li diffusion leading to a homogeneous narrowing of the central line (motional narrowing). The dipolar motional narrowing of the central line is shown in Fig. 9.2.6. For a better comparison, the measured data points are normalized such as to take values between 1 in the very low temperature limit ( $< 200$  K) and 0 in the high-temperatures limit. The temperature at which the narrowing starts,  $T_{\text{onset}}$ , shifts to higher temperatures with increasing Na content ( $1-x$ ) showing qualitatively that the  $\text{Li}^+$  diffusivity is strongly reduced. For instance, at  $\sim 400$  K, the narrowing of the central line is just at the beginning for the composition  $x = 0.3$ ; however, in the case of the pure lithium glass ( $x = 1$ ) it is almost finished at this temperature. Thus, one can conclude that the Li-jump rates of these two samples differ by several orders of magnitude. Applying the semi-empirical equation of Waugh and Fedin equation, the activation energies for  $\text{Li}^+$  diffusion can be calculated (estimated) from the  $T_{\text{onset}}$  temperatures.  $E_A$  values lie between 0.4 and 0.75 eV. This line narrowing gives a qualitative indication about the  $\text{Li}^+$  dynamics. However, diffusion parameters cannot be extracted from the motional narrowing because of the absence of a meaningful model that correlates NMR motional narrowing to diffusion parameters, in most cases.

The  ${}^{23}\text{Na}$  solid-echo spectra for all compositions do not show any central line narrowing in the measured temperature range (i.e. up to 500 K) as shown at the top of Fig. 9.2.7(a). This emphasizes that  $\text{Na}^+$  diffuses substantially slower than  $\text{Li}^+$ .

### 9.2.4 The Dependence of the Central Linewidth on the Lithium Content

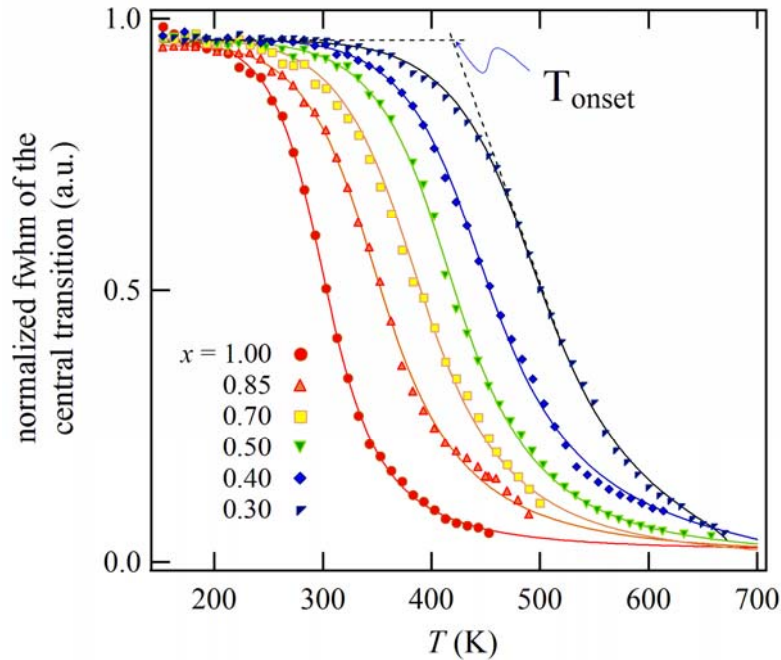


Fig. 9.2.6: The motional narrowing of the  ${}^7\text{Li}$  central line (full width at half maxima) obtained from the solid echoes for the glasses  $0.33[x\text{Li}_2\text{O} \cdot (1-x)\text{Na}_2\text{O}] \cdot 0.33\text{Nb}_2\text{O}_5 \cdot 0.33\text{SiO}_2$  with different lithium contents,  $x$ . The data are normalized to have values between 0 and 1 for a better comparison. The solid lines shown correspond to fits after the Abragam formalism only for guiding the eye.

Fig. 9.2.7 (a) shows that with increasing Na content ( $1-x$ ) there is a systematic decrease in the  ${}^7\text{Li}$  central linewidth (fwhm) measured in the solid lattice range. On the other hand, in the case of  ${}^{23}\text{Na}$  the central linewidth seems to be independent of composition as it stays nearly unchanged with changing  $x$  values (within the experimental error). The values of the fwhm in the rigid lattice are plotted against the alkali content in the glass as shown in Fig. 9.2.7 (b) for  ${}^7\text{Li}$  (bottom) and  ${}^{23}\text{Na}$  (top). The fwhm is linked to the Li-Li ion distance ( $r$ ) according to the van Vleck formula, Eq. (7.2.11). Substituting  $\text{Na}^+$  for  $\text{Li}^+$  the distance between two lithium cations increases and the rigid linewidth ( $\text{fwhm} = f(T)$ ) should decrease. This may be understood as a homogeneous, random distribution of  ${}^7\text{Li}$  cations. Whereas, in the  $\text{Na}^+$  case, the unchanged fwhm of the rigid lattice as a function of composition implies that the distance between two adjacent Na cations remains constant. Thus, with this significant change obtained in the fwhm in case of Li relative to the constant fwhm for Na, clustering is less probable for Li than for Na. Nevertheless, clustering cannot be completely excluded or proven here, since the fwhm would depend also on the number of clusters per unit volume and their expansion. This could cause a decrease of the linewidth, too.

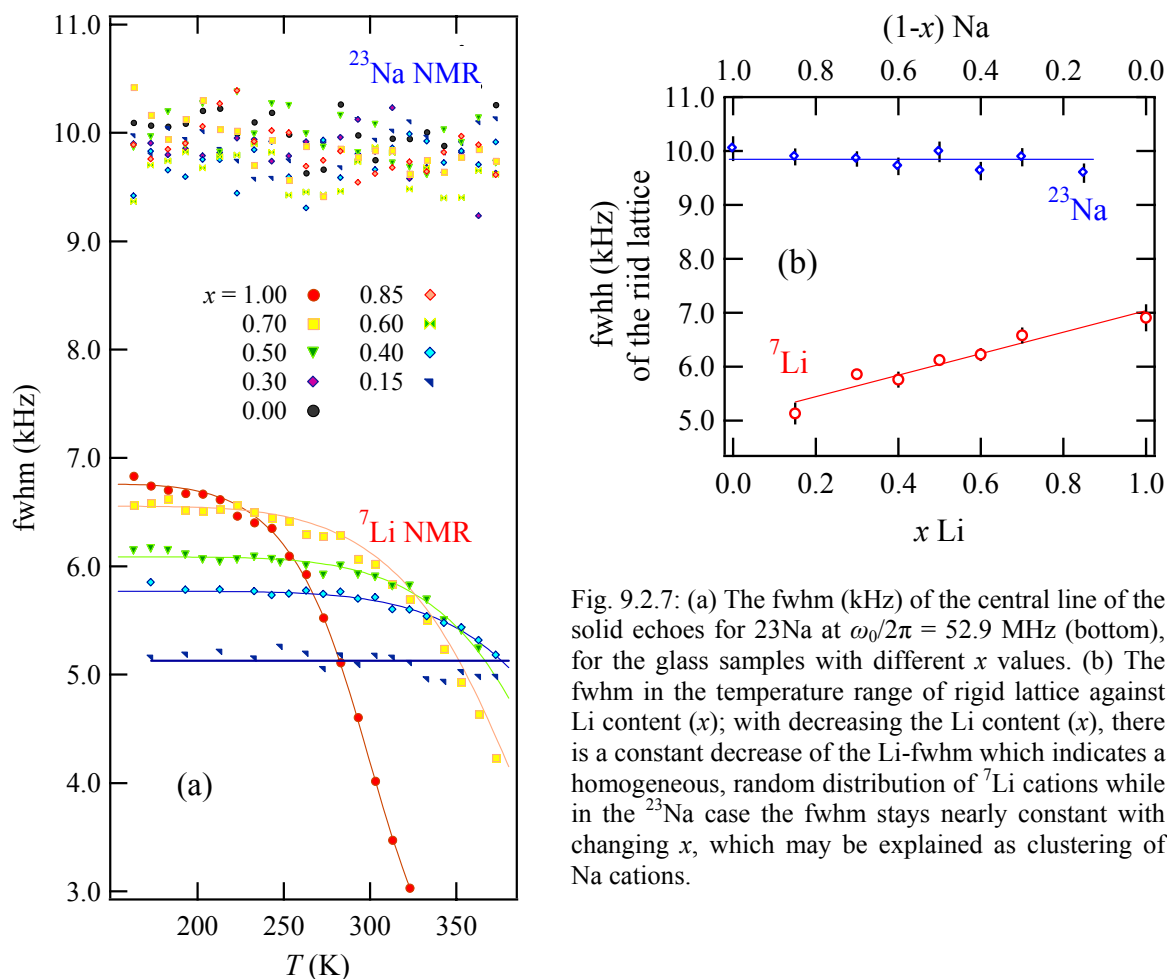


Fig. 9.2.7: (a) The fwhm (kHz) of the central line of the solid echoes for  $^{23}\text{Na}$  at  $\omega_0/2\pi = 52.9$  MHz (bottom), for the glass samples with different  $x$  values. (b) The fwhm in the temperature range of rigid lattice against Li content ( $x$ ); with decreasing the Li content ( $x$ ), there is a constant decrease of the Li-fwhm which indicates a homogeneous, random distribution of  $^7\text{Li}$  cations while in the  $^{23}\text{Na}$  case the fwhm stays nearly constant with changing  $x$ , which may be explained as clustering of Na cations.

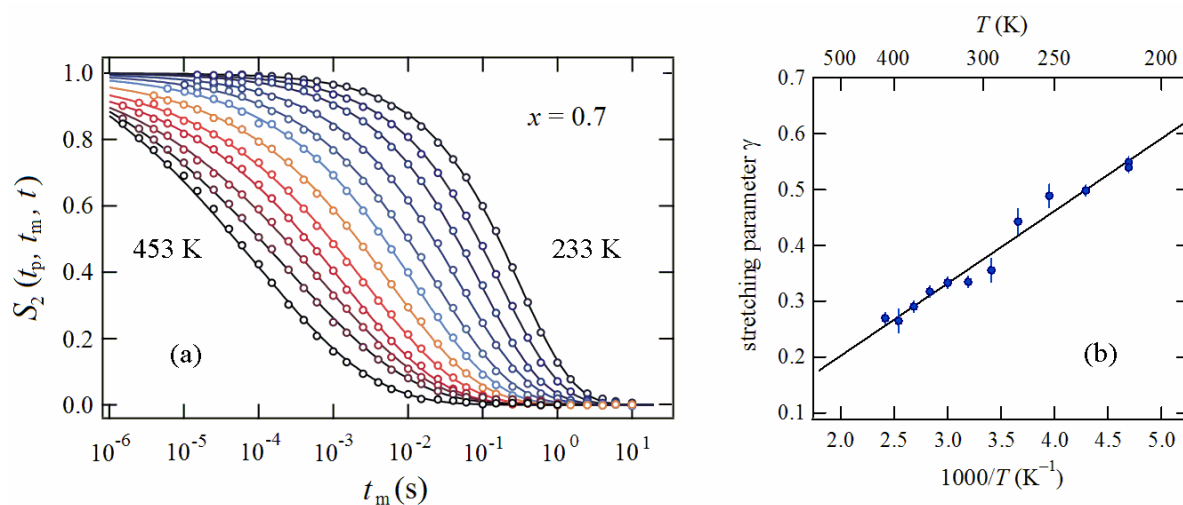


Fig. 9.2.8: (a) Jeener Broekaert (spin-alignment) echo amplitudes  $S_2(t_p, t_m, t)$  of  $^7\text{Li}$  in the glass  $0.33[x\text{Li}_2\text{O} \cdot (1-x)\text{Na}_2\text{O}] \cdot 0.33\text{Nb}_2\text{O}_5 \cdot 0.33\text{SiO}_2$  with  $x = 0.7$ , measured at a Larmor frequency of 77.7 MHz and a fixed evolution time  $t_p = 12 \mu\text{s}$ . Echo amplitudes were determined at  $t = t_p$ . The solid lines show fits with stretched exponential decay functions. (b) The stretching factors ( $\gamma$ ) vs. reciprocal temperature ( $1/T$ ). The stretched factors increase with increasing  $T$ .

### 9.2.5 $^7\text{Li}$ Spin-Alignment Stimulated Echoes \*

With stimulated-echo measurements, the Li dynamics can be monitored more quantitatively. The spin-alignment echo amplitudes were recorded at temperatures between 140 and 430 K. Fig. 9.2.8(a) shows a set of typical two-times correlation functions  $S_2$  measured at  $\omega_0/2\pi = 77.7$  MHz as a function of mixing time ( $t_m$ ) in a semi-logarithmic representation for the glass sample with  $x = 0.7$ . Using small evolution times  $t_p = 12 \mu\text{s}$ , the stimulated spin-alignment echoes are dominated by quadrupole contributions. A successful separation of dipolar influences from the echo amplitude can be achieved for short evolution times and when the echo amplitude is read out at  $t = t_p$ . Fig. 9.2.8(a) shows that with increasing temperature the correlation functions shift to smaller mixing times, indicating a thermally activated  $\text{Li}^+$ -jump process. Within the indicated temperature range, the dependence of the echo amplitudes on the mixing time can be fitted in each case with stretched exponential decay functions with stretching factors  $\gamma$  ( $0.2 < \gamma < 0.6$ ). These stretching factors follow a linear trend of the reciprocal temperature, as shown in Fig. 9.2.8(b). The non-single exponential decay of the echo and the temperature dependence of  $\gamma$  imply a distribution of correlation times, as expected for a disordered (glassy) material.

As expected, at a given temperature the echo amplitude changes as a function of the glass composition. Fig. 9.2.9 compares the decay functions for the glasses with  $x = 1, 0.85, 0.7, 0.5$  and  $0.3$ , all measured at same temperature (373 K). With increasing sodium content the decay curves shift to longer mixing times,  $t_m$ , clearly illustrating the blocking influence of the less mobile  $\text{Na}^+$  on the fast  $\text{Li}^+$  diffusion. By replacing 70 % of the  $\text{Li}^+$  ion from the pure Li sample (i.e. by going from  $x = 1$  to  $0.3$ ), the decay rate ( $1/\tau$ ) of the corresponding decay curves (shown in Fig. 9.2.9) decreases by a factor of about 180. Table 9.2.3 gives an overview of  $1/\tau$  and  $\gamma$  for different compositions at  $T = 373$  K.

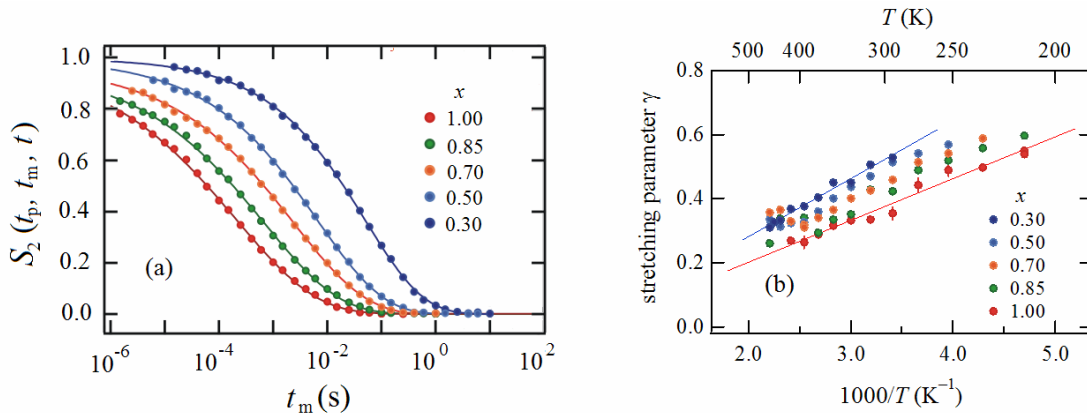


Fig. 9.2.9: (a)  $^7\text{Li}$  spin-alignment echo decay amplitude  $S_2(t_p, t_m, t = t_p)$  recorded at 77.7 MHz and  $t_p = 12 \mu\text{s}$  for glasses of the composition  $0.33[x \text{Li}_2\text{O} \cdot (1-x)\text{Na}_2\text{O}] \cdot 0.33\text{Nb}_2\text{O}_5 \cdot 0.33\text{SiO}_2$  with  $x$  in the range of 0.3 to 1. With increasing Na-content,  $1-x$ , the decay process slows down and points clearly to the blocking effect of the less mobile sodium ions. (b) The appropriate stretching exponents of the exponential decay functions (the solid lines in (a)) as a function of  $1/T$ . With rising the temperature and with decreasing the Na-content the decay curves follow higher stretched exponential functions.

$x$	$\tau_{t=t_p}^{-1}$ ( $s^{-1}$ )	$\gamma$ ( $\pm 0.05$ )
1.00	8709	0.31
0.85	2595	0.34
0.70	803	0.37
0.50	351	0.40
0.30	48	0.45

Table 9.2.3: Decay rates  $1/\tau$ , determined from spin-alignment echo amplitudes shown in Fig. 9.2.9 (a) measured at  $T = 373$  K. The associated stretching factors  $\gamma$  are compared<sup>259</sup>.

To have a meaningful comparison in both Fig. 9.2.9 and Table 9.2.3, the correlation functions and the decay rates were taken at 373 K that lies in the temperature range in which the decay process at low temperatures is negligible (as will be illustrated in the following).

The temperature dependence of the decay rate,  $1/\tau$  ( $1/T$ ), is shown in Fig. 9.2.10 for a variety of Li contents,  $x$ . The Li decay rate ( $1/\tau$ ) cannot be interpreted following a single Arrhenius relation in the examined temperature range. I. e. the echo decay does not take place via a single process; however, it can be clearly separated into two distinct processes. At low temperatures, the measurable decay rates ( $1/\tau$ ) follow an Arrhenius behavior with activation energies ( $E_{a,i}$ ) scattered around a constant value of 0.2 eV independently of the glass composition. In comparison with the  $^7\text{Li}$   $1/T_1$  data (Fig. 9.2.4 and Table 9.2.2), it

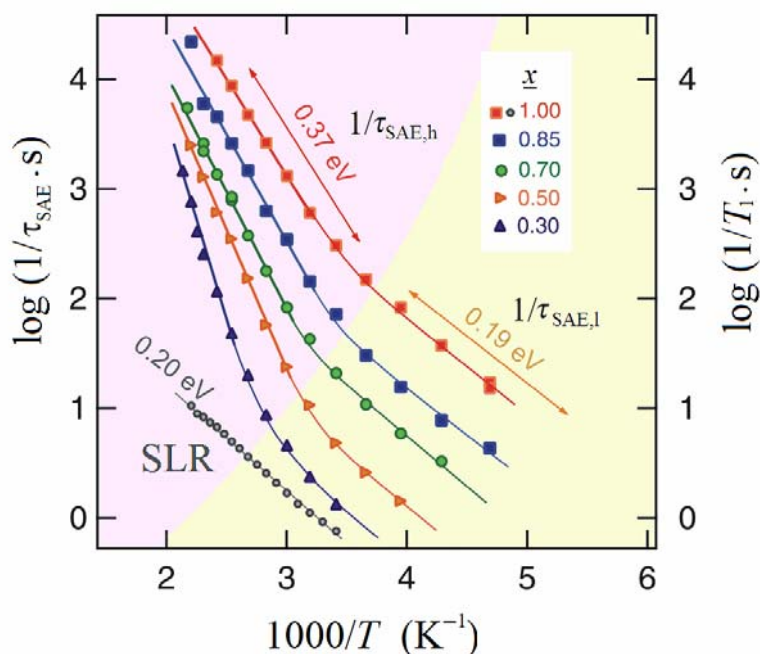


Fig. 9.2.10:  $^7\text{Li}$  spin-alignment decay rates  $1/\tau$  measured at  $\omega_0/2\pi = 77.7$  MHz and  $t_p = 12$   $\mu\text{s}$  as function of reciprocal temperature ( $1/T$ ) for different compositions ( $x = 1, 0.85, 0.7, 0.5,$  and  $0.30$ ). Within the low-temperature range the decay rates are independent of  $x$  and possess an activation energy of 0.2 eV. The corresponding spin-lattices relaxation rates  $1/T_1$  show a similar behavior concerning their temperature dependence and composition independence. For comparison, the SLR rates ( $1/T_1$ ) for  $x = 1$  is shown as an example, too. However, in the high-temperature range the decay rates are more temperature dependent and their activation energies increase with decreasing  $x$ .

can be seen clearly that  $1/\tau_1$  and  $1/T_1$  follow similar temperature dependence for all samples. However, spin-lattice relaxation is obviously affected by and could be interpreted in terms of a dipolar spin-lattice relaxation (rate  $1/T_{1d}$ ). On the other hand, at higher temperatures, the rates ( $1/\tau_h$ ) follow Arrhenius laws with a different activation energies which depend clearly on the composition,  $x$ . As opposed to  $1/\tau_1$ ,  $1/\tau_h$  is considerably more thermally activated.  $E_{a,h}$  ranges from 0.37 to 0.65 eV. A similar behavior was found in the case of amorphous  $\text{LiNbO}_3$ <sup>259</sup>.

Fig. 9.2.11 shows the change in the decay rate ( $1/\tau_h$ ) at 393 K in comparison with the change of the activation energy,  $E_{a,h}$ , as a function of the glass composition  $x$ . A gradual exchange of  $\text{Li}^+$  ions with the slower  $\text{Na}^+$  ions degrades the lithium jump rates by almost three orders of magnitude.

In agreement to that finding, the lithium-activation energy  $E_{a,h}$  increases from approximately 0.37 at  $x = 1$  to about 0.65 eV at  $x = 0.3$ . The decay rates of the echo amplitudes in the high-temperature range,  $1/\tau_h$ , obey a clear exponential decay dependence with increasing  $\text{Na}^+$  content. In Fig. 9.2.12 the decay rates at 393 K are plotted against the lithium content,  $x$ , in a semi-logarithmic plot. The straight lines

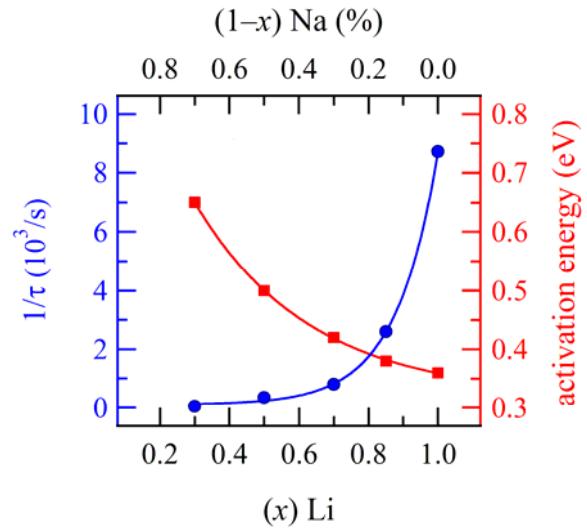


Fig. 9.2.11:  $^7\text{Li}$  spin-alignment decay rates  $1/\tau_h$  at  $T = 393$  K and the dependence of the activation energies  $E_{a,h}$  dependence on the glass-composition,  $x$ . With increasing the concentration of the less mobile  $\text{Na}$ -ions the lithium diffusion rate ( $1/\tau_h$ ) slows down from  $8700 \text{ s}^{-1}$  in the pure  $\text{Li}$  sample to about  $50 \text{ s}^{-1}$  after replacing 70 % of the  $\text{Li}^+$  by  $\text{Na}^+$ .

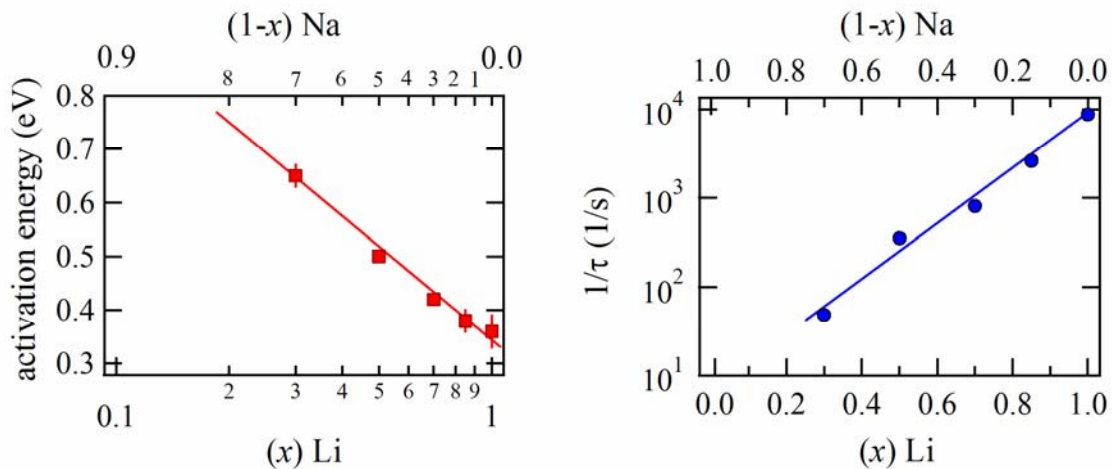


Fig. 9.2.12: The dependence of the activation energy ( $E_{a,h}$ ) and of the decay rates ( $1/\tau_h$ ) on the  $\text{Li}$ -content,  $x$ , determined from  $^7\text{Li}$  spin-alignment measurements at  $t_p = 12 \mu\text{s}$  with 393 K. It is:  $1/\tau_h \propto \exp k(1-x)$  and  $E_{a,h} \propto \log_{10}(1-x)$ .

obtained for temperatures other than 393 K are only shifted parallel to the ordinate. The change of the  $\text{Li}^+$ -activation energy ( $E_{a,h}$ ) shows also a linear dependence on  $\log_{10} x$ .

### 9.2.6 Discussion

Ferroelectric  $\text{LiNbO}_3$  glasses and glass-ceramics with different compositions were prepared by several methods such as sol-gel<sup>415</sup> or heat treatment of glasses with a suitable composition<sup>416</sup>. Using a similar conventional melt-quenching method,  $\text{LiNbO}_3$  was precipitated from  $0.34\text{SiO}_2 \cdot 0.33\text{Li}_2\text{O} \cdot 0.33\text{Nb}_2\text{O}_5$  glass by heat-treatment. It showed a conductivity-activation energy of 0.54 eV. As expected, the dc-conductivity and the dielectric constant decrease with increasing treatment temperature because the number of the free network  $\text{Li}^+$  ions, the main contributor to the conduction, is decreasing due to the growth of the crystalline phase that contains the lithium ions<sup>250</sup>. Prasad *et al.*<sup>251</sup> used a similar method to prepare glass material with 65 %  $\text{LiNbO}_3$ : 35 %  $\text{SiO}_2$  doped and undoped with 0.1 mol %  $\text{Fe}_2\text{O}_3$ . They obtained activation energies of conductivity of 0.54 and 0.67 eV for the undoped and the doped glasses respectively. Glasses and glass-ceramics with a composition  $95\text{SiO}_2 - 2.5\text{Li}_2\text{O} - 2.5\text{Nb}_2\text{O}_5$  were prepared by sol-gel followed by controlled heating at temperatures between 773 – 1173 K. The conductivity was found to decrease with increasing the treatment temperature (823 to 873 K) and its activation increases from 0.58 to 0.64 eV<sup>415</sup>. These values compare well with the value of (0.61 eV) obtained here for the pure Li glass. On the other hand, not so much work was done on the conductivity of the sodium glass. Hiriyama *et al.* found that increasing the niobia content in  $\text{Nb}_2\text{O}_5$ - $\text{Na}_2\text{O}$ - $\text{SiO}_2$  increases the dielectric constant even at high frequencies due to the high charge and small ionic radius of the  $\text{Nb}^{5+}$  ions<sup>252</sup>.

According to our knowledge, this is the first investigation of the electrical conductivity of a mixed (lithium sodium) niobosilicate glass. The pure sodium niobosilicate glass showed a lower conductivity and a higher activation energy; as expected from its bigger size and the consequent reduced diffusivity. Most interestingly, the lithium-sodium glasses showed a minimum in the conductivity when plotted against the composition,  $x$ , at  $x = 0.37$ . This large deviation from simple additive behavior upon mixing of two different types of mobile ions has a strong effect on the glass properties which are affected by long range motions of ions<sup>417</sup>. Furthermore, the conductivity activation energies ( $0.61(1) \leq E_A^{\sigma_{dc}} \leq 0.91(1)$  eV) showed a maximum at the same  $x$  value. These findings are in agreement with the typical mixed-alkali effect phenomena. In contrast to the dc-conductivity measurement that can detect the overall charge carrier diffusion, with NMR techniques the  $\text{Li}^+$  and  $\text{Na}^+$  diffusion can be studied independently.

The  $^7\text{Li}$  and  $^{23}\text{Na}$  SLR rate ( $T_1^{-1}$ ) for the samples with different compositions showed similar activation energies of the low-temperature flank of about 0.25 and 0.3 eV, respectively. These values may be due to dipolar relaxation or due to local diffusional processes and not due to the long-range diffusion. However, the motional narrowing of the central transition measured by solid echoes showed that the Li-ion diffusiv-



ity decreases by decreasing the temperature and by replacing Li with Na in the glass system keeping the overall-alkali content constant, while the Na lines do not show any change emphasizing that Na is the slower diffusing ion or completely immobile in the measured system below 450 K. Furthermore, the fwhm in the rigid lattice as a function of  $x$  gives evidence of the on homogeneous distribution of Li ions and a possibility of clustering in the Na case.

When Li ion is replaced by sodium the tracer diffusion coefficients of Li,  $D_{\text{Li}}$ , always decrease and  $D_{\text{Na}}$  always increase (and vice versa). These changes in the diffusivities are caused by changes in the respective activation energies such that  $D_A$  and  $D_B$  vary by several orders of magnitude at low temperatures. If the mixing were additive,  $E_a^{\text{Li}}$  and  $E_a^{\text{Na}}$  should be invariant upon mixing.

Spin-alignment echoes were applied here to record two-time correlation functions which probe the Li-jump rates. The Li-jumps rates for the different samples were found to decrease exponentially with the introduction of Na ions.

In the dynamic structure model<sup>418,419</sup> based on EXAFS experiments<sup>420</sup>, it was suggested that the A and B ions can create their own distinct local environments in the glass. Thereby preferred diffusion paths for each type of ion are formed and the dependence of the connectivity of these diffusion paths on the ionic composition was shown to provide a possible explanation for both the MAE and the steep increase of the conductivity with ionic concentration in the single modified glasses<sup>421</sup>.

The activation energies  $E_a^{\text{SAE}}$  show a logarithmic increase with increasing Na content. The previous observation agrees with the literature where it was found that the activation energies  $E_{A,B}$  in the single modifier glasses decrease logarithmically with the ionic concentration  $c_{A,B}$ . i.e.  $E_{A,B}^{(0)} = \beta_{A,B} - \gamma_{A,B} \log c_{A,B}$  where  $\beta_{A,B}$  and  $\gamma_{A,B}$  are constants independent of  $c_{A,B}$ . This is in agreement with experimental results for modifier contents of about 5-40 mol %<sup>418-419,422</sup>.

Hunt<sup>423</sup> suggested that the diffusion paths may be associated with a random energy landscape in the glass, where the lower energy states are located at different positions for different types of ions. A critical path analysis<sup>424</sup> allowed him to identify the distinct diffusion paths as consisting of sites within a certain energy range, and to calculate the changes in the activation energies  $E_A$  and  $E_B$  both in single and mixed ion glasses<sup>425,426</sup>. The direction of changes in the activation energies in qualitative agreement with the experimental data, but when considering the mixed-alkali effect, the dependence of  $dE_A(x)/dx$  and  $dE_B(x)/dx$  on the mixing ratio  $x = c_B/c$  was not correctly reproduced ( $c = c_A + c_B$  denotes the total concentration of mobile ions). As a consequence, the 'curvatures'  $\partial^2 \log D_A / \partial x^2$  and  $\partial^2 \log D_B / \partial x^2$  have the wrong sign in comparison with that found in the experiments. To obtain the right sign of the curvatures is, however, an important issue, since otherwise the MAE can be explained essentially by the concentration dependence in single modified glasses under the assumption that ions of different hops do not interfere with each other. In this non-interfering case one would obtain  $E_A(x) = E_A^{(0)}(xc)$  and

$E_B(x) = E_B^{(0)}((1-x)c)$  where  $E_{A,B}^{(0)}$  are the activation energies in the corresponding single modified glasses. The curvature problem was resolved by taking Coulomb interaction between the mobile ions into account. Moreover, by considering the connection between the random energy landscape and the local network structure more explicitly, it was possible to explain the origin of the mixed-alkali internal friction peak<sup>427-429</sup>.

Unfortunately spin-alignment echoes are not applicable for nuclei with large quadrupolar effects, i.e. with those having a quadrupole coupling constant in the MHz range like  $^{23}\text{Na}$ . In such a case the quadrupolar interaction will dominate the spectra. Thus the expected spectra are broad and a non-selective excitation via r.f.-pulse is not possible.

## References

---

- <sup>1</sup> W. Puin, S. Rodewald, R. Ramlau, P. Heitjans, and J. Maier, "**Local and Overall Ionic Conductivity in Nanocrystalline  $\text{CaF}_2$** ", *Solid State Ionics* **131** (2000) 159-164
- <sup>2</sup> R. Winter, K. Siegmund, and P. Heitjans, "**Nuclear Magnetic and Conductivity Relaxations by Li Diffusion in Glassy and Crystalline  $\text{LiAlSi}_4\text{O}_{10}$** ", *J. Non-Cryst. Solids* **212** (1997) 215-224
- <sup>3</sup> S. Indris, P. Heitjans, H. Roman, and A. Bunde, "**Nanocrystalline Versus Microcrystalline  $\text{Li}_2\text{O}:\text{B}_2\text{O}_3$  Composites: Anomalous Ionic Conductivities and Percolation Theory**", *Phys. Rev. Lett.* **84** (2000) 2889-2892
- <sup>4</sup> D. Bork, and P. Heitjans, "**NMR Relaxation Study of Ion Dynamics in Nanocrystalline and Polycrystalline  $\text{LiNbO}_3$** ", *Phys. Chem. B* **102** (1998) 7303
- <sup>5</sup> D. Bork, and P. Heitjans, "**NMR Investigations on Ion Dynamics and Structure in Nanocrystalline and Polycrystalline  $\text{LiNbO}_3$** ", *Phys. Chem. B* **105** (2001) 9162
- <sup>6</sup> M. Wilkening, D. Bork, S. Indris and P. Heitjans, "**Diffusion in Amorphous  $\text{LiNbO}_3$  studied by  $^7\text{Li}$  NMR - Comparison with the Nano- and Microcrystalline Materials**", *Phys. Chem. Chem. Phys.* **4** (2002) 3246-3251
- <sup>7</sup> P. Heitjans and S. Indris, "**Diffusion and Ionic Conduction in Nanocrystalline Ceramics**", *J. Phys.: Condens Matter* **15** (2003) R1257-R1289
- <sup>8</sup> P. Heitjans, J. Kärger eds., "**Diffusion in Condensed Matter – Methods, Materials, Models**", (Springer, Berlin, 2005)
- <sup>9</sup> W. Puin, P. Heitjans, W. Dickenscheid, and H. Gleiter, "**NMR Study of Dynamics Processes In Nanocrystalline  $\text{CaF}_2$** ", in "**Proceedings of the XII International Conference on Defects in Insulating Materials**"; O. Kanert, J. Spaeth, (World Scientific: Singapore, 1993) 137-139
- <sup>10</sup> W. Puin and P. Heitjans, "**Frequency Dependent Ionic Conductivity in Nanocrystalline  $\text{CaF}_2$  Studied by Impedance Spectroscopy**", *Nanostructured Materials* **6** (1995) 885-888
- <sup>11</sup> R. Winter and P. Heitjans, "**Li Diffusion and its Structural Basis in the Nanocrystalline and Amorphous Forms of Two-Dimensional Ion-Conducting  $\text{Li}_x\text{TiS}_2$** ", *J. Phys. Chem. B* **105** (2001) 6108
- <sup>12</sup> R. Winter and P. Heitjans, "**Intergranular Structure of Nanocrystalline Layered  $\text{Li}_x\text{TiS}_2$  as Derived from  $^7\text{Li}$  NMR Spectroscopy**", *J. Non-Cryst Solids* **293-295** (2001) 19
- <sup>13</sup> H. Schmalzried, "**Chemical Kinetics of Solids**", (Weinheim, VCH, 1995)
- <sup>14</sup> H. Rickert, "**Electrochemistry of Solids-An Introduction**", (Berlin, Springer, 1982)
- <sup>15</sup> H. Gleiter, "**Materials with Ultrafine Microstructures: Retrospectives and Perspectives**", *Nanostruct. Mater.* **1** (1992) 1-19
- <sup>16</sup> R. Siegel In "**Encyclopedia of Applied Physics**" eds. G. Trig, E. Immergut, E. Vera, and W. Greulich; (VCH, New York, 1994) 173-200
- <sup>17</sup> R. Siegel, "**Nanophase Materials Assembled From Atomic Clusters**", *Mater. Res. Soc. Bull.* **XV 10** (1990) 60-67.
- <sup>18</sup> C. An, K. Tang, C. Wang, G. Z. Shen, Y. Jin, and Y. Qian, "**Characterization of  $\text{LiNbO}_3$  Nanocrystals Prepared Via Convenient Hydrothermal Route**", *Mater. Res. Bull.* **37** (2002) 1791-1796
- <sup>19</sup> M. Pooley and A. Chadwick, "**The Synthesis and Characterization of Nanocrystalline Lithium Niobate**", *Radiat. Eff. Defects Solids* **158** (2003) 197-201
- <sup>20</sup> A. Chadwick, M. Pooley, and S. Savin, "**Lithium-Ion Transport and Microstructure in Nanocrystalline Lithium Niobate**", *Phys. Stat. Sol. (c)* **2**[1] (2005) 302-305
- <sup>21</sup> M. Niederberger, N. Pinna, J. Polleux, and M. Antonietti, "**A General Soft-Chemistry Route to Perovskite and Related Materials: Synthesis of  $\text{BaTiO}_3$ ,  $\text{BaZrO}_3$ , and  $\text{LiNbO}_3$  Nanoparticles**" *Angew. Chem. Int. Ed.* **43** (2004) 2270-2273
- <sup>22</sup> H. Fecht in "**Nanophase Materials**", eds G. Hadjipanayis, and W. Seigel; (Kluwer Academic Publishers, Netherlands, 1994) 125
- <sup>23</sup> H. Schaefer, R. Wuerschum, R. Brringer, and H. Gleiter, "**Structure of Nanometer-Sized Polycrystalline Iron Investigated by Positron Lifetime Spectroscopy**" *Phys. Rev. B* **38**[14-15] (1988) 9545-9554
- <sup>24</sup> S. Ramasamy, J. Jiang, H. Gleiter, R. Brringer, and U. Gonser, "**Investigation of Nanocrystalline  $\text{FeF}_2$  by Mössbauer Spectroscopy**", *Solid State Commun.* **74**[8] (1990) 851-855.

## References

- <sup>25</sup> R. Elliot, *"Physics of amorphous materials"*, (Longman group Ltd, London, 1983) p. 5
- <sup>26</sup> C. Yu and S. Coppersmith, *"Gravity-Induced Flow of a Structural Glass at Zero Temperature"*, *J. non-cryst. Solids*, **131-133**[1] (1991) 476-478
- <sup>27</sup> F. Ernsberger, *"Glass: Science and Technology"*, eds. D. Uhlmann and N. Kreidle, (Acad., New York, 1980,) Vol. V, Ch. 1.
- <sup>28</sup> W. Zachariasen, *"The Atomic Arrangement in Glass"*, *J. Amer. Chem. Soc.* **54**[10] (1932) 3841-3851
- <sup>29</sup> B. Warren, *"The X-Ray Diffraction of Vitreous Silica"*, *Z. Kristallogr. Kri.* **86** (1933) 349-358
- <sup>30</sup> Y. Tu, J. Tersoff, G. Grinstein and D. Vanderbilt, *"Properties of a Continuous-Random-Network Model for Amorphous Systems"*, *Phys. Rev. Lett.* **81**[22] (1998) 4899-4902
- <sup>31</sup> A. Cooper, *"W.H. Zachariasen - The Melody Lingers On"*, *J. Non-Cryst. Solids* **49**[1-3] (1982) 1-17
- <sup>32</sup> G. Greaves, *"EXAFS and the Structure of Glass"*, *J. Non-Cryst. Solids* **71**[1-3] (1985) 203-217
- <sup>33</sup> P. Duwez and R. Willens, *"Rapid Quenching of Liquid Alloys"*, *Trans Met. Soc. AIME* **227** (1963) 362-365
- <sup>34</sup> R. Roberge and H. Herman, *"A Novel Method for Rapid Quenching of Liquid Alloys: Torsion-Catapult"*, *Mater. Sci. Eng.* **3** (1968/69) 62-63
- <sup>35</sup> M. Moss, *"Dispersion Hardening in Al-V by Plasma-Jet Spray-Quenching"*, *Acta Metallurgica* **16** (1968) 321-326
- <sup>36</sup> H. Chen and C. Miller, *"A Rapid Quenching Technique for Preparation of Thin Uniform Films of Amorphous Solids"*, *Rev. Sci. Instrum.* **41**[8] (1970) 1237
- <sup>37</sup> P. Richet and P. Gillet, *"Pressure-Induced Amorphization of Minerals: A Review"*, *Eur. J. Mineral.* **9**[6] (1997) 907-933
- <sup>38</sup> L. Howe and M. Rainville, *"A Study of the Irradiation Behavior of Zirconium-Aluminum (Zr<sub>3</sub>Al)"*, *J. Nucl. Mater.* **68**[2] (1977) 215-234
- <sup>39</sup> S. Sharma and S. Sikka, *"Pressure Induced Amorphization of Materials"*, *Progr. Materials Sci.* **40**[1] (1996) 1-77
- <sup>40</sup> W. Johnson, *"Thermodynamic and Kinetic Aspects of the Crystal to Glass Transformation in Metallic Materials"*, *Prog Mater Sci.* **30**[2] (1986) 81-134.
- <sup>41</sup> A. Meldrum, L. Boatner, W. Weber, and R. Ewing, *"Amorphisation and Recrystallization of the ABO<sub>3</sub> Oxides"*, *Journal of nuclear Materials* **300** (2002) 242-254
- <sup>42</sup> K. Varma, K. Hershavardhan, K. Rao, and C. Rao, *"Ferroelectric-Like Dielectric Anomaly in RF-Sputtered Amorphous LiNbO<sub>3</sub> Films"*, *Material Research Bulletin* **20** (1980) 315-320
- <sup>43</sup> O. Mishima, L. Calvert and E. Whalley, *"Melting ice' I at 77 K and 10 kbar-A New Method of Making Amorphous Solids"*, *Nature* **310** (1984) 393-395
- <sup>44</sup> R. Hemley, in *"High Pressure Research in Mineral Physics"*, eds by M. Manghni and Y. Syono (Terra Scientific, Tokyo, 1987) 347-359
- <sup>45</sup> Y. Lin, Y. Li, Y. Xu, G. Lan, and H. Wang, *"Raman-Scattering Study on Pressure Amorphisation of LiNbO<sub>3</sub> crystal"*, *J. Appl. Phys.* **77**[7] (1995) 3584-3585
- <sup>46</sup> Y. Lin, G. Lan, and H. Wang, *"An irreversible Pressure-Induced Amorphisation of LiTaO<sub>3</sub> Crystal"*, *Solid State Commun.* **91**[11] (1994) 879-881
- <sup>47</sup> P. Tick, N. Borrelli, and I. Reaney, *"The Relationship Between Structure and Transparency in Glass-Ceramic Materials"*, *Opt. Mater.* **15**[1] (2000) 81-91
- <sup>48</sup> L. Randonjic, M. Todorovic, and J. Miladinovic, *"Nanostructured Sodium Niobate Obtained by Glass Crystallization"*, *Materials Chemistry and Physics* **88** (2004) 427-432
- <sup>49</sup> V. Astakhova, N. Nikonorov, E. Pomyshva, V. Savvin, I. Tunimanova, and V. Tsekhomskii, *" "*, *Glass Phys. Chem.* **18**[2] (1992) 107.
- <sup>50</sup> N. Borrelli, and M. Lyton, *"Dielectric and Optical Properties of Transparent Ferroelectric Glass-Ceramic Systems"*, *J. Non-Cryst. Solids* **6** (1971) 197-212
- <sup>51</sup> A. Glass, *"The Photorefractive Effect"*, *Opt. Eng.* **17**[5] (1978) 470-479

- <sup>52</sup> G. Beall and D. Duke, "**Transparent Glass-Ceramics**", *J. Mater. Sci.* **4** (1969) 340-352
- <sup>53</sup> M. Volmer and A. Weber, "**Nuclei Formation in Supersaturated States**", *Z. Phys. Chem.* **119** (1926) 277
- L. Farkas, "**The Velocity of Nucleus Formation in Supersaturated Vapors**", *Z. Phys. Chem.* **125** (1927) 236-242
- R. Becker and W. Döring, "**The Kinetic Treatment of Nuclear Formation in Supersaturated Vapors**", *Ann. Phys.* **24** (1935) 719-752
- J. Zeldovich, "**Theory of New Phase Formation: Cavitation**", *Acta Physicochim.* **18** (1943) 1-22
- <sup>54</sup> S. Coleman, "**Fate of the False Vacuum: Semi-Classical Theory**", *Phys. Rev. D* **15**[10] (1977) 2929-2936
- <sup>55</sup> N. Wong and C. Knobler, "**Light Scattering Studies of Phase Separation in Isobutyric Acid + Water Mixtures**", *J. Chem Phys* **69** (1978) 725-735
- E. Siebert and C. Knobler, "**Measurements of Homogeneous Nucleation Near a Critical Solution Temperature**", *Phys. Rev. Lett.* **52** (1984) 1133-1136
- <sup>56</sup> D. Herrmann, W. Klein, and D. Stauffer, "**Spinodals in a Long-Range Interaction System**", *Phys. Rev. Lett.* **49** (1982) 1263-1264
- <sup>57</sup> P. Voorhees and R. Schaefer, "**In-Situ Observation of Particle Motion and Diffusion Interactions During Coarsening**", *Acta Metall.* **35**[2] (1987) 327-339
- <sup>58</sup> H. Yinnon and D. Uhlmann, "**Applications of Thermoanalytical Techniques to the Study of Crystallization Kinetics in Glass-Forming Liquids, Part I: Theory**", *J Non-Cryst Solids* **54** (1983) 253-275
- <sup>59</sup> W. Kingery, H. Bowen, and D. Uhlman, "**Introduction to Ceramics**", Second Edition; (John Wiley, New York, 1976).
- <sup>60</sup> A. Ballman, "**Growth of Piezoelectric and Ferroelectric Materials by the Czochralski Technique**", *J. Am. Ceram. Soc.* **48** (1965) 112
- <sup>61</sup> P. Lerner, C. Legras and P. Dumas, "**Stoichiométrie des Monocristaux de Métaniobate de Lithium**", *J. Cryst. Growth* **3**[4] (1968) 231-235
- <sup>62</sup> S. Abrahams, J. Bernstein, W. Hamiltons, H. Levinstein, and J. Reddy, "**Ferroelectric Lithium Niobate .3. Single Crystal X-ray Diffraction Study at 24 °C**", *J. Phys. Chem. Solids* **27**[6-7] (1966) 997
- <sup>63</sup> H. Megaw, "**A Note on the Structure of Lithium Niobate  $\text{LiNbO}_3$** ", *Acta Cryst. Section A: Crystal physics diffraction theoretical and general crystallography A* **24**[6] (1968) 583 H. Megaw, "**A Note on the Structure of Lithium Niobate,  $\text{LiNbO}_3$** ", *Acta Cryst. A* **24** (1968) 583-589
- <sup>64</sup> R. Weis and T. Gaylord, "**Lithium Niobate: Summary of Physical Properties and Crystal Structure**", *Appl. Phys. A* **37**[4] (1985) 191-203
- <sup>65</sup> A. Glass, D. Linde, and T. Negran, "**High-Voltage Bulk Photovoltaic Effect and the Photorefractive Process in  $\text{LiNbO}_3$** ", *Appl. Phys. Lett.* **25**[4] (1974) 233-235
- <sup>66</sup> M. Abouelleil and F. Leonberger, "**Wave-Guides in Lithium Niobate**", *J. Am. Ceram. Soc.* **72** (1989) 1311
- <sup>67</sup> C. Tsai, "**Integrated Acoustooptical Circuits for Real-Time Wideband Signal-Processing**", *Jpn. J. Appl. Phys.*, **19** [Suppl. 1] (1980) 661-665
- <sup>68</sup> A. Räuber, in "**Current Topic Materials Science**", ed E. Kaldis, (North-Holland, Amsterdam, 1978) 481
- <sup>69</sup> K. Wong (ed.), "**Properties of Lithium Niobate**", (INSPEC, UK, 2002)
- <sup>70</sup> S. Abrahams, W. Hamilton and J. Reddey, "**Ferroelectric Lithium Niobate.4. Single Crystal Neutron Diffraction Study at 24 °C**", *J. Phys. Chem. Solids* **27** (1966) 1013
- <sup>71</sup> S. Abrahams and P. Marsh, "**Defect Structure on Composition in Lithium Niobate**", *Acta Cryst. B* **42** (1986) 61-68
- <sup>72</sup> R. Holmes and D. Smyth, "**Titanium Diffusion into  $\text{LiNbO}_3$  as a Function of Stoichiometry**", *J. Appl. Phys.* **55** (1984) 3531
- <sup>73</sup> J. Carruthers, G. Peterson, and M. Grasso, "**Nonstoichiometry and Crystal Growth of Lithium Niobate**", *J. Appl. Phys.* **42**[5] (1971) 1846-1851.
- <sup>74</sup> M. Wohlecke, G. Corradi, and K. Betzler, "**Optical Methods to Characterise the Composition and Homogeneity of Lithium Niobate Single Crystals**", *Appl. Phys. B* **63** (1996) 323

## References

- 
- <sup>75</sup> P. Gallagher and H. O'Bryan, "**Characterization of  $\text{LiNbO}_3$  by Dilatometry and DTA**", *J. Am. Ceram. Soc.* **68**[3] (1985) 147-150
- <sup>76</sup> O. Schirmer, O. Thiemann, and M. Wohlecke, "**Defects in  $\text{LiNbO}_3$ -I. Experimental Aspects**", *J. Phys. Chem. Solids* **52**[1] (1991) 185-200
- <sup>77</sup> H. Fay, W. Alford, and H. Dess, "**Dependence of Second-Harmonic Phase-Matching Temperature in  $\text{LiNbO}_3$  Crystals on Melt Composition**", *Appl. Phys. Lett.* **12**[3] (1968) 89-92
- <sup>78</sup> K. Nassau, and M. Lines, "**Stacking-Fault Model for Stoichiometry Deviations in  $\text{LiNbO}_3$  and  $\text{LiTaO}_3$  and the Effect on the Curie Temperature**", *J. Appl. Phys.* **41**[2] (1970) 533-535
- <sup>79</sup> S. Abrahams and P. Marsh, "**Defect Structure Dependence on Composition in Lithium Niobate**", *Acta Cryst. B*, **42** (1986) 61-68
- <sup>80</sup> W. Bollmann and H. Stoehr, "**Incorporation and Mobility of OH-Ions in  $\text{LiNbO}_3$  Crystals**", *Phys. Stat. Sol. (a)*, **39**[2] (1977) 477-484
- <sup>81</sup> W. Bollmann, "**Stoichiometry and Point-Defects in Lithium-Niobate Crystals**", *Cryst. Res. Technol.* **18**[9] (1983) 1147-1149.
- <sup>82</sup> P. Jorgensen and R. Bartlett, "**High Temperature Transport Processes in Lithium Niobate**" *J. Phys. Chem. Solids* **30**[12] (1969) 2639
- <sup>83</sup> R. Pareja, R. Gonzalez, and M. Pedrosa, "**Study of Thermodynamically Reduced and Electron-Irradiated  $\text{LiNbO}_3$  Single Crystals by Positron-Annihilation and Optical Absorption Measurements**", *Phys. Solidi A- Applied Research* **84**[1] (1984) 179
- <sup>84</sup> E. Hodgson and F. Agullo-Lopeyz, "**Oxygen Vacancy Centres Induced by Electron Irradiation In  $\text{LiNbO}_3$** ", *Solid State Commun.*, **64**[6] (1987) 965-968
- <sup>85</sup> S. Bredikhin, S. Scharner, M. Klingler, V. Kveder, B. Redikin, and W. Weppner, "**Change of the Stoichiometry and Electrocoloration Due to the Injection of Li and O Ions Into Lithium Niobate Crystals**", *Ionics* **3** (1997) 470-476
- <sup>86</sup> S. Bredikhin, S. Scharner, M. Klingler, V. Kveder, B. Redikin, and W. Weppner, "**Nonstoichiometry and Electrocoloration Due to Injection of  $\text{Li}^+$  and  $\text{O}^{2-}$  Ions Into Lithium Niobate Crystals**", *J. Appl. Phys.*, **88**[10] (2000) 5687-5694
- <sup>87</sup> N. Iyi, K. Kitamura, F. Izumi, J. Yamamoto, T. Hayashi, H. Asano, and S. Kimura, "**Comparative Study of Defect Structures in Lithium Niobate With Different Compositions**", *J. Solid State Chem* **101**[2] (1992) 340-352
- <sup>88</sup> D. Smyth, "**Defects and transport in  $\text{LiNbO}_3$** ", *Ferroelectrics* **50** (1983) 93-102
- <sup>89</sup> E. Chang, A. Mehta, and D. Smyth, *Adv. In Ceram.* **23** (1987) 351
- <sup>90</sup> D. Smyth, *Proceeding of the Sixth IEEE Int. Symp. On application of Ferroelectronics*, ISAF '86' (1986) 115
- <sup>91</sup> H. Donnerberg, S. Tomlinson, C. Catlow, and O. Schirmer, "**Computer-Simulation Studies of Intrinsic Defects in  $\text{LiNbO}_3$  Crystals**", *Phys. Rev. B*, **40** (1989) 11909-11916
- <sup>92</sup> Y. Watanabe, T. Sota, K. Suzuki, N. Iyi, and K. Kimura, "**Defect Structures in  $\text{LiNbO}_3$** ", *J. Phys. Condens. Matter.* **7** (1995) 3627-3635
- <sup>93</sup> A. Kling, L. Rebouta, J. Marques, J. Correia, M. daSilva, E. Dieguez, F. AgulloLopez, and J. Soares, "**Ion Beam Channeling and Hyperfine Interaction Analysis for the Characterization of Stoichiometry and Anti-site Population in  $\text{LiNbO}_3$** ", *Nucl. Instrum. Methods Phys. Res. Sect. B-Beam Interact. Mater. Atoms* **118**[1-4] (1996) 622-625
- <sup>94</sup> N. Zotov, H. Boysen, F. Frey, T. Metzger, and E. Born, *J. Phys. Chem. Solids* **55**, 149, (1994).
- <sup>95</sup> J. Blümel, E. Born, and Th. Metzger, "**Solid State NMR Study Supporting the Lithium Vacancy Defect Model in Congruent Lithium Niobate**", *J. Phys. Chem. Solids* **55**[7] (1994) 589-593
- <sup>96</sup> K. Polgar, L. Jeszensky, K. Raksaenyi, and E. Hartmann, *Acta Phys. Acad. Sci. Hung.*, **47**, 125, (1979).
- <sup>97</sup> H. O'Bryan, P. Gallagher, and C. Brandle, "**Congruent Composition and Li-Rich Phase Boundary of  $\text{LiNbO}_3$** " *J. Am. Ceram. Soc.* **68**[9] 493-496 (1985).
- <sup>98</sup> J. Bergmann, A. Askhin, A. Ballmann, J. Dziedio, H. Levinstein, and R. Smith, "**Curie Temperature, Birefringence, and Phase-Matching Temperature Variations in  $\text{LiNbO}_3$  as a Function of Melt Stoichiometry**", *Appl. Phys. Lett.*, **12**[3] (1968) 92-94

- 
- <sup>99</sup> J. Midwinter, "**Lithium Niobate: Effects of Composition on the Refractive Indices and Optical Second-Harmonic Generation**", *J. Appl. Phys.* **39**[7] (1966) 3033
- <sup>100</sup> I. Bodnar and V. Yarunichev, "**Dependence of Refractive-Indexes Dispersion For LiNbO<sub>3</sub> On Impurity**", *Cryst. Res. Technol.* **18** (1983) 1161-1164
- <sup>101</sup> I. Foeldvari, K. Polgar, R. Voszka, R. Balasanyan, "**A Simple Method to Determine the Real Composition of LiNbO<sub>3</sub> Crystals**", *Cryst. Res. Technol.* **19**[12] (1984) 1659-1661
- <sup>102</sup> H. Megaw, "**The Seven Phases of Sodium Niobate**", *Ferroelectrics* **7** (1974) 87-89
- <sup>103</sup> B. Matthias and J. Remeika, "**Dielectric Properties of Sodium and Potassium Niobates**", *Phys. Rev.* **82**[5] (1951) 727-729.
- <sup>104</sup> V. Tennery, "**High-Temperature Phase Transition in NaNbO<sub>3</sub>**", *J. Am. Ceram. Soc.* **48**[10] (1965) 537-539
- <sup>105</sup> M. Francmbe, "**High Temperature Structure Transition in Sodium Niobate**", *Acta Cryst.* **9** (1956) 256-259
- <sup>106</sup> E. Wood, "**Polymorphism in Potassium Niobate, Sodium Niobate and Other ABO<sub>3</sub> Compounds**", *Acta Cryst.* **4** (1951) 353-362
- <sup>107</sup> G. Shirane, R. Newnham, and R. Pepinsky, "**Dielectric Properties and Phase Transitions of NaNbO<sub>3</sub> and (Na,K)NbO<sub>3</sub>**", *Phys. Rev.* **96** (1954) 581-589
- <sup>108</sup> F. Kracek, *J. Am. Chem. Soc.* **61** (1939) 2869
- <sup>109</sup> V. Babushkin, G. Matveyev, and O. Mchedlov-Petrosyan, "**Thermodynamics of Silicates**", (Springer, Berlin, 1985)
- <sup>110</sup> E. Vogel, S. Kosinski, D. Krol, J. Jackel, S. Friberg, M. Oliver, and J. Powers, "**Structural and Optical Study of Silicate Glasses for Nonlinear Optical Devices**", *J. Non-Cryst. Solids* **107** (1989) 244-250
- <sup>111</sup> G. Petrovski, Z. Shceglava, and I. Evtushenko, *Fiz. Khim. Stekla* **5** (1979) 302
- <sup>112</sup> B. Samuneva, S. Kralchev, and V. Dimitrov, "**Structure and Optical Properties of Niobium Silicate Glasses**", *J. Non-Cryst. Solids* **129**[1-3] (1991) 54-63
- <sup>113</sup> N. Borrelli, and M. Lyton, "**Dielectric and optical Properties of Transparent Ferroelectric Glass-Ceramic Systems**", *J. Non-Cryst. Solids* **6** (1971) 197-212.
- <sup>114</sup> N. Borrelli, "**Electro-optic Effect in Transparent Niobate Glass-Ceramic Systems**" *J. Appl. Phys.* **38**[11] (1967) 4243-4237
- <sup>115</sup> N. Borrelli, A. Herczog, and R. Maurer, "**Electro-optic Effect of Ferroelectric Microcrystals in a Glass Matrix**" *Appl. Phys. Lett.* **7**[5] (1965) 117-118
- <sup>116</sup> C. Hirayama and D. Berg., "**Dielectric properties of Glasses in the system Nb<sub>2</sub>O<sub>5</sub>-Na<sub>2</sub>O-SiO<sub>2</sub>**", *J. Am. Ceram. Soc.* **46**[2] (1963) 85-89.
- <sup>117</sup> M. Lyton, and A. Herczog, "**Structure and Crystallization of Glasses of low Network-Former Content**", *Glass Technol.* **10**[2] (1969) 50-53
- <sup>118</sup> Bh. Jankiramarao, "**Neo-Ceramic Glasses and Their Structure**", *Glass Technol.* **5**[2] (1964) 67-77
- <sup>119</sup> D. Vernacotola and J. Shelby, "**Potassium Niobate Silicate Glasses**", *Phys. Chem. Glasses* **35**[4] (1994) 153-59
- <sup>120</sup> M. Layton and A. Herczog, "**Nucleation and Crystallization of NaNbO<sub>3</sub> from Glasses in the Na<sub>2</sub>O-Nb<sub>2</sub>O<sub>5</sub>-SiO<sub>2</sub> system**", *J. Am. Ceram. Soc.* **50**[7] (1967) 369-375
- <sup>121</sup> M. Layton, and A. Herczog, "**Structure and Crystallization of Glasses of Low Network-former Content**", *Glass Technol.* **10**[2] (1969) 50-53
- <sup>122</sup> T. Kudo, K. Fueki, "**Solid state ionics**", (Tokyo, VCH, 1990)
- <sup>123</sup> H. Mehrer and F. Wenwer, "**Diffusion in Materials**" in "**Diffusion in Condensed Matter**", eds J. Kärger, P. Heitjans and R. Haberlandt (Springer, Berlin, 1998) 1-39
- <sup>124</sup> J. Crank, "**The Mathematic of Diffusion**", 2<sup>nd</sup> ed., (Oxford Univ. Press, Oxford, 1975)
- <sup>125</sup> A. Smigelskas and E. Kirkendall. "**Zinc Diffusion in Alpha Brass**", *Trans. Amer Inst. Min. Met. Engrs.* **171**(1947) 130-142.

## References

- <sup>126</sup> A. Einstein, "On the Motion of Small Particles Suspended in Liquids", *Ann. Phys., Lpz.* **17** (1905) 549-560
- <sup>127</sup> M. Smoluchowski, "Zür kinetischen Theorie der Brownschen Molekularbewegung und der Suspensionen", *Ann. Phys., Lpz.* **21** (1906) 756-780
- <sup>128</sup> F. Beniere in "Physics of Electrolytes" ed. J. Hladik (London, Academic, 1972)
- <sup>129</sup> G. Murch, "The Haven Ratio in Fast Ionic Conductors", *Solid State Ion.* **7** (1982) 177-198
- <sup>130</sup> M. Kleitz and J. Dupuy Eds, "Electrode Processes in Solid State Ionics", *NATO Conference, Ajaccio* (1975).
- <sup>131</sup> R. Armstrong in "Fast Ion Transport in Solids, Solid State Batteries and Devices", ed. W. Gool, (North-Holland, Amsterdam, 1973) p.269
- <sup>132</sup> J. Corish and P. Jacobs, "Ionic Conductivity of Silver Chloride Single Crystals", *J. Phys. Chem. Solids*, **33**[9] (1972) 1799-1818
- <sup>133</sup> H. Gleiter, "Nanocrystalline Materials", *Prog. Mater. Sci.* **33**[4] (1989) 223-315
- <sup>134</sup> H. Gleiter, "Diffusion in Nanostructured Metals", *Phys. Status Solidi B* **172**[1] (1992) 41-51
- <sup>135</sup> J. Horvath, R. Birringer, and H. Gleiter, "Symmetry Breaking Commensurate-Incommensurate Transition of Monolayer Xe Physisorbed on Pt(111)", *Solid State Commun.* **62**[6] (1987) 391-394
- <sup>136</sup> A. Körblein, P. Heitjans, H.-J. Stöckmann, F. Fujara, H. Ackermann, W. Buttler, K. Dörr, and H. Grupp, "Diffusion Processes in Solid Li-Mg and Li-Ag Alloys and the Spin-Lattice Relaxation of  $^8\text{Li}$ ", *J. Phys. F: Met. Phys.* **15** (1985) 561-577
- <sup>137</sup> J. Isard, "The Mixed Alkali Effect in Glasses", *J. Non-Crystal. Solids* **1** (1969) 235-61
- <sup>138</sup> M. Ingram, "Ionic-Conductivity in Glasses", *Phys. Chem. Glasses* **28**[6] (1987) 215-234
- <sup>139</sup> D. Day, "Mixed Alkali Glasses-Their Properties and Uses", *J. Non-Cryst. Solids* **21** (1976) 343-372
- <sup>140</sup> O. Mazurin, "Structure of Glasses", Vol. 4, Consultants Bureau, New York (1965) 5-55.
- <sup>141</sup> B. Lengyel and Z. Bosksay, *Z. Phys. Chem.-Leipzig* **203** (1954) 96
- <sup>142</sup> J. Stevels, "The Electrical Properties of Glass" *Handbuch der Physik* Vol. 20, Ed. Flugge, (Springer-Verlag, Berlin, 1957).
- <sup>143</sup> J. Hendrickson, and P. Bray, "A Theory for the Mixed Alkali Effect in Glass, Part I", *Phys. Chem. Glasses* **13**[2] 43-49 (1972).
- <sup>144</sup> J. Hendrickson, and P. Bray, "A Theory for the Mixed Alkali Effect in Glass, Part II", *Phys. Chem. Glasses* **13**[4] (1972) 107-115.
- <sup>145</sup> G. Tomandl, and H. Schaeffer, "Mixed Alkali Effect-A Permanent Challenge", *J. Non-Cryst. Solids* **73** (1985) 179-196
- <sup>146</sup> W. LaCourse, "A Defect Model for the Mixed Alkali Effect", *J. Non-Cryst. Solids* **95-96** (1987) 905-912
- <sup>147</sup> M. Tomozawa, "Alkali Ionic Transport in Mixed Alkali Glasses", *J. Non-Cryst. Solids* **152** (1993) 59-69
- <sup>148</sup> M. Tomozawa, and V. McGahay "Mechanism of the Mixed Alkali Effect Based upon the Thermodynamic State of the glass", *J. Non-Cryst. Solids* **128** (1991) 48-56
- <sup>149</sup> J. Lapp, and J. Shelby, "The Mixed Alkali Effect in Sodium and Potassium Glliosilicate Glasses I, Glass transformation temperatures", *J. Non-Cryst. Solids* **84** (1986) 463-467
- <sup>150</sup> J. Lapp, and J. Shelby, "The Mixed Alkali Effect in Sodium and Potassium Glliosilicate Glasses II, DC Electrical Conductivity", *J. Non-Cryst. Solids*, **86** (1986) 350-60
- <sup>151</sup> C. Kuppinger, and J. Shelby, "Viscosity and Thermal Expansion of Mixed Alkali Sodium-Potassium Borate Glasses", *J. Am. Ceram. Soc.* **68**[9] (1985) 463-467
- <sup>152</sup> J. Shelby, "Thermal Expansion of Mixed Alkali Germanates", *J. Appl. Phys.* **46**[1] (1975) 193-196
- <sup>153</sup> Yu Feldman, A. Andrianov, E Polygalov, G. Romanychev, I. Ermolina, Yu Zuev and B. Milgotin, "Time Domain Dielectric Spectroscopy: An Advanced Measuring System", *Rev. Sci. Instrum.* **67**[9] (1996) 3208-3216
- <sup>154</sup> A. Jonscher, "Dielectric Relaxation in Solids", *J. Phys. D: Appl. Phys.* **32** (1999) R57-R70.
- <sup>155</sup> J. Macdonald, ed., "Impedance Spectroscopy - Emphasizing Solid Materials and Systems". 1st ed., (John Wiley & Sons, New York, 1987)



- 
- <sup>156</sup> R. Buchanan, "*Ceramics Materials for Electronics, Processing, Properties, and Applications*", (New York Marcel Dekkerjp 110, 1986)
- <sup>157</sup> M. Haile, L. West, and J. Campbell, "*The Role of Microstructure and Processing on the Proton Conducting Properties of Gadolinium-Doped Barium cerate*", *J. Mater. Res.* **13**[6] (1998) 1576
- <sup>158</sup> D. Macdonald, "*Transient Techniques in Electrochemistry*", (Plenum Press, New York, 1977)
- <sup>159</sup> C. Schiller, "*About Electrochemical Impedance Spectroscopy EIS; Basics and Applications of the EIS*", in "*Thales IM 6 Owner's Manual*", Zahner Messtechnik, Kronach
- <sup>160</sup> A. Bard, and L. Faulkner, "*Electrochemical Methods - Fundamentals and Applications*", 2<sup>nd</sup> ed., (John Wiley & Sons, New York, 2001)
- <sup>161</sup> C. Hamann, A. Hamnett and W. Vielstich, "*Electrochemistry*", 1<sup>st</sup> ed. (Wiley-VCH, Weinheim, New York, 1998)
- <sup>162</sup> C. Hsu, and F. Mansfeld, "*Concerning the Conversion of the Constant Phase Element Parameter  $Y_0$  into a Capacitance*", *Corrosion* **57** (2001) 747
- <sup>163</sup> V. Jovic, "*Determination of the Correct Value of  $C_{dl}$  from the Impedance Results Fitted by the Commercially Available Software*", Distributed Courtesy of Gamry Instruments. Inc., <http://www.gamry.com>
- <sup>164</sup> W. Mulder, J. Sluyters, T. Pajkossy, and L. Nyikos, "*Tafel Current At Fractal Electrodes-Connection with Admittance Spectra*", *J. Electroanal. Chem.*, **285**[1-2] (1990) 103-115
- <sup>165</sup> J. Fleig, J. Jamnik, J. Maier, and J. Ludvig, "*Inductive Loops in Impedance Spectroscopy Caused by Electrical Shielding*", *J. Electrochem. Soc.*, **143** (1996) 3636.
- <sup>166</sup> P. Debye, "*Some Results of a Kinetic Theory of Insulators*", *Phys. Z.* **13** (1912) 97-100
- <sup>167</sup> P. Debye, "*Polar Molecules*", (Dover, New York, 1945)
- <sup>168</sup> S. Havriliak and S. Havriliak, "*Dielectric and Mechanical Relaxation in Materials: Analysis, Interpretation, and Application to Polymers*", (Hanser Gardner Publ., Munich, 1997)
- <sup>169</sup> A. Jonscher, "*Dielectric Relaxation in Solids*", (Chelsea Dielectrics, London, 1983)
- <sup>170</sup> J. Dyre, "*Some Remarks on AC Conduction in Disordered Solids*", *J. Non-Crystal. Solids* **135**[2-3] (1991) 219-226
- <sup>171</sup> V. Bryksin, "*Frequency Dependence of the Hopping Conductivity for Three-Dimensional Systems in the Framework of the Effective-Medium Method*", *Sov. Phys. Solid State* **22**[8] (1980) 1421-1426
- <sup>172</sup> K. Funke, "*Jump Relaxation Model and Coupling Model-A Comparison*", *J. Non-Crystal. Solids* **172-174**[2] (1994) 1215-1221
- <sup>173</sup> K. Funke, "*Mechanisms of Ionic Conduction in Solid Electrolytes*", *Defect Diffus. Forum* **143-147**[2] (1997) 1243-1257
- <sup>174</sup> C. Cramer, K. Funke, M. Buscher, A. Happe, T. Saatkamp and D. Wilmer, "*Ion Dynamics in Glass-Forming Systems .2. Conductivity Spectra Above The Glass Transformation Temperature*", *Phil. Mag.* **71**[4] (1995) 713-719
- <sup>175</sup> C. Cramer, K. Funke, B. Roling, T. Saatkamp, D. Wilmer, M. Igram, A. Pradel, M. Ribes and G. Taillades, "*Ionic and Polaronic Hopping in Glass*", *Solid State Ionics* **86-88**[1] (1996) 481-486
- <sup>176</sup> C. Cramer, K. Funke, T. Saatkamp, D. Wilmer and M. Ingram, "*High-Frequency Conductivity Plateau and Ionic Hopping Processes in a Ternary Lithium Borate Glass*", *Z. Naturf. a* **50**[7] (1995) 613-623
- <sup>177</sup> A. Bunde, K. Funke and M. Ingram, "*A Unified Site Relaxation Model for Ion Mobility in Glassy Materials*", *Solid State Ionics* **86-88**[2] (1996) 1311-1317
- <sup>178</sup> A. Bunde, M. Ingram, and P. Maass, "*The Dynamic Structure Model for Ion-Transport In Glasses*", *J. Non-Crystal. Solids* **172-174**[2] (1994) 1222-1236
- <sup>179</sup> A. Jonscher and M. Frost, "*Weakly Frequently-Dependence Electrical-Conductivity In A Chalcogenide Glass*", *Thin Solid Films* **37**[2] (1976) 267-273
- <sup>180</sup> A. Jonscher, "*Universal Relaxation Law*", (London: Chelsea Dielectrics, 1996)
- <sup>181</sup> D. O'Neill, R. Bowman, and J. Gregg, "*Dielectric Enhancement and Maxwell-Wagner Effects in Ferroelectric Superlattice Structures*", *Appl. Phys. Lett.* **77**[10] (2000) 1520-1522

- <sup>182</sup> A. Jonscher, "**Low-loss Dielectris**", *J. Mater. Sci.* **34** (1999) 3071-3082
- <sup>183</sup> H. Günther, "**NMR Spectroscopy: Basic Principles, Concepts, and Applications in Chemistry**", 2. ed, (Wiley, Chichester; New York, 1995)
- <sup>184</sup> D. Grant and R. Harris, "**Encyclopedia of Nuclear Magnetic Resonance**", 1-9 Willy, 2002
- <sup>185</sup> N. Bloembergen, E. Burcell, and R. Pound, "**Relaxation Effects in Nuclear Magnetic Resonance Absorption**", *Phys. Rev.* **73**[7] (1948) 679-712
- <sup>186</sup> C. Sholl, "**Nuclear Spin Relaxation by Translational Diffusion in Liquids and Solids : High- and Low-Frequency Limits**", *J. Phys. C: Solid State Phys.* **14** (1981) 447-664
- <sup>187</sup> J. Bjorkstam and M. Villa, "**NMR and EPR Studies of Superionic Conductors**", *Magn. Res. Rev.* **6**[1] (1980) 1-57
- <sup>188</sup> E. Goebel, W. Müller-Warmuth, H. Olyschläger, and H. Dutz, "**Lithium-7 NMR Spectra, Nuclear Relaxation, and Lithium-Ion Motion in Alkali Silicate, Borate, and Phosphate Glasses**", *J. Magn. Reson.* **36**[3] (1979) 371-387
- <sup>189</sup> D. Knödler, P. Pendzig, and W. Dieterich, "**Ion Dynamics in Structurally Disordered Materials: Effects of Random Coulombic Traps**", *Solid State Ionics* **86-88** (1996) 29
- <sup>190</sup> K. Ngai and O. Kanert, "**Comparisons Between The Coupling Model Predictions, Monte-Carlo Simulations and Some Recent Experimental-Data of Conductivity Relaxations in Glassy Ionics**", *Solid State Ionics* **53-56**[2] (1992) 936-946
- <sup>191</sup> K. Funke, "**Jump Relaxation in Solid Electrolytes**", *Progr. Solid State Chem.* **22**[2] (1993) 111- 195
- <sup>192</sup> Kärger, P. Heitjans, R. Haberlandt, eds, "**Diffusion in Condensed Matter**", Vieweg: Brawnschweig, Springer, 1998, p.120
- <sup>193</sup> J. Hendrickson and P. Bray, "**Phenomenological Equation for NMR Motional Narrowing in Solids**", *J. Magn. Res.*, **9**[3] (1973) 341-357
- <sup>194</sup> A. Abragam, "**The Principle of Nuclear Magnetism**", (Oxford, Clarendon Press, Oxford, 1961).
- <sup>195</sup> J. Waugh and E. Fedin, "**Determination of Hindered-Rotation Barriers in Solids**", *Sov. Phys. Solid State* **4**[8] (1963) 1633-1636
- <sup>196</sup> M. Wilkening and P. Heitjans, "**Ultraslow Diffusion in Polycrystalline h-LiTiS<sub>2</sub> Studied by <sup>7</sup>Li Spin-Alignment Echo NMR Spectroscopy**", *Defect Diffus. Forum* **237-240** (2005) 1182-1187
- <sup>197</sup> P. Heitjans, S. Indris and M. Wilkening, "**Solid-State Diffusion and NMR**", *Diffusion Fundamentals*, Leipziger Universitätsverlag, Leipzig (2005) 226-245
- <sup>198</sup> J. Jeener, P. Broekaert, "**Nuclear Magnetic Resonance in Solids: Thermodynamic Effects of a Pair of RF Pulses**", *Phys. Rev.*, **157** (1967) 232.
- <sup>199</sup> R. Böhmer, "**Multiple-Time Correlation Functions in Spin-3/2 Solid-State NMR Spectroscopy**" *J. Magn. Res.* **147**[1] (2000) 78-88
- <sup>200</sup> F. Qi, T. Jörg, and R. Böhmer, "**Stimulated-Echo NMR Spectroscopy of <sup>9</sup>Be and <sup>7</sup>Li in Solids: Method and Application to Ion Conductors**", *Solid State Nucl. Magn. Res.* **22**[4] (2002) 484-500
- <sup>201</sup> F. Qi, G. Diezemann, H. Böhm, J. Lambert, and R. Böhmer, "**Simple Modeling of Dipolar Coupled <sup>7</sup>Li Spins and Stimulated-Echo Spectroscopy of Single-Crystalline  $\beta$ -Eucryptite**", *J. Magn. Res.* **169**[2] (2004) 225-239
- <sup>202</sup> A. Körblein, P. Heitjans, H. J. Stöckmann, F. Fujara, H. Ackermann, W. Buttler, K. Dörr, and H. Grupp, "**Diffusion processes in solid Li-Mg and Li-Ag alloys and the Spin-Lattice Relaxation of <sup>8</sup>Li**", *J. Phys. F: Met. Phys.* **15**[3] (1985) 561-577
- <sup>203</sup> E. Schneider, J. Stebbins, and A. Pines, "**Speciation and Local-Structure in Alkali and Alkaline-Earth Silicate-Glasses – Concepts from <sup>29</sup>Si NMR –Spectroscopy**", *J. Non-Cryst. Solids* **89** (1987) 371
- <sup>204</sup> J. Stebbins, "**NMR Spectroscopy and Dynamic Processes in Mineralogy and Geochemistry**", in "**Spectroscopic Methods in Mineralogy and Geology**", ed. F. Hawthorne, (Mineralogical Society of America, Washington D. C., 1988). 405-430
- <sup>205</sup> P. Lee, P. Citrin, P. Eisenberger, and B. Kincaid, "**Extended X-ray Absorption Fine Structure–Its Strengths and Limitations as a Structural Tool**", *Rev. Mod. Phys.* **53** (1981) 769-806.

- 
- <sup>206</sup> D. Sayers, E. Stern, and F. Lytle, "**New Technique for Investigating Noncrystalline Structures: Fourier Analysis of the Extended X-Ray—Absorption Fine Structure**", *Phys. Rev. Lett.* **27** (1971) 1204–1207
- <sup>207</sup> J. Rehr, in *Proceedings of the VII<sup>th</sup> International Conference on X-ray Absorption Fine Structure (XAFS)* [*Jpn. J. Appl. Phys. Suppl.* **32-2**, 8 (1993)].
- <sup>208</sup> S. Gurman, "**Interpretation of EXAFS Data**", *J. Synchrotron Rad.* **2** (1995) 56-63.
- <sup>209</sup> S. Hasnain, "**Application of EXAFS and XANES to Metalloproteins**", *Life Chem. Reports* **4** (1987) 273-331.
- <sup>210</sup> C. Macgillivray, and G. Rieck (Eds.), "**International Tables for X-ray Crystallography, Vol. III: Physical and Chemical Tables**" (Lonsdale, K. gen. Ed.), International Union of Crystallographers. (Kynoch Press, Birmingham, England. 1962)
- <sup>211</sup> D. Koningsberger, and R. Prins, "**X-ray Absorption: Principles, Applications, Techniques of EXAFS, SEXAFS, and XANES**", (Wiley, New York, 1988):
- <sup>212</sup> A. Benninghoven, F. Rüdenauer, and H. Werner, "**Secondary Ion Mass Spectrometry: Basic Concepts, Instrumental Aspects, Applications, and Trends**", (Wiley, New York, 1987).
- <sup>213</sup> P. Mazur and J. Sanders, "**On Derivation Of Range Equation For Energetic Particles In Amorphous Materials**" *Physica* **44** (1969) 444
- <sup>214</sup> P. Sigmund, "**Theory of Sputtering. I. Sputtering Yield of Amorphous and Polycrystalline Targets**", *Phys. Rev.*, **184**, (1969) 383-416
- <sup>215</sup> J. Vickerman, A. Brown, and N. Reed, "**Secondary Ion Mass Spectroscopy: Principles and Applications**", (Clarendon Press, Oxford, 1989)
- <sup>216</sup> G. McMahon, L. Cabri, "**The SIMS Technique in Ore Mineralogy, in Modern Approaches to Ore and Environmental Mineralogy**", Eds. L. Cabri and D. Vaughan, Mineralogical Association of Canada, Short Course **27**, (1998) 199-223.
- <sup>217</sup> D. Greenaway and G. Harbeke, "**Optical Properties and Band Structure of Semiconductors**", (Pergamon Press, Oxford, New York, 1968) pp. 23-26
- <sup>218</sup> E. Wiesendanger and G. Guntherodt, "**Optical Anisotropy of LiNbO<sub>3</sub> and KNbO<sub>3</sub> in the Interband Transition Region**", *Solid State Commun.* **14**[4] (1974) 303
- <sup>219</sup> G. Boyd, W. Boyd, and H. Carter, "**Refractive Index as a Function of Temperature in LiNbO<sub>3</sub>**", *J. Appl. Phys.* **38**[4] (1967) 1941-1943
- <sup>220</sup> I. Földvari, K. Polgar, R. Voszka, and R. Balasanyan, "**A Simple Method to Determine the Real Composition of LiNbO<sub>3</sub> Single Crystals**", *Cryst. Res. Technol.* **19**[12] (1984) 1659-1661
- <sup>221</sup> S. Hongye and L. Guoxiang, "**Crystallization Processes in Amorphous LiNbO<sub>3</sub>**", *Ferroelectrics* **101** (1990) 11-18
- <sup>222</sup> H. Chen and C. Miller, "**A Rapid Quenching Technique for the Preparation of Thin Uniform Films of Amorphous Materials**", *Rev. Sci. Instrum.* **41** (1970) 1237-1238
- <sup>223</sup> T. Zuzuki and A-M Anthony, "**Rapid Quenching on the Binary Systems of High Temperature Oxides**", *Mat. Res. Bull.* **9** (1974) 745-754
- <sup>224</sup> K. Nassau, "**Rapid Quenched Glasses**", *J. Non-Crystal. Solids* **42** (1980) 423-432
- <sup>225</sup> M. Tatsumisago and T. Minami, "**Lithium-Ion Conducting Glass Prepared by Rapid Quenching**", *Mater. Chem. Phys.* **18**[1-2] (1987) 1-17
- <sup>226</sup> K. Varma, "**Twin Roller Quenching Technique and Preparation of glasses of High Melting Ionic Solids**", *Bull. Mater. Sci.* **9**[1] (1987) 1-5
- <sup>227</sup> M. Lonhardt, M. Jurisch, U. Böttcher, and A. Luft, "**A TEM Study of the Microstructure of Fe-6.25 wt.%Si Ribbons Prepared by Twin Roller Quenching**", *Mater. Sci. Eng.* **A133** (1991) 620-623
- <sup>228</sup> Y. Yue, S. Jensen, and J. Christiansen, "**Physical Aging in a Hyperquenched Glass**", *Appl. Phys. Lett.* **81**[16] (2002) 2983-2985
- <sup>229</sup> A. Glass, M. Lines, K. Nassau, and J. Shiever, "**Anomalous Dielectric Behavior and Reversible Pyroelectricity in Roller-Quenched LiNbO<sub>3</sub> LiTaO<sub>3</sub> Glass**", *Appl. Phys. Lett.* **31**[4] 249-251

## References

- <sup>230</sup> A. Glass, K. Nassau, and T. Negran, "**Ionic-Conductivity of Quenched Alkali Niobate and Tantalate Glasses**", *J. Appl. Phys.* **49**[9] (1978) 4808-4811
- <sup>231</sup> S. Ono, H. Mochizuki, and S. Hirano, "**Preparation and Characterization of Amorphous LiNbO<sub>3</sub> Powders from Completely Hydrolysed Metal Alkoxides**", *J. Cer. Soc. Jap.*, **104**, (1996) 574-578
- <sup>232</sup> S. Hirano and K. Kato, "**Formation of LiNbO<sub>3</sub> Films by Hydrolysis of Metal Alkoxides**", *J. Non-Cryst. Solids* **100** (1988) 538-541
- <sup>233</sup> S. Hirano and K. Kato, "**Synthesis of LiNbO<sub>3</sub> by Hydrolysis of Metal Alkoxides**", *Adv. Ceram. Mater.* **2**[2] (1987) 142-145
- <sup>234</sup> M. Dinges, "**Strukturelle Charakterisierung von Sol-Gel Prozessen**", *Ph. D. Thesis*, Technische Hochschule Darmstadt, 1997
- <sup>235</sup> D. Bork, "**NMR-Untersuchungen zur Ionendynamik und Struktur in Nano- und Polykristallinem LiNbO<sub>3</sub>**", *Ph. D. Thesis*, Universiaet Hannover, 1997
- <sup>236</sup> S. Indris, D. Bork, and P. Heitjans, "**Nanocrystalline Oxide Ceramics Prepared by High-Energy Ball Milling**", *J. Mater. Synth. Proc.* **8**[3-4] (2000) 245-250.
- <sup>237</sup> Reference for  $\alpha$ -alumina is 1997 JCPDS 46-1212.
- <sup>238</sup> W. Rachinger, "**A Correction for the  $\alpha_1\alpha_2$  Doublet in the Measurement of Widths of X-ray Diffraction Lines**" *J. Sci. Inst.* **25** (1948) 254-255
- <sup>239</sup> B. Waren, "**X-ray Diffraction**", (Addison-Wesley, New York, 1969).
- <sup>240</sup> R. Pease, "**The Resolution of X-ray Doblel Diffraction Lines into  $\alpha_1\alpha_2$  Components**" *J. Sci. Inst.* **25** (1948) 353.
- <sup>241</sup> H. Klug and L. Alexander, "**X-Ray Diffraction Procedures : for Polycrystalline and Amorphous Materials**", (Wiley, New York, 1974)
- <sup>242</sup> G. Williamson, and W. Hall, "**X-Ray Line Broadening From Filed Aluminium and Wolfram**", *Acta Metallurgica* **1** (1953) 22-31
- <sup>243</sup> G. Rush, A. Chadwich, I. Kosacki and U. Anderson, "**An EXAFS Study of Nanocrystalline Yttrium Stabilized Cubic Zirconia Films and Pure Zirconia Powders**", *J. Phys. Chem B* **104** (2000) 9597-9606
- <sup>244</sup> H. Zeng and S. Tung, "**Synthesis of Lithium Niobate Gels Using a Metal Alkoxide-Metal Nitrate Precursor**", *Chem. Mater.* **8** (1996) 2667-2672
- <sup>245</sup> J-M. Jehng and I. Wachs, "**Structural Chemistry and Raman Spectra of Niobium Oxides**", *Chem. Mater.* **3** (1991) 100-107
- <sup>246</sup> S. Ross, "**The Vibrational Spectra of Lithium Niobate, Barium Sodium Niobate and Barium Sodium Tantalate**", *J. Phys. C: Solid St. Phys.* **3** (1970) 1785-1790
- <sup>247</sup> R. Schaufele, and M. Weber, "**Raman Scattering by Lithium Niobate**", *Phys. Rev.* **152** (1966) 705-708
- <sup>248</sup> S. Hirano, T. Yogo, K. Kikuta, and Y. Isobe, "**Study of Crystallization of LiNbO<sub>3</sub> Films from Metal Alkoxides**", *J. Mater. Res. Sci.* **28** (1993) 4188-4192
- <sup>249</sup> Y. Kong, J. Xu, X. Chen, C. Zhang, W. Zhang, and G. Zhang, "**Ilmenite-Like Stacking Defect in Non-Stoichiometric Lithium Niobate Crystals Investigated by Raman Scattering Spectra**", *J. Appl. Phys.* **87**[9] (2000) 4410-4414
- <sup>250</sup> M. Graca, M. Valente, and M. Silva, "**Electrical Properties of Lithium Niobium Silicate Glasses**", *J. Non-Crystal. Solids* **325** (2003) 267-274
- <sup>251</sup> E. Prasad, M. Sayer, and H. Vyas, "**Li<sup>+</sup> Conductivity in Lithium Niobate: Silicate Glasses**", *J. Non-Crystal. Solids* **40** (1980) 119-134
- <sup>252</sup> C. Hirayama, and D. Berg, "**Dielectric Properties of Glasses in the System Nb<sub>2</sub>O<sub>5</sub>-Na<sub>2</sub>O-SiO<sub>2</sub>**", *J. Am. Ceram. Soc.* **46** [2] (1963) 85-88
- <sup>253</sup> A. Herczog, "**Phase Distribution and Transparency in Glass-Ceramics Based on a Study of the Sodium Niobate Silica System**", *J. Am. Ceram. Soc.* **73**[9] (1990) 2743-2746
- <sup>254</sup> Maksimova, Korzunova, and Milberg, "**Microliquefaction in Glasses of the System Li<sub>2</sub>O-Nb<sub>2</sub>O<sub>5</sub>-SiO<sub>2</sub>**", *Neorganicheskie Stekla, Pokrytiya, i Materialy* **1** (1975) 99-102

- <sup>255</sup> B. Boukamp, "*Equivalent Circuit (Version 4.51)*" Computer program for IBM-PC computers and compatibles, 1993 and *User Manual*, 2<sup>nd</sup> revised edition, 1988/89, 53 pages, Dept. Chemical Technology, University of Twente, Netherlands.
- <sup>256</sup> R. Kappes "*Impedanz- und NMR-Spektroskopische Untersuchungen an Wasserhaltigen Alumosilikatgläsern*", *Ph D. Thesis*, Hannover University 2002.
- <sup>257</sup> D. Messurier, "*An Investigation into the Interfacial Region of a Sol-Gel Prepared Nanocrystalline Zirconia-Alumina Composite and Metasilicate Glass Matrix*", *M. Sc. Thesis*, University of Wales-Aberystawyth 2003
- <sup>258</sup> E. Fukushima and S. Roeder, "*Experimental Pulse NMR*", (Addison-Wesley, London, 1981)
- <sup>259</sup> M. Wilkening "*Ultralangsame Ionenbewegung in Festkörpern: NMR-spektroskopische Studien an Lithium-Ionenleitern*", *Ph. D. Thesis*, Hannover University 2005.
- <sup>260</sup> F. Qi, G. Diezemann, H. Böhm, J. Lambert, and R. Böhrer, "*Simple Modeling of Dipolar Coupled <sup>7</sup>Li Spins and Stimulated-Echo Spectroscopy of Single-Crystalline  $\beta$ -Eucryptite*", *J. Magn. Res.* **169** (2004) 225
- <sup>261</sup> D. Massiot, F. Fayon, M. Capron, I. King, S. Calve, B. Alonso, J. Durand, B. Bujoli, Z. Gan, and G. Hoatson, "*Modelling One- and Two-Dimensional Solid-state NMR Spectra*", *Magn. Reson. Chem.* **40** (2002) 70-76
- <sup>262</sup> J. Shelby, "*Introduction to Glass Science and Technology*", (The Royal Society of Chemistry, Cambridge, 1997), 78
- <sup>263</sup> H. Stockmann and P. Heitjans, "*Low-Temperature Nuclear-Spin-Lattice Relaxation in Glasses – Homogeneous and Inhomogeneous Averaging*", *J. Non.-Cryst. Solids* **66**[3] (1984) 501-509
- <sup>264</sup> CCLRC Daresbury Laboratory computer programs (<http://srs.dl.ac.uk/xrs/Computing/help.html>)
- <sup>265</sup> N. Binsted, (1998) EXCURV98: CCLRC Daresbury Laboratory computer program. S. Gurman, N. Binsted, and I. Ross, "*A Rapid, Exact Curved-Wave Theory for EXAFS Calculations*", *J. Phys. C: Solid State Phys.* **17** (1984) 143-151
- <sup>266</sup> L. Svaasand, M. Eriksrud, G. Nakken, and A. Grande, "*Solid-Solution Range of LiNbO<sub>3</sub>*", *J. Cryst. Growth* **22**[3] (1974) 230-232
- <sup>267</sup> R. De Souza, and M. Martin, "*Secondary Ion Mass Spectroscopy: A Powerful Tool for Diffusion Studies in Solids*", *Arch. Metall. Mater.* **49**[2] (2004) 431-446
- <sup>268</sup> Topas V. 2.0, "*General Profile and Structure Analysis Software for Powder Diffraction Data*", Bruker AXS, Karlsruhe, Germany, 2000.
- <sup>269</sup> J. Hennel and J. Klinowski, "*Fundamentals of Nuclear Magnetism*", (Longman Scientific and Technical, Harlow, 1993)
- <sup>270</sup> M. Cohen, F. Reif, in: "*Solid St. Physics*" Vol. 5, (Academic Press, New York, 1975)
- <sup>271</sup> T. Das and R. Bersohn, "*Variation Approach to the Quadrupolar Polarizability of Ions*", *Phys. Rev.* **102** (1956) 733- 738
- <sup>272</sup> T. Halstead, "*Temperature Dependence of the Li NMR Spectrum and Atomic Motion in LiNbO<sub>3</sub>*", *J. Chem. Phys.* **53**[9] (1970) 3427-3435
- <sup>273</sup> G. Peterson, P. Bridenbaugh, and P. Green, "*NMR Study of Ferroelectric LiNbO<sub>3</sub> and LiTaO<sub>3</sub>. II*", *J. Chem. Phys.* **48** (1968) 3402-3406
- <sup>274</sup> V. Bogdanov, V. Lemanov, V. Klyuev, and S. Fedulov, "*Nuclear Magnetic Resonance in Lithium Niobate Crystals*", *Sov. Phys. Solid State* **10** (1968) 886-890
- <sup>275</sup> R. Pound, "*Nuclear Quadrupole Interaction in Crystals*", *Phys. Rev.* **79** (1950) 685-705
- <sup>276</sup> G. Burns, "*Polarizabilities and Antishielding Factors of 10 and 18 Electron Closed Shell Atoms*", *Phys. Rev.* **127** (1962) 1193-1197
- <sup>277</sup> G. Peterson, P. Bridenbaugh, and P. Green, "*NMR Study of Ferroelectric LiNbO<sub>3</sub> and LiTaO<sub>3</sub>. I*", *J. Chem. Phys.* **46**[10] (1967) 4009-40114
- <sup>278</sup> V. Gabrielyan, V. Kasperovich, S. Klimko, and E. Charnaya, "*NMR of <sup>7</sup>Li in Lithium Niobate Crystals with Various Nonstoichiometries*", *Phys. Solid State* **38**[6] (1996) 1041

## References

- 279 E. Charnaya, V. Gabrielyan, V. Kasperovich, and S. Klimko, "<sup>7</sup>Li NMR in LiNbO<sub>3</sub> Crystals with Different Non-stoichiometries", *Ferroelectrics* **202** (1997) 115-119
- 280 E. Charnaya, V. Kasperovich, and M. Shelyapina, "**Quadrupole Splitting of the <sup>7</sup>Li NMR Line in LiNbO<sub>3</sub> Crystals**", *Ferroelectrics* **208-209** (1998) 225-236
- 281 A. Yatsenko, "**Characterization of Dynamics of LiNbO<sub>3</sub> Monocrystal Structures According to Li-7 NMR Data**", *Russ. Phys. Solid St.* **37**[7] (1995) 2203
- 282 S. Choh, I.-W. Park, J. Ahm, I. Kim and Y. Choi, "", *Ferroelectrics* **156** (1994) 255
- 283 L. Baiqin, W. Yening, and X. Ziran, "**NMR Study of Anomalous Properties of LiNbO<sub>3</sub> Crystal at 292-363 K**", *J. Phys. C.: Solid State Phys.* **21** (1988) L251-L255.
- 284 A. Yatsenko, N. Sergeev, "**Peculiarities of <sup>7</sup>Li nuclear magnetic resonance absorption spectra in LiNbO<sub>3</sub>**", *Ukr. J. Phys.* **30** (1985) 118-120
- 285 A. Yatsenko, N. Sergeev, in Extended Abstracts 28<sup>th</sup> Congress AMPERE, University of Kent, England, 1996, p.279.
- 286 A. Yatsenko, in Extended Abstracts 28<sup>th</sup> Congress AMPERE, University of Kent, England, 1996, p.281.
- 287 A. Yatsenko, E. Ivanova, N. Sergeev, "**NMR Study of Intrinsic Defects in Congruent LiNbO<sub>3</sub> 1. Unoverlapping defects**", *Physica B* **240** (1997) 254-262
- 288 J. Davis, D. Tinetti, J. Fripiat, J. Amarilla, B. Casal, and E. Ruiz-Hitzky, "**<sup>51</sup>V and <sup>93</sup>Nb High Resolution NMR Study of NbVO<sub>5</sub>**", *J. Mater. Res.* **6**[2] (1991) 393-400
- 289 P. Man, H. Theveneau, and R. Papon, "**Investigation of the Central Line of Nb-93 by a Two-Dimensional NMR Method**", *J. Magn. Reson.* **64**[3] (1985) 271-277
- 290 S. Prasad, P. Zhao, J. Huang, J. Fitzgerald, and J. Shore, "**Niobium-93 MQMAS NMR Spectroscopic Study of Alkali and Lead Niobates**", *Solid State Nucl. Magn. Reson.* **19** (2001) 45-62
- 291 R. Kind, H. Gracnicer, B. Derighetti, F. Waldner, and E. Brun, "**NMR of <sup>93</sup>Nb in Ferroelectric LiNbO<sub>3</sub>**", *Solid State Commun.* **6** (1968) 439-440
- 292 M. Cohen and F. Reif, "**Quadrupole Effects In Nuclear Magnetic Resonance Studies of Solids**", *Solid State Phys.* **5** (1957) 321-438
- 293 G. Peterson and A. Carnevale, "**<sup>93</sup>Nb NMR Linewidths in Nonstoichiometric Lithium Niobate**", *J. Chem. Phys.* **56**[10] (1972) 4848
- 294 L. Hu, Y. Chang, C. Chang, S. Yang, M. Hu, and W. Tse, "**Raman and NMR Study in MgO-Doped LiNbO<sub>3</sub> Crystal**", *Modern Physics Letters B* **5** (1991) 789-797
- 295 D. Douglass, G. Peterson, and V. McBrierty, "**Re-examination of the Local Electric Field Gradients in LiNbO<sub>3</sub>**", *Phys. Rev. B* **40** (1989) 10694-10703
- 296 A. Yatsenko, H. Maksimova, and N. Sergeev, "**NMR Study of Intrinsic Defects in Congruent Lithium Niobate**", *Cryst. Res. Technol.* **34**[5-6] (1999) 709-713
- 297 A. Yatsenko, and E. Ivanova, "**Study of Non-Stoichiometric LiNbO<sub>3</sub> Crystals by the NMR Technique**", *Solid St. Phys.* **37**[8] (1995) 2262-2268
- 298 N. Zotov, H. Boysen, F. Frey, T. Metzger, and E. Born, "**Cation Substitution Models of Congruent LiNbO<sub>3</sub> Investigated by X-ray and Neutron Powder Diffraction**", *J. Phys. Chem. Solids.* **55**[2] (1994) 145-152
- 299 D. Bradley and C. Holloway, "**Nuclear Magnetic Resonance Studies on Niobium and Tantalum Penta-Alkoxides**", *J. chem. Soc. (A) -Inorg. Phys. Theor.* **2** (1968) 219
- 300 D. Eichorst, and D. Payne, "**Evolution of Molecular Structure in Alkoxide-Derived Lithium Niobate**" in "**Better Ceramics Through Chemistry IV**", eds J. Zelinski, C. Brinker, D. Clark, and D. Ulrich (*Mater. Res. Soc. Symp. Proc.* **180**, Pittsburgh, PA, 1990), 669-674.
- 301 D. Eichorst, D. Payne, S. Wilson, and K. Howard, "**Crystal Structure of LiNb(OCH<sub>2</sub>CH<sub>3</sub>)<sub>6</sub>: A Precursor for Lithium Niobate Ceramic**", *Inorganic Chemistry* **29** (1990) 1458-1459
- 302 V. Joshi and M. Mecartney, "**The Influence of Water of Hydrolysis on Microstructural Development in Sol-Gel Derived LiNbO<sub>3</sub> Thin Films**", *J. Mater. Res.* **8**[10] (1993) 2668-2678

- <sup>303</sup> A. Chadwick, M. Pooley, K. Rammutla, S. Savin, and A. Rougier, "**A Comparison of the Extended X-ray Absorption Fine Structure of Nanocrystalline ZrO<sub>2</sub> Prepared by High-Energy Ball Milling and Other Methods**", *J. Phys.: Condens. Matter* **15** (2003) 431-440
- <sup>304</sup> A. Chadwick, and G. Rush, in "**Nanocrystalline Metals and Oxides: Selected Properties and Applications**", eds. P. Knauth and J. Schoonman, Ch. 5, (Kluwer, Boston, 2001)
- <sup>305</sup> J. Löffler, and J. Weissmüller, "**Grain-Boundary Atomic Structure in Nanocrystalline Palladium From X-Ray Atomic Distribution Function**", *Phys. Rev. B* **52**[10] (1995) 7076-7093
- <sup>306</sup> X. Zhu, R. Birringer, U. Her, and H. Gleiter, "**X-Ray Diffraction Studies of Nanometer-Sized Crystalline Materials**", *Phys. Rev. B* **35**[17] (1987) 9085-9090
- <sup>307</sup> T. Haubold, R. Birringer, B. Lengeler, and H. Gleiter, "**EXAFS Studies of Nanocrystalline Materials Exhibiting a New Solid State Structure with Randomly Arranged Atoms**", *Phys. Lett. A*, **135**[8-9] (1989) 461-466
- <sup>308</sup> G. Thomas, R. Siegel, and J. Eastman, "**Grain Boundaries in Nanophase Palladium: High Resolution Electron Microscopy and Image Simulation**", *Acta Metall. Mater.* **24** (1990) 201-206
- <sup>309</sup> J. Eastman, M. Fitzsimmons, M. Müller-Stach, G. Wallner, and W. Elam, "**Characterization of Nanocrystalline Pd by x-ray Diffraction and EXAFS**", *Nanostruct. Mater.* **1** (1992) 47-52.
- <sup>310</sup> E. Stern, R. Seigle, M. Newville, P. Sanders, and D. Haskell, "**Are Nanophase Grain Boundaries Anomalous?**", *Phys. Rev. Lett.*, **75**[21] (1995) 3874-3877.
- <sup>311</sup> S. de Panfilis, F. d'Acapito, V. Haas, H. Konrad, J. Weissmüller and F. Boscherini, "**Local Structure and Size Effects in Nanophase Palladium: An x-ray Absorption Study**", *Phys. Lett. A* **207** (1995) 397-403
- <sup>312</sup> S. Davis, A. Chadwick, and J. Wright, "**A Combined EXAFS and Diffraction Study of Pure and Doped Nanocrystalline Tin Oxide**", *J. Phys. Chem. B* **101**[48] (1997) 9901-9908
- <sup>313</sup> A. Chadwick, A. Harsch, N. Russel, K. Tse, A. Whitham, and A. Wilson, "**Nanocrystalline Copper Doped Zinc Oxide Gas Sensors**", *Radiat. Eff. Defects Solids* **137**[1-4] (1995) 1277-1281
- <sup>314</sup> G. Rush, A. Chadwick, I. Kosacki, and H. Anderson, "**An EXAFS Study of Nanocrystalline Thin Films**", *Radiat. Eff. Defects Solids* **156** (2001) 117-121
- <sup>315</sup> K. Funke, C. Cramer and B. Roling, "**Dynamics of Mobile Ions in Glass-What Do Conductivity Spectra Tell Us?**", *Glass. Sci. Technol.-Glastechnische Berichte* **73**[8] (2000) 244-254
- <sup>316</sup> F. Henn, J. Giuntini, and J. Zanchetta, "**AC Conductivity in Ionic Glasses: Analysis of Different Methods of Investigation**", *J. Non-Cryst. Solids* **131-133** (1991) 1084-1088
- <sup>317</sup> S. Summerfield, "**Universal Low-Frequency Behavior in the AC Hopping Conductivity of Disordered-Systems**", *Philos. Mag. B-Phys. Condens. Matter Stat. Mech. Electron. Opt. Magn. Prop.* **52** (1985) 9-22
- <sup>318</sup> J. Lee, J. Hwang, J. Mashek, T. Mason, A. Miller and R. Siegel, "**Impedance Spectroscopy of Grain Boundaries in Nanophase ZnO**", *J. Mater. Res.* **10**[9] (1995) 2295
- <sup>319</sup> M. Kleitz and J. Kennedy, "**Complex Plane Analysis of the Impedance and Admittance of Polycrystalline Sodium-Beta-Alumina Doped with Transition-Metal Ions**", in "**Fast Ion Transport in Solids: Electrodes and Electrolytes**", eds by P. Vashishta, J. Mundy and G. Shenoy, (North-Holland, Amsterdam, 1979) 185
- <sup>320</sup> P. Macedo, C. Moynihan, and R. Rose, "**Role of Ionic Diffusion in Polarization in Vitreous Ionic Conductors**", *Phys. Chem. Glasses* **13**[6] (1972) 171-179
- <sup>321</sup> D. Almond and A. WEST, "**Impedance and Modulus Spectroscopy of Real Dispersive Conductors**", *Solid State Ion* **11**[1] (1983) 57-64
- <sup>322</sup> C. Moynihan, L. Boesch, and N. Laberge, "**Decay Function for Electric Field Relaxation in Vitreous Ionic Conductors**", *Physics and Chemistry of Glasses* **14** (1973) 122-125
- <sup>323</sup> Ref. 322 and copy of the tables previously obtained on request from C. T. Moynihan
- <sup>324</sup> Y.-H Hwang, S. Kim, J. Kim, S. Kim, J. Oh, and M. Jang, "**A Study of Temperature Dependent  $\epsilon''(\omega)$  in Amorphous LiNbO<sub>3</sub> and KNbO<sub>3</sub>: Mode Coupling Theory Analysis**", *J. Kor. Phys. Soc.* **35** (1999) S1354-S1358
- <sup>325</sup> S. Kim, Y. Jang, H. Kim, N. Ryu, and M. Jang, "**Relaxation and Conduction of Amorphous LiNbO<sub>3</sub>**", *Ferroelectrics* **196** (1997) 261-264
- <sup>326</sup> S. Kim, S. Lee, Y. Yang, B. Chae, J. Kim, and M. Jang, "**Universal Behavior of Amorphous LiNbO<sub>3</sub>**", *J. Kor. Phys. Soc.* **30** (1997) 618-622

- <sup>327</sup> S. Lanfredi and A. Rodrigues, "*Impedance Spectroscopy Study of the Electrical Conductivity and Dielectric Constant of Polycrystalline LiNbO<sub>3</sub>*", *J. Appl. Phys.* **86**[4] (1999) 2215-2219.
- <sup>328</sup> A. Mansingh and A. Dhar, "*The AC Conductivity and Dielectric-Constant of Lithium Niobate Single Crystals*", *J. Phys. D: Appl. Phys.* **18**[10] (1985) 2059-2071
- <sup>329</sup> W. Bollmann and M. Gernand, "*Disorder of LiNbO<sub>3</sub> Crystals*", *Phys. Status Solidi A* **9**[1] (1972) 301
- <sup>330</sup> S. Kaul and K. Singh, "*Anomaly in Electrical-Resistivity of LiNbO<sub>3</sub> and its Eutectic with 3(Li<sub>2</sub>O)·Nb<sub>2</sub>O<sub>5</sub>*", *Solid State Commun.* **26** (1978) 365
- <sup>331</sup> G. Bergmann, "*Electrical Conductivity of LiNbO<sub>3</sub>*", *Solid State Commun.* **6**[2] (1968) 77
- <sup>332</sup> L. Kovacs, I. Fodvari and K. Polgar, "*Characterization of LiNbO<sub>3</sub> Crystals Resistant to Laser Damage*", *Acta Phys. Hung.* **61**[2] (1987) 223-226
- <sup>333</sup> Y. Limb, K. Cheng, and D. Smyth, "*Composition and Electrical-Properties in LiNbO<sub>3</sub>*", *Ferroelectrics* **38**[1-4] (1981) 813-816
- <sup>334</sup> A. Glass, K. Nassau and T. Negran, "*Ionic Conductivity of Quinched Alkali Niobate and Tantalate*", *J. Appl. Phys.* **49**[9] (1978) 4808
- <sup>335</sup> S. Kim, M. Jang, B. Chae and Y. Yang, "*A Study of Dielectric Properties of Amorphous Ferroelectric LiNbO<sub>3</sub>*", *J. Korean Phys. Soc.* **32** (1998) S807-S810
- <sup>336</sup> M. Lines, "*Microscopic Model for a Ferroelectric Glass*", *Phys. Rev. B* **15**[1] (1977) 388-395.
- <sup>337</sup> K. Varma, K. Hershavardhan, K. Rao, and C. Rao, "*Ferroelectric-Like Dielectric Anomaly in RF- Sputtered Amorphous LiNbO<sub>3</sub> Films*", *Mater. Res. Bull.* **20** (1980) 315-320
- <sup>338</sup> N. Sata, K. Eberman, K. Ebert, and J. Maier, "*Mesoscopic Fast Ionic Conduction in Nanometer-Scale Planar Heterostructure*", *Nature* **408** (2000) 946-949.
- <sup>339</sup> R. De Souza and R. Chater, *to be submitted to SSI.*
- <sup>340</sup> IUPAC ref. K. Rosman and P. Taylor, "*Isotope Compositions of the Elements 1997*", *Pure Appl. Chem.* **70**[1] (1998) 217-235
- <sup>341</sup> P. Fielitz and G. Borchardt, "*On the Accurate Measurement of Oxygen Self Diffusivities and Surface Exchange Coefficients in Oxides via SIMS Depth Profiling*", *Solid State Ionics* **144** (2001) 71
- <sup>342</sup> A. Mehta, E. Chang, and D. Smyth, "*Ionic Transport in LiNbO<sub>3</sub>*", *J. Mater. Res.* **6**[4] (1991) 851-854
- <sup>343</sup> P. Fielitz, G. Borchardt, M. Schmücker, H. Schneider, M. Wiedenbeck, D. Rhede, S. Weber, and S. Scherrer, "*Secondary Ion Mass Spectroscopy Study of Oxygen-18 Tracer Diffusion in 2/1-Mullite Single Crystals*", *J. Am. Ceram. Soc.* **84** [12] (2001) 2845
- <sup>344</sup> S. Abrahams, H. Levinstein, and J. Reddy, "*Ferroelectric Lithium Niobate. 5. Polycrystal X-Ray Diffraction Study Between 24° and 1200 °C*", *J. Phys. Chem. Solids* **27** (1966) 1019
- <sup>345</sup> D. Birnie, "*Review Analysis of Diffusion in Lithium Niobate*", *J. Mater. Sci.* **28** (1993) 302-315
- <sup>346</sup> F. Henn, J. Giuntini, and J. Zanchetta, "*AC Conductivity in Ionic Glasses: Analysis of Different Methods of Investigation*", *J. Non.-Cryst. Solids* **131-133** (1991) 108-1088
- <sup>347</sup> K. Sweeney and L. Halliburton, "*Oxygen Vacancies in Lithium-Niobate*", *Appl. Phys. Lett.* **43**[4] (1983) 336-338
- <sup>348</sup> B. Dischler, "*Correlation Of Photorefractive Sensitivity In Doped LiNbO<sub>3</sub> With Chemically-Induced Changes In Optical—Absorption Spectra*", *Solid State Commun.* **14**[11] (1974) 1233-1236
- <sup>349</sup> L. Radonjic, M. Todorovic, and J. Miladovic, "*Nanostructured Sodium Niobate Obtained by Glass Crystallization*", *Mater. Chem. Phys.* **88** (2004) 427-432
- <sup>350</sup> M. Layton and J. Smith, "*Pyroelectric Response in Transparent Ferroelectric Glass-Ceramics*", *J Am. Ceram. Soc.* **58** [9-10] (1975) 435-37
- <sup>351</sup> F. Liebau, "*Untersuchungen an Schichtsilikaten des Formeltyps A<sub>m</sub>(Si<sub>2</sub>O<sub>5</sub>)<sub>n</sub>. I. Die Kristallstruktur der Zimmertemperaturform des Li<sub>2</sub>Si<sub>2</sub>O<sub>5</sub>*", *Acta Cryst.* **14** (1961) 389-395
- <sup>352</sup> F. Liebau, "*Untersuchungen an Schichtsilikaten des Formeltyps A<sub>m</sub>(Si<sub>2</sub>O<sub>5</sub>)<sub>n</sub>. II. Über die Kristallstruktur des α-Na<sub>2</sub>Si<sub>2</sub>O<sub>5</sub>*", *Acta Cryst.* **14** (1961) 395-398



- <sup>353</sup> Y. Le Page and G. Donnay, *"Refinement of the Crystal Structure of Low-Quartz"*, *Acta Cryst. B* **32** (1976) 2456-2459
- <sup>354</sup> D. Peacor, *"High-Temperature Single-Crystal Study of the Cristobalite Inversion"*, *Z. Kristallogr.* **138** (1973) 274-298
- <sup>355</sup> M. Ohgaki, K. Tanaka, and F. Marumo, *"Structure Refinement of lithium (I) Niobium (V) Trioxide, with Anharmonic Thermal Vibration Model"*, *Mineral. J* **16** (1992) 150-160
- <sup>356</sup> S. Solov'ev, Zu. Venevtsev, and G. Zhdanov, *"An X-Ray Study of Phase Transitions in  $\text{NaNbO}_3$ "*, *Kristallografiya* **6** (1961) 218-224
- <sup>357</sup> A. Hewat, *"Neutron Powder Profile Refinement of Ferroelectric and Antiferroelectric Crystal Structures: Sodium Niobate at 22 °C"*, *Ferroelectrics* **7** (1974) 83-85
- <sup>358</sup> F. Wolf, D. Kline, and H. Story, *" $^{93}\text{Nb}$  and  $^{23}\text{Na}$  NMR in Polycrystalline Sodium Niobate"*, *J. Chem. Phys.* **53**[9] (1970) 3538-3543
- <sup>359</sup> J. Murdoch, J. Stebbins, and I. Carmichael, *"High resolution  $^{29}\text{Si}$  NMR Study of Silicate and Aluminosilicate Glasses: the Effect of Network-Modifying Cations"*, *Am. Mineral.* **70** (1985) 332-343
- <sup>360</sup> B. Sherriff, H. Grundy, and J. Hartman, *"The Relation Between  $^{29}\text{Si}$  MAS NMR Chemical Shift and Silicate Mineral Structure"*, *Eur. J. Mineral.* **3** (1991) 751-768
- <sup>361</sup> J. Smith, and C. Blackwell, *"Nuclear Magnetic Resonance of Silica Polymorphs"*, *Nature* **303** (1983) 223-225
- <sup>362</sup> M. Mägi, E. Lippmaa, A. Samosen, G. Engelhardt, and A. Grimmer, *"Solid-State High-Resolution Silicon-29 Chemical Shifts in Silicates"*, *J. Phys. Chem.* **88** (1984) 1518-1522
- <sup>363</sup> G. Huanxin, W. Zhongcai, and W. Shizhuo, *"Properties and Structure of Niobosilicate Glasses"*, *J. Non-Cryst. Solids* **112** (1989) 332-335
- <sup>364</sup> S. Nemilov, *"Thermodynamic and Kinetics Aspects of the Vitreous State"*, (CRC, Boca Raton, FL, 1995).
- <sup>365</sup> I. Gutzov and J. Schmelzer, *"The Vitreous State: Thermodynamics, Structure, Rheology and Crystallization"*, (Springer, Berlin, 1995).
- <sup>366</sup> C. Hermann, *Z. Kristallogr.* **69** (1929) 533-555
- <sup>367</sup> W. Borchardt-Ott, *"Crystallography"*, 2<sup>nd</sup> Ed., (Springer-Verlag, Berlin, 1995)
- <sup>368</sup> V. Shuvaeva, M. Yu., S. Linderman, O. Fesenko, V. Smotrakov, ? Yu., and T. Struchkov, *"X-Ray Diffraction Study of  $\text{NaNbO}_3$  Single Crystals in Electric Field"*, *Kristallografiya* **37** (1992) 1502-1507
- <sup>369</sup> P. Tarte, *"Physics of Non-Crystalline Solids: Proceedings"*, ed. J. Prins, (Northen Holland, Amsterdam, 1965), 549
- <sup>370</sup> T. Kokubo, M. Nishimura, and M. Tashiro, *"Glass Formation in Systems  $(\text{K or Cs})_2\text{O}-(\text{Nb or Ta})_2\text{O}_5-\text{Al}_2\text{O}_3$ "* *J. Non-Cryst. Solids*, **15**[2] (1974) 329-33
- <sup>371</sup> T. Kokubo, M. Nishimura, and M. Tashiro, *"Infrared Transmission of  $(\text{R}_2\text{O or R}'\text{O})-(\text{TiO}_2, \text{Nb}_2\text{O}_5 \text{ or } \text{Ta}_2\text{O}_5)-\text{Al}_2\text{O}_3$  Glasses"*, *J. Non-Cryst. Solids* **22**[1] (1976) 125-134
- <sup>372</sup> L. Hench, *"Characterization of Glass Corrosion and Durability"*, *J. Non-Cryst. Solids* **19** (1975) 27-39
- <sup>373</sup> M. Prassas, J. Phalippou, L. Hench, and J. Zarzycki, *"Preparation of  $x\text{Na}_2\text{O}-(1-x)\text{SiO}_2$  Gels for the Gel-Glass Process. I. Atmospheric Effect on the Structural Evolution of the Gels"*, *J. Non-Cryst. Solids* **48** (1982) 79-95
- <sup>374</sup> E. Lippincott, A. Van Valkenburg, C. Weir, and E. Bunting, *"Infrared Studies on Polymorphs of Silicon Dioxide and Germanium Dioxide"*, *J. Res. Nat. Bur. Stand.* **61** (1958) 61-70
- <sup>375</sup> B. Samuneva, Y. Dimitreiv, I. Ivanova, V. Dimitrov, E. Kashchieva, and P. Djambazki, in Proc. 15<sup>th</sup> Int. Congress on Glass, vol. 2a p. 26 Leningrad 1989
- <sup>376</sup> R. Hanna, *"Infrared Absorption Spectrum of Silicon Dioxide"*, *J. Am. Ceram. Soc.* **48** (1965) 595
- <sup>377</sup> P. Sarjeant and R. Roy, *"New Glassy and Plymorrhpic Oxide Phases Using Rapid Quenching Techniques"*, *J. Am. Ceram. Soc.* **50**[10] (1967) 500
- <sup>378</sup> P. Sarjeant and R. Roy, *"Experimental Data on Formation of New Non-Crystalline Solids (NCS) Phases"*, in *"The Reactivity of Solids: Proceedings of the 6<sup>th</sup> International Symposium on the Reactivity of Solids"*, Eds J. Mitchell, R. DeVries, R. Roberts, and P. Cannon (Wiley, New York, 1969) 725-732.

## References

- 379 P. McMillan, "**Structural Studies of Silicate-Glasses and Melts-Applications and Limitations of Raman Spectroscopy**", *Amer. Mineral.* **69**[7-8] (1984) 622-644
- 380 K. Fukumi and S. Sakka, "**Coordination State of Nb<sup>5+</sup> Ions in Silicate and Galate Glasses as Studied by Raman-Spectroscopy**", *J. Mater. Sci.* **23**[8] (1988) 2819-2823
- 381 J. Scott, "**Temperature Study of the Polarized Raman Spectra of Strontium Barium Niobate**", *J. Appl. Phys.* **44**[11], (1973) 5192-5193.
- 382 K. Fukumi and S. Sakka, "**Structure of Alkali or Alkaline Earth Niobium Gallate Glasses**", *J. Non-Cryst. Solids* **110** (1989) 61-68
- 383 E. Husson, and Y. Repelin, "**Vibrational Spectroscopy of Sodium and Silver Niobates of Perovskite Structure**", *Spectroc. Acta Pt. A-Molec. Biomolec. Spectr.* **40 A** (1984) 315-321
- 384 V. Kolobkova, E. Kolobkova, I. Morozova, and A. Chikovskii, "**Spectroscopic Investigation of Niobium Silicate Glasses**", *Fiz. Khim. Stekla*, **12**[3] (1986) 352-358
- 385 E. Husson, Y. Rerelin, N. Dao, and H. Brusset, "**Normal Coordinate Analysis of MNb<sub>2</sub>O<sub>6</sub> Series of Columbite Structure (M = Mg, Ca, Mn, Fe, Co, Ni, Cu, Zn, Cd)**", *J. Chem. Phys.* **67** (1977) 1157-1163
- 386 L. Randonjic, M. Todorovic, and J. Miladinovic, "**Nanostructured Sodium Niobate Obtained by Glass Crystallization**", *Mater. Chem. Phys.* **88** (2004) 427-432
- 387 W. Weyl and E. Marboe, "**The Constitution of Glasses**", Vol. II, Part 1 (Interscience, New York, 1964) 512.
- 388 E. Levin, "**Structural Interpretation of Immiscibility in Oxide Systems .4. Occurrence Extent and Temperature of Monotectic**", *J. Am. Ceram. Soc.* **50** (1967) 29
- 389 Y. Hu and C. Huang, "**Crystallization Kinetics of LiNbO<sub>3</sub>-SiO<sub>2</sub>-Al<sub>2</sub>O<sub>3</sub> glass**", *J. Non-Crystal. Solids* **278** (2000) 170-177
- 390 J. Hsu and R. Speyer, "**Crystallization of Li<sub>2</sub>O-Al<sub>2</sub>O<sub>3</sub>-6SiO<sub>2</sub> Glasses Containing Niobium Pentoxide as Nucleating Dopant**", *J. Am. Ceram. Soc.* **74**[2] (1991) 395-399
- 391 H. Kim, T. Komatsu, R. Sato, and K. Matusita, "**Crystallization of LiNbO<sub>3</sub> in Tellurite glasses**", *J. Non-Crystal. Solids* **162** (1993) 201-204
- 392 T. Komatsu, H. Tawarayama, H. Mohri, and K. Matusita, "**Properties and Crystallization Behavior of TeO<sub>2</sub>-LiNbO<sub>3</sub> Glasses**", *J. Non-Crystal. Solids* **135** (1991) 105-113
- 393 H. Kim and T. Komatso, "**Fabrication and Properties of Transparent Glass-Ceramic in Na<sub>2</sub>O-Nb<sub>2</sub>O<sub>5</sub>-TeO<sub>2</sub> System**", *J. Mater. Sci. Lett.* **17** (1998) 1149-1151
- 394 G. Maciel, N. Rakov, C. Araujo, A. Lipovskii, and D. Tagantsev, "**Optical Limiting Behavior of Glass-Ceramic Containing Sodium Niobate Crystallites**", *Appl. Phys. Lett.* **79**[5] (2001) 584-586
- 395 D. Vemacotola, "**Glasses and Glass-Ceramics in the Potassium Niobium Silicate System**", *M.Sc. Thesis*, Alfred University, Alfred, New York 1993
- 396 D. Vemacotola and J. Shelby, "**Ceramic Transactions: Conference on Advances in the Fusion and Processing of Glass**", **29** (1993) 215
- 397 Bh. Rao, "**Dual Role of Niobium in System K<sub>2</sub>O-SiO<sub>2</sub>-Nb<sub>2</sub>O<sub>5</sub> and its Relation to Structure of Glass**", *J. Sci. Industr. Res. B* **21** (1962) 108
- 398 D. Vemacotola and J. Shelby, "**Potassium Niobium Silicate Glasses**", *Phys. Chem. Glasses* **35**[4] (1994) 153-159
- 399 W. Zhongcai, S. Bingkai, and W. Shizhuo, "**Investigation of the Network Structure of Niobium Borate Glasses**", *J. Non-Cryst. Solids* **80** (1986) 160
- 400 T. Kokubo, Y. Inaka, and S. Sakka, "**Formation and Optical Properties of (R<sub>2</sub>O or R'O)-Nb<sub>2</sub>O<sub>5</sub>-Ga<sub>2</sub>O<sub>3</sub> Glasses**", *J. Non-Cryst. Solids* **81**[3] (1986) 337-350
- 401 K. Fukumi, S. Sakka and T. Kokubo, "**Properties and Structure of Cs<sub>2</sub>O-Nb<sub>2</sub>O<sub>5</sub>-Al<sub>2</sub>O<sub>3</sub> Glasses**", *J. Non-Cryst. Solids* **93**[1] (1987) 190-202
- 402 G. Blasse, "**Vibrational Spectra of Yttrium Niobate and Tantalate**", *J. Solid State Chem.* **7**[2] (1973) 169-171
- 403 E. Kolobkova, "**Raman Investigation of the Structure of Niobium Germanate Glasses**", *Fiz. Khim. Stekla*, **13**[3] (1987) 352-358

- 
- <sup>404</sup> S. Karpov and E. Kolobkova, "**Raman Spectra and Structure of Niobium Phosphate Glasses**", *Fiz. Khim. Stekla* **17**[3] (1991) 425-435
- <sup>405</sup> E. Kolobkova, "**Coordination State Niobium and its Structural Role in Lanthanoborate Glasses According to Data of Vibration Spectroscopy**", *Fiz. Khim. Stekla* **14** (1988) 490-493
- <sup>406</sup> T. Sidorov, "**IR and Raman Spectra in Relation to the Structure of Glasses in the System  $\text{Na}_2\text{O-Nb}_2\text{O}_5\text{-SiO}_2$** ", *J. Appl. Spect.* (1970) 1124
- <sup>407</sup> N. M. Kokubo et al., *J. Non-Cryst. Solids*, **90** (1987) 612
- <sup>408</sup> W. Weyl and E. Marboe, "**Conditions of Glass Formations Among Simple Compounds Part III**", *Glass Ind.* **41**[12] (1960) 687-715
- <sup>409</sup> D. Vemacotola and J. Shelby, "**Ceramic Transactions: Conference on Advances in the Fusion and Processing of Glass**", **29** (1993) 215
- <sup>410</sup> C. Hirayama and D. Berg, "**Dielectric Properties of Glasses in the System  $\text{Nb}_2\text{O}_5\text{-Na}_2\text{O-SiO}_2$** ", *J. Am. Ceram. Soc.*, **46**[2] (1963) 85-88.
- <sup>411</sup> S. Ito, T. Kokubo, and M. Tashiro, "**Transparency of  $\text{LiTaO}_3\text{-SiO}_2\text{-Al}_2\text{O}_3$  Glass-Ceramics in Relation to their Microstructure**", *J. Mater. Sci.* **13**[5] (1978) 930-938
- <sup>412</sup> H. C. Zeng, K. Tanaka, K. Hirano, and N. Soga, "**Crystallization and Glass Formation in  $50\text{Li}_2\text{O-50Nb}_2\text{O}_5$  and  $25\text{Li}_2\text{O-25Nb}_2\text{O}_5\text{-50SiO}_2$** ", *J. Non-Cryst. Solids* **209** (1997) 112-121
- <sup>413</sup> C. Shaw and J. Shelby, "**Barium Gallosilicate Glasses I. Transformation Range Behavior**", *Phys. Chem. Glasses* **31**[5] (1990) 199
- <sup>414</sup> J. Shelby, "**Formation and Properties of Calcium Aluminosilicate Glasses**", *J. Am. Ceram. Soc.* **68**[3] (1985) 155
- <sup>415</sup> M. Garca, M. Silva, and M. Valente "**Electrical Properties of Lithium Niobosilicate Gel Derived Glass and Glass-Ceramics**", *Key Eng. Mat.* **230-232** (2002) 161-164
- <sup>416</sup> M. Todorovic and L. Radonjic, "**Lithium-Niobate Ferroelectric Material Obtained by Glass Crystallization**", *Ceram. Int.* **23** (1997) 55-60
- <sup>417</sup> D. Day, "**Mixed Alkali Glasses-Their Properties and Uses**", *J. Non-Cryst. Solids* **21**[3] (1976) 343-372
- <sup>418</sup> A. Bunde, M. Ingram, and P. Maass, "**The Dynamic Structure Model for Ion-Transport in Glasses**", *J. Non-Cryst. Solids* **72**[2] (1994) 1222-1236
- <sup>419</sup> P. Maass, A. Bunde, and M. Ingram, "**Ion Transport Anomalies in Glasses**", *Phys. Rev. Lett.* **68**[20] (1992) 3064-3067
- <sup>420</sup> G. Greaves, S. Gurman, C. Catlow, A. Chadwick, S. Houde-Walter, C. Henderson, and B. Dobson, "**A Structural Basis For Ionic-Diffusion In Oxide Glasses**", *Philos. Mag. A* **64**[5] (1991) 1059-1072
- <sup>421</sup> C. Hunter and M. Ingram, " **$\text{Na}^+$  Conducting Glasses**", *Solid state Ionics* **14**[1] (1984) 31-40
- <sup>422</sup> A. Pradel and M. Ribes, "**Ion-Transport in Superionic Conducting Glasses**", *J. Non-Cryst. Solids* **172**[2] (1994) 1315-1323
- <sup>423</sup> A. Hunt, "**Non-Debye Relaxation and the Glass-Transition**", *J. Non-Cryst. Solids* **160**[3] (1993) R183-227
- <sup>424</sup> V. Ambegaokar, B. Halperin, and J. Langer, "**Hopping Conductivity in Disordered Systems**", *Phys. Rev. B* **4**[8] (1971) 2612-2620
- <sup>425</sup> A. Hunt, "**An Explanation for the Kauzmann Paradox And Its Relation To Relaxation-Times**", *J. Non-Cryst. Solids* **175**[2-3] (1994) 129-136
- <sup>426</sup> A. Hunt, "**Mixed-alkali Effect: Some new Results**", *J. Non-Cryst. Solids* **255**[1] (1999) 47-55
- <sup>427</sup> W. Zdaniewski, G. Rindone and D. Day, "**The Internal Friction of Glasses**", *J. Mater. Sci.* **14**[4] (1979) 763
- <sup>428</sup> B. Roling and M. Ingram, "**Determination of Divalent Cation Mobilities in Glass by Dynamic Mechanical Thermal Analysis (DMTA): Evidence for Cation Coupling Effects**", *Solid State Ionics* **105**[1] (1998) 47-53
- <sup>429</sup> P. Green, D. Sidebottom, R. Brow and J. Hudgens, "**Mechanical Relaxation Anomalies in Mixed Alkali Oxides**", *J. Non-Cryst. Solids* **231**[1] (1998) 89-98

## List of Figures

Figure	page
1.1.1	1
2.1.1	9
2.1.2	10
2.1.3	11
2.3.1	15
2.3.2	16
2.3.3	20
3.1.1	23
3.1.2	24
3.1.3	24
3.1.4	25
3.2.1	25
3.4.1	28
3.4.2	28
3.5.1	29
4.1.1	36
4.1.2	38
4.1.3	39
4.1.4	39
4.1.5	41
4.1.6	43
4.1.7	43

List of Figures

---

Figure		page
4.1.8	The basic principle of capacitance bridges .....	44
4.1.9	Basic principle of the manual bridge .....	45
4.1.10	The distributed capacitance, resistance, and inductance in a coaxial cable .....	45
4.1.11	The four-terminal configuration of an impedance cell .....	46
4.1.12	The sample inside a Faraday cage .....	47
4.1.13	Principle of the virtual ground "shielding" .....	47
4.1.14	Schematic TD response $f(t)$ of two types of dielectric materials one dominated by dipoles and the other by hopping charge carriers .....	48
4.1.15	The real and imaginary components of the complex dielectric susceptibility for the Debye process .....	49
4.1.16	(a) A near-Debye response showing the characteristic deviation from the Debye shape. (b) The generalized form of a non-Debye loss peak with the rising and falling branches following power laws with exponents $m$ and $1 - n$ , respectively .....	49
4.1.17	The dielectric behavior of a material in which slowly mobile charge carriers such as ions or hopping electrons dominate the dielectric response .....	50
4.1.18	The frequency dependence of electrical conductivity $\sigma(\omega) = \epsilon_0 \omega \chi''(\omega)$ for the same conditions as those shown for the susceptibility in Fig. 4.1.17 .....	52
4.2.1	A general schematic layout of the main components in the NMR experiment .....	53
4.2.2	Zeeman splitting of the nuclear energy level due to interaction of the nuclear spins with a static external field $B_0$ .....	55
4.2.3	The effect of the perpendicular $B_1$ field on the magnetization vector in the rotating frame .....	57
4.2.4	The obtained FID's for when the reference frequency and the precession frequency of the nuclei are: (a) "on resonance", (b) "off resonance" .....	57
4.2.5	The internuclear vector at an angle $\beta$ to the static field is rotated about the magic angle $\theta_m$ by spinning of the rotor to give an average orientation similar as the magic angle .....	59
4.2.6	The dependence of the static NMR lineshape on the symmetry and orientation of the molecular segment relative to the applied field and the stimulated static and MAS lineshapes .....	60
4.2.7	Lorentzian spectral density functions for three different temperatures .....	62
4.2.8	Schematic plot demonstrating the characteristic temperature and frequency dependence of the diffusion induced SLR rate ( $1/T_1$ ) for 3D systems at three different Larmor frequencies $\omega_0$ .....	63
4.2.9	Schematic representation of log (SLR rate) vs. log (correlation time) (corresponding to reciprocal temperature) for diffusion in the BPP case and the expected deviations for 2D systems and disordered systems .....	64
4.2.10	Schematic representation of log (SLR rate) vs. log (Larmor frequency) (or magnetic field) for the BPP case and the expected deviations for 2D systems and disordered systems .....	64
4.2.11	Illustration for the recovery of the magnetization as a function of the delay time ( $\tau$ ). It shows the exponential recovery to the maximum magnetization $M_0$ at three different stages .....	65
4.2.12	$^{29}\text{Si}$ chemical shift (ppm) with respect to TMS for various possible silicate structural configurations $Q^n$ .....	69

List of Figures

---

Figure	page
4.3.1	71
4.3.2	71
4.3.3	72
4.3.4	75
4.3.5	77
4.4.1	81
4.4.2	83
4.4.3	85
4.4.4	86
4.4.5	87
4.4.6	88
4.4.7	88
4.4.8	88
5.1.1	94
5.1.2	95
5.1.3	97
5.1.4	98
5.1.5	99
5.1.6	100
5.1.7	101
5.1.8	101
5.3.1	103
6.1.1	106
6.1.2	106
6.2.1	108

List of Figures

---

Figure		page
6.2.2	NMR samples; sealed quartz ampoule, and 4-mm diameter cylindrical zirconia tube with its plastic turbine-shaped rotor cap .....	109
6.2.3	A schematic electronic diagram for the LRC circuit used in the home-built NMR probe .....	109
6.2.4	(a) Top of MAS probe after being disassembled, (b) Bottom of the MAS probe showing the knob used to match the resonance circuit to the 50 $\Omega$ cable coming from the spectrometer and the knob for tuning the correct frequency for the sample nucleus capacitors .....	110
6.5.1	JEOL JEM-2100F-UHR TEM microscope .....	119
6.5.2	Field-Emission SEM JEOL JSM-6700F .....	119
6.5.3	IFS 66v/S Vacuum FT-IR spectrometer and Bruker RFS100/S Raman spectrometer .....	120
7.1.1	$^7\text{Li}$ NMR spectra for amorphous, 16 h HEBM nanocrystalline (23 nm), sol-gel prepared nanocrystalline (27 nm), and microcrystalline $\text{LiNbO}_3$ measured at 77.7 MHz .....	125
7.1.2	$^7\text{Li}$ NMR narrow line relative contribution to the total area under the whole line. For nanocrystalline samples of comparable grain sizes, one prepared by sol-gel (27 nm) and the other by HEBM (23 nm) .....	125
7.1.3	Illustration of the effect of the introduction of crystal imperfections on the intensities of the quadrupole satellites in static $^7\text{Li}$ NMR lines measured at 155.5 MHz going from the single crystal and microcrystalline through the nanocrystalline HEBM for different periods ending with the amorphous $\text{LiNbO}_3$ .....	126
7.1.4	$^{93}\text{Nb}$ MAS-MNR spectra measured at Larmor frequency 97.98 MHz with spinning rate 12.5 kHz for single-crystal powder, microcrystalline, nanocrystalline HEBM .....	130
7.1.5	Second-order powder pattern neglecting the effects of dipolar broadening .....	131
7.1.6	(a) Nb K-edge EXAFS for microcrystalline $\text{LiNbO}_3$ obtained in transmission mode and their FTs .....	133
7.1.7	The temperature dependence of the Debye-Waller factors for microcrystalline $\text{LiNbO}_3$ . Comparison between experimental data (points) and calculated results (lines) for the niobium-oxygen and niobium-niobium shells .....	135
7.1.8	Niobium K-edge measured at 80 K for: the microcrystalline, ball milled nanocrystalline, and sol-gel prepared amorphous $\text{LiNbO}_3$ : EXAFS spectra (a), and their FT's (b) .....	136
7.1.9	Nb K-edge XAFS of nanocrystalline $\text{LiNbO}_3$ , with the fit obtained by a linear combination of the EXAFS curves for the microcrystalline and the amorphous measured at the same temperatures .....	137
7.1.10	Niobium K-edge (a) EXAFS for nanocrystalline $\text{LiNbO}_3$ at 140 K, and (b) their FTs. Fitted using the multiple cluster model with the indicated different mixing coefficients .....	138
7.1.11	The change in $R_{\text{EXAFS}}$ (%) for the multiple clusters fitting with changing ratio of amorphous and microcrystalline clusters .....	139
7.1.12	The TEM image of nanocrystalline $\text{LiNbO}_3$ prepared by: (a) HEBM for 32 h (average crystallite size 23 nm) and (b) heating the double alkoxide sol-gel amorphous sample for 1 h at 773 K (average grain size 27 nm) .....	140
7.2.1	Conductivity log-log spectra for amorphous $\text{LiNbO}_3$ for temperatures from 313 to 454 K measured under oxygen atmosphere in the frequency range from 5 Hz to 13 MHz .....	143

List of Figures

Figure		page
7.2.2	Conductivity master curves obtained by normalizing the $y$ -axis over $\sigma_{dc}$ and the $x$ -axis over the product ( $\sigma_{dc} \cdot T$ ) for different LiNbO <sub>3</sub> samples .....	144
7.2.3	Temperature dependence of $\sigma_{dc}$ for the different forms of LiNbO <sub>3</sub> .....	145
7.2.4	Complex plane representation of resistivity data measured at 370 K for different forms of LiNbO <sub>3</sub> and their fits obtained using the Equivalent Circuit program .....	146
7.2.5	(a) Real and (b) imaginary parts of the electric modulus for nanocrystalline LiNbO <sub>3</sub> HEBM for 64 h at temperatures from 313 to 453 K, (c) shows the positioning of the $M''$ peak at around the center of the dispersion region of $M'$ (markers are the measured points while the solid lines are the fits with the KWW stretched function) .....	147
7.2.6	Temperature dependence of relaxation time of the electric modulus, $\tau_p$ , for microcrystalline, nanocrystalline and amorphous LiNbO <sub>3</sub> .....	148
7.2.7	The frequency dependence of $\varepsilon'$ for amorphous LiNbO <sub>3</sub> for different temperatures between 313 K and 453 K from 5 to 10 <sup>7</sup> Hz, the inset shows the re-scaled area from 10 <sup>2</sup> to 10 <sup>7</sup> Hz .....	149
7.2.8	Temperature dependence of the real part of the dielectric constant measured at different arbitrary frequencies and the dielectric constant calculated at the relaxation frequency .....	150
7.2.9	Dielectric constants, calculated at the relaxation frequencies for microcrystalline, nanocrystalline and amorphous LiNbO <sub>3</sub> .....	151
7.2.10	Temperature dependence of $\sigma_{dc}$ for microcrystalline, nanocrystalline LiNbO <sub>3</sub> . A comparison between pure samples with the impure samples .....	151
7.2.11	Temperature dependence of $\sigma_{dc}$ for, microcrystalline, nanocrystalline, and amorphous LiNbO <sub>3</sub> ; a comparison between the conductivities measured under O <sub>2</sub> and He atmosphere .....	152
7.2.12	The complex plane plot of impedance data for partially (1/3) hydrolyzed LiNbO <sub>3</sub> at 413 and 433 K with the theoretical fits obtained using the Equivalent Circuit program and the individual contribution of the sub-circuits ( $R_1Q_1$ ) and ( $R_2Q_2$ ) .....	153
7.2.13	Comparison between the temperature dependence of $\sigma_{dc}$ for the sol-gel prepared amorphous LiNbO <sub>3</sub> fully and partially hydrolyzed .....	154
7.2.14	(a) Temperature dependence of $\sigma_{dc}$ for the chemically prepared (sol-gel) LiNbO <sub>3</sub> heat treated at different temperatures and times (b) Comparison with the commercial microcrystalline (Alfa) and nanocrystalline HEBM for 16 h .....	155
7.2.15	Temperature dependence of the <sup>7</sup> Li spin-lattice relaxation rates ( $1/T_1$ ) for amorphous, nanocrystalline and microcrystalline LiNbO <sub>3</sub> measured at $\omega_0/2\pi = 77.7$ MHz .....	159
7.2.16	The temperature dependence of the <sup>7</sup> Li NMR SLR rates ( $1/T_1$ ) measured at $\omega_0/2\pi = 77.7$ MHz for the microcrystalline and the HEBM nanocrystalline LiNbO <sub>3</sub> showing the impurity effect ..	160
7.2.17	The temperature dependence of the <sup>7</sup> Li NMR SLR rates ( $1/T_1$ ) measured at $\omega_0/2\pi = 77.7$ MHz for the microcrystalline and the HEBM nanocrystalline LiNbO <sub>3</sub> showing the preparation route effect on the amorphous LiNbO <sub>3</sub> prepared by double alkoxide sol-gel with partial and full hydrolysis and on the nanocrystalline form prepared by HEBM and chemically by sol-gel .....	160
7.2.18	The temperature dependence of the full width at half maximum (fwhm) of the <sup>7</sup> Li central transition NMR-line for the amorphous, the nanocrystalline (16 h HEBM), and the microcrystalline LiNbO <sub>3</sub> sample .....	164
7.2.19	The temperature dependence of the full width at half maximum (fwhm) of the central transition <sup>7</sup> Li-NMR line for the amorphous LiNbO <sub>3</sub> prepared by the double alkoxide sol-gel method with one of them fully hydrolyzed and the other partially (1/3) hydrolyzed .....	165



List of Figures

Figure		page
7.2.20	The temperature dependence of the full width at half maximum (fwhm) of the $^7\text{Li}$ central transition for nanocrystalline $\text{LiNbO}_3$ prepared by HEBM for 16 h, and double alkoxide sol-gel fully hydrolyzed and heated for 1 h at 773 K .....	166
7.2.21	SIMS depth profiles of the relative $^{18}\text{O}$ concentration measured in $\text{LiNbO}_3$ single crystal after diffusion annealing in $^{18}\text{O}_2$ gas atmosphere (200 mbar) at 973, 1073, and 1188 K for 184200, 23700, and 4200 s, respectively, with diffusion direction parallel and perpendicular to the $c$ -axis .....	169
7.2.22	Oxygen diffusion coefficients ( $D$ ) and oxygen exchange coefficients ( $K$ ) measured in single crystal $\text{LiNbO}_3$ , with the filled markers representing the diffusion $\parallel$ the optical $c$ -axis while the open markers are used for the diffusion $\perp$ the optical $c$ -axis .....	171
7.2.23	Oxygen diffusion coefficients, $D$ , measured here by SIMS in single crystalline $\text{LiNbO}_3$ , a comparison with literature .....	172
8.1.1	Ex-situ XRD patterns for the composite $n\text{-LiNbO}_3\cdot g\text{-NaSi}_{1.5}\text{O}_{3.5}$ after 2 h of heating at 873, 973, 1073, 1173, 1273 K .....	178
8.1.2	The molar % of crystalline phases in the composite $n\text{-LiNbO}_3\cdot\text{NaSi}_{1.5}\text{O}_{3.5}$ showing the effect of heating for 2 h at temperatures ranging from 873 to 1273 K for $\text{LiNbO}_3$ , $\text{NaNbO}_3$ , quartz low, cristobalite low and $(\text{Li,Na})_2\text{Si}_2\text{O}_5$ .....	179
8.1.3	In-situ x-ray for the composite $n\text{-LiNbO}_3\cdot g\text{-NaSi}_{1.5}\text{O}_{3.5}$ showing the transformation of $\text{LiNbO}_3$ to $\text{NaNbO}_3$ with heating up .....	181
8.1.4	Raman spectra showing the heating effect (2 h) on the composite $n\text{-LiNbO}_3\cdot\text{NaSi}_{1.5}\text{O}_{3.5}$ at 873, 973, 1073, 1173, 1273 K .....	182
8.1.5	(a) $^{29}\text{Si}$ NMR lines for the composite $n\text{-LiNbO}_3\cdot g\text{-NaSi}_{1.5}\text{O}_{3.5}$ heated for 2 h at the indicated temperatures. (b) Abundance, (c) FWHM, (d) chemical shift values of $Q^n$ 's. (e) The percentage of the non-bonding oxygens to the total number of oxygen around $^{29}\text{Si}$ .....	183
8.1.6	(a) $^{93}\text{Nb}$ NMR lines for the $n\text{-LiNbO}_3\cdot g\text{-NaSi}_{1.5}\text{O}_{3.5}$ composite after heating for 2 h at the indicated temperatures measured at 97.8 MHz and fitted using the $^{93}\text{Nb}$ NMR lines of commercial $\text{LiNbO}_3$ and $\text{NaNbO}_3$ as standards and the relative contribution of $\text{LiNbO}_3$ and $\text{NaNbO}_3$ , respectively .....	184
8.1.7	The relative percentage of $\text{LiNbO}_3$ and $\text{NaNbO}_3$ obtained from Nb NMR fit in comparison with those obtained from Rietveld refinement of the XRD data .....	185
8.1.8	$^{23}\text{Na}$ MAS-NMR lines for the $n\text{-LiNbO}_3\cdot g\text{-NaSi}_{1.5}\text{O}_{3.5}$ measured at room temperature and 105.8 MHz after being heated for 2 h at the indicated temperatures at a spinning rate of 12.5 kHz .....	185
8.1.9	(a) Arrhenius plots for the $n\text{-LiNbO}_3\cdot g\text{-Na}_2\text{Si}_3\text{O}_7$ composites heated for 2 h at 873, 973, 1073, 1173, 1273 K, and for the as-mixed composite. The lines represent the best Arrhenius fit. (b) Variation in the dc-conductivity and its activation energy with changing treatment temperature .....	186
8.2.1	Ex-situ XRD pattern for the composite $(x)n\text{-LiNbO}_3\cdot(1-x)g\text{-NaSi}_{1.5}\text{O}_{3.5}$ after heating for 2 h at 1173 K with $x$ : 0.0, 0.2, 0.4, 0.6, 0.8, 1.0 .....	188
8.2.2	Mole % of $\text{LiNbO}_3$ , $\text{NaNbO}_3$ in the crystalline phase obtained after heat treatment for 2 h at 1173 K in the composite $(x)n\text{-LiNbO}_3\cdot(1-x)g\text{-NaSi}_{1.5}\text{O}_{3.5}$ , showing the effect of varying the starting compositions, $x$ .....	189

List of Figures

Figure		page
8.2.3	Raman spectra for the composite $(x)\text{n-LiNbO}_3 \cdot (1-x)\text{g-NaSi}_{1.5}\text{O}_{3.5}$ showing the composition effect on samples heated at 1173 K for 2 h .....	189
8.2.4	(a) Simulated $^{29}\text{Si}$ MAS NMR spectra of the composite $(x)\text{n-LiNbO}_3 \cdot (1-x)\text{NaSi}_{1.5}\text{O}_{3.5}$ with $x = 0$ (glass), 0.20, 0.50, 0.80 after heating for 2 h at 1173 K. (b) $Q^n$ abundance, (c) fwhm, (d) chemical shift values $\delta$ , and (e) the percentage of the NBO to the total number of oxygen atoms around the $^{29}\text{Si}$ atom .....	190
8.2.5	(a) $^{93}\text{Nb}$ (b) $^{23}\text{Na}$ MAS-NMR lines for the composite $(x)\text{n-LiNbO}_3 \cdot (1-x)\text{g-NaSi}_{1.5}\text{O}_{3.5}$ with $x = 0.2, 0.5, 0.8$ after heating for 2 h at 1173 K, with a spinning frequency of 12.5 kHz .....	191
8.2.6	(a) Arrhenius plot for the $(x)\text{n-LiNbO}_3 \cdot (1-x)\text{g-Na}_2\text{Si}_3\text{O}_7$ composite heated for 2 h at 1173 K for $x$ ranging from 0.0 to 0.9. The lines represent the best linear fit. (b) The variation in the activation energy and the dc-conductivity with changing the composite composition at three chosen temperatures 573, 623, 673 K .....	192
8.3.1	The crystallographic point groups and their subgroups, after Hermann. The figure shows two symmetry pathways from $\text{LiNbO}_3$ to $\text{NaNbO}_3$ (direct and indirect) .....	195
9.1.1	(a) XRD pattern for glasses $0.33[x\text{Li}_2\text{O} \cdot (1-x)\text{Na}_2\text{O}] \cdot 0.33\text{Nb}_2\text{O}_5 \cdot 0.33\text{SiO}_2$ , with $0 \leq x \leq 1$ , showing only the FSDPs and the change in their positions and widths vs. $x$ value .....	200
9.1.2	Infrared spectra for the glasses $0.33[x\text{Li}_2\text{O} \cdot (1-x)\text{Na}_2\text{O}] \cdot 0.33\text{Nb}_2\text{O}_5 \cdot 0.33\text{SiO}_2$ .....	200
9.1.3	(a) Raman spectra for the glasses $0.33[x\text{Li}_2\text{O} \cdot (1-x)\text{Na}_2\text{O}] \cdot 0.33\text{Nb}_2\text{O}_5 \cdot 0.33\text{SiO}_2$ , with $0 \leq x \leq 1.00$ ; (b) the ratio between the heights of the Raman at 875 and 815 $\text{cm}^{-1}$ vs. $x$ .....	201
9.1.4	$^7\text{Li}$ , (b) $^{93}\text{Nb}$ , and (c) $^{23}\text{Na}$ MAS-NMR for $0.33[x\text{Li}_2\text{O} \cdot (1-x)\text{Na}_2\text{O}] \cdot 0.33\text{Nb}_2\text{O}_5 \cdot 0.33\text{SiO}_2$ glasses with $x = 1.00$ , $x = 0.50$ , and $x = 0.0$ measured at room temperature with a spinning frequency of 12.5 kHz, at the indicated resonance frequencies .....	202
9.1.5	(a) $^{29}\text{Si}$ MAS-NMR for $0.33[x\text{Li}_2\text{O} \cdot (1-x)\text{Na}_2\text{O}] \cdot 0.33\text{Nb}_2\text{O}_5 \cdot 0.33\text{SiO}_2$ glasses with $x = 0$ , $x = 0.5$ , $x = 1$ . The effect of changing $x$ is shown on: the relative abundances of the Q species (b), their widths (c), their positions (d), and the percentage of the NBOs to the total number of oxygen surrounding the silicon atoms .....	203
9.1.6	Raman spectra of: (a) $x\text{Li}_2\text{O} \cdot (1-x)/3[\text{Nb}_2\text{O}_5 \cdot 2\text{SiO}_2]$ glasses for various $\text{Li}_2\text{O}$ concentration, $x$ ( $x = 0.35, 0.40, 0.45$ ) and (b) $(1-y)/2[\text{Li}_2\text{O} \cdot \text{SiO}_2] \cdot y\text{Nb}_2\text{O}_5$ glasses for various $\text{Nb}_2\text{O}_5$ concentration, $y$ , ( $y = 0.10, 0.20, 0.33$ ) .....	205
9.1.7	$^{29}\text{Si}$ MAS-NMR spectra for $x\text{Li}_2\text{O} \cdot (1-x)/3[\text{Nb}_2\text{O}_5 \cdot 2\text{SiO}_2]$ glasses with $x = 0.35, 0.40, 0.45$ . The effect of changing the $\text{Li}_2\text{O}$ concentration, $x$ , is shown on: the relative abundances of the Q species (b), their widths (c), their positions (d), and the percentage of the NBOs to the total number of oxygen surrounding the Si atoms .....	207
9.1.8	$^{29}\text{Si}$ MAS-NMR for $(1-y)/2[\text{Li}_2\text{O} \cdot \text{SiO}_2] \cdot y\text{Nb}_2\text{O}_5$ glasses with $y = 0.10, 0.20, 0.33$ . The effect of changing the $\text{Nb}_2\text{O}_5$ concentration, $y$ , is shown on: the relative abundances of the Q species (b), their widths (c), their positions (d), and the percentage of the NBOs to the total number of oxygen surrounding the Si atoms .....	208
9.1.9	<i>In-situ</i> x-ray diffractograms showing the development of the crystalline phases and their growth in the glass $0.33[x\text{Li}_2\text{O} \cdot (1-x)\text{Na}_2\text{O}] \cdot 0.33\text{Nb}_2\text{O}_5 \cdot 0.33\text{SiO}_2$ with $x = 0, 0.3, 0.5, 0.7, 1$ with heating at the indicated temperatures .....	210
9.1.10	Samples $0.33[x\text{Li}_2\text{O} \cdot (1-x)\text{Na}_2\text{O}] \cdot 0.33\text{Nb}_2\text{O}_5 \cdot 0.33\text{SiO}_2$ , with different $x$ values after being heated in the in-situ experiment: (a) the XRD patterns, (b) the percentage of $\text{LiNbO}_3$ and $\text{NaNbO}_3$ , in the crystalline niobate phase, and the percentage of Cristobalite in the total crystalline phase, (c) their particle sizes .....	211

Figure		page
9.1.11	Raman spectra for samples $0.33[x\text{Li}_2\text{O} \cdot (1-x)\text{Na}_2\text{O}] \cdot 0.33\text{Nb}_2\text{O}_5 \cdot 0.33\text{SiO}_2$ , after being heated in the in the situ XRD experiment with different $x$ values .....	213
9.2.1	(a) Log-log plots for the frequency dependence of the conductivity, $\sigma$ , for the glass $0.33[x\text{Li}_2\text{O} \cdot (1-x)\text{Na}_2\text{O}] \cdot 0.33\text{Nb}_2\text{O}_5 \cdot 0.33\text{SiO}_2$ ( $x = 0.5$ ), (b) the complex plane representation for the same sample for temperatures 598-674 K .....	217
9.2.2	Arrhenius plots for the glasses $0.33[x\text{Li}_2\text{O} \cdot (1-x)\text{Na}_2\text{O}] \cdot 0.33\text{Nb}_2\text{O}_5 \cdot 0.33\text{SiO}_2$ , with $0 \leq x \leq 1$ . The lines represent the best linear fit .....	218
9.2.3	Variation in $\sigma_{\text{dc}}$ with changing $x$ value. $\sigma_{\text{dc}}$ values for the temperatures 473, 523, 573, 623 and 673 K) in comparison with $E_{\text{a}}^{\sigma_{\text{dc}}}$ . While $\sigma_{\text{dc}}$ shows its MAE minima at $x = 0.37$ , the $E_{\text{a}}^{\sigma_{\text{dc}}}$ shows an absolute maximum at the same $x$ value .....	218
9.2.4	The temperature dependence of the spin-lattice relaxation rates ( $1/T_1$ ) for the glasses $0.33[x\text{Li}_2\text{O} \cdot (1-x)\text{Na}_2\text{O}] \cdot 0.33\text{Nb}_2\text{O}_5 \cdot 0.33\text{SiO}_2$ , with $0 \leq x \leq 1$ ; (a) $^7\text{Li}$ SLR rates measured at $\omega_0/2\pi = 77.7$ MHz, (b) $^{23}\text{Na}$ SLR rates measured at $\omega_0/2\pi = 52.9$ MHz .....	220
9.2.5	$^7\text{Li}$ solid echo spectra of $0.33[x\text{Li}_2\text{O} \cdot (1-x)\text{Na}_2\text{O}] \cdot 0.33\text{Nb}_2\text{O}_5 \cdot 0.33\text{SiO}_2$ glasses measured at 77.7 MHz: (a) for the pure Li sample ( $x = 1.0$ ) upon heating from 153 to 453 K, showing the disappearance of the contribution of quadrupolar satellites at high temperatures, (b) for different compositions, $x$ , measured within the rigid lattice range (193 K) .....	221
9.2.6	The motional narrowing of the $^7\text{Li}$ central line (fwhm) obtained from the solid echoes for the glasses $0.33[x\text{Li}_2\text{O} \cdot (1-x)\text{Na}_2\text{O}] \cdot 0.33\text{Nb}_2\text{O}_5 \cdot 0.33\text{SiO}_2$ with different lithium contents, $x$ .....	223
9.2.7	(a) The fwhm of the central line of the solid echoes for $^{23}\text{Na}$ at $\omega_0/2\pi = 52.9$ MHz, and for $^7\text{Li}$ at $\omega_0/2\pi = 77.7$ MHz for the glass $0.33[x\text{Li}_2\text{O} \cdot (1-x)\text{Na}_2\text{O}] \cdot 0.33\text{Nb}_2\text{O}_5 \cdot 0.33\text{SiO}_2$ with different $x$ values. (b) The fwhm in the temperature range of rigid lattice against the Li content .....	224
9.2.8	(a) Jeener Broekaert (spin-alignment) echo amplitudes $S_2(t_p, t_m, t)$ of $^7\text{Li}$ in the glass $0.33[x\text{Li}_2\text{O} \cdot (1-x)\text{Na}_2\text{O}] \cdot 0.33\text{Nb}_2\text{O}_5 \cdot 0.33\text{SiO}_2$ with $x = 0.7$ , measured at a Larmor frequency of 77.7 MHz and a fixed evolution time $t_p = 12 \mu\text{s}$ . (b) The stretching factors ( $\gamma$ ) vs. reciprocal temperature ( $1/T$ ). The stretched factors increase with increasing $T$ .....	224
9.2.9	(a) $^7\text{Li}$ spin-alignment echo decay amplitude $S_2(t_p, t_m, t = t_p)$ recorded at 77.7 MHz and $t_p = 12 \mu\text{s}$ for glasses of the composition $0.33[x\text{Li}_2\text{O} \cdot (1-x)\text{Na}_2\text{O}] \cdot 0.33\text{Nb}_2\text{O}_5 \cdot 0.33\text{SiO}_2$ with $x$ in the range of 0.3 to 1. (b) The appropriate stretching exponents of the exponential decay functions as a function of $1/T$ .....	225
9.2.10	$^7\text{Li}$ spin-alignment decay rates $1/\tau$ measured at $\omega_0/2\pi = 77.7$ MHz and $t_p = 12 \mu\text{s}$ as function of reciprocal temperature ( $1/T$ ) for different compositions ( $x = 1, 0.85, 0.7, 0.5$ , and $0.30$ ). Within the low-temperature range the decay rates are independent of $x$ and possess an activation energy of 0.2 eV .....	226
9.2.11	$^7\text{Li}$ spin-alignment decay rates $1/\tau_h$ at $T = 393$ K and the dependence of the activation energies $E_{\text{a,h}}$ dependence on the glass-composition, $x$ .....	227
9.2.12	The dependence of the activation energy ( $E_{\text{a,h}}$ ) and of the decay rates ( $1/\tau_h$ ) on the Li-content, $x$ , determined from $^7\text{Li}$ spin-alignment measurements at $t_p = 12 \mu\text{s}$ with 393 K .....	227

## List of Tables

Table		page
2.3.1	The seven phases of sodium niobate, their space groups and temperatures of transformation.	19
4.1.1	Different circuit elements, their symbols, frequency response of the of $V(t)$ and $I(t)$ in their circuits and the complex plane impedance plots.	37
4.1.2	Comparison between the impedance $Z^*$ of a resistor ( $R$ ) and a capacitor ( $C$ ) connected in series and in parallel .....	40
5.1.1	The results of the chemical analyses done by ICP-AES and/or delivered by the manufacturing companies for the different LiNbO <sub>3</sub> samples .....	92
5.1.2	The grain sizes $L_0$ (in nm) and the strain $\varepsilon$ for the nanocrystalline LiNbO <sub>3</sub> prepared by HEBM .....	96
5.1.3	Band locations (cm <sup>-1</sup> ) for the observed Raman bands for LiNbO <sub>3</sub> in comparison with those found in the literature .....	100
5.2.1	Weights of n-LiNbO <sub>3</sub> and g-Na <sub>2</sub> Si <sub>3</sub> O <sub>7</sub> used to prepare 5-g batches the composite (x)n-LiNbO <sub>3</sub> ·(1-x)g-NaSi <sub>1.5</sub> O <sub>3.5</sub> with different x values .....	102
5.3.1	Weights of Li <sub>2</sub> CO <sub>3</sub> , Na <sub>2</sub> CO <sub>3</sub> , Nb <sub>2</sub> O <sub>5</sub> , and SiO <sub>2</sub> used to prepare 5-g batches of 0.33[xLi <sub>2</sub> O·(1-x)Na <sub>2</sub> O]·0.33Nb <sub>2</sub> O <sub>5</sub> ·0.33SiO <sub>2</sub> glass with different compositions, x .....	103
5.3.2	Weights of Li <sub>2</sub> CO <sub>3</sub> , Na <sub>2</sub> CO <sub>3</sub> , Nb <sub>2</sub> O <sub>5</sub> , and SiO <sub>2</sub> used to prepare 5-g batches the glasses (1-y)/2[Li <sub>2</sub> O·SiO <sub>2</sub> ]·yNb <sub>2</sub> O <sub>5</sub> and xLi <sub>2</sub> O·(1-x)/3[Nb <sub>2</sub> O <sub>5</sub> ·2SiO <sub>2</sub> ] with different y and x values	103
6.4.1	Annealing conditions of the LiNbO <sub>3</sub> single crystal samples with the diffusion parallel to (  ) or perpendicular to (⊥) the optical c-axis .....	116
7.1.1	Literature values of the quadrupole coupling constant for LiNbO <sub>3</sub> in single crystal and powder forms at room temperature .....	128
7.1.2	Comparison between the radial distributions for LiNbO <sub>3</sub> for single crystal data (from the literature), fitting results for microcrystalline and amorphous LiNbO <sub>3</sub> .....	134
7.1.3	Static and vibration frequency of Nb-O and Nb-Nb shells obtained from fitting the curves in Fig. 7.1.6 .....	136
7.1.4	The values of the mixing coefficients for the microcrystalline (M) and the amorphous (A) standards that gave the best fit for the nanocrystalline EXAFS .....	138
7.2.1	Comparison between the activation energy of the dc conductivity, $E_{a,\sigma}$ , and the activation energy of the semicircle relaxation frequency, $E_{a,r}$ .....	145
7.2.2	The fitting parameters (activation energies, $W$ , and the logarithm of the pre-exponential factors, $\log(\tau_0)$ ) obtained from the Arrhenius plots for $M'$ , Fig. 7.2.6 and for $M''$ .....	148
7.2.3	Comparison between the activation energy of the dc conductivity, $E_{a,\sigma}$ , of the pure LiNbO <sub>3</sub> samples (Alfa) with the impure sample (Aldrich) .....	151
7.2.4	Comparison between the activation energy of the dc conductivity, $E_{a,\sigma}$ , for different forms of LiNbO <sub>3</sub> under oxygen and under helium .....	153
7.2.5	Comparison between the activation energy of the dc conductivity, $E_{a,\sigma}$ , and the activation energy of the semicircle relaxation frequency, $E_{a,r}$ .....	154

Table		page
7.2.6	Values of the activation energies of the low-temperature flank of $^7\text{Li}$ SLR rates ( $1/T_1$ ) obtained from the plots of Fig. 7.2.15 (with and without background correction) .....	150
7.2.7	The activation energies for the low-temperature flank of the $^7\text{Li}$ SLR rates ( $1/T_1$ ) obtained from the plots of Fig. 7.2.17 (with and without background correction) .....	161
7.2.8	Fitting parameters of the temperature-dependent MN obtained by different equations ad hoc, and Waugh Fedin), the activation energies of the low-temperature flank of the SLR rate are also given for comparison .....	164
7.2.9	The experimental parameters obtained from fitting the curves in Fig. 7.2.21 .....	170
7.2.10	Summary for the fitting parameters of the Arrhenius plots of the oxygen diffusion coefficients and oxygen exchange coefficients obtained by fitting the plots in Fig. 7.2.22 .....	171
8.1.1	The molar percentages of $\text{LiNbO}_3$ , $\text{NaNbO}_3$ (summation of Lueshite high, Lueshite low, and orthorhombic $\text{NaNbO}_3$ ) and the other new phases relative to the total crystalline phases obtain by Rietveld-structure refinement of the XRD diffractograms for the composite $n\text{-LiNbO}_3\text{-g-NaSi}_{1.5}\text{O}_{3.5}$ after heating for 2 h at the indicated temperatures .....	179
8.1.2	The crystallographic (literature) details for $\text{LiNbO}_3$ and some of $\text{NaNbO}_3$ phases, phases ( <i>I</i> , <i>III</i> , <i>V</i> ) were detected and refined in the x-ray diffractograms while phases <i>II</i> and <i>IV</i> are known phases which may be metastable phases .....	180
8.2.1	Mole % of $\text{LiNbO}_3$ , $\text{NaNbO}_3$ in the crystalline phase obtained after heat treatment for 2 h at 1173 K for the composite: $(x)n\text{-LiNbO}_3 \cdot (1-x)\text{g-NaSi}_{1.5}\text{O}_{3.5}$ with different starting compositions, $x$ .....	189
9.1.1	Result of the Rietveld refinement for the crystalline phases in the glass-ceramics with the starting glass compositions $0.33[x\text{Li}_2\text{O} \cdot (1-x)\text{Na}_2\text{O}] \cdot 0.33\text{Nb}_2\text{O}_5 \cdot 0.33\text{SiO}_2$ for the indicated $x$ values after the growth of the crystalline particles by heat treatment .....	212
9.2.1	Arrhenius parameters (activation energy, $E_a^{\sigma_{ac}}$ , and the logarithm of the pre-exponential factor) of the plots shown above in Fig. 7.3.10 .....	218
9.2.2	The activation energies for the $^7\text{Li}$ and $^{23}\text{Na}$ SLR rates ( $1/T_1$ ) obtained from the plots of Fig. 9.2.4 (with and without background correction) .....	221
9.2.3	Decay rates $1/\tau$ , determined from spin-alignment echo amplitudes shown in Fig. 9.2.9 (a) measured at $T = 373$ K. The associated stretching factors $\gamma$ are compared .....	226

# CURRICULUM VITAE

## PERSONAL:

Name : **Muayad Masoud Mahmoud Maasoud**  
Place of Birth : **Burqa, Nablus, WestBank, Palestine**  
Date of Birth : **Sep. 24<sup>th</sup>, 1973**  
Marital Status : **Single**  
Nationality : **Palestinian**

## EDUCATION:

**HANNOVER UNIVERSITY, Hannover, Germany**  
*Ph. D. Student, Physical chemistry (2002- 2005)*

**Thesis:** "Diffusivity and Ionic Conductivity in Lithium Niobate and Related Glasses and Glass Ceramics".

**AN-NAJAH N. UNIVERSITY, Nablus, Palestine**  
*M. Sc., Chemistry. (1996-2001)*

**Cumulative average:** 86.3%, **Rating:** *V. good.*

**Thesis:** "Surface Modification of n-GaAs Semiconductor with Metalloporphyrin / Polysiloxane Matrices: Effect of Modification on Band-Edge Positions, Short Circuit Current and Surface Stability Aqueous Photoelectrochemistry".

**AL-YARMOUK UNIVERSITY, IRBID, JORDAN**  
*B. Sc., Chemistry. (1992-1996) Honor list: 7 semesters*

**Cumulative average:** 89.8%, **Rating:** *Excellent.*

**BURQA SEC. SCHOOL, BURQA, NABLUS, WEST BANK**  
*General School Certificate, (Tawjeehi), Science Stream: 95.5%, (1992)*

## RESEARCH & TEACHING EXPERIENCE:

### Research Techniques:

- Solid state NMR for structure and dynamic characterization [Static and MAS-NMR-solid echoes-Spin lattice relaxation (solid state diffusion)].
- Impedance spectroscopy (conductivity- complex-plane impedance-dielectric constant-Modulus).
- Electrochemistry: Surface Analytical Techniques (e.g. Cyclovoltammetry etc.),
- Semiconductor Current Voltage (I-V) plots Capacitance-Voltage (Mott-Schottky)
- X-ray diffraction, in-situ XRD and Extended X-ray Atomic Absorption Fine Structure (EXAFS).
- AAS, HPLC, UV/Visible, FT-IR, Raman Spectroscopy in addition to computer skills.

### Teaching Experiences:

- 1) Chemistry teacher (High School) 1996-2002.
- (1996-1997) Burqa Sec. School For Boys and Salim/Dair Al-Hatab Sec. School For Boys- Nablus-Westbank-Palestine
  - (1997-2001) Burqa Sec. School for Boys-Nablus-Westbank-Palestine

I was involved in many scholastic activities being a high-school chemistry teacher in addition to teaching several subjects like general science, physics, mathematics and computer for basic levels, besides being responsible about computer and science laboratories, a member of teaching developing team in the school as well as a member of the subject "Chemistry" committee in Nablus directorate for several years.

2) Selected for the position of chemistry director (supervisor) in the Ministry of Education- Nablus Directorate 2002 (only for 2 weeks and then started PhD).

## INVITED PRESENTATION AND CONFERENCES

Title	Conference	Date & Place
surface modified n-GaAs semiconductor with metalloporphyrinatomanganese(III) encapsulated in polysiloxane matrices: effect of modification on the semiconductor characteristics at the solid/liquid junctions. (oral contribution)	2 <sup>nd</sup> International Conference on Pure, Applied and Environmental Chemistry	17-21/04/(2000) - Yarmouk University, Irbid,
n-GaAs Band edge repositioning by modification with metalloporphyrin/polysiloxane matrices (oral contribution: 4-SMOA07)	The 7 <sup>th</sup> Arab International Solar Energy Conference and Regional World Renewable Energy Conference	19-22/02/(2001) - Sharjah, UAE
Stability and Cell Efficiency Enhancement of n-GaAs Electrodes by Metalloporphyrin Complexes Embedded Inside Polysiloxane Matrice . (Poster Contribution: P17)	World Renewable Energy Congress VII	29/06-05/07/(2002) - Cologne-Germany
Impedance spectroscopy study of Li ion dynamics in microcrystalline, nanocrystalline, and Amorphous LiNbO <sub>3</sub> (Poster Contribution)	Deutsche Physikalische Gesellschaft (DPG) "spring meeting of the Division Condensed Matter Physics"	24-28/03/(2003) - Dresden-Germany
Impedance Spectroscopy Analysis of Li Ion Dynamics in Single Crystal, Microcrystalline, Nanocrystalline, and amorphous LiNbO <sub>3</sub> (oral contribution)	Sixth International Conference on DIFFUSION IN MATERIALS (DIMAT 2004)	18-23/07/(2004) - Krakow-Poland
Mixed Alkali Effect in (Li, Na) Niobium Silicate Glasses-Probing Cation Dynamics by Impedance spectroscopy and by Solid-echo and Multiple-time Spin-Alignment Echo <sup>7</sup> Li NMR Spectroscopy (Poster Contribution)	Deutsche Physikalische Gesellschaft (DPG) "Spring Meeting of the Division Condensed Matter Physics"	04-09/03/(2005) - Berlin-Germany
Oral contribution: Impedance and NMR Study of Amorphous and Nanocrystalline LiNbO <sub>3</sub> : Influence of Preparation Routes	1 <sup>st</sup> International Student Workshop (Germany-Japan-Korea) Solid State Ionics: Session IV: Novel Materials and Spectroscopic Studies-	15-16/07/(2005) - Geissen-Germany

## PUBLICATIONS:

- 1) H. S. Hilal, M. A. Suleiman, W. J. Jondi, S. Khalaf, M. Masoud, "***Poly(siloxane)-Supported Decacarbonyldimanganese(0) Catalyst for Terminal Olefin Hydrosilylation Reactions: The Effect of the Support on the Catalyst Selectivity, Activity and Stability***", *Journal of Molecular Catalysis A-Chemical*, **144**[1] (1999) 47-59
- 2) H. S. Hilal, M. Masoud, S. Shakhshir, N. Jisrawi, "***Metalloporphyrin/polysiloxane modified n-GaAs surfaces: effect on photoelectrochemical efficiency and surface stability***", *Journal of Electroanalytical Chemistry* **527**[1-2] (2002) 47-55
- 3) H. S. Hilal, M. Masoud, S. Shakhshir, "***n-GaAs band-edge repositioning by modification with metalloporphyrin/polysiloxane matrices***", *Active and Passive Electronic Components* **26**[1] (2003) 11-22
- 4) M. Masoud, P. Heitjans, "***Impedance Spectroscopy Study of Li Ion Dynamics in Single Crystal, Microcrystalline, Nanocrystalline, and Amorphous LiNbO<sub>3</sub>***", *Defect and Diffusion Forum* **237-240** (2005) 1016-1021

**In preparation:**

M. Masoud, P. Heitjans, D. Bork, D.-M. Fischer, A. Dent, "*Comparative EXAFS Analysis of Microcrystalline, Nanocrystalline, and Amorphous LiNbO<sub>3</sub>: Nature of the Grain-Boundaries Region*", ready for submission

M. Masoud, P. Heitjans, Fielitz, G. Borchardt, R. A. De Souza, M. Martin, "*Oxygen-18 Surface Exchange and Diffusion in Single Crystalline Lithium Niobate*", ready for submission

M. Masoud and P. Heitjans, T Gesing, and R. Winter, "*Mixed Alkali Niobosilicate Glasses and Glass Ceramics: Structural Aspects by Multi nuclear magnetic resonance, XRD, I.R., and Raman Spectroscopy*", In preparation

M. Masoud, M. Wilkening, R. Winter, and P. Heitjans, "*Mixed Alkali Effect in (Li, Na) Niobium Silicate Glasses: Probing Cation Dynamics by Impedance Spectroscopy and by Solid-Echo and Multiple-Time Spin-Alignment Echo <sup>7</sup>Li NMR Spectroscopy*", In preparation

**AWARDS & RESEARCH GRANTS:**

- Graduate Program "New materials with tailored properties" fellowship supported financially by Georg Christoph Lichtenberg-fellowships sponsored by the State of Niedersachsen, (02/2002-02/2005)
- Conference grants "financial support for young scientists" in The Sixth International Conference on DIFFUSION IN MATERIALS (DIMAT 2004), Krakow-Poland, 18-23 July 2004.



# Appendixes

## A.1 Trails to Prepare Quenched Amorphous LiNbO<sub>3</sub>

Several attempts were made to initiate a collaboration to prepare amorphous LiNbO<sub>3</sub>. The required conditions were really hard. Firstly, LiNbO<sub>3</sub> has a high melting point (1538 K), it is highly reactive with the atmosphere in the molten state. Secondly, a high cooling rate of 10<sup>6</sup> K/s is required to get really amorphous phase. It should be kept in mind that LiNbO<sub>3</sub> is an ionic conductor, so it is not possible to heat it inductively. Several trails to contact people were done in Germany (Göttingen, Freiberg, Dresden, Düsseldorf, Jena) as well as abroad (USA, France, Japan, Korea, India, Denmark)

### Göttingen:

Physikalisches Institut-Universität Göttingen-Bunsenstr. 9, D-37073 (Tel.: +49 551 39 7602, Fax.: +49 551 39 2328). Prof. K. Samwer (Tel. 7601, e-mail: [ksamwer@gwdg.de](mailto:ksamwer@gwdg.de)); Dr. B. Damaschke (Tel. 7623, e-mail: [bdamasc1@gwdg.de](mailto:bdamasc1@gwdg.de)); Mrs. Uta Bete (Tel. 7622, e-mail: [ubete@gwdg.de](mailto:ubete@gwdg.de)).

On the 9<sup>th</sup> of July 2002, the following possibilities to prepare amorphous samples were found during a visit to the institute: (i) Splat-quenching: for this method, a conducting and nearly spherical (3 mm-diameter) sample (not only pressed one) is needed. The sample is levitated electrostatically which is not possible with LiNbO<sub>3</sub>. (ii) Melt-spinning/Copper molt casting: the (conducting) sample is heated inductively in a quartz tube, and then sprayed onto a copper wheel or a Cu molt for solidification. A compacted sample is needed for this technique. The suggestion was to use laser heating instead of inductive heating which proved to be practically impossible. Alternatively one has to design a metallic sample holder (the tube in which the sample is heated). The main point was whether the cooling rate will be high enough. The velocity of the wheel of this melt-spinning facility was 40 m/s which is much slower than the speed needed for quenching LiNbO<sub>3</sub> (5000 r.p.m.) besides the uncontrolled sample thickness.

### Freiberg

Freiberger, Compound Materials GmbH, Am Junger Löwe Schacht 5, D-09599 Freiberg / Sachsen – Tel. (+49) 3731 2 80-0 Fax (+49) 3731 2 80-1 06, E-mail [info@fcm-germany.com](mailto:info@fcm-germany.com). Dr. Manfred Jurisch, e-mail: [jurisch@fcm-germany.com](mailto:jurisch@fcm-germany.com)

Dr. Jurisch offered four possibilities to prepare amorphous LiNbO<sub>3</sub>; two of them (double roller equipments) were left at 1992 in the Institute of Solid State Physics and Materials Research in Dresden: (i) a big machine for strip casting with a ribbon thickness around 2 mm. This machine was dismantled and shipped to the National Iron and Steel Institute- Brazil. (ii) A small machine used for thin ribbon casting of Fe-Si-alloys and for splat-cooling of a glass containing barium-hexa-ferrite (under the disposal of Dr. Wolfgang Loeser (a former coworker). (iii) Another double roller is active in the MPI für Eisenforschung in Düsseldorf (Dr. Achim-Ruediger Buechner. It is a part of a former medium size double roller of his group in Dresden. It is used for strip casting of steel alloys. (iv) A small double roller for splat cooling of different glasses was used in Jena (Prof. Peter Goernert).

### Dresden

Dr. Wolfgang Löser, e-mail: W.Löser@ifw-dresden.de

Dr. Löser answered on 5 Aug 2002. He has searched for the twin-roller history. The smaller caster has also been dismantled two years ago and nothing remained. He advised me to contact Dr. A. Büchner, MPI für Eisenforschung Düsseldorf who probably continued research in twin-roller technology.

### Düsseldorf

Max-Planck-Institut für Eisenforschung Abteilung Metallurgie, 40237 Düsseldorf, Dr. rer. nat. Achim R. Büchner (Tel.: +49 211 6792 328, Fax.: +49 211 6792 390)

On the 23<sup>rd</sup> of July 2002 I received the answer of Dr. Büchner. He assumed that the cooling rates in a twin roller are not large enough to produce amorphous LiNbO<sub>3</sub> and suggested that single roller could be a better technique, which is available also in the same institute with Prof. Frommeyer (e-mail: frommeyer@mpie.de).

### Jena

IPHT Jena (Magnetik), Winzerlaer Str. 10, 07745 Jena, Tel. +49 3641-206-109, fax: +49 3641-206-199, (www.ipht-jena.de). Dr. Robert Müller e-mail: robert.mueller@ipht-jena.de

On the 24<sup>th</sup> July 2002, Dr. Müller answered upon a request from Prof. Goernert. He told that the twin roller is used up to now. The technical parameters are:  $T_{\max} = 1450$  °C, air atmosphere, and quenching rate =  $10^4$  K/s. The used heating is a resistance one, there should be no gas formation, the used material must not react with Pt-crucible and should be soluble in an acid to clean the crucible. All the previous conditions are suitable for LiNbO<sub>3</sub>; however, the cooling rate is not high enough and it is not possible to use powder samples (only pieces with diameter > 4mm can be used) and therefore a previous melting step is needed.

### USA

1) Bell Laboratories-600 Mountain Avenue-Murray Hill, NJ 07974-Tel.: 908-582-3000 (<http://www.bell-labs.com/employment>). There was no answer.

2) University of Wisconsin-Madison- 4623 Engineering Hall - 1415 Engineering Drive -Madison, WI 53706. Prof. Leon McCaughan (Tel: 608/262-0311, e-mail: mccaughan@engr.wisc.edu) I contacted Prof. McCaughan for the possibility to prepare amorphous LiNbO<sub>3</sub> by chemical vapor deposition (C.V.D.) according to their reports about "Amorphous LiNbO<sub>3</sub>: Entryway to 2D and 3D Oxide Structures" in ([http://mrsec.wisc.edu/individ\\_nuggets/irgl/Amorphous\\_LiNbO3.htm](http://mrsec.wisc.edu/individ_nuggets/irgl/Amorphous_LiNbO3.htm)), but unfortunately they did not answer.

### France

Several publications about ionic conductive glasses, mainly Li-ion conductors were produced by twin-roller quenching device. For this many trails have been made to contact Prof. Annie Pradel (apradel@lpmc.univ-montp2.fr). But there was no positive response.

### Japan

1) Tokyo University of Agriculture and Technology, Laboratory of Ceramics, Department of Applied Chemistry, Faculty of Technology, 2-24-16, Naka-cho, Tokyo 184-8588, Japan  
Prof. Takeyuki Suzuki (Tel. and Fax: +81-423-88-7039, e-mail: takeyuki@cc.tuat.ac.jp)

Sat, 13 Jul 2002, he answered telling me that I took him back to 30 years ago. He heard at that time that LiNbO<sub>3</sub> can be made into amorphous not only by twin roller but also by single roll method. Now, he works on another theme and cannot help anymore.

2) Tohoku University, Institute of Multidisciplinary Research for Advanced Materials, Division of Advanced System.  
Prof. Masahiko Shimada (e-mail: shimada@tagen.tohoku.ac.jp). There was no answer.

3) Tohoku University, Department of Applied Chemistry of Molecular Systems, Synthetic Chemistry of Advanced Materials.  
Prof. Tadashi Endo (Tel. +81-222177225, Fax. +81-222177228, e-mail: endo@aim.che.tohoku.ac.jp)

I contacted Prof. Endo asking about the apparatus of twin-roller quencher that was used for the preparation of glasses, especially  $\text{KNbO}_3\text{-Nb}_2\text{O}_5$  glasses. There was no answer.

4) Osaka Prefecture University, Department of Applied Chemistry, Gakuen-cho, Sakai, Osaka 599-8531, Japan (Tel: +81-72-252-9291, Fax: +81-72-254-9910, e-mail: office@chem.osakafu-u.ac.jp)  
An e-mail was sent to the Department of Applied Chemistry to ask about the apparatus of thermal-image furnace combined with twin roller quencher that was used for the preparation of  $\text{Li}_2\text{O-RO-Nb}_2\text{O}_5$  glasses. There was no answer

5) Tohoku University, The Department of Molecular Chemistry and Engineering (*Prof. Masahiko Shimada*, e-mail: shimada@tagen.tohoku.ac.jp)  
Prof. Shi that was used for the preparation of glasses, especially  $\text{KNbO}_3\text{-Nb}_2\text{O}_5$  glasses, but there was no answer.

### **Korea:**

Research Center for Dielectric and Advanced Matter Physics, Dept. of Physics in Graduate School Pusan National University, Pusan 609-735, Korea (idecmail@idec.pusan.ac.kr)  
There were more than 7 papers published in the period from 1995 to 1999, on pure amorphous  $\text{LiNbO}_3$ . This was prepared by the twin roller quencher designed by Kim which has a rate of cooling of about  $10^6$  K/sec and the thermal and electrical properties of the resultant amorphous  $\text{LiNbO}_3$  was studied.

Professor Yoon-Hwae Hwang (e-mail: yhwang@hyowon.pusan.ac.kr), Professor Min-Su Jang (e-mail: msjang@hyowon.pusan.ac.kr) without getting any answer from them. After that, on the 11<sup>th</sup> of July 2002. Dr. Hwang, Sang-Moon (e-mail: hwang@pusan.ac.kr) answered telling me that in their previously published works, they used the sample which was prepared in other professor's lab in their research institute. His name is Prof. Yong Suk Yang, (Tel: 82-515102958, Fax:82-515165682, e-mail: ysyang@pusan.ac.kr)

I received the 1<sup>st</sup> response on 12<sup>th</sup> Jul 2002 from Prof. Yang. He accepted to prepare the samples, but he commented that producing  $\text{LiNbO}_3$  glass needs some care because its reaction with environmental material during melting is very strong. He said that it will take time to ensure the sample is pure glass without impurities. After two month, he claimed that the preparation of bulk glass is extremely hard because it actively reacts with other materials and the quenching rate has to be high. Thus, he suggested adding glass former ( $\text{SiO}_2$ ) and said that only  $\text{LiNbO}_3$  characteristics can be obtained. He proposed to send samples with different mole ratio of  $\text{SiO}_2$ . It was surprising that in his recent publications "about systems with  $\text{SiO}_2$ " the cooling rate was  $3\text{--}4\cdot 10^4$  K/sec and not  $10^6$  K/sec as was mentioned in the old 7 publications. Then he commented with unclear sentences that "the previously published papers were from Prof. M. S. Jang group for a student who has a name similar to his English name. Nevertheless, they often used his twin roller quenching equipment. He found that it was not easy to make  $\text{LiNbO}_3$  bulk glasses. The previously published results were almost the same as the result of  $\text{LiNbO}_3 : \text{SiO}_2 = 2 : 1$ . Consequently, he thinks that the former results are partially acceptable.

### **India:**

Indian Institute of Science, Materials Research Centre, Bangalore-560 012, India. Prof. K. B. R. Varma (Fax: 91-0803600683, Tel.: (Off) 3092914 (Res) 3600208, e-mail: kbrvarma@mrc.iisc.ernet.in)

On the 11<sup>th</sup> of July 2002, Prof. Varma told me that he does not prepare pure flakes of  $\text{LiNbO}_3$  etc by twin roller quenching technique anymore. Alternatively, He suggested to send samples of many ferroelectric nanocrystals embedded in a glass matrix and to try to locate the samples prepared using the twin roller quenching method more than 18 years ago. When I insisted on preparing new glassy  $\text{LiNbO}_3$ , he mentioned that it is difficult for him to get back to this particular piece of work because none of his students is working on this problem. And again he suggested to send  $\text{LiNbO}_3$  microcrystals dispersed in a  $\text{TeO}_2$  matrix. However, he was ready to prepare the pure amorphous  $\text{LiNbO}_3$  again.

### **Denmark**

Section of Chemistry-Aalborg University-Sohngaardsholmsvej 57-DK-9000, Aalborg, Prof. Yuanzheng Yue (Tel.: +45 9635 8522, Fax: +45 9635 0558, e-mail: yy@bio.auc.dk, http://iprod.auc.dk/forsk/poly/proj/renate.htm)

The first response from Prof. Yue was received on the 31<sup>st</sup> of July 2003. He was interested in the topic as  $\text{LiNbO}_3$  is a quite fragile system and that they are studying some hyperquenched fragile systems at the actual time. Their method requires at least 300 grams in order to get 10 grams of good fibers. After that there was a period of interruption until Prof. Heitjans phoned him on the 20<sup>th</sup> of Nov. 2003 and he agreed to prepare the hyper quenched  $\text{LiNbO}_3$  fibers. Two packages (100 g each) of microcrystalline  $\text{LiNbO}_3$  were sent to him. He received them within three days and told me that he was planning to make the fibbers in one or two weeks. There were some problems with the fibber spinning equipment besides being busy with teaching. Two months later he asked about the exact melting point of  $\text{LiNbO}_3$  and complained that 200 g may be not enough. On the 18<sup>th</sup> of Feb. 2004, i.e. after additional one month and a half, he apologized for the delay as they spent some time to change their facility in the way they hope to be able to make glass from such fragile system as  $\text{LiNbO}_3$ . He told that in the last week he with Rockwool people, have tried to make hyperquenched glass from  $\text{LiNdO}_3$ . But unfortunately it was not successful experiment. A DSC measurement,  $c_p$  curve, of the hyperquenched sample shows an exothermic peak between 450 and 520 °C. This peak could be associated with the enthalpy relaxation of hyper-quenched sample indicating that some glass is obtained by hyper-quenching. But the main part of the samples was crystalline material. He said that he will send the hyper quenched samples back but he did not. He justified the failure by:

- 1)  $\text{LiNbO}_3$  melt is too fragile, in other words, the viscosity is too low slightly above the liquidus temperature (1275 °C).
- 2) The rotating wheel is not hot enough. There are technical difficulties to get it very hot.
- 3) The amount of raw materials is not enough to get the melt well attached on the wheel.

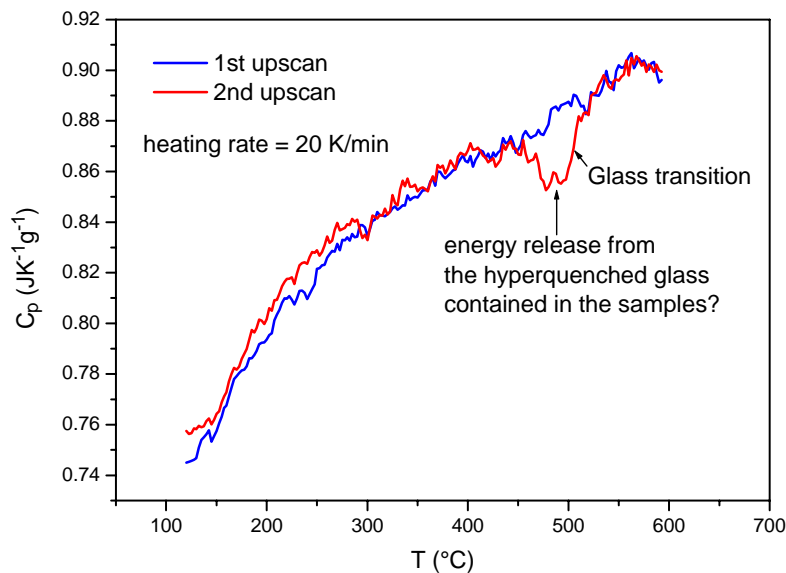
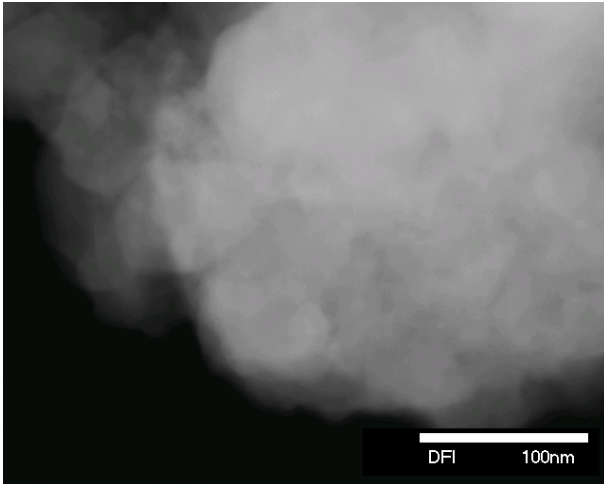


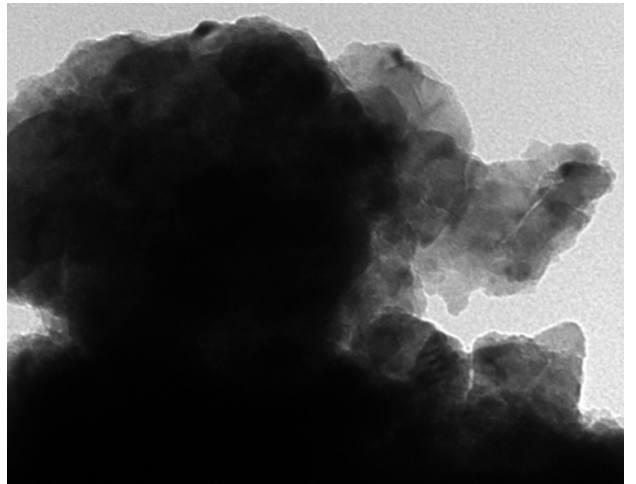
Fig. A: DSC measurement,  $c_p$  curve, of the hyperquenched sample shows an exothermic peak between 450 and 520 °C in the first heating scan. This peak could be due to the glass transition of the hyper-quenched sample. This confirms that some glass is obtained, but the main part of the samples was crystalline material.

**A.2 TEM Images for Nanocrystalline  $\text{LiNbO}_3$  Prepared by HEBM and by Sol-gel**

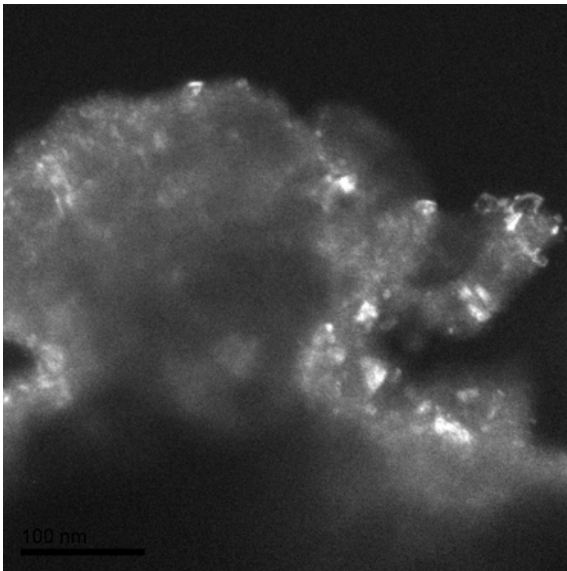
Nanocrystalline  $\text{LiNbO}_3$  HEBM 16 h (site 1)



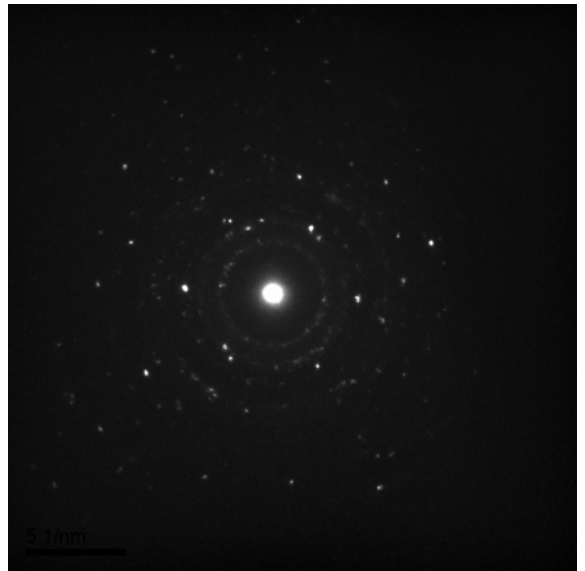
STEM02.dm6



Q-16h-01-DF



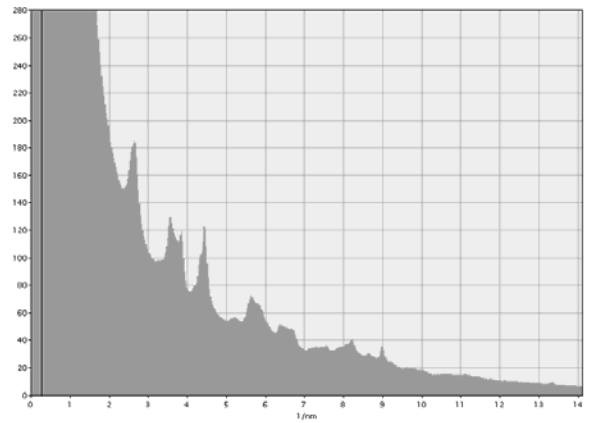
Q-16h-DF-03



Q-SAED-01-gefiltert

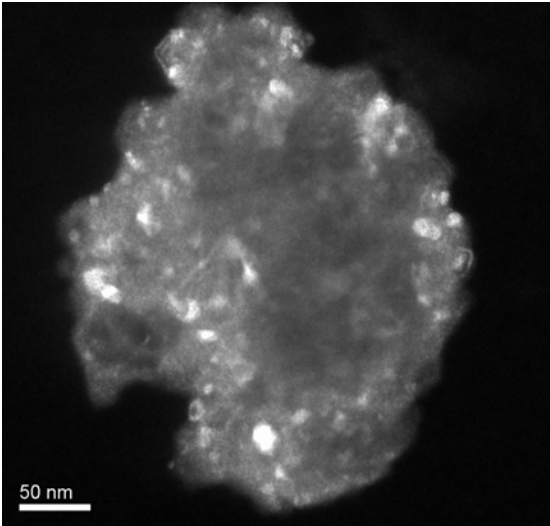


Q-SAED-02-Rotational Average

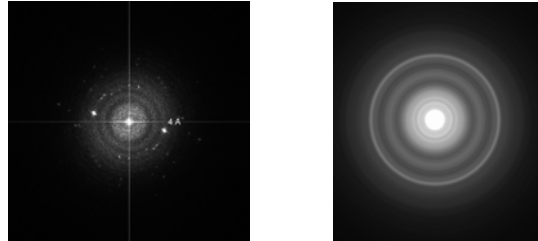
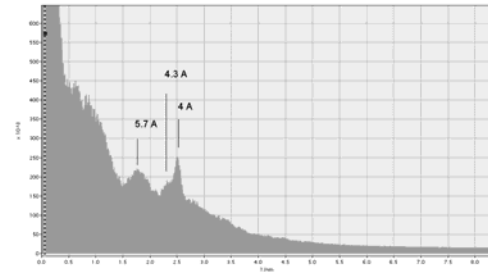


Q-SAED-Radial Intensity

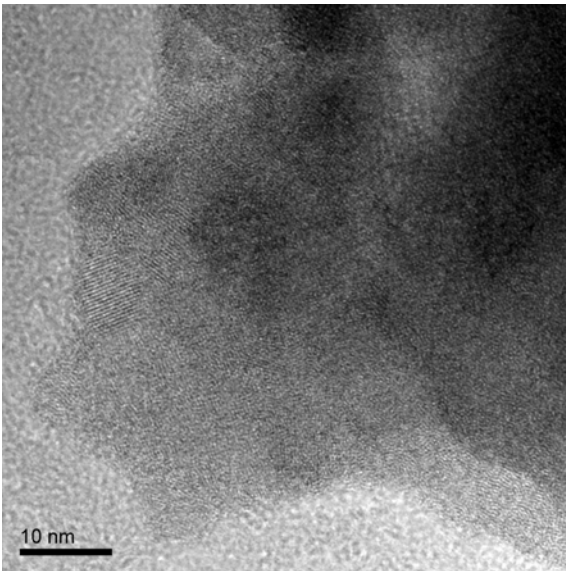
Nanocrystalline LiNbO<sub>3</sub> HEBM 16 h (site 2)



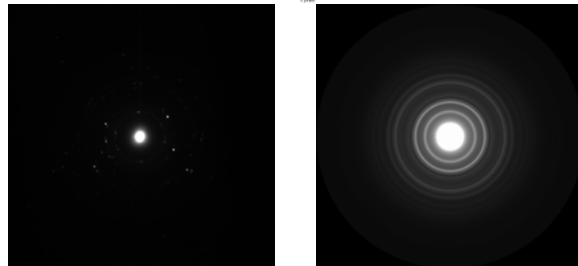
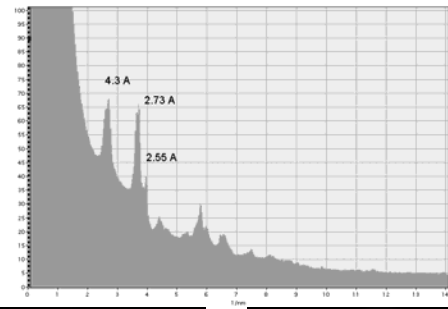
Q-BF03



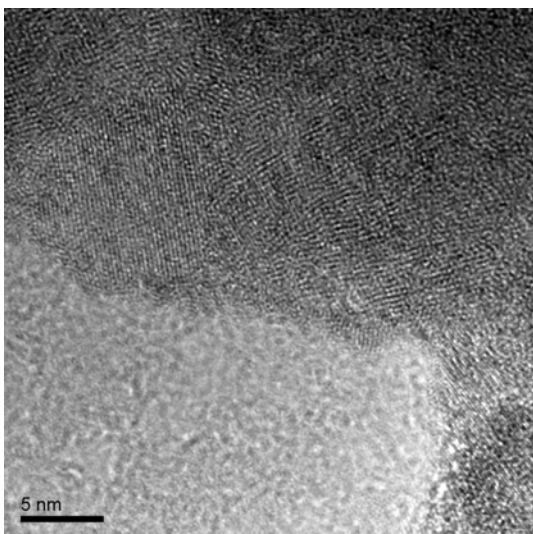
Q-HRTEM03-FFT-Radial Intensity, SAED, & Rotational Average



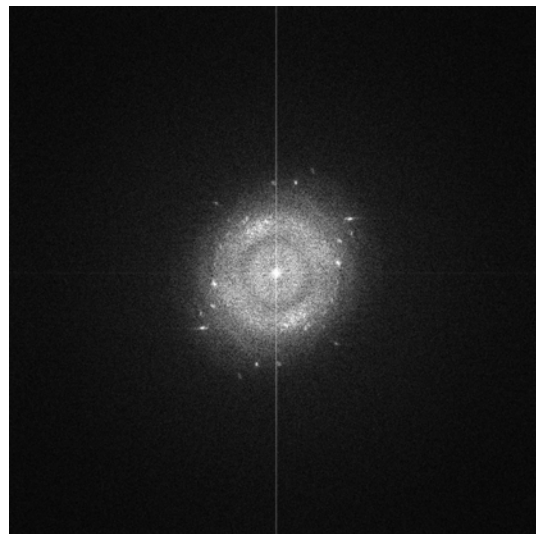
Q-HRTEM04



Q-SAED-Radial Intensity, SAED, & Rotational Average

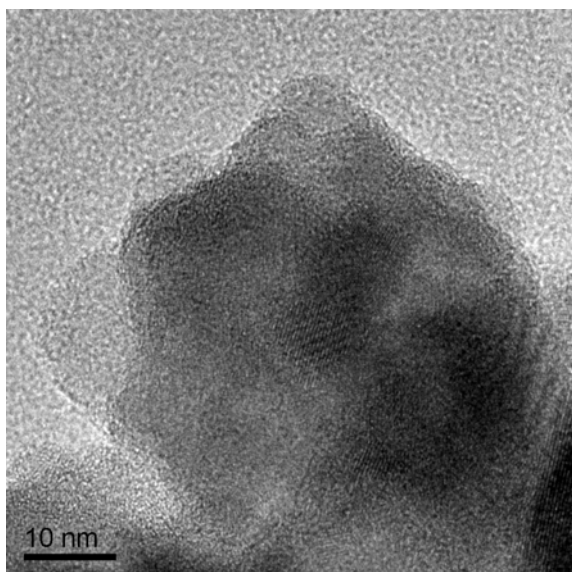


Q-HRTEM06

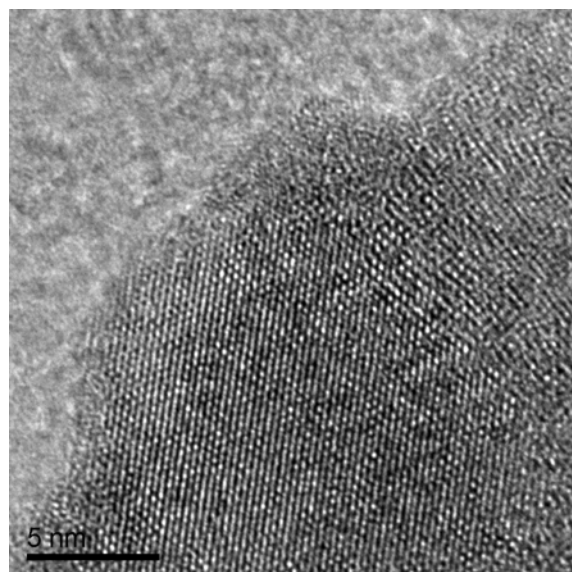


Q-HRTEM06-FFT

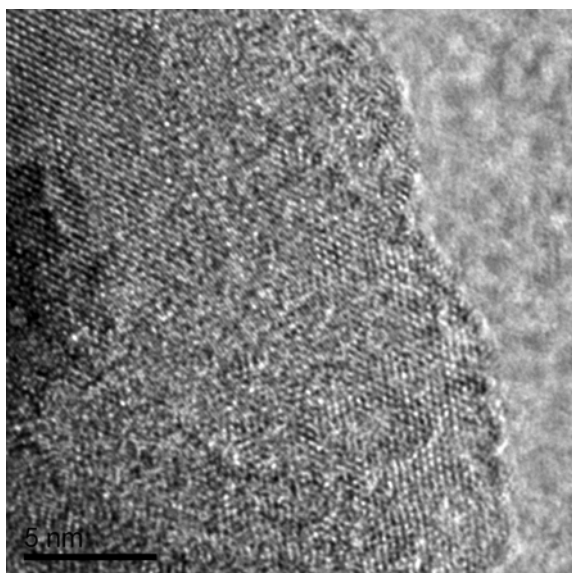
Nanocrystalline  $\text{LiNbO}_3$  HEBM 16 h (site 3)



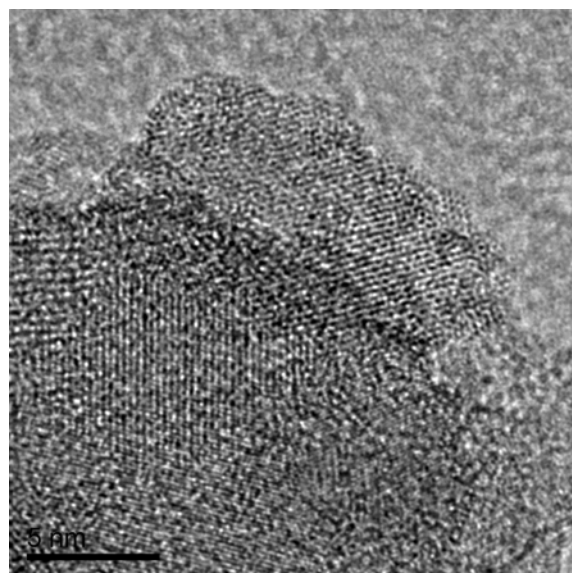
Q-HRTEM01



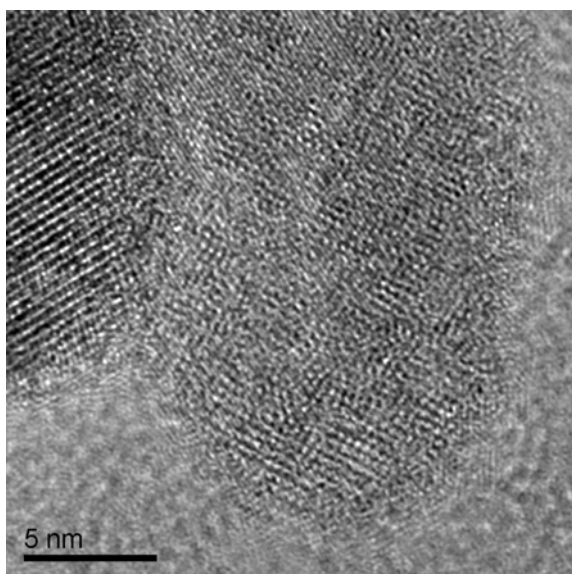
Q-HRTEM05



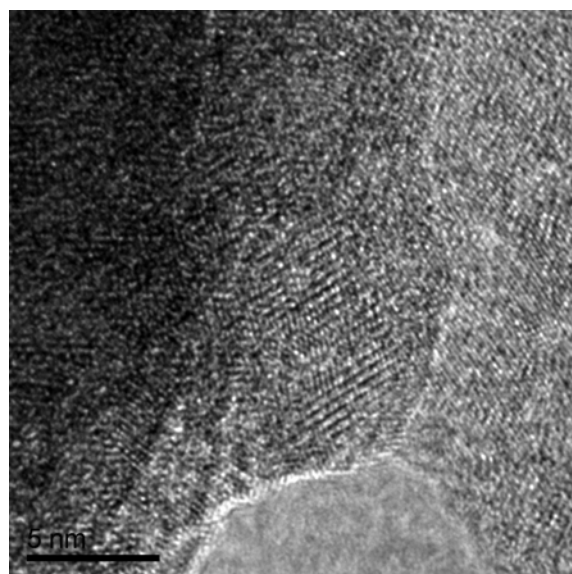
Q-HRTEM06



Q-HRTEM07

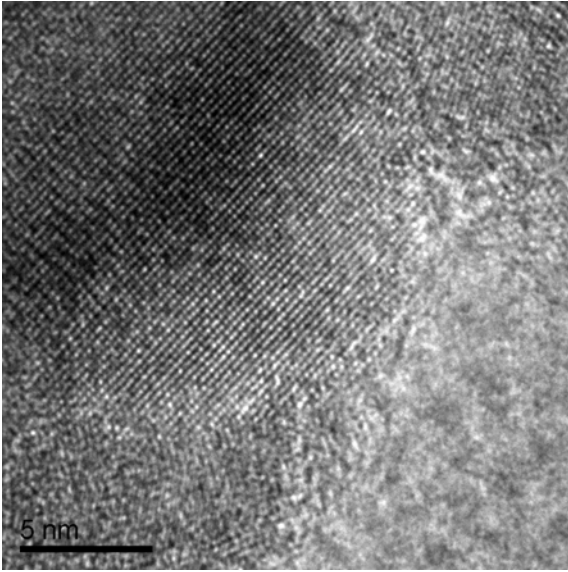


Q-HRTEM08

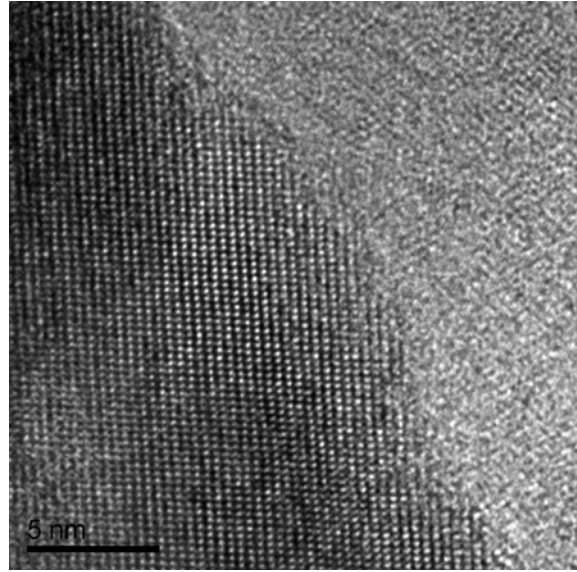


Q-HRTEM09

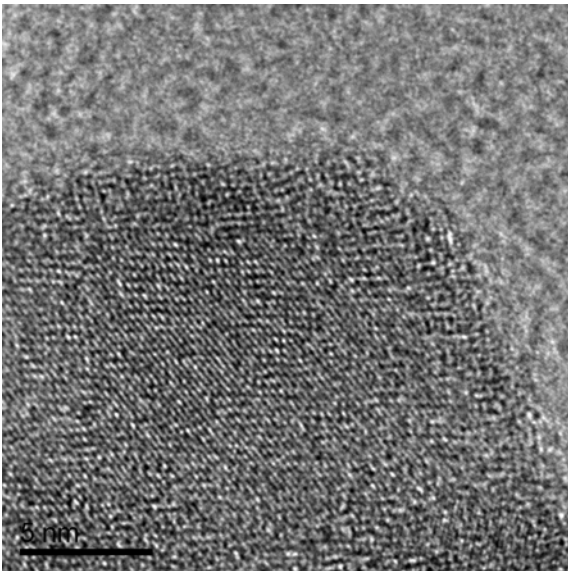
Nanocrystalline LiNbO<sub>3</sub> HEBM 16 h (site 4)



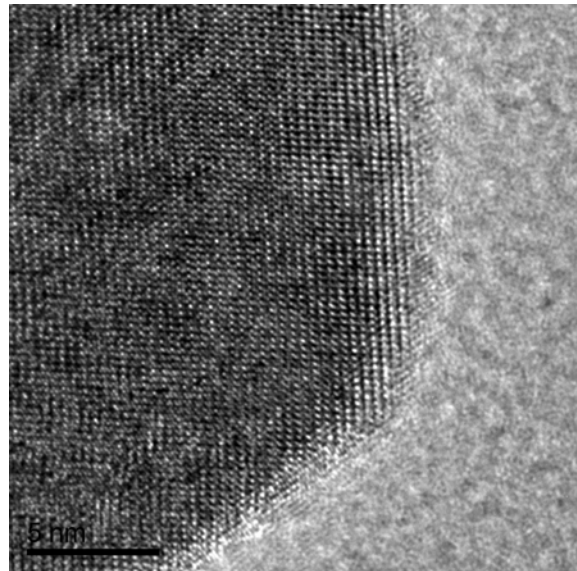
Q-HRTEM01



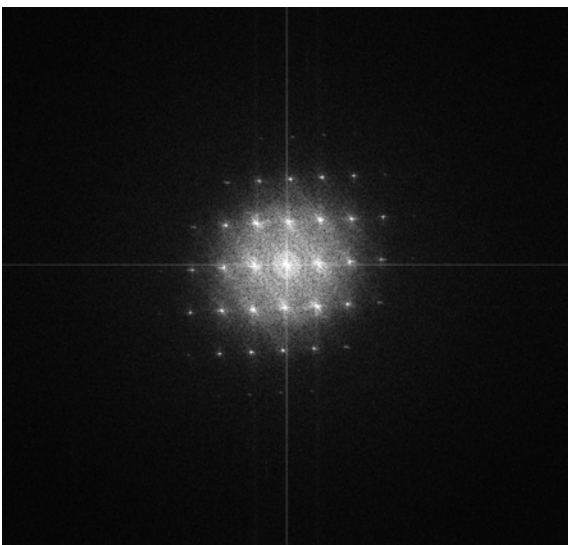
Q-HRTEM02



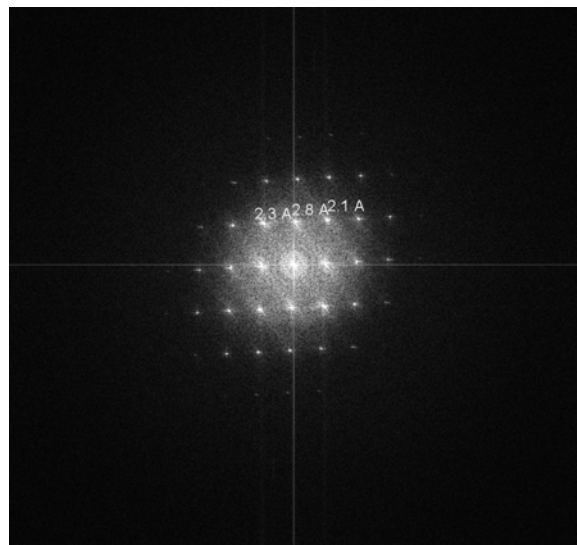
Q-HRTEM03



Q-HRTEM04



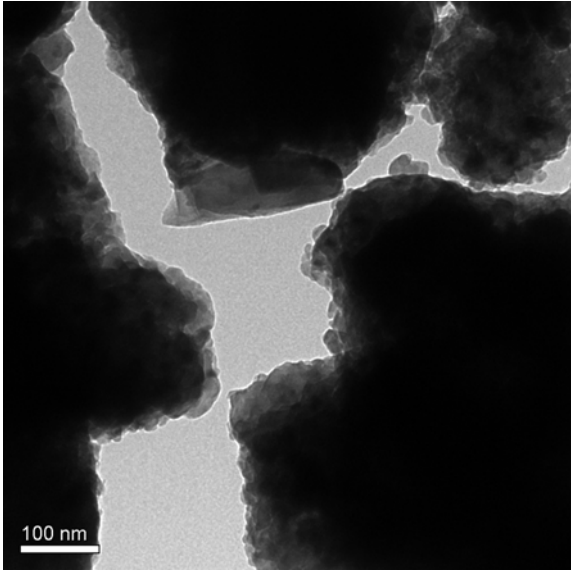
Q-HRTEM04-FFT



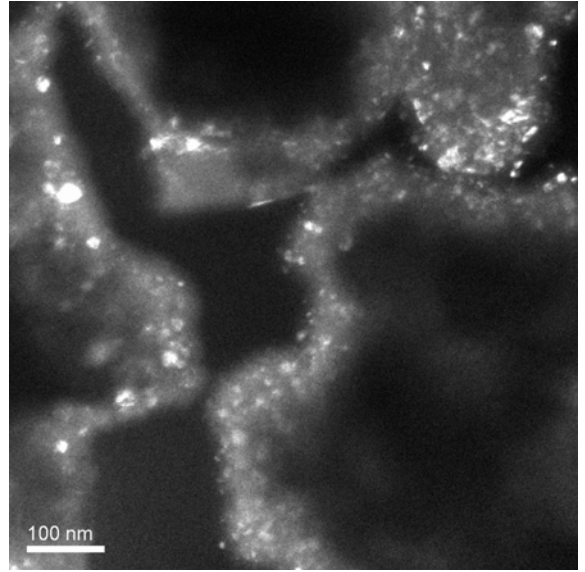
Q-HRTEM04-FFTb



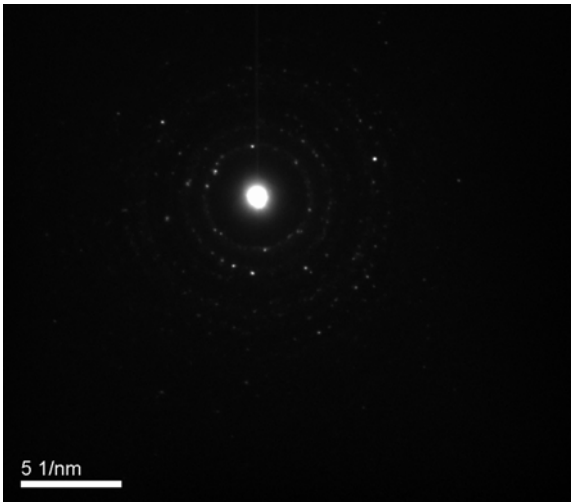
Nanocrystalline LiNbO<sub>3</sub> HEBM 32 h (site 1)



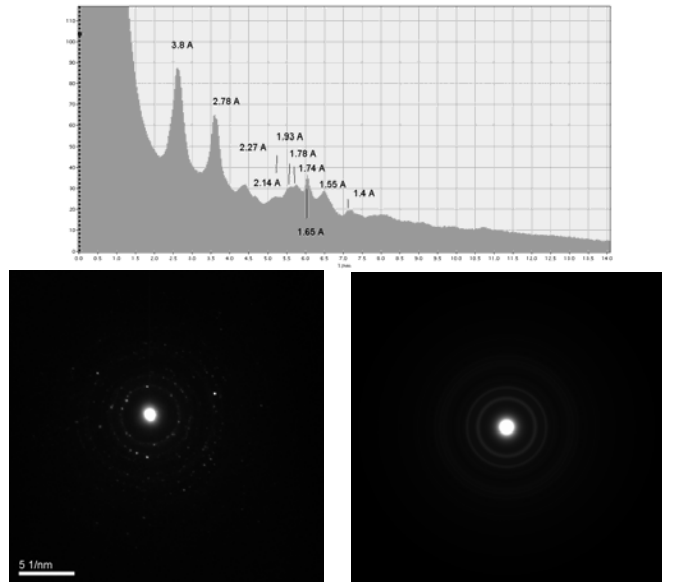
B-BF



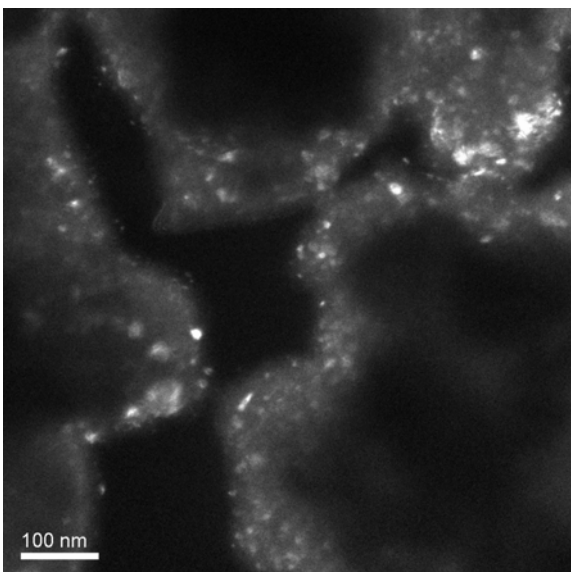
B-DF01



B-SAED01

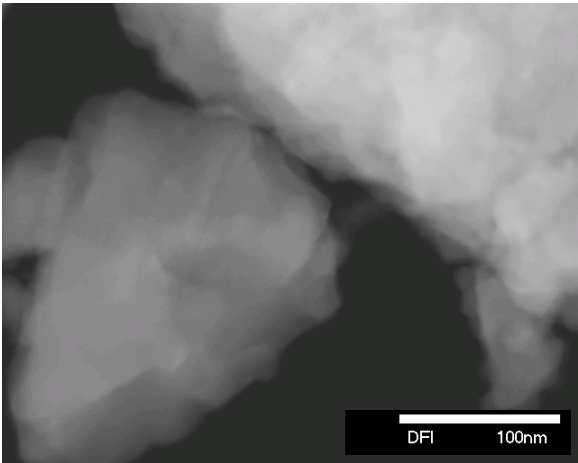


B--01-SAED02 Radial Intensity, & Rotational Average

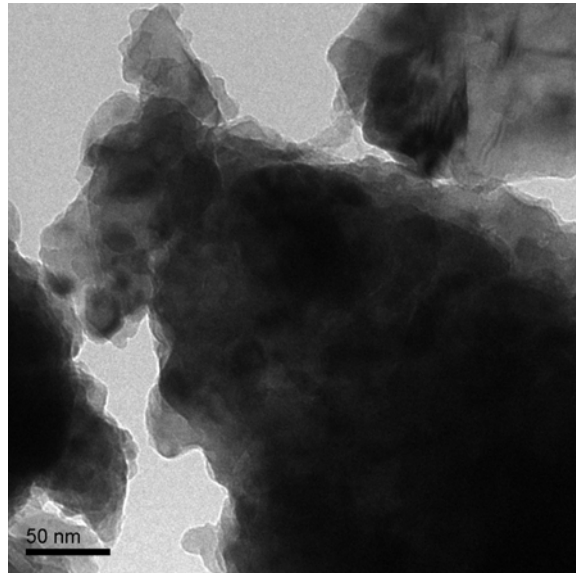


B-01-DF02

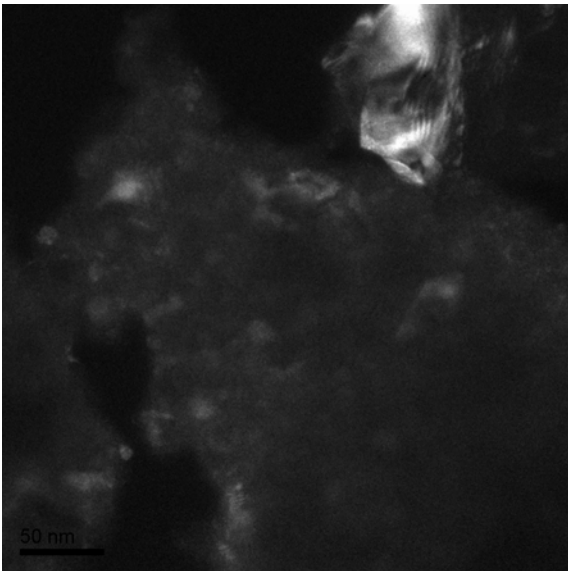
Nanocrystalline LiNbO<sub>3</sub> HEBM 32 h (site 2)



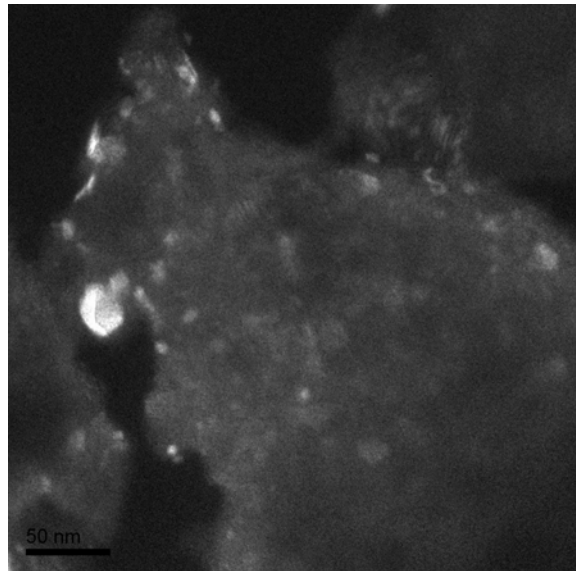
B-STEM02.dm4



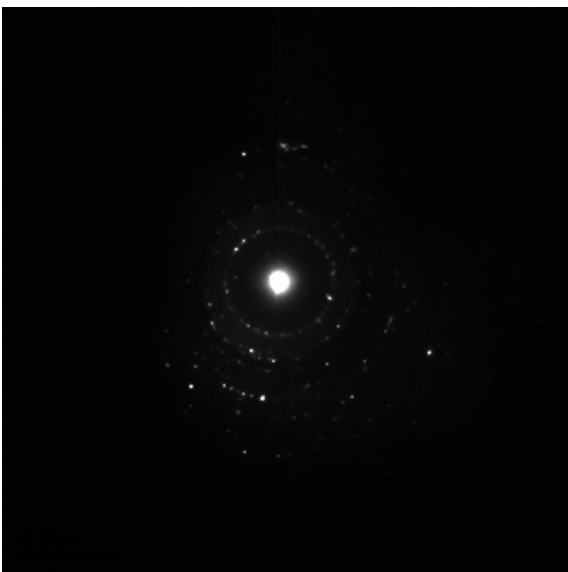
B-02-BF



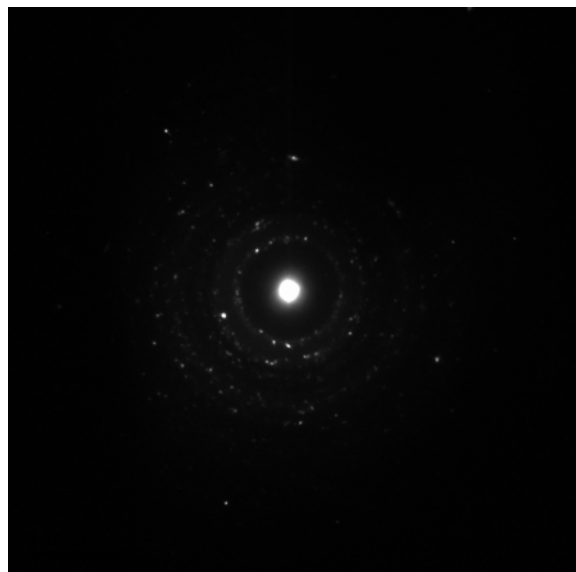
B-BF01



B-BF02

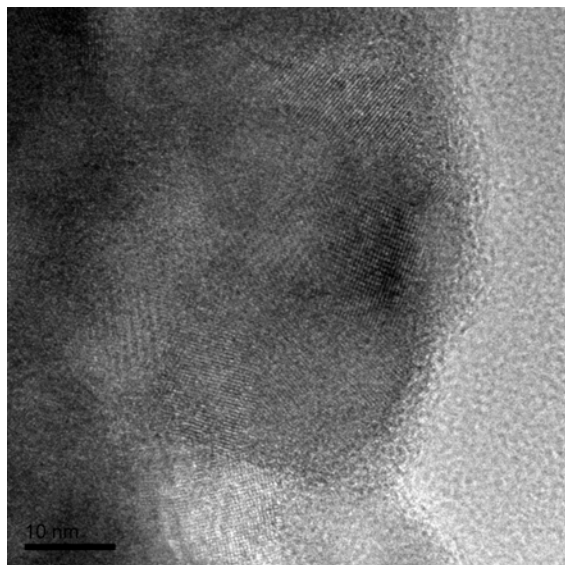


B-SAED-10microns

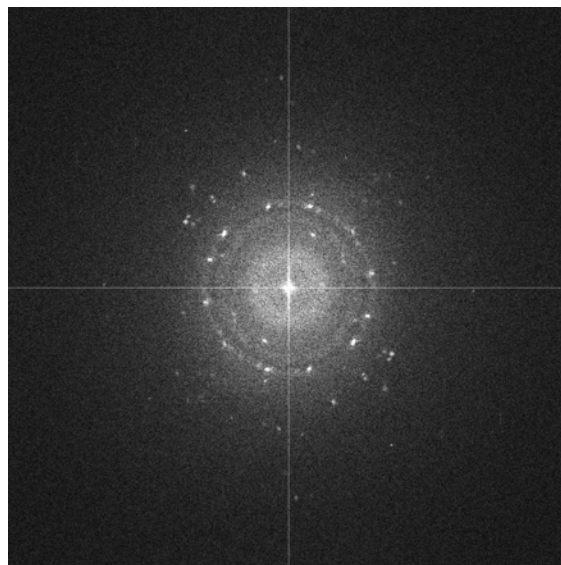


B-SAED

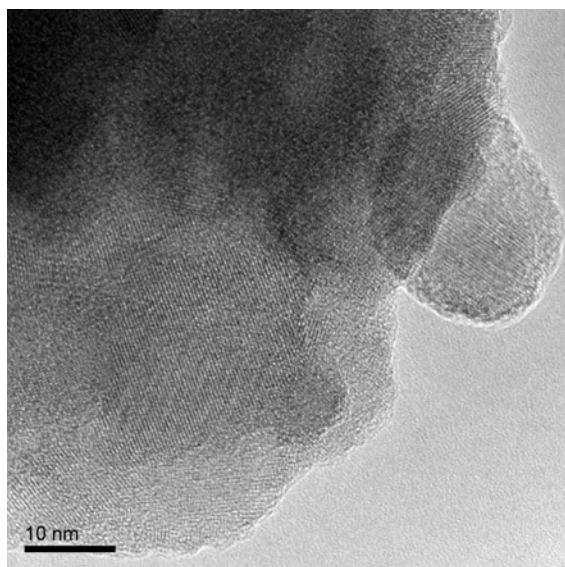
Nanocrystalline  $\text{LiNbO}_3$  HEBM 32 h (site 3)



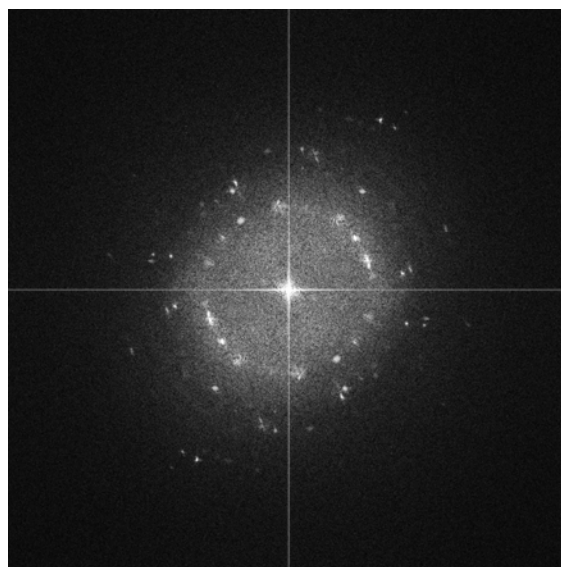
B-HRTEM01



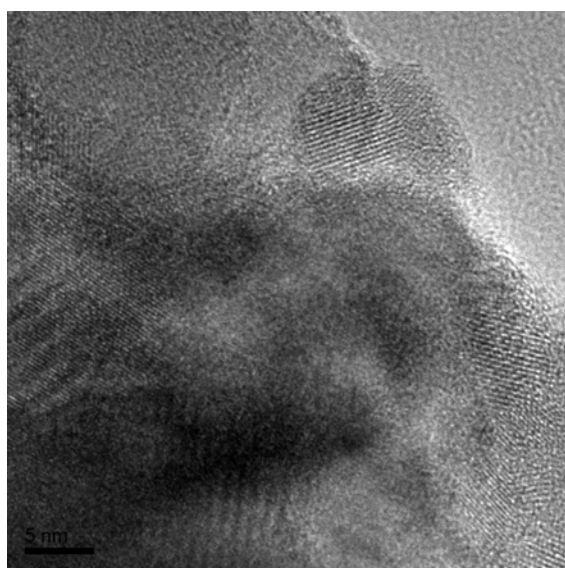
B-HRTEM01-FFT



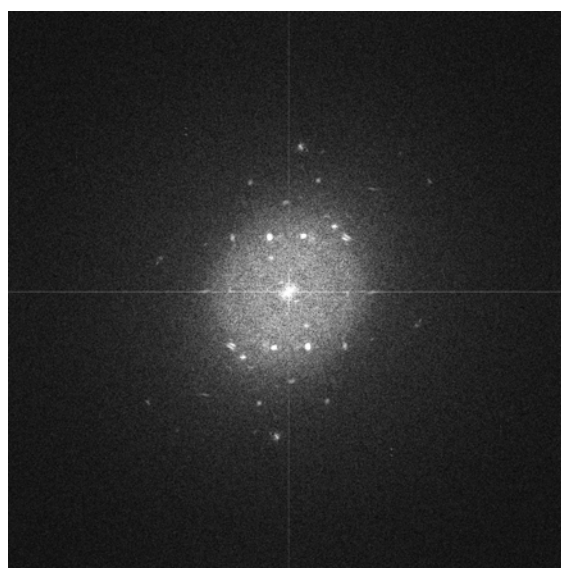
B-HRTEM03



B-HRTEM03-FFT

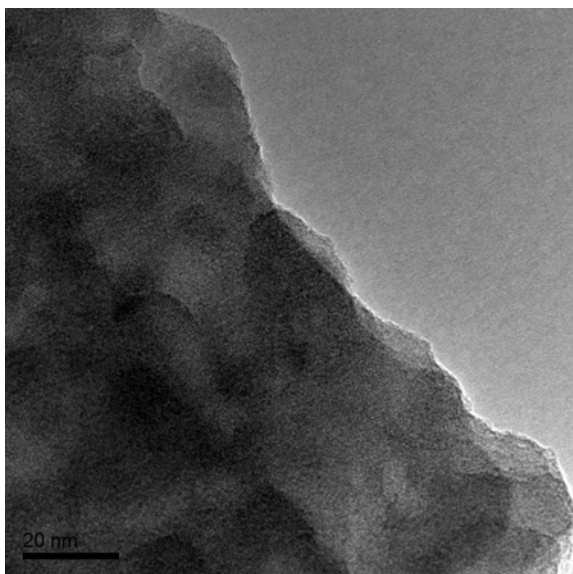


B-HRTEM04

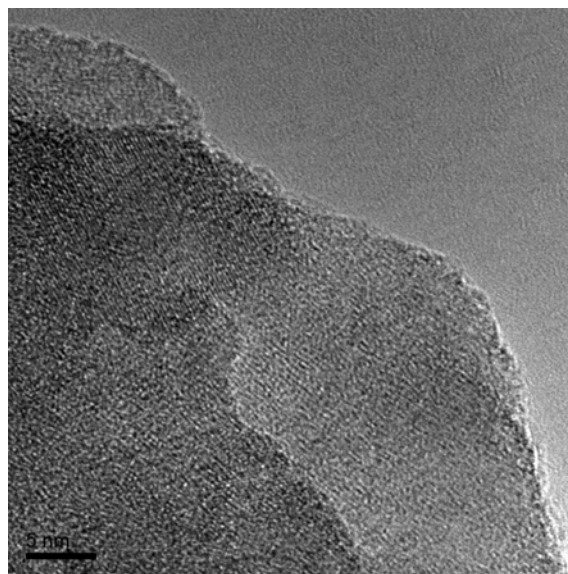


B-HRTEM04-FFT

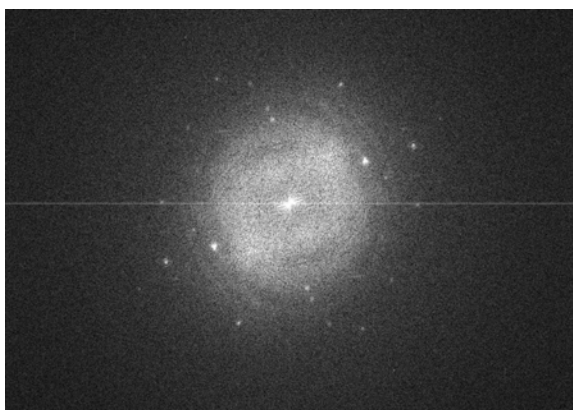
Nanocrystalline LiNbO<sub>3</sub> HEBM 32 h (site 4)



B-BF

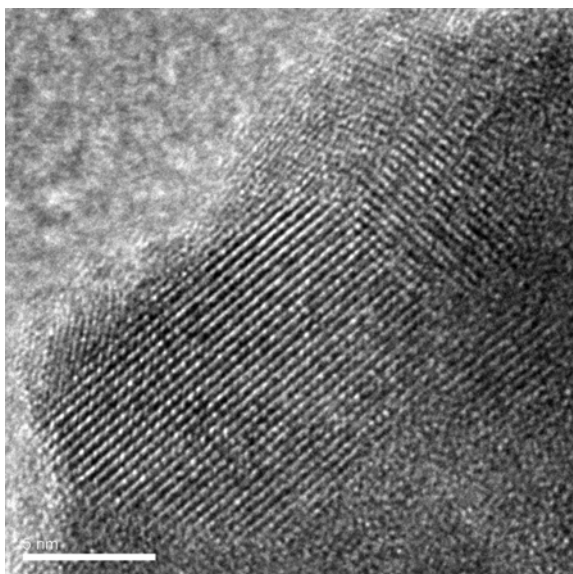


B-HRTEM01

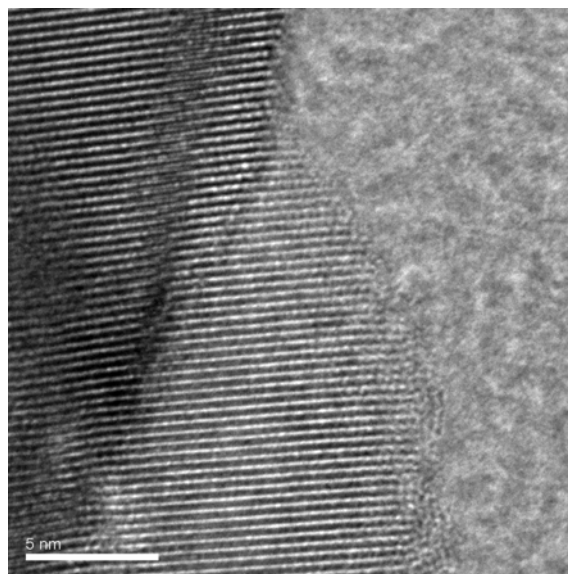


B-HRTEM01-FFT

Nanocrystalline LiNbO<sub>3</sub> HEBM 32 h (site 5)

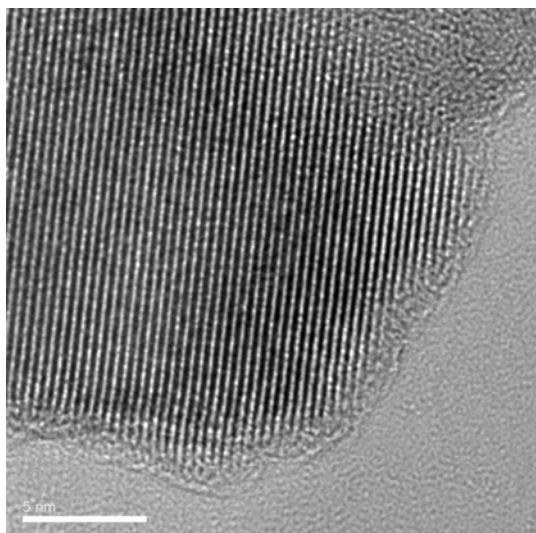


B-HRTEM01

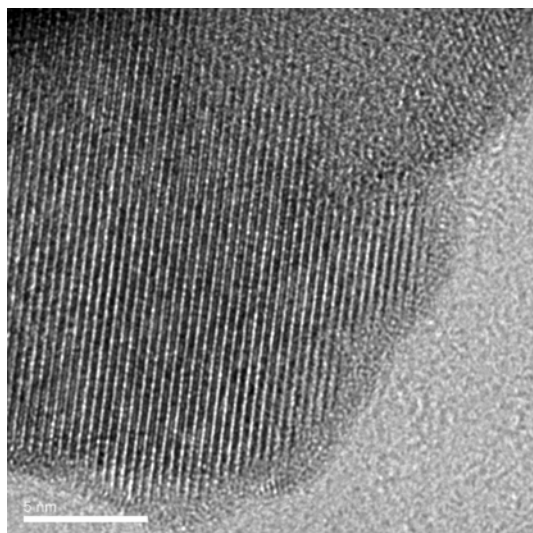


B-HRTEM02

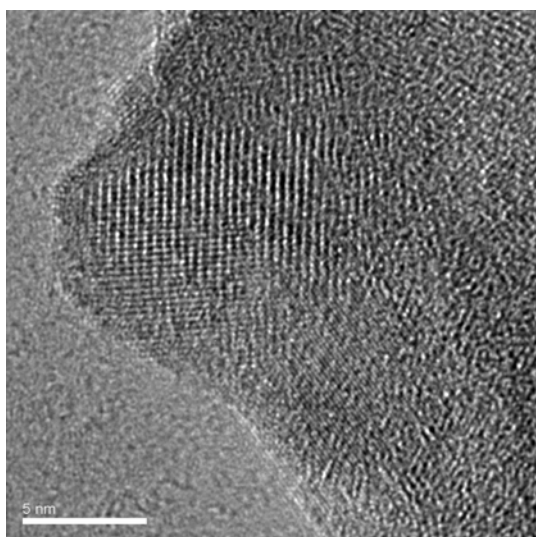
Nanocrystalline  $\text{LiNbO}_3$  HEBM 32 h (site 6)



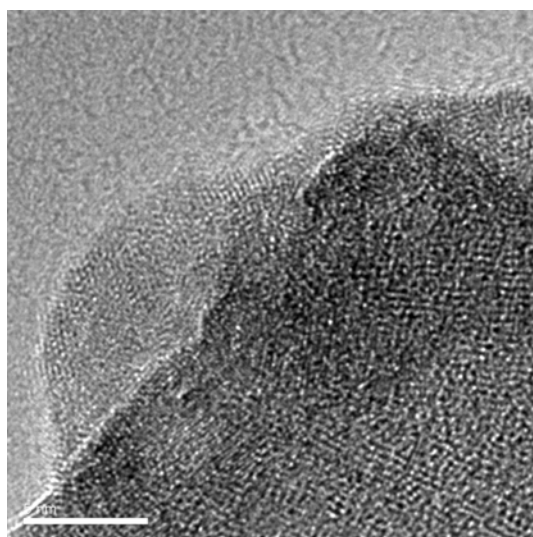
B-HRTEM01



B-HRTEM02

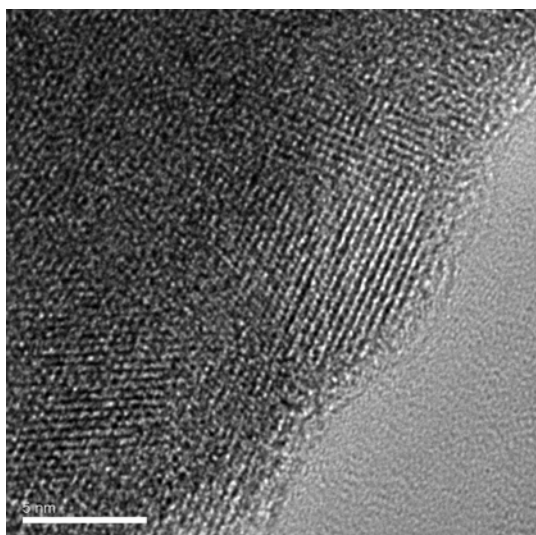


B-HRTEM03

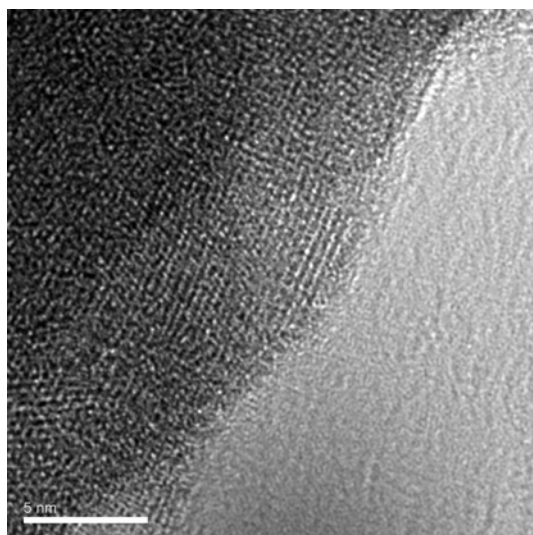


B-HRTEM04

Nanocrystalline  $\text{LiNbO}_3$  HEBM 32 h (site 7)

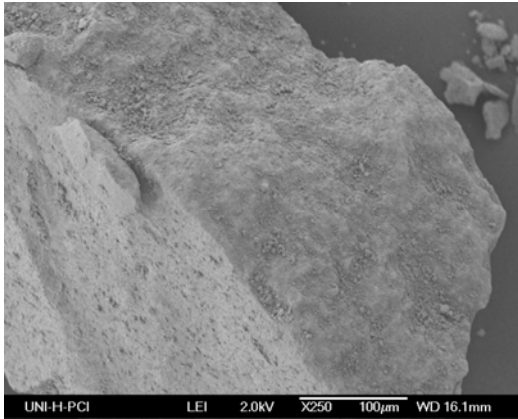


B-HRTEM03

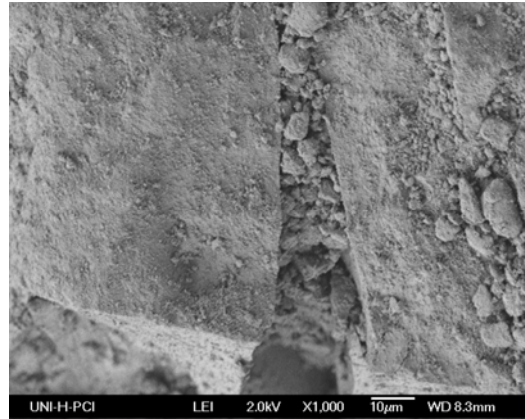


B-HRTEM03-elastisch

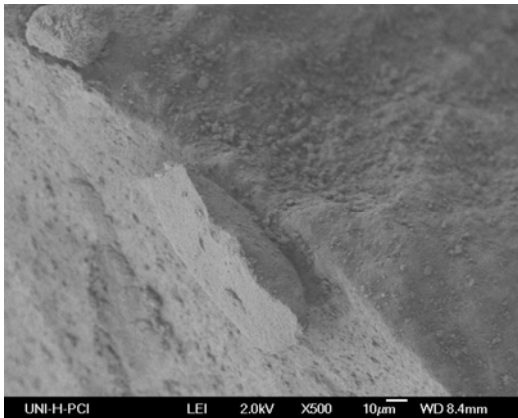
SEM images for Nanocrystalline  $\text{LiNbO}_3$  Prepared by Sol-gel (heated 1 h at 773 K)



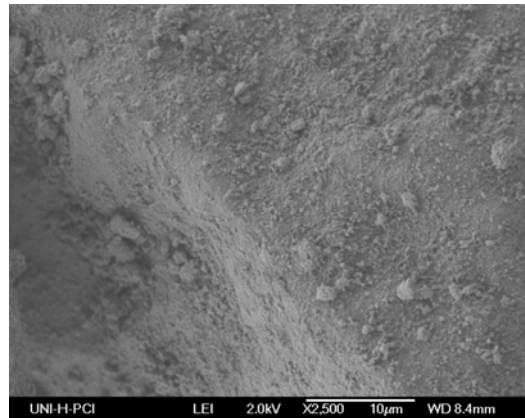
08



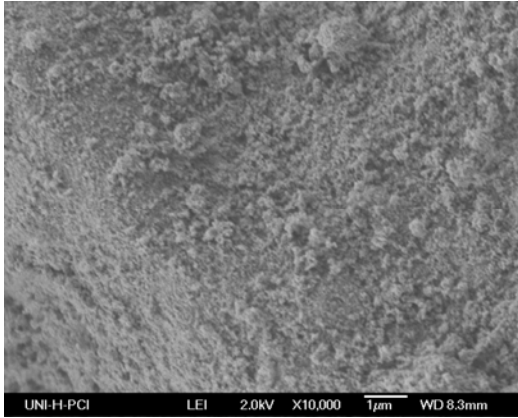
04



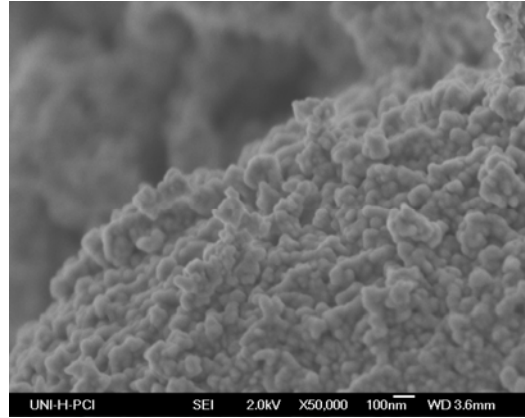
10



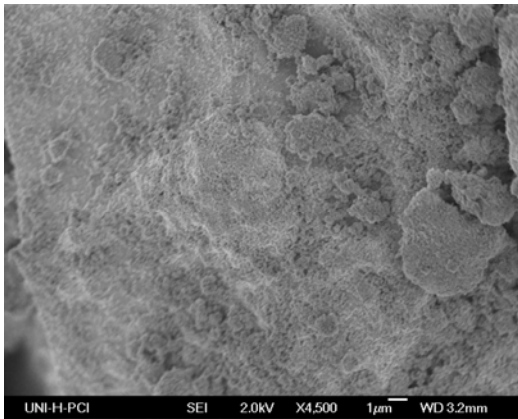
12



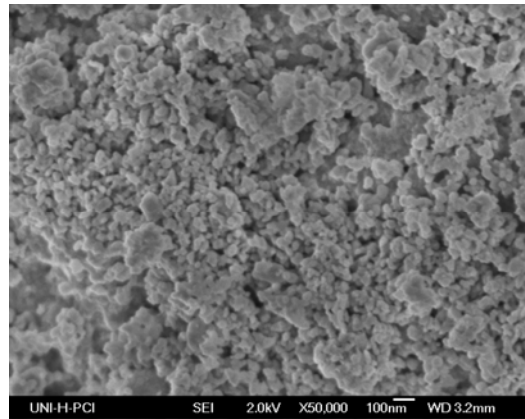
14



20

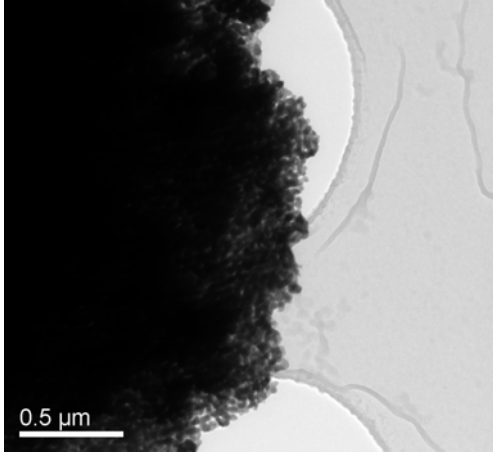


06

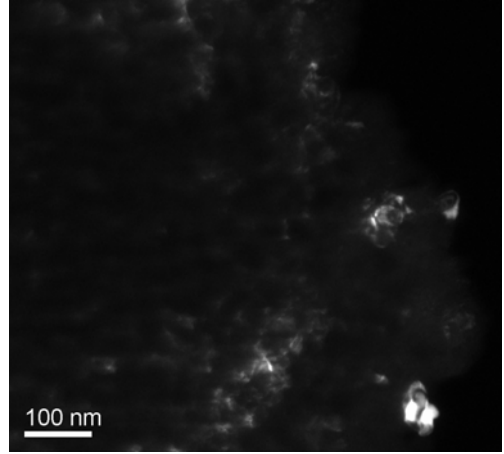


08

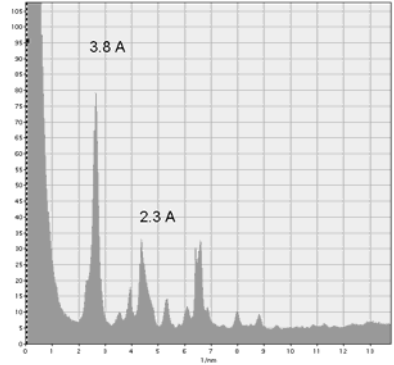
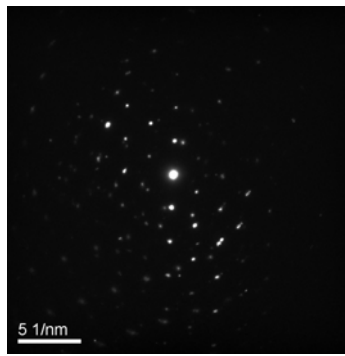
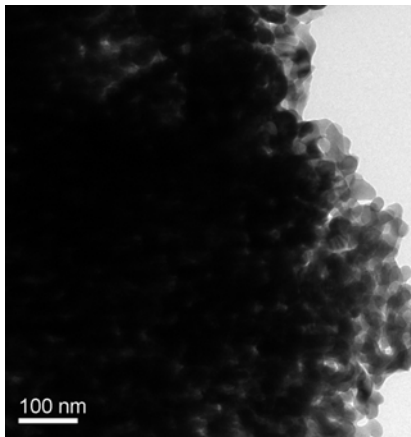
SEM images for Nanocrystalline  $\text{LiNbO}_3$  Prepared by Sol-gel (heated 1 h at 773 K)



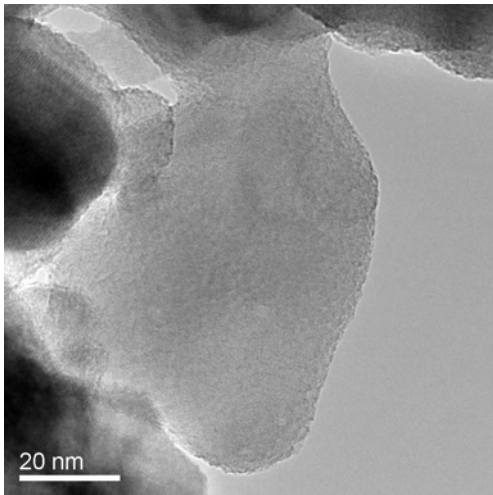
BF01



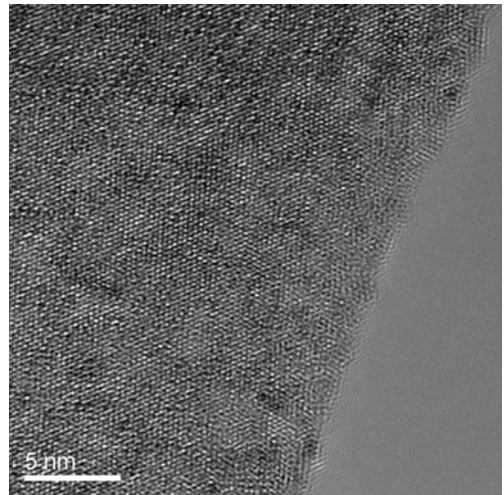
BF02-DF02



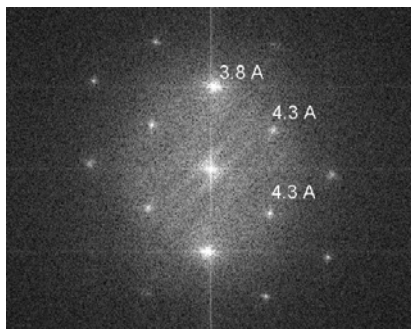
BF02 & BF02-SAED & BF02-SAED-Radial Intensity



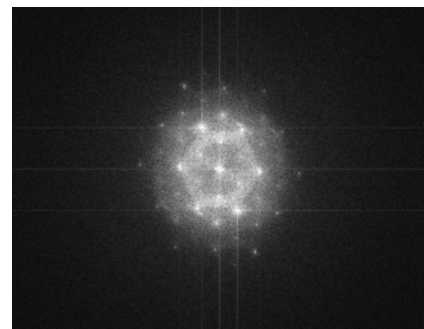
BF02-HRTEM02



BF02-HRTEM03



BF02-HRTEM01-FFTb



BF02-HRTEM03-FTT

A.3 Moynihan's Tables for fitting the dielectric Modulus

Tables for the relaxation function  $N^*(\omega)$  based on the Decay function:

$$\varphi(t) = \exp\left[-\left(\frac{t}{\tau}\right)^\beta\right] = \sum_{i=1}^n g_i \exp\left(-\frac{t}{\tau_i}\right)$$

$$N^*(\omega) = N'(\omega) - iN''(\omega)$$

$$= \sum_{i=1}^n g_i \left[ \frac{1}{1+(\omega\tau_i)^2} \right] - i \sum_{i=1}^n g_i \left[ \frac{\omega\tau_i}{1+(\omega\tau_i)^2} \right]$$

Table A:  $(1-N'(\omega))$  as a function of  $\log \omega\tau_0$  and  $\beta$

$\beta$ Log( $\omega\tau_0$ )	1.00	0.95	0.90	0.85	0.80	0.75	0.70	0.65	0.60	0.55	0.50	0.45	0.40	0.35	0.30
-3.0	0.000	0.000	0.000	0.000	0.000	0.000	0.000	0.000	0.000	0.000	0.000	0.000	0.000	0.000	0.001
-2.8	0.000	0.000	0.000	0.000	0.000	0.000	0.000	0.000	0.000	0.000	0.000	0.000	0.000	0.001	0.002
-2.6	0.000	0.000	0.000	0.000	0.000	0.000	0.000	0.000	0.000	0.000	0.000	0.000	0.000	0.001	0.005
-2.4	0.000	0.000	0.000	0.000	0.000	0.000	0.000	0.000	0.000	0.000	0.000	0.000	0.001	0.003	0.009
-2.2	0.000	0.000	0.000	0.001	0.001	0.001	0.001	0.000	0.000	0.000	0.000	0.001	0.002	0.006	0.017
-2.0	0.000	0.000	0.001	0.001	0.001	0.001	0.001	0.001	0.000	0.000	0.001	0.002	0.005	0.012	0.029
-1.8	0.000	0.001	0.001	0.001	0.002	0.002	0.002	0.001	0.001	0.001	0.003	0.006	0.011	0.023	0.045
-1.6	0.001	0.001	0.001	0.002	0.002	0.002	0.002	0.002	0.003	0.004	0.007	0.012	0.023	0.041	0.068
-1.4	0.002	0.002	0.002	0.002	0.002	0.003	0.004	0.005	0.007	0.011	0.016	0.026	0.043	0.067	0.098
-1.2	0.004	0.004	0.003	0.004	0.004	0.006	0.008	0.012	0.017	0.025	0.035	0.051	0.073	0.101	0.133
-1.0	0.010	0.010	0.010	0.011	0.013	0.016	0.021	0.028	0.038	0.052	0.069	0.090	0.116	0.145	0.176
-0.8	0.025	0.026	0.029	0.033	0.038	0.045	0.054	0.065	0.080	0.098	0.120	0.144	0.170	0.196	0.222
-0.6	0.059	0.066	0.074	0.083	0.094	0.105	0.119	0.134	0.151	0.170	0.191	0.212	0.233	0.253	0.272
-0.4	0.137	0.149	0.161	0.174	0.188	0.203	0.218	0.233	0.249	0.264	0.278	0.291	0.303	0.314	0.324
-0.2	0.285	0.294	0.304	0.314	0.324	0.334	0.344	0.353	0.361	0.367	0.371	0.374	0.376	0.377	0.377
0.0	0.500	0.499	0.497	0.495	0.493	0.491	0.487	0.483	0.478	0.472	0.465	0.457	0.448	0.439	0.430
0.2	0.715	0.702	0.688	0.673	0.657	0.641	0.624	0.607	0.589	0.571	0.554	0.536	0.518	0.500	0.481
0.4	0.863	0.843	0.823	0.801	0.778	0.755	0.731	0.707	0.682	0.657	0.632	0.607	0.582	0.556	0.530
0.6	0.941	0.921	0.901	0.879	0.857	0.833	0.809	0.783	0.757	0.729	0.701	0.672	0.641	0.610	0.577
0.8	0.975	0.960	0.943	0.926	0.907	0.886	0.864	0.841	0.816	0.788	0.759	0.727	0.693	0.658	0.621
1.0	0.990	0.980	0.968	0.955	0.940	0.924	0.905	0.884	0.861	0.835	0.806	0.774	0.740	0.702	0.661
1.2	0.996	0.990	0.983	0.974	0.963	0.950	0.934	0.916	0.896	0.872	0.845	0.814	0.780	0.741	0.699
1.4	0.998	0.995	0.990	0.984	0.976	0.966	0.954	0.939	0.921	0.901	0.876	0.847	0.814	0.776	0.732
1.6	0.999	0.997	0.994	0.989	0.983	0.976	0.967	0.955	0.941	0.923	0.901	0.875	0.844	0.806	0.763
1.8	1.000	0.998	0.995	0.992	0.988	0.983	0.976	0.967	0.955	0.940	0.921	0.898	0.869	0.833	0.790
2.0	1.000	0.999	0.997	0.995	0.992	0.988	0.983	0.976	0.966	0.954	0.938	0.917	0.890	0.857	0.815
2.2	1.000	0.999	0.999	0.997	0.995	0.992	0.988	0.982	0.975	0.964	0.951	0.932	0.908	0.877	0.838
2.4	1.000	1.000	0.999	0.998	0.997	0.995	0.992	0.987	0.981	0.972	0.960	0.945	0.923	0.894	0.857
2.6	1.000	1.000	0.999	0.999	0.998	0.996	0.994	0.990	0.985	0.978	0.968	0.955	0.936	0.910	0.874
2.8	1.000	1.000	0.999	0.999	0.998	0.997	0.995	0.993	0.989	0.983	0.975	0.963	0.946	0.923	0.890
3.0	1.000	1.000	1.000	0.999	0.999	0.998	0.997	0.995	0.992	0.987	0.980	0.970	0.955	0.934	0.904
3.2	1.000	1.000	1.000	1.000	0.999	0.999	0.998	0.996	0.994	0.990	0.985	0.976	0.963	0.944	0.916
3.4	1.000	1.000	1.000	1.000	1.000	0.999	0.998	0.997	0.995	0.992	0.988	0.980	0.969	0.952	0.926
3.6	1.000	1.000	1.000	1.000	1.000	0.999	0.999	0.998	0.996	0.994	0.990	0.984	0.974	0.958	0.935
3.8	1.000	1.000	1.000	1.000	1.000	1.000	0.999	0.998	0.997	0.995	0.992	0.987	0.978	0.964	0.943
4.0	1.000	1.000	1.000	1.000	1.000	1.000	0.999	0.999	0.998	0.996	0.993	0.989	0.982	0.970	0.951



Table B:  $N''(\omega)$  as a function of  $\log \omega\tau_0$  and  $\beta$

$\beta$	1.00	0.95	0.90	0.85	0.80	0.75	0.70	0.65	0.60	0.55	0.50	0.45	0.40	0.35	0.30
Log( $\omega\tau_0$ )															
-3.0	0.001	0.001	0.001	0.001	0.001	0.001	0.001	0.001	0.002	0.002	0.002	0.002	0.003	0.005	0.009
-2.8	0.002	0.002	0.002	0.002	0.002	0.002	0.002	0.002	0.002	0.003	0.003	0.004	0.005	0.008	0.014
-2.6	0.003	0.003	0.003	0.003	0.003	0.003	0.003	0.004	0.004	0.004	0.005	0.006	0.008	0.012	0.020
-2.4	0.004	0.004	0.004	0.005	0.005	0.005	0.005	0.006	0.006	0.007	0.008	0.010	0.013	0.019	0.030
-2.2	0.006	0.007	0.007	0.007	0.008	0.008	0.008	0.009	0.010	0.011	0.013	0.016	0.020	0.029	0.041
-2.0	0.010	0.010	0.011	0.011	0.012	0.012	0.013	0.014	0.015	0.017	0.020	0.024	0.032	0.042	0.056
-1.8	0.016	0.016	0.016	0.017	0.018	0.018	0.020	0.021	0.024	0.027	0.031	0.038	0.047	0.060	0.072
-1.6	0.025	0.025	0.025	0.026	0.027	0.029	0.031	0.034	0.038	0.042	0.049	0.057	0.069	0.081	0.090
-1.4	0.040	0.040	0.040	0.041	0.043	0.045	0.048	0.053	0.059	0.066	0.074	0.084	0.095	0.104	0.108
-1.2	0.063	0.064	0.065	0.067	0.069	0.073	0.077	0.083	0.090	0.099	0.108	0.118	0.125	0.128	0.125
-1.0	0.099	0.101	0.104	0.108	0.112	0.116	0.122	0.128	0.135	0.142	0.149	0.154	0.155	0.150	0.141
-0.8	0.155	0.159	0.164	0.169	0.174	0.179	0.184	0.188	0.191	0.193	0.193	0.189	0.181	0.169	0.153
-0.6	0.236	0.241	0.245	0.248	0.252	0.254	0.254	0.253	0.250	0.243	0.233	0.220	0.203	0.184	0.162
-0.4	0.344	0.342	0.339	0.335	0.331	0.325	0.317	0.307	0.295	0.279	0.260	0.239	0.217	0.192	0.167
-0.2	0.451	0.439	0.425	0.411	0.395	0.378	0.360	0.340	0.319	0.296	0.272	0.247	0.222	0.196	0.169
0.0	0.500	0.481	0.461	0.440	0.418	0.394	0.370	0.346	0.321	0.296	0.271	0.246	0.220	0.194	0.168
0.2	0.451	0.435	0.418	0.400	0.381	0.361	0.341	0.320	0.299	0.278	0.256	0.234	0.212	0.188	0.164
0.4	0.344	0.336	0.328	0.319	0.310	0.300	0.289	0.277	0.264	0.250	0.234	0.217	0.199	0.179	0.158
0.6	0.236	0.237	0.238	0.238	0.237	0.236	0.233	0.230	0.224	0.217	0.208	0.196	0.183	0.168	0.150
0.8	0.155	0.161	0.167	0.172	0.177	0.181	0.184	0.185	0.185	0.184	0.180	0.174	0.165	0.154	0.141
1.0	0.099	0.107	0.116	0.123	0.130	0.137	0.142	0.147	0.150	0.153	0.153	0.152	0.148	0.141	0.131
1.2	0.063	0.070	0.078	0.086	0.093	0.100	0.107	0.114	0.120	0.125	0.128	0.130	0.130	0.127	0.121
1.4	0.040	0.045	0.051	0.058	0.064	0.072	0.079	0.086	0.094	0.100	0.106	0.111	0.113	0.114	0.110
1.6	0.025	0.029	0.033	0.038	0.044	0.051	0.058	0.065	0.073	0.080	0.087	0.094	0.098	0.101	0.101
1.8	0.016	0.019	0.022	0.026	0.031	0.037	0.043	0.049	0.057	0.064	0.071	0.078	0.084	0.089	0.091
2.0	0.010	0.013	0.015	0.019	0.022	0.027	0.032	0.037	0.044	0.051	0.058	0.065	0.072	0.078	0.082
2.2	0.006	0.008	0.010	0.013	0.016	0.019	0.023	0.028	0.033	0.040	0.047	0.054	0.061	0.068	0.073
2.4	0.004	0.005	0.007	0.008	0.011	0.013	0.017	0.021	0.025	0.031	0.037	0.045	0.052	0.059	0.065
2.6	0.003	0.003	0.004	0.005	0.007	0.009	0.012	0.015	0.019	0.024	0.030	0.037	0.044	0.051	0.058
2.8	0.002	0.002	0.003	0.004	0.005	0.007	0.009	0.011	0.015	0.019	0.024	0.030	0.037	0.045	0.052
3.0	0.001	0.001	0.002	0.003	0.004	0.005	0.007	0.009	0.012	0.015	0.020	0.025	0.031	0.039	0.046
3.2	0.001	0.001	0.001	0.002	0.003	0.004	0.005	0.006	0.009	0.012	0.016	0.020	0.026	0.033	0.040
3.4	0.000	0.001	0.001	0.001	0.002	0.002	0.003	0.005	0.006	0.009	0.012	0.016	0.022	0.028	0.035
3.6	0.000	0.000	0.001	0.001	0.001	0.002	0.002	0.003	0.005	0.007	0.009	0.013	0.018	0.024	0.031
3.8	0.000	0.000	0.000	0.001	0.001	0.001	0.002	0.003	0.004	0.005	0.008	0.011	0.016	0.021	0.028
4.0	0.000	0.000	0.000	0.000	0.001	0.001	0.001	0.002	0.003	0.004	0.007	0.009	0.013	0.019	0.025

- Computer generated values of  $[1-N'(\omega)]$  and  $N''(\omega)$  have been rounded to off to the nearest integer in the third decimal place.

-  $[1-N'(\omega)]$  and  $N''(\omega)$  values for  $\beta$  values that are not tabulated may be obtained by linear interpolation at a fixed frequency.

#### A.4 Error accumulation caused by errors in $^{18}\text{O}$ concentration measurements by SIMS

Simple error estimation is possible in the following way: Eq. (6.3.7) can be approximated with errors less than 10 % for  $t/\tau \geq 3$  as follows

$$c_s(t) - c_\infty \cong (c_g - c_\infty) \left( 1 - \frac{1}{\sqrt{\pi}} \sqrt{\frac{\tau}{t}} \right) \quad \text{for } \frac{t}{\tau} \geq 3 \quad (\text{A.4.1})$$

Neglecting the small background value of  $^{18}\text{O}$ ,  $c_\infty$ , and taking into account  $\tau = D/K^2$  we obtain approximately for the surface exchange coefficient

$$K \cong \frac{1}{\sqrt{\pi}} \sqrt{\frac{D}{t}} \frac{c_g}{c_g - c_s} \quad \text{for } \frac{t}{\tau} \geq 3 \quad (\text{A.4.2})$$

Time measurement errors are negligible, so that the error accumulation of  $K$  is generally given by

$$\left| \frac{\Delta K}{K} \right| = \frac{1}{K} \left\{ \left| \frac{\partial K}{\partial D} \Delta D \right| + \left| \frac{\partial K}{\partial c_g} \Delta c_g \right| + \left| \frac{\partial K}{\partial c_s} \Delta c_s \right| \right\} \quad (\text{A.4.3})$$

With equations (A.4.2) and (A.4.3) one gets approximately (taking into account  $D = \sigma^2/(4t)$ )

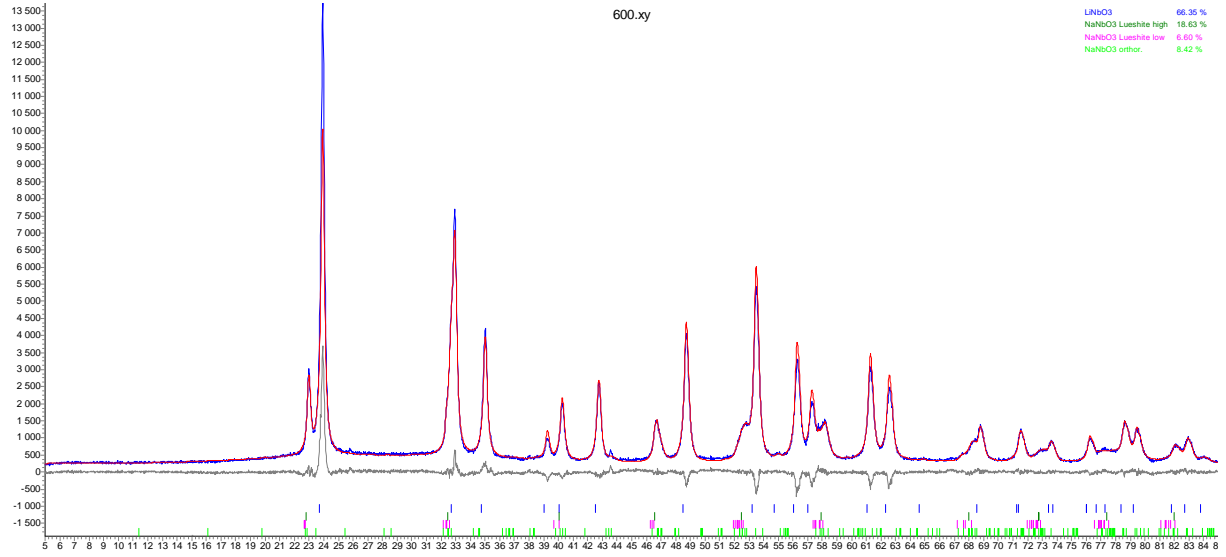
$$\left| \frac{\Delta K}{K} \right| \cong \left| \frac{\Delta x}{x} \right| + \frac{c_s}{c_g - c_s} \left( \left| \frac{\Delta c_g}{c_g} \right| + \left| \frac{\Delta c_s}{c_s} \right| \right) \quad \text{for } \frac{t}{\tau} \geq 3 \quad (\text{A.4.4})$$

where  $\Delta x/x$  is the percentage error of the SIMS crater depth measurement. If one assumes an error of the concentration measurements of about 4% and an error of the SIMS crater depth measurement of about 10% one calculates an error for the  $K$  values measured at 1073 K of about 55% ( $t/\tau \approx 14$ , see Table 7.2.9). Therefore, the scatter of the measured  $K$  values in the Arrhenius diagram (see Fig. 7.2.21(b)) can be explained by error accumulation which is mainly caused by errors of the concentration measurements.

### A.5 Rietveld structure refinement

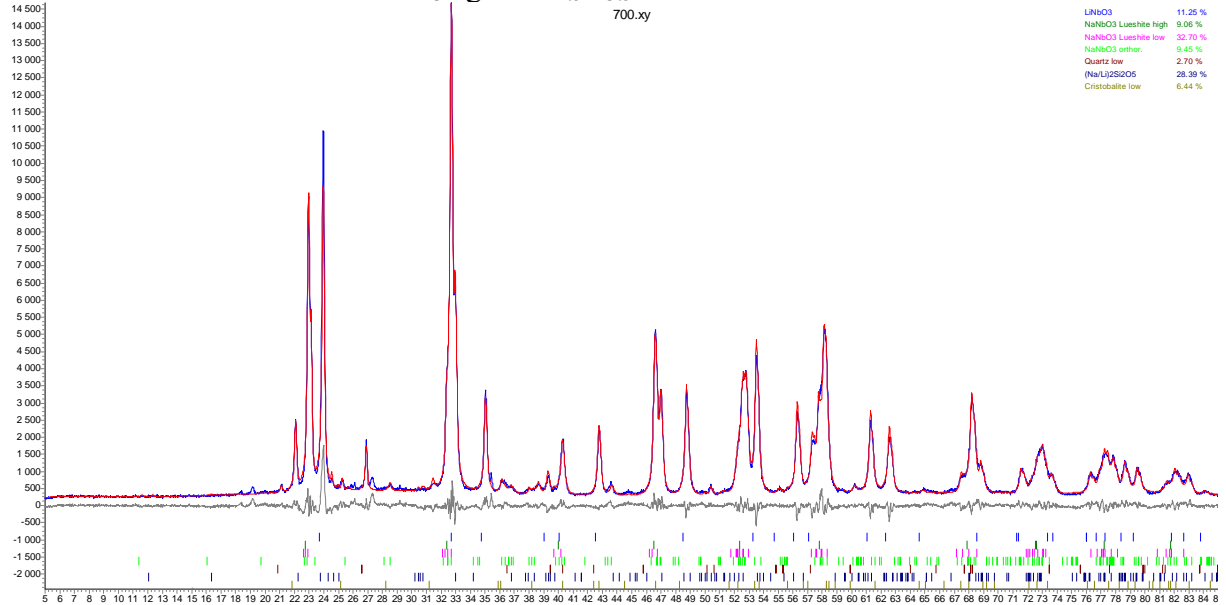
#### A.5.1 Heating Effect in the composite n-LiNbO<sub>3</sub> · g-NaSi<sub>1.5</sub>O<sub>3.5</sub>

n-LiNbO<sub>3</sub> · g-NaSi<sub>1.5</sub>O<sub>3.5</sub> heated for 2 h at 873 K



phase	%	crystallite size (nm)	s. g.	Cryst. sys.	lattice parameters			
					a	b	c	
LiNbO <sub>3</sub>	66.35	36.2237	R 3 c H	Trigonal	5.1565	-	13.8437	
NaNbO <sub>3</sub> Lueshite high	18.63	55.1362	P m -3 m	Cubic	3.8956	-	-	
NaNbO <sub>3</sub> Lueshite low	06.60	101.1784	P 1 2/m 1	Monoclinic	3.9196	3.9129	3.9036	β = 90.71°
NaNbO <sub>3</sub> orthor.	08.42	25.7726	P b m a	Orthorhombic	5.5613	15.5409	5.5002	

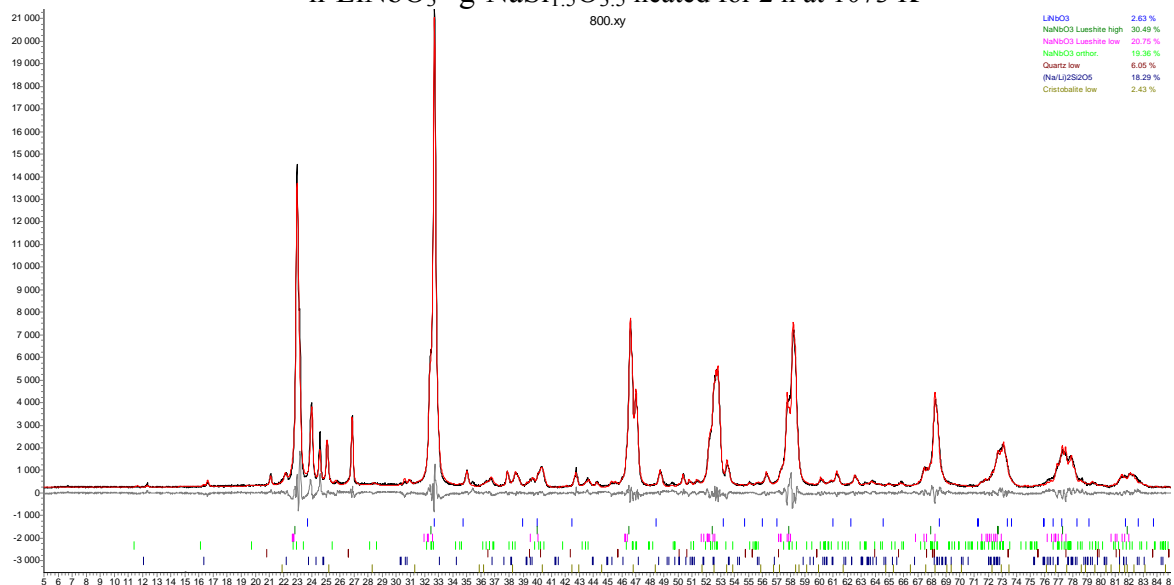
n-LiNbO<sub>3</sub> · g-NaSi<sub>1.5</sub>O<sub>3.5</sub> heated for 2 h at 973 K



phase	%	Crystallite size (nm)	s. g.	Cryst. sys.	lattice parameters			
					a	b	c	
LiNbO <sub>3</sub>	11.25	57.91366	R 3 c H	Trigonal	5.157490		13.8400	
NaNbO <sub>3</sub> Lueshite high	9.06	78.02710	P m -3 m	Cubic	3.900375			
NaNbO <sub>3</sub> Lueshite low	32.70	252.52247	P 1 2/m 1	Monoclinic	3.926284	3.920427	3.91261	β = 90.91°
NaNbO <sub>3</sub> orthor.	9.45	56.82099	P b m a	Orthorhombic	5.565713	15.53646	5.512832	
Quartz low	2.70	74.37845	P 3 2 1	Trigonal	4.917407		5.405329	
(Na,Li) <sub>2</sub> Si <sub>2</sub> O <sub>5</sub>	28.39	140.06978	C 1 c 1	Monoclinic	5.831111	14.64911	4.764476	β = 89.39°
Cristobalite low	6.44	65.793	P 4 1 2 1 2	Tetragonal	5.002070		6.993845	

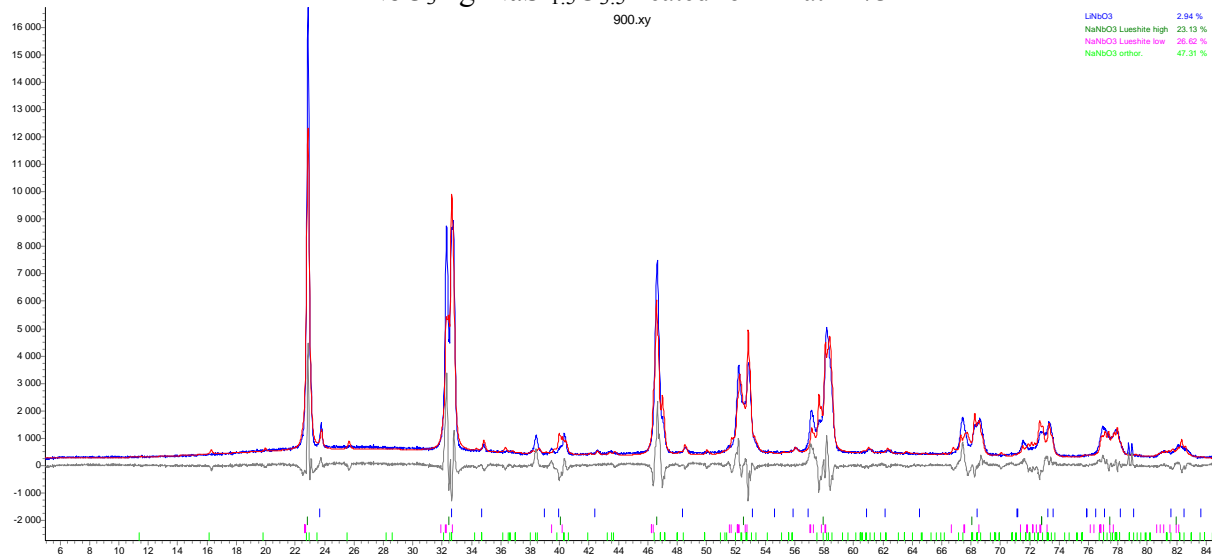
Appendixes

n-LiNbO<sub>3</sub> · g-NaSi<sub>1.5</sub>O<sub>3.5</sub> heated for 2 h at 1073 K

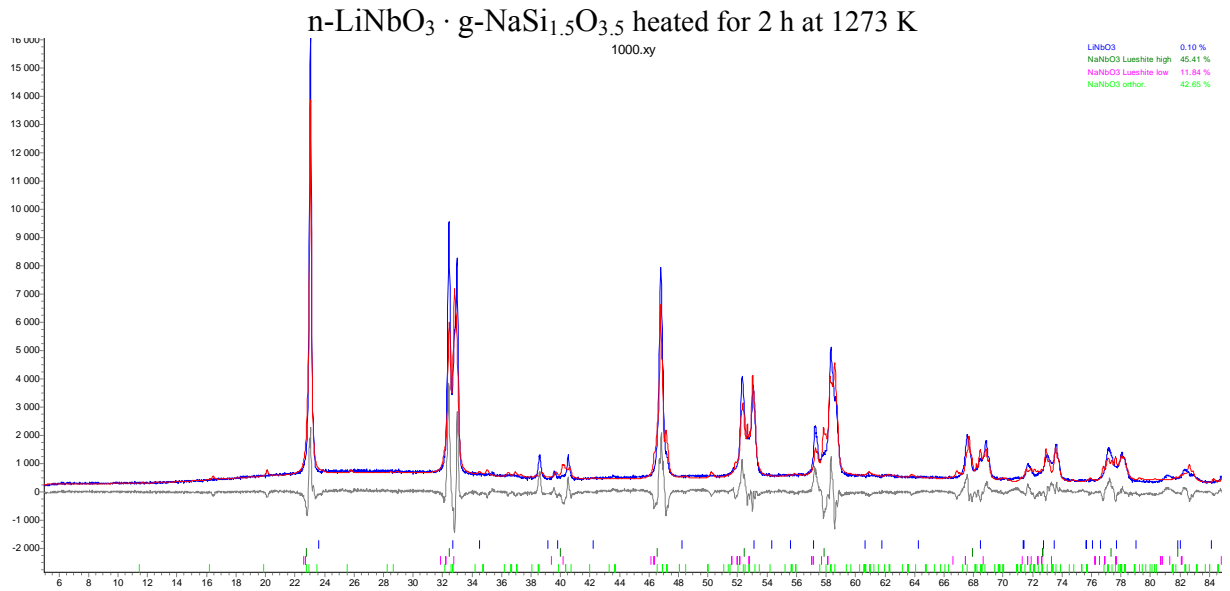


phase	%	crystallite size (nm)	s. g.	Cryst. sys.	Lattice parameters			
					a	B	c	
LiNbO <sub>3</sub>	2.63	67.6553	R 3 c H	Trigonal	5.1595		13.8509	
NaNbO <sub>3</sub> Lueshite high	30.49	85.83271	P m -3 m	Cubic	3.9002			
NaNbO <sub>3</sub> Lueshite low	20.75	116.5818	P 1 2/m 1	Monoclinic	3.9281	3.9215	3.9130	$\beta = 91.07^\circ$
NaNbO <sub>3</sub> orthor.	19.36	63.4087	P b m a	Orthorhombic	5.5684	15.5287	5.5074	
Quartz low	6.05		P 3 2 1	Trigonal				
(Na/Li) <sub>2</sub> Si <sub>2</sub> O <sub>5</sub>	18.29		C 1 c 1	Monoclinic				
Cristobalite low	2.43							

n-LiNbO<sub>3</sub> · g-NaSi<sub>1.5</sub>O<sub>3.5</sub> heated for 2 h at 1173 K



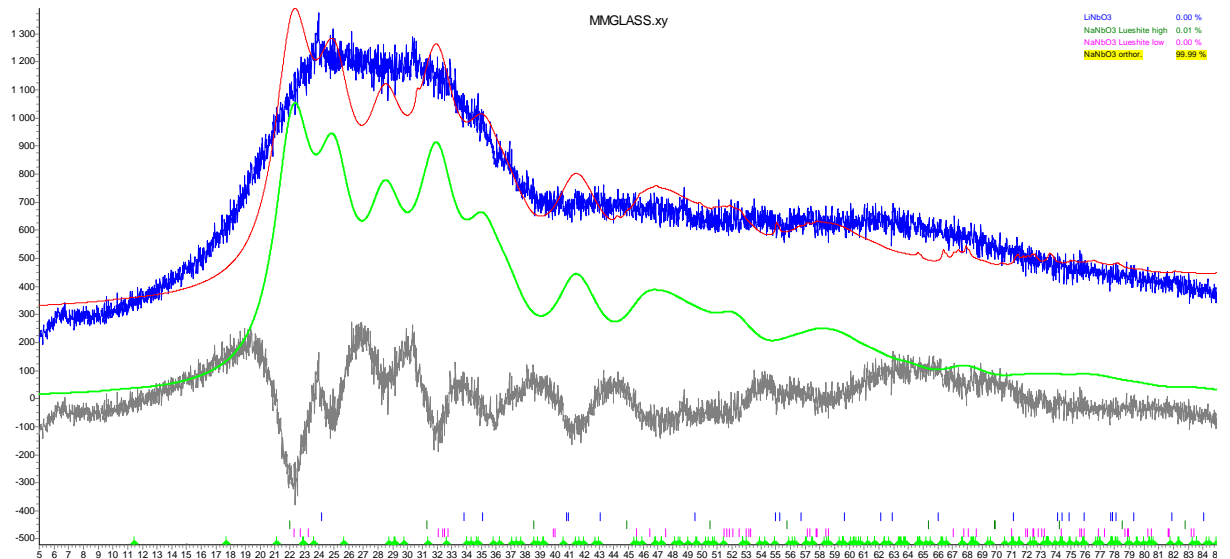
phase	%	crystallite size (nm)	s. g.	Cryst. sys.	lattice parameters			
					A	b	c	
LiNbO <sub>3</sub>	02.94	78.7177	R 3 c H	Trigonal	5.1677	-	13.8641	
NaNbO <sub>3</sub> Lueshite high	23.13	138.1501	P m -3 m	Cubic	3.8950	-	-	
NaNbO <sub>3</sub> Lueshite low	26.62	79.3451	P 1 2/m 1	Monoclinic	3.9243	3.9220	3.9125	$\beta = 91.39^\circ$
NaNbO <sub>3</sub> orthor.	47.31	77.4768	P b m a	Orthorhombic	5.5701	15.5004	5.4791	



phase	%	crystallite size (nm)	Space group	Cryst. sys.	lattice parameters			
					a	b	c	
LiNbO <sub>3</sub>	00.10	114.6803	R 3 c H	Trigonal	5.1970	-	13.7990	
NaNbO <sub>3</sub> Lueshite high	45.41	130.2393	P m -3 m	Cubic	3.8995	-	-	
NaNbO <sub>3</sub> Lueshite low	11.84	74.7673	P 1 2/m 1	Monoclinic	3.9174	3.9348	3.9162	$\beta = 91.50^\circ$
NaNbO <sub>3</sub> orthor.	42.65	72.9257	P b m a	Orthorhombic	5.5635	15.4810	5.4681	

### A.5.2 Composition Effect in the composite (x)n-LiNbO<sub>3</sub> · (1-x)g-NaSi<sub>1.5</sub>O<sub>3.5</sub>

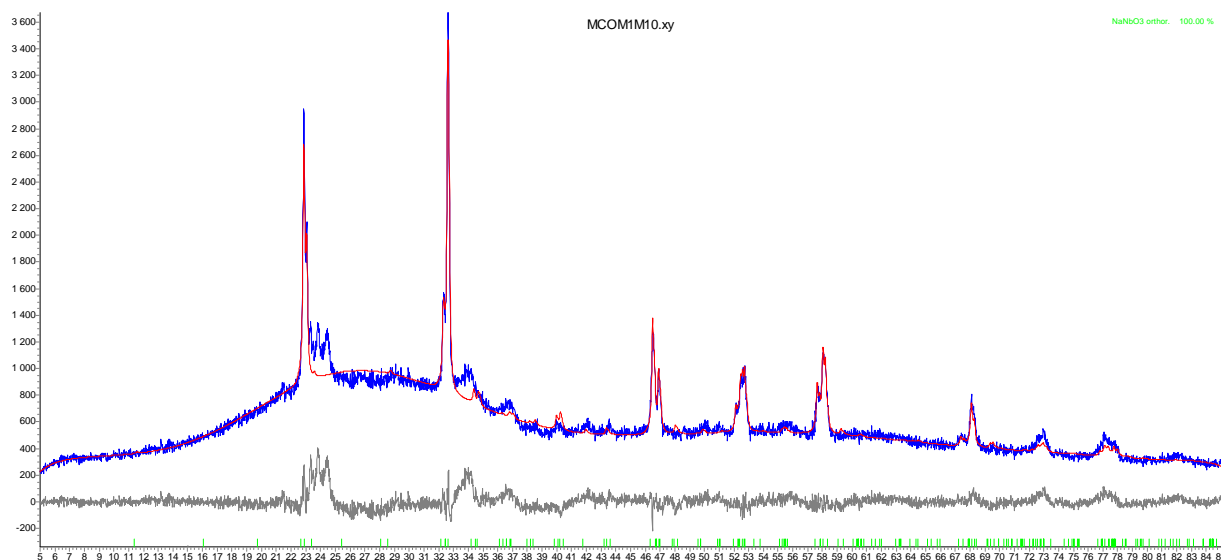
0.0n-LiNbO<sub>3</sub> · 1.0g-NaSi<sub>1.5</sub>O<sub>3.5</sub> [Na<sub>2</sub>Si<sub>3</sub>O<sub>7</sub> glass] heated for 2 h at 1173 K



Grain size is limited to 3nm but must be smaller

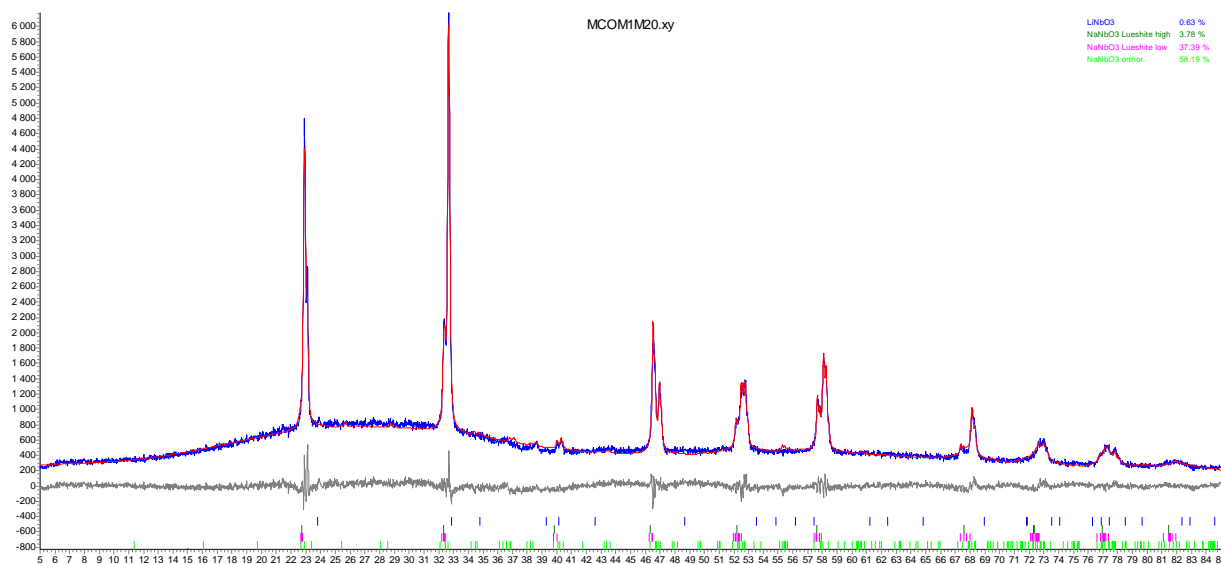
Appendix

0.1n-LiNbO<sub>3</sub> · 0.9g-NaSi<sub>1.5</sub>O<sub>3.5</sub> heated for 2 h at 1173 K



phase	%	crystallite size (nm)	s. g.	Cryst. Sys.	Lattice parameters			
					a	b	c	
NaNbO <sub>3</sub> orthorhombic	100.00	81.93	P b m a	Orthorhombic	5.5674	15.5397	5.5137	c = 5.3605

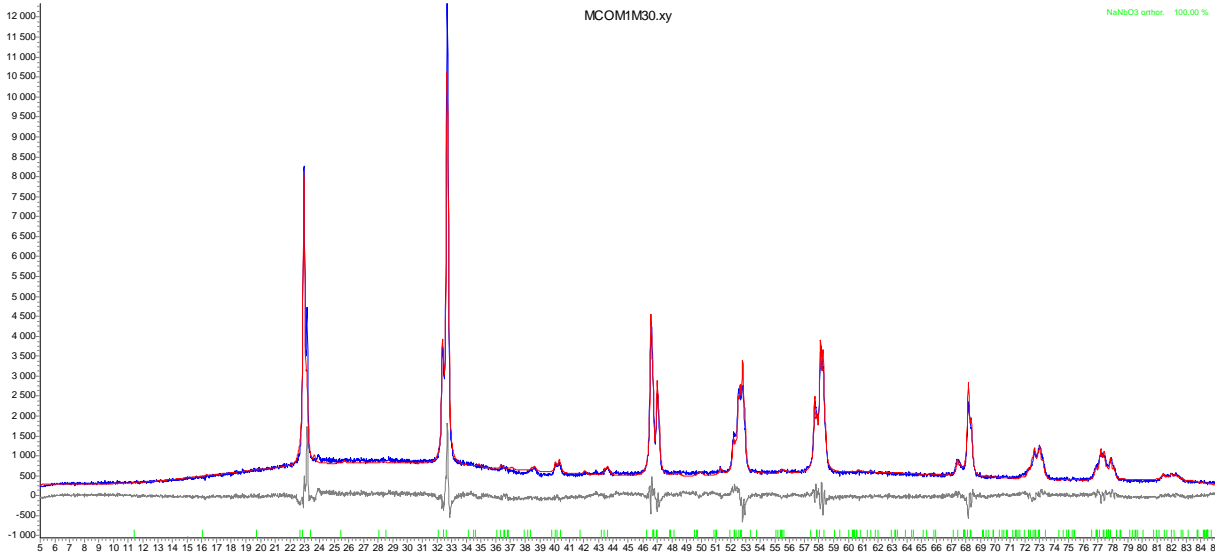
0.2n-LiNbO<sub>3</sub> · 0.8g-NaSi<sub>1.5</sub>O<sub>3.5</sub> heated for 2 h at 1173 K



phase	%	crystallite size (nm)	s.g.	Cryst. Sys.	lattice parameters			
					a	b	c	
LiNbO <sub>3</sub>	00.63	7.1804	R 3 c H	Trigonal	5.1491	-	13.7385	
NaNbO <sub>3</sub> Lueshite high	03.78	3.0000	P m -3 m	Cubic	3.9160	-	-	
NaNbO <sub>3</sub> Lueshite low	37.39	97.5183	P 1 2/m 1	Monoclinic	3.9229	3.9095	3.9041	β = 90.49°
NaNbO <sub>3</sub> orthor	58.19	100.8585	P b m a	Orthorhombic	5.5707	15.5350	5.5125	

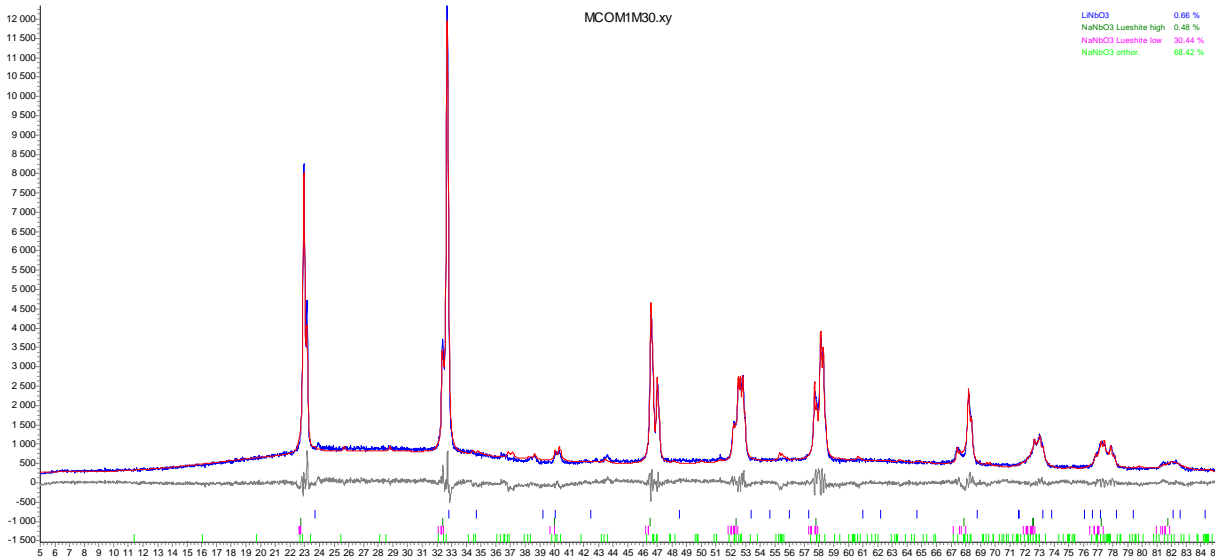
Appendixes

0.3n-LiNbO<sub>3</sub> · 0.7g-NaSi<sub>1.5</sub>O<sub>3.5</sub> heated for 2 h at 1173 K



phase	%	crystallite size (nm)	s. g.	Cryst. Sys.	Lattice parameters		
					<i>a</i>	<i>B</i>	<i>c</i>
NaNbO <sub>3</sub> orthor	100.00	91.2038	P b m a	Orthorhombic	5.5714	15.5381	5.5145

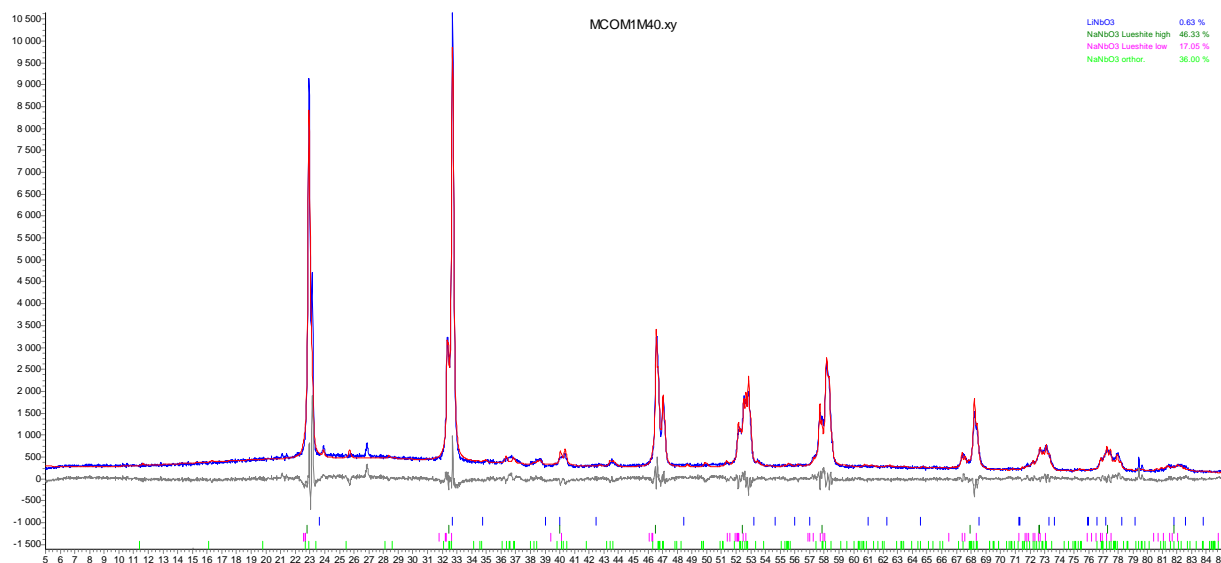
0.3n-LiNbO<sub>3</sub> · 0.7g-NaSi<sub>1.5</sub>O<sub>3.5</sub> heated for 2 h at 1173 K



phase	%	crystallite size (nm)	s. g.	Cryst.sys.	lattice parameters		
					<i>a</i>	<i>B</i>	<i>c</i>
LiNbO <sub>3</sub>	00.66	16.2054	R 3 c H	Trigonal	5.1595	-	13.7710
NaNbO <sub>3</sub> Lueshite high	00.48	12.0639	P m -3 m	Cubic	3.9040	-	-
NaNbO <sub>3</sub> Lueshite low	30.44	146.3883	P 1 2/m 1	Monoclinic	3.9260	3.9131	3.9099 β = 90.63°
NaNbO <sub>3</sub> orthor.	68.42	103.6606	P b m a	Orthorhombic	5.5721	15.5360	5.5136

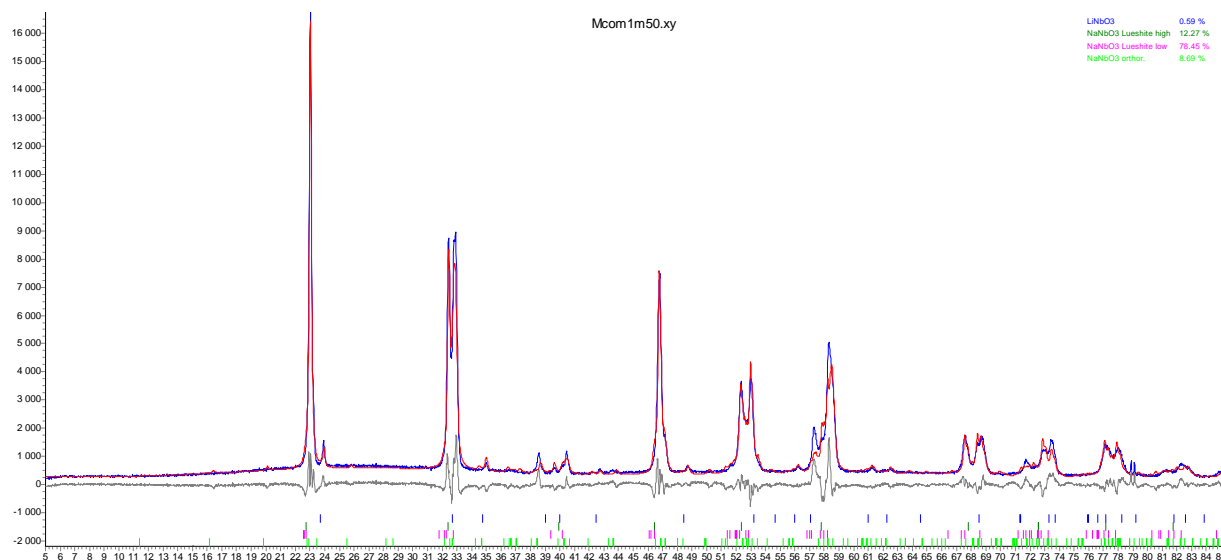
Appendix

0.4n-LiNbO<sub>3</sub> · 0.6g-NaSi<sub>1.5</sub>O<sub>3.5</sub> heated for 2 h at 1173 K



phase	%	crystallite size (nm)	s. g.	Cryst. Sys.	lattice parameters		
					a	b	c
LiNbO <sub>3</sub>	0.63	138.1018	R 3 c H	Trigonal	5.1635	-	13.8399
NaNbO <sub>3</sub> Lueshite high	46.33	86.2364	P m -3 m	Cubic	3.9010	-	-
NaNbO <sub>3</sub> Lueshite low	17.05	150.5148	P 1 2/m 1	Monoclinic	3.9363	3.9209	3.9182 β = 91.39°
NaNbO <sub>3</sub> orthor.	36.00	91.0865	P b m a	Orthorhombic	5.5727	15.5188	5.5072

0.5n-LiNbO<sub>3</sub> · 0.5g-NaSi<sub>1.5</sub>O<sub>3.5</sub> heated for 2 h at 1173 K

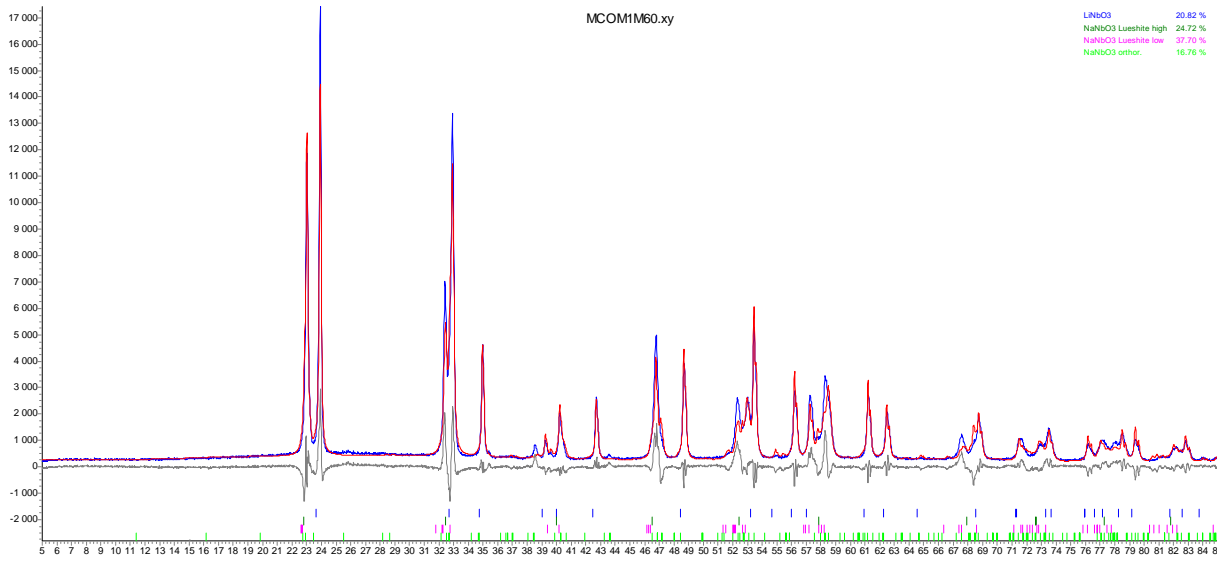


phase	%	Crystallite size (nm)	s. g.	Cryst. Sys.	Lattice parameters		
					a	b	c
LiNbO <sub>3</sub>	00.59	93.1581	R 3 c H	Trigonal	5.1621	-	13.8338
NaNbO <sub>3</sub> Lueshite high	12.27	107.4926	P m -3 m	Cubic	3.9053	-	-
NaNbO <sub>3</sub> Lueshite low	78.45	72.5207	P 1 2/m 1	Monoclinic	3.9352	3.9283	3.9099 β = 91.62°
NaNbO <sub>3</sub> orthor.	08.69	64.2199	P b m a	Orthorhombic	5.5610	15.4967	5.4779



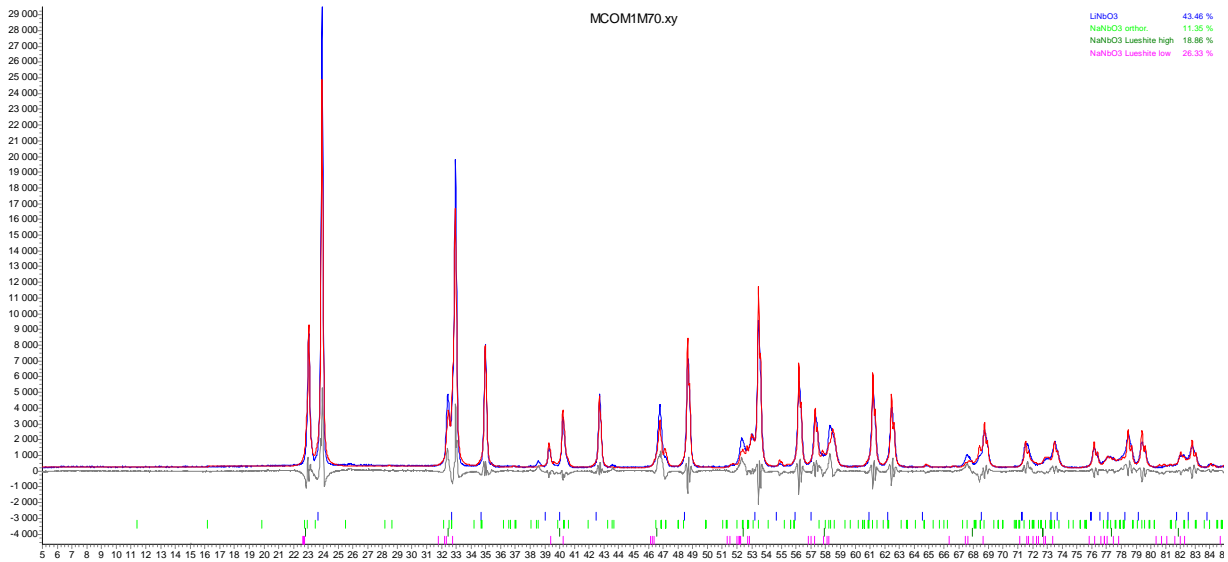
Appendixes

0.6n-LiNbO<sub>3</sub> · 0.4g-NaSi<sub>1.5</sub>O<sub>3.5</sub> heated for 2 h at 1173 K



phase	%	crystallite size (nm)	s. g.	Cryst. Sys.	lattice parameters			
					a	b	c	
LiNbO <sub>3</sub>	20.82	93.6706	R 3 c H	Trigonal	5.1631	-	13.8461	
NaNbO <sub>3</sub> Lueshite high	24.72	157.1079	P m -3 m	Cubic	3.9011	-	-	
NaNbO <sub>3</sub> Lueshite low	37.70	74.1369	P 1 2/m 1	Monoclinic	3.9327	3.9215	3.9156	β = 91.69°
NaNbO <sub>3</sub> orthor.	16.76	58.9359	P b m a	Orthorhombic	5.5654	15.4993	5.4742	

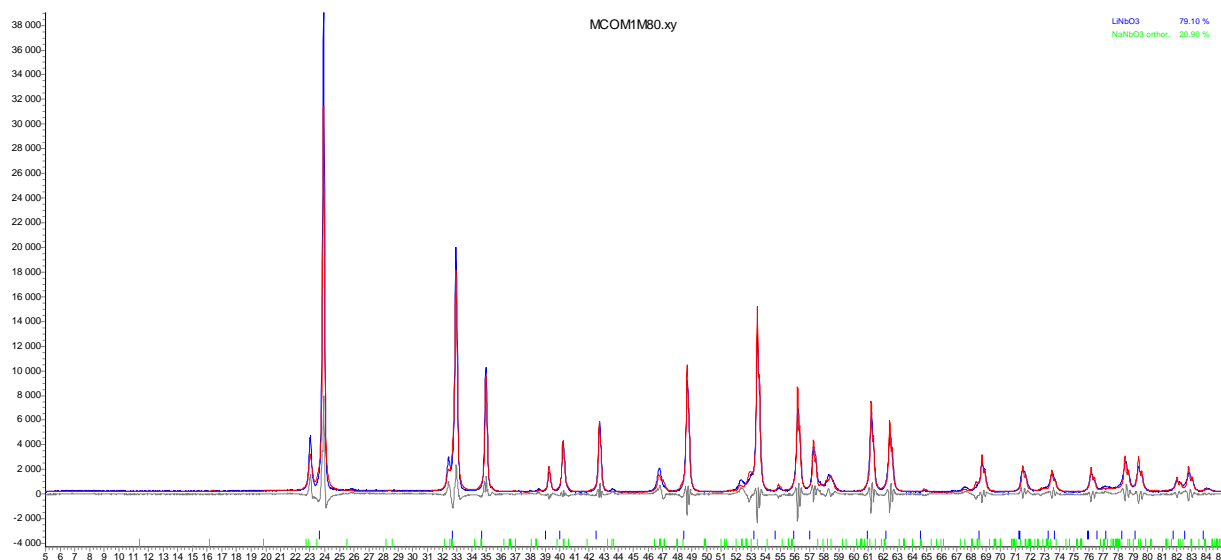
0.7n-LiNbO<sub>3</sub> · 0.3g-NaSi<sub>1.5</sub>O<sub>3.5</sub> heated for 2 h at 1173 K



phase	%	crystallite size (nm)	s. g.	Cryst. Sys.	lattice parameters			
					a	b	C	
LiNbO <sub>3</sub>	43.46	98.1922	R 3 c H	Trigonal	5.1652	-	13.8395	
NaNbO <sub>3</sub> Lueshite high	11.35	186.7708	P m -3 m	Cubic	3.8992	-	-	
NaNbO <sub>3</sub> Lueshite low	18.86	90.9666	P 1 2/m 1	Monoclinic	3.9322	3.9189	3.9136	β = 91.72°
NaNbO <sub>3</sub> orthor.	26.33	66.1871	P b m a	Orthorhombic	5.5653	15.4911	5.4786	

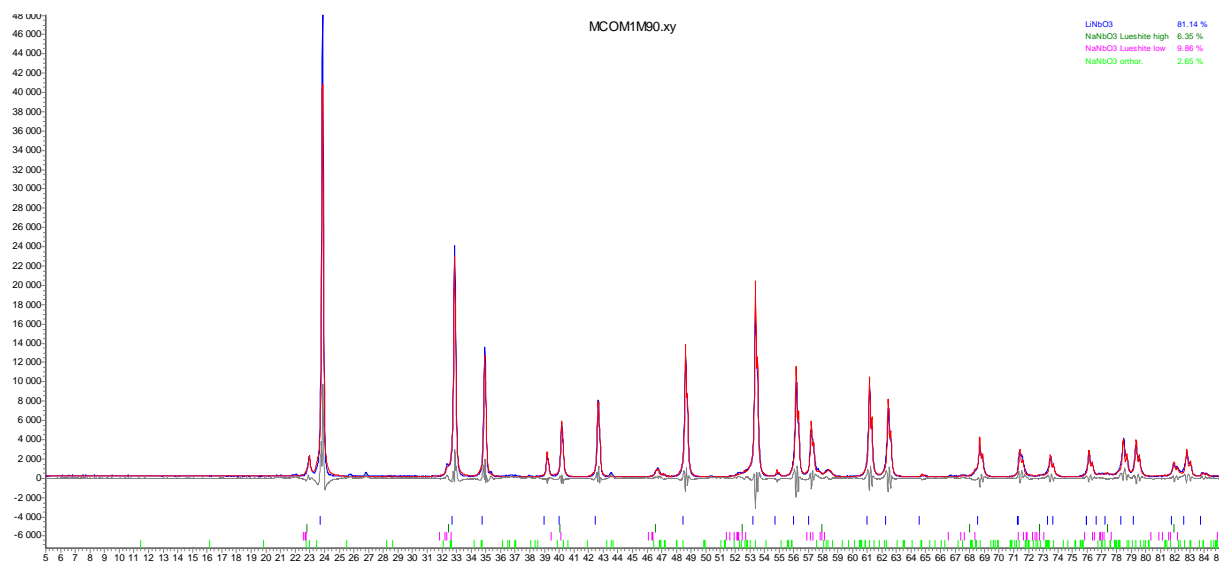
Appendixes

0.8n-LiNbO<sub>3</sub> · 0.2g-NaSi<sub>1.5</sub>O<sub>3.5</sub> heated for 2 h at 1173 K



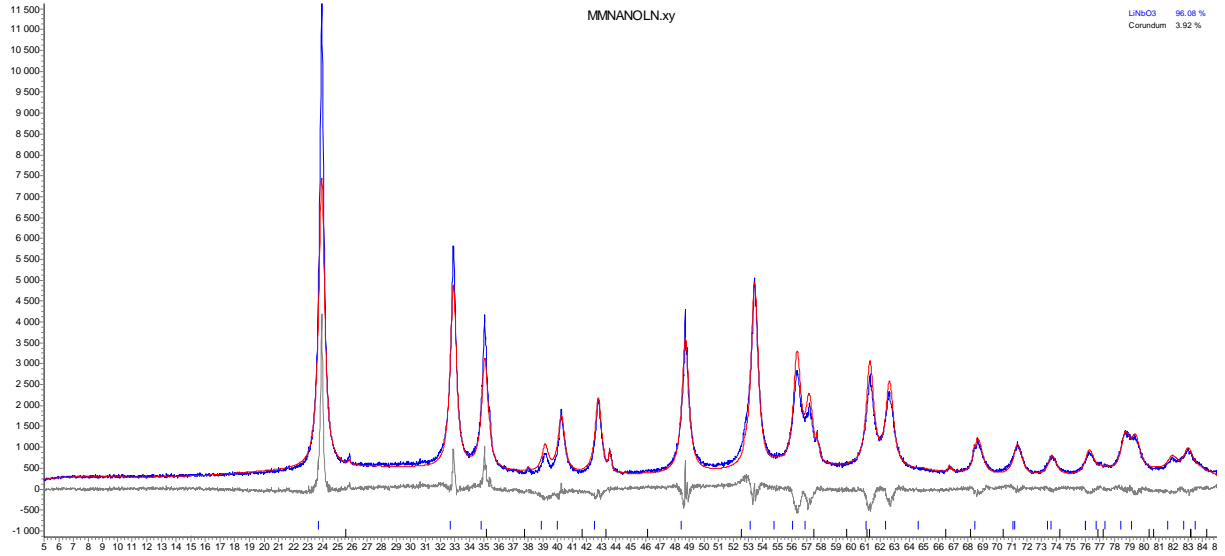
phase	%	crystallite size (nm)	s. g.	Cryst. Sys.	lattice parameters		
					a	b	c
LiNbO <sub>3</sub>	79.10	93.3168	R 3 c H	Trigonal	5.1642	-	13.8425
NaNbO <sub>3</sub> orthor.	20.90	55.8001	P b m a	Orthorhombic	5.5640	15.5237	5.4778

0.9n-LiNbO<sub>3</sub> · 0.1g-NaSi<sub>1.5</sub>O<sub>3.5</sub> heated for 2 h at 1173 K



Phase	%	crystallite size (nm)	s. g.	Cryst. Sys.	lattice parameters		
					a	B	c
LiNbO <sub>3</sub>	81.14	109.8059	R 3 c H	Trigonal	5.1608	-	13.8476
NaNbO <sub>3</sub> Lueshite high	06.35	154.9914	P m -3 m	Cubic	3.8968	-	-
NaNbO <sub>3</sub> Lueshite low	09.86	104.7457	P 1 2/m 1	Monoclinic	3.9384	3.9182	3.9114 β = 91.37°
NaNbO <sub>3</sub> orthor.	02.65	70.1210	P b m a	Orthorhombic	5.5695	15.4736	5.4810

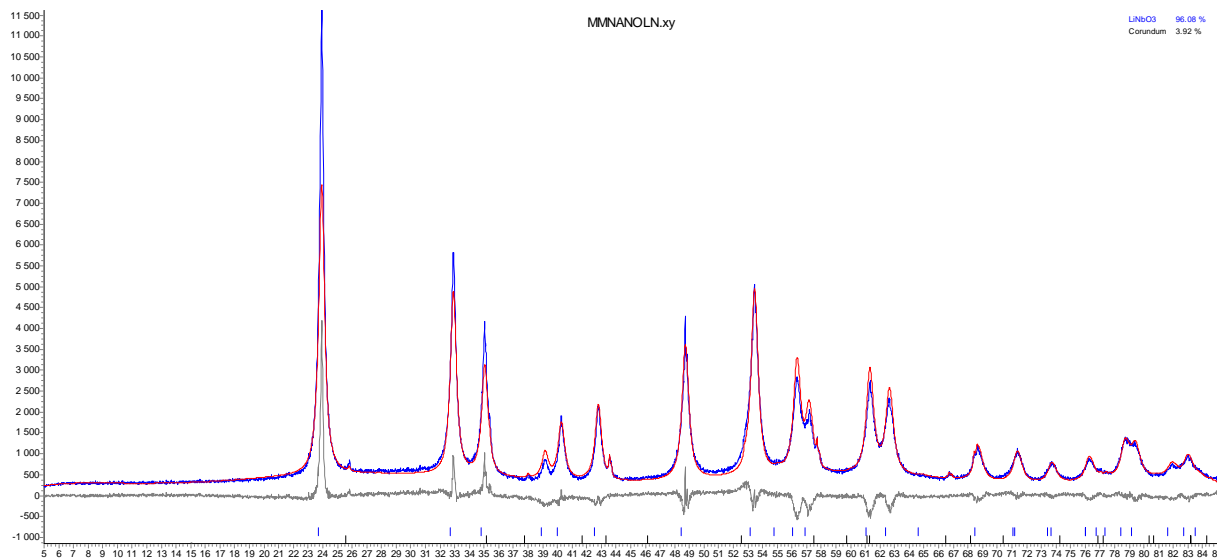
1.0n-LiNbO<sub>3</sub> · 0.0g-NaSi<sub>1.5</sub>O<sub>3.5</sub> (n-LiNbO<sub>3</sub> HEBM for 16 h without heating)



Sample	phase	%	crystallite size (nm)	s. g.	Cryst. Sys.	lattice parameters		
						A	b	C
nanocrystalline LiNbO <sub>3</sub> (HEBM 16h)	LiNbO <sub>3</sub>	96.08	20.3810	R 3 c H	Trigonal	5.1530	-	13.8797
	Corundum	03.92	114.6065	R -3 c H	Trigonal	4.7614	-	12.9952

A.5.3 Composition of glass ceramics formed after heating the glasses 0.33[xLi<sub>2</sub>O · (1-x)Na<sub>2</sub>O] · 0.33Nb<sub>2</sub>O<sub>5</sub> · 0.33SiO<sub>2</sub>

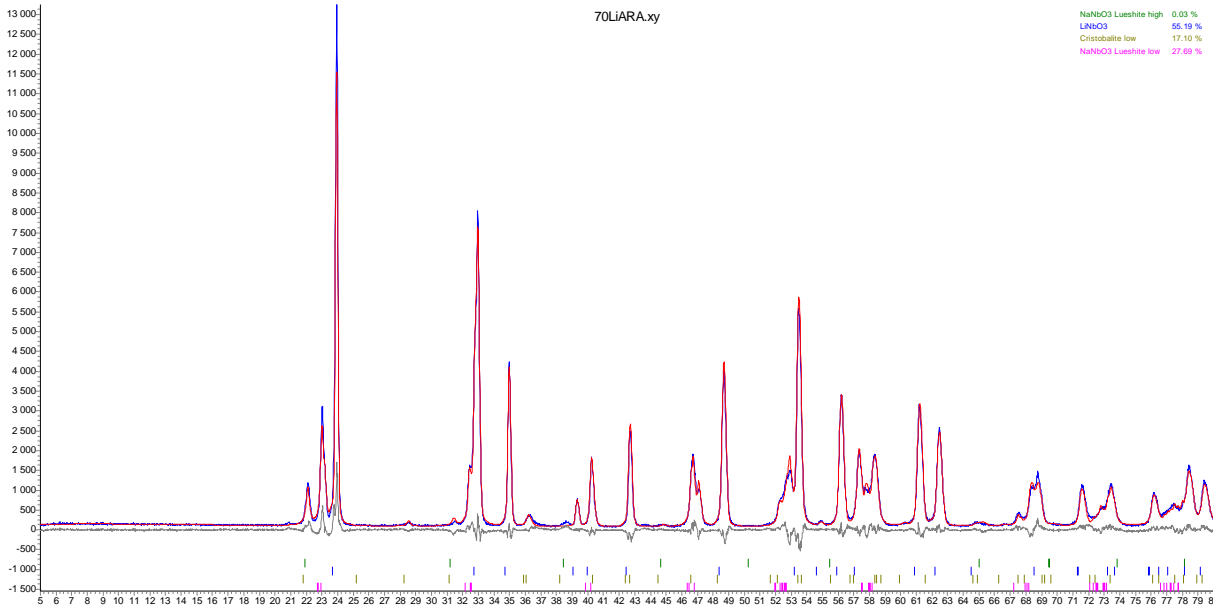
0.33Li<sub>2</sub>O · 0.33Nb<sub>2</sub>O<sub>5</sub> · 0.33SiO<sub>2</sub> · glass ceramic (after rotating anode)



phase	%	crystallite size (nm)	s. g.	Cryst. Sys.	lattice parameters		
					a	b	c
LiNbO <sub>3</sub>	22.70	186.4579	R 3 c H	Trigonal	5.16081	-	13.82911
Cristobalite low	77.30	16.2498	P 41 21 2	Tetragonal	4.99376	-	7.04342

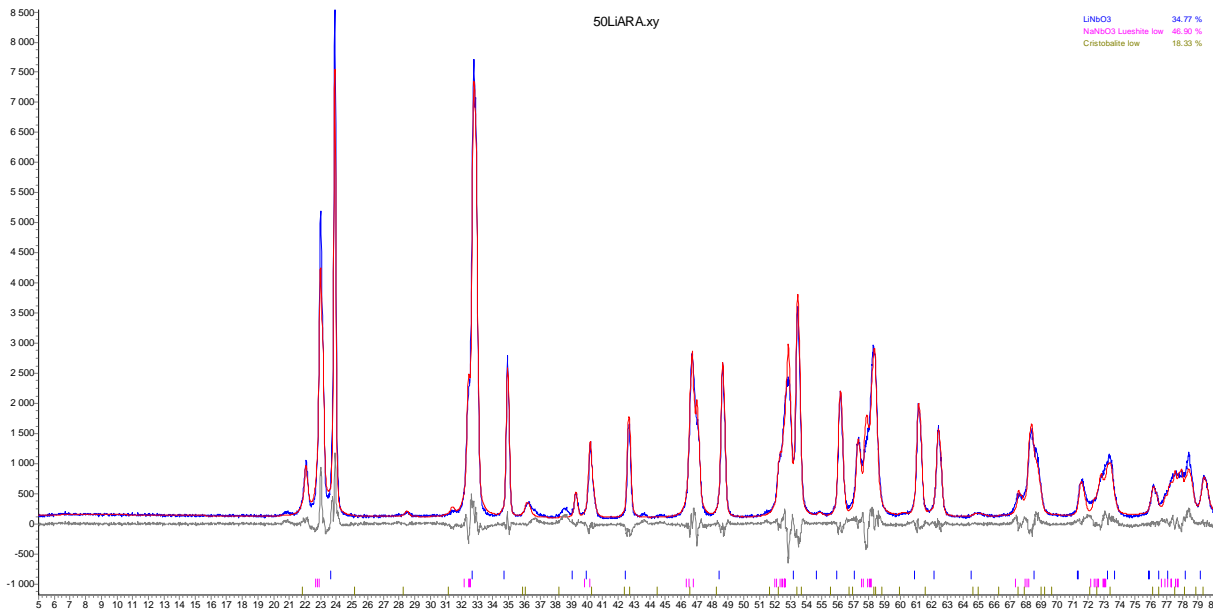
Appendixes

0.33[0.7Li<sub>2</sub>O · 0.3Na<sub>2</sub>O] · 0.33Nb<sub>2</sub>O<sub>5</sub> · 0.33SiO<sub>2</sub> glass ceramic (after rotating anode)



phase	%	crystallite size (nm)	s. g.	Cryst. Sys.	lattice parameters			
					a	b	c	
LiNbO <sub>3</sub>	55.19	270.7321	R 3 c H	Trigonal	5.16843	-	13.83634	
NaNbO <sub>3</sub> Lueshite high	0.03	47.4024	P m -3 m	Cubic	4.05465	-	-	
NaNbO <sub>3</sub> Lueshite low	27.69	62.6565	P 1 2/m 1	Monoclinic	3.91711	3.87817	3.90609	β = 90.70 °
Cristobalite low	17.10	40.50277	P 41 21 2	Tetragonal	4.99838	-	7.01184	

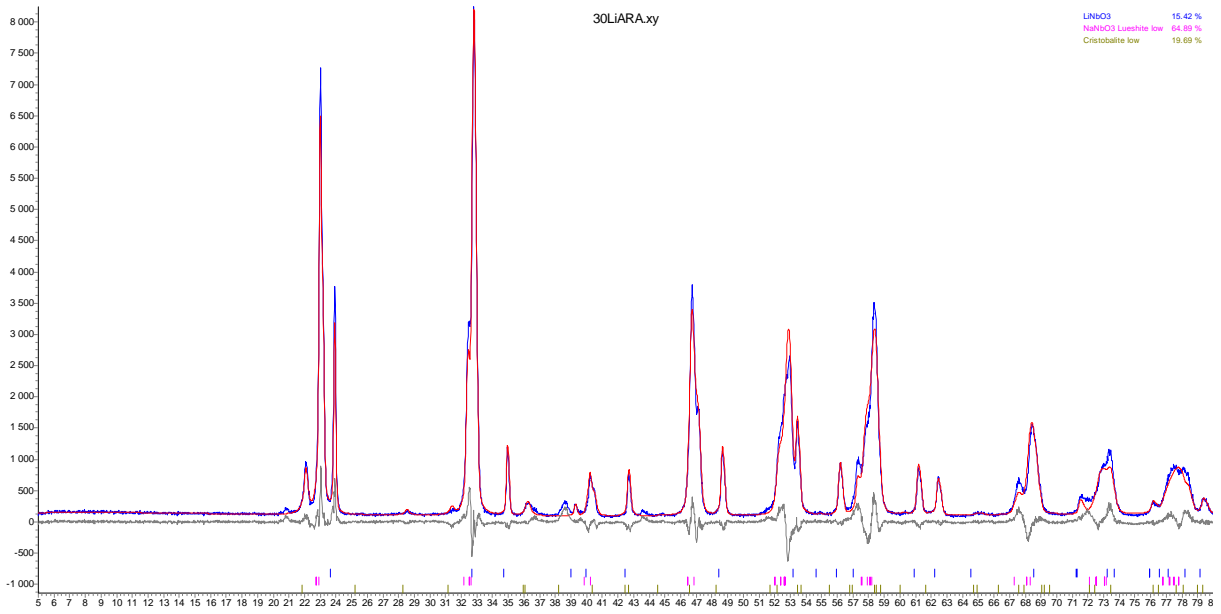
0.33[0.5Li<sub>2</sub>O · 0.5Na<sub>2</sub>O] · 0.33Nb<sub>2</sub>O<sub>5</sub> · 0.33SiO<sub>2</sub> glass ceramic (after rotating anode)



phase	%	crystallite size (nm)	s. g.	Cryst. Sys.	lattice parameters			
					a	B	c	
LiNbO <sub>3</sub>	34.77	247.4768	R 3 c H	Trigonal	5.16771	-	13.83506	
NaNbO <sub>3</sub> Lueshite low	46.90	58.9300	P 1 2/m 1	Monoclinic	3.91442	3.87971	3.90223	β = 90.66 °
Cristobalite low	18.33	36.6846	P 41 21 2	Tetragonal	4.99932	-	7.00469	

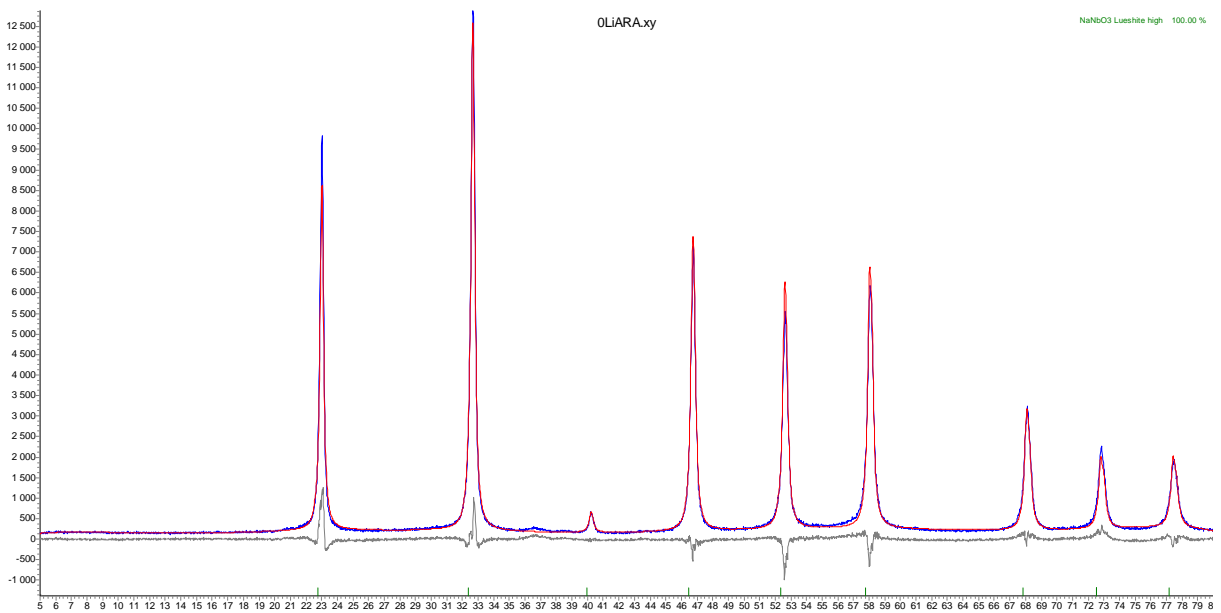
Appendixes

0.33[0.3Li<sub>2</sub>O · 0.7Na<sub>2</sub>O] · 0.33Nb<sub>2</sub>O<sub>5</sub> · 0.33SiO<sub>2</sub> glass ceramic (after rotating anode)



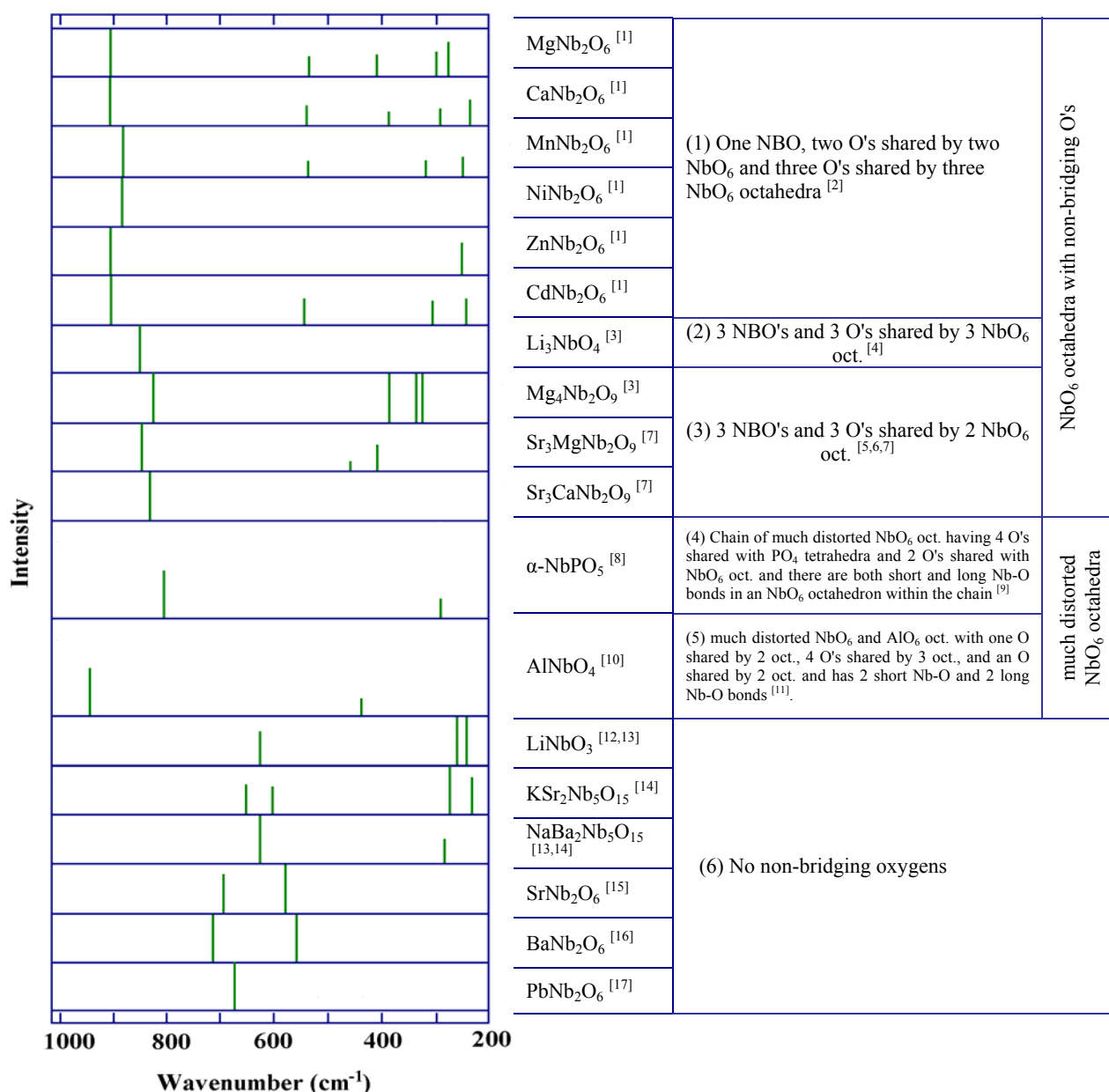
phase	%	crystallite size (nm)	s. g.	Cryst. Sys.	lattice parameters			
					a	b	c	
LiNbO <sub>3</sub>	15.42	256.1600	R 3 c H	Trigonal	5.16681	-	13.83846	
NaNbO <sub>3</sub> Lueshite low	64.89	116.3126	P 1 2/m 1	Monoclinic	3.90838	3.87714	3.90721	β=90.75 °
Cristobalite low	19.69	33.6273	P 41 21 2	Tetragonal	4.99437	-	7.01213	

0.33Na<sub>2</sub>O · 0.33Nb<sub>2</sub>O<sub>5</sub> · 0.33SiO<sub>2</sub> glass ceramic (after rotating anode)



phase	%	crystallite size (nm)	s. g.	Cryst. Sys.	lattice parameters			
					a	B	c	
NaNbO <sub>3</sub> Lueshite high	100	42.2495	P 1 2/m 1	Monoclinic	3.91061	3.90146	3.90553	β=90.21 °

## A.6 Raman Spectroscopy of Nb compounds.



(1–2) An increasing number of NBO's in an NbO<sub>6</sub> octahedron which possesses NBO's decreases the wavenumber of the region above about 800 cm<sup>-1</sup>.

(3) The peak wavenumber of the band in the region above 800 cm<sup>-1</sup> may decrease with decreasing number of oxygens shared by three NbO<sub>6</sub> octahedra in an octahedron with non-bridging oxygens.

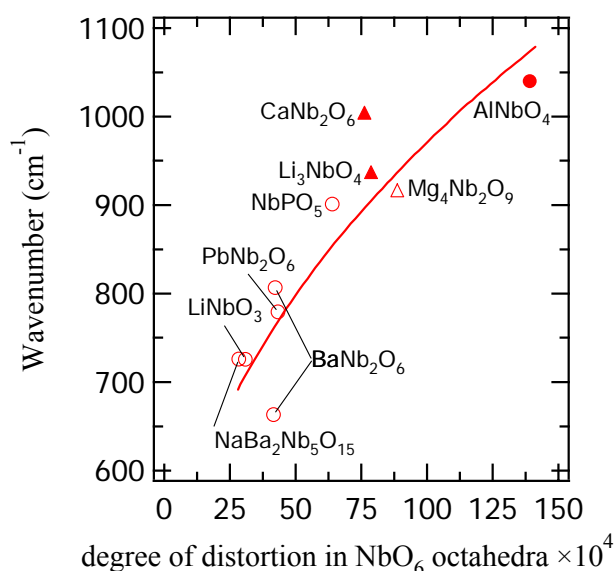
(4–5) an increase of distortion and/or increase in the number of the oxygens shared by three or four polyhedra may increase the peak wavenumber of the band in the region above about 800 cm<sup>-1</sup>.

(6) less distorted NbO<sub>6</sub> octahedra with no non-bridging oxygens.

The band above about 800 cm<sup>-1</sup> is assigned to the vibration of NbO<sub>6</sub> octahedra. The location of this band shifts with composition and is related to the structure change of NbO<sub>6</sub> octahedra. The band shifts to higher wave number with increasing the distortion of NbO<sub>6</sub> octahedra. The next Figure shows the peak wavenumber of the strong Raman scattering peak in various niobate crystals vs. the degree of distortion of NbO<sub>6</sub> octahedra  $\left\langle \left( R - \bar{R} \right)^2 / \bar{R}^2 \right\rangle$  proposed by Shannon [18] where  $R$  and  $\bar{R}$  represent

the distance of each Nb–O bond and the mean Nb–O bond distance in NbO<sub>6</sub> octahedra, respectively and the bracket means the calculation for the average of the respective bonds. The crystals consisting of severely distorted NbO<sub>6</sub> octahedra show strong Raman peak above ~800 cm<sup>-1</sup> while those consist-

ing of less distorted  $\text{NbO}_6$  octahedra display peak at  $600\text{--}700\text{ cm}^{-1}$ . This indicates that the Raman band above  $\sim 800\text{ cm}^{-1}$  in the glasses is assigned to the vibration of short Nb–O bonds in a severely distorted  $\text{NbO}_6$  octahedron. The distorted  $\text{NbO}_6$  octahedra in niobate crystals often have non-bridging or three-fold coordinated oxygens.



The relation between the wavenumber of strong Raman peak and degree of distortion of  $\text{NbO}_6$  octahedra:  $\circ$  with neither non-bridging oxygens ( $\text{O}_{\text{nb}}$ ) nor three- or four-fold oxygens ( $\text{O}_{\text{t}}$ ),  $\bullet$  with no  $\text{O}_{\text{nb}}$  but  $\text{O}_{\text{t}}$ ,  $\blacktriangle$  with both  $\text{O}_{\text{nb}}$  and  $\text{O}_{\text{t}}$ ,  $\triangle$  with no  $\text{O}_{\text{t}}$  but  $\text{O}_{\text{nb}}$ .

- [1] E. Husson, Y. Repelin, "Infrared and Raman Spectrophotometric Studies of Niobates of Columbite Structure", *Spectrochim. Acta Pt. A-Mol. Bio.*, **33** [11] (1977) 995-1001
- [2] J.P. Cummings, and Simonsen, "The crystal structure of Calcium niobate ( $\text{CaNb}_2\text{O}_6$ )", *Am. Mineral.* **55** (1970) 90-97
- [3] G. Blasse and G. P. M. Van Den Heuvel, "Vibrational-Spectra of Some Oxidic Niobates", *Z. Phys. Chem. Frankfurt* **84**[1-4] (1973) 114-120
- [4] J.-C. Grenier, C. Martin, and A. Durif, " ", *Bull. Soc. Fr. Miner. Crist.* **87** (1964) 316-330 Bulletin de la Société Française de Minéralogie et de Cristallographie 1964
- [5] E. F. Bertaut, L. Corliss, F. Forrat, R. Aleonard, R. Pauthenet, "Etude De Niobates Et Tantalates De Metaux De Transition Bivalents", *J. of Phys. Chem. Solids* **21**[3-4] (1961) 234-251
- [6] F. Galasso and J. Pyle, "Ordering of the Compounds of the  $A(\text{B}_{0.33}\text{Ta}_{0.67})\text{O}_3$ ", *Inorg. Chem.* **2** (1963) 482-
- [7] G. Blasse and A. F. Corsmit, "Vibrational Spectra of 1-2 ordered Perovskites", *J. Solid State Chem.* **10**[1] (1974) 39-45
- [8] G. T. Stranford, and R. A. Condrate, "The Vibrational-spectra of  $\alpha\text{-MoPO}_5$  ad  $\text{NbPO}_5$ ", *J. Solid State Chem.* **52**[3] (1984) 248-253
- [9] J. M. Longo and P. Kierkagaard, "Crystal Structure of  $\text{NbOPO}_4$ ", *Acta Chem. Scand.* **20**[1] (1966) 72-
- [10] G. Blasse and R. 't Lam, "Some Optical Properties of Aluminum and Gallium Niobate", *J. Solid State Chem.* **25**[1] (1978) 77-83
- [11] P. F. Pedersen, "Crystal Structure of Aluminum Niobium Oxide ( $\text{AlNbO}_4$ )", *J. Solid State Chem.* **16**[2] (1962) 421-
- [12] R. F. Schaufele and M. J. Weber, "Raman Scattering of Lithium Niobate", *Phys. Rev.* **152**[2] (1966) 705-
- [13] S. D. Ross, "Vibrational Spectra of Lithium Niobate, Barium Sodium Niobate and Barium Sodium Tantalate", *J. Phys C* **3**[8] (1970) 1785
- [14] G. Burns, J. D. Axe and D. F. Okane, "Raman Measurements of  $\text{NaBa}_2\text{Nb}_5\text{O}_{15}$  and Related Ferroelectrics", *Solid State Commun.* **7**[13] (1969) 933-
- [15] Y. Repelin, E. Husson, N. Q. Dao, and H. Brusset, "IR Absorption Spectroscopy and Raman Diffusion Spectroscopy of Compounds with 1X2 block Structure .2. Study on Strontium Niobate, Calcium Tantalate and Barium Tantalate", *Spectrochim. Acta A* **35** [10] (1979) 1165-1175
- [16] Y. Repelin, E. Husson, and H. Brusset " IR Absorption Spectroscopy and Raman-Scattering Study of  $A^{\text{II}}\text{B}^{\text{V}}_2\text{O}_6$  Compounds with "1X2 block" Structure .1. Study of Barium Niobate ", *Spectrochim. Acta A* **35**[8] (1979) 937- 948
- [17] Y. Repelin, E. Husson, N. Q. Dao, and H. Brusset, " IR Absorption Spectroscopy and Raman Diffusion Spectroscopy of Compounds with "1X2 block" Structure .3. Study of Niobate and Tantalate and Barium Tantalate of  $\text{PbNb}_2\text{O}_6$  and  $\text{PbTa}_2\text{O}_6$  Phombohedral Lead", *Spectrochim. Acta A* **36**[3] (1980) 253-258
- [18] R.D. Shannon, "Revised Effective Ionic Radii and Systematic Studies Distances in Halides and Chacofenides", *Acta Cryst. A* **32** (1976) 751-767